Development of porous carbon- and nitrogen-based polymeric nanomaterials and their application in wastewater remediation

Thesis submitted by

Dimitra Das

Doctor of Philosophy (Engineering)

School of Materials Science and Nanotechnology
Faculty of Interdisciplinary studies, Law and Management (FISLM)
Jadavpur University
Kolkata, India

2023

INDEX NO.: D-7/ISLM/19/18

1. **Title of the thesis:** Development of porous carbon- and nitrogen-based polymeric nanomaterials and their application in wastewater remediation

2. **Name, Designation & Institution of the Supervisor/s:**

Prof. Somnath Mukherjee (Supervisor)
Professor
Department of Civil Engineering,
Jadavpur University,
Kolkata-700032,
India
Email: mukherjeesomnath19@gmail.com

Prof. Kalyan Kumar Chattopadhyay (Co-supervisor)
Professor
Department of Physics,
School of Materials Science and Nanotechnology,
Jadavpur University,
Kolkata-700032,
India
Email: kalyan_chattopadhyay@yahoo.com, kkc.juphy@gmail.com

3. **List of Publications:**

❖ **International Journals:**

i. Highly exfoliated graphitic carbon nitride for efficient removal of wastewater pollutants: Insights from DFT and statistical modeling
Dimitra Das, Bikram Kumar Das, Ratna Sarkar, Somnath Mukherjee, Kalyan Kumar Chattopadhyay, 2023, ***Environmental Research***, 115263.

ii. Copper and nickel decorated g-C_3N_4 as superior catalysts for reduction of toxic pollutants: A combined experimental and theoretical approach
Dimitra Das, Bikram Kumar Das, Ratna Sarkar, Somnath Mukherjee, Kalyan Kumar Chattopadhyay, 2022, ***Applied Surface Science***, *580*, 152137.

iii. A morphology-tailored triazine-based crystalline organic polymer for efficient mercury sensing
Dimitra Das, Anuradha Mitra, Rituparna Chatterjee, Sumanta Sain, Kalyan Kumar Chattopadhyay, 2019, ***New Journal of Chemistry***, 43(11), 4364-4376.

iv. Nickel Doped Graphitic Carbon Nitride Nanosheets and Its Application for Dye Degradation by Chemical Catalysis
Dimitra Das, Diptonil Banerjee, Monojit Mondal, Avik Shett, Biswajit Das, Nirmalya S. Das, Uttam K. Ghorai, Kalyan Kumar Chattopadhyay, 2018, ***Materials Research Bulletin***, *101*, 291-304.

v. Low temperature Ssynthesis of Ggraphitic Ccarbon nitride nanorods for heavy metal ions sensing
Dimitra Das, Diptonil Banerjee, Nirmalya S Das, Biswajit Das, Uttam K Ghorai, Kalyan Kumar Chattopadhyay, 2018, ***Solid State Sciences***, *82*, 99-105.

vi. Effect of cobalt doping into graphitic carbon nitride on photo induced removal of dye from water
Dimitra Das, Diptonil Banerjee, Biswajit Das, Nirmalya S. Das, Kalyan Kumar Chattopadhyay, 2017, ***Materials Research Bulletin***, *89*, 170-179.

vii. Defect induced tuning of photoluminescence property in graphitic carbon nitride nanosheets through synthesis conditions
Dimitra Das, Diptonil Banerjee, Debabrata Pahari, Uttam K. Ghorai, Samrat Sarkar, Nirmalya S. Das, Kalyan K. Chattopadhyay, 2017, ***Journal of Luminescence***, *185*, 155-165.

viii. A Review on Luminescence Based Metal Ion Sensing Efficacy of Graphitic Carbon Nitride Nanostructures
Dimitra Das, Amit K. Sharma, Kalyan K. Chattopadhyay, Diptonil Banerjee, 2023, ***Journal of Alloys and Compounds***, 170689.

ix. Dye Removal Ability of Pure and Doped Graphitic Carbon Nitride
Dimitra Das, Amit K. Sharma, Kalyan Kumar Chattopadhyay, Diptonil Banerjee, 2022, ***Current Analytical Chemistry***, *18*(3), 309-340.

x. Oxygen Vacancy-Induced Band Engineering and Metal Unsaturation in MoS_2–MoO_3 with Spillover-Based Confined Catalysis
Dipayan Roy, Bikram Kumar Das, S.N. Riaz, **Dimitra Das**, Sourav Sarkar, and Kalyan K. Chattopadhyay, 2023, ***ACS Applied Energy Materials***.

xi. Probing the emission dynamics in nitrogen-doped carbon dots by reversible capping with mercury (ii) through surface chemistry
Dipayan Roy, Antika Das, Rajarshi Roy, **Dimitra Das**, Bikram Kumar Das, Uttam Kumar Ghorai, Kalyan Kumar Chattopadhyay, Sourav Sarkar, 2022, ***New Journal of Chemistry***, *46*(30), 14690-14702.

xii. Manipulating dielectric relaxation via anisotropic field deviations in perovskite titanate grain–grain boundary heterostructure: a joint experimental and theoretical venture

Souvik Bhattacharjee, Ratna Sarkar, Pratik Chattopadhyay, Anibrata Banerjee, Nirmalya Sankar Das, **Dimitra Das**, Kalyan Kumar Chattopadhyay, 2022, ***Applied Physics A***, *128*(6), 501.

xiii. Hydrothermal synthesis of GO wrapped BiOCl nanosheet and its application in visible light assisted catalytic degradation of Rhodamine B dye
Ratna Sarkar, **Dimitra Das**, Kausik Chanda, Brahami Das, Subrata Sarkar, Kalyan Kumar Chattopadhyay, 2022, ***Materials Chemistry and Physics***, *279*, 125796.

xiv. Morphology tuning of bismuth oxychloride nano-crystals by citric acid variation: Application in visible light-assisted dye degradation and hydrogen evolution by electrochemical method
Ratna Sarkar, Dipayan Roy, **Dimitra Das**, Subrata Sarkar, Kalyan Kumar Chattopadhyay, 2021, ***International Journal of Hydrogen Energy***, *46*(30), 16299-16308.

xv. Hollow micro-spherical bismuth oxy-chloride for superior visible light induced dye-sensitized photocatalytic activity and its theoretical insight
Ratna Sarkar, **Dimitra Das**, Bikram Kumar Das, Anuradha Mitra, Nirmalya S Das, Subrata Sarkar, Kalyan K Chattopadhyay, 2020, ***Materials Research Bulletin***, *125*, 110778.

xvi. Size-modulation of functionalized Fe_3O_4: nanoscopic customization to devise resolute piezoelectric nanocomposites
Souvik Bhattacharjee, Nilesh Mazumder, Suvankar Mondal, Karamjyoti Panigrahi, Anibrata Banerjee, **Dimitra Das**, Saikat Sarkar, Dipayan Roy, Kalyan Kumar Chattopadhyay, 2020, ***Dalton Transactions***, *49*(23), pp.7872-7890.

xvii. $CsPbBrCl_2/g\text{-}C_3N_4$ type II heterojunction as efficient visible range photocatalyst
Tufan Paul, **Dimitra Das**, Bikram Kumar Das, Saikat Sarkar, Soumen Maiti, Kalyan Kumar Chattopadhyay, 2019, ***Journal of hazardous materials***, *380*, 120855.

xviii. 1D-2D Hybrids as Efficient Optoelectronic Material: A Study on Graphitic Carbon Nitride Nanosheets Wrapped Zinc Oxide Rods
Avik Sett, **Dimitra Das**, Diptonil Banerjee, Uttam K. Ghorai, Nirmalya S. Das, Biswajit Das, Kalyan K. Chattopadhyay, 2018, ***Dalton Transactions***, *47*(13), 4501-4507.

- **Conference Proceedings:**

i. Magnesium incorporated graphitic carbon nitride for effective removal of fluoride ions
Dimitra Das, Kalyan Kumar Chattopadhyay, Somnath Mukherjee, 2019, ***Journal of Indian Chemical Society***, *96*, 455-460.

ii. Sodium borohydride assisted reduction of toxic pollutants by silver coordinated melamine based polymeric material
Dimitra Das, Ratna Sarkar, Somnath Mukherjee, Kalyan Kumar Chattopadhyay, 2021, ***Materials Today: Proceedings***, *44*, 444-452.

iii. Efficient photocatalytic activity of bismuth oxyhalides with preferentially oriented (210) facets under visible light
Ratna Sarkar, **Dimitra Das**, Brahami Das, Subrata Sarkar, Kalyan Kumar Chattopadhyay, 2020, In ***AIP Conference Proceedings*** (Vol. 2220, No. 1, p. 020030), AIP Publishing LLC.

iv. Faceted Growth of Morphologically Tuned of BiOCl
Ratna Sarkar, **Dimitra Das**, Anuradha Mitra, Subrata Sarkar, Kalyan Kumar Chattopadhyay, 2019**,** ***Materials Today: Proceedings***, *18*, 1086-1095.

- **Book Chapter:**

i. Sodium Borohydride Assisted Catalytic Reduction of Toxic Pollutants by Carbon and Nitrogen Based Poly-meric Compounds: A Review
Dimitra Das, Kalyan K. Chattopadhyay, Somnath Mukherjee, 2022, September. In ***International Conference on Environmental Geotechnology, Recycled Waste Materials and Sustainable Engineering*** (369-395). Singapore: Springer Nature Singapore.

This thesis is based on the above-mentioned published works (i-iii) in international journals.

4. **List of Patents:** Nil

5. **List of Presentations in National/ International/ Conferences/ Workshops:**

i. Magnesium doped graphitic carbon nitride for effective removal of fluoride ions
Dimitra Das, Kalyan Kumar Chattopadhyay, Somnath Mukherjee, International Conference on Advanced Technologies for Industrial Pollution Control (ATIPC-2018), IIEST, Shibpur, 2018 (**Oral Presentation**).

ii. Catalytic reduction of 4-nitrophenol by rod-like silver-melamine coordination polymer
Dimitra Das, Somnath Mukherjee, Kalyan Kumar Chattopadhyay, 3rd International Conference on Materials Sciences and Nanomaterials (ICMSN 2019), University of Oxford, UK, 2019 (**Oral presentation**).

iii. Thermally stable triazine-based organic polymeric nanodendrites for mercury sensing

Dimitra Das, Somnath Mukherjee, Kalyan Kumar Chattopadhyay, International Conference on Nano Science and Technology (ICONSAT 2020), Kolkata, 2020 (**Poster presentation)**.

iv. Sodium borohydride assisted reduction of toxic pollutants by silver coordinated melamine based polymeric material
Dimitra Das, Ratna Sarkar, Somnath Mukherjee, Kalyan Kumar Chattopadhyay, 11th Conference on Materials Processing and Characterization (ICMPC 2020), IIT Indore, 2020 (**1st prize in Oral presentation)**.

v. Review on sodium borohydride assisted catalytic reduction of toxic pollutants by carbon and nitrogen based polymeric compounds
Dimitra Das, Somnath Mukherjee, Kalyan Kumar Chattopadhyay, 2nd National Conference on Materials and Devices (NCMD 2021), Teerthanker Mahaveer University, 2021 (**1st prize in Oral presentation**).

vi. Sodium borohydride assisted catalytic reduction of toxic pollutants by carbon and nitrogen based polymeric compounds: A review
Dimitra Das, Kalyan Kumar Chattopadhyay, Somnath Mukherjee, 3rd International Conference on Environmental Geotechnology, Recycled Waste Materials and Sustainable Engineering (EGRWSE 2022), Dokuz Eylul University, Turkey, 2022 (**Oral presentation**).

"Statement of Originality"

I, **Dimitra Das** registered on **19.01.2018** do hereby declare that this thesis entitled **"Development of porous carbon- and nitrogen-based polymeric nanomaterials and their application in wastewater remediation"** contains literature survey and original research work done by the undersigned candidate as part of Doctoral studies.

All information in this thesis have been obtained and presented in accordance with existing academic rules and ethical conduct. I declare that, as required by these rules and conduct, I have fully cited and referred all materials and results that are not original to this work.

I also declare that I have checked this thesis as per the "Policy on Anti Plagiarism, Jadavpur University, 2019", and the level of similarity as checked by iThenticate software is __8__%.

Signature of Candidate: Dimitra Das

Date: 20.09.2023

Certified by Supervisor(s):

(Signature with date, seal)

20/9/23

1. Prof. Somnath Mukherjee (Supervisor)
   Department of Civil Engineering,
   Jadavpur University, Kolkata-700032

DR. S. N. MUKHERJEE
Professor
CIVIL ENGINEERING DEPT.
JADAVPUR UNIVERSITY
KOLKATA-700032, (W.B)

20.9.23

2. Prof. Kalyan Kumar Chattopadhyay (Co-supervisor)
   Department of Physics,
   School of Materials Science and Nanotechnology,
   Jadavpur University, Kolkata-700032

Dr. K. K. Chattopadhyay
Professor
Head, Department of Physics
Jadavpur University
Kolkata-700 032

CERTIFICATE FROM THE SUPERVISOR/S

This is to certify that the thesis entitled "**Development of porous carbon- and nitrogen-based polymeric nanomaterials and their application in wastewater remediation**" submitted by **Smt Dimitra Das**, who got her name registered on **19.01.2018** for the award of Ph.D. (Engineering) degree of Jadavpur University is absolutely based upon her own work under the supervision of **Prof. (Dr.) Somnath Mukherjee** and **Prof. (Dr.) Kalyan Kumar Chattopadhyay**, Jadavpur University, and that neither her thesis nor any part of the thesis has been submitted for any degree/diploma or any other academic award anywhere before.

1. 20/9/23

Signature of the Supervisor and
date with Official Seal

DR. S. N. MUKHERJEE
Professor
CIVIL ENGINEERING DEPT.
JADAVPUR UNIVERSITY
KOLKATA-700032, (W.B)

2. 20.09.23

Signature of the Supervisor and
date with Official Seal

Dr. K. K. Chattopadhyay
Professor
Head, Department of Physics
Jadavpur University
Kolkata-700 032

Acknowledgements

This thesis would not have seen the light without the contribution from several incredible individuals, who accompanied me and guided me in every juncture of my five-year long journey towards achieving my dream. I would like to take this moment to convey my profound gratitude towards my respected supervisors, Prof. Somnath Mukherjee and Prof. Kalyan Kumar Chattopadhyay. I wish to extend my appreciation to Prof. Somnath Mukherjee for his invaluable guidance and unwavering support throughout every phase of this research endeavour. His constructive and timely guidance played an instrumental role in ensuring the seamless progression of this thesis towards its successful culmination. I wish to express my utmost and heartfelt appreciation to my co-supervisor, Prof. Kalyan Kumar Chattopadhyay, for granting me the invaluable chance to conduct research within his esteemed research group. His profound understanding of the expansive domains of physics, chemistry, materials science, and nanotechnology inspired and motivated me to embark on my own journey within this scientific realm. I am eternally indebted to both my supervisors for their scientific mentorship, patient guidance, and encouragement that nurtured independent and perceptive research pursuits. In this context, I would like to take the opportunity to express my deepest gratitude towards my senior lab-mate and collaborator, Dr. Anuradha Mitra. She has provided unwavering support in every facet of this journey, and consistently inspired and encouraged me to excel. Her profound expertise in chemistry, adeptness in manuscript writing, and effective communication has been instrumental in enhancing my own capabilities.

Being a member of the Thin Film and Nanoscience Laboratory has been a blessing for me during my doctoral research works. The laboratory environment has been influential in cultivating collaborative efforts with esteemed and diligent researchers, contributing to my personal growth over the subsequent years. The lessons that I have learnt in this lab will always be my guiding light in every spheres of my life. In this regard, I would like to acknowledge Dr. Diptonil Banerjee, who guided me during my M.Tech project days and helped me to develop my research interest on carbon-based nanomaterials. I would also like to thank my senior lab-mates Dr. Uttam Kumar Ghorai, Dr. Rajarshi Roy, Dr. Nilesh Mazumder, Dr. Dipayan Sen, Dr. Nirmalya Sankar Das, Dr. Samrat Sarkar, Karam Da, Madhupriya Di, Partha Da, Promita Di, Nripen Da, Rituparna Di, Rimpa Di, and Subhasish Da, for supporting me throughout my research journey and providing me with consistent assistance whenever I required it. I am eternally thankful to my lab-mates Tufan, Shrabani, Dipayan, Brahami, Dipanwita, and Suvankar for all the scientific discussions and collaborative research works. My gratitude extends to my junior Ratna whose contributions were helpful in carrying out experimental research tasks and providing valuable assistance across various laboratory activities. I would also like to express my appreciation to two of my cherished junior colleagues in the lab, Suvra and Nabanita, for creating a comforting ambiance within our workspace. The strong bond that I shared with my M.Tech juniors - Tanay, Riaz, Avinash, Mrinmoy, Imran, and Tanbir - will always have a special place in my heart. They had the remarkable ability to replace my moments of frustration with laughter and humour.

I am forever grateful to ‘Hindol’ for gifting me with some of the most unforgettable moments in my life. My Ph.D. journey wouldn't have been as vibrant without them. I extend my heartfelt thanks to the exceptionally talented individuals - Mustafa, Manas, Banhi, and Aditya - who infused my mundane days with melodies, conversations, whimsy, and unadulterated fun.

Never could I have envisioned that during my PhD journey, I would be fortunate enough to find friends who would not only become my close-knit family but possibly even more. The incredible individuals comprising the 'Dimbo' group effortlessly turned this into reality. Expressing my gratitude will always fall short for whatever they did for me and are still continuously doing for me over the past six years. I am eternally indebted to Baccha (Anibrata), Arya, Robu (Souvik), Saikat, Jyoti Da, Chitrak Da, and Arnab. Bachha, akin to a true brother, has been my continuous support-system in every situation. Despite our frequent episodes of fighting followed by not talking to each other for days together, the special bond we share remains irreplaceable. Life would have been too much boring without our customary heart-to-heart conversations, Arya and I. Our mutual passion for rock music (especially Fossils) has strengthened our bond to such an extent that I cannot imagine a single ‘adda’ session without this gem of a human being, Arya. I can’t thank him enough for being there whenever I needed him. Robu stands out as the most meticulous individual I've encountered in my entire life. His profound knowledge in Physics is one of the many things about him that I admire the most. Beyond his outwardly serious demeanour, there's a delightfully fun and crazy side of his personality that he reveals only to his closest confidants - I consider myself really lucky to have glimpsed that side of him. I am also grateful to Robu for providing me with some much-needed advice during my Ph.D. journey. I must thank Jyoti Da for being the craziest and most eccentric member of the ‘Dimbo’ group. Although unquestionably the most irritating person in my life, Jyoti Da has consistently assumed the role of a guardian, always treating me as his younger sister. I would also like to acknowledge Chitrak Da (affectionately known as Tuban) who has transcended the role of a senior to become more of a companion and confidant, engaging in random gossips with me. I am thankful to Saikat for his selfless assistance in analysing my experimental results whenever I faced challenges in tackling them independently. Throughout my Ph.D. journey, he has not only been a wonderful friend but also an exceptionally talented research colleague. Finally, I would like to acknowledge Arnab for his amusing and hilarious anecdotes, often shared at rather unconventional moments, and for making the lab-life more tolerable during the intense final stages of my research works.

I wish to express my sincere gratitude to the Director of School of Materials Science and Nanotechnology, Dr. Sourav Sarkar, along with other esteemed faculty members Dr. Chandan Kumar Ghosh and Dr. Mahua Ghosh Chaudhuri, for their unwavering support and motivation during my Ph.D. journey. Additionally, my thanks extend to the staff members of the Department of Physics and the School of Materials Science and Nanotechnology at Jadavpur University, whose genuine assistance in conducting some of my experiments over the past few years have been invaluable. I would like to take this opportunity to acknowledge Prof. Tuhin Ghosh (my dearest Tuhin Kaku), from the School of Oceanographic Studies, for being my go-to person whenever I encountered the slightest difficulties at my university. I thank him for his invaluable assistance in every aspect of my PhD journey. I would also like to thank Dr. Abhra Chanda (Secretary, FISLM) for guiding me through various complicated official procedures and providing me with exceptional support.

I would like to acknowledge the University Grants Commission (UGC), the Government of India, for the 'University with potential for excellence (UPEII) (Grant No.: F-1-10/12(NSPE))' scheme for their support in facilitating various research endeavors. I wish to thank the Department of Science and Technology (DST), Govt. of India, for granting me the DST INSPIRE fellowship [Reg. No.: IF170684] which helped me to conduct my Ph.D. research works for the past five years.

My journey through the darkest days of my PhD life would have been unimaginable without my support system - the Bangla rock band Fossils. Through relentless mental pressure, panic attacks, frustrations, and crippling anxiety, and the times when I felt utterly defeated, the lyrics and music crafted by Fossils became my guiding light. Their music not only helped me to conquer my deepest fears but also instilled in me the resilience to confront every challenge head-on. Without their deeply empathetic, emotionally-charged, and relatable compositions, I would not have the power or the ability to endure the hardships that I faced during my PhD days. The music and lyrics of Fossils have not only been my source of strength but continue to serve as a source of inspiration in all aspects of my life. I owe an everlasting debt of gratitude to each band member of Fossils for helping me become a resilient individual.

Finally, I would like to express my profound appreciation to my family members, whose unwavering support was absolutely crucial for me to persevere through my challenging times. I am forever thankful to Bikram, my best-friend, closest confidant, and life partner, for always being my pillar of strength, my safe place, and my most enthusiastic cheer-leader. I thank him for being an attentive listener to all my endless ranting, and offering me wise advices whenever necessary. I am also grateful to him for always believing in me, even when I questioned myself and had severe self-doubts, and for never losing hope. Without Bikram's steadfast support and constant encouragement, it would have been impossible for me to achieve so much in life. He taught me to dream unconditionally and helped me to bring out the best version of myself. I am eternally grateful to my Baba and Ma for believing in my abilities and always inspiring me to strive for excellence. Their boundless love, continuous guidance, and endless sacrifices have shaped me into the person I am today. The values, wisdom, and life-lessons they have instilled in me help me to navigate life's challenges with grace and confidence. I thank my Kutty, Kaku, and Kamma for their unwavering support which has been the foundation of my success and happiness. I am forever grateful to my late Dadu and Thamma for bestowing upon me unconditional love and care. I thank my dearest brother Aniket (whom I lovingly call Gublai) for being an integral part of my life's journey. Through the ups and downs, he has been a constant source of support, understanding, and companionship. Lastly, I would like to dedicate this thesis to my beloved parents.

20.09.2023

Dimitra Das

Dimitra Das

Dedicated to my parents

TABLE OF CONTENTS

CHAPTER 6: RESULTS AND DISCUSSION PART 1 …………………………..101-141

CHAPTER 6: RESULTS AND DISCUSSION PART 2 ………………………… 143-239

List of Abbreviations

2,4-DNP = 2,4-Dinitrophenol

AOP = Advanced Oxidation Process

AP = Aminophenol

APC = Advanced Polymer Chromatography

AR = Analytical Research

BBD = Box–Behnken Design

BET = Brunauer-Emmett-Teller

BJH = Barrett-Joyner-Halenda

C_3N_4 = Carbon Nitride

CA = Citric Acid

CASTEP = CAmbridge Serial Total Energy Package

CB = Conduction Band

CBM = Conduction Band Minima

CR = Congo Red

Cr(III) = Trivalent Chromium

Cr(VI) = Hexavalent Chromium

CsI = Caesium Iodide

CTF = Covalent Triazine Frameworks

CV = Crystal Violet

CVD = Chemical Vapour Deposition

DFT = Density Functional Theory

DI = Deionized

DMF = Dimethylformamide

DRS = Diffuse Reflectance Spectroscopy

EDS = Energy-Dispersive X-ray Spectroscopy

EDTA = Ethylenediaminetetraacetic Acid Disodium Salt Dehydrate

E_F = Fermi Energy Level

ELF = Electron Localization Function

FA = Formic Acid

FESEM = Field Emission Scanning Electron Microscope

FTIR = Fourier-Transform Infrared

GCN = Graphitic Carbon Nitride

GCNB = Bulk GCN

GCNX = Exfoliated GCN

GGA = Generalized Gradient Approximation

GPa = Giga Pascal

h = hour

HC = High Concentration

Hg(II)/Hg^{2+} = Mercury(II) cation

HOMO = Highest Occupied Molecular Orbital

HRTEM = High-Resolution Transmission Electron Microscope

HSAB = Hard Soft Acid Base

ICDD = International Centre for Diffraction Data

IPA= Isopropyl Alcohol

IR = Infrared

JCPDS = Joint Committee on Powder Diffraction Standards

KBr = Potassium Bromide

LC = Low Concentration

L_D/LOD = Limit of Detection

LMB = Leucomethylene Blue

LUMO = Lowest Unoccupied Molecular Orbital

M = Molar

M.W. = Molecular Weight

List of Abbreviations

MB = Methylene Blue

MG = Malachite Green

mg = milligram

mg/L = milligram/Litre

min = minute

mM = millimolar

MO = Methyl Orange

MPa = Mega Pascal

MR = Methyl Red

NHE = Normal Hydrogen Electrode

nm = nanometer

nM = nanomolar

NMP = N-Methyl-2-Pyrrolidone

NMR = Nuclear Magnetic Resonance

NNI = National Nanotechnology Initiative

NO = Nitric Oxide

NP = Nitrophenol

OA = Oxalic Acid

PAW = Projector Augmented Wave

PBE = Perdew–Burke–Ernzerhof

PDOS = Projected Density of States

PL = Photoluminescence Spectroscopy

PMMA = Poly(methyl methacrylate)

ppb = parts per billion

ppm = parts per million

RB = Rose Bengal

RhB = Rhodamine B

ROS = Reactive Oxygen Species

rpm = Revolutions per minute

RSM = Response Surface Methodology

s/sec = second

TA = Terephthalic Acid

TC = Tetracycline

TDOS = Total Density of States

TGA = Thermogravimetric Analysis

UV = Ultraviolet

VASP = Vienna ab-initio Simulation Package

VB = Valence Band

VBM = Valence Band Maxima

Vis = Visible

WHO = World Health Organization

XPS = X-ray Photoelectron Spectroscopy

XRD = X-Ray Diffraction

$ZnCl_2$ = Zinc Chloride

ZnO = Zinc Oxide

β-C_3N_4 = β–phase of Carbon Nitride

Abstract

Nanoscience and nanotechnology have a vast potential in the modern world since these exciting fields help to explore and understand the fundamental properties of matter in the nanoscale dimension. Since nanomaterials exhibit distinctive behaviours which significantly differ from their bulk equivalents, this enables scientists, engineers, and researchers to design and develop innovative solutions with extraordinary precision. This interesting branch of science has immense prospective for environmental applications, like in wastewater remediation. Nanomaterials can be employed to remove contaminants like heavy metals, organic impurities, pathogens, and other pollutants from water resources with excellent efficiency. Moreover, nanocatalysts can significantly contribute to enhancing the efficiency of wastewater treatment procedures by converting contaminants into less toxic or non-toxic products. The present dissertation encompasses the synthesis and characterization of carbon- and nitrogen-based polymeric nanomaterials in their pristine and doped forms. The physiochemical properties of these nanomaterials have been modified by varying the synthesis techniques. Finally, the suitability and applicability of the as-synthesized nanomaterials in the fields of wastewater remediation have been extensively investigated following different methodologies.

Carbon- and nitrogen-based nanomaterials consisting of triazine cores as the fundamental building blocks have immense potentiality in numerous targeted applications owing to their fascinating characteristics. The reason for choosing this class of materials is their low cost of synthesis, straightforward synthesis technique, large yield of production, and the raw materials required for their synthesis purposes are cheap and easily available. Moreover, these materials are non-toxic in nature, which facilitates their utilization in environmental applications. Their two-dimensional conjugated matrix provides a stable support for anchoring metal nanoparticles, and their covalent network gives rise to chemical and thermal stability. These nanomaterials have abundant reactive sites on their surface owing to their nitrogen-rich nature, which is highly beneficial for sensing and catalytic applications. A novel triazine-based organic polymeric material (MEG_{10}) possessing some interesting features like crystallinity, thermal stability, and nanodendrite-like morphology, along with abundant surface functional groups, was developed in this dissertation. Graphitic carbon nitride (GCN) belongs to the class of triazine-based polymeric materials, which has colossal significance for implementation in the fields of environmental remediation. In the present dissertation, GCN was synthesized in its pristine form with substantial modification in its surface and physiochemical properties through thermal treatment and exfoliation procedures. Moreover, GCN was decorated with transition metal ions like Cu and Ni to modify its surface properties and to enhance its effectiveness in rapidly degrading hazardous wastewater contaminants. All the triazine-based nanomaterials synthesized during the research works were thoroughly characterized employing modern characterization techniques to unravel their intrinsic properties in details.

Fluorescence detection technique is a highly selective, sensitive, and rapid method for the detection of heavy metals from aquatic environment. Until now, the majority of previous studies have indicated that triazine-based polymers used for sensing mercury ions (Hg^{2+}) necessitate the incorporation of sulfur-based functional groups due to the strong affinity of Hg^{2+} towards sulfur. Nonetheless, MEG_{10} polymer sensor demonstrated an impressive level of sensitivity, with a value of approximately 8.18×10^6 M^{-1}, and ability to selectively detect Hg^{2+} ions at an incredibly low concentration (1.95 nM) without the requirement of any sulfur-mediated modifications. This is because the covalent MEG_{10} polymer is rich in nitrogen and oxygen functional groups, which facilitated the ultra-trace level detection of mercury ions. The underlying sensing phenomenon was thoroughly elucidated to comprehend the material's practicality and potential applications.

Until now, the majority of reports on enhancing the photocatalytic activity of GCN have necessitated complex procedures involving the creation of heterojunctions or the integration of metals or non-metals into the GCN framework. However, these approaches often introduce toxicity to GCN, which can lead to secondary contamination, rendering the utilization of such materials impractical and challenging in real-world scenarios. In contrast, a straightforward synthesis method for metal-free pristine GCN was undertaken in the present dissertation. It focused on modifying GCN through exfoliation, eliminating the need for intricate functionalization while achieving remarkable catalytic properties. The conventional bulk GCN suffers from a limited surface area, resulting in clustered sheets that poorly adsorb pollutants on its surface. To overcome this limitation, the surface area of GCN was successfully increased to a value of 88.735 m^2/g through exfoliation; thereby creating a greater number of active sites. This enhancement led to improved adsorption of contaminants, ultimately resulting in superior catalytic activity. This exfoliated GCN (GCX) was subsequently implemented in the photocatalytic reduction of some conventional harmful pollutants found in aquatic environments, specifically targeting the removal of rhodamine B dye (RhB) and hexavalent chromium (VI) (Cr(VI)) heavy metal. By harnessing visible-light source, GCNX was capable of rapidly degrading RhB dye within just 30 min when combined with the electron-capturing reagent H_2O_2. Additionally, it could efficiently convert chromium from its hexavalent to trivalent form in less than 2 h when FA was introduced into the system as the hole-capturing reagent. In order to comprehend the intricate interplay between the factors influencing catalytic activity, a comprehensive statistical assessment was conducted using the response surface methodology. Additionally, first-principles calculations based on density functional theory was undertaken to further investigate the reduction efficiency of the GCN catalyst.

Though metal nanoparticles exhibit remarkable potentiality in catalysing the reduction of hazardous pollutants following catalytic hydrogenation technique, nevertheless, metal nanoparticles are costly, prone to agglomeration with repeated usage, and exhibit poor stability. These factors hinder their practical application as catalysts in wastewater treatment. To address these limitations, researchers have sought to immobilize or anchor nanoparticles onto the two-dimensional matrix of GCN. The majority of existing studies focus on incorporating noble metals (like Au, Ag, Pt) into the GCN sheets, which poses practical

limitations due to their high cost, limited availability, and the need for controlled synthesis approaches. In contrast, transition metals such as Cu and Ni are widely abundant on earth and offer a more cost-effective solution for practical applications. In the present dissertation, promising catalyst materials were developed by integrating Cu and Ni into the GCN conjugated network. The as-synthesized nanomaterials were extensively employed to catalytically degrade a wide spectrum of pollutants commonly present in wastewater, including textile pollutants and nitrophenol compounds, utilizing the $NaBH_4$-mediated catalytic hydrogenation method. The catalysts decorated with metals exhibited an impressive ability to rapidly and completely reduce these pollutants in just a matter of minutes, demonstrating nearly 100 % decolourizing efficiency in all the cases. The effectiveness of the catalyst was confirmed by conducting detailed first-principles-based rigorous theoretical calculations. By exploring atomic-level reactions, the most viable reaction pathways for selected pollutants were identified, highlighting the crucial role of $NaBH_4$ in facilitating the electron-relay process.

Therefore, the inexpensive nanomaterials discussed earlier can serve as highly effective sensors and catalysts for identifying and breaking down various pollutants commonly found in wastewater. In wastewater remediation, these polymeric materials exhibit exceptional performance, making them viable substitutes for certain conventional catalysts.

Keywords: nanomaterials, polymers, triazine-core, metal-doping, exfoliation, heavy metals, organic dyes, nitrophenols, sensing, photocatalysis, catalytic hydrogenation, first principles calculation, DFT, reaction pathways.

Dimitra Das
20.09.2023
Signature of Candidate with date

20/9/23
Signature of Supervisor
DR. S. N. MUKHERJEE
Professor
CIVIL ENGINEERING DEPT.
JADAVPUR UNIVERSITY
Department of Civil Engineering,
Jadavpur University,
Kolkata-700032,
India

20.09.23
Signature of Supervisor
Dr. K. K. Chattopadhyay
Professor
Head, Department of Physics
Jadavpur University
Kolkata-700 032
School of Materials Science and
Nanotechnology,
Jadavpur University,
Kolkata-700032,
India

CHAPTER 1:

INTRODUCTION

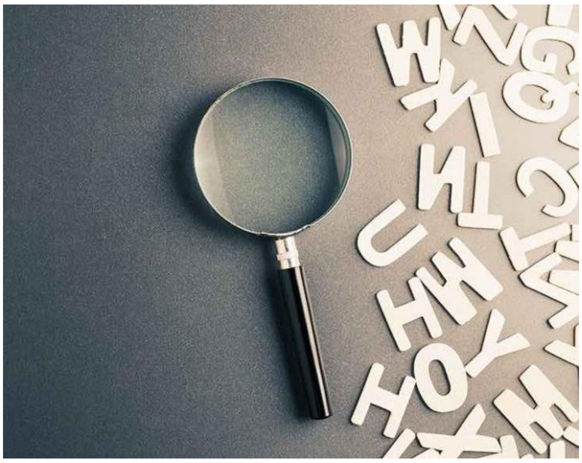

Introduction

1.1. Overview:

The challenging responsibility of environmental scientists and engineers is to provide safe and whole-some water to the community by continuous exploration of new and appropriate technologies, along with up-gradation of existing procedures with cost-optimization. The target objective is to supply water that should be free from undesirable contaminants like toxic metals, metalloids, organic pollutants, and disease causing organisms. Over the century, consolidated efforts have been endeavoured by the researchers through interdisciplinary approaches, using experimentations and software tools, coupled with application of technology, new materials development, different statistical modelling, process modifications and knowledge of advance level of physical, chemical, biological, and engineering science. Different novel materials with their uptake of different pollutants that are normally unable to be removed by conventional processes are being currently focused in the application of water pollution amendments fields. In quest of such developments, nanomaterials and their application are now being very much imprinted in various literatures profusely [1].

The concept of "nanotechnology" has grasped the attention of the world in recent times. This relatively new branch of science has intrigued and fascinated scientists from all over the world, so much so, that it has been considered as a revolution in the field of modern science and technology. As defined by the National Nanotechnology Initiative (NNI), nanotechnology deals with matter having dimensions in nanoscale range, i.e. between 1 and 100 nm [2]. Materials exhibit unique properties at such small dimensions, which eventually enables their novel applications in numerous fields of science and technology. The manipulating and engineering of materials in nano-dimension to modulate their properties constitute the basics of nanoscience and nanotechnology. This interdisciplinary branch of science brings together materials scientists, physicists, chemists, biologists, computer scientists, mechanical, electrical, electronics, and environmental engineers to modulate molecular properties at the nanoscale level for contributions in respective disciplines.

Nanomaterials may exist naturally, and can also be manufactured from various precursors in research laboratories by different procedures. The synthesis methods of nanomaterials can be broadly classified into two distinct categories: "top-down approach" and "bottom-up approach". In the top-down method, materials in nano-dimension are produced by step-by-step breaking down of bulk materials. In contrast, the bottom-up approach deals with the rearrangement and accumulation of atomic clusters or molecules to gradually assemble into nanostructures. Nanomaterials synthesized through the bottom-up approach possess ordered structures, less number of defects, and homogeneous chemical compositions as compared to those synthesized via the top-down method. Nanomaterials exhibit highly interesting optical, electrical, electronic, quantum, mechanical, and magnetic properties because they attribute some unique characteristics as compared to their bulk equivalent. These include their large surface to volume ratio, high percentage of surface atoms and molecules, their interesting scattering properties, their size and shape determining their interesting physicochemical properties, and they have interesting electronic band structure resulting from confined energy states which gives rise to their unique opto-electronic properties. Furthermore, surface driving forces impart an important role in modulating their characteristics [3].

The immense prospects of nanotechnology have resulted in its breakthrough applications in various spheres of the modern world. Nanomaterials are currently being implemented in rapidly developing areas like medical science and health sectors, environmental management, structural and construction engineering, textile engineering, pharmaceutical industries, batteries and fuel cells, flexible electronics, and information and communication technology. Scientists, researchers, and technologists all around the world are persistently striving towards making the utilization of nanomaterials economical and feasible in different fields of applications. **Fig. 1.1** gives the schematic depiction of various applications of nanotechnology in distinct fields of the modern world.

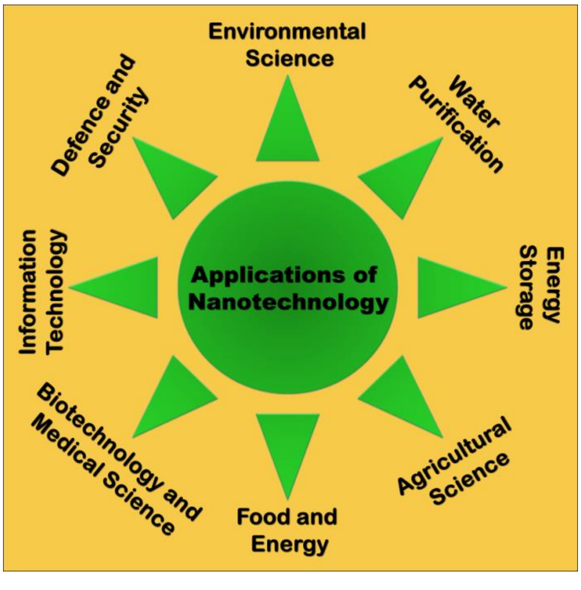

Fig. 1.1: *Implementation of nanotechnology in different areas*

Environmental pollution has severely aggravated in modern times due to the rapid burgeoning of pharmaceutical and textile industries which not only pose as a serious threat to the aquatic ecosystem but also is equally hazardous to human health. It is thus of immense importance to take appropriate measures to achieve environmental sustainability and alleviate water pollution. There are several problems encountered by industries in removing pollutants from the environment. Some of the most significant challenges are described below:

- A huge amount of pollutants is generated by industries. Cleaning them up requires a massive effort, man-power, profits, and resources.
- Different pollutants exhibit distinct complexities arising from their different chemical and physical properties. Thus different techniques are required for their removal from the environment. Moreover, some pollutants require additional treatment for their removal than others.
- Treatment and removal of certain complex pollutants require sophisticated techniques and instrumentations, which are expensive to bear the cost for small-scale industries. Thus many industries become reluctant sometimes to invest in pollution control technologies because of economic reasons.
- Last but not the least, some pollution control techniques produce secondary pollutants which lead to further contamination of natural resources and have negative environmental impacts.

Conventional bulk materials generally used for attenuation of pollutants suffer from several drawbacks which limit their performance efficiency. Moreover, traditional methodologies employed for wastewater remediation have several disadvantages involving the cost, time of treatment, and competence issues. Some of these limitations are given below point-wise:

- Requirement of material in high dosages for application purposes
- Less number of surface active sites in bulk materials
- Sludge production and management issues
- High cost arising from large requirement of material and expensive processes
- Low removal efficiency of targeted pollutants
- Requires periodic regeneration and cannot be recycled
- Leaching of materials in treated water can cause secondary contamination
- Poor selectivity for targeted pollutants

With the view-point of above issues as-described, the need of nanotechnology using nanomaterials becomes evident in the modern world. The drawbacks of conventional materials and methodologies have led to the urge for the search of potential nanomaterials for efficient removal of all kinds of pollutants from water and wastewater environment. Nanomaterials offer several advantages for pollution control in industries. Some of the key benefits are described below:

- Enhancement of efficiency: Nanomaterials exhibit a high ratio of surface area to its volume than bulk materials. The higher surface area with abundant reactive sites makes them more efficient at capturing pollutants.
- Versatility: Nanomaterials can be tailored according to specific pollutants. This makes them more effective in environmental remediation than conventional pollution control technologies. The high selectivity of nanomaterials towards certain pollutants can additionally help in their efficient removal.
- Lower cost: Though the initial cost of nanomaterials may be high owing to their synthesis strategies, but their increased efficiency means that less amount of material is required during applications, which can decrease the overall cost of pollution control in industries.
- Environmental benefits: Nanomaterials can be designed to be biodegradable or environmentally benign. This reduces the negative impact of pollution control technologies on the environment.
- Improved safety: Nanomaterials can be designed to be less toxic than traditional pollution control materials, reducing the risk to workers and the environment.
- Recyclable properties: Nanomaterials can be recycled up to several times during catalytic activity for degradation of pollutants. They do not lose their efficiency after repeated use. This reduces the cost of materials and treatment procedure.

Nanocatalysts or nanoadsorbents are specifically designed nanomaterials applied for the effective treatment of industrial wastewater to remove hazardous pollutants from water-bodies. Nanomaterials exhibit superior efficiency in degradation of these pollutants to non-toxic end products and complete removal of these pollutants from the aquatic environment. As compared to traditional bulk materials, this high efficiency of nanomaterials results from their impressive surface area and large number of surface active sites. The common constraints of bulk materials can be overcome by proper selection of nanomaterials for application in wastewater remediation. Selection of nanomaterials for practical implementation should be done by considering the economic factors, that is, feasible synthesis procedure, large yield, abundantly available raw precursors, and most importantly non-toxic nature of the synthesized material so that it does not cause any further contamination. Sustainable technologies involving inexpensive and readily available materials should be made use of instead of relying on expensive and rare resources [4]. Nanomaterials composed of basic elements like carbon and nitrogen can perhaps fulfil the above-mentioned criteria to a great extent.

Carbon- and nitrogen-based conjugated organic materials having triazine frameworks (like graphitic carbon nitride and other triazine-based derivatives) are metal free, economically cheap and viable nanomaterials having good surface area and porosity, impressive thermal and chemical stability along with tunable band gap. This particular class of nanomaterials has achieved immense prominence in recent times owing to their distinctive physiochemical, electronic, and optical properties. They can be synthesized adopting affordable and cost-effective techniques that make them even more attractive for numerous applications. Graphitic carbon nitride (GCN) is a special class of covalently bonded carbon- and nitrogen-based polymeric nanomaterial having the chemical formula C_3N_4. This material has achieved high popularity among scientists and researchers from every sector, especially energy harvesting and environmental fields, owing to its many lucrative attributes. GCN has been extensively utilized as a multi-functional catalyst material to initiate and carry forward many important chemical reactions like photochemical water-splitting, oxidation reactions of alkanes, olefins, alcohols, and heteroatoms, trimerization reactions, Friedel-crafts reactions to activate benzene, Fenton reactions, carbon dioxide reduction reactions (both electrocatalytic and photocatalytic), hydrogenation reactions, NO decomposition, and many more [5-11]. GCN has also been employed as a biosensor and gas sensor [12,13], as a light-emitting diode [14], and as efficient energy storage devices [15]. Most importantly, GCN has tremendous potential in environmental remediation fields owing to its photocatalytic [16], adsorption [17], and selective sensing properties [18].

Triazine-based materials exhibit impressive catalytic and adsorption properties for the effective degradation and removal of wastewater pollutants [19-21]. Conventional adsorption procedure is a comparatively time-consuming process, requires high adsorbent dosage, and problem arises regarding the safe disposal of the adsorbent material. Since the target pollutant remains adsorbed on the adsorbent’s surface, if the adsorbent is not properly disposed of, then it can lead to secondary contamination of the environment. In this regard, photocatalysis and catalytic hydrogenation techniques have several advantages over adsorption procedure since these processes can rapidly and completely degrade conventional hazardous pollutants to non-toxic end products. The end-products do not cause any harmful effects on the environment, and the nanocatalyst material can be recovered and reused for further applications. Since GCN is a semiconducting nanomaterial with appropriate electronic band gap and band edge potentials for visible-light utilization, it can readily perform catalytic reduction of harmful non-degradable pollutants in presence of a suitable light source [22]. Catalytic hydrogenation technique is an even more rapid, cost-effective, and efficient procedure for reduction of pollutants as compared to photocatalytic dye degradation. In this technique, instead of an irradiation source, an additional reducing agent helps the catalyst material to reduce pollutants within few minutes [23]. Hence, in the present research work, different kinds of catalytic reactions have been conducted using GCN as a catalyst material for the efficient degradation and removal of hazardous pollutants from water environment. Furthermore, triazine-based nanomaterials have interesting fluorescence properties owing to which they can act as distinctly sensitive as well as selective fluorescent probes for the sensing and detection of toxic heavy metals contaminants from aqueous environment [24]. These technologies motivate new researchers to further accelerate the utilization of nanomaterials in different sectors of environmental remediation.

The limitation of earlier works towards the i) heavy metal detection by self-functionalized triazine-based polymers, ii) rapid degradation of diverse toxic chemical pollutants following catalytic hydrogenation method by non-noble-metal (transition metal) decorated GCN, and iii) also by photo-fenton like catalytic procedure employing pristine GCN, along with iv) inadequate reports on substantial theoretical explanations to justify the efficiency of these materials in environmental remediation, were the motivation to undertake this research work.

The hypothesis of the present research problem is that the development and subsequent suitable modification of carbon-nitrogen based organic nanomaterials can enhance their efficiency in removing some specific industrial pollutants from wastewater. The research aims to address the limitations of earlier works in heavy metal detection, rapid degradation of hazardous organic and inorganic pollutants, and theoretical explanations related to the efficiency of these materials in environmental remediation. Such inadequacy and limitations of previous studies in various aspects of triazine-based nanomaterials for wastewater remediation also gave rise to the genesis of the research problem. Thus, the current dissertation problem tried to explore mainly the different facets of carbon- and nitrogen-based polymeric nanomaterials for wastewater remediation, seeking to overcome the identified limitations and contribute to the field.

A research carried out in the direction of application of triazine-based nanomaterials in environmental remediation by employing simple and effective methodologies along with substantial theoretical validation is very much urged in the present context. In this regard, the broad objective of the proposed research work is to develop triazine-based covalent organic conjugated polymers including GCN, to carry out detailed characterizations of the as-synthesized materials, and to finally investigate the capability of these materials in degradation and removal of various conventional pollutants present in wastewater emitted from different industries.

The novelties of the proposed research works are given below:

- The first work involves the design and development of a novel conjugated organic polymer containing triazine units and exhibiting some unique properties. The as-synthesized material has been successfully employed for the selective sensing of Hg(II) ions from aqueous environment. Interestingly, the novelty of this work stems from the fact that the material possesses inherent detection ability for mercury ions owing to its electron donating nitrogen and oxygen-based functional groups. This is in contrast to other reported triazine-based polymers which require sulphur-based modifications for Hg(II) detection.
- In the next phase of work, metal-free pristine GCN with high surface area has been developed and employed for the photo-fenton like degradation of textile pollutant RhB dye and heavy metal Cr(VI) from aquatic environment. In this work, original theoretical investigation has been performed to provide detailed information on the degradation mechanism of the targeted pollutants. Additionally, statistical modelling has been conducted to analyse the effect of interactions between the different catalytic parameters on the catalytic degradation efficiency.
- Finally, GCN has been decorated with transition metal ions like Cu(II) and Ni(II) for the rapid degradation of a variety of textile dyes and nitrophenol compounds following catalytic hydrogenation reactions. This work’s novelty comes from the fact that detailed in-depth theoretical calculations have been conducted to understand the role of the incorporated metal atom within the GCN matrix towards the catalytic reduction mechanisms.

The expected outcomes of the above-mentioned proposed researches are appended below:

A novel triazine-based polymeric nanomaterial will be synthesized following novel synthetic strategies which will be established as a highly sensitive as well as selective fluorescent probe for detecting heavy metal pollutants. Additionally, a well-established triazine-based material GCN will be developed following modification of established synthesis techniques to modulate its surface properties, along with its physio-chemical and opto-electronic properties. GCN will also be doped with transition metal atoms to improve its performance efficiency. GCN in its pristine form along with its various derivatives will be effectively applied in water remediation procedures including removal and degradation of both organic and inorganic toxic contaminants like heavy metals, textile dyes, and nitrophenol compounds. The proposed nanomaterials and methodologies implemented in the present research work are expected to replace some expensive traditional adsorbents and catalysts, and conventional wastewater remediation procedures thereby achieving more economy as compared to traditional practises.

1.2. Organization of the thesis:

The research endeavours conducted in the present dissertation are structured and presented as distinct chapters. The layout of the entire thesis is outlined as follows:

Chapter 1 introduces the contextual backdrop of the research works that have been carried out. It delves into the justification of the research works, elucidates the hypothesis and genesis of the research problem, outlines the broad aim of the research subject, highlights the novelties of the proposed research undertakings, and finally anticipates some potential research outcomes.

Chapter 2 provides a comprehensive literary overview of carbon- and nitrogen-based triazine units containing polymeric nanomaterials with special focus on graphitic carbon nitride, along with the identification of potential application areas concerning wastewater remediation through an in-depth analysis of existing literature.

Chapter 3 elucidates the objectives and scope of the research topic after analysing the research gaps identified from extensive literature survey.

Chapter 4 describes the various instruments and equipment employed to carry out the synthesis of the triazine-based nanomaterials. This chapter also describes in brief the tools and devices used for characterizing and analysing the properties of the nanomaterials. The different methodologies implemented to explore the applications of the as-synthesized nanomaterials in wastewater purification, have additionally been discussed in this chapter.

Chapter 5 deals with the materials and chemical reagents utilized during the synthesis of triazine-based polymers and their elaborate synthesis protocols. This section also includes discussion of diverse characterization techniques deployed to probe the nanomaterials' properties, and finally the test programs and analytical methods used to perform the application procedures involving these nanomaterials.

Chapter 6 has been divided into two broad sections: Part 1 and Part 2.

Part 1 presents the characterization results of the as-synthesized nanomaterials obtained from the various experiments performed during the course of the research works. This section also provides the relevant discussions to justify the results obtained from the different characterization techniques.

Part 2 delves into the experiments conducted on the as-synthesized nanomaterials to implement them in wastewater remediation. This section has been again divided into three portions based on the three different applications of the nanomaterials in wastewater purification. These include: (a) fluorescence detection of mercury heavy metal by a novel triazine-based nanomaterial, (b) photocatalytic degradation of toxic pollutants like organic dye and heavy metal chromium by GCN, and (c) catalytic reduction of textile pollutants and nitrophenol compounds by metal decorated GCN. Plausible mechanisms are explained to understand the activity of these nanomaterials in degradation of toxic compounds from water environment.

Chapter 7 is the concluding chapter comprising of a recapitulation of the research investigations conducted, their resultant findings, and the attained outcomes. Additionally, potential avenues for further exploration of the research conducted herein are deliberated upon.

CHAPTER 2:

LITERATURE REVIEW

Literature Review

This chapter presents a detailed literature review concerning the development of triazine-based polymeric nanomaterials and their subsequent utilization in wastewater treatment. Multifaceted functionalities of these nanomaterials in the environmental sector concerning wastewater remediation have been surveyed by intensive reviewing of existing literatures. Among different types of carbon-and nitrogen-based nanomaterials, primary focus is given on polymeric materials based on triazine building blocks, along with special attention to graphitic carbon nitride. Review of past works necessitates identifying the existing gaps in the present research fields. It enhances the motivation for development of novel synthesis approaches, or to modify existing synthesis methods to modulate the characteristics of triazine-based nanomaterials. The use of these samples are required to be thoroughly investigated in elimination of perilous contaminants from polluted water environment only after conducting exhaustive research of the published literature reports.

2.1. Carbon- and nitrogen-based nanomaterials:

Organic frameworks consisting of covalently bonded carbon and nitrogen atoms have gained expansive attention in recent times due to the potentiality to device nanomaterials having multifaceted and modifiable functionality [5]. Covalent triazine frameworks (CTF) are a class of carbon- and nitrogen-based organic materials having impressive chemical stability and porosity arising from their aromatic C=N or triazine linkages [25,26]. CTFs are polymeric nanomaterials composed of these repeated triazine units which act as monomers or the fundamental building blocks of CTFs. The concept of CTFs was initially proposed by Thomas et al. in 2008 [27] when they reported the synthesis of a series of polymeric compounds having triazine linkages following dynamic condensation chemical reactions. The interesting π-π interactions, highly delocalized electron distribution, nitrogen rich chemical structure, tendency to form hydrogen bonding, and appropriate structural motif for metal chelation, are some of the unique characteristics of CTFs which make them an impressive topic of research in supramolecular chemistry. The π-conjugated scaffolds of CTFs with permanent nanopores within the framework, along with abundant nitrogen content, bestow CTFs with distinctive advantages and make it a prospective material for various industrial applications including energy storage and conversion [28,29], heterogeneous catalysis [30,31], photocatalysis [32,33], adsorption [34,35], and so on [26]. One of the most promising materials that belong to the class of CTFs is Graphitic carbon nitride (GCN/g-C_3N_4).

2.1.1. Graphitic carbon nitride (GCN):

2.1.1.1. Brief history of GCN:

Graphitic carbon nitride (GCN) is a special class of covalently bonded carbon- and nitrogen-based polymeric nanomaterial having the chemical formula C_3N_4. This material has achieved high popularity among scientists and researchers from every sector, especially energy harvesting and environmental fields, owing to its many lucrative attributes.

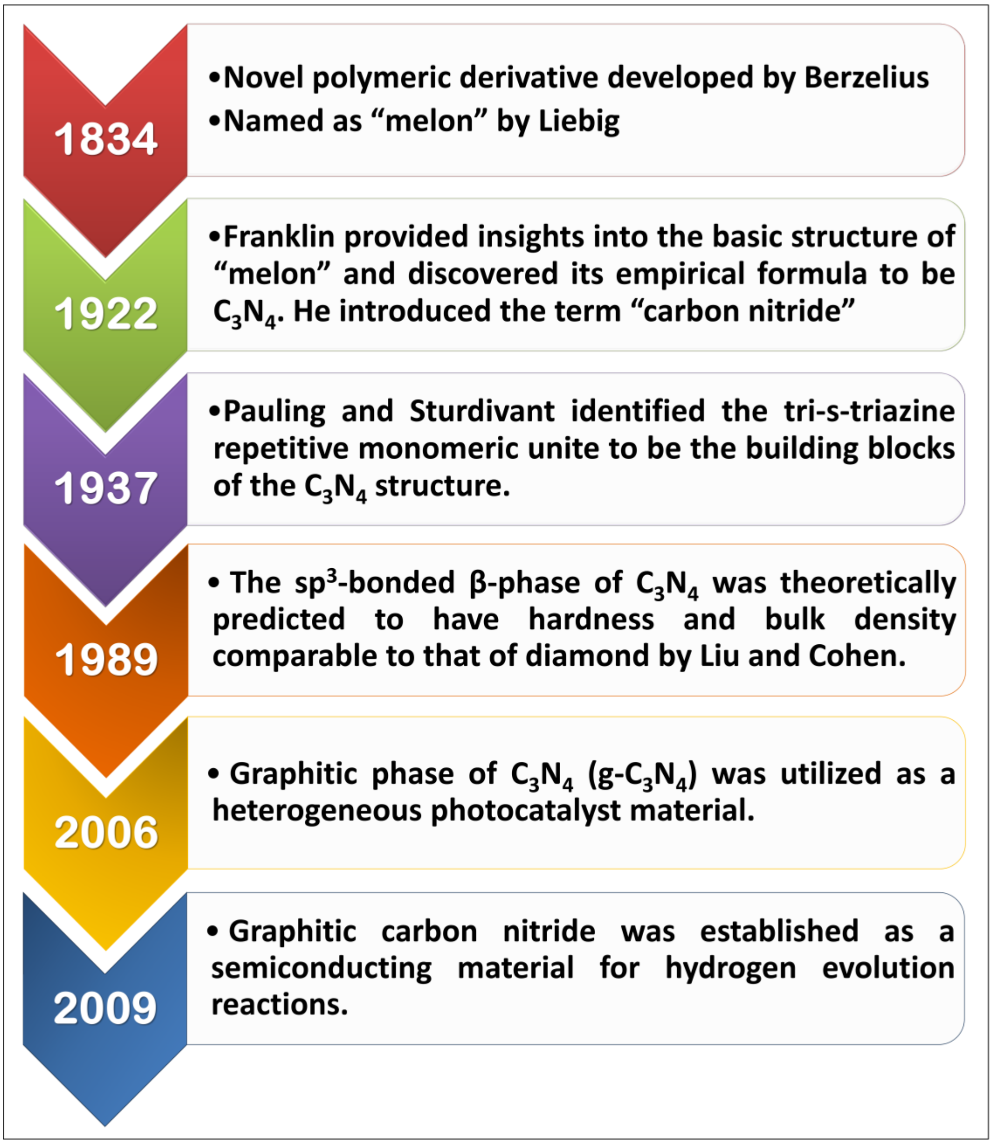

1834

- Novel polymeric derivative developed by Berzelius
- Named as "melon" by Liebig

1922

- Franklin provided insights into the basic structure of "melon" and discovered its empirical formula to be C_3N_4. He introduced the term "carbon nitride"

1937

- Pauling and Sturdivant identified the tri-s-triazine repetitive monomeric unite to be the building blocks of the C_3N_4 structure.

1989

- The sp^3-bonded β-phase of C_3N_4 was theoretically predicted to have hardness and bulk density comparable to that of diamond by Liu and Cohen.

2006

- Graphitic phase of C_3N_4 (g-C_3N_4) was utilized as a heterogeneous photocatalyst material.

2009

- Graphitic carbon nitride was established as a semiconducting material for hydrogen evolution reactions.

Fig. 2.1: *Schematic depiction of the brief history of GCN*

The history of carbon nitride polymers or oligomers dates back to as early as 1834, when Berzelius developed a novel polymeric derivative which was eventually termed as “melon” by Liebig [36]. A general formula of the as-synthesized material was proposed as $(C_3N_3H)_n$ [37]. In 1922, Franklin provided significant insights into the basic structure of this “melon” compound [38]. Around 1989, Liu and Cohen’s theoretical work predicted that the β–phase of carbon nitride (β-C_3N_4) has diamond-like characteristics in terms of hardness and compressibility [39]. However, the graphitic phase of carbon nitride is contemplated to be the stable allotrope of C_3N_4 at ambient conditions [40]. The schematic representation of the brief history of GCN is given in **Fig. 2.1**.

2.1.1.2. Basic structure and properties of GCN:

The full potential of GCN has only been unveiled quite recently when extensive researches on this material revealed its interesting surface properties resulting from basic surface active sites [41]. Being a member of the CTF class of materials, GCN shows a π-conjugated polymeric nature. GCN is structurally quite similar to graphite, where instead of the C-C bonds in graphite, each layer of GCN is composed of C-N covalent bonds. The layers of GCN are joined together by weak forces corresponding to van der Waals interaction [37]. Ideally, GCN sheets should be solely composed of C and N elements with C:N ratio being exactly 0.75, and the material should only consist of C-N bonds with absence of localization of electrons in the π-states [42]. However, in reality, GCN is prepared by polycondensation reactions from nitrogen-rich precursors like urea, melamine, dicyandiamide etc. During synthesis, incomplete condensation may result in the incorporation of some hydrogen in the conjugated system, which may be present as a part of the edge-terminated primary or secondary amine (N-H) groups within the GCN motif. The presence of these groups (rather the dangling bonds arising from the edge-terminated groups) results in surface defects and can stimulate delocalization of π-electrons on the GCN surface. This also enhances the Lewis-base property of GCN which helps in coordination chemistry and catalytic applications [41]. Moreover, GCN exhibits thermal stability up to 600 °C in air [11], and chemical stability in acidic, neutral, or basic conditions [43] because of the N-bridged tri-s-triazine ring-like framework along with high degree of condensation [37]. Thus GCN can be successfully employed in liquid or gaseous environments, and also at high temperatures. This increases the potentiality of the material for extensive applications in numerous fields.

Fig. 2.2 shows the different surface functionalities of GCN which contribute significantly to its interesting properties, some of which are described below:

(i). The metal-free nature and simple constitution of graphitic carbon nitride has prompted a huge interest among researchers for multi-dimensional applications. Carbon, nitrogen and some residual hydrogen are the compositional elements of GCN. This renders the biocompatible and low cytotoxicity character of GCN, because of which GCN can safely be utilized in biological applications [44]. Due to its metal-free nature, GCN is also considered as a potential candidate for different environmental applications, particularly in water and wastewater treatment. It does not cause any metal-leaching or secondary contamination in soil and water when used as an attenuation material for respective environmental remediation fields.

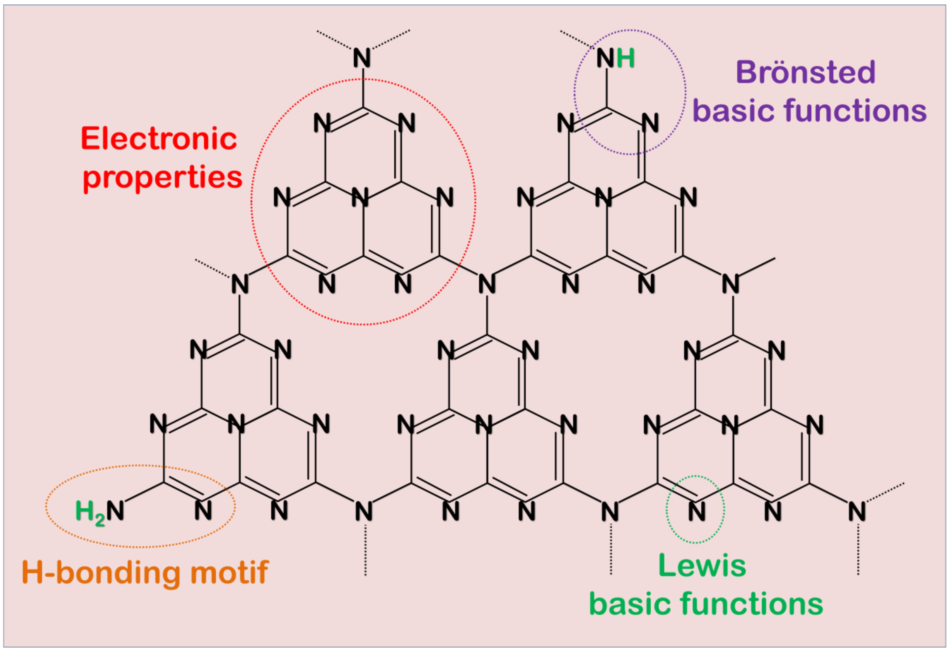

Fig. 2.2: *The different surface functionalities of GCN giving rise to its interesting properties [41]*

(ii). GCN is a polymeric semiconducting material. Its interesting electronic features arise from the sp^2 hybridization of carbon and nitrogen atoms to form a highly delocalized π-conjugated system [45]. The lone pair of electrons of the nitrogen atoms plays the most important role in modulating the electronic structure of GCN. GCN is typically an ‘n’-type semiconducting material with an indirect optical band gap of about 2.7 eV. First principles theoretical investigations have suggested that the HOMO or the VB of GCN is comprised of the p_z orbitals of the nitrogen atoms. These lone pair of electrons basically forms the nonbonding orbitals (n). The LUMO or CB of GCN is made up of the carbon p_z orbitals, i.e. the sp^2 hybridized clusters of C-N bonds. They constitute the π^*-antibonding orbital [46].

The interesting optical properties of GCN have been extensively researched by employing UV-vis diffuse reflectance spectroscopy (DRS) and photoluminescence spectroscopy (PL). The material exhibits significant light absorption in the visible range of the electromagnetic spectrum, with an absorption edge near 420-470 nm wavelengths. Band to band transition of photogenerated charge carriers occurs from n to π^* orbitals, and maximum emission is observed around 440 nm [47]. Thus it emits intense blue light at room temperature. GCN can also utilise wide range of the visible scale (430-550 nm), because of which it shows potential application in visible-light induced photocatalytic reactions, light-emitting devices, and in opto-electronic fields [48,49,14]. Additionally, the electronic band-structure of GCN makes it suitable for use in photo-electrochemical cells, photo-detectors and solar cells [50,51].

(iii). GCN is a two-dimensional layered nanomaterial with prolific specific surface area, porosity, and rich in surface defects. Unfortunately, simple thermal treatment of nitrogen-rich precursors results in the formation of bulk GCN sheets. Bulk sheets suffer from inferior physicochemical, electronic and optical properties because of high probability of recombination of photogenerated charge carriers (electrons and holes) in the valence and conduction band of GCN, poor specific surface area, and moderate quantum yield [45,52]. Low surface area arises from the bulk clustered sheets which remain in agglomerated condition. Exfoliation of bulk sheets to produce thin nanosheets of GCN [53] along with tuning the morphology of GCN to form one-dimensional nanorods or nanotubes, and zero-dimensional quantum dots [54,55] can lead to enhancement in light absorption and harvesting, improvement in specific surface area, faster transport of charge carriers, easy absorption and transportation of reactant, and lesser probability of carrier recombination [56]. Recently, GCN quantum dots have gained quite prominence owing to their attractive characteristics which include high quantum yield, quantum confinement, intense fluorescence, chemical stability, improved surface area, and biocompatibility [57]. Thus GCN quantum dots are effectively utilised as fluorescent probes for sensing applications. Their water-soluble, non-toxic, and stable nature is appropriate for environmental and biological applications [58].

(iv). Among the different allotropes of C_3N_4, tri-s-triazine-based GCN exhibits the highest stability. From thermogravimetric analysis (TGA), it is evident that GCN can withstand thermal treatment up to a temperature as high as 600 °C. At temperatures higher than 750 °C, GCN undergoes complete decomposition or sublimation in presence of oxygen atmosphere to produce oxides of nitrogen and carbon [59,60]. Such high thermal stability is quite rare among organic materials, thus GCN exhibits promising efficiency in high temperature applications. Additionally, GCN shows exceptional chemical steadiness in acidic, alkaline or neutral environment. GCN is not soluble in most common solvents like water, alcohols, toluene, tetrahydrofuran, diethylether, dimethylformamide and so on [59]. GCN layers are stacked in a kind of way that van der Waals interactions exist in optimal condition between the individual layers, which renders its insoluble nature in common solvents. Thus GCN suspension in aqueous solution remains highly stable for several days without any signs of agglomeration or precipitation.

2.2. Synthesis and development of covalent triazine-based polymers:

2.2.1. Synthesis techniques of triazine-based polymers:

The first development of crystalline covalent organic polymers was reported by Cote et al. in 2005 [61]. Simple one-step condensation reactions were performed by them to develop several highly cross-linked crystalline mesoporous and microporous covalent organic polymers with rigid frameworks, unusual thermal stability, high surface area, along with permanent porosity. The outcome of this research paved the way for extensive research on the evolution of several other crystalline polymers containing triazine-based frameworks.

Highly stable amorphous micro-porous triazine-based polymeric network was first synthesized by Kuhn et al. in 2008 employing ionothermal trimerization reaction [27]. Their pioneer work involved the dynamic trimerization of nitrile monomers in molten $ZnCl_2$ where the carbonitrile and $ZnCl_2$ were heated at a temperature of 400 ºC. However, this ionothermal procedure had some limitations resulting from the extreme reaction conditions, long time duration of reaction, and contamination of the as-synthesized organic polymers with the $ZnCl_2$ metallic catalyst. Zhang et al. reported a time-efficient synthesis procedure involving polymerization reactions following microwave-assisted ionothermal process [62]. This method exhibited amorphous triazine-based polymers with improvement in surface area.

Schwab et al. (2009) prepared a melamine-based highly cross-linked polymer with substantial surface area and micro-porous properties [63]. They followed a catalyst-free Schiff-base reaction procedure. The as-prepared material had high nitrogen content and exhibited impressive thermal as well as chemical stability. Modak et al. designed a triazine functionalized organic polymer via electrophilic substitution reaction [64]. The material had substantial surface area and was highly porous with pore size varying from micropores to mesopores. The triazine functional groups enabled the generation of electron-donating nitrogen-sites which functioned as Lewis basic sites on the surface of the as-prepared polymeric framework. Similarly, triazine-based polymers can be prepared via nucleophilic substitution reactions. Cyanuric chloride is typically used as a precursor for this type of reaction since it already contains a built-in triazine block [30,65,66]. Another synthesis procedure of triazine-based polymers is through condensation reactions with triazine-containing amine compounds and various dianhydrides [67]. Liebl et al. employed this technique to produce triazine-based polyimides with impressive thermal and chemical stability [67]. They also obtained a high surface area of the polymer.

Lee et al. followed a simple one-pot catalyst-free technique of polymerization between cyanuric chloride and an amino group containing compound to develop a novel aromatic triazine-based polymer [68]. The introduction of the aromatic ring into the triazine framework already rich with nitrogen content led to the significant enhancement of the thermal stability. Similarly, Peng et al also followed a catalyst-free synthesis route to develop triazine-based polymeric materials under mild synthesis condition [69]. Single-step polycondensation reaction involving melamine as the precursor, and phthalic, isophthalic, and terephthalic acids as the initial monomers, was performed at a mild reaction temperature of 180 °C and at atmospheric pressure to produce the triazine-based polymers.

Though there are plenty of other literatures on the varied synthesis procedures to develop highly functional triazine-based porous organic polymers, the above mentioned discussions have been reported on the basis of most preferred and relevant ones.

2.2.2. Synthesis techniques of GCN:

By searching “graphitic carbon nitride” in various search engines while setting the time span from 2019 to 2023 yields about 17,800 results. This indicates the vast interest and extensive on-going researches on GCN in recent times. This stems from the fact that GCN can be prepared in large amount following uncomplicated and cost-effective synthesis strategies using cheap and abundantly available raw precursors. The commonly used precursors for the synthesis and growth of GCN generally have certain similar characteristics viz. reactive in nature, fertile in nitrogen content, preferably oxygen-free, and they contain covalently bonded C-N structures, like triazine or heptazine blocks.

However, most of these precursors are not stable and are highly explosives due to their chemically reactive nature [41]. Owing to the poor thermodynamic stability, the development of single-phase, highly crystalline, ordered, sp^3-hybridized C_3N_4 phase with appropriate C:N ratio of 0.75 is an extremely challenging task [70]. The difficulties encountered during the synthesis of the ideal C_3N_4 phase have eventually led to the increase in the popularity and demand of the defect-rich graphitic phase (GCN). Compared to ideal C_3N_4, GCN has become more valuable in recent times, particularly for catalytic applications, because of its surface defect sites. Thus, the next section will try to put forth the different synthesis techniques of GCN with defects since it is currently an extremely interesting and relevant topic of research.

The conventional precursors used for the synthesis of GCN are CN_xH_y compounds like urea, cyanamide, dicyandiamide, melamine, thiourea, and sometimes their mixtures [71]. The traditional synthesis procedures are thermal polycondensation, solvothermal treatment, chemical vapour deposition, and plasma sputtering deposition [71]. However, thermal treatment of carbon and nitrogen containing precursors remains the most dominating and frequently used procedure compared to the other techniques.

Although, GCN was discovered by Berzelius and Liebig in 1834, it was not before 1991 that researches took serious interest in this material. In 1991, Maya et al. attempted the synthesis of amorphous carbon nitride by a high pressure (225 MPa) and high temperature (700 °C) decomposition technique using organic sources containing C-H-N elements [70]. Kouvetakis et al. in 1994 reported the synthesis of amorphous C_3N_4 thin films by decomposing triazine-containing precursors in a low-pressure reactor at an optimum temperature of 450-500 °C following CVD [72]. In 1999, Alves et al. reported the preparation of graphitic phase of C_3N_4 by polycondensation reaction of triazine-block containing precursor melamine in a nitriding solvent hydrazine under high pressure and temperature (3 GPa, 800 ^oC) [73].

Montigaud et al. performed two types of solvothermal synthesis strategies to produce macroscopic C_3N_4 samples [74]. The first condensation route produced weakly condensed and poorly ordered carbon nitride with many dangling amino groups. The second synthesis route performed at a high temperature of 800 ^oC generated graphite-like framework with stoichiometry near to that of ideal C_3N_4. However, at such a high temperature, depletion of nitrogen takes place; hence the final product contains lesser amount of nitrogen. Then Gu et al. resumed this work in 2003 and was able to synthesize carbon nitride by a reaction between the two precursor: cyanuric chloride and calcium cyanamide [75]. They carried out the synthesis at a moderate temperature of 500 to 550 ºC and finally they obtained carbon nitride with proper stoichiometry, order, and composition. A detailed work by Lotsch and Schnick reported the development of a series of triazine-based (C_3N_3) non-metal tricyanomelaminates compounds as potential precursors for the synthesis of GCN [76]. They showed that these novel precursors first undergo transformation to form melem $(C_6N_7)(NH_2)_3$, which after further polymerization form semi-crystalline graphitic phase of carbon nitride (CN_xH_y) materials. A benchmark work by Bojdys et al. in 2008 was able to synthesize crystalline, ordered, and condensed GCN by ionothermal synthesis technique [77]. They obtained a GCN species whose sheets were made up of hexagonally arranged C_6N_7 or s-heptazine units having pronounced graphitic stacking. A highly cited work by Zhang et al. published in 2010 reported a very simple copolymerization technique between dicyandiamide and organic monomer barbituric acid for the generation of polymeric C_3N_4 [78]. The precursors were thermally treated at 550 °C for 4 hr. to obtain the final products.

In most of the earlier works discussed so far, they have extensively used cyanamide and dicyandiamide to synthesize GCN samples. Unfortunately, these precursors are expensive, difficult to obtain, virulent, and can have fatal effects on human beings and also on the environment. They are also highly chemically reactive, unstable, and are cannot be synthesized in large-scales. To overcome such difficulties, next generation researchers started synthesizing GCN employing melamine as a lucrative precursor. Till 2009, researchers tried to synthesize GCN from melamine under supercritical conditions. Most researchers reported thermal pyrolysis of melamine at elevated temperatures, high pressures, or in low-vacuum system. Though they were successful in obtaining highly ordered and properly stacked GCN samples, however, considering a practical viewpoint in terms of large-scale industrial application, the above-mentioned procedures were not considered as feasible and realistic. Thus researchers started venturing on the production of GCN under ambient condition, applying facile and cost-effective technologies.

A highly cited work in this regard is a report by Yan et al. published in 2009, which basically helped to optimize the reaction conditions for preparation of graphitic phase of carbon nitride [9]. They followed a straight-forward method by directly heating melamine in two-step process carried out in a semi-closed system. They were able to obtain proper graphitic phase with many surface active sites. Following this work, Liu et al. in 2011 chose urea as the starting material for the synthesis of GCN [79]. Urea is a very common cheap raw material readily available and widely-used in the chemical industry. Urea can act as a reactive molecular precursor for the genesis of melamine and biuret in industries [80]. Thermal decomposition of urea at 350 °C can produce a mixture of cyanuric acid, melamine, and ammelide, provided the reaction occurs in an open reaction vessel [81]. Thus urea is a much cheaper raw material than melamine. Liu et al. was able to obtain GCN in large-scale by thermal treatment of urea at a temperature corresponding to 550 °C for 3 hr. [79]. The reaction was carried out in ambient pressure, and the simplicity of this method lies in the fact that no external assistance for modulating the reaction atmosphere and pressure was required or needed. Moreover, a nearly ideal stoichiometric C:N ratio of 0.73 was obtained in this method. Thus this strategy of synthesizing GCN became widely-popular.

There are plenty of works in this regard where urea or melamine has been used as a raw precursor for the synthesis of GCN. Most of the literatures report the pyrolysis of urea or melamine at an optimum temperature of 550-600 °C. Urea/melamine is taken in an alumina or quartz crucible which is suitably covered with a lid, then the system is placed in a muffle furnace, and the thermal polycondensation reactions proceed under ambient pressure in presence of air. It generally takes 3-4 hr. for the reaction to complete. A pale-yellow coloured powder product is obtained at the end. The heating rate is preferably maintained at 5-10 °C/min. Some reports suggest the drying of urea at 80 °C in an oven for 10-12 hr. prior to the thermal treatment. Though urea (CH_4N_2O) is a desirable precursor in terms of cost-effectiveness, however, since urea contains oxygen in its chemical structure, GCN compounds synthesized from urea occasionally contain oxygen as impurities, which may affect the C:N elemental ratio. Thus, melamine ($C_3H_6N_6$) is more preferably employed for synthesizing impurity free ideal GCN material. Moreover, melamine inherently possesses the triazine unit which acts as an added benefit. Conversely, GCN produced from pyrolysis of urea generally shows much higher surface area as well as porosity, with somewhat small crystalline domains as compared to GCN synthesized from melamine [82]. Zhou et al. [83], Huang et al. [84], Yao et al. [85], Fang et al. [86], and others have demonstrated direct pyrolysis of urea to produce GCN; whereas, Zhai et al. [87], Zhang et al. [88], Praus et al. [89], Shcherban et al. [90], and many other researchers synthesized GCN by direct thermal treatment of melamine in air or in inert (argon) atmosphere. Some researchers have also tried to synthesize GCN by mixing two or more precursors before heat treatment at the optimum temperature [91-93]. Mixing precursors have resulted in increase in the yield of the final product, increased the surface area as well as porosity, and also affected the nitrogen content in GCN thereby affecting its overall surface properties.

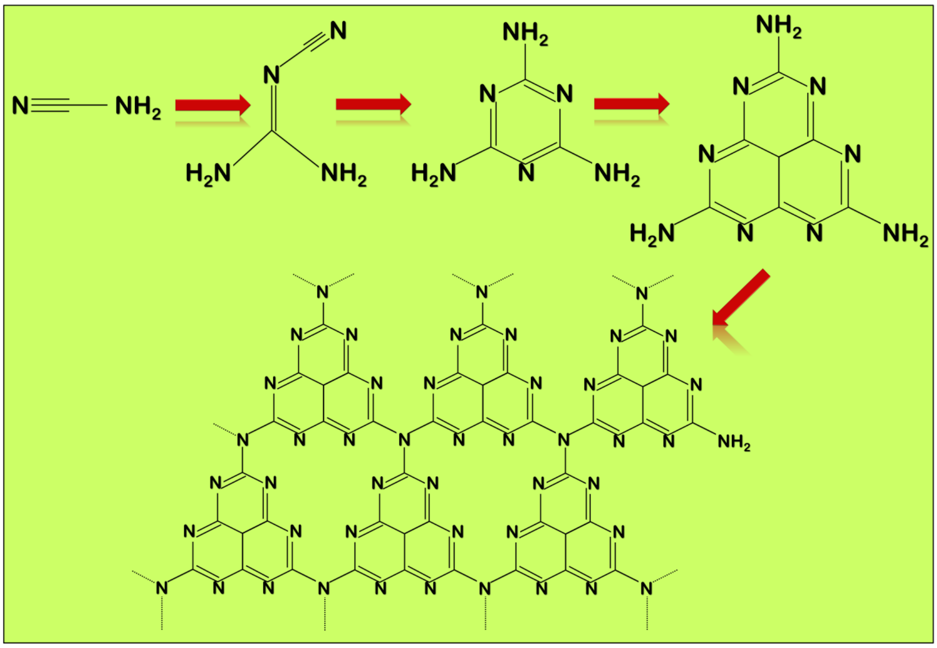

Fig. 2.3: *Reaction pathway showing the gradual formation of GCN from cyanamide precursor [40]*

The reaction steps that occur in the course of generation of GCN are described below and additionally the schematic provided in **Fig. 2.3** shows the gradual formation of GCN from its precursor cyanamide through several steps. Combined polyaddition and polycondensation reactions take place in the time of synthesis of GCN.

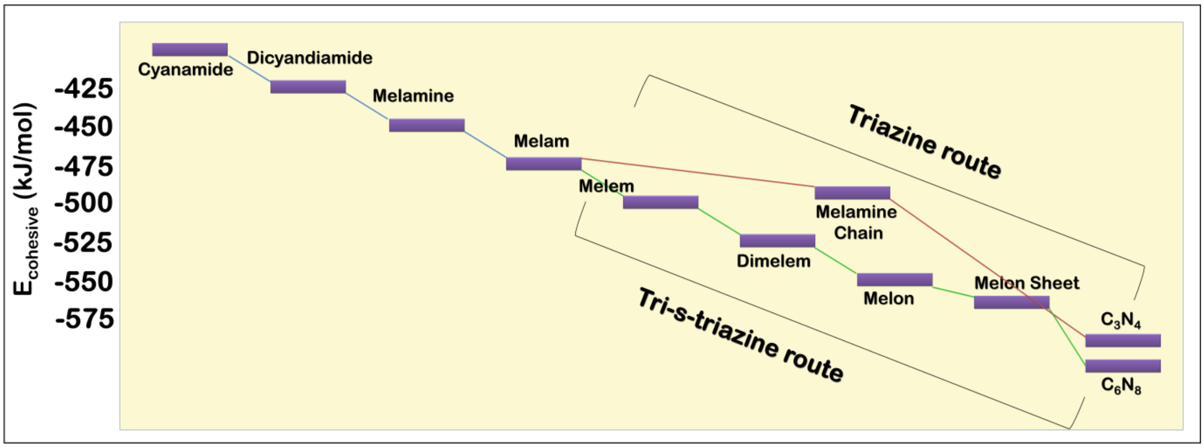

Fig. 2.4: *Cohesive energy diagram for the development of GCN from cyanamide following triazine and tri-s-triazine routes [40]*

If we consider the most conventionally-used precursor urea, then in the first step of reaction, urea undergoes condensation reaction to form an intermediate product called melamine. Depending upon whether the reactions are performed in an open or closed environment, the products may differ; however, in the second-step, ammonia is eliminated by condensation reactions. Generally, melamine-based intermediate compounds are formed up to a temperature of 350 °C. Around 390 °C, tri-s-triazine structures start to form by rearrangements of melamine-like products. Subsequent polymerization reactions involving condensation of these tri-s-triazine units yield the final network of polymeric GCN. This occurs at around 550 °C. The material starts to become slightly unstable after 600 °C [40]. The cohesive energy diagram for the formation of GCN is given in **Fig. 2.4**.

Theoretical *ab initio* calculations have further supported and correlated the experimental data which have helped to predict the reaction pathways more clearly. The intermediate products like melamine and melem formed by condensation reactions are basically molecular crystals. Inside the crystal structure, the molecules remain bound together by strong covalent bonds, while combination of hydrogen bonding and van der Waals interactions helps to held together the crystal structure. There has been some uncertainty regarding the next step of reaction, whether GCN sheets are formed based on triazine units or tri-s-triazine units. Both these units can act as tectonic units to form the GCN sheets, however, they differ from each other in their stability resulting from the dimension of the nitride pores, and the dissimilar electronic environment of nitrogen atoms. The two probable pathways are stated below:

(i). Condensation reactions may progress through the polymerization of melamine crystals and lead to the formation of *triazine* units-based C_3N_4 sheet-like structures.

(ii). Formation of melem molecules from melamine molecules by condensation, followed by polymerization of these melem molecules to form *tri-s-triazine* units-based C_6N_8 sheet-like structures.

Extensive experimental works by Lotsch et al. have proved that melem is indeed the most probable product formed after polymerization of melamine [94]. This indicates that pathway (ii) is the most plausible and preferred way for the genesis of GCN, and polymerization occurs via tri-s-triazine path. Additionally, Kroke et al. performed theoretical calculations and found that GCN formed via the tri-s-triazine structure is energetically more favourable and stable [95]. The next step involves the generation of dimelem molecules, which are formed by joining of the adjacent molecules within the melem crystal system. This step is followed by condensation reactions of dimelem molecules to form linear polymeric chains of tri-s-triazine units called melons. The final step involves the polymerization or fusion of the melon chains to ultimately produce GCN sheets. Depending on the degree of condensation, there are several ways to attach the melon chains into graphitic sheet-like GCN structure. As suggested by Lotsch et al. [96], one possibility is to join the melon chains in a particular way so that every alternate melon chain remains inverted. This gives rise to a framework in which the tri-s-triazine blocks fit into each other compactly. Hydrogen bonding between the amine groups (NH_2) and the edge-terminated nitrogen atoms hold together the GCN structure. Interestingly the GCN sheets are significantly buckled near the edges. This transpires as a result of the repulsion occurring between the edge-terminated nitrogen atoms in the tri-s-triazine units as these units come in close proximity to each other within the GCN motif.

The GCN products obtained after direct pyrolysis of the precursors at requisite temperature exhibit bulk features and have sheets or layers stacked in agglomerated clusters. These types of samples generally suffer from inferior physiochemical properties and cannot be fully utilized for application purposes without further modifications. Some conventional strategies to convert bulk GCN into its nano-dimensional counterpart in order to enhance its features are discussed below:

2.2.2.1. Exfoliation of GCN:

Exfoliation is a method to transform the bulk layered sheets of GCN into thin or ultrathin nanosheets so that the specific surface area gets enhanced, leading to some interesting electronic properties and improved host capabilities for promising application in catalysis and energy storage. Niu et al. [97] were the first to try exfoliating GCN by Hummer’s method, since this was already an established method for exfoliating graphite into graphene layers [98]. However, they did not succeed, since Hummer’s method resulted in large aggregates of GCN particles having dimension of several hundred nanometres. Moreover, this method completely destroyed the planar atomic framework of GCN. Hence Liu et al. tried to discover an alternative route for exfoliating GCN and developed an “etching” process of bulk GCN [97]. This etching was performed by direct thermal oxidation in air. They successfully obtained GCN nanosheets having thickness of about only 2 nm. Zhang et al. published a work on the exfoliation of as-synthesized bulk GCN into ultrathin nanosheets by liquid exfoliation technique [44]. Bulk GCN was dispersed in deionized (DI) water and then subjected to ultrasonication treatment for 16 hr., followed by centrifugation to remove the unexfoliated GCN nanoparticles. Yang et al. also followed a similar exfoliation strategy like Zhang et al., where they dispersed bulk GCN into various solvents like isopropyl alcohol (IPA), water, ethanol, acetone, or N-Methyl-2-pyrrolidone (NMP) and sonicated the dispersed solution for 10 hr. to obtain nanosheets of GCN [99]. The nanosheets had thickness in the scale of 2 nm. Sun et al. obtained exfoliated GCN nanosheets by thermal oxidation technique [100]. Bulk GCN powder was first dispersed in IPA solvent, the mixture was then put into a crucible, which was then placed in a furnace for thermal oxidation at 550 °C for 2 hr. Apart from these chemical exfoliation techniques, several researchers have reported "green exfoliation" of GCN where GCN is dispersed in water instead of any other chemical solvents for the process of exfoliation. This type of exfoliation is cost-effective, environment-friendly, and yields large scale products. Chebanenko et al. reported exfoliation of GCN by simple ultrasonic treatment [101]. GCN powder was dispersed in DI water and magnetically stirred for 15 min, followed by ultrasonic treatment for 2 hr.

Besides exfoliation, modification of GCN to enhance its inherent properties and increase its potentiality has been performed by incorporating metal ions into the GCN matrix. In the next section, a detailed review has been put forward on the different synthesis strategies of metal-doped GCN nanomaterials.

2.2.2.2. Metal doping of GCN:

Incorporation of metals into GCN have proved to significantly modify its crystal structure, textural properties, along with electronic band structure, thereby remarkably improving its light absorption properties, quantum yield, and facilitating charge carrier separation to prolong the carrier lifetime [102]. The process of doping is to basically introduce impurities deliberately into the pristine GCN system in order to tune the electronic band gap of GCN along with the band edge potentials. GCN has been doped with different types of:

(i) Alkali metals such as lithium (Li), sodium (Na), potassium (K), rubidium (Rb), and cesium (Cs).
(ii) Alkaline earth metals like magnesium (Mg), calcium (Ca), strontium (Sr), and barium (Ba).
(iii) Transition metals like titanium (Ti), vanadium (V), manganese (Mn), iron (Fe), cobalt (Co), nickel (Ni), copper (Cu), zinc (Zn), and molybdenum (Mo).
(iv) Noble metals nanoparticles like palladium (Pd), silver (Ag), platinum (Pt), and gold (Au).

There are several literatures on transition metal doping in GCN [103-111]. All the doped samples exhibited shifting of optical band gaps to lower energy values, which facilitated to produce additional photogenerated charge carriers under light irradiation, promoted visible-light utilization, and improved efficiency of charge separation. Doping also resulted in the generation of abundant active sites on the porous surface of GCN. As the current topic of research suggests, only the most relevant types of doping of GCN and their synthesis strategies have been listed in **Table 2.1**.

Table 2.1: Different types of metal dopants incorporated into the GCN matrix.

Sample	Precursors for GCN	Precursors for metal dopant	Reaction conditions	References
K-GCN	Thiourea	Potassium bromide	550 °C, 2 hr. in air	Xiong et al. [112]
Na-GCN	Thiourea	Sodium bromide	550 °C, 2 hr. in air	Xiong et al. [112]
Li-GCN	Melamine	Lithium chloride	550 °C, 4 hr. in N_2	Ge et al. [113]
Cs-GCN	Dicyandiamide	Caesium chloride	550 °C, 4 hr. in air	Kumar et al. [114]
Rb-GCN	Dicyandiamide	Rubidium chloride	550 °C, 4 hr. in air	Kumar et al. [114]
Mg-GCN	Urea	Magnesium chloride	550 °C, 2 hr. in air	Deng et al. [115]
Ca-GCN	Cyanamide	Calcium chloride	550 °C, 3 hr. in argon	Fronczak et al. [116]
Sr-GCN	Melamine	Strontium nitrate	520 °C, 4 hr. in air	Zhou et al. [117]
Ba-GCN	Melamine	Barium nitrate	550 °C, 3 hr. in air	Bui et al. [118]
Ti-GCN	Urea	Tetrabutyl titanate	550 °C, 3 hr. in air	Wang et al. [103]
V-GCN	Urea	Ammonium metavanadate	400 °C, 2 hr. in air	Reddy et al. [104]
Mn-GCN	Urea	Potassium permanganate	550 °C, 4 hr. in N_2	Li et al. [105]
Fe-GCN	Melamine	Ferric chloride	-	Tonda et al. [106]
Co-GCN	Melamine	Cobalt phthalocyanine	550 °C, 4 hr. in air	Chen et al. [107]
Ni-GCN	Melamine	Nickel nitrate	550 °C, 5 hr. in air	Pham et al. [108]
Cu-GCN	Dicyandiamide	Cupric chloride	550 °C, 4 hr. in air	Li et al. [109]
Zn-GCN	Urea	Zinc chloride	400 °C, 4 hr. in air	Zhu et al. [110]
Mo-GCN	Melamine	Molybdenum diacetylacetonate dioxide	550 °C, 2 hr. in air	Goncalves et al. [111]
Pd-GCN	Melamine	Hydrogen chloropalladate	-	Jin et al. [119]
Ag-GCN	Urea	Silver nitrate	550 °C, 3 hr. in air	Paul et al. [120]
Pt-GCN	Dicyandiamide	Chloroplatinic acid hexahydrate	550 °C, 4 hr. in N_2	Li et al. [121]
Au-GCN	Melamine	Chloroauric acid	-	Cheng et al. [122]

2.3. Conventional pollutants present in aquatic environment, their sources of emission, and harmful effects:

Population influx is a consequential threat to the global environment and ecosystems in the modern world. With exponential increase in human population, the world has experienced a rapid growth in industries and factories to fulfil the need of 8 billion people (current global population as on 15th November 2022) [123]. Most factories and plants in a developing country like India lack appropriate knowledge regarding the proper disposal of waste materials generated as by-products from manufacturing processes. Due to poor economic condition, many factories suffer from scarcity of proper facilities and amenities required for treatment of waste products prior to their discharge in the environment, whose consequences is the unregulated emission of pollutants from these places. Water resource is one of the most salient natural resources required for human existence and survival. Unfortunately, human activities are the main reason for contamination of water-bodies (like groundwater, lakes, rivers, oceans, and reservoirs) by releasing harmful matters into water and making it unsuitable for drinking and other purposes [124]. Thus, water treatment, remediation, and preservation of this human elixir are of utmost concern of today for the engineering and scientific community.

2.3.1. Sources of pollutants present in wastewater:

Industries are bulk pollution causing sources, particularly those which are using huge amount of water for processing and manufacturing of products. Different industries emanate various kinds of pollutants of organic and inorganic nature along with varied amount of discharged effluents. One example of such industries is textile which consumes large amount of water during manufacturing processes, and hence it is one of the major producers of wastewater [125]. Apparel industry alone can contribute to about one-fifth of the earth’s total water pollution [126]. Textile manufacturing processes require various chemical compounds for pre-treatment, and dyeing and printing of textiles. Thus wastewater emitted from textile industries is laden with highly toxic non-degradable chemicals, which when discharged into aquatic environment without proper treatment can lead to disastrous damage to the ecosystem.

Commonly emitted chemicals from textile industries include coloured organic dye compounds like rhodamine B (RhB), methyl orange (MO), methylene blue (MB), etc. Approximate quantity of dyes produced in dye manufacturing industries world-wide annually is 800,000 tons [127]. Around 10,000 synthetic dyes are required during textile manufacturing processes [127]. More than 10% of these dye compounds are discharged into the planet’s water resources as residual dye present in textile effluent during aqueous dyeing process. Synthetic dyes are the most complicated and difficult-to-treat environmental pollutants because of their big molecular weight, complex chemical structures and properties, non-degradable nature, and toxicity [128]. Other than textile industries, synthetic dyes are also released from leather tanning, printing, paint, food-processing, tannery, cosmetics, and pharmaceutical industries [128,129]. Industrial effluents primarily contain both organic and inorganic products because different types of chemicals are used during various manufacturing and processing stages [127,130]. Thus some heavy metals like chromium (Cr), arsenic (As), copper (Cu), and zinc (Zn) is present in industrially emitted wastewater along with dye compounds [127].

Other than heavy metals and organic dyes, nitroaromatic compounds are also released from leather tanning, explosives, pesticides, fungicides, insecticides, pigment, and drug manufacturing industries are a group of extremely hazardous pollutants which cause detrimental effects to the environment [131]. Nitrophenol compounds fall under this category. These chemicals are considered as “priority pollutants” by several environmental organizations because of their highly soluble and stable nature in aqueous solution [132].

Heavy metal pollutants are inorganic pollutants that can cause severe environmental damage owing to their high solubility in water. Presence of these metals even in trace amounts can have hazardous effects on living organisms. Heavy metal emission into aquatic environment majorly results from tanneries, metal and alloy processing, mining, pesticides, fungicides, pharmaceuticals, rubber and plastics, and electronic device manufacturing industries [133]. Heavy metals containing runoff water from industrial sites is transported downstream where it contaminates other water resources [134]. Heavy metals can also exist naturally in the environment owing to geological cycles and can contaminate water resources through rainfall and other natural calamities [135]. Hexavalent chromium Cr(VI) is one such major pollutant primarily released from leather tanneries [136]. This heavy metal can also be emitted into wastewater from electroplating, anodizing baths, and alloy manufacturing industries [137]. The World Health Organization (WHO) recommends that the maximum permissible Cr(VI) concentration in drinking water sources should be 0.05 mg/L [138]. The trivalent form of chromium (Cr(III)) is an essential micronutrient which can exist in the environment naturally, in contrast to Cr(VI) which is generated from industrial processes [138]. Another hazardous heavy metal which when present in aquatic system can cause critical health hazards to human beings is mercury (Hg). Mercury in its divalent form Hg(II) is discharged into water-bodies because of nuclear fuel production [139], artisanal gold mining [140], hydroelectric industries, cement industries, and are also present in combusted hydrocarbons released from refineries and petrochemical industries [141]. WHO recommends the maximum allowable Hg(II) concentration in drinking-water sources to be 0.002 mg/L [140].

2.3.2. Harmful effects of pollutants:

The pollutants released from industries possess adverse consequences on the ecosystem. Not only they have fatal consequences to human beings, but they equally destroy the ecosystem thereby affecting aquatic plants and organisms. The huge environmental damage caused by industrial effluents is the reason why wastewater treatment and water remediation is of utmost importance in the modern world. Researchers all around the world should focus more on developing appropriate and sustainable materials and methods to combat the hazardous effects of pollutants on our planet.

The effects of toxic textile effluents on aquatic environments are far-reaching and can have significant economic, social, and environmental consequences. Textile dyes like RhB, MB, MO etc. are coloured chemical compounds which when released into water-bodies can form impermeable layers on the water-surface. These layers block the penetration of sunlight to the bottom and severely affect the aquatic organisms [142]. Moreover, the presence of these highly stable non-degradable complex chemicals in the water-bodies results in eutrophication and reduction in the reoxygenation capacity which can disrupt the natural equilibrium of water bodies, leading to increased toxicity levels [143,144]. Most of the textile dyes are carcinogenic and mutagenic in nature [145]. These chemicals exhibit some common toxicity and health hazards in human beings like vomiting tendency, gastrointestinal disorder, diarrhoea, respiratory problems, skin diseases, adverse effects on reproductive system, digestive tract infection, allergies, jaundice, cyanosis, cardiovascular problems, tissue necrosis, neurotoxicity, oxidative stress, and inflammation [146-149].

Like textile dyes, nitroaromatic compounds have severe negative effects on human-bodies. Nitrophenol compounds like 4-nitrophenol (4-NP) have carcinogenic and mutagenic effects on human-bodies [150]. These chemicals can cause hazardous side effects in human body like liver damage, stomach-upset, anaemia, irritation in skin and respiratory system, and fatigue [131,151]. Even for a short-time exposure, 4-NP can cause irritation in mucous membrane accompanied with headache, nauseating feeling, and vomiting [151]. Long-time exposure can have adverse effects on peripheral and central nervous system, and can damage the liver as well as kidney permanently [151]. Presence of these compounds in excess in the environment can cause eutrophication thereby damaging the aquatic ecosystem [152].

Heavy metal poisoning is an extremely serious issue in developing and third-world countries where industrial effluents are constantly emitted into the environment in unrestricted manner thereby contaminating the precious drinking water resources. Heavy metals including lead, chromium, and mercury can accumulate in the tissues of aquatic organisms, leading to long-term health effects and even leads to death. These metal ions exhibit high solvation energy, thus detecting and removing them from aqueous medium is a very challenging task [153]. The strong affinity of Hg towards sulphur groups renders its high toxicity in biological system [153]. Moreover, in aqueous media, Hg undergoes microbiological transformation to form methylmercury which is a lipophilic organic product, thus making Hg prone to biomagnification and bioaccumulation in food chains [154]. Foetus and infants are highly prone to Hg-related toxicity. Children exposed to Hg poisoning show signs of dyslexia and poor brain functions. Exposure to Hg environment can cause trouble in the central nervous system in case of adults. Disruption in motor functioning, and disturbance in verbal memory and attention are some of the symptoms in adults [154]. Hg can also cause other health hazards like cardiovascular, neurological, immunological, genetic, and nephrological disorders and can even cause Alzheimer’s and Parkinson’s disease [154]. The significant solubility and mobility of Cr(VI) in water render its highly toxic nature, thus equally affecting human health and marine life [137]. Cr(VI) has carcinogenic, mutagenic, as well as teratogenic properties because of which it is widely considered as a topmost priority pollutant [155]. Human beings are exposed to Cr(VI) contamination by ingestion, inhalation, and contact though skin [156]. Cr(VI) can lead to several health hazards like allergies, bronchial asthma, ulcers in lungs and respiratory tract, problems in reproductive system along with developmental problems [156]. In case of extreme exposure, Cr(VI) contamination can lead to death. Conversely, Cr(III) is less toxic than Cr(VI), so most Cr(VI) removal methods deal with reduction of Cr from its hexavalent to trivalent form. The pollutants considered for treatment purposes in the present research work include different types of textile dyes (like RhB, MB, MO, RB, CR, and MR), nitrophenol compounds (like 4-NP, 3-NP, and 2-NP) and heavy metals (Cr^{6+} and Hg^{2+}).

The above discussion as collated from literature review clearly signifies why it is critical that chemical manufacturers must take steps to reduce their environmental footprint and adopt sustainable practices to minimize the negative effects of their operations to preserve healthy earth. **Fig. 2.5** depicts the sources of some conventional pollutants present in wastewater and their harmful effects on human-bodies and other living organisms.

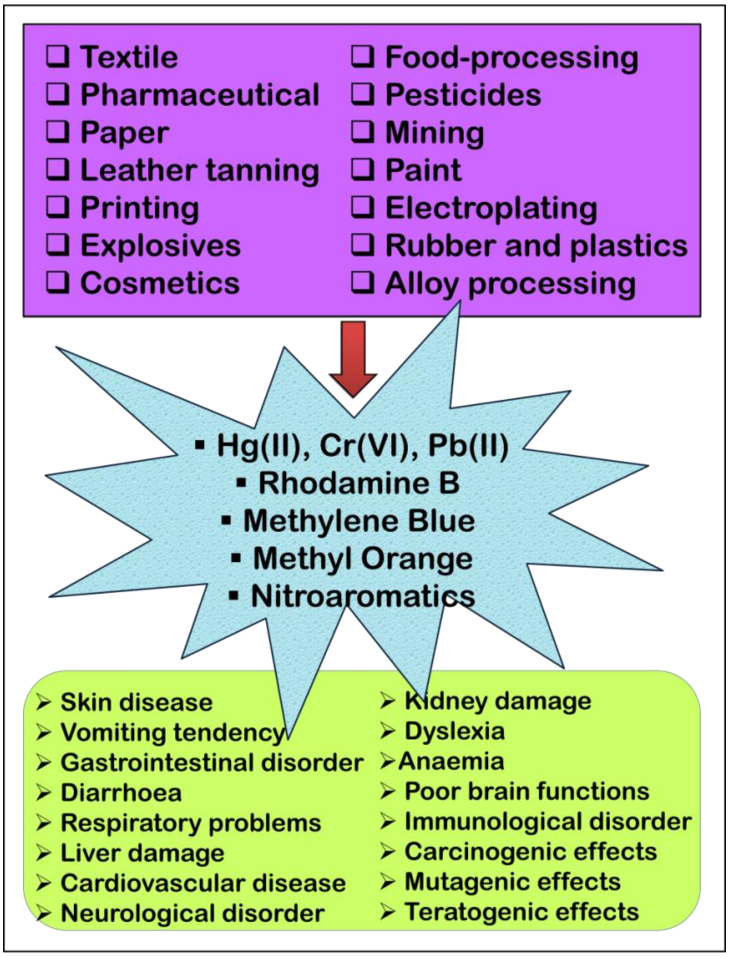

Fig. 2.5: *Sources of some conventional pollutants present in wastewater and their harmful reactions on human-bodies*

2.4. Application of nanomaterials for wastewater remediation:

Nanomaterials exhibit promising efficiency in removing various types of pollutants from industrial effluents. Typical methodologies employed for pollution remediation are adsorption, photocatalysis, and catalytic hydrogenation reactions. All these methods are discussed in details in subsequent chapters (chapter 4). Nanoparticles generally exhibit high surface area because of their nano-dimension, and act as very good adsorbents for different heavy metals as well as textile dyes [157,158]. Carbon nanotubes, graphene oxides, surface-functionalized polymeric materials and electrospun nanofibres also exhibit high removal efficiency in removing heavy metal ions from contaminated water-bodies [159-162]. These nanomaterials are also extensively used for the adsorption of textile dye pollutants like MB, acid red 183, RhB, and MO [163,164]. Additionally, nanoparticles can also perform as highly efficient photocatalyst materials for photocatalytically degrading textile pollutants like RhB, MO, MB, reactive yellow, Congo red and many others [165-168]. Metal and metal oxide nanoparticles are widely used for the reduction of these colored dyes from aqueous medium employing visible or UV radiation source. These nanoparticles can also rapidly reduce pollutants to their non-toxic forms following catalytic hydrogenation reactions without employing any photon irradiation [169,170]. Noble metal nanoparticles like silver (Ag) and palladium (Pd) exhibit exceptionally high efficiency in this regard [171,172]. Co-doping of bimetallic nanoparticles and metal-oxide nanoparticles with other noble or non-noble metals result in fast reduction of nitrophenol and dye compounds by hydrogenation reaction [173,174].

However, nanoparticles have certain disadvantages which need to be addressed:

- Nanoparticles suffer from agglomeration tendency owing to their high surface energy because of which they cannot be reused or recycled, thus decreasing their efficiency significantly. Nanoparticles also show inferior stability and durability during practical usage. Additionally, nanoparticles can be very easily oxidized which again affects the efficiency. Moreover, nanoparticles are non-uniformly dispersed in different solvents, thus separating them from solvents becomes a difficult task.
- Synthesis strategies of most nanoparticles are quite expensive and require costly raw materials and sophisticated instruments. In most cases, the volume of production is very low. Thus employing nanomaterials for practical industrial application still remains a far-fetched idea.
- Due to the relatively recent development of nanotechnology, there is limited understanding of the long-term effects of exposure to nanoparticles on human health along with that on the environment. This lack of knowledge makes it difficult to accurately assess the risks and dangers resulting from their usage.
- Nanoparticles can be difficult to dispose of safely, as they may not degrade easily and can be difficult to separate from other materials. This can expedite accumulation of nanoparticles in landfills, potentially resulting in environmental contamination.
- Nanoparticles can have large band gap energies owing to the effects of quantum confinement. This limits the absorption of light by the nanomaterials in the UV region of the electromagnetic spectrum.

Scientific researchers are continuously working on developing sustainable nanomaterials to combat the above-mentioned disadvantages. The need for metal-free carbon- and nitrogen-based materials becomes quite evident in this scenario. Carbon- and nitrogen-based polymeric materials like graphitic carbon nitride are non-toxic, environment-friendly, sustainable nanomaterials which can be synthesized in large quantity using abundantly available cheap precursors and cost-effective synthesis methods. Moreover, the conjugated layered GCN matrix provides a support for metal nanoparticles in order to prevent their agglomeration. GCN shows amazing capability in wastewater treatment in its pristine, modified, and functionalized forms [103,112,116].

2.5. Application of covalent triazine-based polymers in wastewater remediation:

Triazine-based polymers have been extensively utilized as sensing materials for detecting heavy metal pollutants from industrially-emitted wastewater. Their conjugated framework along with abundant nitrogen lone pairs helps in capturing the metal ions into their triazine cores. Their superior specific surface area and high porosity with large pore volumes also help in the adsorption of different harmful pollutants on their surface. Thus, these polymers act as good adsorbents for the removal of pollutants from water environment. Moreover, owing to their interesting band structure and light harvesting properties, they additionally exhibit good photocatalytic properties in degradation of hazardous textile pollutants.

2.5.1. Triazine-based polymers as heavy metal ions sensors:

Triazine-based polymers have been employed for selectively detecting certain heavy metals present in wastewater which are frequently emitted from factories and plants. These toxic heavy metals include mercury (Hg), iron (Fe), lead (Pb), silver (Ag), copper (Cu) etc. The most conventional method employed for heavy-metal ions detection is fluorescence-based quenching techniques. Shan et al. [24] performed selective sensing of Hg(II) ions from aqueous solution using a triazine-based nitrogen-rich porous polymeric material having a high surface area and π-π conjugated network giving rise to intense fluorescence properties. The as-synthesized polymer showed superior detection efficiency for Hg(II) having concentration around 1 ppm or more in wastewater [24]. Moreover, the presences of other cations like alkali metal ions or alkaline earth metal ions or some other transition metal ions like Cu(II) and Ag(I) did not reveal any considerable impact on the fluorescence quenching of the polymer. This proved the selective detection capability of the as-synthesized polymer material. GCN, a type of triazine-based polymer has been successfully employed for the fluorescence detection of Hg(II) in both its pristine and surface-functionalized forms. Li et al. [175] and Zhuang et al. [18] reported the fluorescence detection of Hg(II) ions from aqueous environment by employing GCN nanosheets. The outstanding fluorescence properties of GCN along with impressive stability rendered the superior sensing capability of toxic Hg(II) ions by GCN nanosheets. Zhuang et al. also achieved a detection limit for Hg(II) ions as low as 0.3 nM [18].

Wang et al. [176] developed a covalent triazine-based framework having fluorescent properties and Hong et al. [177] synthesized a fluorescent conjugated triazine polymer based on anthracene, and both these polymeric materials were utilized for the selective detection of Fe(III) ions from water environment. Fluorescence quenching mechanism was applied for detection of Fe(III) ions. Wang et al. attained a detection limit as low as 0.78 μM, whereas, the polymer as synthesized by Hong et al. showed high selectivity for Fe(III) ions even at a very less concentration of $1.1 \text{ X } 10^{-5}$ M. The improved surface area as well as good stability of the polymers additionally helped in the sensing application. Guo et al. [178] and Tang et al. [179] employed GCN nanosheets for the selective fluorescence detection of Fe(III) ions. The detection limits as obtained by above-mentioned reports were 0.086 μmol/L and 2.06 μM, respectively [178,179]. The ultrathin GCN nanosheets as synthesized by Guo et al. [178] exhibited strong fluorescence properties along with good chemical and photo-stability. Based on these properties, they were capable of designing a novel "on-off-on" fluorescent switching Fe(III) ions sensor. The GCN nanosheets as prepared by Tang et al. possessed a substantial surface area and exhibited interesting optical properties. Moreover, the high-dispersed nature of the GCN sheets in aqueous media made it possible to be applied as a fluorescent probe for the highly sensitive detection of Fe(III) ions.

GCN in its different forms have been employed as an efficient sensor for detecting Cu(II) ions by fluorescence detection technique. Cheng et al. [180] and Tian et al. [181] applied GCN nanosheets as a fluorosensor for the sensing of Cu(II) ions. The detection limit as obtained by Cheng et al. and Tian et al. was 1.2 nM and 0.5 nM, respectively. Both the sensors exhibited high sensitivity and selectivity in detecting Cu(II) ions from aqueous environment. The quenching of the fluorescence intensity of GCN nanosheets in presence of Cu(II) ions occurred due to the photoinduced charge transfer between Cu(II) ions and GCN. Bian et al. [182] and Huang et al. [183] reported that the fluorescence detection of Ag(I) ions by employing GCN. Bian et al. [182] developed GCN nanosheets which acted as a fluorescent probe for Ag(I) detection. The mechanism for detection exhibited high sensitivity and quite rapid analysis time, and detection limit about 27 nM was achieved. Conversely, Huang et al. [183] developed solid nanofilms of GCN which acted as a recyclable and sensitive fluorescent probe for Ag(I) detection. They obtained a detection limit of 20 nM. Zhang et al. [184] developed GCN with nanocones like morphology for the fluorescent-based detection of Pb(II) ions. In contrast to the fluorescence quenching method observed for detecting other heavy metals, interestingly while detecting Pb(II) ions, fluorescence enhancement of GCN occurred. A sensing limit of about 0.0438 $\mu mol \cdot dm^{-3}$ was estimated for Pb(II) ions.

Though substantial amount of researches have already been performed on the fluorescent-based detection of heavy metals by GCN in its pristine, functionalized, and doped forms, however, unfortunately, triazine-based carbon and nitrogen containing polymers other than GCN have not been extensively utilized for heavy metal sensing. Most of the reported triazine-based materials require exclusive functionalization by incorporating different functional groups into the nanostructure, or by doping with different metals and non-metals. For example, most of the reported triazine-based polymers which have been utilized for Hg(II) sensing require additional incorporation of sulphur-based functional groups into the conjugated network. It is a known fact that sulphur can induce toxic effects in human bodies. Similarly, by introducing other metal or non-metal dopants into the polymeric matrix can result in increasing the polymer's toxicity level. Thus, developing a polymeric material only consisting of carbon and nitrogen elements, which have the capability to efficiently function as a sensitive fluorescent probe for detecting heavy metals without the need or requirement of any functionalization or modification, is indeed a challenge.

2.5.2. Triazine-based polymers as adsorbents of hazardous pollutants:

Triazine-based polymers are also employed for efficiently adsorbing hazardous textile dyes, heavy metals, and toxic non-metals from water environment. The large surface area along with abundant surface reactive sites enables these conjugated polymers to function as efficient adsorbents. Moreover, their environment-friendly nature, low cost, easy regeneration abilities, high selectivity towards targeted contaminants, and compatible nature make them favourable candidates as pollutant adsorbents. Afshari et al. were able to synthesize a novel nitrogen-rich covalent organic framework for removing Direct Fast Sarlet-4BS textile dye from wastewater [185]. The impressive specific surface area (328 m^2/g), mesoporous character, and the nitrogen-abundant surface of the triazine-based framework resulted in its large adsorption capacity for the removal of the textile pollutant. Shan et al. applied nitrogen-rich triazine-based polymer for adsorption of Hg(II) heavy metal from contaminated solutions [24]. They achieved a removal efficiency of 99.99% within 20 min of contact time. Coordination chemistry associated with cationic and π-interactions along with high concentration of electronic-charge in the triazine-based polymer resulted in its impressive performance in removal of Hg(II). Liu et al. utilized nitrogen-abundant porous triazine-based polymers for high adsorption of iodine [186]. The high surface area, hierarchical porosity, and presence of plenty of N-H bonds in the triazine-polymeric framework resulted in the efficient uptake of iodine. Thus, triazine-based conjugated polymers exhibit impressive adsorption properties in removing organic dyes, heavy metals, and non-metals.

GCN can function as a very good adsorbent material in its pure and different modified forms for removing toxic pollutants from contaminated water sources. Mohanraj et al. developed water-soluble GCN and used MB dye as an adsorbate model for its removal from water medium [187]. Nearly 80% of dye adsorption efficiency was achieved without the requirement of any additional physio-chemical stimulation. Yousefi et al. synthesized oxidized GCN nanosheets which were able to efficiently adsorb several popular organic dyes like MB, MG, RB, RhB, MO, and antibiotic drug tetracycline (TC) [188]. The removal performance of modified GCN was comparable with conventional adsorbents like graphene and carbon-based porous materials. Xiao et al. published a very important report on removing different cationic and anionic heavy metals from contaminated water-sources by GCN nanosheets following adsorption technology [189]. Toxic cations like Cd(II) and Pb(II) and anion like Cr(VI) were effectively adsorbed by GCN nanosheets having a substantial surface area of 111.2 m^2/g. The nitrogen-rich surface of GCN along with the tri-s-triazine blocks was responsible for the superior adsorption of heavy metals. Peng et al. reported the adsorption of Hg(II) and Pb(II) cations by nanosheets like structures of boron doped carbon nitride [190]. High removal efficiency was achieved for both the heavy metal pollutants. Availability of literature on the anionic heavy metal adsorption by GCN is very much limited. Access to one such publication by Georgiou et al. [191] is one of the very few landmarks for anion removal by GCN. They developed and investigated a hybrid nanomaterial based on GCN by decorating the surface of GCN with Fe nanoparticles. This nano-hybrid was implemented for the uptake of As(III) ions and an adsorption capacity of 76.5 mg/g was achieved. This value was higher than the adsorptive removal capacities of most reported conventional carbonaceous materials.

Though GCN and its derivatives have been extensively employed as high-functioning adsorbent materials for the uptake and removal of various types of hazardous pollutants like textile dyes and heavy metals (both cationic and anionic), however, there are no such reports on the adsorption of non-metals like fluoride ions or others. Introduction of appropriate dopants into GCN matrix can lead to surface modification which eventually enhances the prospective of GCN to be utilized as an adsorbent material for up-taking of non-metals. The choice of dopants in this regard remains a challenging task till date.

Though adsorption technology is a facile, economic, and straight-forward method for removing toxic compounds from polluted water-bodies, however, this method suffers from several disadvantages which tend to restrict their application in practical scenarios. Few of such limitations arise from the time-consuming procedure, high requirement of adsorbent dosage to achieve maximum efficiency of adsorption, weak specificity and precision for targeted pollutants, and generation of waste products after completion of the process. Moreover, the used adsorbents are required to be repeatedly charged to continue the adsorption process, which results in difficulty in reusing and recycling of the adsorbents, along with increase in the overall cost of the procedure [192]. Additionally, while conducting adsorption experiments for removal of pollutants, several parameters are required to be considered because these parameters have huge impacts on the overall performance of the adsorbent. These include initial pollutant concentration, dosage of adsorbent, pH, temperature, contact time between adsorbent and adsorbate, stirring speed, and existence of additional cations and anions in the aqueous media [192,193]. To combat these limitations, new methodologies are being developed in recent times for the relatively fast, efficient and economical removal of contaminants from wastewater sources.

2.5.3. Triazine-based polymers as catalysts for degradation of hazardous pollutants:

Advanced oxidation processes (AOPs) are newly developed techniques which are regarded as efficient methodologies to remove organic pollutants from water environment. This particular class of oxidation technique is comprised of various other methodologies like heterogeneous photocatalysis, electrocatalysis, Fenton-like reactions, ozonation, sonolysis and others. All of these processes possess the capability of breaking-down organic pollutants to non-toxic CO_2 and H_2O as final products by primarily generating reactive oxygen species (ROS). For a particular material to function as a promising catalyst and to take part in AOPs, it should possess appropriate semiconducting band gap, capability to utilize and harvest visible-light energy, proper band edge potentials for carrying out necessary redox reactions, and should be able to prevent the recombination of photogenerated charge-carriers like electrons and holes. Triazine-based polymers, especially GCN, luckily possess some of these features because of which they have been widely applied for degrading toxic contaminants by AOPs.

Xu et al. employed a novel covalent organic polymer for catalytically degrading both acidic (MO) and basic (MB, RhB) dyes [19]. The catalytic investigations were performed under LED light or natural illumination in presence of H_2O_2. Scavenging experiments are generally conducted to identify the reactive radicals participating in the catalytic degradation of dyes. In this case, hydroxyl radicals (•OH) and photogenerated holes (h^+) were revealed as the main active species for dye degradation. Du et al. developed a novel triazine-based framework rich in catalytic-active sites, which also exhibited impressive light absorption capability along with good thermal and light stability. The material effectively degraded a variety of conventional pollutants (MO, CR, MB, and RhB) emitted from textile industries [194]. In this case, superoxide radicals ($•O_2^-$) were established as the major reactive species. Geng et al. designed donor-acceptor covalent triazine-based polymers and employed them for the visible-light induced reduction of Cr(VI) heavy metal [195]. To ameliorate the photocatalytic activity, hole trapping agent isopropanol (IPA) was additionally used. Photogenerated electrons were the primary contributor in reducing hexavalent Cr to its non-toxic trivalent form.

The unique structural and interesting opto-electronic features of GCN enable its exclusive utilization in photocatalytic dye degradation. The GCN motif is inherently functionalized with amine groups which are present as structural defects as a result of synthesis conditions involving incomplete polymerization and polycondensation reaction [41]. Zhu et al. suggested that this defect-rich and nitrogen-abundant conjugated structure of GCN induces electron delocalization on its surface, which renders the Lewis base characteristics of GCN [41]. The electron-rich surface of GCN, along with its thermally and chemically stable nature is the major driving forces behind the excellent catalytic activity of GCN. Additionally, GCN possesses a wide band gap corresponding to the visible-spectrum, and suitable CB and VB potentials necessary for the redox reactions to take place in order to carry out the catalytic reduction of targeted dye pollutants. However, as-discussed earlier, bulk GCN structures have lower surface area, low porosity, poor quantum yield, inferior photon-harvesting and absorption property, high probability of recombination of photogenerated electrons and holes, and they have agglomerated sheets clustered together resulting in inefficient utilization of the surface [196]. All these major drawbacks can be amended by different simple ways: i) exfoliation of bulk sheets to form nanosheets of GCN to improve the surface area, ii) tuning of the conventional sheet-like structure of GCN to form different other morphologies in different dimensions (nanofibres, nanorods, nanospheres, quantum dots, etc.), iii) modification of the band gap as well as light-harvesting property of GCN by incorporating different types of dopant atoms into its matrix, and iv) designing of different types of GCN-based heterojunctions and nanocomposites with other appropriate semiconducting materials to modulate the band edge potentials. All these modifications eventually result in enhancement of the catalytic property of GCN for application in treatment of polluted water.

There are innumerable reports on the photo-degradation of organic textile dyes by GCN in its pristine and modified forms. Kumar et al. developed few-layered porous environmental-friendly GCN exhibiting high specific surface area (76 m^2/g) and uniformly distributed pores on the layered sheets, which helped in the visible-light assisted decolouration of RhB dye [197]. Cui et al. reported the photodegradation of RhB dye under visible-light irradiation by a hollow-spherical morphology of GCN [198]. Wang et al. developed porous nanosheets of GCN having increased number of catalytic surface-active sites, cross-plane diffusion channels for facile transport of mass and charge, and enhanced charge separation efficiency, which helped in the complete degradation of RhB [199]. Pawar et al. developed one-dimensional micro-rods like morphology of GCN having nanoporous features [200]. Changing the morphology from 2-D to 1-D resulted in improved carrier lifetime, increased band gap due to quantum confinement, increase in surface-active sites, and improved electron-hole separation resulting in better charge transport and carrier mobility. These modifications ultimately resulted in the enhancement of photodegradation ability of GCN in removing MB dye.

Doping with non-metal elements has proved to considerably boost the photocatalytic efficiency of GCN by tuning its electronic band structure and narrowing its optical band gap. There are several literatures in this regard where GCN has been doped with oxygen [201], nitrogen [202], carbon [203], and sulphur dopants [204]. In all these cases, the doped samples exhibited many-fold enhancement in degradation efficiency and degradation rate compared to un-doped GCN. There are also many research works on the enhanced photocatalytic activity of GCN compared to its pristine form when decorated with various metal dopants, especially transition metals and noble metals. Cu-doped GCN are primarily employed for the photo-fenton like reactions in degradation of pollutants. Zhu et al. decorated GCN with Cu(II) atoms such that the sample contained abundant Cu-N$_x$ species, which helped in the rapid degradation of RhB, MO, and MB dyes [205]. Besides Cu, there are several reports on doping of GCN with other metal atoms like Fe [106], Co [206], and noble-metals like Ag [207] for successful utilization in reduction of organic dye contaminants like RhB, Eosin B, MB, CV, and RB.

Fabricating binary and tertiary heterojunctions of GCN with other suitable semiconducting materials have also proved to significantly improve the photodegradation capability of GCN. The formation of heterojunctions enhances the dissociation of photogenerated charges carriers by preventing their recombination [208]. Paul et al. developed a perovskite-based type 2 heterojunction of GCN and employed the material for photoreduction of Eosin B dye [209]. The synergistic effect between the two individual materials helped in enhancing the photocatalytic performance of the composite material. It is also to be noted that GCN can function as a potential catalyst material for reduction of hexavalent Cr heavy metal. Wu et al. supported Pt nanocubes uniformly on GCN surface and the nanocomposite was used as an efficient photocatalytic material for visible-light assisted reduction of Cr(VI) to Cr(III) [210]. Formic acid (FA) acted as a reducing agent to accelerate the catalytic activity. The interesting reports along with the experimental conditions and calculated rate constant values are listed in a tabular form and provided in **Table 2.2**.

Table 2.2: Application of pristine, functionalized, and modified GCN samples in the catalytic degradation of dye pollutants

Material	**Pollu-tants**	**Light source**	**Conc. of Pollutants**	**Amount of Catalyst**	**Rate constant (min^{-1})**	**Active Radicals**	**Ref.**
GCN	RhB	Visible	10 ppm	10 mg/100 mL	0.0029	-----------	Paul et al. [211]
	MB				0.0076		
	MO				0.0008		
GCN	MB	Simulated solar radiation	10 ppm	10 mg/100 mL	0.0081	$\bullet O_2^{-}$, h^{+}	Paul et al. [212]
Porous GCN	RhB	Visible	50 mL, 10 mg/L	25 mg	-----------	$\bullet OH$, $\bullet O_2^{-}$	Kumar et al. [197]
Mesoporous GCN	RhB, MO, MB	Visible and UV	10 mg/L	25 mg	-----------	-----------	Erdogan et al. [213]
Hollow-spherical GCN	RhB	Visible	10^{-5} mol/L	40 mg	-----------	-----------	Cui et al. [198]

Porous GCN nanosheet	RhB	Visible	30 mL, 10 mg/L	10 mg	0.217	•O_2^-, h^+	Wang et al. [199]
Folded porous GCN	MB	Visible	100 mL, 10 mg/L	100 mg	0.0216	•O_2^-	Li et al. [214]
Porous micro-rod like GCN	MB	Visible	250 mL/ 3.2 mg/L	50 mg	0.0156	•O_2^-, h^+	Pawar et al. [200]
Water-dispersible GCN	MB	Visible	50 mL, 10 ppm	10 mg	0.0251	-----------	Nguyen et al. [22]
Oxygen-doped GCN	RhB	Visible	100 mL, 10^{-5} mol/L	50 mg	0.249	h^+	Wei et al. [201]
Nitrogen-doped GCN	RhB	Visible	50 mL, 20 mg/L	50 mg	-----------	•O_2^-, h^+	Qi et al. [202]
Carbon-doped GCN	RhB	Visible	50 mL, 10 mg/L	50 mg	0.042	•OH, •O_2^-	Wang et al. [203]
Sulphur-doped GCN	AO7	Ultra-violet A	150 mL, 25 mg/L	10 mg	0.113	-----------	Praus et al. [204]
Cu-doped GCN	RhB, MB, MO	Dark condition	50 mL, 10 mg/L H_2O_2 conc.: 1.5 mL	10 mg	-----------	•OH, •O_2^-, $^1O_2$	Zhu et al. [205]
Cu-doped GCN	MO	Visible	100 mL, 10 mg/L	50 mg	-----------	•O_2^-, h^+	Le et al. [215]
Fe-doped GCN	RhB	Sunlight	250 mL, 5 mg/L	100 mg	-----------	•OH, •O_2^-, h^+	Tonda et al. [106]
Co-doped GCN	Eosin B	Visible	60 mL, 10^{-5} M	15 mg	0.0111	-----------	Das et al. [206]
Ag-doped GCN	MB	Visible	100 mL, 10 ppm	10 mg	0.0275	•O_2^-	Paul et al. [207]
	CV				0.01237		
	RB				0.01247		
GCN isotype	MB	Visible	50 ppm	20 mg/L	0.0799	•O_2^-, h^+	Sundaram et al. [208]
$CsPbBrCl_2$/GCN	Eosin B	Visible	40 mL, 10^{-5} M	20 mg	0.00967	•OH, •O_2^-, h^+	Paul et al. [209]
Ag/ZnO/S-GCN	MB	Sunlight	100 mL, 10 mg/L	10 mg	0.023	•OH, •O_2^-	Iqbal et al. [216]
Pt-doped GCN	Cr(VI)	Visible	3 mL, 50 mmol/L $K_2Cr_2O_7$, 3 mL FA	0.3 mL, 2.0 mg/mL	0.0224	h^+, e^-	Wu et al. [210]

Photocatalytic mechanism is undoubtedly a very efficient wastewater remediation technology to degrade toxic organic pollutants. However, this method can sometimes become expensive due to the requirement of costly lamp sources (like Xenon or Hg lamp). Moreover, the design of an efficient photocatalytic reactor is quite expensive. Additionally, this technique requires the development of materials possessing some unique features like suitable band gap, band edge potentials, semiconducting properties, light absorption properties, efficient charge separation properties, quantum yield, and others to mention a few. This narrows down the possibility of utilization of conventional low-cost materials in photocatalytic applications. Though GCN has been substantially utilized as a photocatalyst material in its pristine metal-free form, however, in order to fulfil the above-mentioned characteristics and to considerably improve the performance efficiency, extensive doping with toxic metals and non-metals has been performed. This can eventually lead to leaching of metals into water-bodies, thereby, resulting in possibility of secondary contamination. Moreover, synthesis strategies that deal with structural modification of GCN are till now quite exorbitant and require high-cost facilities. Thus, it is of immense necessity to develop facile and straight-forward synthesis techniques to achieve metal-free GCN with enhanced properties and improved catalytic activity without any metal or non-metal incorporation.

2.5.4. Triazine-based polymers for degradation of hazardous pollutants by catalytic hydrogenation technique:

The short-comings of adsorption and photocatalysis procedures have motivated next generation global researchers to develop facile and rapid degradation techniques for removing hazardous pollutants from contaminated water resources. Catalytic hydrogenation is one such recently developed technique, which besides being cost-effective, is a very efficient and rapid method to achieve complete reduction of conventional pollutants. In this method, beside the catalyst, an additional reducing agent (like sodium borohydride-$NaBH_4$) is required to initiate the catalytic reduction mechanism. Interestingly, unlike photocatalysis, this procedure does not require any irradiation sources, and the whole reduction process is executed only in presence of an appropriate catalyst and $NaBH_4$ at room temperature. Thus, the overall cost of the mechanism is largely reduced. The basic requirement of this procedure is the facile transfer of electrons from $NaBH_4$ to the pollutants via the nanocatalyst material. The more feasible the relay of electrons, higher is the reduction efficiency. Till date, mostly noble metal nanoparticles have been utilized regarding this purpose because they possess large surface area owing to which both $NaBH_4$ and the target contaminants can readily adsorb on their surface. This in turn facilitates the process of electron relay between these molecules. However, as discussed previously, noble-metal nanoparticles are not only costly, but they also suffer from inferior stability arising from their tendency to agglomerate. This restricts the usage of noble-metal nanoparticles in real-life water treatment procedures. These complications have resulted in the immobilization of metal nanoparticles on carbon- and nitrogen- based supports and other polymeric matrices which are rich in -OH, -COOH, or -NH_2 functional groups. Anchoring metal nanoparticles on polymeric supports not only increases their stability and reduces their aggregation tendency, but also prevents their leaching into the environment thereby decreasing the chances of secondary contamination. Triazine-based polymers including GCN provide excellent support to metal nanoparticles owing to their structural and functional motif.

Rezaei et al. used a covalent organic polymer for supporting Ag nanoparticles on its porous surface and applied the as-synthesized material for the catalytically reducing nitroaromatic compounds like 4-NP, 2-NP, 3-nitroaniline, and 4-nitroaniline [217]. Very less amount (about 5 mg) of the sample could reduce 3 mL of 4-NP solution having concentration of 10^{-4} mol/L in presence of 600 μL of freshly prepared $NaBH_4$ (concentration of stock: 10^{-1} mol/L) 5 min. The rate constant value obtained was 0.0181 s^{-1}. Similarly, Subodh et al. decorated Ag nanoparticles on triazine-based covalent microspheres for reducing 4-NP, 2,4-dinitrophenol (2,4-DNP), and 2,4,6-trinitrophenol (picric acid) [218]. The experimental conditions were: 2 mg catalyst, 4 mL of pollutant containing solution having concentration of 25 mM, and $NaBH_4$ (about 100 equivalents to the pollutants). Under these reaction conditions, 4-NP was degraded within 120 sec (rate constant: 0.0226 s^{-1}), 2,4-DNP was reduced within 200 sec (rate constant: 0.0191 s^{-1}), and picric acid achieved complete reduction within 180 sec (rate constant: 0.0130 s^{-1}).

GCN in its modified forms have been largely used for catalytic hydrogenation reactions of different pollutants. In most cases, GCN has been decorated with noble-metal nanoparticles like Ag, Au, and Pd, and sometimes bimetallic doping has also been accomplished to execute the $NaBH_4$-induced reduction of contaminants. There are also plenty of reports on the designing of several heterojunctions of GCN and anchoring nanoparticles on those heterojunctions to enhance the pollutant reduction capability of GCN.

Wang et al. immobilized Ag nanoparticles on GCN nanosheets, Nguyen et al. synthesized a nanocomposite of Au decorated on GCN, and Gu et al. developed a well-connected interface between Pd nanosheets and GCN nanosheets, and all these samples were utilized for the rapid reduction of toxic nitrophenol compounds to non-toxic aminophenol [219-221]. Zhou et al. incorporated Au nanoparticles on GCN [222], Kumar et al. synthesized nitrogen-rich porous nanosheets of GCN which helped in the strong immobilization of Pd nanoparticles on the GCN surface [223] Saravanakumar et al. decorated GCN nanosheets with Ag, Au, and Pd

[224], and all of these above-mentioned samples were employed for ultrafast degradation of various pollutants like 4-NP MR, MB, and RhB. Fang et al. loaded GCN ultrathin nanosheets with bimetallic Pd/Au nanoparticles which showed excellent performance in reducing 4-nitrophenol [225]. The Pd/Au-GCN sample exhibited much higher reduction efficiency than either Pd/GCN or Au/GCN hybrid.

Besides noble-metal nanoparticles, transition metals like Cu, Co, and Ni have been embedded into the GCN matrix and applied for $NaBH_4$-assisted catalytic hydrogenation of toxic pollutants [226,227,47]. Huang et al. reported the synthesis of Cu nanoparticles decorated GCN with large number of catalytic active sites for the efficient reduction of 4-NP [226]. Within the nanocomposite structure, Cu nanoparticles promoted separation of charges at the metal-semiconductor interface, whereas, GCN acted as a strong support for the Cu atoms, thereby improving the catalytic activity many-folds.

Fabrication of GCN-based heterostructures has proved to significantly enhance the reduction efficiency in degrading wastewater pollutants [228-234]. Aditya et al. reported the homogeneous dispersion of both CuO and Cu_2O on GCN nanosheets and employed the samples for catalytically reducing 4-NP to 4-AP [228]. Similarly, Mitra et al. designed a nanocomposite with Cu_2O and GCN which was able to efficiently reduce MO dye to the non-toxic reduced products: *N*,*N′*-dimethyl-*p*-phenylenediamine and sodium salt of sulphanilic acid [229]. Kumar et al. fabricated a complex heterostructure or nano-assembly comprising of biochar, GCN, $Bi_2O_2CO_3$, and $CoFe_2O_4$ [230], whereas, Ayodhya et al. developed a heterojunction of GCN and CdS [231], and both these samples were employed for the efficient conversion of 4-NP to 4-AP. Due to the large number of existing reports concerning this research area, the most important results are provided in a tabular form shown in **Table 2.3**.

Table 2.3: Application of pristine, functionalized, and modified GCN samples in the $NaBH_4$-assisted catalytic hydrogenation of dye pollutants.

Catalyst	**Pollutant Conc.**	**$NaBH_4$ Conc.**	**Catalyst Dosage (mg)**	**Time (min)**	**Apparent Rate Constant (min^{-1})**	**Ref.**
Ag/GCN	4-NP, $1.03 x 10^{-4}$ M (150 mL)	0.3 M (3 mL)	15	14	0.186	Wang et al. [219]
Au-GCN	2-NP, 3-NP, 4-NP, 10 mM (40 μL)	0.1 M (0.04-0.16 mL)	2	10	0.9	Nguyen et al. [220]
Pd/GCN	4-NP, 0.145	1 M (50 μL)	0.0000125	6	0.76	Gu et al.

	mM (2.5 mL)					[221]
Au-GCN	4-NP, 0.1 mM (2 mL)	0.1 M (1 mL)	0.0255	3.33	0.9726	Zhou et al. [222]
Pd/nitrogen-rich GCN	4-NP [0.2 mM (0.2 mL)]	0.4 M (0.5 mL)	0.02	1	0.2526	Kumar et al. [223]
	MR [0.02 mM (0.2 mL)]			2	0.1266	
	MB [0.02 mM (0.2 mL)]			1.33	0.1224	
	RhB [0.02 mM (0.2 mL)]			1	0.2268	
Ag, Au, Pd-GCN	4-NP, 1 mM	0.1 M	5	16 (Ag)	0.301 (Ag)	Saravanakumar et al. [224]
				6 (Au)	0.649 (Au)	
				4 (Pd)	1.141 (Pd)	
Pd/Au@GCN-N	4-NP, 14.37 mM (1 mL)	1.43 M (1 mL)	0.25	5	0.7907	Fang et al. [225]
Au@S-GCN	4-NP, 1 mM (10 mL)	1 mM (1 mL)	0.5	5	0.751	Balakumar et al. [234]
Cu/GCN	4-NP, 0.01 M (40 μL)	0.5 M (80 μL)	0.05	6	1.116	Huang et al. [226]
Cu/GCN	4-NP, 0.01 M (0.05 mL)	0.5 M (2 mL)	0.5	7	0.103	Nisha et al. [227]
Ni-doped GCN	MO, 0.1 mM	0.1 M	1	4	1.4219	Das et al. [47]
Copper Oxide-GCN	4-NP, $5x10^{-5}$ M (3 mL)	1.6 mM (3 mL)	1	4	1.19	Aditya et al. [228]
Cu_2O/GCN	MO, 0.1 mM (3 mL)	$2x10^{-3}$ mM (0.3 mL)	1	4.7	1.3	Mitra et al. [229]
Ag-Cu_xO-GCN	4-NP, 100 ppm (1.5 mL)	0.01 M (1.5 mL)	0.05	4	0.334	Verma et al. [232]
Au/polydopamine-decorated GCN	2-NP, 0.2 mM (15 mL)	10, 20, 40, 60, 80 mM (15 mL)	5	1	2.904	Qin et al. [233]
	4-NP, 0.2 mM (15 mL)			1	3.084	
	MO, 0.2 mM (15 mL)			0.67	5.298	
	CR, 0.2 mM (15 mL)			3	1.17	
Biochar-GCN/$Bi_2O_2CO_3/CoFe_2O_4$	4-NP, 10 mM (2 mL)	0.05 M (20 mL)	----	5	0.783	Kumar et al. [230]
GCN/CdS	4-NP, 0.1 mM (1 mL)	10 mM (1 mL)	10 mg/L	18	0.0388	Ayodhya et al. [231]

As evident from the review of the past works, most existing reports on catalytic hydrogenation of organic non-degradable pollutants are based on incorporation of noble-metal nanoparticles in triazine-based polymeric matrices. Also, a large number of reports are based on the fabrication of complex heterostructures which requires expensive and sophisticated synthesis techniques and instrumentations. Moreover, the yield of product is so less in these cases that the catalysts cannot be implemented in practical scenarios involving industrial applications. Researchers should take into account these limitations and try to develop cost-effective nanocatalysts with high yield for utilization in catalytic reduction of harmful contaminants. Researchers should also take initiative in incorporating non-noble-metal nanoparticles like transition metals in the GCN framework for reducing the cost of the application process.

2.6. Limitations of GCN in practical environmental applications:

A sizable amount of past researches and on-going investigations are described in various publications. However, there are some research gaps which need to be addressed to establish GCN as one of the leading nanomaterials in the area of wastewater and environmental remediation. Several strategies have been performed to increase the surface area of GCN, improve its porosity, tune its band gap to appropriate range, increase its light absorption and harvesting properties, and improve carrier mobility. Unfortunately, most of these strategies and experimental designs are highly sophisticated and complicated. Major drawback lies in the fact that these processes lack scalability, sustainability, and environment-friendly green synthesis protocol of GCN [235]. Though such advanced modification techniques involving nano-engineering of GCN can result in enhancement of its properties and performance, but these processes are not feasible in practical industrial situations. Very commonly, GCN is doped with noble metals like Pd, Pt, Au or Ag to improve its hydrogen evolution reaction rates and other catalytic properties. Nevertheless, noble metals are highly expensive for usage in practical scenarios. Hence the cost-effective nature of GCN is compromised. Researchers must shift their focus towards non-noble metals like Cu, Co or Ni to function as co-catalysts in photocatalytic experiments. Much effort should be given to design metal-free pristine GCN nanosheets with enhanced properties so that complicated fabrication of nanocomposites or heterojunctions of GCN can be avoided. Moreover, decorating GCN with metal particles sometimes leads to leaching of the metal nanoparticles to the environment thus causing secondary contamination. This may negatively impact the application of GCN in environmental remediation.

Very few reports are found on actual implementation of GCN in industrial application, particularly on effluent treatment. Experimental set-ups in laboratories use high quality water and sacrificial agents while conducting experiments with GCN. This is however not the case in real life scenario, where polluted water discharged directly from industries is required to be treated. Hence, it is difficult in obtaining proper results for performance analysis [235]. Thus attempt should be made to improve the capability of GCN to be employed in practical situations. Researches should be conducted maintaining a balance between strengthening the efficiency and developing sustainable synthesis techniques besides intensive studying of the material’s fundamental properties [235].

2.7. Research Gaps:

The extensive research and review on existing literature reports concerning the development of triazine-based polymeric nanomaterials for application in wastewater remediation has helped us to identify the research gaps prevailing in this particular area of research.

☐ Till now, most of the existing reports on triazine-based polymers for Hg(II) ion sensing require the introduction of sulphur-based groups or sulphur-mediated fuctionalizations owing to the high affinity of Hg(II) towards sulphur. However, sulphur is quite toxic to human beings. Such modifications induce toxic effects in the polymeric materials; hence, introduction of sulphur groups can decrease the practical feasibility of the materials for environmental application. Moreover, there are very few reports on the inherent detection capability of sulphur-free triazine-based polymers without any modifications for detecting Hg(II) heavy metals from aqueous medium.

☐ Pristine GCN is not yet quite developed for the fenton-like photocatalytic degradation of toxic organic textile pollutants and heavy metal like Cr(VI). Most reports till date try to modify the surface features of GCN along with its opto-electronic properties by extensive doping and fabrication of sophisticated heterostructures or composites. These procedures not only result in increase in the cost of materials, but also the very poor yield during synthesis limits their large-scale practical applications.

☐ Currently, most published works on reduction of harmful nitroaromatic compounds and textile pollutants employing catalytic hydrogenation techniques by GCN are based on incorporating highly expensive noble-metal nanoparticles into the GCN framework. This again compromises the overall cost of the catalyst and makes it unsuitable for realistic applications.

☐ Most importantly, there are not many significant reports which have performed substantial theoretical calculations by employing first principles density functional theory (DFT) to provide circumstantial insights into the fundamental reaction mechanisms involving both photocatalytic and catalytic hydrogenation techniques in removing wastewater contaminants. To understand the basic concept regarding how pollutants are reduced to their non-toxic final products during catalysis, elaborate theoretical studies are required to be performed at the atomic level. This is essential to understand the reaction chains and also to provide a clear picture to future researchers for further conceptual analysis.

☐ Along with theoretical analysis, mathematical and statistical analysis is equally important to validate the catalytic model's efficiency. There are currently only some sporadic accounts on the application of statistical models like response surface methodology to optimize the catalytic parameters and comprehend the effect of interaction between different parameters on catalytic efficiency.

Summarization of literature survey:

A detailed overview of carbon- and nitrogen-based polymeric materials with emphasis on GCN has been given in this chapter. Various reports on synthesis techniques of triazine-based polymers in their pristine and modified forms along with their many interesting properties have been summarised and discussed. A separate section has been provided to discuss about the different types of pollutants present in water, their harmful effects on human beings, and their treatment procedures. Extensive literature survey has been done to summarise the application of triazine-based materials in remediation of pollutant-containing contaminated water-bodies by adsorption and catalysis techniques. Finally, the research gaps in the relevant fields of application have been identified to accordingly formulate the research problem presented in this dissertation.

CHAPTER 3:

OBJECTIVES AND SCOPE

Objectives and Scope

3.1. Objectives of the research topic:

The objectives of the proposed research work are to develop novel synthetic strategies for carbon and nitrogen containing triazine-based conjugated polymeric nanomaterials, modification of the structural and surface characteristics of the nanomaterials, and subsequent impregnation of non-noble metal dopants into the polymeric frameworks for enhancement of the properties of the basic polymeric materials, and subsequently to investigate some performance studies regarding their applications for removal of certain specific pollutants like textile dyes, nitrophenol compounds and heavy metals from aquatic system.

In order to achieve the target objectives, the following scopes are considered:

3.2. Scope of the research topic:

- Development of novel synthetic strategies of carbon and nitrogen containing conjugated covalent organic polymers having triazine units as the building blocks.
- Modification of established synthesis methods for enhancement of specific surface area along with porosity of these nanomaterials to achieve improved properties for application optimization.
- Incorporation of various non-noble metals (preferably transition metals) into the triazine-based conjugated polymeric matrices for enhancement of intrinsic properties.
- Utilisation of the as-synthesized polymeric nanomaterials for detection and sensing of heavy metal ions like Hg^{2+} dissolved in aquatic system by fluorescence detection technique.
- Application of the triazine-based nanomaterials in their pristine and modified forms for accomplishing removal and degradation of various toxic organic and inorganic pollutants like textile dyes, nitrophenol compounds, and heavy metal Cr(VI) from contaminated water by adsorption, photocatalysis, and catalytic hydrogenation mechanisms.
- Determination of rate limiting factors by experimentally varying the parameters (like dosage, initial pollutant concentration, pH etc.) that directly influence the removal and degradation activity of the nanomaterials.
- Application of statistical modelling involving various factors to achieve optimization of the performance efficiency of the nanomaterials.

- Exhaustive theoretical investigation following first principles calculations to reveal the fundamental reaction mechanisms occurring at atomic level during the catalytic degradation of some targeted pollutants.

CHAPTER 4:

CHARACTERIZATION TOOLS AND METHODOLOGIES

Characterization Tools and Methodologies

This chapter scripted a brief description on the various instruments and equipment employed to carry out the synthesis of the triazine-based nanomaterials. The tools and devices used for analysing the phase formation of the materials, their structural variations, surface properties, compositional studies, chemical nature, optical properties and others are also described in this chapter. Finally, the different methodologies implemented to explore the applications of the as-synthesized nanomaterials in wastewater purification, has been discussed in this section.

4.1. Equipment required during synthesis procedures:

4.1.1. Equipment for synthesis of triazine-based polymeric nanomaterial:

In the present work, triazine-based polymeric nanomaterial has been primarily synthesized by hydrothermal/solvothermal process. The synthesis procedure was executed in an autoclave arrangement shown in **Fig. 4.1(a)**. An autoclave reactor is an apparatus designed for heating an aqueous solution of organic solvents at a high temperature, preferably above the solvents' boiling point, and at a high pressure, higher than the normal atmospheric pressure. While performing the hydrothermal synthesis of a given material, the autoclave should always be maintained at a maximum temperature below 240 °C, while the working pressure should be maintained at less than 3 MPa. The reactor consists of a cylindrical shaped jacket made of stainless steel which is tightly fitted with a screw cap. Prior to the initiation of the hydrothermal reaction, this screw cap is to be tightly fitted to ensure that the autoclave system can withstand the high-pressure generated within the steel jacket during the reaction. There is a cylindrical container made of Teflon fitted with a Teflon cap inside the steel jacket chamber. The given solution undergoing hydrothermal treatment is placed inside this container, which functions as the reaction chamber. The Teflon-made cylinder is placed inside the stainless steel jacket, and fitted with the screw cap before the initiation of the synthesis procedure. The Teflon cylinder is generally available in different capacities viz. 50 mL, 100 mL etc. It is to be strictly followed that maximum 80 % of the total volume should be filled with the solution. The autoclave is finally placed inside an oven pre-heated to the requisite temperature.

Since the preferred reaction temperature required to carry out hydro (solvo) thermal reactions should stay within the limit of 240 °C, hence a low temperature oven is sufficient to conduct the experiment. The image of the oven is shown in **Fig. 4.1(b)**. An electronic temperature controller is used to control the oven's temperature with an accuracy of ± 0.5 °C. Ovens are also employed to dry samples after synthesis and washing.

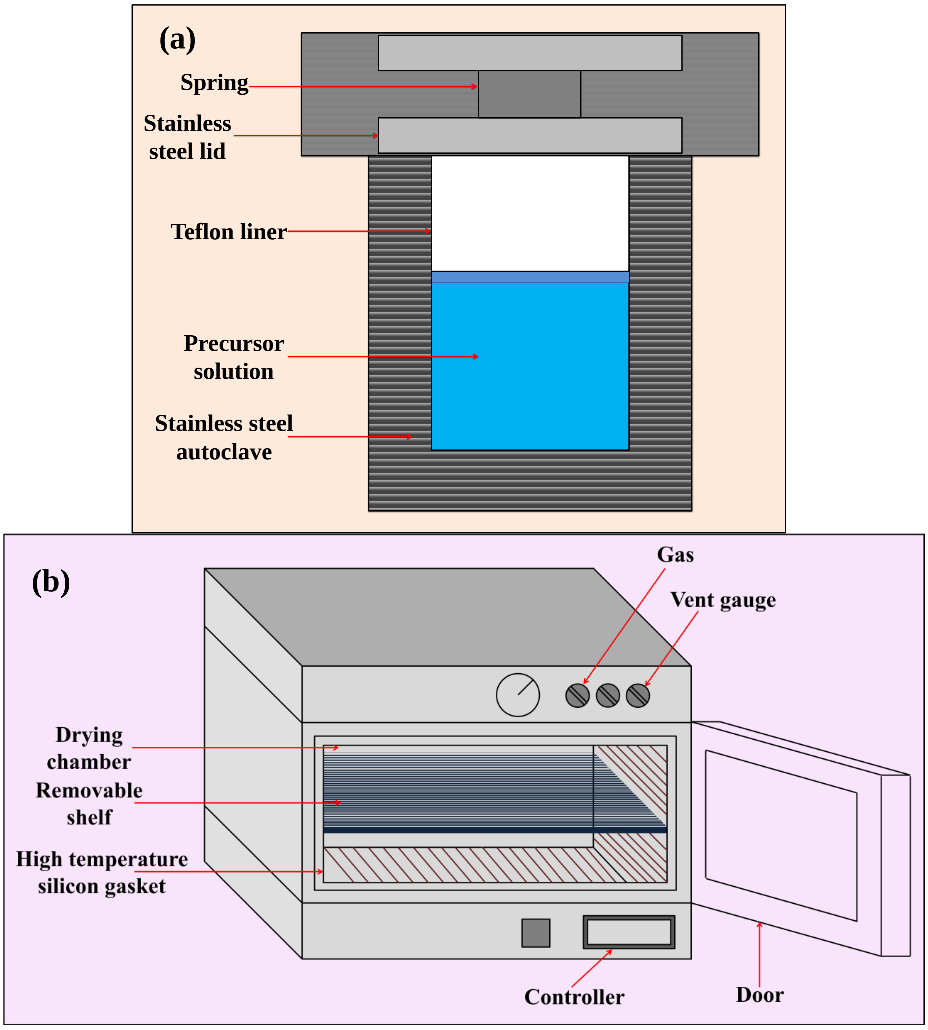

***Fig. 4.1**: Schematic depiction of (a) hydrothermal synthesis using a teflon-lined autoclave, and (b) an oven*

4.1.2. Equipment for synthesis of GCN:

GCN has been synthesized by thermal condensation method carried out in a high temperature muffle furnace or box furnace. The furnace used in the synthesis of GCN has a front-loading system with a box-type design, accompanied with a programmable digital controller. The ramp of the reaction, sintering steps, and the temperature can be programmed and modulated by the digital controller. The operating principle of a muffle furnace is based on heating of the furnace to a requisite temperature by conduction, convection, or blackbody radiation. The source of this radiation is electrical resistance heating elements. The chamber of the furnace is made with refractory bricks avert heat loss. The main advantage of a muffle or box furnace is that during heating of a material, it can isolate the material from fuel as well as the by-products generated due to combustion. Other advantages include cost-effective operating system, energy-efficient, good thermal conductivity, robust, and flexible temperature ranges (200-1300 °C). The digital image of a furnace is provided in **Fig. 4.2(a).** The precursors are taken in crucible and boats made of alumina to undergo heat treatment in the reaction chamber of the furnace.

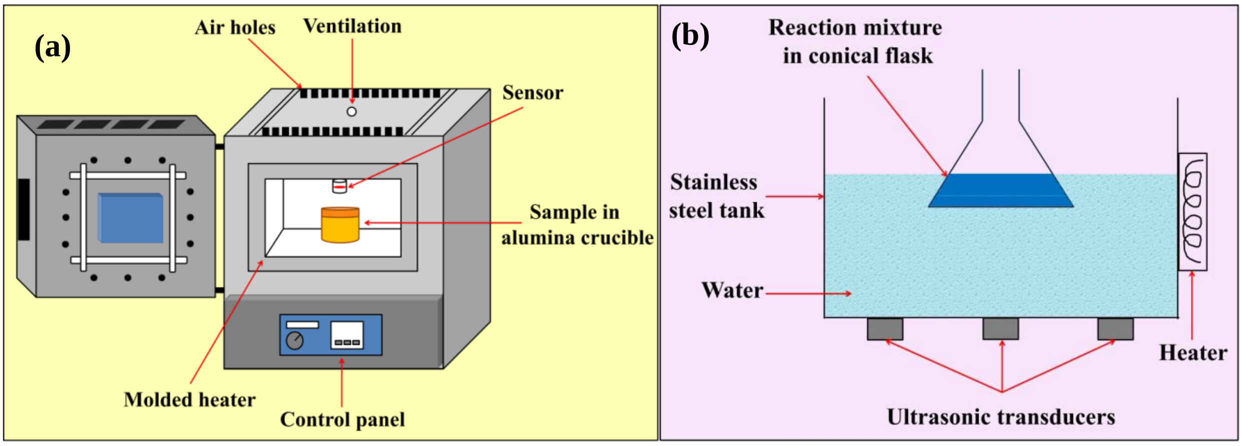

***Fig. 4.2**: Schematic depiction of (a) muffle furnace, and (b) an ultrasonic bath sonicator*

For exfoliation of GCN, an ultrasonic bath sonicator has been employed. The image is given in **Fig. 4.2(b)**. This low-cost device operates on a moderate ultrasonic intensity. The rectangular ultrasonic bath sonicator used in the current experiments has been manufactured by Labman-LMUC, has a total volume of 2.5 L, and operates on 2 A current and 40 KHz frequency, providing an output power of 50 W. An ultrasonic transducer is used to produce high-frequency sound waves inside the liquid (deionized water). These waves cause agitation in the water in order to generate cavitation bubbles. The GCN sample that requires exfoliation is dispersed in acetone taken in a glass beaker. This beaker is then partially immersed inside the bath sonicator containing water, and is held in position by means of a stand, so that the beaker does not get submerged in the water. The sound waves generated in the water due to sonication are transmitted to the beaker containing dispersed GCN. This eventually causes agitation in the GCN-dispersed acetone solution which helps in the exfoliation of the bulk GCN sheets.

4.2. Characterization tools:

Different instrumentations have been employed to confirm the formation of the nanomaterials and also to investigate their interesting characteristics in details. This section describes the basic features and operating principles of some commonly employed instruments in the present experimental studies.

4.2.1. X-Ray diffraction (XRD):

The first step after synthesis of a nanomaterial is to confirm its phase purity. X-ray diffraction (XRD) analysis helps in proper identification of the phases of the as-synthesized nanomaterials. After the discovery of X-ray by Roentgen in 1895, gradual research led to the understanding of its diffraction patterns by crystal's atomic planes. This eventually revealed a whole new direction for precisely investigating the structure of matter of either amorphous or crystalline form.

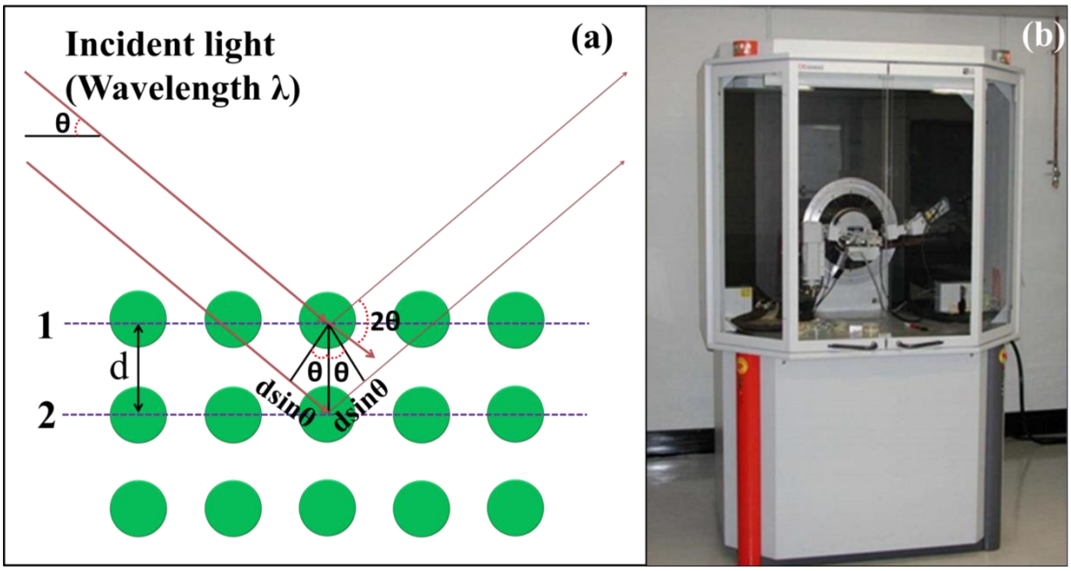

Fig 4.3: (a) Schematic depiction of Bragg's law, (b) digital image of the experimental set-up of an XRD instrument

When an X-ray of monochromatic nature is incident on a crystal lattice, reflection of these X-rays are caused by the atomic planes, where each atom functions as an epicentre of scattering. The schematic representation is shown in **Fig. 4.3(a)**, where two atomic planes are denoted as 1 and 2. Reflected X-rays from plane 1 and plane 2 will have a path difference in between them. Only those reflected beams will undergo constructive interference when their path difference is an integral multiple of the incident X-ray's wavelength. This phenomenon is described by the Bragg's law [236], which is given as below:

$$2d\sin\theta = n\lambda \quad \text{……………….. (4.1)}$$

where, ‘n’ is an integer, denoted as the order of diffraction, ‘λ’ is the incident X-ray beam’s wavelength, ‘θ’ is the glancing angle, also known as the Bragg’s angle, and ‘d’ is the interplanar spacing representing the distance between two consecutive atomic planes.

To carry out the X-ray diffraction analysis of the synthesized nanomaterials in the present work, a Rigaku Ultima III X-ray diffractometer has been employed, the digital image of which is shown in **Fig. 4.3(b)**. The diffraction pattern has been recorded in θ-2θ configuration, and Cu Kα X-ray having a wavelength λ of 1.5404 Å has been used as the source of irradiation of the samples under investigation. The diffractometer operates at a voltage of 40 kV and current of 30 mA. To collect the data, the samples have been scanned with a rate of 2^{o}/min. After collection of data, the XRD pattern has been background corrected for further analysis. Additionally, the observed peaks have been confirmed from the International Centre for Diffraction Data (ICDD) resource.

4.2.2. Fourier-transform infrared spectroscopy (FTIR):

Molecular vibrational frequencies of a material can be detected in the infrared region of the electromagnetic (EM) spectrum. FTIR spectroscopic measurement is an important tool to confirm and understand the different vibrational modes of the chemical bonds present in a sample. An FTIR instrument makes use of an interferometer and implements the Fourier transformation mathematical method to analyse the chemical bond formation. The advantage of this method lies in the minimum time required to produce the desired data. Commercially employed FTIR spectrometers generally use Michelson interferometer whose working principle is shown in **Fig. 4.4**. The components of a Michelson interferometer are:

- A light source of polychromatic nature, emitting light of wavelengths in the mid-IR region.
- A beam splitter generally made of KBr or CsI
- Two surface-coated mirrors, one of which is movable and the other remains fixed
- A detector

To analyse a sample by FTIR spectroscopy, the sample in powder form is mixed with KBr uniformly, following which a pallet having 8 mm diameter is prepared by employing a palletizer. The data is taken in transmittance mode. The experimental set-up's diagram is provided in **Fig. 4.4(inset)**.

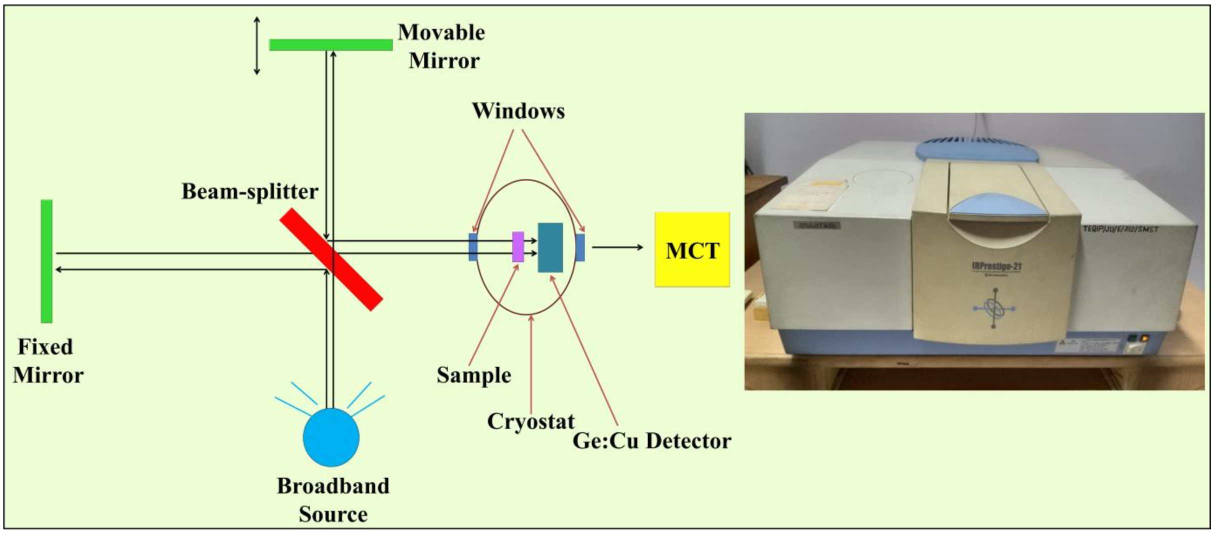

Fig 4.4: *Schematic depiction of working principle of FTIR, (inset) digital image of the experimental set-up of an FTIR instrument*

4.2.3. X-ray photoelectron spectroscopy (XPS):

XPS is among the most authentic surface-sensitive techniques to accurately determine the chemical states of the constituent elements of a material, as well as to provide detailed information regarding the qualitative elemental survey and quantitative composition. In this method, first an X-ray photon having 1-15 KeV of energy is incident on the sample's surface. This X-ray interacts with the solid surface, resulting in emission of electrons from the sample's surface. The incident X-ray can not only eject outer shell electrons but is equally efficient in ejecting electrons from the core shells of the elements. A schematic depiction of the working principle of XPS is described in **Fig. 4.5(a)**. Since the incident X-ray's energy is a known factor, the characteristic binding energy (B.E.) of a core-level photoelectron directly corresponds to its kinetic energy (K.E.). The primary objective of an XPS spectrometer is to determine an electron's binding energy, which is analysed using the following equation:

$$\boldsymbol{B.E. = h\nu - K.E. - W_f} \quad \ldots\ldots\ldots\ldots\ldots\ldots.. (4.2)$$

where, 'W_f' is the work function of the sample undergoing analysis.

The experimental set-up (as shown in **Fig. 4.5(b)**) of an XPS is comprised of:

- a source of X-ray

- an analysing system to measure electron energy, equipped with a detection system
- a sample stage

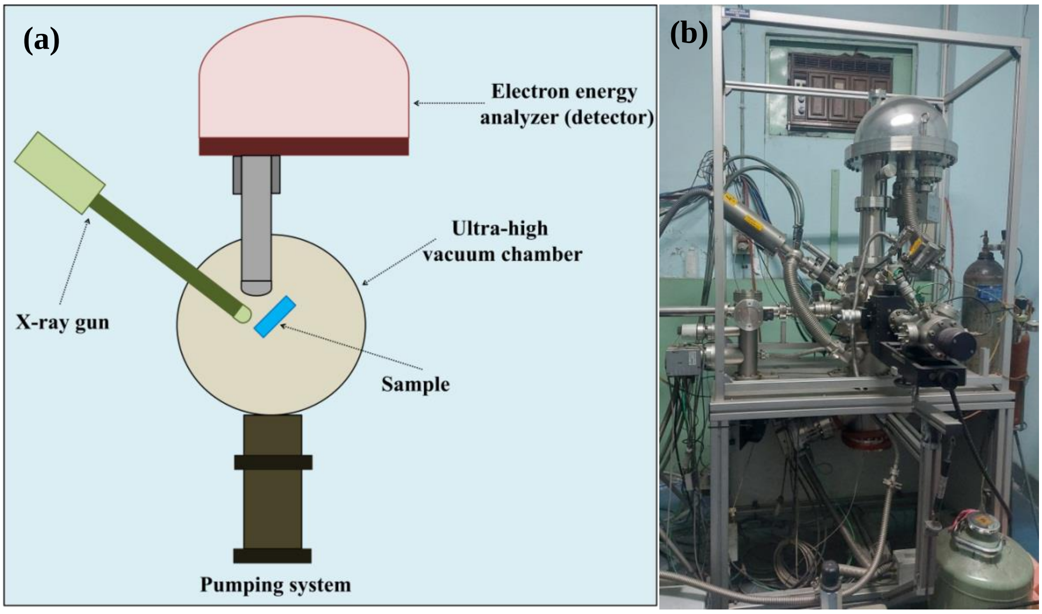

Fig 4.5: *(a) Schematic depiction of working principle of XPS, (b) digital image of the experimental set-up of an XPS instrument*

The plot of the XPS spectrum signifies the number (intensity) of electrons observed at a particular binding energy. In the present work, XPS analysis of the samples have been carried out in SPECS instrument equipped with an energy analyser of hemispherical shape (HSA 3500). Monochromatic Al Kα X-ray, having energy (hν) of 1486.6 eV is used as the source of excitation. The XPS system operates at a voltage and anode current of 10 kV and 17 mA respectively, and a pressure range of 10^{-8}-10^{-9} Torr are maintained during the measurement. To perform the XPS analysis of powder samples, a pallet having diameter of 12 mm is prepared to improve the ratio of signal to noise. The digital photograph of the XPS instrument is provided in **Fig. 4.5(b)**.

4.2.4. Ultraviolet-visible spectroscopy (UV-Vis):

Optical properties of a material are measured by UV-Vis spectroscopy. This method generally refers to absorption, transmittance, or reflectance spectroscopy in the UV, visible, and near IR range of the electromagnetic spectrum. The underlying concept of this technique is the absorption of photon energy by a material corresponding to UV or visible wavelength, resulting in the generation of distinct spectra in the UV-visible region. The photon energy absorbed by the sample material corresponds to its band gap energy. When a material absorbs a photon, excitation of an electron occurs to higher energy states or molecular orbitals (MO) denoted as the excited states.

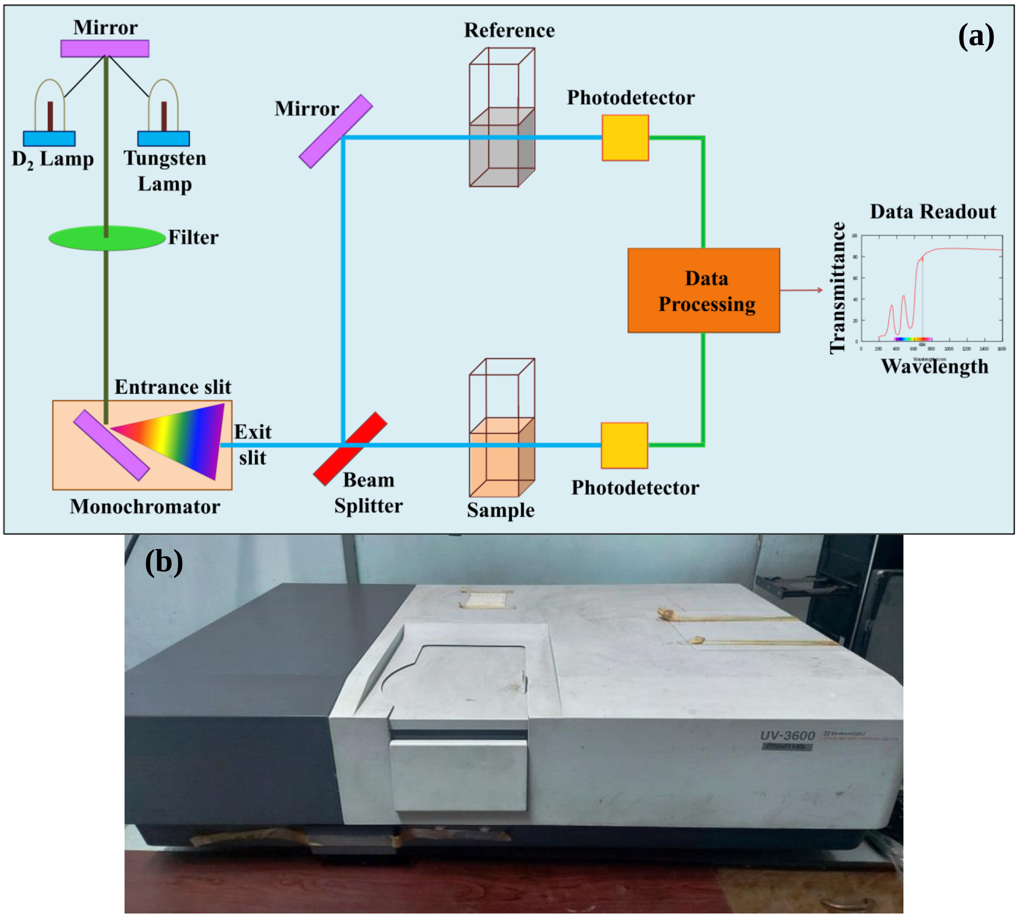

Fig 4.6: (a) Schematic depiction of working principle of UV-Vis, (b) digital image of the experimental set-up of an UV-Vis instrument

The concept of absorption of light by a material is explained from two laws, Lambert’s law and Beer’s law. The UV-vis measurement of a material dispersed in a solvent is carried out in a cuvette made of quartz material. A photon is incident on this cuvette with an intensity of I_0. Some of the photon energy is absorbed by the material and the rest gets transmitted through the material with a reduced intensity of I. The ratio of (I/I_0) is known as the transmittance (T). Absorbance (A) of a material is defined as $(-\log_{10}T)$, which represents the amount of photon energy absorbed by the molecules in a material. The Lambert’s law states that this absorbance has a direct proportional relation to the cuvette’s thickness (10 mm) that is the path length traversed by the light. Beer’s law states that concentration of the material in the solution is directly proportional to the absorbance. Combination of these two laws gives the Beer-Lambert’s law stated below:

$$\boldsymbol{log_{10}\left(\frac{I_0}{I}\right) = A = \alpha c d} \;\ldots\ldots\ldots\ldots\ldots\ldots.. (4.3)$$

where, ‘α’ is a constant termed as molar absorptivity, ‘c’ is concentration of the solution, and ‘d’ is the path length. A schematic depiction is given in **Fig. 4.6(a)**. The constituent parts of an UV-vis spectrometer along with the digital image of the instrument are given in **Fig. 4.6(b)**. The instrument consists of: (i) a light source, (ii) a monochromator; which is again composed of an entrance slit, a dispersive element, and an exit slit, and (iii) a detector.

UV-vis measurement of a material is primarily performed to calculate its band gap, which helps in providing information about the opto-electronic properties of the material. In case of liquid samples, homogenous solutions, solid samples which can be uniformly dispersed in a solvent, and thin-film samples, UV-vis measurement in absorbance or transmittance mode is performed to calculate their respective band gaps following Tauc’s plot method. Conversely, for powder samples, measurement is done in reflectance mode (also known as diffuse reflectance spectroscopy or DRS), and in this case Kubelka-Munk method is employed for calculating the optical energy gaps of the samples. The Tauc’s equation and Kubelka-Munk equation are given as equation (4.4) and (4.5) respectively.

$$\boldsymbol{\alpha h v = A(hv - E_g)^n} \;\ldots\ldots\ldots\ldots\ldots\ldots.. (4.4)$$

$$\boldsymbol{[F(R_\infty)hv] = A(hv - E_g)^n} \;\ldots\ldots\ldots\ldots\ldots\ldots.. (4.5)$$

$$\boldsymbol{[F(R_\infty)] = \frac{k}{s} = \frac{(1-R_\infty)^2}{2R_\infty}} \;\ldots\ldots\ldots\ldots\ldots\ldots.. (4.6)$$

where, ‘A’ is a constant, ‘υ’ is denoted as the light-wave’s frequency, ‘E_g’ is the band gap, ‘k’ is the absorption coefficient (similar to α), ‘s’ is the scattering coefficient, ‘R_∞’ is the diffuse reflectance, and [F(R_∞)] is the Kubelka-Munk function. ‘n’ represents the nature of electronic transition, whether the transition is direct or indirect in nature. Values of ‘n’ as 1/2, 3/2, 2, and 3 denote direct allowed, direct forbidden, indirect allowed, and indirect forbidden transitions respectively. Tauc’s plot is a typical plot between $(\alpha h\upsilon)^{1/n}$ in the ordinate and (hυ) in the abscissa. A tangent is drawn passing through the linear region of this plot which cuts the x-axis at a particular value, denoted as the band gap E_g value.

The UV instrument used in the research works is Shimadzu 3600 UV-Vis-NIR spectrophotometer, which employs deuterium lamp as the source of light for the UV range, and halogen lamp as the light source for visible and near IR range. For measuring the reflectance of a powder sample, barium sulphate is employed as the reference since it exhibits 100 % reflectance in the UV-vis-NIR region. For absorbance measurement of a sample dispersed in a solvent, the solvent without the sample dispersed in it is considered as the reference.

4.2.5. Field emission scanning electron microscope (FESEM):

FESEM analysis is performed to examine the morphologies of the as-prepared samples in the present investigation. It is an electron microscopy instrument operating in a high-vacuum system and employs an electron beam emitted from a field emission source. The interaction between an electron beam and the atoms of a matter results in two kinds of scattering phenomena: elastic and inelastic. For electrons which are scattered elastically, their direction can change with collision, but their velocity and kinetic energy remain constant. Conversely, for inelastic scattering, the incident beam of electrons has the ability to displace the electrons from the orbits surrounding the nuclei of the atom of the sample under investigation. These interacting electrons can generate signals depending upon the target sample's morphology as well as composition [237]. Moreover, secondary electrons are generated due to the interaction occurring between the surface of the sample and the incident electron beam, and these electrons can be converted into voltage.

A schematic depiction of the construction of an FESEM instrument is given in **Fig. 4.7(a)**. The machine consists of a field emission gun to produce an electron beam, electromagnetic lenses and apertures for focusing the electron beam, a detector, and an ultra-high vacuum system. The electron gun has the capability to generate a stable beam of electron having characteristics of (i) high current, (ii) small spot size, (iii) adjustable energy, and (iv) small dispersion of energy. Tungsten hairpin or lanthanum hexaboride (LaB_6) are employed as the field emission sources in modern-day FESEM instruments. A high intensity electric field formed on the very finely oriented tip of the source (which acts as the cathode) facilitates the electron emission. These electrons are attracted towards the anode, forming a powerful electron beam. The electron beam is finally focused strongly on the material under investigation by the combined help of the various types of electromagnetic lenses and apertures. These lenses are also used to control the size and position of the electron beam.

In the present works, an FESEM instrument (FESEM, S-4800, Hitachi) developed by Hitachi has been utilized in studying the morphologies of the samples. The machine operates at an accelerating voltage less than 15 kV. For samples with insulating properties, coating of its surface with Au or Ag nanoparticles is required to exclude the surface charge imbalance and to achieve better resolution. Powder samples are pasted on carbon tape prior to measurement. The digital image of an FESEM instrument is provided in **Fig. 4.7(b)**.

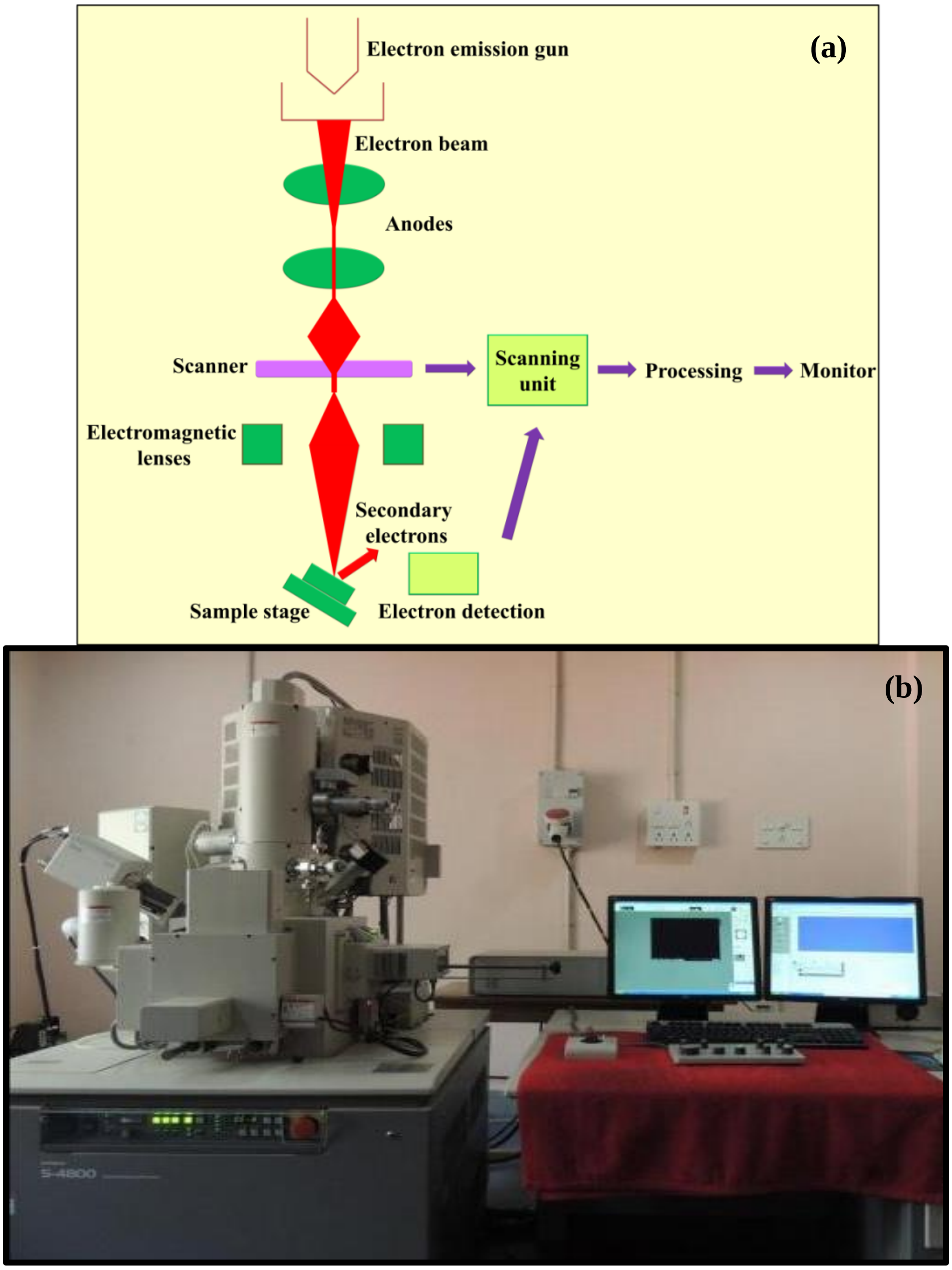

***Fig 4.7**: (a) Schematic depiction of working principle of FESEM, (b) digital image of the experimental set-up of an FESEM instrument*

Generally, energy-dispersive X-ray spectroscopic analysis (EDS) is performed in association with FESEM measurement. EDS is an efficient analytical tool to analyse the elemental composition of the specimens under investigation. During EDS measurement, inside an electron microscope, bombardment of the target material is done by an electron beam. The incident electrons with high intensity undergo collision with the target sample's atom, thus knocking off some of the electrons from the inner shells of the atom in the process. The void left behind by the inner shell electrons after their emission is eventually filled up by the electrons from the outer shell having higher energy. The energy difference existing between the higher energy and the lower energy shells are released or emitted as X-rays from the atoms. X-ray energies are characteristic of the element's atomic structure from which they are emitted, thereby facilitating in measuring the chemical composition of the sample. In the present works, EDS analysis has been performed by an EDS part attached with the FESEM Hitachi instrument. This attachment has been manufactured by Thermo Scientific having the model: Noran System - Thermo Scientific UltraDry EDS Detector.

4.2.6. High-resolution transmission electron microscope (HRTEM):

HRTEM is an important and useful tool for characterisation purpose of microstructure of the nanomaterials along with their detailed crystal structure at atomic level by implementing the concept of diffraction and imaging technologies. In contrast to FESEM analysis, whose resolution is only limited up to the nanometric scale; HRTEM can provide detailed information about the inter-lattice spacing (d) of the nanomaterial under investigation. The accelerating voltage of electrons in HRTEM is much higher (about 160-300 kV) as compared to FESEM (5-30 kV). Such high accelerating voltage enables the electrons to move almost with the speed of light, resulting in much higher resolution of images. Like FESEM, HRTEM also operates in a high-vacuum (~ 10^{-10} Pa) system. In a conventional HRTEM instrument, an electron beam having uniform current density is generated from an electron gun source which is either made of tungsten or LaB_6. The instrument employs sets of electromagnetic lenses made of Cu, and they are: (i) two condenser lenses, (ii) one objective lens, and (iii) six image forming lenses. The electron beam passes through these series of lenses along with apertures to illuminate the sample. The collimated electron beam gets transmitted through the nanomaterial and the corresponding image is digitally recorded with help of a charge coupled device (CCD) camera. The working principle of HRTEM along with its digital image is displayed in **Fig. 4.8(a,b)**.

For investigating the nanostructures of the as-synthesized samples, minute quantity of the powder sample is first uniformly dispersed in a solvent (preferably ethanol) by ultrasonication. Then the solution is carefully drop-casted on a carbon-coated copper grid.

After the grid is properly dried, the sample is used for measurement using an HRTEM instrument manufactured by JEOL (model: JEOL JEM-2100).

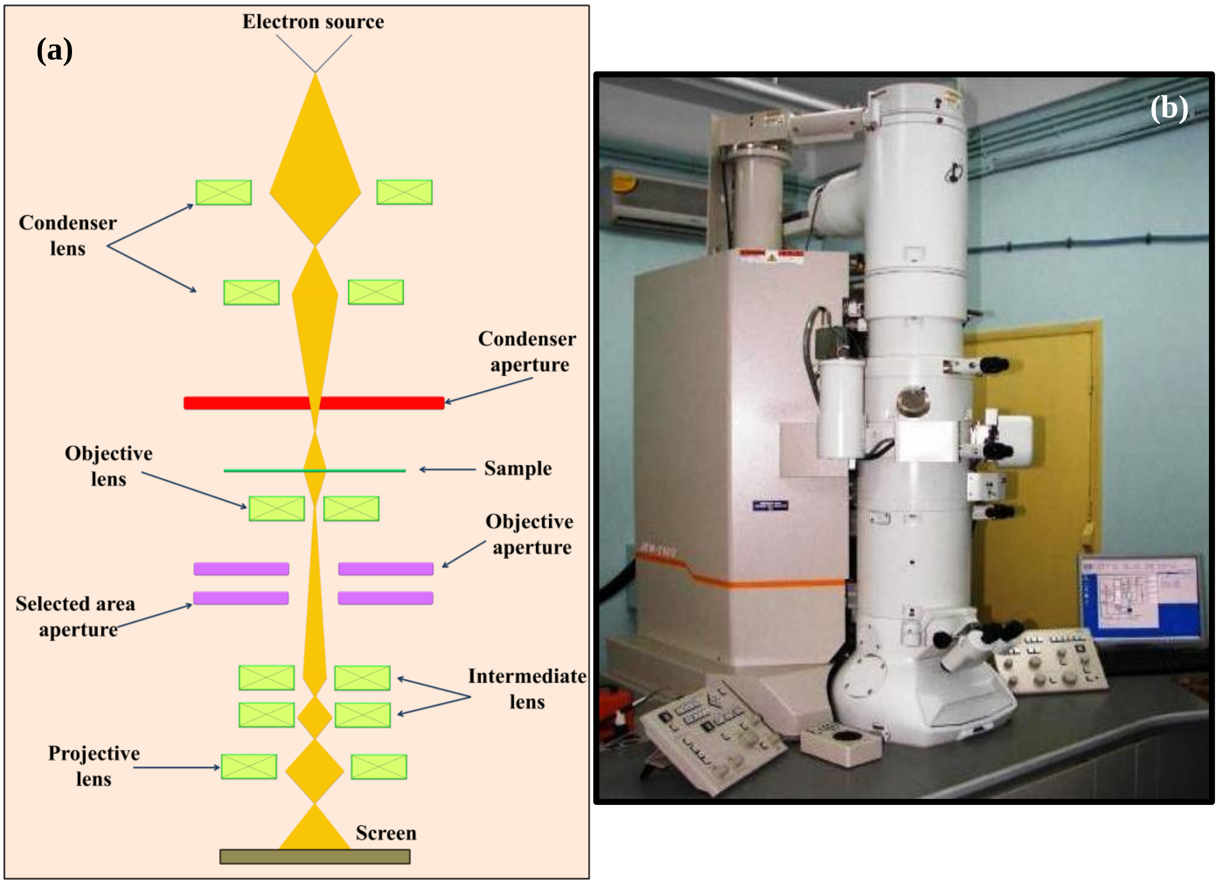

Fig 4.8: (a) Schematic depiction of working principle of HRTEM, (b) digital image of the experimental set-up of an HRTEM instrument

4.2.7. Brunauer-Emmett-Teller (BET) analysis:

BET measurement is performed to investigate the specific surface area (m^2/g) of a nanomaterial along with its porosity and pore size distribution. This multi-point measurement is performed by physical adsorption of an inert gas like nitrogen on the solid sample. The sample is kept under continuous flow of nitrogen gas prior to analysis for sufficient time period to ensure the adsorption of nitrogen on the sample's surface. The gas molecules are adsorbed on the solid material's porous surface owing to van der Waals forces, thus creating a monolayer formed of adsorbed gas molecules. These gas molecules pass into all the surface pores and cracks, hence BET measurement probes the solid sample's entire microscopic surface area. Standard BET measurement is performed at 77 K which is the temperature of boiling of liquid nitrogen. The analytical method employs a measurement technique based on physisorption, and the BET model is based on the quantity of absorbed gas molecules which is given as a function of the relative pressure (P/P_0). ‘P’ is the adsorptive pressure, and ‘P_0’ is the saturated vapour pressure at fixed temperature. The typical measurement technique employs: (i) taking a known amount of material in a sample holder, (ii) outgassing the sample for removal of impurities and moisture, (iii) gradually increasing the pressure of nitrogen gas and subsequently measuring the amount of gas absorbed on the material’s surface, (iv) the saturation vapour pressure P_0 can be measured simultaneously.

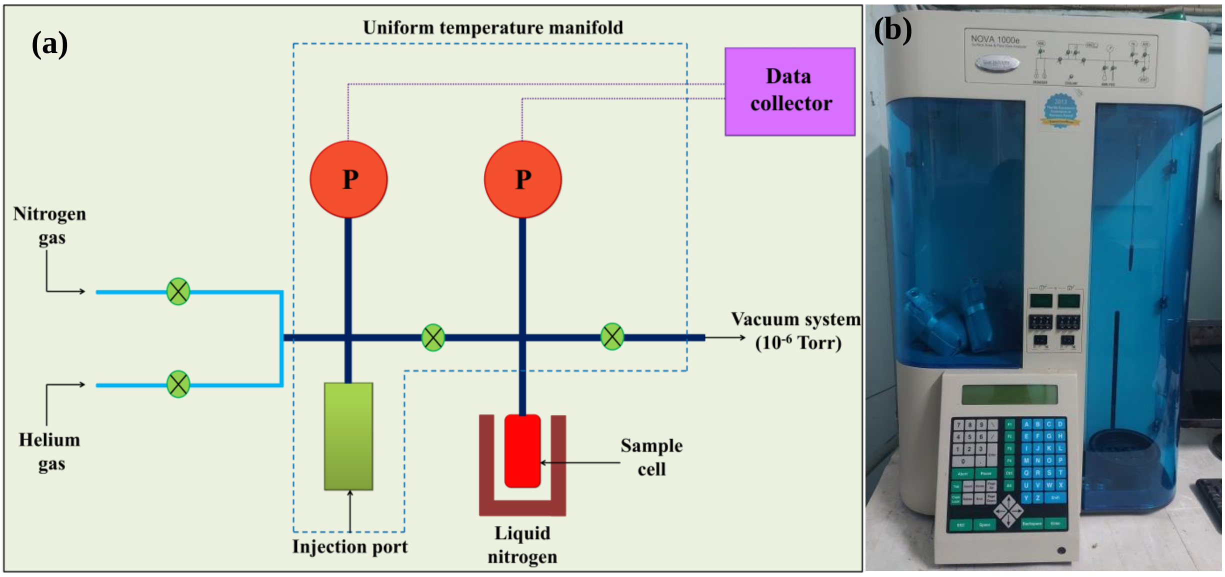

Fig 4.9*: (a) Schematic depiction of working principle of BET analyser, (b) digital image of the experimental set-up of a BET instrument*

BET analysis involves the study of an adsorption isotherm, which is basically a plot between ‘amount of gas molecules adsorbed’ and ‘relative pressure’. In the present work, Quantachrome Nova 1000e BET analyser has been employed for surface area measurements of the as-synthesized samples. The instrument operated at 77 K and 1 bar. The schematic depiction of a BET analyser along with the digital photograph of BET instrument is provided in **Fig. 4.9(a,b)**.

4.2.8. Photoluminescence spectroscopy (PL):

PL is an important characterization method to investigate the opto-electronic properties of semiconducting nanomaterials. When a photon of appropriate energy comparable to or higher than the band gap energy of a particular material is incident on that material, then the material’s electrons will absorb this photon energy, get excited, and will undergo transition from ground level to a higher energy excited state, leaving behind a hole in this process. After some time period, relaxation of this excitation will take place, resulting in the return of the electrons to the ground state. By doing so, some amount of energy will be released in the form of photon as well as heat. The returning of electrons to the ground state will result in the recombination of electrons and holes and their subsequent annihilation. When only photon energy is emitted during the recombination, then the process is termed as radiative recombination. However, sometimes, the excitation energy undergoes relaxation by dissipation of heat (as lattice vibrations), thus emitting a phonon during the process. This recombination type is known as non-radiative recombination. Thus PL spectroscopy provides in-depth analysis of the different types of electronic transitions occurring inside a semiconducting material arising due to band-to-band transitions as well as transitions from intermediate defect or trap states.

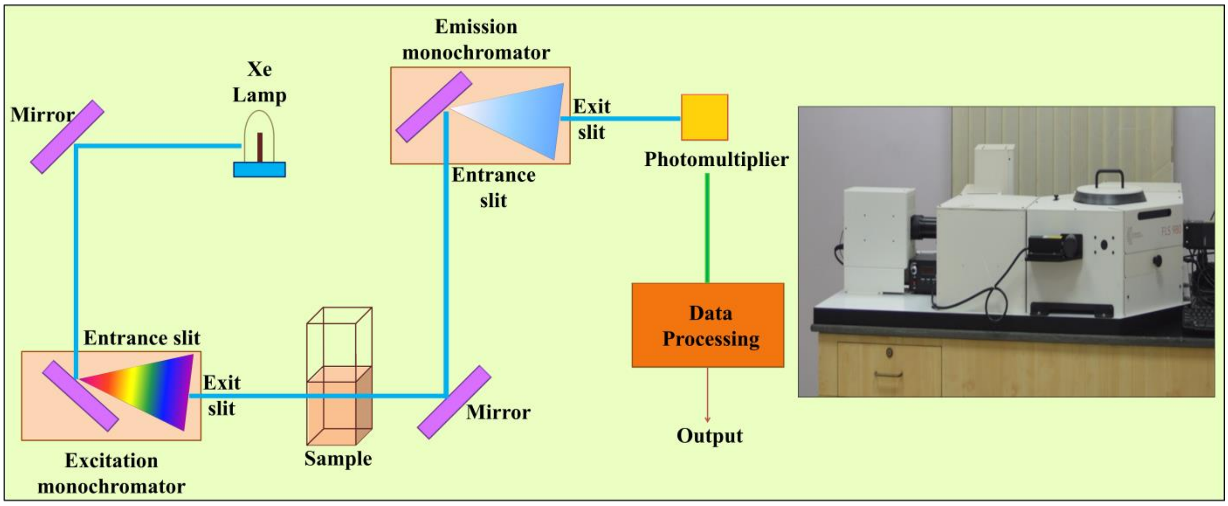

Fig 4.10: Schematic depiction of working principle of PL spectroscopy, (inset) digital image of the experimental set-up of a PL instrument

The PL spectrofluorometer consists of the following components: excitation monochromator, cell holder, emission monochromator, and photomultiplier tubes. The schematic depiction of the working principle of a PL instrument is given in **Fig. 4.10**. In the present work, PL measurements of the samples were conducted with a Shimadzu RF-6000 Spectro Fluorophotometer. The digital image of the instrument is provided in **Fig. 4.10(inset)**. The measurement yields an emission spectrum with respect to wavelength, when the sample is excited with appropriate photon energy. Generally, the emitted photon has a lower energy than the absorbed photon, thus emission occurs at a longer wavelength as compared to the absorption wavelength.

4.3. Methodologies:

This section deals with the explanation and discussion about the different methodologies followed during the detection, degradation, and removal of hazardous pollutants from contaminated water resources using carbon- and nitrogen-based nanomaterials.

4.3.1. Fluorescence detection technique:

Photoluminescence spectroscopy employing fluorescence phenomenon is an important tool used for the detection of heavy metal pollutants. As discussed earlier, this method is a fast and effective technique for sensing of pollutants present in contaminated water. When an electron in a semiconducting material is excited by an incident photon having energy higher than the band gap energy of the nanomaterial, this electron gets excited and moves to the material's CB and leaves behind a hole in the VB. It is a natural tendency of any material to achieve its lowest possible thermodynamically stable energy state. Thus, the exited electron, upon relaxation, comes back to the ground state or the VB by emitting energy in the form of photon. This phenomenon is called band-to-band luminescence, and the recombination of the electron-hole pair is radiative in nature. However, for materials having indirect band gaps, or defect and trap states in between the CB and VB, non-radiative recombination of electrons and holes can take place. The series of transitions that occur between the absorption and emission of photon energy by a material is illustrated by the Jablonski diagram, shown in **Fig. 4.11**.

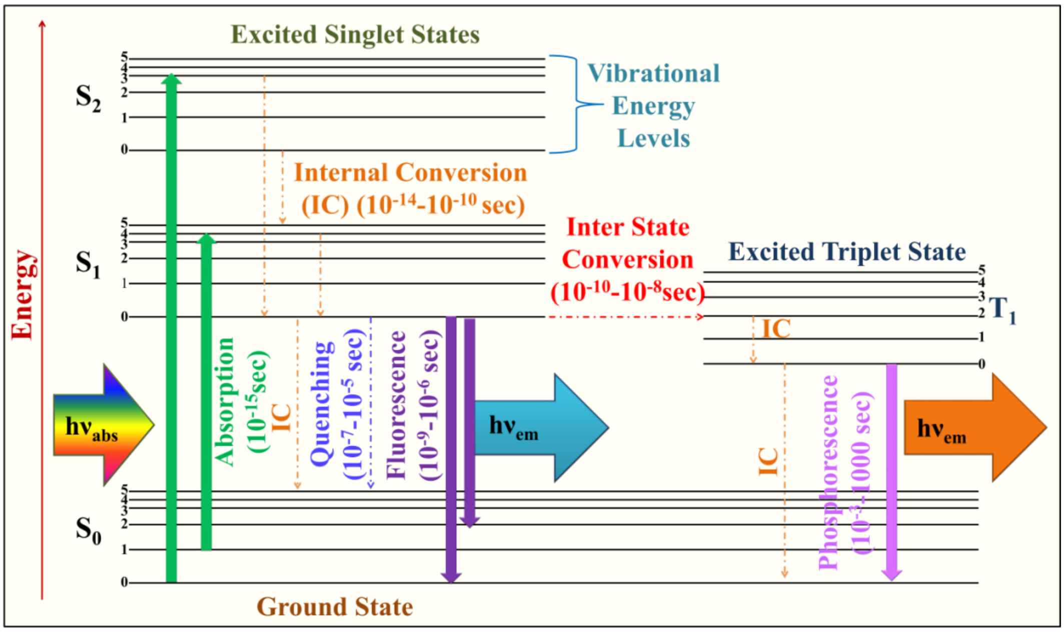

***Fig 4.11**: Schematic depiction of the Jablonski energy diagram*

It is established, that each electronic energy levels of a particular material is composed of several vibrational energy levels. In the diagram, the electronic energy levels are indicated as S_0, S_1, and S_2 for ground state, 1st excited state, and 2nd excited state respectively. Each vibrational levels are represented as 0, 1, 2 etc. Radiative recombination processes are depicted by solid arrows, whereas, the non-radiative phenomena are indicated with dotted arrows in the diagram. A material or a chemical compound which exhibits photoluminescence activity is known as a fluorophore. Let us consider that the molecules of this fluorophore remain in the ground state (S_0) prior to excitation with photon energy. When a photon is incident on the fluorophore, absorption of the light energy takes place, which initiates a chain of processes. The electrons in the fluorophore get excited to some higher electronic energy levels like S_1 or S_2. Now each electronic level has several vibrational levels. The electrons from 0 vibrational level of S_0 can get excited to higher vibrational levels of higher electronic states, suppose 4 of S_2. Subsequently, these electrons will rapidly undergo relaxation and will return back to the lowest vibrational level 0 of S_1 excited state. This rapid process is called the internal conversion which takes place within 10^{-14} to 10^{-10} sec. This process does not involve the emission of any photon. Moreover, electrons from 0 state of S_0 can get excited to higher excited vibrational state of S_1, suppose 5 of S_1. These electrons shall undergo vibrational relaxation that involves their transmission from higher excited vibrational level of S_1 to lowest vibrational state of S_1 (0) following a non-radiative process. Finally, the successive relaxation of the electrons from this lowest vibrational level of S_1 (0) to a higher excited vibrational level of the ground state S_0 accompanied by the emission of photon energy is called fluorescence. This is a radiative phenomenon having lifetime of about 10^{-8} sec. Again, vibrational relaxation will lead to the return of the electrons from the higher vibrational levels of S_0 to the ground state of S_0. Lifetime of vibrational relaxation is around 10^{-12} sec. The electronic states discussed till now are excited singlet states, which mean that the electron in the excited state has opposite spin with respect to the electron in the ground state. The orientation of the electron’s spin in the ground and excited state of the singlet configuration allows the return of the excited electron to the ground state. This spin allowed process results in rapid transition of the electrons to their thermally equilibrium state by a photon emission, a process that is termed as fluorescence. A flurophore’s lifetime (τ) is defined as the average time spent between the excitation of the fluorophore and its relaxation to the ground state. Electrons present in the excited S_1 state can travel to an excited triplet level T_1 by spin conversion. An electron in the triplet excited states has same spin with respect to the ground level electron. Thus the return of the electrons from T_1 excited state to

S_0 ground level is a forbidden process, and is not feasible without a spin conversion. The conversion of S_1 to T_1 is known as inter-state conversion. Emission of photon from the T_1 state is called phosphorescence, which has a much higher lifetime of 10^{-3}-1000 sec as compared to fluorescence.

Quenching is a phenomenon which refers to the decrease or reduction in the fluorescence emission intensity of a material caused by molecular interactions in presence of a quencher molecule. This process can result from reactions in the excited state, complex-formation, energy transfer reactions, and others. Thus, fluorescence quenching mechanism is important for measuring the binding affinity of a particular molecule to the fluorescent material. This technique is used in detecting heavy metal ions since they are capable in forming strong complexes with triazine-based fluorescent materials. Quenching phenomena are primarily of two types viz. static and dynamic [238]. In static quenching, interaction between the fluorophore and the quencher occurs at the ground state leading to the formation of a complex before excitation can take place. Thus, the complex is not transferred to the excited state, or it may happen that the complex in the ground level is slightly excited to a higher energy level. The complex then rapidly returns to the ground energy level without the emission of any radiation. Conversely, dynamic quenching, also known as collisional quenching, occurs when the fluorophore which is already present in the excited state comes in contact with a quencher molecule, undergoes collision, and returns to the ground level depending on the interaction between the fluorophore and the quenching molecule. This type of quenching process results in the non-radiative emission like charge and energy transfer in the ground state.

4.3.2. Catalysis:

Heterogeneous catalysis is an efficient methodology to treat wastewater pollutants by degrading them into non-toxic final products. Catalytic reactions can be induced by many factors, like light energy, reducing agents, electron or hole capturing agents, or a combination of all these elements. In the present works, two types of catalytic procedures for degradation of varieties of pollutant compounds have been investigated. They are described below:

4.3.2.1. Photocatalysis: Photocatalysis is a type of advanced oxidation processes (AOPs) which employs a catalyst material and light energy depending upon the band gap energy of the catalyst material to degrade hazardous compounds. In this method, photon energy excites a semiconducting material with suitable energy gap so as to initiate a chain of redox reactions taking place in the CB and VB of the material. These reactions are able to generate reactive oxygen species like superoxide anionic radicals ($•O_2^{-}$) or hydroxyl radicals (•OH). These active radicals along with photogenerated electrons (e^-) and holes (h^+) are capable of reducing toxic compounds.

When a photon with appropriate energy (hν) comparable to the catalyst material's band gap energy is incident on the catalyst, electrons are excited to the CB of the material leaving behind positively charged holes in the VB. The catalysis procedure takes place in an aqueous medium. Depending upon the CB band edge potential of the catalyst, the CB electrons are capable of carrying out some reduction reactions to generate $•O_2^{-}$ radicals from dissolved oxygen. Similarly, if the catalyst material's VB band edge potential is suitable enough, then oxidation reactions can take place in presence of the photogenerated holes to generate •OH radicals from H_2O. These active species can further degrade the toxic pollutants dissolved in the aqueous medium to organic species like CO_2 and H_2O. The photogenerated VB holes can directly reduce toxic compounds to non-toxic organic species. Apart from these conventional reactions, other redox reactions can also take place depending upon the catalyst material's band edge potentials to ultimately generate $•O_2^{-}$ and •OH radicals. Most importantly, the catalyst material should not undergo any degradation, consumption, or phase change during the catalytic reactions, and should remain unchanged throughout the process. The redox potential values with respect to normal hydrogen electrode (NHE) are given as: O_2/ $•O_2^{-}$ (-0.046 V), O_2/H_2O_2 (0.69 V), OH^-/•OH (1.99 V), H_2O/•OH (2.37 V). The plausible reactions that occur during catalysis are as follows:

$\text{Catalyst} + h\nu \longrightarrow e_{CB}^- + h_{VB}^+$

$O_2 + e_{CB}^- \longrightarrow •O_2^{-}$

$O_2 + 2e^- + 2H^+ \longrightarrow H_2O_2$

$H_2O_2 + e^- \longrightarrow •OH$

$h_{VB}^+ + \text{Pollutant} \longrightarrow CO_2 + H_2O$

$•OH + \text{Pollutant} \longrightarrow CO_2 + H_2O$

$•O_2^{-} + \text{Pollutant} \longrightarrow CO_2 + H_2O$

These radicals are highly active species which can perform complete mineralization of the toxic pollutant compounds, thus converting contaminated water-bodies to innocuous system. A catalyst material should be efficiently capable in preventing the recombination and subsequent annihilation of the photogenerated electrons and holes. Sufficient time should be provided for the electrons and holes to travel to the catalyst material's surface from the bulk portion since the pollutant remains adsorbed on the catalyst's surface. The recombination and annihilation of photogenerated charge carriers result in the loss of these redox species, thus, no electrons or holes would be available to initiate the redox reactions. Sometimes, to enhance the catalytic efficiency, electron or hole capturing agents are used which are able to generate more active radicals and subsequently improve the overall catalytic performance.

4.3.2.2. Catalytic hydrogenation reactions: Catalytic hydrogenation technique for reduction of pollutant compounds employs a cheap and convenient reducing agent (preferably sodium borohydride, $NaBH_4$) along with a suitable catalyst nanomaterial, and the process takes place in absence of any source of irradiation. The concept of this type of reduction reactions is solely based on the relay or transport of electrons from the $NaBH_4$ compound to the organic pollutant compounds via the catalyst material. The primary criterion for initiating this type of reaction is the proper adsorption of both $NaBH_4$ and pollutant compounds on the catalyst's surface. Moreover, the catalyst material should be capable of providing a smooth transmission channel for the passage of electrons from $NaBH_4$ to the pollutants. The sources of H^+ and e^- required for the pollutant reduction process are identified as H_2O and $NaBH_4$ respectively. These active charges following a series of chemical reactions can reduce the toxic pollutants to their less-toxic or non-toxic forms.

There are plenty of on-going researches to unravel the plausible reactions that occur during catalytic hydrogenation method; however, there are very few reports which have been able to successfully prove them. Nonetheless, this extremely rapid, cost-effective, simple, and efficient method has been extensively employed to perform the reduction of various toxic compounds commonly existing in wastewater. In the present works, we have tried to provide some fundamental ideas regarding this technology following substantial theoretical calculations. The detailed discussions will be provided in the following chapters.

Summary of the chapter:

In this chapter, different useful equipment required for the synthesis of triazine-based polymers has been discussed in details. The various characterization instruments and techniques employed for the detailed study of the as-synthesized materials' properties have also been described. The fundamental concepts and working principles of these instruments have been explained. Finally, the methodologies implemented for the application purposes of the nanomaterials have also been discussed in details.

CHAPTER 5:

MATERIALS AND METHODS

Materials and Methods

This chapter deals with the materials used during the synthesis of triazine-based polymers, their elaborate synthesis procedures, the different characterization techniques employed to investigate the properties of the nanomaterials, and finally the methods used to perform the application procedures of these materials.

5.1. Synthesis procedures:

5.1.1. Synthesis of a novel triazine-based polymer (MEG_{10}):

Materials: The materials were used as received. All the chemicals were of AR grade. Melamine ($C_3H_6N_6$, M.W: 126.12 g/mol) was purchased from Loba Chemie. Ethylene glycol ($C_2H_6O_2$, M.W: 62.07 g/mol), nitric acid (HNO_3, M.W: 63.01 g/mol, 69-70% v/v), and ammonia solution (NH_4OH, M.W: 35.04 g/mol, ~25% v/v), were procured from Merck. All the experiments were carried out in deionised water (18.3 MΩ).

Synthesis procedure: 0.78 g melamine (M; 0.0062 moles) was dissolved in 26.67 mL of ethylene glycol (EG; 0.43 moles) followed by drop-wise addition of 53.34 mL of 0.1 M HNO_3 such that the molar composition between melamine and ethylene glycol is 1:69. A copious white precipitate appeared and the pH of the solution was ~4. To this, concentrated NH_3 solution was added drop-wise to get a clear solution till the pH reached ~6, 10 or 12 and the stirring was continued for 1 hr. This solution was transferred into a 100 mL hydrothermal Teflon-lined container and was subjected to hydrothermal treatment for 24 hr. at 120 °C with a ramp of 2 °C/min. Post-hydrothermal treatment, the clear liquid was then dried in an oven at 60 °C. The powder, so obtained, was washed with excess ethanol to remove the impurities (unreacted reactants) and dried at 60 °C overnight. The powders, so obtained at different pH (pH= 6, 10 and 12) are designated as MEG_6, MEG_{10} and MEG_{12}, respectively.

5.1.2. Synthesis of pristine GCN and GCN-based materials:

Materials: For the synthesis of pristine GCN, urea (CH_4N_2O, M.W: 60.06 g/mol) having purity greater than 99% was purchased from Merck. Melamine ($C_3H_6N_6$, M.W: 126.12 g/mol) purchased from Merck was also used as a precursor for the synthesis of pure GCN. For the exfoliation of bulk GCN into nanosheets, acetone (C_3H_6O, M.W: 58.08 g/mol) purchased from Merck was used. All chemicals used were of AR grade.

For the synthesis of Cu-doped and Ni-doped GCN samples, copper chloride dihydrate ($CuCl_2·2H_2O$, M.W: 170.48 g/mol), nickel chloride hexahydrate ($NiCl_2·6H_2O$, M.W: 237.69 g/mol), and hydrochloric acid (HCl, 37 wt%) were purchased from Merck. Deionized water was used throughout all experimental procedures.

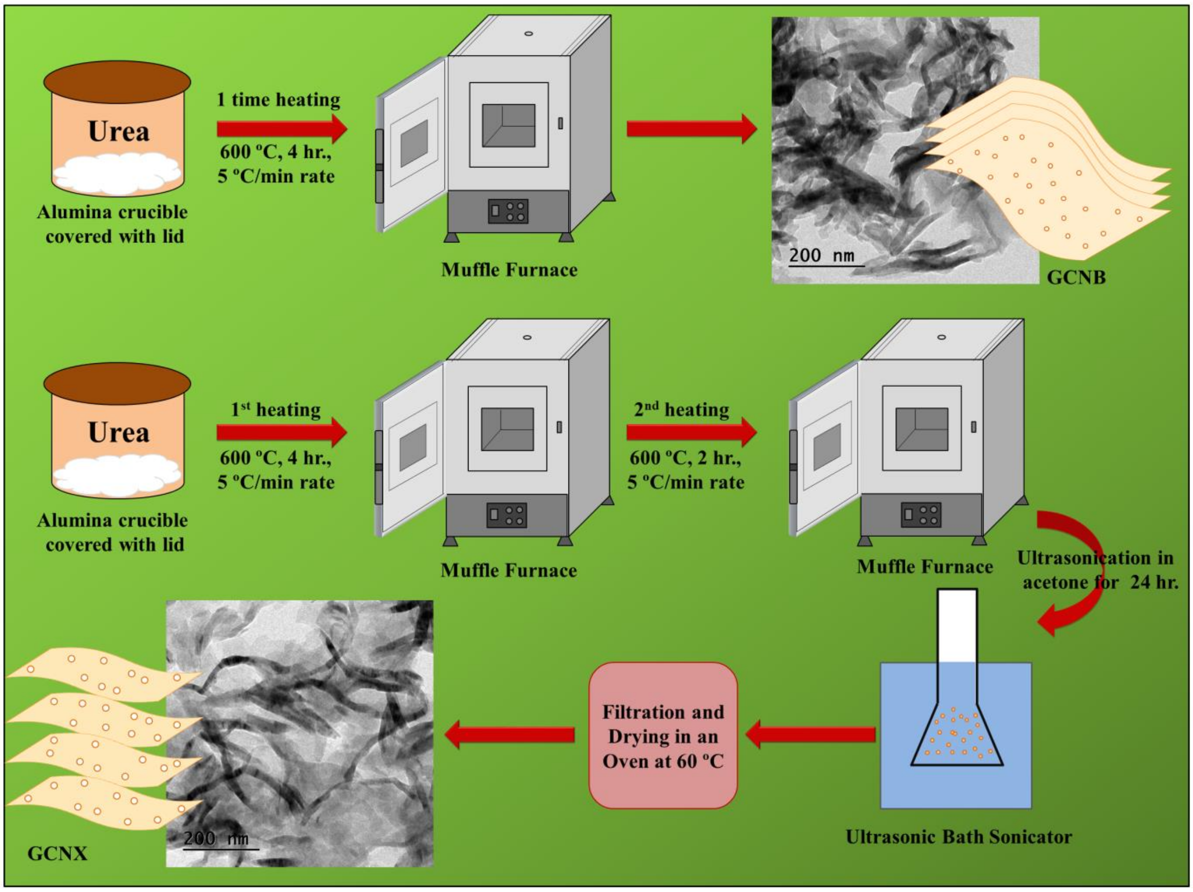

***Fig. 5.1**: Schematic representation of the synthesis procedures of GCNB/GCN and GCNX*

5.1.2.1. Synthesis procedure of pristine GCN:

Bulk GCN was synthesised by thermal treatment of urea taken in a tightly-covered alumina crucible in a muffle furnace at 550 °C - 600 °C in air for 4 hr. at 5 °C/min heating rate. The light yellow coloured sample obtained after pyrolysis was named as GCN/GCNB. For synthesis of pure GCN from melamine, melamine was taken in a well-covered alumina crucible attached with a lid which was then subjected to thermal treatment at 550 °C for 4 hr. at 5 °C/min heating rate in air in a muffle furnace. In this case also, a pale yellow coloured powder sample was obtained which was named as GCN.

5.1.2.2. Synthesis procedure of exfoliated GCN:

For the synthesis of exfoliated GCN (GCNX), urea was subjected to thermal treatment at 600 °C for 4 hr. at 5 °C/min heating rate. After completion of the heating procedure, the sample was allowed to cool down to room temperature. The light yellow coloured sample obtained after the first thermal treatment was again subjected to thermal treatment for the second time in a muffle furnace at 600 °C for 2 hr. at 5 °C/min heating rate. This powder like product was then dispersed in acetone and ultrasonicated in a water bath for 24 hr. The sample was then filtered and dried in an oven at 60 °C overnight to obtain the final product GCNX. The synthesis procedures of bulk and exfoliated GCN are schematically represented in **Fig. 5.1**.

5.1.2.3. Synthesis procedure of Cu-doped and Ni-doped GCN:

The synthesis procedure followed in this work is according to a report by Zhu et al [205] with minor modification. 0.04 mol of $CuCl_2{\cdot}2H_2O$ was initially dissolved in 300 mL of concentrated HCl (37 wt%) at room temperature to form a green coloured solution. 0.08 mol of melamine powder was then added slowly into this solution along with continuous stirring until the solution turned yellow in colour. The molar ratio of $CuCl_2{\cdot}2H_2O$ and melamine was maintained at 1:2. The change in colour from green to yellow upon the addition of melamine suggested the formation of Cu-melamine (CuM) supramolecular complex. The yellow product was collected by repeated centrifugation and washing vigorously with concentrated HCl for 5 times. The product was then dried at 60 ºC overnight to obtain the yellow coloured powder form. Some amount of this product was then taken in an alumina crucible which was properly covered with a lid. This was then subjected to thermal treatment in a muffle furnace at 550 ºC for 2 hr. at 5 ºC/min heating rate. A brown coloured product was obtained which was grind into fine powder by mortar and pestle. The sample obtained was named as CuCN. Similar procedure was followed with $NiCl_2{\cdot}6H_2O$ as the precursor. After dissolution of $NiCl_2$ into 37 wt% HCl, a green coloured solution was formed which turned into whitish-green after addition of appropriate amount of melamine. The molar ratio of the precursors was again maintained at 1:2. The whitish-green powder (NiM) was obtained after repeated washing, centrifugation and drying at 60 ºC overnight. Some amount of the powder sample was heated in a muffle furnace at 550 ºC for 2 hr. at 5 ºC/min heating rate. The brownish-yellow coloured sample was obtained after finely grinding the powder with a mortar and pestle. This sample was named as NiCN. The synthesis procedure of CuCN is schematically depicted in **Fig. 5.2**.

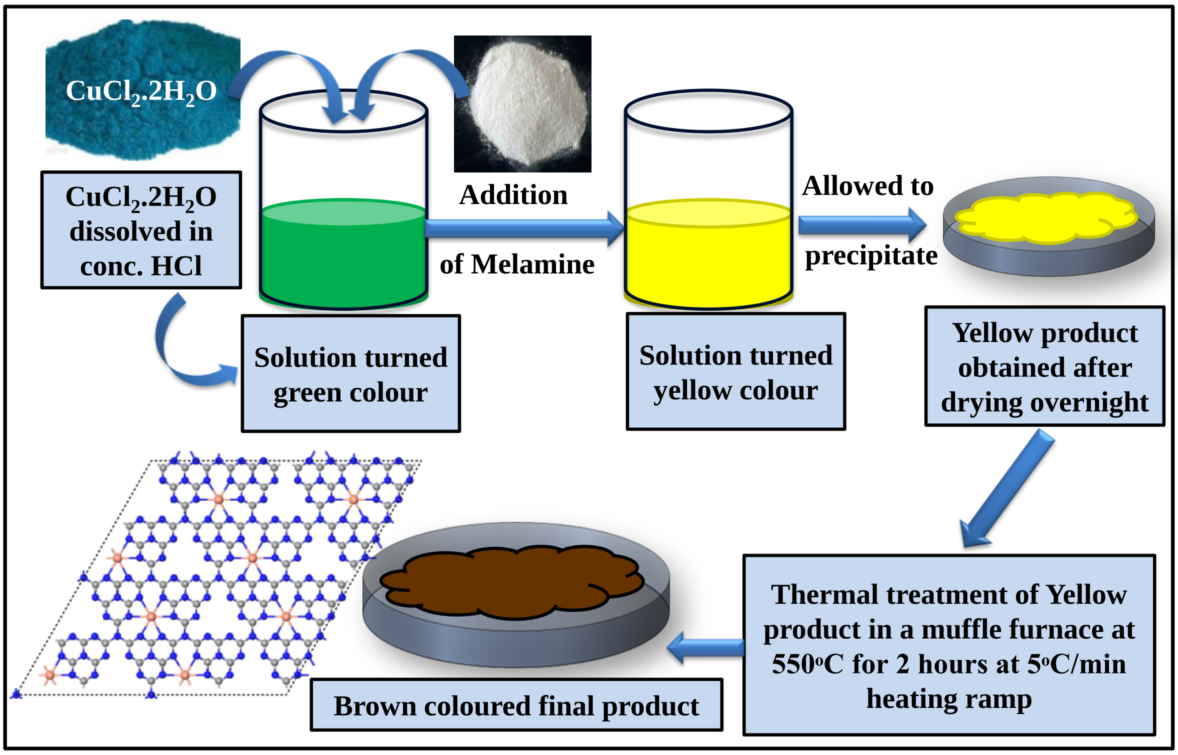

Fig. 5.2: *Schematic representation of synthesis procedure of CuCN*

5.2. Characterization techniques:

5.2.1. Characterization of triazine-based polymer MEG_{10}:

Thermogravimetric analysis (TGA) of the powdered sample was done using Perkin Elmer Diamond Pyris 480 thermogravimetric analyser with the N_2 flow rate of 150 mL/min and heating rate of 15 °C/min. X-Ray diffraction (XRD) studies were performed using Bruker D8 advanced diffractometer (1.2 kW, Cu Kα source λ =1.5405Å) while the low angle XRD profile was acquired by Rigaku XRD (1.3 kW, Cu Kα source, λ =1.5405Å). To study the chemical structure of the polymers Fourier transform infrared (FTIR) spectra, X-ray photoelectron spectroscopy (XPS) of the powder sample, and Raman spectra were carried out using Shimadzu FTIR-8400S, Kratos AXIS ULTRA XPS (monochromatic Al source; 117 W), and Witec Raman spectrophotometer excited at 532 nm, respectively. The survey scans and high resolution elemental scans for XPS analysis were carried out with pass energy of 160 at 1.00 eV energy step and pass energy of 20 and 0.1 eV energy step, respectively. The molecular weight distribution analysis of the polymer was carried out using ACQUITY advanced polymer chromatography (APC) system equipped with a refractive index detector. Dimethylformamide (DMF) was used as the mobile phase and the sample for measurement was prepared by dissolving 1 mg of MEG_{10} in 1 ml of DMF. The flow rate of DMF was maintained at 0.5 mL/min and the measurement was carried out at a temperature of 45 ºC. Poly(methyl methacrylate) (PMMA) standards were used to obtain the calibration curves and the columns are packed with ethylene bridged hybrid particles. Zeta potential of MEG_{10} was measured by Malvern Zeta sizer Nano-ZS 90 instrument. Field emission scanning electron microscopic studies and high resolution transmission electron microscopic studies were carried out using JEOL 6340F FEG-SEM and JEOL-JEM 2100 (200 kV), respectively. For Raman spectroscopy, FESEM and TEM analyses the aqueous dispersion of the samples were drop-casted on cleaned Al-foil substrate, on single-side polished Si-wafer and on C-coated Cu grids (300 mesh), respectively. The elemental ratios of the polymer were evaluated using elemental XPS through CasaXPS software (version 2.3.25) and energy dispersive X-ray (EDX) analyser equipped with the FESEM instrument. UV-visible diffuse reflectance spectrum (DRS) of the powder sample was obtained by UV–Vis spectrophotometer (Shimadzu 3600 UV-Vis-NIR) using $BaSO_4$ as a reflectance standard. Photoluminescence (PL) emission spectra of the aqueous sample dispersion of the polymer in presence of different metal salts were recorded in Shimadzu RF-6000 spectrofluorometer (150 watt Xe lamp source; $\lambda ex = 257.8$ nm). Fluorescence time decay was measured by Edinburgh FLS980 spectrometer. BET measurements were performed by N_2-BET Surface Area and Pore size Analyzer (NOVA 1000e) operating at 77K and 1 bar. The sample was degassed at 60 °C for 4 hours prior to the measurements.

Rietveld analysis: For the MEG_{10} polymer, X-ray powder diffraction (XRD) in conjunction with the Rietveld whole profile fitting method [239-241], which is regarded as the best known method for (micro)structure characterization, was adopted to obtain quantitative information on different structure and microstructure parameters (viz. lattice parameters, crystallite size, r.m.s. lattice strain, fractional atomic coordinates, etc.) simultaneously through a Marquardt least-square refinement procedure using Rietveld refinement software MAUD (V2.71) [242]. Primarily, this method involves simulating of a large portion of the experimental XRD pattern with analytical functions, in which the intensity is directly corresponded to the structure of each studied phase [243]. For the instrumental correction, the Cagliotti parameters [244], the instrumental asymmetry, and Gaussianity parameters were obtained for the XRD setup using standard Si. The shape of the peak broadening was represented by a pseudo-Voigt (pV) function, a combination of Cauchy (attributed to crystallite size effect) and Gaussian functions (attributed to r.m.s. strain effect). The orientation of crystallites in a polycrystalline assembly has a deep impact on some physical properties viz. anisotropy of bulk properties [245]. Presence of preferred orientation plays a significant role in changing the relative intensities of the Bragg peaks which can be accommodated by incorporating a mathematical modelling using March-Dollase function [246] into the calculation. The amount of texturing was determined by March-Dollase coefficient (r), where r>0 and r = 1 signified the distribution of the orientation to be random. The convergence of the fitting residual of this iterative method is achieved by minimizing the weighted residual parameter, $\boldsymbol{R_{wp}}$, with the help of the following expression:

$$\boldsymbol{R_{wp}} = \left\{\frac{\sum_i \left|\boldsymbol{w_i(I_{oi} - I_{ci})^2}\right|}{\sum_i \boldsymbol{w_i(I_{oi})^2}}\right\}^{\frac{1}{2}} \ldots\ldots\ldots\ldots\ldots\ldots.. \quad (5.1)$$

and the goodness of fitting (GoF) is monitored by comparing $\boldsymbol{R_{wp}}$ with

$$\boldsymbol{R_{exp}} = \left[\frac{\boldsymbol{(N-P)}}{\sum_i \boldsymbol{w_i(I_{oi})^2}}\right]^{\frac{1}{2}} \ldots\ldots\ldots\ldots\ldots\ldots.. \quad (5.2)$$

where w_i is the statistical weight, I_{oi} and I_{ci} are the observed and calculated XRD intensities, N is the weight and number of experimental observation and P is the number of fitting parameters.

5.2.2. Characterization of pristine and modified GCN:

The phase formation, chemical structure, morphology, surface area, and optical properties of pristine GCN, exfoliated GCN, and doped-GCN samples were analysed by several characterization techniques. The phase formation of the samples was confirmed from X-Ray Diffraction (XRD) employing a Rigaku Miniflex 600 X-Ray Diffractometer with Cu Kα as the source of radiation having wavelength λ = 1.54056 Å. A scan rate (2Θ) of 2° min^{-1} was used during analysis. The chemical structures of the samples were characterized by Fourier transform infrared spectroscopy (FTIR, Shimadzu FTIR-8400S). Different chemical bonding of the pristine and doped samples were confirmed from X-Ray Photoelectron Spectroscopic (XPS) analysis (Thermo Fisher Scientific Pvt. Ltd., UK, ESCALAB Xi+, WF = 4.39 eV, employing Al Kα source). For morphological analysis of the different synthesized samples, field emission scanning electron microscopic studies were performed using FESEM instrument (FESEM, Carl Zeiss Model Supra 55 Germany; JEOL 6340F FEG-SEM; and Hitachi S-4800 FESEM). Besides FESEM, transmission electron microscopic (TEM) analysis (by JEOL JEM 2100 PLUS) were performed to observe the morphologies of the samples. The elemental composition was evaluated by energy dispersive X-ray spectroscopy (EDS) recorded by Oxford Instrument EDS detector. The samples were coated with Pd-Au in a spin coater before EDS measurement. The optical properties of the samples were analysed by Diffuse Reflectance Spectroscopic (DRS) measurements employing Shimadzu-3600 UV-Vis-NIR spectrophotometer. Barium sulphate powder was used as the reflectance standard during DRS measurements. Photoluminescence spectroscopic studies were performed by employing Shimadzu RF-6000 spectrofluorometer. Brunauer–Emmett–Teller (BET) measurements were carried out employing an N_2-BET surface area and pore size analyser (Quantachrome NOVA 1000e) which operated at 77 K and 1 bar.

5.3. Test programs and analytical methods followed for application of different parametric estimations:

The different methodologies followed for wastewater remediation by triazine-based nanomaterials are discussed in this section. These methodologies include detection and sensing of heavy metal ions by fluorescence quenching technique, photocatalytic degradation of textile pollutants and heavy metal Cr(VI), and finally the reduction of toxic chemical pollutants by catalytic hydrogenation technique.

5.3.1. Fluorescence detection of heavy metals by MEG_{10}:

5.3.1.1. Materials and chemical reagents:

All the chemicals used were of AR grade. Lead nitrate ($Pb(NO_3)_2$, M.W: 331.2 g/mol) and ethylenediaminetetraacetic acid disodium salt dihydrate ($C_{10}H_{14}N_2Na_2O_8$, M.W: 336.21 g/mol, abbreviated as 'EDTA') were purchased from Loba Chemie. Calcium nitrate tetrahydrate ($Ca(NO_3)_2.4H_2O$, M.W: 236.15 g/mol), magnesium nitrate hexahydrate ($Mg(NO_3)_2.6H_2O$, M.W: 256.41 g/mol), sodium nitrate ($NaNO_3$, M.W: 84.9947 g/mol), potassium nitrate (KNO_3, M.W: 101.1032 g/mol), cadmium nitrate tetrahydrate ($Cd(NO_3)_2.4H_2O$, M.W: 308.49 g/mol), iron nitrate nonahydrate ($Fe(NO_3)_3.9H_2O$, M.W: 403.95 g/mol), cobalt nitrate hexahydrate ($Co(NO_3)_2.6H_2O$, M.W: 291.03 g/mol), nickel nitrate hexahydrate ($Ni(NO_3)_2.6H_2O$, M.W: 290.81 g/mol), copper nitrate trihydrate ($Cu(NO_3)_2.3H_2O$, M.W: 241.60 g/mol), zinc nitrate hexahydrate ($Zn(NO_3)_2.6H_2O$, M.W: 297.5 g/mol), silver nitrate ($AgNO_3$, M.W: 169.87 g/mol) and mercury nitrate monohydrate ($Hg(NO_3)_2.H_2O$, M.W: 342.62 g/mol) were procured from Merck. All the experiments were carried out in deionised water (18.3 MΩ).

5.3.1.2. Metal ion sensing performance:

0.05 g MEG_{10} dissolved in 10 ml DI water was used as 'MEG_{10} stock'. 5x10^{-3} g/mL, 1x10^{-3} g/mL and 1x10^{-4} g/mL metal salt stock solutions were prepared using calculated amounts of Ca, Mg, K, Na, Cd, Fe, Co, Ni, Cu, Zn, Pb, Ag, Hg metal salts in appropriate amount of DI water. For detection of ultra-trace level of Hg^{2+} ions the 1x10^{-4} g/mL Hg^{2+} solution was further diluted by 10, 100 and 1000 times such that the respective concentrations are 1x10^{-5} g/mL, 1x10^{-6} g/mL and 1x10^{-7} g/mL. The compositions given as set no. 1-5 in **Table 5.1** were prepared using the 5x10^{-3} g/mL, 1x10^{-3} g/mL and 1x10^{-4} g/mL solutions and their respective PL was recorded after ~5-10 min of incubation time. For 'ultra-trace' Hg^{2+} ion detection compositions no 6 & 7 were followed using the 10^{-5}-10^{-7} g/mL solutions. To test the potential of the MEG_{10} as an "ON/OFF" fluorescent sensor of Hg^{2+} ions we added 0.15 mL of 0.05 M EDTA solution to composition set no. 8 (shown in Table 1) to observe necessary changes in the PL intensity before and after EDTA addition. The pH was maintained at a buffer value of 6 for all sensing purposes.

Table 5.1. Composition of solutions for ion detection:

Set No.	MEG_{10} stock (mL)	Metal salt stock (mL)	DI water (mL)
1	0.3	0	2.7
2	0.3	1.2	1.5
3	0.3	1.7	1
4	0.3	2.2	0.5
5	0.3	2.7	0
6	0.3	0.1	2.6
7	0.3	0.2	2.5
8	0.15	1.2	1.5

Additionally, to test the efficiency of MEG_{10} as selective Hg^{2+} ion sensor in a mixture of aqueous solution of ions a 'combo stock solution' comprising of 6.43 x 10^{-3} M each of Fe^{2+}, Co^{2+}, Ni^{2+}, Cu^{2+}, Zn^{2+} and Ag^{+} ions was used as follows: 0.3 mL MEG_{10} stock solution, 1.5 mL DI water and 1 mL of combo stock were added and the PL was recorded. Then 0.2 mL of 2.92 x 10^{-3} M Hg^{2+} was added to this solution and PL was recorded again.

The MEG_{10} polymer was further employed to detect trace mercury ions present in tap water samples to prove its practical applicability. The tap water was collected from Jadavpur area, West Bengal, India, which was centrifuged at 10000 rpm followed by filtration through Millipore filter papers before sensing purposes to remove any insoluble. The procedure proposed by Lu et al. [247] and Wang et al. [248] was followed in this regard. The as obtained tap water samples were then injected with standard solutions of Hg^{2+} by varying the concentration of Hg^{2+} from 2 nM to 10 nM. The concentration of MEG_{10} was kept constant at 0.5 mg/mL.

5.3.1.3. Mathematical calculations:

The fluorescence quenching efficiency of triazine-based MEG_{10} polymer in presence of various heavy metal ions with different concentrations was measured through the Stern-Volmer equation (5.3) to compare the sensitivities of various analyte:

$$\frac{\boldsymbol{I_0}}{\boldsymbol{I}} = \mathbf{1} + \boldsymbol{K_{S-V}} . [\boldsymbol{Q}] \dots\dots\dots\dots\dots\dots \quad (5.3)$$

where, I and I_0 are the fluorescence intensities at the concentrations of metal ion analyte [Q] and in absence of any analyte, respectively, and the K_{sv} is the Stern-Volmer quenching effect coefficient of the sensing material for a given analyte. For Hg^{2+} the limit of detection (L_D) is calculated from equation (5.4):

$$\boldsymbol{L_D} = \mathbf{3}\ \boldsymbol{X}\ \frac{\boldsymbol{Standard\ Deviation}}{\boldsymbol{Slope}} \dots\dots\dots\dots\dots\dots \quad (5.4)$$

5.3.2. Photocatalytic degradation of toxic pollutants by exfoliated GCN:

5.3.2.1. Materials and chemical reagents:

All the chemicals used for application purpose were of AR grade. The materials required were rhodamine B dye ($C_{28}H_{31}ClN_2O_3$, M.W: 479.02 g/mol), potassium dichromate ($K_2Cr_2O_7$, M.W: 294.18 g/mol), hydrogen peroxide (H_2O_2, M.W: 34.01 g/mol, Density: 1.45 g/cm^3), and formic acid (85%) (HCOOH, M.W: 46.03 g/mol, Density: 1.22 g/cm^3). Other chemicals used were sodium chloride (NaCl), sodium bromide (NaBr), sodium sulphate (Na_2SO_4), sodium carbonate (Na_2CO_3), sodium bicarbonate ($NaHCO_3$), sodium nitrate ($NaNO_3$), calcium chloride ($CaCl_2$), magnesium chloride ($MgCl_2$), terephthalic acid (TA, $C_8H_6O_4$), isopropyl alcohol (IPA, C_3H_8O), ethylenediaminetetraacetic acid (EDTA, $C_{10}H_{16}N_2O_8$), silver nitrate ($AgNO_3$), citric acid ($C_6H_8O_7$), oxalic acid ($C_2H_2O_4$), methyl orange (MO, $C_{14}H_{14}N_3NaO_3S$), and methylene blue (MB, $C_{16}H_{18}ClN_3S$). Deionized water (DI) was used for experimental purposes.

5.3.2.2. Catalysis procedure:

The photocatalytic experiments for both RhB dye degradation and Cr(VI) reduction were carried out at ambient temperature employing a high pressure mercury lamp which acted as the visible light source. The lamp was equipped with a UV cut-off filter. The catalytic activity was carried out in a double-walled glass beaker specially designed to prevent the over-heating of the beaker by circulation of cold water through the hollow space between the walls. For RhB dye degradation, a 40 mL dye solution having a concentration of 10^{-5} M was prepared at first. This was followed by the dispersion of 20 mg of the as-prepared catalyst samples into the dye solution by vigorous stirring for 1 hr. in dark condition. After a desired adsorption-desorption equilibrium condition was achieved, some amount of H_2O_2 was added into the solution. Then the catalytic system was irradiated by the visible-light source. 4 mL of solution was collected at 15 min interval which was centrifuged to separate out the solid catalyst. The absorbance of the solutions were analysed by a UV-vis spectrophotometer. The initial concentration of the dye solution was varied as 10, 20, 30, and 40 µM; the catalyst dosage was varied as 10, 20, 30 and 40 mg; and the concentration of H_2O_2 was varied as 0, 0.1, 1, 5, 10, 15 and 20 mL/L. Necessary variation of the pH of the aqueous dye solution was achieved by mixing appropriate amount of HCl or NH_4OH to make the pH 2 and 11.5, respectively.

To study the effect of anions on the catalytic activity, 0.5 g/L of anionic salts like NaCl, NaBr, Na_2SO_4, Na_2CO_3, $NaHCO_3$ and $NaNO_3$ were added into the catalytic system. Similarly cationic salts like $CaCl_2$ and $MgCl_2$ were added in the same concentration to study the effect of cations. For scavenger studies to identify the active radicals in the catalytic process, IPA, EDTA and $AgNO_3$ were added into the system as scavengers for ·OH radicals, holes and electrons respectively. Terephthalic acid test (TA) was performed to detect the production of ·OH radicals with time in presence of H_2O_2 and the photocatalyst material under visible light irradiation. For this test, a 40 mL solution containing 20 mg GCNX and 10 mL/L H_2O_2 was prepared initially. Then 3 mM TA and 0.01 M NaOH was added into the above solution followed by switching on the visible light source. 4 mL of this solution was collected at 15 min time intervals and centrifuged to separate out the catalyst before analysing the emission spectrum of the solutions by PL spectroscopy. The excitation wavelength used was 315 nm. To study the effect of other interfering dyes on the catalytic activity of RhB, methyl orange (MO) and methylene blue (MB) dyes were chosen for experiments. For the RhB + MO mixed dye solution, 5 µM RhB and 5 µM MO were mixed together in 40 mL DI water; while for the

RhB + MB mixed dye solution, 5 µM MB was added with 5 µM RhB in 40 mL aqueous solution. Catalyst dosage and H_2O_2 concentration were maintained at 20 mg and 10 mL/L respectively.

For the Cr(VI) reduction process, a stock solution of concentration of 800 mg/L was prepared by dissolving dried anhydrous $K_2Cr_2O_7$ in DI. During the catalytic procedure, 5 mL of this stock solution was added into 40 mL DI followed by the addition of catalyst. The solution was then stirred continuously for an hour in dark before the addition of desired amount of formic acid (FA). This system was then subjected to visible light irradiation. At regular time intervals, 4 mL of this solution was collected and centrifuged before analysing them by UV-vis spectroscopy. Variations in the catalysis influencing parameters were performed by varying the catalyst dosage as 10, 20 and 30 mg; varying the FA amount as 0, 0.1, 0.45, 0.8, 1.6 and 2.4 mL; varying the initial Cr(VI) concentration as 0.4, 0.8 and 1.2 mg/mL; and varying the pH (by adding HCl or NH_4OH) as 2, 5, 6.5, 9 and 11.5. Besides FA, the effect of other organic acids on the reduction activity of Cr(VI) was studied by addition of citric acid, oxalic acid or EDTA into the catalytic system. Amount of organic acids were maintained at 0.1 g in 40 mL catalytic solution, GCNX dosage was maintained at 20 mg and Cr(VI) concentration was taken as 0.8 mg/mL. The effect of co-existing inorganic ions on the reduction of Cr(VI) was analysed by adding 0.5 g/L NaCl or Na_2SO_4 in the catalytic aqueous solution. In all cases GCNX dosage, FA amount and Cr(VI) concentration were maintained at 20 mg, 0.8 mL, and 0.8 mg/mL respectively.

To study its stability and practical applicability, the catalyst material was reused up to several catalytic cycles for both pollutants. After each cycle, the catalyst was collected, centrifuged and washed several times with DI followed by drying the sample overnight in an oven at 60 ^{o}C. Tap water was collected from a tap located at Jadavpur University, Kolkata, West Bengal, India. River water was collected from River Ganga flowing near Belur, Howrah, West Bengal, India. The river water was kept in static condition for five days to separate the clear water from the sediments. The clear water was again subjected to filtration prior to the photocatalysis procedure. For RhB degradation in actual water systems, the catalytic parameters were maintained as 20 mg GCNX, 10 mL/L H_2O_2 and 20 µM RhB solutions. For Cr(VI) reduction in river water system, 20 mg GCNX amount, 0.8 mg/mL Cr(VI) concentration, and 0.8 mL FA amount were used; while for carrying out reduction in tap water system, 0.4 mg/mL Cr(VI) solution was used keeping the other parameters same.

5.3.2.3. Mathematical calculations:

For H_2O_2-assisted photocatalytic dye degradation, the reactions are considered to follow a pseudo-first-order kinetics model because the rate of the catalytic degradation reactions remained independent of the H_2O_2 concentration. Thus, as per Langmuir–Hinshelwood kinetics, the pseudo-first-order reaction is given as:

$$-\frac{d\boldsymbol{C_{RhB}}}{dt} = \boldsymbol{kC_{RhB}\,C_{OH*}} \ldots\ldots\ldots\ldots\ldots\ldots..(5.5)$$

where C_{RhB} represents the RhB dye concentration and C_{OH*} indicates the hydroxyl radical concentration. In excess H_2O_2 (in excess water), the C_{OH*} term remains constant, and the reaction rate is independent of this factor. Thus, following the pseudo-first-order hypothesis, equation (5.5) can be further simplified as follows:

$$-\frac{d\boldsymbol{C_{RhB}}}{dt} = \boldsymbol{kC_{RhB}} \ldots\ldots\ldots\ldots\ldots\ldots..(5.6)$$

Finally, after the integration of equation (5.6),

$$\int_{C_{RhB0}}^{C_{RhB}} -dC_{RhB} = k\int_{0}^{t} dt \ldots\ldots\ldots\ldots\ldots\ldots..(5.7)$$

$$ln\frac{C_{RhB0}}{C_{RhB}} = kt \ldots\ldots\ldots\ldots\ldots\ldots.. (5.8)$$

where C_{RhB} (or C_T) denotes the concentration of RhB at irradiation time t = T, and C_{RhB0} (or C_0) denotes the initial RhB concentration at time t = 0. The value of the rate constant (k) in min^{-1} is calculated from the slope of the linearized plot of $ln(C_0/C_T)$ versus irradiation time in min. Additionally, non-linear fitting of the pseudo-first-order model has been performed following the equation:

$$C_T = C_0\, X\, e^{-kt} \ldots\ldots\ldots\ldots\ldots\ldots..(5.9)$$

The value of k is obtained from the converged non-linear best regression fitting of the data points in the plot of C_T versus irradiation time (t).

Similar to the H_2O_2-assisted catalytic degradation of RhB, the FA-mediated Cr(VI) reduction also followed pseudo-first order kinetics because FA was maintained at a higher concentration than the pollutant during the catalysis process. The photoreduction efficiency in terms of percentage (η) has been calculated by the equation (5.10):

$$\eta\ (\%) = \frac{C_0 - C_T}{C_0}\ X\ 100 \ldots\ldots\ldots\ldots\ldots\ldots..(5.10)$$

where C_T denotes the concentration of Cr(VI) at irradiation time t = T, and C_0 denotes the initial Cr(VI) concentration at time t = 0.

5.3.2.4. Statistical modelling:

The net number of experiments to be performed to assess the synergistic effects of the parameters on the catalytic degradation of RhB and Cr(VI) was determined and optimised using Box–Behnken design (BBD) in this work. This method suggests that if N is the number of required experiments, K is the number of catalytic parameters, and C_0 is the number of mid-points, then [249]:

$$N = 2K(K-1) + C_0 \ldots\ldots\ldots\ldots\ldots\ldots..(5.11)$$

BBD can be employed to study the response function with three-level variables by conducting the minimum number of runs. BBD was applied in this present work to achieve the best degradation efficiency by optimising the experimental conditions using the GCNX photocatalyst and visible light irradiation. The three parameters that were chosen in the case of RhB degradation were the amount of catalyst (mg) (X_1), H_2O_2 concentration (mL/L) (X_2), and RhB concentration (µM) (X_3). Similarly, for Cr(VI) reduction, the three chosen factors were the amount of catalyst (mg) (X_1), FA amount (mL) (X_2), and Cr(VI) concentration (mg/mL) (X_3).

The experimental levels and ranges for each independent catalytic variable are shown in **Table 5.2** (for RhB) and **Table 5.4** (for Cr(VI)), respectively. Fifteen experimental runs were performed following equation (5.11) (K = 3, C_0 = 3) with their respective low (−1), mid-point (0), and high (+1) values. To estimate the error, the midpoint (0) of the BBD was calculated three times. The ranges of the catalytic parameters were chosen following preliminary experiments, and the variables were selected by determining the parameters which had the most influential effects on the photocatalytic activity. **Table 5.3** for RhB and **Table 5.5** for Cr(VI) reduction give complete lists of the fifteen experimental runs.

Table 5.2. The experimental levels and ranges for each independent catalytic variable for RhB degradation:

Variable Design	Factors	Range and Levels		
		-1	0	1
X_1	Catalyst amount (mg)	10	20	30
X_2	H_2O_2 concentration (mL/L)	5	10	15
X_3	RhB concentration (μM)	10	20	30

Table 5.3. The complete list of the fifteen experimental runs for RhB degradation:

Run Order	Coded-level of variables			Actual level of variables			Degradation Efficiency	
	X_1	X_2	X_3	X_1	X_2	X_3	Observed	Predicted
1	0	1	-1	20	15	10	99.53	100.00
2	-1	0	1	10	10	30	76.11	77.287
3	0	-1	-1	20	5	10	98.41	99.233
4	-1	1	0	10	15	20	91.64	91.287
5	0	1	1	20	15	30	97.47	96.633
6	1	0	-1	30	10	10	99.47	98.283
7	1	-1	0	30	5	20	98.42	98.763
8	0	0	0	20	10	20	98.97	98.958
9	0	0	0	20	10	20	98.63	98.958
10	-1	0	-1	10	10	10	93.75	92.697
11	0	0	0	20	10	20	99.29	98.958
12	0	-1	1	20	5	30	88.80	87.403
13	-1	-1	0	10	5	20	81.13	81.357
14	1	0	1	30	10	30	96.53	97.573
15	1	1	0	30	15	20	99.99	99.753

Table 5.4. The experimental levels and ranges for each independent catalytic variable for Cr(VI) reduction:

Variable Design	Factors	Range and Levels		
		-1	0	1
X_1	Catalyst amount (mg)	10	20	30
X_2	FA amount (mL)	0.1	0.45	0.8
X_3	Cr(VI) concentration (mg/mL)	0.4	0.8	1.2

Table 5.5. The complete list of the fifteen experimental runs for Cr(VI) reduction:

Run Order	**Coded-level of variables**			**Actual level of variables**			**Reduction Efficiency**	
	X_1	**X_2**	**X_3**	**X_1**	**X_2**	**X_3**	**Observed**	**Predicted**
1	0	1	-1	20	0.8	0.4	95.94	100.00
2	-1	0	1	10	0.45	1.2	26.14	22.7
3	0	-1	-1	20	0.1	0.4	89.62	84.48
4	-1	1	0	10	0.8	0.8	57.03	55.46
5	0	1	1	20	0.8	1.2	34.77	40.02
6	1	0	-1	30	0.45	0.4	98.61	100.00
7	1	-1	0	30	0.1	0.8	58.86	60.55
8	0	0	0	20	0.45	0.8	61.78	61.1
9	0	0	0	20	0.45	0.8	61.94	61.1
10	-1	0	-1	10	0.45	0.4	81.48	78.00
11	0	0	0	20	0.45	0.8	59.44	61.1
12	0	-1	1	20	0.1	1.2	31.75	26.72
13	-1	-1	0	10	0.1	0.8	38.55	47.22
14	1	0	1	30	0.45	1.2	35.04	38.64
15	1	1	0	30	0.8	0.8	90.79	82.23

The observed degradation and reduction efficiencies are the values obtained from equation (5.10) by conducting experiments, whereas the predicted efficiencies are calculated from a second-order polynomial equation (equation (5.12)) which has been generated using Minitab Statistical Software (2021 Minitab, LLC, version 20.3). The equation has been derived by considering all the linear, square, and interaction terms between the variables [250].

$$\boldsymbol{Y = \beta_0 + \sum_{i=1}^{K}\beta_i X_i + \sum_{i=1}^{K-1}\sum_{j=2}^{K}\beta_{ij}X_iX_j + \sum_{i=1}^{K}\beta_{ii}X_i^2 + e_i} \text{ ………………. (5.12)}$$

$$\boldsymbol{Y = \beta_0 + \beta_1X_1 + \beta_2X_2 + \beta_3X_3 + \beta_{12}X_1X_2 + \beta_{13}X_1X_3 + \beta_{23}X_2X_3 + \beta_{11}X_1^2 + \beta_{22}X_2^2 + \beta_{33}X_3^2} \text{ ………………. (5.13)}$$

where Y(%) = the response variable, that is, the predicted degradation/reduction efficiency,

β_0 = interception coefficient, a constant

β_{11}, β_{22}, β_{33} = quadratic terms,

β_{12}, β_{13}, β_{23} = interaction coefficients.

e_i = random error constant

As obtained from the Minitab software, equation (5.13) can be written as the following:

For RhB degradation,

$$\boldsymbol{Degradation\ Efficiency}\ (\%) = \mathbf{68.77} + \mathbf{2.510}\boldsymbol{X_1} + \mathbf{1.318}\boldsymbol{X_2} - \mathbf{0.667}\boldsymbol{X_3} - \mathbf{0.05378}\boldsymbol{X_1^2} - \mathbf{0.0316}\boldsymbol{X_2^2} - \mathbf{0.02120}\boldsymbol{X_3^2} - \mathbf{0.0447}\boldsymbol{X_1X_2} + \mathbf{0.03675}\boldsymbol{X_1X_3} + \mathbf{0.0377}\boldsymbol{X_2X_3} \ldots\ldots\ldots\ldots\ldots\ldots \text{(5.13.1)}$$

For Cr(VI) reduction,

$$\boldsymbol{Reduction\ Efficiency}\ (\%) = \mathbf{88.7} + \mathbf{1.47}\boldsymbol{X_1} - \mathbf{4.0}\boldsymbol{X_2} - \mathbf{66.3}\boldsymbol{X_3} - \mathbf{0.0122}\boldsymbol{X_1^2} + \mathbf{12.1}\boldsymbol{X_2^2} + \mathbf{3.1}\boldsymbol{X_3^2} + \mathbf{0.96}\boldsymbol{X_1X_2} - \mathbf{0.514}\boldsymbol{X_1X_3} - \mathbf{5.9}\boldsymbol{X_2X_3} \ldots\ldots\ldots\ldots\ldots\ldots \text{(5.13.2)}$$

5.3.2.5. Theoretical methods:

The first principles calculations were carried out within the framework of density functional theory (DFT) using the Vienna ab-initio simulation package (VASP) [251,252]. All the calculations were performed using the projector augmented wave (PAW) [253] method. The Perdew–Burke–Ernzerhof (PBE) functional [254] within the generalized gradient approximation (GGA) was adopted for the exchange-correlation terms. An energy cut-off of 600 eV was utilized throughout all the calculations. The structural optimizations were performed at the Γ point. All the systems were allowed to relax until the total energies converged below 10^{-5} eV/ atom. The effect of the dispersive forces were taken into account using the DFT+D3 (Grimme's) method with the Becke-Johnson damping function [255] as implemented in VASP. The GCN blocks were modelled by considering a triangular GCN unit with the edge dangling bonds functionalized with hydrogen/ functional groups and was placed in a cubic cell of length 25 Å to avoid interaction between its recurrent images. All the calculations were carried out in a spin unrestricted manner.

The adsorption energy of a H_2O_2/HCOOH molecule on edge-functionalized GCN blocks was calculated using the following formula:

$$\boldsymbol{E_{Ads}} = \boldsymbol{E_{GCN+Ad}} - \boldsymbol{E_{GCN}} - \boldsymbol{E_{Ad}} \ \ldots\ldots\ldots\ldots\ldots\ldots.. \text{(5.14)}$$

Where E_{GCN+Ad}, E_{GCN} and E_{Ad} are the ground state energies of adsorbed-H_2O_2/HCOOH GCN, pure GCN block, and one free adsorbate molecule respectively as computed from the DFT calculations.

5.3.3. Catalytic hydrogenation induced reduction of pollutants by doped-GCN:

5.3.3.1. Materials and chemical reagents:

All materials used were of AR grade. The materials required for application purpose were 4-nitrophenol, 3-nitrophenol, 2-nitrophenol (NP, $C_6H_5NO_3$, M.W: 139.11 g/mol), methyl orange (MO, $C_{14}H_{14}N_3NaO_3S$, M.W: 327.33 g/mol), methylene blue (MB, $C_{16}H_{18}ClN_3S$, M.W: 319.85 g/mol), methyl red (MR, $C_{15}H_{15}N_3O_2$, M.W: 269.30 g/mol), congo red (CR, $C_{32}H_{22}N_6Na_2O_6S_2$, M.W: 696.66 g/mol), rose Bengal (RB, $C_{20}H_2Cl_4I_4Na_2O_5$, M.W: 973.67 g/mol), rhodamine B (RhB, $C_{28}H_{31}ClN_2O_3$, M.W: 479.02 g/mol), and sodium borohydride ($NaBH_4$, M.W: 37.83 g/mol). All these materials of highest purity were purchased from Merck. Deionized water was used throughout all experimental procedures.

5.3.3.2. Catalysis procedure:

For the catalytic study of degradation of nitrophenol (NP) compounds, stock solutions of 1 mM 4-Nitrophenol (4-NP), 3-NP and 2-NP were prepared by dissolving 10 mg NP compounds in 50 mL DI water. $NaBH_4$ stock solutions were freshly prepared in different concentrations (0.01 M, 0.05 M, 0.1 M, 0.5 M and 1 M) and catalyst materials were taken in 1 mg, 2 mg, 4 mg and 6 mg dosages. During the study of catalytic activity, some amount of the catalyst was taken in a quartz cuvette having 10 mm path length, followed by the immediate addition of 3 mL of $NaBH_4$ stock solution and 0.3 mL of NP stock solution. The total volume of the solution was maintained at 3.3 mL and the concentration of 4-NP in the cuvette was 0.09 mM. The yellow colour of the solution rapidly turned colourless and the corresponding UV spectrum was measured by a Shimadzu-3600 UV-Vis-NIR spectrophotometer.

To study the effect of increased concentrations of 4-NP on the catalytic activities, 5 mM, 10 mM, and 15 mM of 4-NP stock solutions were prepared and the degradation activities were measured by similar procedure. It is to be noted that the stock solution of 4-NP had a neutral pH of 7, whereas the stock solution of 0.1 M $NaBH_4$ had a slightly basic pH value. Hence the reaction solution (4-NP + $NaBH_4$) inside the cuvette had a pH value of 9. The catalytic activity of the as-prepared catalyst in reduction of 1 mM 4-NP was studied at a basic pH value (pH = 11.5) by adding appropriate amount of 0.1 M of NH_4OH in the reaction solution. The stability of the catalysts was examined by reusing them for more than one catalytic cycle. This was performed by extracting the used catalyst from the dye-$NaBH_4$ solution after completion of a particular catalytic cycle through filtration, then washing it repeatedly with DI water, and finally drying it at 50 ^{o}C to obtain the product.

For the catalytic study of degradation of different cationic and anionic dyes, 0.1 mM of dye solutions (MO, MB, MR, CR, RB, and RhB) were prepared by individually mixing appropriate amount of dye compounds in 50 mL DI water. 0.1 M $NaBH_4$ solution was freshly prepared in DI water. Catalyst dosage was varied as 1 mg, 2 mg and 4 mg. During the catalytic activity, measured amount of catalyst materials were taking in a quartz cuvette followed by the addition of $NaBH_4$ and dye solution. The concentrations of MO dye were varied in such a way so that the final concentrations of the dye in the cuvette were $9.09\text{x}10^{-6}$ M, $3.34\text{x}10^{-5}$ M, $6.67\text{x}10^{-5}$ M, and $8.34\text{x}10^{-5}$ M whereas the corresponding concentrations of $NaBH_4$ were varied as 0.09 M, 0.067 M, 0.034 M, and 0.016 M respectively. The concentration of MB and RhB dyes were varied as $9.09\text{x}10^{-6}$ M, $3.34\text{x}10^{-}5$ M, and $6.67\text{x}10^{-5}$ M whereas that of MR was varied as $3.34\text{x}10^{-5}$ M, $6.67\text{x}10^{-5}$ M, and $8.34\text{x}10^{-5}$ M. For the RB and CR dyes, concentration of dyes in the cuvette was varied as $3.34\text{x}10^{-5}$ M and $6.67\text{x}10^{-5}$ M.

For the study of degradation of mixed dye, initially three 20 mL solutions of MO, MR and CR dyes were prepared each having concentration of 0.1 mM. These three individual solutions were mixed together to form a bright reddish orange coloured solution termed as Mixed Dye 1 (Mxd. Dye 1). Another 50 mL, 0.1 mM solution of MB dye was prepared separately. 5 mL of Mxd. Dye 1 and 5 mL of MB solution were finally mixed together to obtain the greenish-blue coloured Mxd. Dye 2 solution. The concentrations of the mixed dyes and $NaBH_4$ were varied along with the variation in the catalyst amount (1 mg, 2 mg, and 4 mg). For the pH variation studies, performed only for MO dye, few drops of 0.1 M HCl and 0.1 M of NH_4OH were added into the reaction solution to make the pH values 2 and 11.5, respectively.

5.3.3.3. Mathematical calculations:

The established concept till date to elucidate the type of reaction kinetics model followed during sodium borohydride mediated heterogeneous catalysis is pseudo-first order reaction model [256]. Throughout the catalysis procedure, the concentration of $NaBH_4$ remained at a much higher value than the concentration of the pollutants. Owing to this, the reaction rates are supposed to be independent of the $NaBH_4$ concentration as it remained unchanged during the reaction time period [47]. The rate of reduction was solely dependent on the concentration of the pollutants. The pseudo-first order reaction equation is given as:

$$\ln\left(\frac{C_0}{C_T}\right) = kt \dots\dots\dots\dots\dots\dots..(5.15)$$

where, C_0 is the concentration of pollutant at time t = 0 and C_T is the concentration at time 't' measured from the corresponding absorption spectra. 'k' is the pseudo-1st order reaction rate constant. A linear plot was obtained by plotting $\ln(C_0/C_T)$ with time, the slope of which gave the value of 'k'.

5.3.3.4. Theoretical Methods:

The first principles calculations were carried out using Vienna ab-initio simulation package (VASP) [251,252,257,258] with the projector augmented wave (PAW) [253] approach. The Perdew-Burke-Ernzerhof (PBE) functional [254] was implemented to describe the exchange correlation parts of the Hamiltonian within the generalized gradient approximation (GGA). During all the structural optimization and electronic property calculations, the plane of basis set cut off was kept 600 eV. During structural optimization, all the systems were allowed to relax until the total free energies converged below 10^{-5} eV/ atom. A vacuum slab of 24 Å was utilized along the **c** direction during all the calculations to ward off any spurious interaction between the periodic images. To study the dye degradation process on Cu decorated GCN, a (2×2) supercell of GCN was considered for 4-NP to minimize the interaction between the periodic images of adsorbed 4-NP along the lateral directions. For the larger MO and MB dye molecules, a (3×3) supercell of GCN was considered for the same reason. As the supercell dimensions were sufficiently large, a Γcentered k-point mesh of (1×1×1) was implemented during the study of dye degradation process on CuCN. Much denser k-point meshes of (15×15×1), (9×9×1) and (5×5×1) were utilized respectively for the DOS and ELF calculation of GCN and CuCN unit cells, Cu decorated (2×2×1) supercell of GCN and Cu decorated (3×3×1) supercell of GCN. As GGA typically underestimate the band gap value, the band structure of the GCN and CuCN unit cells were calculated using the hybrid HSE06 functional [259]. The effect of the van der Waals interaction was taken into account using the DFT + D2 (Grimme's) method [260] as implemented in VASP.

The formation energy of Cu decorated GCN was computed using the following relation:

$$\mathbf{E_{for} = E_{CuCN} - E_{GCN} - n_{Cu}\mu_{Cu}} \text{ ……………….. (5.16)}$$

Where E_{CuCN} and E_{GCN} are the total ground state energies of the Cu decorated GCN and GCN cell of same dimension respectively. n_{Cu} is the number of Cu atom incorporated in the GCN system and μ_{Cu} is the chemical potential of Cu calculated using the FCC Cu as the reference system.

The dye adsorption energies on the CuCN systems were calculated using the following formula:

$$\mathbf{E_{ads} = E_{CuCN\text{-}dye} - E_{CuCN} - E_{dye}} \text{ ……………….. (5.17)}$$

Where, $E_{CuCN\text{-}dye}$ and E_{CuCN} are the total ground state energies of the dye adsorbed and bare CuCN system respectively. E_{dye} is the ground state energy of a dye molecule as computed from the DFT calculations. The relative energy change of each reaction step throughout the dye degradation processes were computed using the following formula taking the energy of the initial step as reference:

$$\mathbf{\Delta E = E_n - E_i} \text{ …………….. (5.18)}$$

Where, E_n is the enthalpy of the system at n^{th} reaction coordinate and E_i is the enthalpy of the system at the initial or very first reaction coordinate. The Mulliken population analysis was carried out using the CAmbridge Serial Total Energy Package (CASTEP) [261] code with the same specifications of the convergence criteria and energy cut-off for different cell sizes as the VASP calculations.

Summary of the chapter:

The detailed synthesis procedures of all the samples used in the present research works were discussed in this chapter. The different characterization techniques used to investigate the structural, chemical, and optical properties of the nanomaterials were also mentioned. Relevant discussions will be done in the next chapter. Finally, the methods implemented for application of these nanomaterials in the field of wastewater remediation were also discussed.

CHAPTER 6:

RESULTS AND DISCUSSION

PART 1

Characterization results of the as-synthesized nanomaterials

This chapter presents the experimental results obtained from the various experiments performed during the course of the research works and their relevant discussions. The results obtained from the different characterization techniques have been discussed in details. The experiments conducted on the as-synthesized nanomaterials to implement them in wastewater remediation have also been discussed. Plausible mechanisms are explained to understand the activity of these nanomaterials in degradation of toxic compounds from water environment.

6.1. Characterization of MEG_{10} triazine-based polymer:

6.1.1. Thermogravimetric Analysis (TGA):

The TGA curves of MEG_x are shown in **Fig. 6.1(a).** It reveals that the polymer prepared at pH 10 under hydrothermal treatment (MEG_{10}) exhibits a stable weight region up to 300 °C whereas MEG_6 and MEG_{12} both lose considerable amount of weight (~10-12%) before 100 °C due to removal of adsorbed water or ammonia (from NH_4OH medium), and finally start decomposing beyond 200 °C. This analysis indicates the non-volatile polymeric nature of MEG_{10}. Considering the greater thermal stability of MEG_{10} powder in comparison to MEG_6, MEG_{12} or in absence of hydrothermal treatment (refer to **Fig. 6.1(b)**), the MEG_{10} sample was chosen for further characterizations.

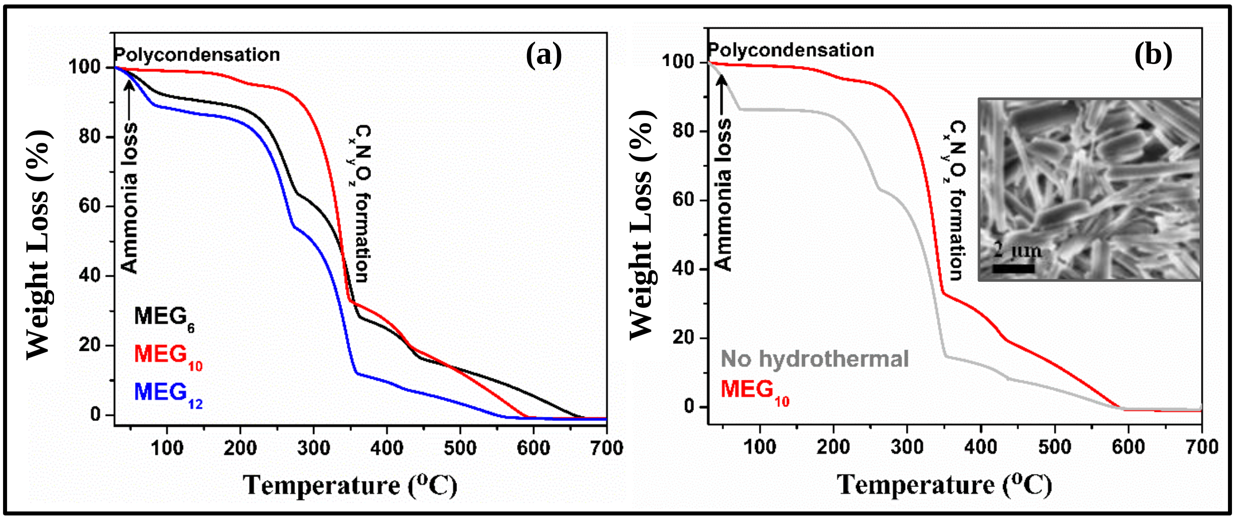

Fig. 6.1: *(a) TGA curves of MEG_x polymers prepared at pH 6, 10 and 12. (b) TGA analysis and FESEM image (inset) of melamine-EG polymer prepared at pH 10 without hydrothermal treatment*

6.1.2. Crystal structure evaluation:

The raw XRD graphical pattern of melamine and MEG_{10} are given in **Fig. 6.2(A)**. Simulated XRD pattern employing the Rietveld whole profile fitting method for polycrystalline melamine is depicted in **Fig. 6.3(a)**. All reflections in the XRD patterns are unambiguously identified comparing with its bulk counterpart (space gr. $P2_1/a$; a= 10.4330 Å, b= 7.4580 Å, c= 7.2380 Å, β= 113.30°) to emanate from monoclinic melamine and are indexed accordingly in **Fig. 6.3(b)** [262]. Textural and (micro)-structure characterizations of the sample are performed utilizing the Rietveld method based on the crystallographic information obtained from its bulk counterpart. Interestingly, the most intense (201) peak of melamine appears stronger than that of its bulk counterpart, resulting in mismatch in intensity (**Fig. 6.3(a)**). This is caused by the preferential growth of lattice planes along <201> crystallographic direction. Considering this effect of texturing, the XRD pattern of melamine is refined further using March-Dollase function and the simulated profile is shown in **Fig. 6.3(b)** [246]. The improvement in quality of fitting is easily noticeable from residue of fitting which confirms preferred orientation along <201> and the degree of orientation obtained from March-Dollase coefficient is found to be 0.4. Similar type of observation was noticed in case of SnO_2 and ZnO nanostructures with preferential growth [263,264].

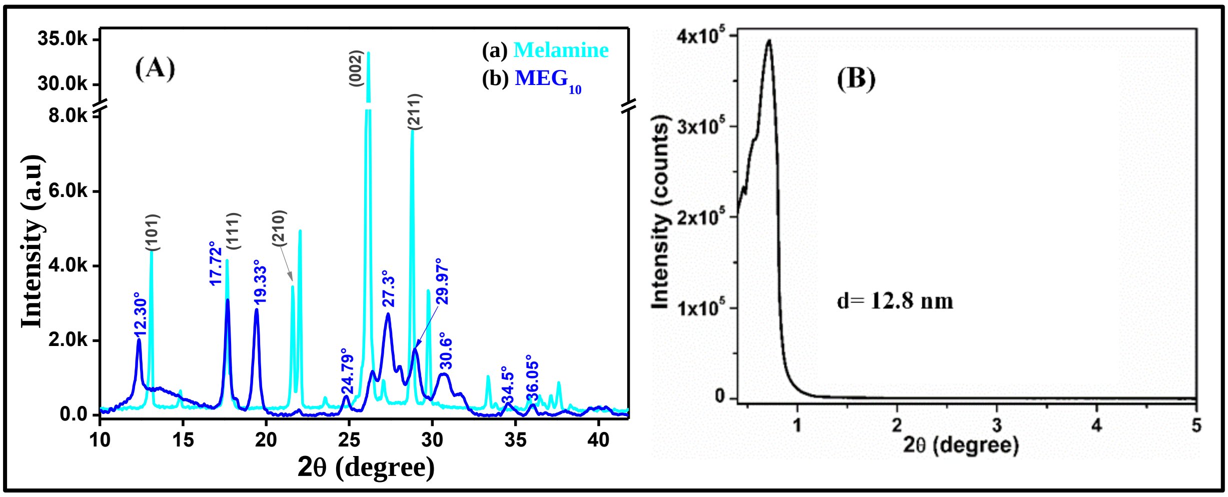

Fig. 6.2: *(A) High angle XRD spectra of (a) pure melamine and (b)* MEG_{10}*. (B) Low angle XRD shows mesoporous nature of* MEG_{10} *polymer*

Different structural parameters obtained from Rietveld analysis of the XRD pattern of polycrystalline melamine are displayed in **Table 6.1**. XRD pattern of MEG_{10}, displayed in **Fig. 6.3(c)**, is seemingly different from that of the polycrystalline melamine and appears to be a completely new phase. However, Rietveld analysis confirms that it comprises similar monoclinic melamine (space gr. $P2_1/a$) with considerably different lattice constants and cell angle compared to that of polycrystalline melamine.

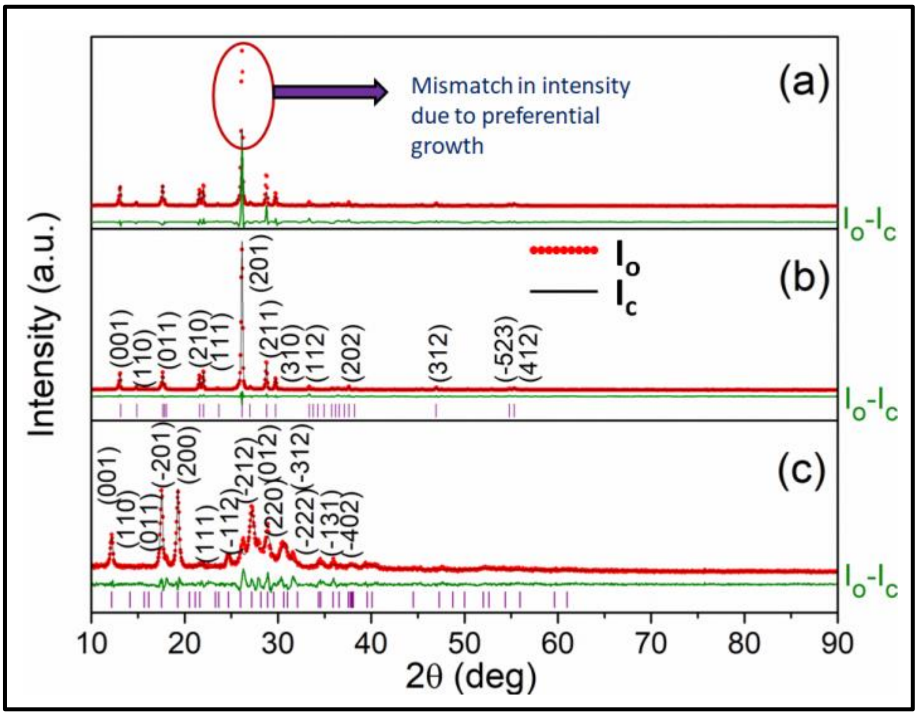

Fig. 6.3: *Simulated XRD spectra of melamine without using any texturing (a), using textural effect (b), and MEG_{10} (c) employing the Rietveld whole profile fitting method. Red dotted and black continuous lines represent the observed (I_o) and computed (I_c) patterns respectively. ($I_o - I_c$) represents the residue of the refinement*

Rietveld analysis in the present study reveals that lattice parameter ‘a’ decreases from 10.6036 Å to 10.1243 Å, whereas both lattice parameters ‘b’ and ‘c’ increase substantially to 8.2604 Å and 7.8860 Å, respectively, with reference to polycrystalline melamine. The cell angle (β) also increases from 112.22° to a value of 116.85°. The significant expansion in the unit cell volume of MEG_{10} to 588.41 Å^3 suggests that the condensation of melamine with ethylene glycol. Preferred orientation (textural effect) inherent to melamine facilitates in providing the rod shape morphology of MEG_{10}. Broader XRD peaks of MEG_{10} compared to those of melamine suggests smaller crystallite size. Rietveld analysis reveals the crystallite size and r.m.s lattice strain of MEG_{10} to be ~38 nm and 1.351×10^{-4} respectively. Different structural parameters obtained from the Rietveld analysis of the XRD pattern of MEG_{10} are tabulated in **Table 6.2**.

Table 6.1. Different structural parameters obtained by refining the XRD pattern of melamine:

Lattice parameters (Å)			**Cell angle (deg)**	**Atom types**	**Fractional coordinates**		
a	**b**	**c**	**β**		**x**	**y**	**z**
10.6036	7.5045	7.2872	112.22	C1	0.1508	0.6056	-0.0054
				C2	0.0595	0.6847	0.3503
				C3	0.1268	0.7692	0.1470
				N1	0.2772	0.9509	-0.1753
				N2	0.1257	0.4270	0.4440
				N3	0.0574	0.9515	0.2355
				N4	0.0050	0.8184	0.2011
				N5	0.1971	0.7794	-0.0348
				N6	0.1367	0.5153	0.2622
				H1	0.3703	0.4166	-0.0822
				H2	0.2446	0.4667	0.0038
				H3	0.0545	0.2026	0.6081
				H4	0.0970	0.5337	0.5542
				H5	-0.0020	0.5011	0.2144
				H6	0.0039	0.0300	0.0726

The unit cell volume of polycrystalline melamine enhances from 517.25 Å^3 to 536.81 Å^3 with respect to its bulk counterpart primarily due the expansion of all the lattice parameters. However, the cell angle (β) reduces marginally from 113.30° to 112.22°. Coherently diffracting domain (crystallite) size and r.m.s. lattice strain of polycrystalline melamine are found to be 253.45 nm and 1.954×10^{-4} respectively.

Table 6.2. Different structural parameters obtained by refining the XRD pattern of MEG$_{10}$:

Lattice parameters (Å)			**Cell angle (deg)**	**Atom types**	**Fractional coordinates**		
a	**b**	**c**	**β**		**x**	**y**	**z**
10.1243	8.2604	7.8860	116.85	C1	0.2798	0.4466	0.0052
				C2	0.2045	0.5430	0.3230
				C3	0.0216	0.8022	0.3561
				N1	0.0964	0.3628	-0.3370
				N2	0.0917	-0.0213	0.4738
				N3	0.0017	0.2037	0.1936
				N4	-0.0017	0.6743	0.5033
				N5	0.3465	0.0740	0.1861
				N6	0.1108	0.2726	0.1151
				H1	0.5662	0.7102	0.3356
				H2	0.0400	0.8303	-0.0151
				H3	0.0072	0.0072	0.7706
				H4	0.0125	0.1735	0.6265
				H5	0.0353	0.8177	0.0061
				H6	0.0270	0.1663	0.6257

6.1.3. Morphological analysis:

FESEM images reveal the presence of nanodendritic clusters composed of several nanowires (**Fig. 6.4(A-D)**) with the diameter in the range of 70-130 nm (**Fig. 6.4(A)**). The C: N: O atomic ratio obtained from elemental EDX analysis is 40.9:43.1:16.0 (shown in **Fig. 6.5**), which is close to that obtained from XPS analysis (C: N: O= 37.42:43.86:18.73). **Fig. 6.4(E)** shows the TEM image of a portion of the nanodendritic structure. The selected area diffraction pattern confirms the highly crystalline nature of the polymer, in agreement with the XRD analysis, with (200) and (220) planes at ~4.54 and 3.05 Å, respectively (**Fig. 6.4(F)**). A broad peak at 0.7° (~12.8 nm) in the low angle XRD profile (**Fig. 6.2(B)**) suggests that the pores are in mesoporous region. This is in agreement to the pore size distribution and the type III isotherm obtained in the N$_2$-BET analysis of MEG$_{10}$ powder (see **Fig. 6.6**).

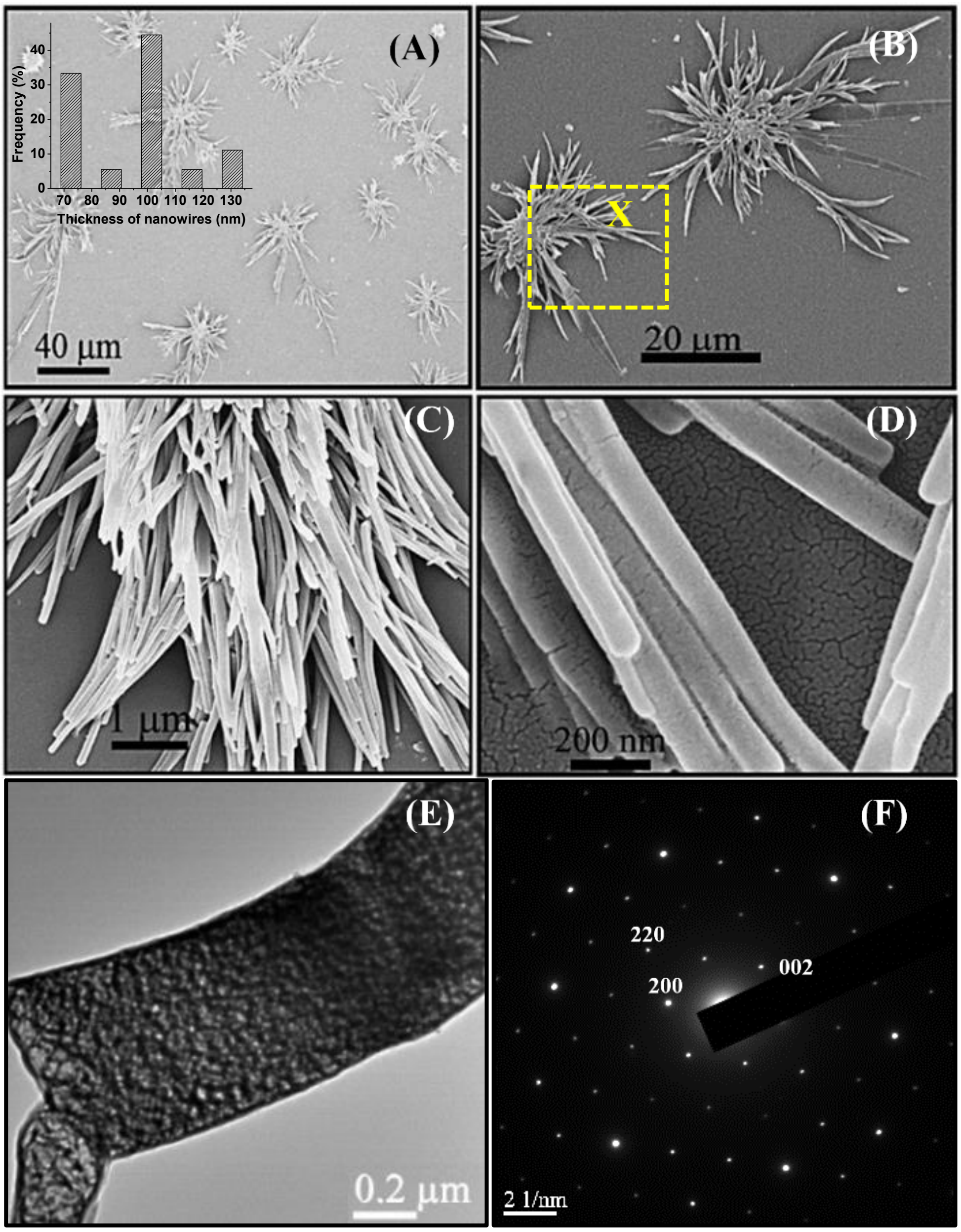

Fig. 6.4: *(A, B) FESEM images of* MEG_{10} *shows dendritic nanofibrous morphology. (A, inset) The histogram shows thickness of the nanowires. (C, D) Magnified views of a portion in (B), marked as 'X', shows distinct nanowires. (E) Low resolution TEM image. (F) SAED pattern shows single crystalline nature of the polymer*

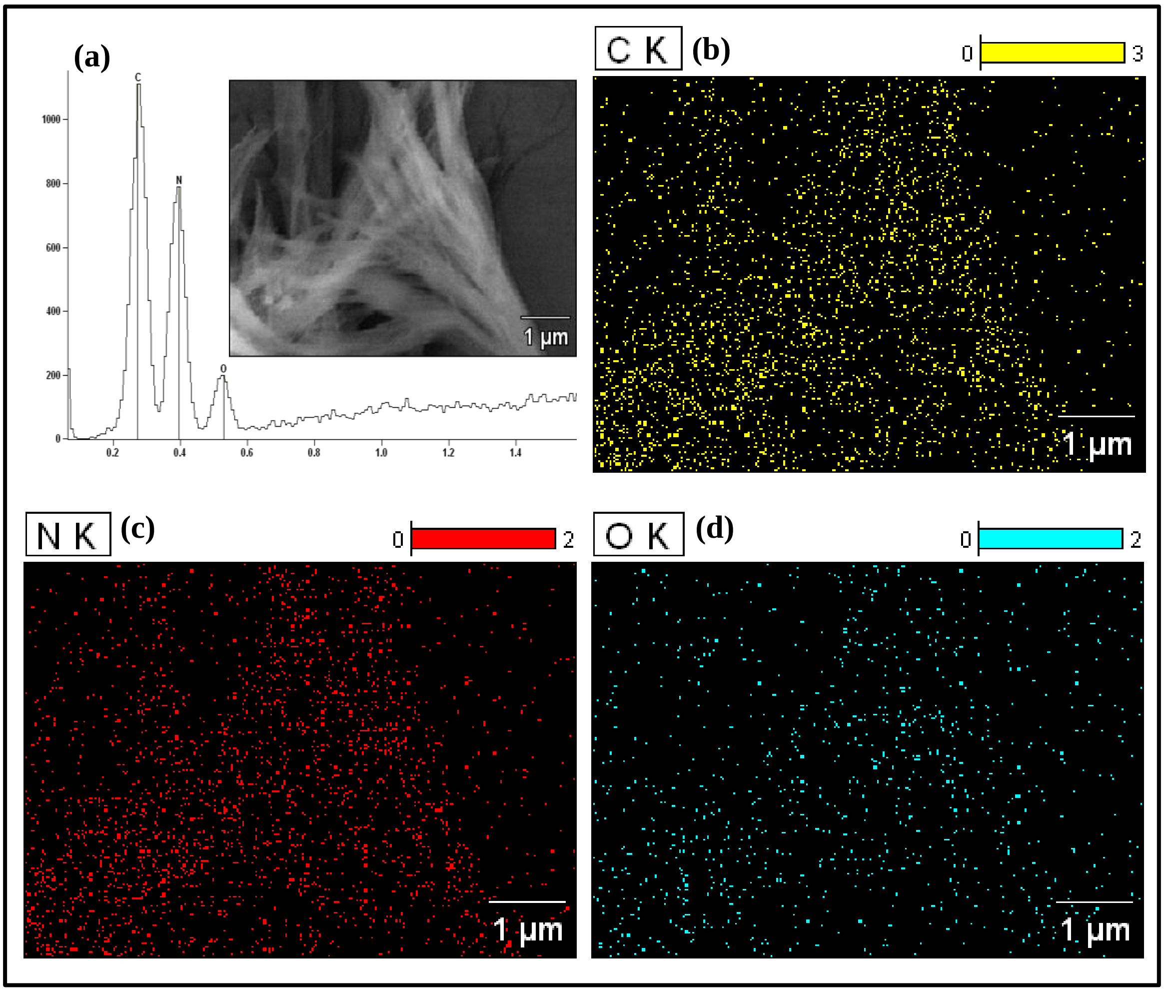

Fig. 6.5: *(a) EDX spectra of* MEG_{10} *showing the presence of C, N and O; corresponding elemental mapping images are shown in (b),(c) and (d) for C, N and O respectively*

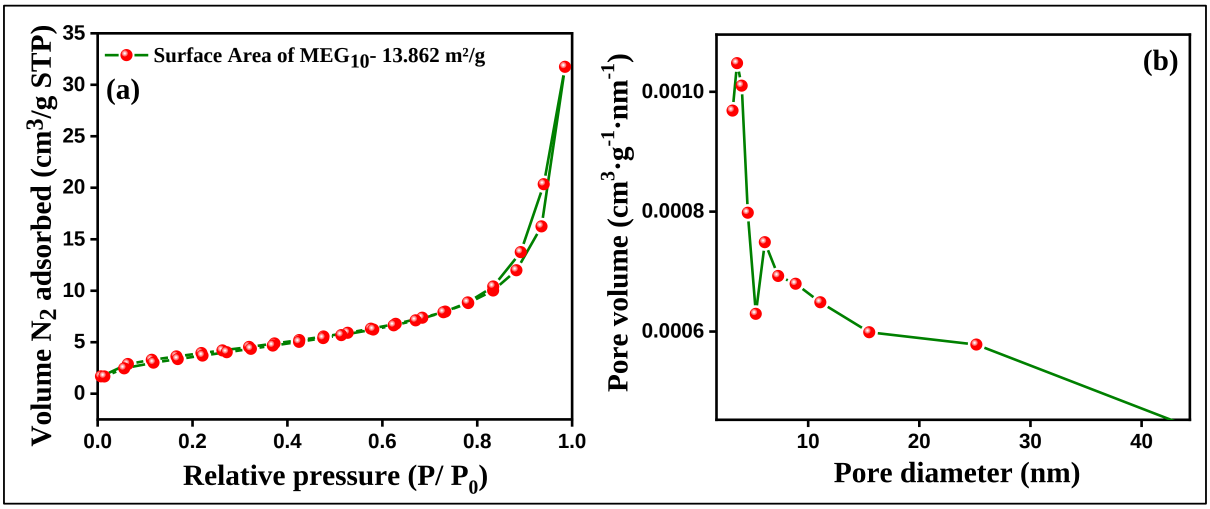

Fig. 6.6: *(a) Nitrogen adsorption-desorption isotherm showing classical type III isotherm and (b) corresponding BJH pore-size distribution curve of* MEG_{10} *polymer with BJH pore diameter of 3.611 nm and average pore diameter of 13.9 nm (total pore volume = 0.03707 cc/g for pores smaller than 65 nm;* $P/P_0 = 0.98530$*)*

As routine analysis we carried out the sorption analysis using N_2 gas at 77K and 1 bar. A low surface area (~13.8 m^2/g) is observed may be due to the common diffusional issues of N_2 molecules inside narrow pores [265,266]. The surface area can also be severly reduced due to the fusion of many pores probably during framework crystallization which results in structural variations like "pore expansion" [267]. However the polymer material may also be non-porous with large number of π stackings and the surface area as obtained from the BET analysis arises mainly due to the external surfaces.

6.1.4. Chemical structure analysis:

To understand the chemical structure of the polymer extensive spectroscopic characterisations were carried out. **Fig. 6.7(A)** shows the FTIR peaks of melamine (**a**) and MEG_{10} (**b**). Pristine melamine consists of prominent peaks at 3466, 3421, 3329 and 3143 cm^{-1} corresponding to the -NH stretching mode of hydrogen bonded primary amine, the peaks at 2204 cm^{-1} and 1410-1577 cm^{-1} region are assigned to the C≡N stretching and the characteristic peaks of triazine ring of melamine, respectively. The disappearance of the peaks at 3466 and 2204 cm^{-1} and a notable peak broadening in the region 3400-2500 cm^{-1} with the peak centred at 3413 along with the appearance of very small peak at 1762 cm^{-1} indicate the formation of 2° amine and –OH groups in MEG_{10}. While, the peaks at 1695-1450 cm^{-1} is attributed to the heptazine ring as observed in case of condensation of melamine units [268]. It is to be noted that the prominent peaks at 2400 and 1380 cm^{-1} are attributed to the combined stretching vibration of C-H and C-C, and the combined vibrations of O-H bending (δ_{O-H}) and C-O stretching (ν_{C-O}) modes, respectively. This symbolize the presence of H-bonded groups (N•••H-O or N-H•••OH) in the polymer. The peak at 813 cm^{-1}, characteristic to the out-of-plane vibration of the ring, confirms that the heterocyclic ring is intact. The relatively small but prominent peaks at 1050-1190 cm^{-1}, shown in the inset of **Fig. 6.7(A)**, are due to $-CH_2-O-CH_2-$ vibrations of ether. Therefore, it may be stated that the M and EG units undergo cross polymerization to yield MEG_{10}.

The Raman spectra, shown in **Fig. 6.7(B)**, shed considerable light into the nature of bonding in MEG_{10}. Raman spectrum of MEG_{10} (**Fig. 6.7(B)(b)**) shows two very intense and sharp peaks at 1061 cm^{-1} and 698.7 cm^{-1}. The former is attributed to the C-O stretching mode [269] whereas the later (~698.7 cm^{-1}) along with the peak at 990.1 cm^{-1} are due to the two ring breathing modes of the heptazine units [270]. The peaks at 401.5 and 483.5 cm^{-1} are assigned to the HNCN torsion mode, while the peak at 579.8 cm^{-1} is due to the out-of-plane C-N-C bending vibration. The small peaks at 1352.5, 1468.5, 1527.9 and 1578.8 cm^{-1} are ascribed to the H-C-H wagging (M) and C-O-H bending (EG), the H-C-H bending and A_1 vibration of heptazine ring, the C-N stretching vibration (M), and secondary vibration of the heterocyclic ring, respectively. The FTIR and Raman spectra confirm the presence of heptazine units bonded together via N-C-N units and possessing –C-OH groups/tails.

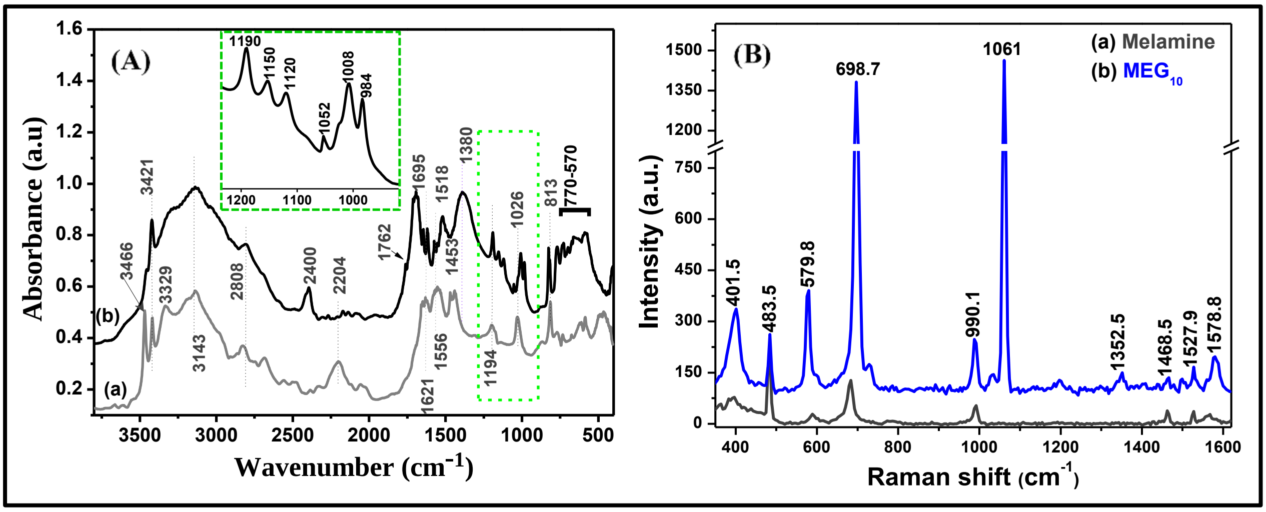

Fig. 6.7: (A) FTIR spectra and (B) Raman spectra of (a) pure melamine and (b) MEG_{10} composite polymer

XPS analysis plot of MEG_{10} is shown in **Fig. 6.8**. Deconvolution of the C1s (**Fig. 6.8(b)**) spectra reveals three peaks at 288.7, 286.6, and 284.6 eV, which correspond to C-O bonding, C-N bond of C-NH group and C=N bond of $[(N-)_2C(=N)]$ group of the heterocyclic ring. The N1s spectra (**Fig. 6.8(c)**) shows a sharp peak at 398.6 eV which are ascribed to the tertiary or secondary N atoms of either $N(–C)_3$ or $H–N–(C)_2$ groups, along with a prominent π-π* satellite peak at 405.8 eV ($\Delta = 7.2$ eV). The O1s peak at 530.5 eV is due to the presence of C-O group (**Fig. 6.8(d)**). The XPS results confirms the presence of heterocyclic rings with C=N, C-N and C-O functional groups.

The H^1-NMR spectra, given in **Fig. 6.9**, further reveal the peaks corresponding to the heptazine repeating units along with the presence of $–CH_3$ groups. Considering the combined results from the FESEM images and FTIR, Raman, NMR and XPS analyses of MEG_{10}, the plausible mechanism for the formation of MEG_{10} is exhibited in **Fig. 6.10**.

Briefly, the M units co-condense into heptazine while the EG undergoes transformation into acetaldehyde intermediate via acidic hydrolysis and hydride shift mechanism. These synthons reacts to produce the possible amine-substituted monomer which condense either through N-

C-N or C-O-C linkages to produce the respective polymers A or B with different steric energies. The presence of both these linkages in MEG_{10} is corroborated in accordance with the FTIR and NMR results. The polymer chains form long nanorods which further reassemble into nanodendrites after the hydrothermal treatment.

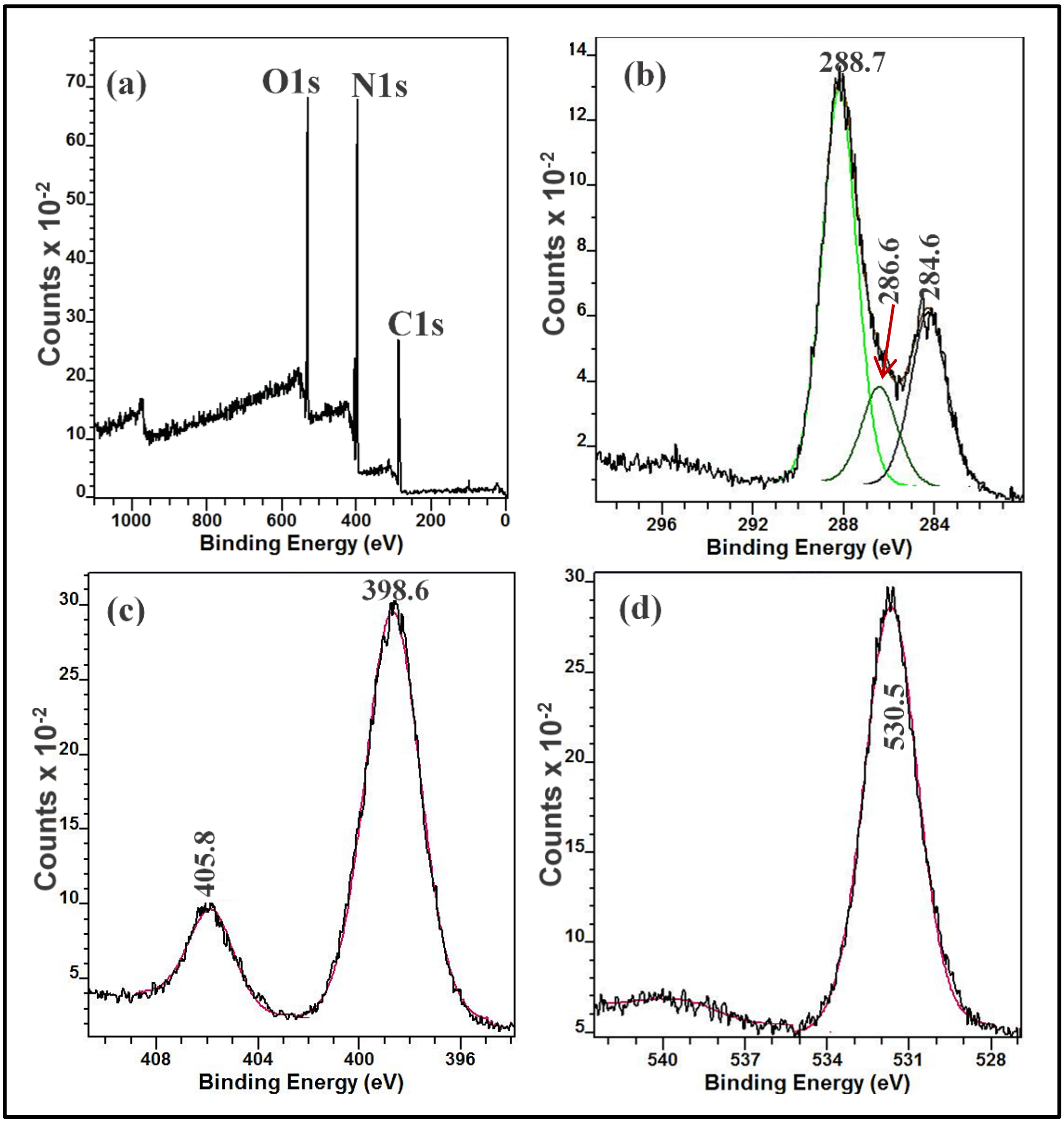

Fig. 6.8: *(a) XPS of MEG_{10} showing the presence of C1s, N1s and O1s peaks along with the elemental scan of (b) C1s, (c) N1s and (d) O1s spectra. The deconvoluted profiles are shown in the respective high-resolution XPS spectra*

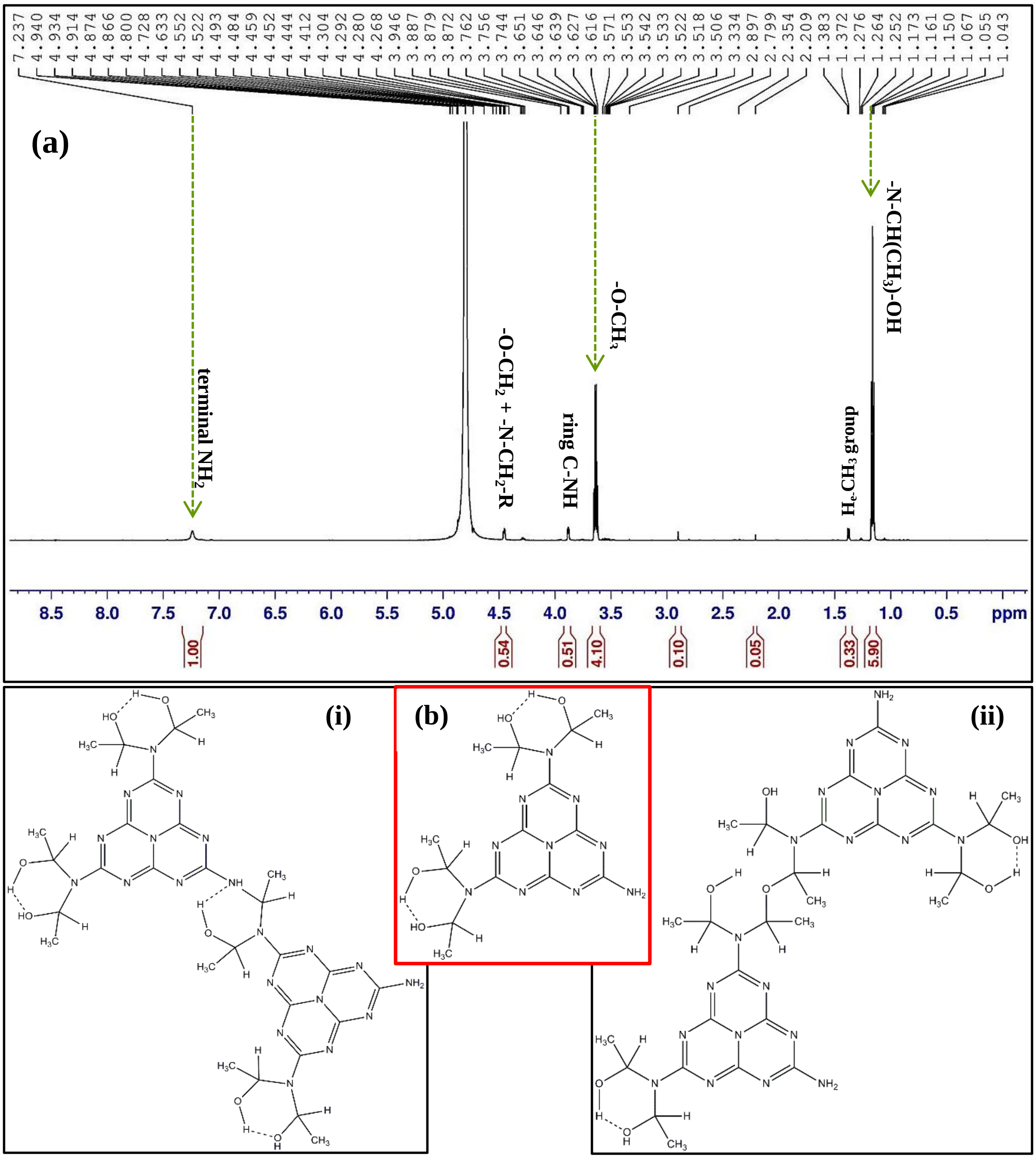

Fig. 6.9: *(a) ^{1}H-NMR spectra of MEG$_{10}$. Possible structures of the repeating unit created from the monomeric structure (b) are shown in (i) and (ii)*

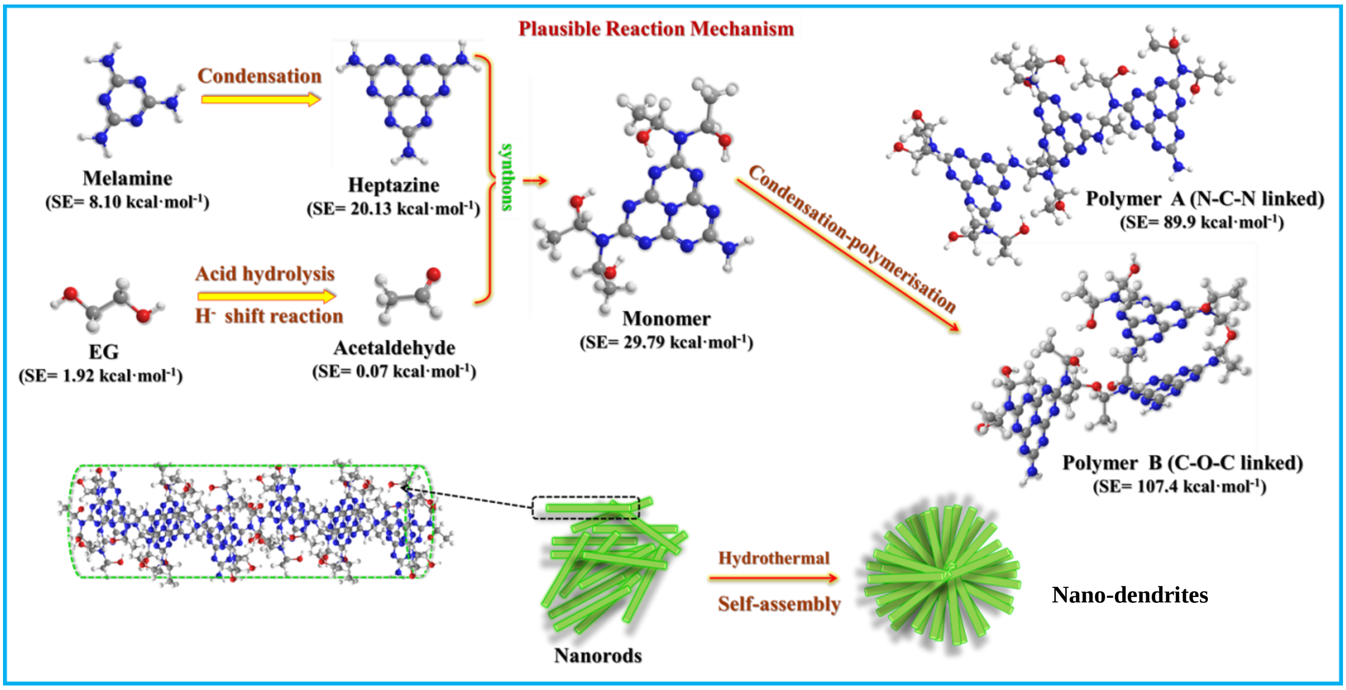

Fig. 6.10: *Synthesis mechanism shows the formation of nano-dendrites from hydrothermal treatment of EG and melamine. The grey, blue, red and white spheres represent C, N, H and O atoms, respectively. Steric energy (SE) of each simulated structures is given in the parentheses*

The molecular weight of the MEG_{10} polymer is evaluated from APC and the corresponding refractive index vs. retention time plot has been plotted in **Fig. 6.11**. As the resulting curve does not show mono-modal distribution, so molecular weight is not determined exactly. However, from the calibration against PMMA standards, the molecular weight of the polymer can be estimated to be around 2500-3000 Da range. As observed from **Fig. 6.9(b)**, the monomeric structure is composed of one heptazine unit and four acetaldehyde units. The molecular weight of one such monomer unit is approximately 300. Hence an average molecular weight of 3000 Da indicates the presence of not more than 10-15 monomeric units. Thus MEG_{10} is a low molecular weight polymer which can be more accurately considered as an oligomer. The deconvolution of the curve shows the existence of three broad regions which suggests the polydispersed nature of the hetero-polymer. The polydispersity of MEG_{10} arises due to its uneven nanodendritic morphology, also clearly evident from the FESEM images showing nanodendrites of varying sizes clustered together. The growth mechanism depends completely on the hydrothermal conditions which results in the inconsistent growth of the polymer. Since hydrothermal synthesis procedure can never lead to mono-dispersed growth of samples, hence growth in some places occurs more prominently than in other places. The inherent non-uniform nature of the polymer results in such deviations in the size distribution.

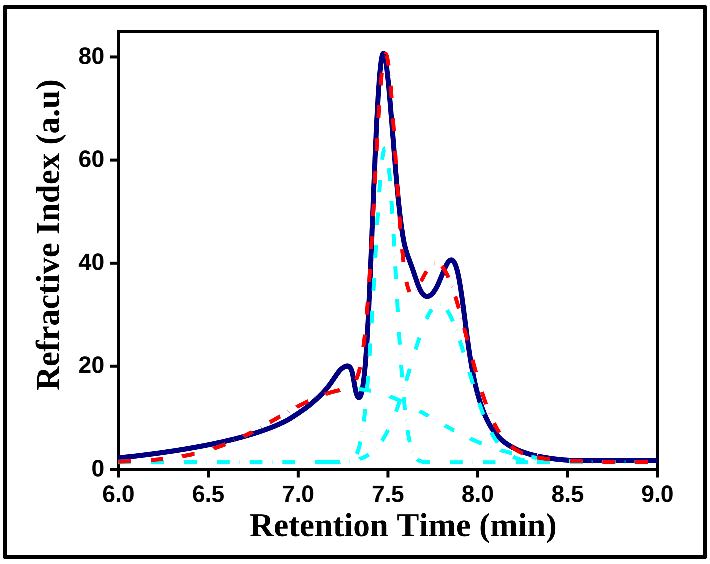

Fig. 6.11: *Molecular weight distribution of MEG_{10} as obtained from APC*

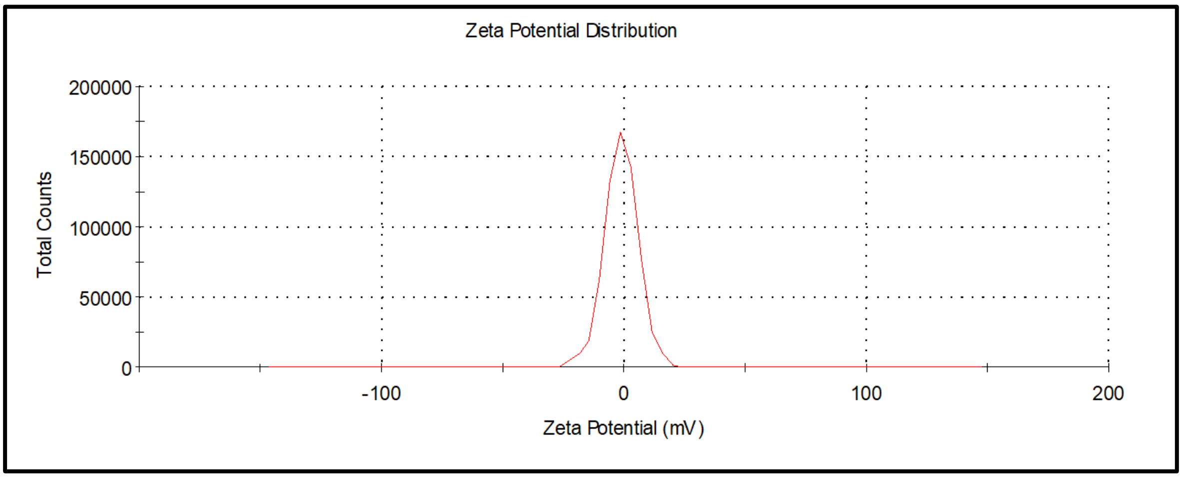

Fig. 6.12: *Zeta Potential distribution curve of MEG_{10} dispersed in deionized water measured at pH 6*

The Zeta potential distribution curve is shown in **Fig. 6.12**, which reveals the existence of negative charge on the surface of MEG_{10} polymer when dispersed in deionized water. The corresponding potential value as obtained from the intensity vs. potential curve is -2.6 mV. The lone pairs of electrons of the edge terminated oxygen and nitrogen bonded groups most possibly render the all-over negative surface charge on the polymer.

The absorbance spectrum as obtained from DRS is presented in **Fig. 6.13(a)**, which clearly shows two prominent peaks at 244 nm and 294 nm corresponding to π-π^* and n-π^* transitions, respectively. The π-π^* transition is perhaps due to the presence of triazine rings in the polymeric framework of MEG_{10} whereas the n-π^* transition most likely occurs due to the presence of C=O or C=N moieties. **Fig. 6.13(b)** shows the photoluminescence excitation and emission spectra of MEG_{10}. The emission peak is at 369.4 nm for an excitation wavelength of 257.8 nm.

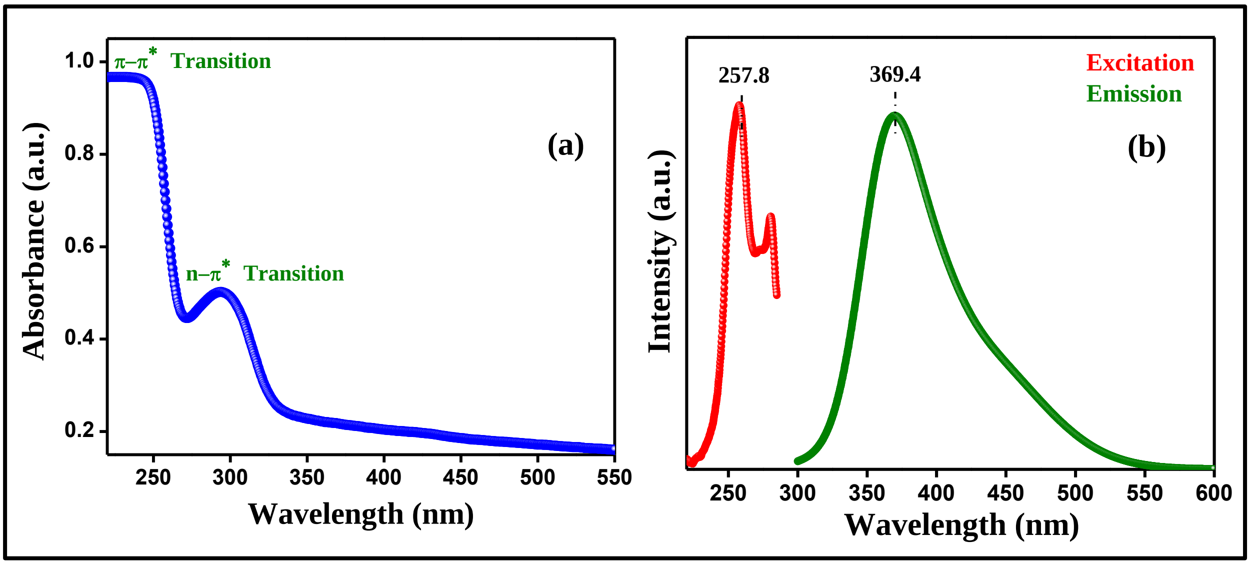

Fig. 6.13: *(a) Absorbance spectrum of MEG_{10} at pH 6; and (b) Photoluminescence excitation and emission spectra of MEG_{10}*

6.2. Characterization of pristine and exfoliated GCN:

6.2.1. Phase formation and chemical structure analysis:

The X-ray diffraction (XRD) patterns of bulk GCN (GCNB) and thermally modified and exfoliated GCN (GCNX) are depicted in **Fig. 6.14(a)**. Two prominent diffraction peaks at $2\theta = 13.03°$ and $2\theta = 27.5°$ are visible in the plots. The short peak corresponds to the (100), whereas the high-intensity peak corresponds to the (002) plane, both characteristic of GCN and matches exactly with JCPDS card no. 87-1526 [271]. The high-angle reflection peak is attributed to the interplanar stacking of the conjugated aromatic system, that is, the graphitic phase of GCN. The lower-angle peak is attributed to the in-plane repeating tri-s-triazine units, which function as the structural packing motif [272]. There is no visible shifting in the characteristic peaks between the two samples; however, it is found that there is a significant decrease in the intensity of GCNX compared to that of GCNB. This indicates that the crystallinity of GCN decreases, and the interlayer stacking order weakens upon thermal modification followed by exfoliation [271]. No other XRD peaks are observed other than the typical peaks.

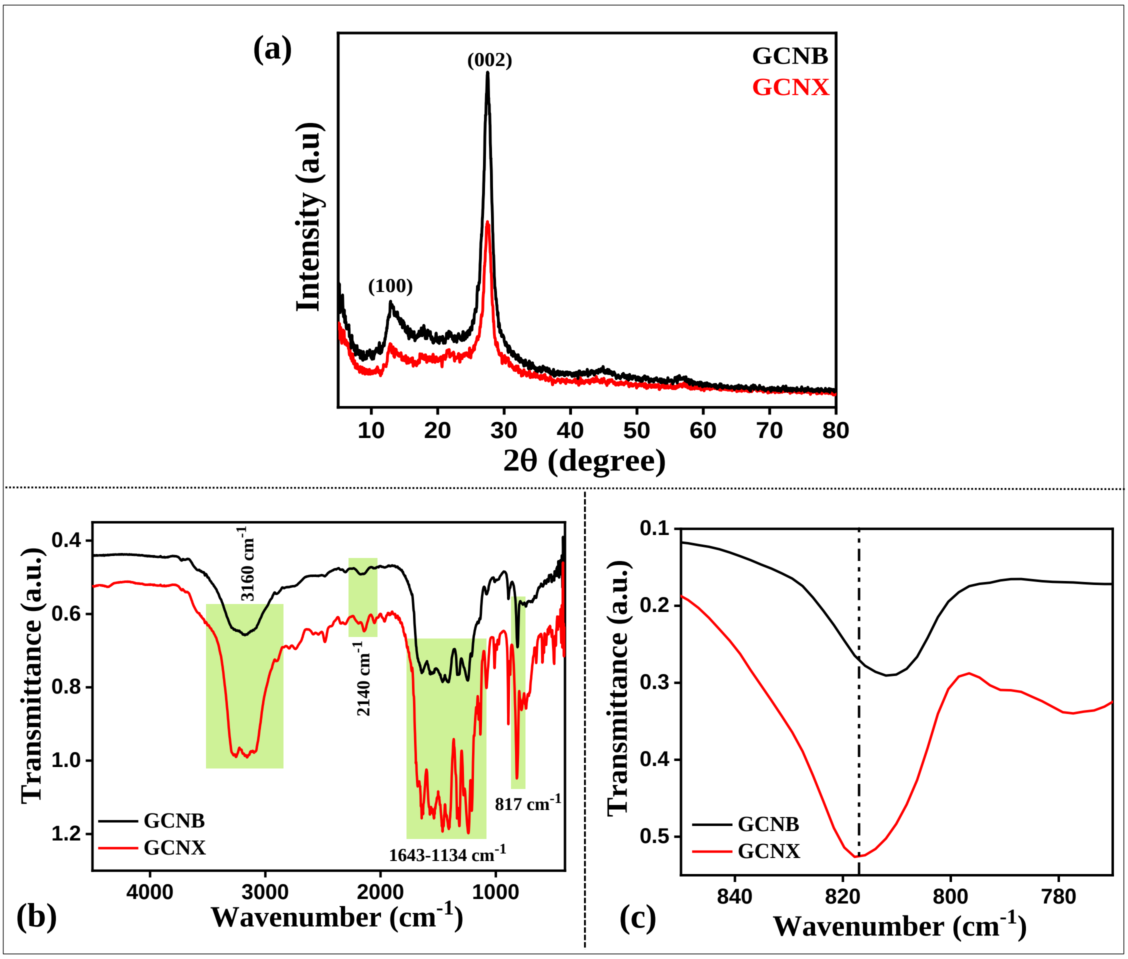

***Fig. 6.14**: (a) XRD, and (b) FTIR spectra of GCNB and GCNX, (c) Magnified FTIR spectra of the region 810 cm^{-1}*

The Fourier transform infrared (FTIR) spectra of GCNX and GCNB are given in **Fig. 6.14(b)**. The characteristic peak of GCN occurs at 810 cm^{-1} due to the breathing mode vibration of the tri-s-triazine CN heterocyclic rings. This peak shifted to a higher wavenumber (817 cm^{-1}) in GCNX (as seen in **Fig. 6.14(c)**). The series of continuous peaks in the region 1643–1134 cm^{-1} are attributed to the stretching vibration modes of the C-N bonds present within the skeletal tri-s-triazine units. The peaks at 1243 and 1317 cm^{-1} can be attributed to the stretching mode vibrations of the C-NH-C and C-N(-C)-C functional units that are possibly due to partial or complete condensation, respectively [79]. The presence of cyano groups is evident from the small hump at 2140 cm^{-1}, which can be attributed to the stretching mode vibration of the C≡N bonds. The absorption band centring around 3160 cm^{-1} indicates the symmetric and asymmetric stretching mode vibrations of the -NH bond of the amino and amine functional groups. These edge-terminated groups occur due to incomplete polymerisation and condensation reactions during the GCN synthesis procedure [131]. This band can also be ascribed to the O-H bonds of adsorbed water molecules. The presence of these characteristic bonds for both GCNB and GCNX suggests the formation of pristine GCN.

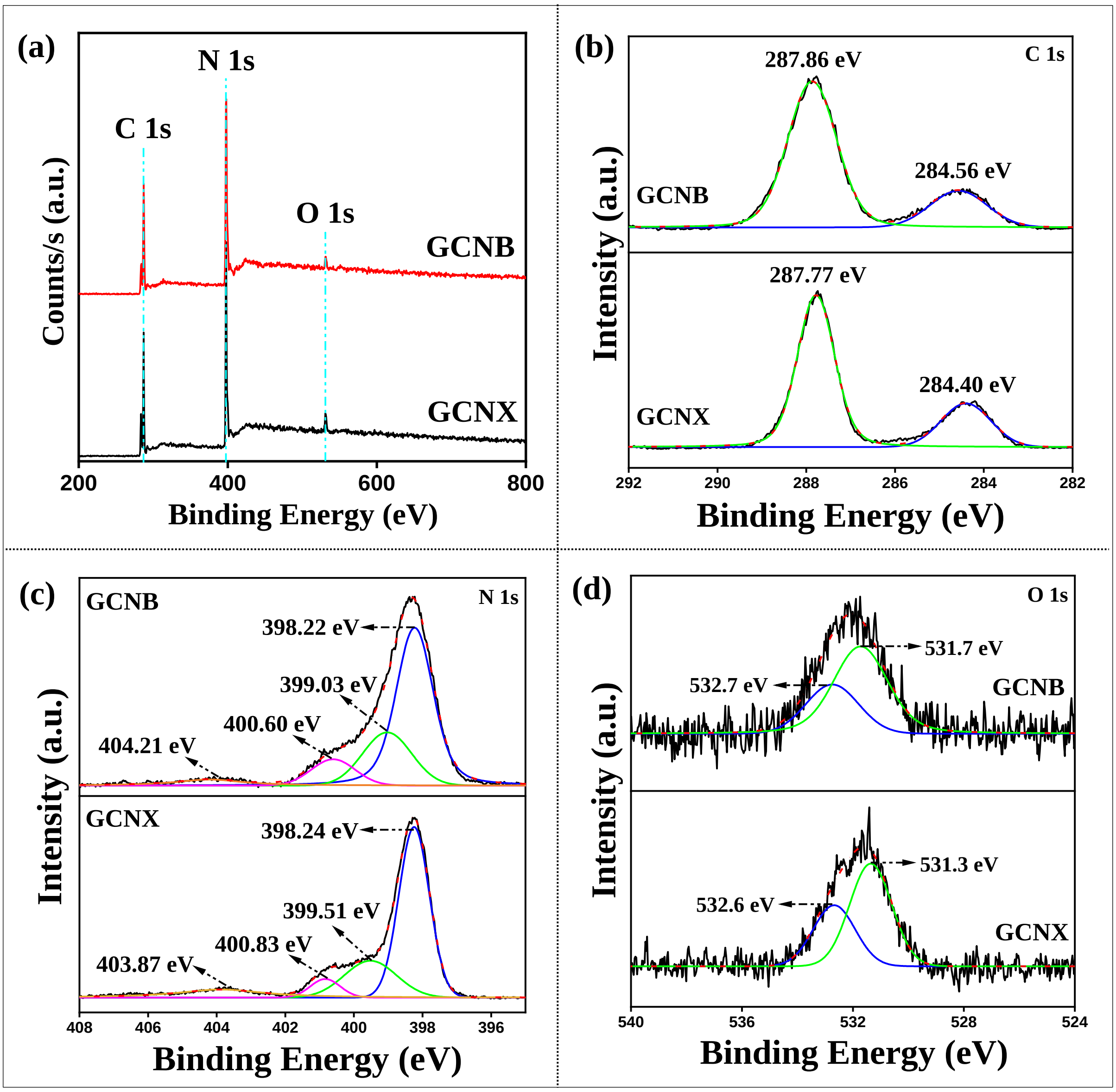

Fig. 6.15: *(a) XPS survey scans of GCNB and GCNX; (b) C1s, (c) N1s, and (d) O1s spectra of GCNB and GCNX*

The X-ray photoelectron spectroscopy (XPS) survey spectra of the as-synthesised samples, as shown in **Fig. 6.15(a),** show that both GCNB and GCNX are comprised of C, N and O without any other impurities. The XPS spectra of the individual elements (C, N, and O) of GCNB and GCNX are shown in **Fig. 6.15(b-d)**. In the C1s spectra of GCNB (**Fig. 6.15(b)**), two prominent peaks are observed at 284.56 and 287.86 eV. For GCNX, a slight shift of these peaks to 284.40 and 287.77 eV is observed. The first peak is attributed to the sp^2-bonded C in the C-C bond present due to the contamination from adventitious carbon [274], and the second peak is attributed to the tertiary carbon in the N=C-N_2 group [275].

The N1s spectra of both samples can be deconvoluted into four significant peaks (**Fig. 6.15(c)**). For GCNB, the peak at 398.22 eV is ascribed to the sp^2-hybridised aromatic nitrogen atom bonded to the carbon atoms in the C-N=C functional groups of the triazine rings. The peak at 399.03 eV is ascribed to the sp^3-hybridised nitrogen atom in the tertiary N-$(C)_3$ functional groups. The peak at 400.60 eV corresponds to the N-H_x amino groups due to imperfect condensation and polymerisation reactions. Finally, the minor component with a binding energy of 404.21 eV is the satellite peak of GCN, which exists due to the π-excitation or charging effect in the -C≡N and heterocyclic functional groups. These characteristic peaks undergo slight shifts in GCNX, and the peak positions become 398.24, 399.51, 400.83 and 403.87 eV [205,276].

The O1s spectra, as shown in **Fig. 6.15(d),** exhibit a prominent peak situated around 532 eV for both the samples, which can be deconvoluted into two peaks. For GCNB, the peaks are at 531.7 and 532.7 eV, whereas for GCNX, they are at 531.3 and 532.6 eV. The peak at a lower binding energy originates from the N-C-O groups, whereas the peak at a relatively higher binding energy occurs due to the presence of C-OH groups [277].

6.2.2. Morphological analysis:

The morphology of the samples is evident from the field emission scanning electron microscopy (FESEM) and transmission electron microscopy (TEM) analyses shown in **Fig. 6.16** and **Fig. 6.17**, respectively. In the FESEM images of GCNB (**Fig. 6.16(a,b)**), bulk sheet-like structures remain stacked together in clusters. In GCNX, these bulk clusters are broken down by the exfoliation process, and smaller sheets are formed (**Fig. 6.16(c,d)**). The TEM images of GCNB (shown in **Fig. 6.17(a-c)**) further illustrate the agglomerated bulk sheets, where the darker regions indicate the stacked GCN layers. Though both samples exhibit two-dimensional sheet-like morphology, the nature of the sheets of GCNX differs markedly from that of GCNB. As observed from the TEM images in **Fig. 6.17(d-i)**, thin nano-sheets several nanometres long are formed in GCNX. Agglomeration is significantly reduced, and the sheets are uniform and well-dispersed. Moreover, the sheets are visibly buckled or folded at their edges. The GCN sheets are edge-terminated by amine and amino groups consisting of nitrogen lone pairs. The electrostatic repulsion between these terminal functional groups results in sheets bending away from each other.

In addition to XPS, energy-dispersive X-ray spectroscopy (EDS) analysis has also been performed to study the composition of the synthesised samples. The corresponding EDS spectra of GCNB and GCNX are provided in **Fig. 6.16(e,f)**. The presence of C, N and O elements are evident from the spectra and no other peaks related to any impurity are observed. The elemental mapping images for GCNB and GCNX are demonstrated in **Fig. 6.16(g)** and **(h)**, respectively. In case of GCNB, the atomic percentages of C, N, and O are 31.14, 61.12, and 7.74 %, respectively; whereas for GCNX, the atomic percentages of elements C, N, and O are 34.90, 55.32, and 9.78 %, respectively. The C:N ratio for GCNB and GCNX are 0.50 and 0.63, respectively. It is evident that there is slight increase in the oxygen content in GCNX as indicated in XPS analysis.

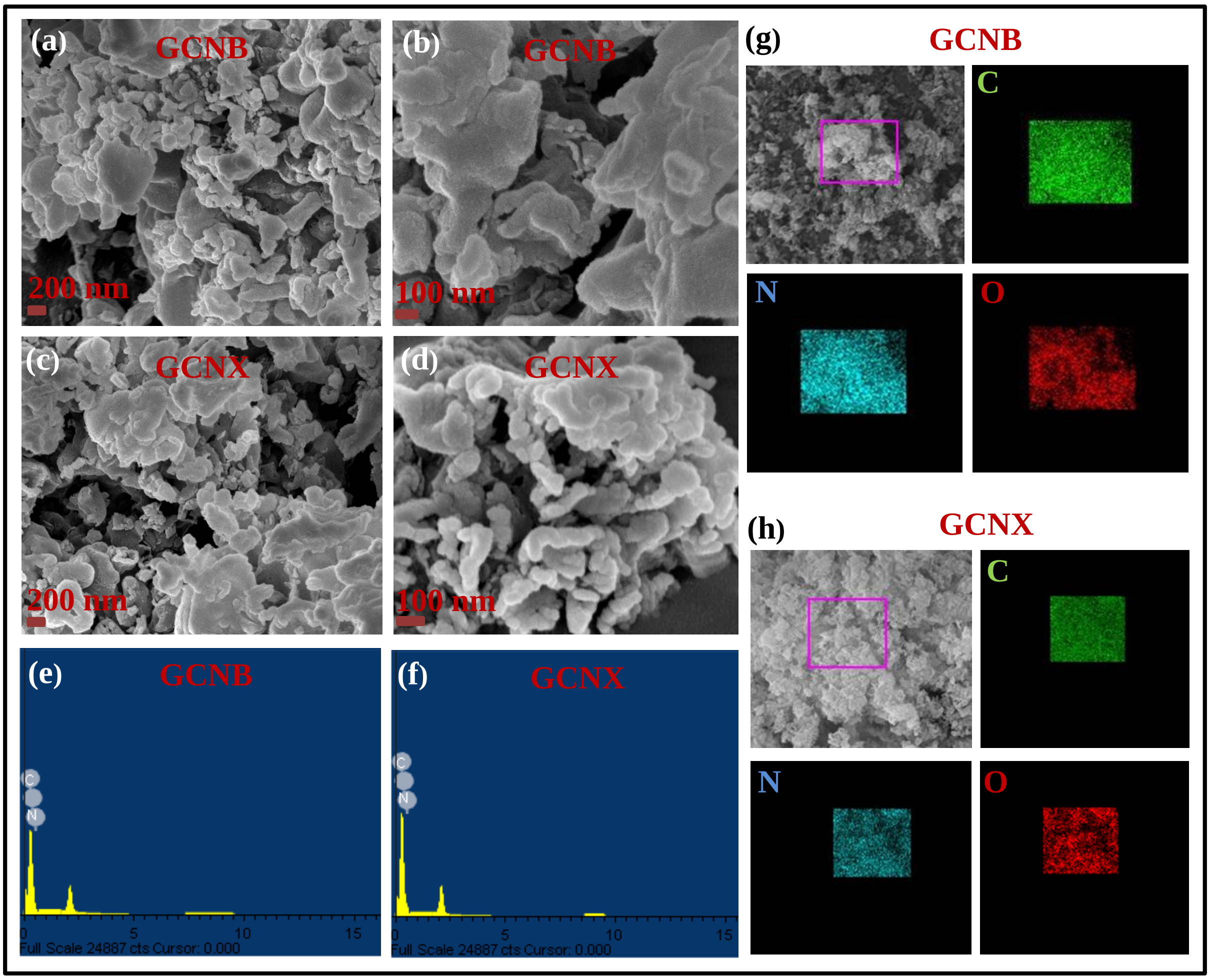

Fig. 6.16: *FESEM images of (a,b) GCNB, and (c,d) GCNX samples; EDS spectra of (e) GCNB, and (f) GCNX; elemental mapping images showing the presence of C, N, O elements in (g) GCNB, and (h) GCNX*

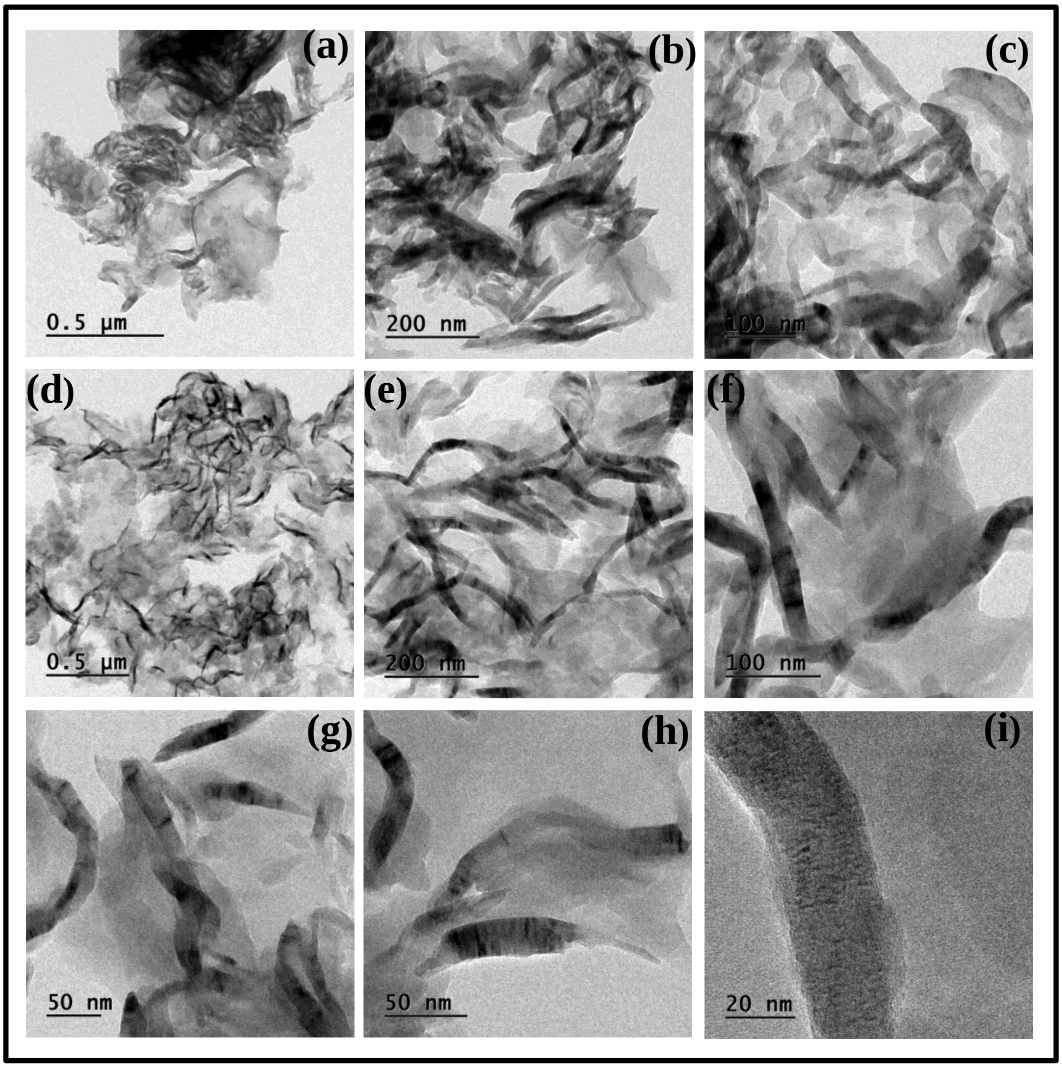

***Fig. 6.17**: TEM and HRTEM images of (a-c) GCNB, and (d-i) GCNX*

The specific surface area of the samples has been measured by Brunauer–Emmett–Teller (BET) analysis, and the corresponding nitrogen adsorption-desorption isotherm plots are shown in **Fig. 6.18(a)**. GCNB and GCNX exhibit higher surface areas than previously reported; however, upon thermal modification and exfoliation, the surface area of GCNX improves significantly. The BET analysis measured the surface area of GCNB and GCNX as 56.088 and 88.735 m^2/g, respectively. The larger specific surface area indicates the porous nature of the GCNX sample; it provides more active sites for catalysis applications. The Barrett-Joyner-Halenda (BJH) pore size distribution of both samples is shown in **Fig. 6.18(b)**. For GCNB, the pore volume and average pore diameter are 0.123 cc/g and 3.168 nm, respectively, whereas for GCNX, the pore volume and diameter are 0.229 cc/g and 4.036 nm, respectively. The increase in the pore volume gives GCNX better adsorption properties than GCNB.

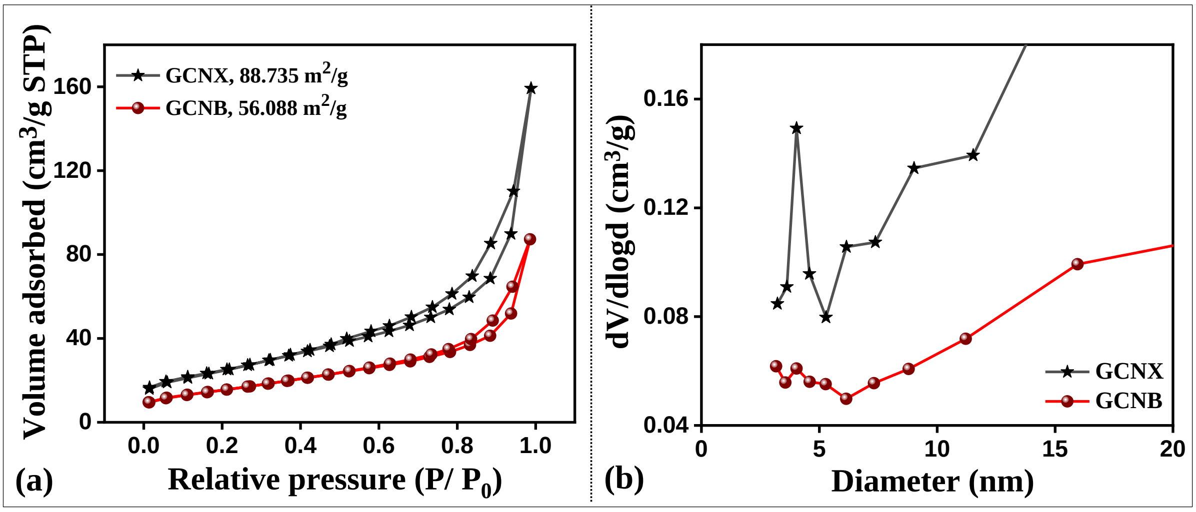

***Fig. 6.18**: (a) BET nitrogen adsorption-desorption isotherm plots of GCNB and GCNX; (b) BJH pore size distribution of GCNB and GCNX*

6.2.3. Optical properties:

The optical properties of the samples have been analysed by UV-vis diffuse reflectance spectroscopy (DRS) and photoluminescence spectroscopy (PL). The DRS spectra of GCNB and GCNX are shown in **Fig. 6.19(a)**. Both samples exhibit high reflectance properties. The samples absorb in the visible region, making them appropriate for photocatalytic applications under visible light irradiation. The initial fall in the reflectance spectra occurs at 456 nm for GCNB and 532 nm for GCNX. The indirect band gap energies of the samples are calculated by the Kubelka–Munk method and are 2.83 and 2.98 eV for GCNB and GCNX, respectively. The corresponding band gap plot is shown in **Fig. 6.19(b).** The band gap of GCNX is larger than that of bulk GCN because of the smaller crystal size of GCN, which results from the exfoliation process. The thin nanosheet-like structure of GCNX results in a significant quantum confinement effect [272].

The PL emission spectra of GCNX and GCNB are shown in **Fig. 6.19(c)**. Upon excitation of the samples with an energy equivalent to 350 nm wavelength, emission at around 450 nm is observed. The emission occurs in the visible region of the UV-vis spectrum. The PL emission intensity decreases significantly in GCNX. This reduced intensity indicates that for GCNX, the recombination of photogenerated electrons and holes is considerably hindered, improving its catalytic property relative to GCNB. The decrease in emission intensity suggests the probable prevention of the annihilation of photogenerated charge carriers. Thus, electrons and holes become freely available to participate in catalytic activity.

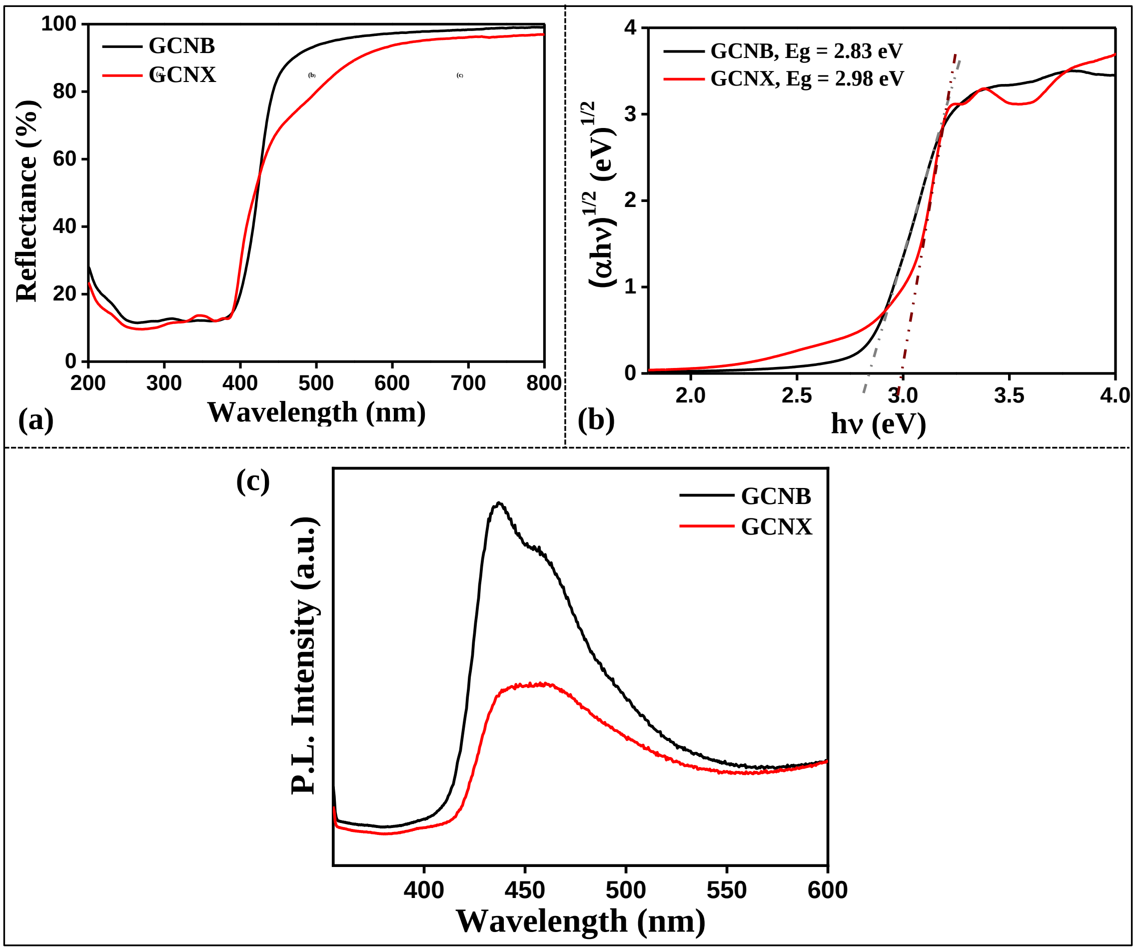

Fig. 6.19: (a) Diffuse reflectance spectra of GCNB and GCNX, (b) Kubelka–Munk plot to evaluate the band gap values of GCNB and GCNX, (c) PL emission spectra of GCNB and GCNX

6.3. Characterization of Cu-doped and Ni-doped GCN:

6.3.1. Phase formation, chemical structure, and compositional analysis:

The XRD spectra of pure Melamine, pure GCN along with supramolecular complexes of CuM and NiM as well as the final products of CuCN and NiCN obtained from precursors CuM and NiM respectively are shown in **Fig. 6.20(a,b)**. The XRD spectra of pure melamine and pure GCN have already been discussed in section 1.2 and 2.1, respectively. Detailed discussions regarding the as-obtained spectra have been provided in the above-mentioned subsections. The XRD peaks of commercially available melamine matches with the JCPDS: 39-1950 index [46]. Similarly, XRD spectra of pure GCN shows the presence of characteristic peaks at 2ϴ = 13.29° and 2ϴ = 27.5° corresponding to the respective (100) and (002) diffraction planes (JCPDS: 87-1526) [278,279]. The interplanar spacing “d” value calculated for the (100) plane is about 0.665 nm which is the distance between the heptazine aromatic units acting as the prime structural-building blocks of GCN within a single layer of GCN [47]. The "d" value calculated for the (002) plane is around 0.324 nm which indicates the distance or separation between two successive graphitic planes of GCN.

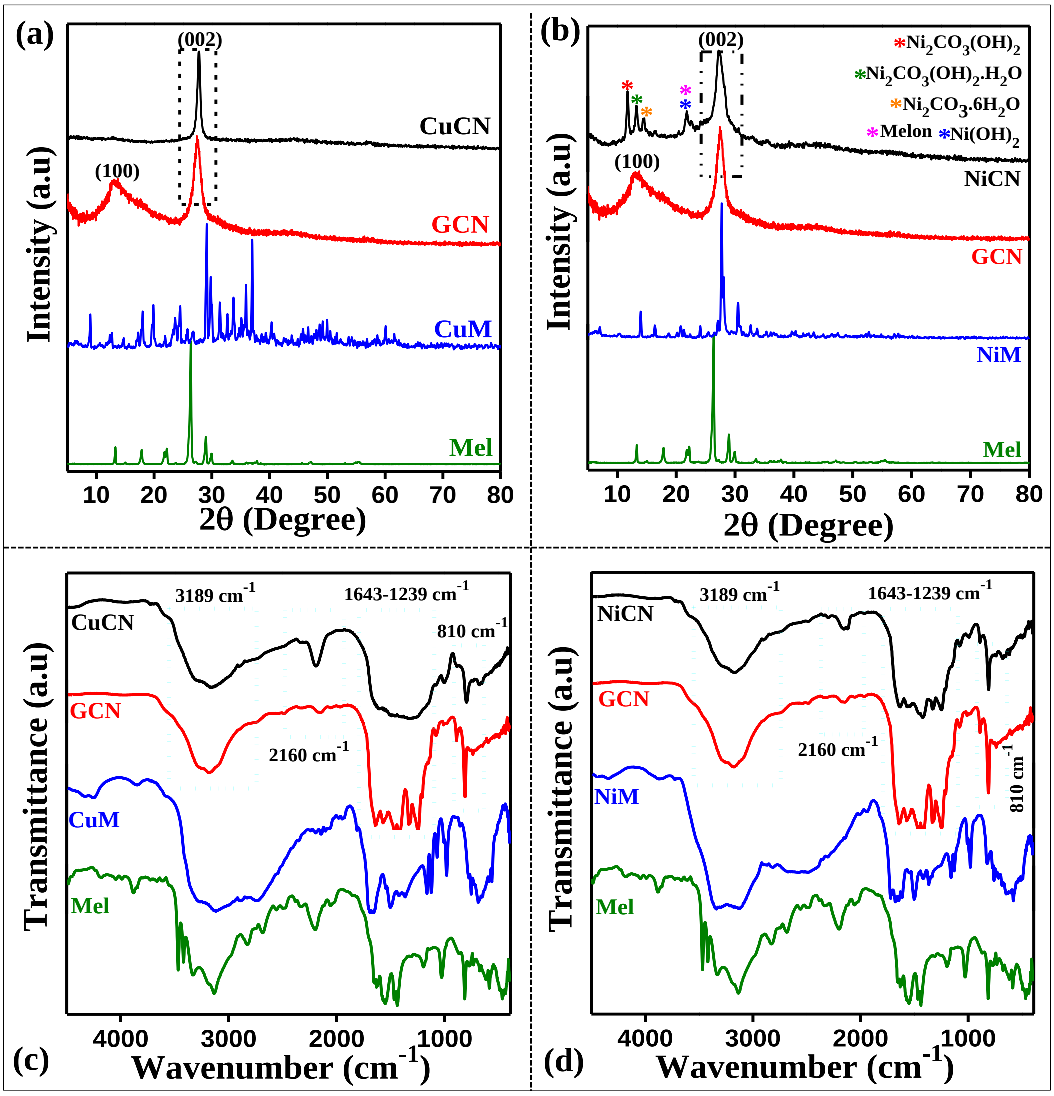

***Fig. 6.20**: XRD spectra of pure GCN and melamine with (a) CuM and CuCN, and (b) NiM and NiCN; FTIR spectra of pure GCN and melamine with (c) CuM and CuCN, and (d) NiM and NiCN*

It can be clearly observed from the XRD spectra of CuCN that the peak around 13° has disappeared indicating that the distance between the heptazine units of the GCN polymeric matrix have now been occupied with Cu [279]. The peak corresponding to the (002) plane undergoes a slight shifting to higher 2Θ value (27.76°) which probably suggests the distortion of the crystal lattice due to incorporation of Cu in-between the graphitic planes of GCN, thereby resulting in the decrease of the "d" value to 0.321 nm [205]. Additionally, no peaks corresponding to the crystalline copper species such as oxides, nitrides, chlorides, or carbides related phases are observed in the CuCN XRD spectrum which suggests that the Cu species remains chemically coordinated to the GCN host via Cu-N bonds [280]. The XRD spectrum of CuM complex shows several peaks corresponding to melamine and Cu related intermediates suggesting the chelation between them, all of which disappears after thermal treatment to form the CuCN material.

The XRD spectrum of NiM complex shows relatively lesser number of peaks, most of which corresponds to melamine peaks with significant shifting. This indicates that Cu has higher probability of forming stable chelating complexes with melamine than Ni. The XRD spectrum of NiCN shows the characteristic (002) plane of GCN with no shifting; however, unlike CuCN, there is presence of several hydroxides and carbonates related groups, including melon related peaks (the condensation product of melamine) in the material as evident from **Fig. 6.20(b)**. This again indicates that the highly crystalline supramolecular complex formed by the coordination of Cu atoms with melamine ligands in CuM proves to be distinctly beneficial as a precursor for the formation of CuCN upon pyrolysis [205], which is in contrast to the NiM precursor since it was not able to produce complex free NiCN. This is also reflected in their individual catalytic activity which is shown in the following sections.

The FTIR spectra of pure melamine and pure GCN match with the existing reports of our group and has been previously discussed in the above sections [47,153,209]. The existence of primary amine groups can be revealed from the notable band around 3466-3143 cm^{-1} region which is due to the -NH stretching mode; whereas the presence of C≡N stretching is evident from the peaks around 2204 cm^{-1} (**Fig. 6.20(c,d)**). The series of peaks from 1577-1410 cm^{-1} indicates the existence of the characteristic triazine ring of melamine [153]. The FTIR spectrum of CuM shows similar nature as melamine, however the sharp peaks around 3466-3143 cm^{-1} becomes significantly inconspicuous suggesting the disruption of the -NH stretching mode due to the formation of the stable Cu-Melamine complex by breaking the hydrogen bonds of the primary amine groups of melamine. The NiM FTIR spectrum matches more appropriately with that of melamine, however similar nature like CuM is observed around primary amine groups related region (**Fig. 6.20(d)**). The FTIR spectrum of pure GCN is also in consistent with our previous report [209]. The wide IR absorption band around 3189 cm^{-1} can be attributed to the stretching mode vibrations of the terminal amino/amine groups present due to synthesis condition induced insufficient polymerization and condensation [279]; the slight hump at 2160 cm^{-1} is associated with the existence of cyano related groups (stretching mode of C≡N); and the intense peak at 810 cm^{-1} can be assigned to the out-of-plane bending modes of s-triazine heterocyclic rings [279,281]. A series of sharp peaks can also be observed around 1643-1239 cm^{-1} which can be attributed to the stretching mode vibrations of tri-s-triazine derived melon blocks which are the repeating units of GCN matrix and also the stretching vibration of C-N(-C)-C or C-NH-C connected units occurring due to complete or partial condensation [79].

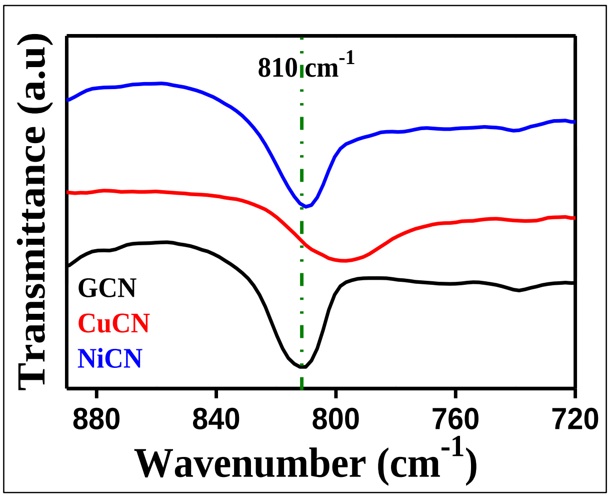

Fig. 6.21*: FTIR spectra of GCN, CuCN and NiCN showing the magnified region around 810 cm^{-1}*

The FTIR spectrum of CuCN (**Fig. 6.20(c)**) reveals a significant decrease in the intensity of the IR absorption band around 3189 cm^{-1} and an increase in the intensity of the cyano related bonds around 2190 cm^{-1}. Moreover, the discrete peaks around 1643-1239 cm^{-1} become visibly less intense resulting in a continuous band like nature thereby indicating the possible attachment of the Cu ions to the heptazine units by means of coordination bonds. However, there is no generation of any new peaks in the spectrum. This suggests that the structural framework of the host GCN has been significantly disrupted upon introduction of Cu in the polymeric matrix but without the formation of any new Cu-related groups. Possibly, Cu forms attachment with the terminal amine/amino groups of GCN resulting in the disordering of these particular bonds. The NiCN FTIR spectrum reveals similar nature, however, the IR peaks around 1643-1239 cm^{-1} remains comparatively more discrete compared to that of CuCN. No new peaks are observed in case of NiCN also. **Fig. 6.21** shows the magnified image of the IR peak at 810 cm^{-1}. It can be seen that the peak shifts significantly to lower wavenumber values as compared to bare GCN, 797.08 cm^{-1} for CuCN and 809.09 cm^{-1} for

NiCN. This suggests the possible interaction of Cu or Ni with the C-N and C=N bonds of the GCN.

The XPS survey scan of pristine GCN is shown in **Fig. 6.22(a)** which reveals the presence of elements C, N and O. The XPS spectra for C1s, N1s and O1s of GCN are given in **Fig. 6.23(a-c)**. The deconvolution of the respective spectra gives information about the different chemical bonds, and chemical and electronic states.

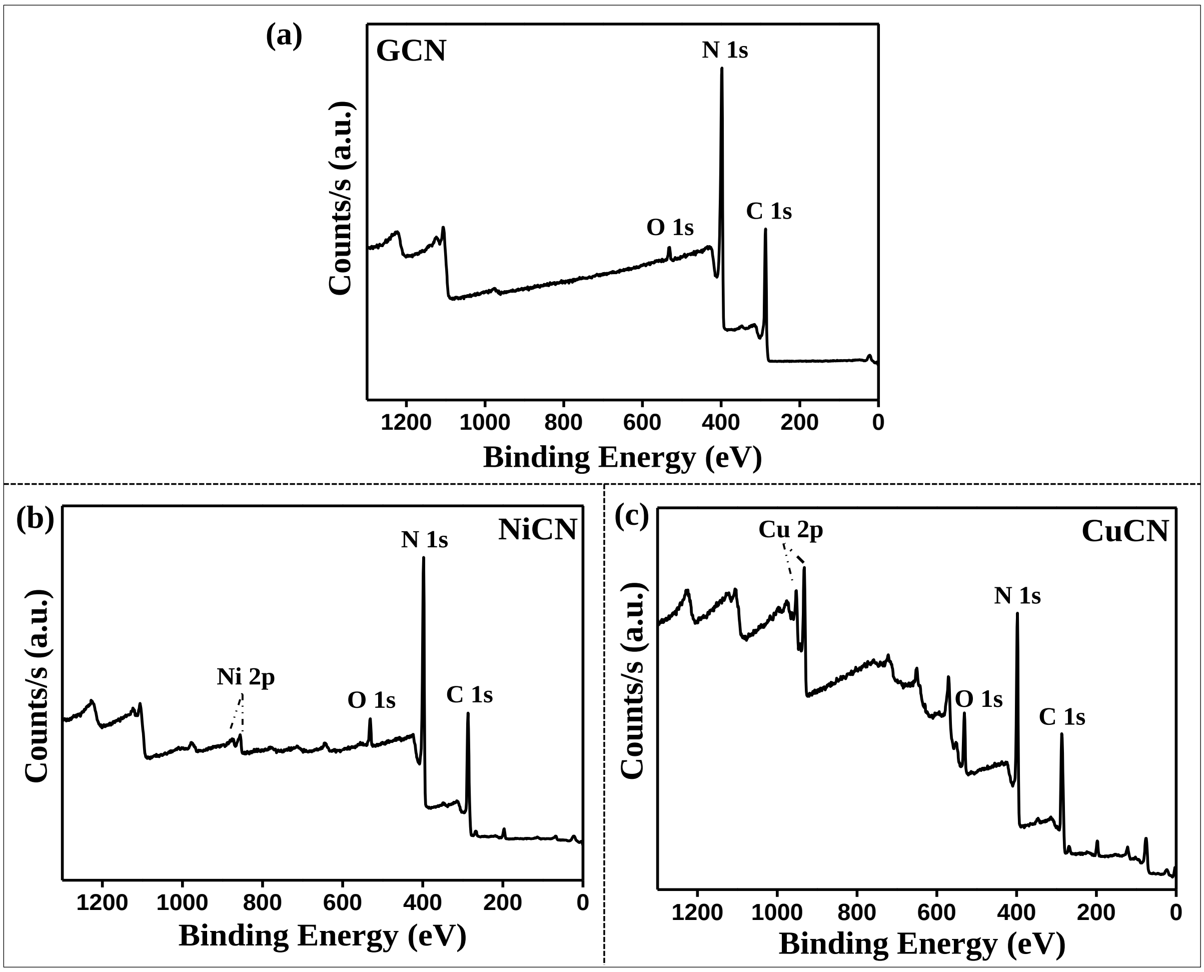

***Fig. 6.22**: XPS survey spectra of (a) pristine GCN, (b) NiCN and (c) CuCN*

As observed from the C1s spectra of pure GCN (**Fig. 6.23(a)**), the peak situated at 284.8 eV can be assigned to the sp^2 hybridized graphitic C-C or C=C present due to external adventitious contamination [274], whereas, the peak situated at 288.19 eV can be ascribed to the sp^2 bonded tertiary carbon of the N-C=N group [275]. Upon doping of GCN with Ni and Cu, it can be observed from the C1s spectra of NiCN (**Fig. 6.23(d)**) and CuCN (**Fig. 6.23(g)**) that there is a significant increase in the intensity of the peak corresponding to the binding energy of 284.8 eV. Similar kind of findings was observed by other researchers

[282,283,279]. Also, a minute shifting of the peak at 288.19 eV towards lower binding energies is observed for the doped samples, where the peak shifts to lower values of 288.13 eV and 288.14 eV for NiCN and CuCN respectively. This phenomenon suggests the possible formation of coordination chemical bonds between the N atoms and the metal ions by partially disrupting the aromatic π bond of N-C=N to N-C-N [283].

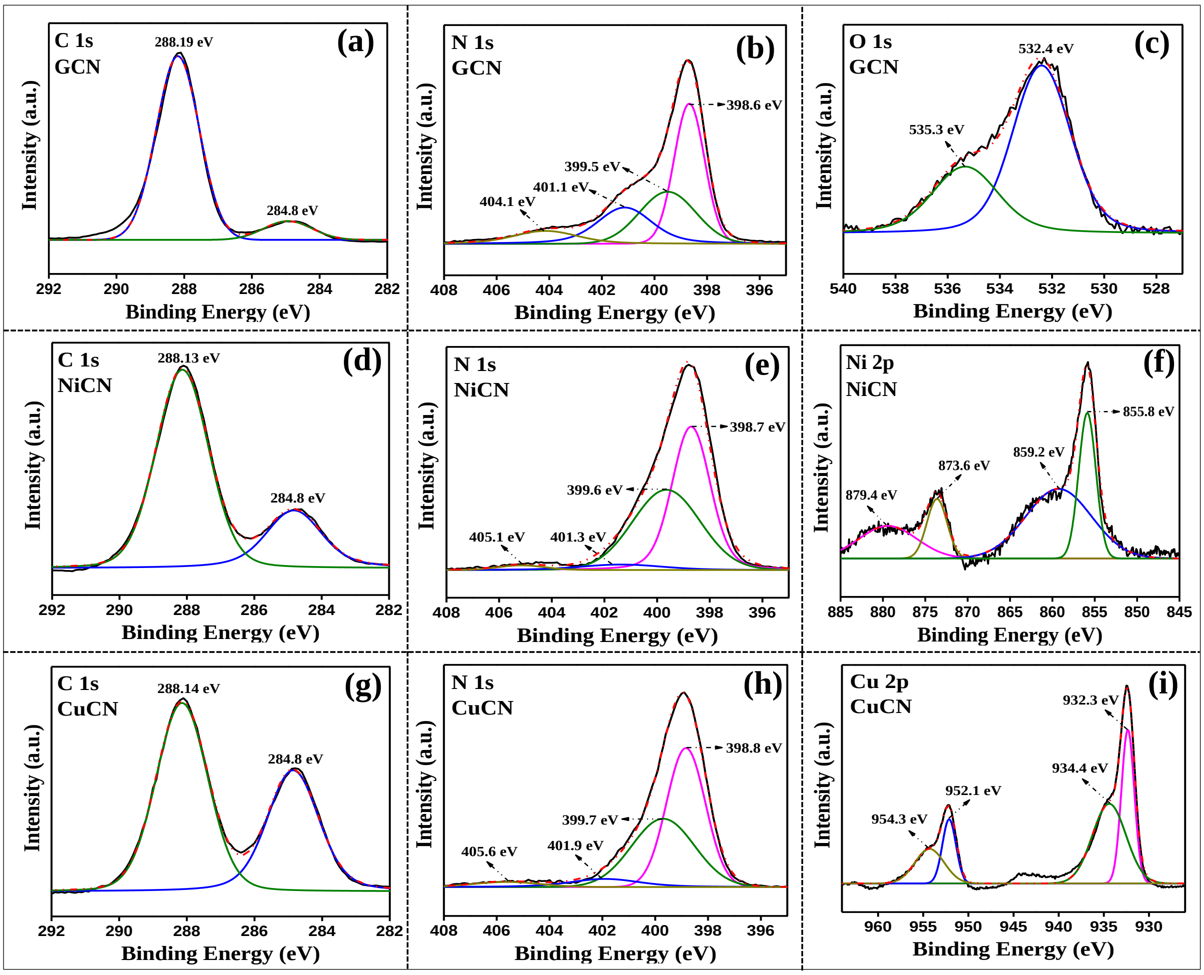

***Fig. 6.23**: XPS spectra of pristine GCN (a-c), NiCN (d-f), and CuCN (g-i) samples*

The N1s spectra of pristine GCN, as shown in **Fig. 6.23(b)**, exhibit four distinct peaks upon deconvolution. The prominent peak at 398.6 eV can be attributed to sp^2 hybridized N atoms bonded to C atoms of the C=N-C groups belonging to the heterocyclic triazine rings [205,276,284]. The next distinct peak situated at 399.5 eV can be allocated to the sp^3 hybridized N atoms of the functional group $N\text{-}(C)_3$ [205,276,284]. Another prominent deconvoluted peak at 401.1 eV can be assigned to the C-N-H related amino groups arising due to partial condensation and incomplete polymerization reactions [284]. Finally, the satellite peak of GCN can be observed as a small inconspicuous hump situated at 404.1 eV. This occurs due to the excitation of π electrons in the cyano groups (-C≡N) and other heterocyclic functional groups [276]. The N1s spectra of NiCN (**Fig. 6.23(e)**) and CuCN (**Fig. 6.23(h)**) show the presence of all the four characteristic peaks with significant shifting to higher binding energies as compared to pure GCN. The binding energy of the peak corresponding to C=N-C groups shifted to 398.7 eV for NiCN and to 398.8 eV for CuCN. Also the binding energy of the N-$(C)_3$ chemical groups increased to values of 399.6 eV and 399.7 eV for NiCN and CuCN respectively. Moreover, the amino related groups also showed an increase in binding energy for the doped samples (401.3 eV for NiCN and 401.9 eV for CuCN). However, there was a significant decrease in the content of amino groups in NiCN and CuCN as compared to pure GCN which is clearly evident from the area of the characteristic deconvoluted peak. The satellite peak shifted to higher binding energies of 405.1 eV and 405.6 eV for NiCN and CuCN respectively. The increased binding energies in the N1s spectra of both the doped samples most probably indicate the possible transfer of electrons between the electron-rich N atoms and the metal ions, thereby forming stable coordination bonds between them [285]. Hence the obtained results suggest the possible interaction of Cu or Ni with N atoms upon incorporation of these metal ions into the GCN matrix. Moreover, there iss absence of any additional peaks in N1s spectra of the metal decorated GCN complexes. Similar observations were made by Ding et al. [280] who suggested that the six N atoms surrounding the metal species within the cavity of the coordination complex are all chemically homogeneous in nature thereby providing a coordination conjugation.

The O1s spectra of pure GCN (**Fig. 6.23(c)**) show the presence of a single prominent peak which upon deconvolution yields two peaks situated at 532.4 eV and 535.3 eV. The peak at 532.4 eV can be assigned to the presence of N-C-O functional groups whereas the peak at 535.3 eV indicates the possible adsorption of water molecules on the sample surface [286,277].

The Ni2p spectra (**Fig. 6.23(f)**) of the NiCN sample show the presence of two distinct peaks situated at 855.8 eV and 873.6 eV which are attributed respectively to the $Ni2p_{3/2}$ and $Ni2p_{1/2}$ states of the $Ni(OH)_2$ phase [287-289]. This also corroborates the observations obtained from the XRD result of NiCN. The other two peaks situated around 859.2 eV and 879.4 eV are assigned as the satellite peaks of $Ni2p_{3/2}$ and $Ni2p_{1/2}$ respectively. Ni is thus present as the Ni^{2+} chemical state in the NiCN sample [290]. The survey scan of NiCN sample shown in **Fig. 6.22(b)** confirms the presence of Ni2p along with the presence of C1s, N1s and O1s.

The XPS spectra of Cu2p shown in **Fig. 6.23(i)** exhibit the presence of two distinct peaks at 932.3 eV and 952.1 eV corresponding to the $Cu2p_{3/2}$ and $Cu2p_{1/2}$ states respectively. Upon deconvolution of these peaks, two shoulder peaks are observed which are situated at 934.4 eV and 954.3 eV. The two distinct peaks indicate the presence of Cu in its Cu^+ ($3d^{10}$) oxidation state whereas the shoulder peaks suggest the possible presence of Cu^{2+} ($3d^9$) species in CuCN [291,292]. The small hump near 940-945 eV is attributed to the shake-up satellite peak of Cu^{2+} [292]. Hence, in CuCN, Cu exists within the GCN matrix primarily in its Cu^+ oxidation state along with a small contribution from Cu^{2+} species. However, unlike NiCN, no X-ray diffraction peaks associated with Cu_2O or CuO were observed in the XRD spectra of CuCN. This implies that the Cu^+ and/or Cu^{2+} ions are properly incorporated or embedded at the interstitial position within the GCN polymeric matrix by forming stable coordination Cu-N bonds with the nitrogen atoms of GCN [205,293]. The XPS survey spectrum of CuCN shown in **Fig. 6.22(c)** further confirms the presence of C1s, N1s, O1s and Cu2p in the sample. The presence of O1s peak is mainly due to the oxygen adsorbed from environment on the CuCN surface on exposure to air and humidity during experimental measurements [292]. It is also to be noted from the XPS survey spectra (**Fig. 6.22(b,c)**) of the metal decorated GCN samples that there is presence of Cl (around 200 eV) in small concentration which comes from the metal salt precursors used during synthesis procedure. The Cl/Cu ratio is calculated to be 0.75 from XPS elemental analysis which is much smaller than the Cl/Cu ratio in the $CuCl_2$ precursor (2:1) used in the synthesis of CuCN [291]. This suggests that the Cu ions are stabilized in the GCN system primarily through coordination bonds with the electron donating N atoms, and the small amount of Cl^- ions present in the system are probably used for charge balance [291,280]. These Cl^- ions do not hinder the catalytic activity of the CuCN catalyst by blocking the Cu active sites. However, in case of NiCN, the presence of Cl is much more prominent and the Cl/Ni ratio as evaluated from XPS analysis is found to be near 2.5. In this case, the Cl^- ions probably occupy the interlayer spaces as well as remain bonded to the coordinated Ni ions in the GCN matrix thereby affecting the catalytic activity of NiCN significantly.

In order to evaluate the elemental compositions of the doped samples, EDS measurements were also performed and the corresponding EDS spectra of CuCN and NiCN are shown in **Fig. 6.24(a,b)**. The spectra show the presence of carbon and nitrogen along with the presence of Ni in NiCN and Cu in CuCN. It is evident from the plots that Cu is present in large concentration in the CuCN sample as compared to the concentration of Ni in NiCN.

Moreover the EDS spectra of both the samples show the presence of Cl in small concentration which is in agreement with the XPS analysis. The atomic percentages of C, N, and Cu in CuCN as measured from EDS are found to be 39.04 %, 58 %, and 2.96 % respectively; whereas the same for C, N, and Ni in NiCN are found to be 41.70 %, 57.75 %, and 0.55 % respectively. For pristine GCN, the atomic percentages of C and N are 41.66 % and 58.34 % respectively. The C:N atomic ratio for bare GCN, CuCN, and NiCN is 0.71, 0.67, and 0.72 respectively.

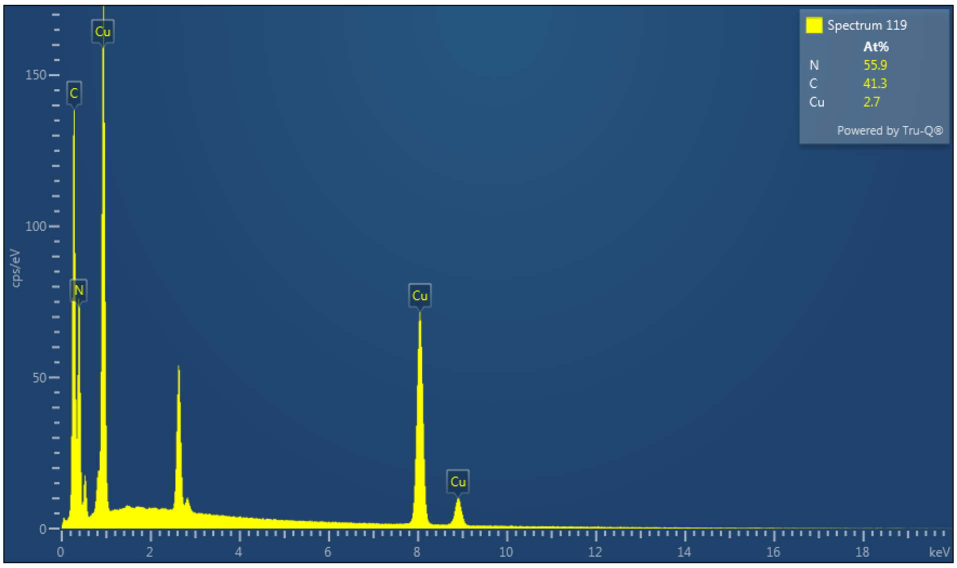

***Fig. 6.24(a)**: EDS spectra of CuCN*

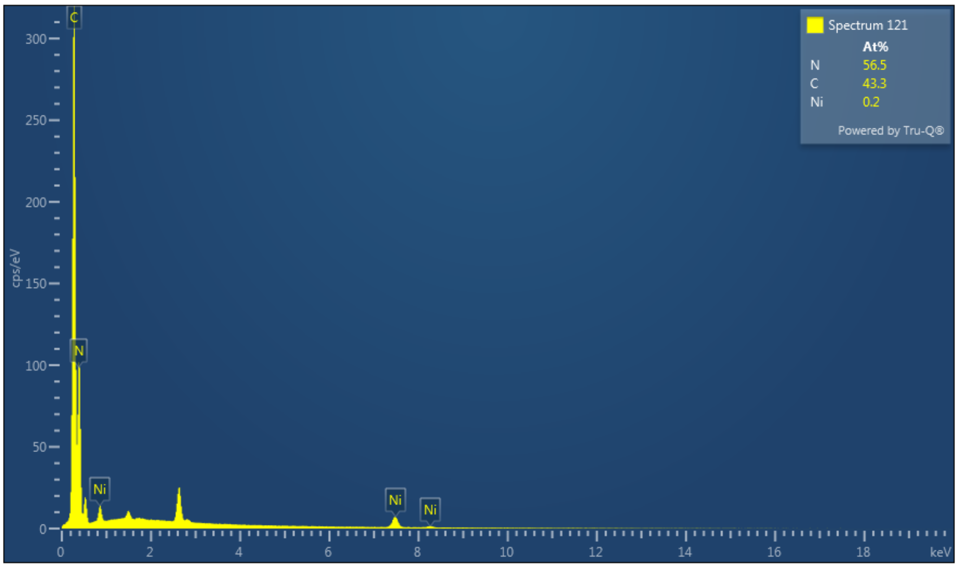

***Fig. 6.24(b)**: EDS spectra of NiCN*

6.3.2. Morphological analysis:

The FESEM images of all the samples are shown in **Fig. 6.25(a-f)**. Pure GCN have layered sheet like structures arranged in stacks. FESEM images of CuM and NiM show the presence of bulk chunks of plate-like micro-crystalline structures clustered or agglomerated together in large dimension. Upon thermal treatment of these complexes, both CuCN and NiCN form sheet like morphology resembling pure GCN. However, the magnified image of CuCN shown in **Fig. 6.25(e)** reveals that the small sheets like structures are clustered in many layers. A stark difference is noticeable in the sheet like structures of NiCN and CuCN. All the three samples, in pure and doped form, exhibit layered sheet-like morphologies.

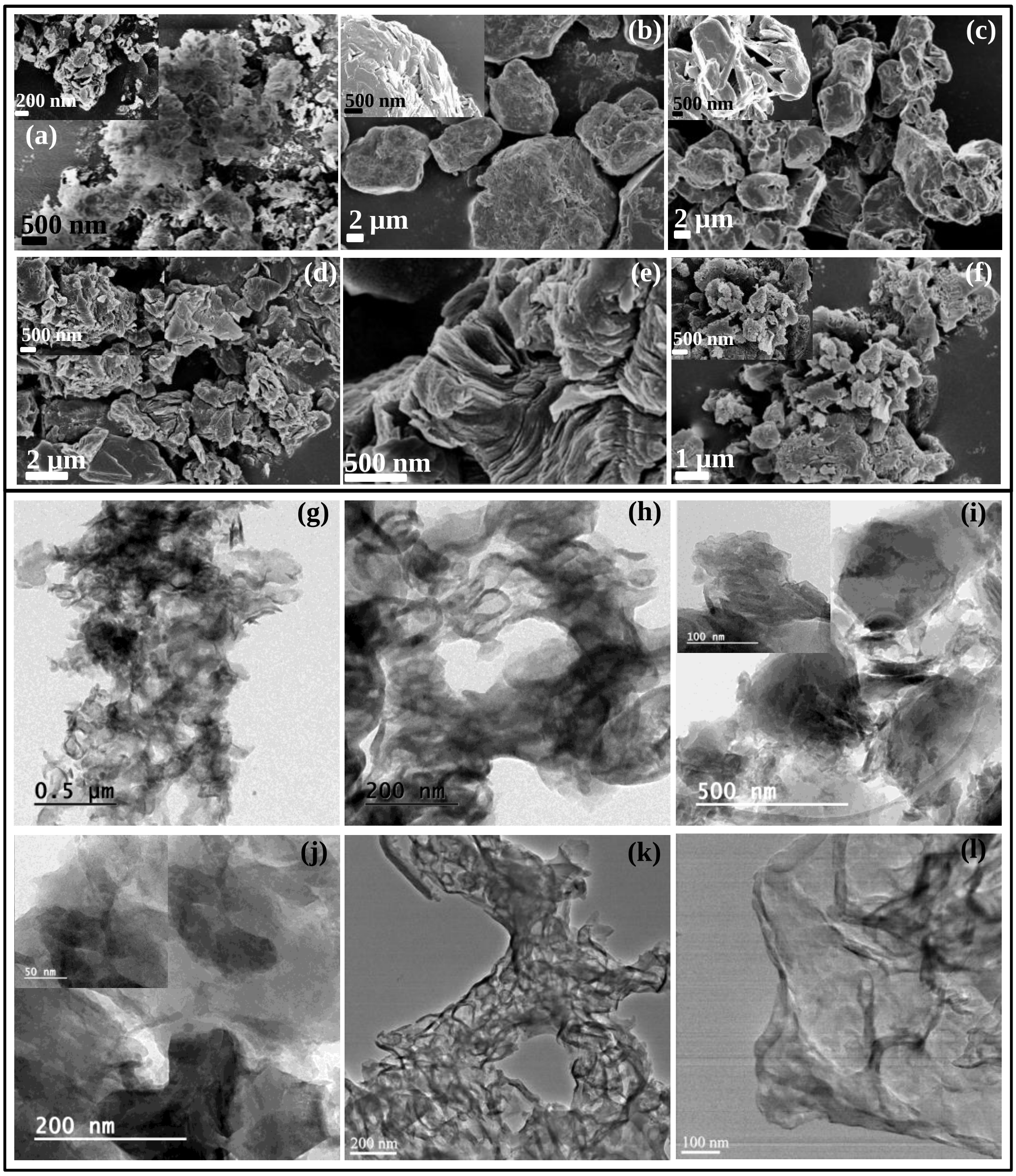

Fig. 6.25*: FESEM images of (a) pristine GCN, (b) CuM, (c) NiM, (d, e) CuCN, and (f) NiCN samples. TEM images of (g, h) pristine GCN, (i, j) CuCN, and (k, l) NiCN samples*

The TEM images of all the pristine and metal decorated samples are shown in **Fig. 6.25(g-l)**. Though all samples exhibit sheet like morphology as evident from the images, however, the sheets are distinct in nature. The irregular nano-sheets of pristine GCN are slightly porous, planar, and stacked in nature (**Fig. 6.25(g,h)**). The sheets of CuCN sample exhibits two-dimensional stacked lamellar nature as shown in **Fig. 6.25(i,j)**, the insets of which show the high resolution images. The corresponding HRTEM images of CuCN are shown in **Fig. 6.26** which also suggests the nano-flakes like nature of the CuCN sheets. It is clearly evident from the CuCN microscopic images that there is complete absence of any crystalline nanoparticles on the stacked sheets of CuCN, which indicates that no oxide species of Cu are deposited on the nano-flakes like sheets [205]. This in turn supports the XRD results. The TEM images of NiCN are given in **Fig. 6.25(k,l)** which also suggest the layered sheet like morphology of the sample. The sheets are slightly buckled near the edges.

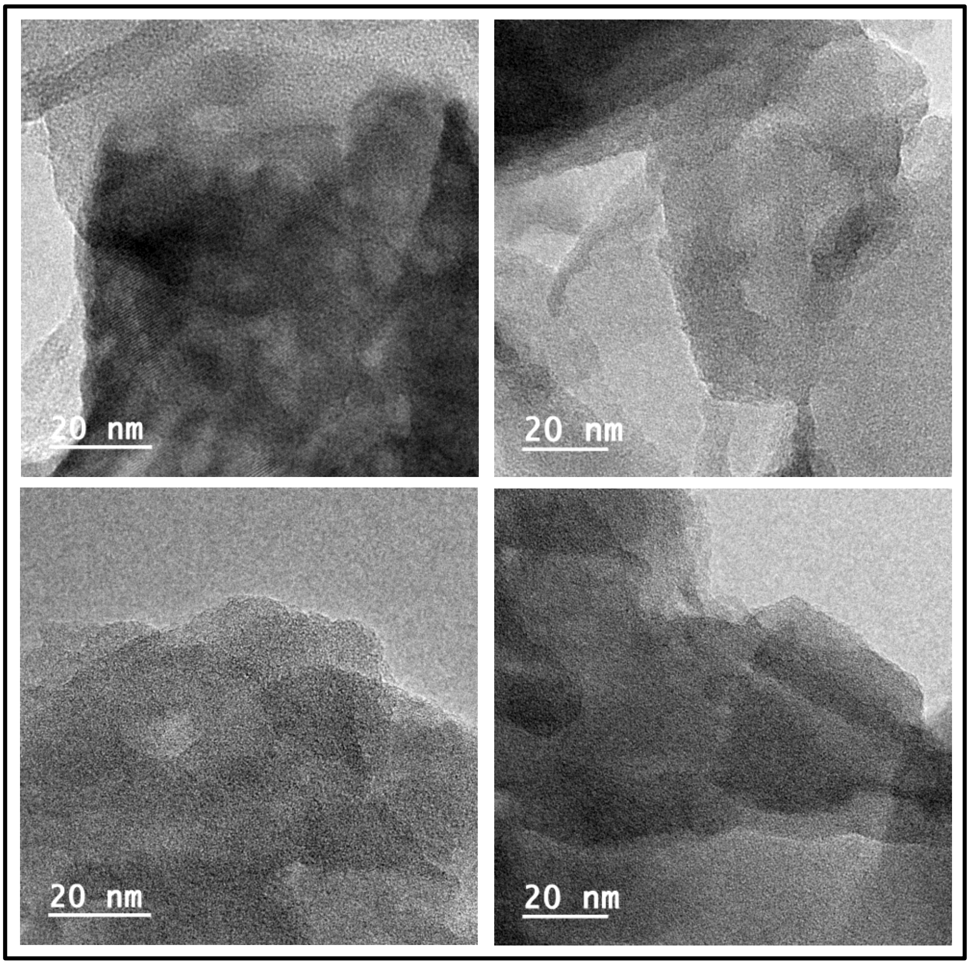

***Fig. 6.26**: HRTEM images of CuCN catalyst*

6.3.3. Optical and electronic properties analyses:

The diffuse reflectance spectra (DRS) of all samples have been measured in the range from 200 to 2200 nm and shown in **Fig. 6.27(a,b)**. Melamine shows a steep fall in the DRS spectrum in the UV region around 325 nm whereas pristine GCN exhibits a strong absorption in the visible region at around 370 nm. The CuM sample reveals the existence of two prominent absorption regions, one in the visible region and the other near IR region, as evident from **Fig. 6.27(a)**. The fall near the IR region is probably due to the presence of Cu related complexes. The DRS spectrum of NiM sample (**Fig. 6.27(b)**) also exhibits many absorption peaks throughout near IR, visible and UV region and an intense fall around 335 nm. This may also be due to the presence of Ni related groups in the Ni-melamine complex. Interestingly, the CuCN sample exhibits intense absorption throughout the whole visible range of the spectrum along with significant expansion of the absorption above 600 nm that is the near IR region. The NiCN DRS spectrum has a fall near 550 nm and absorption peak near 375 nm which is also at a slightly higher wavelength than GCN.

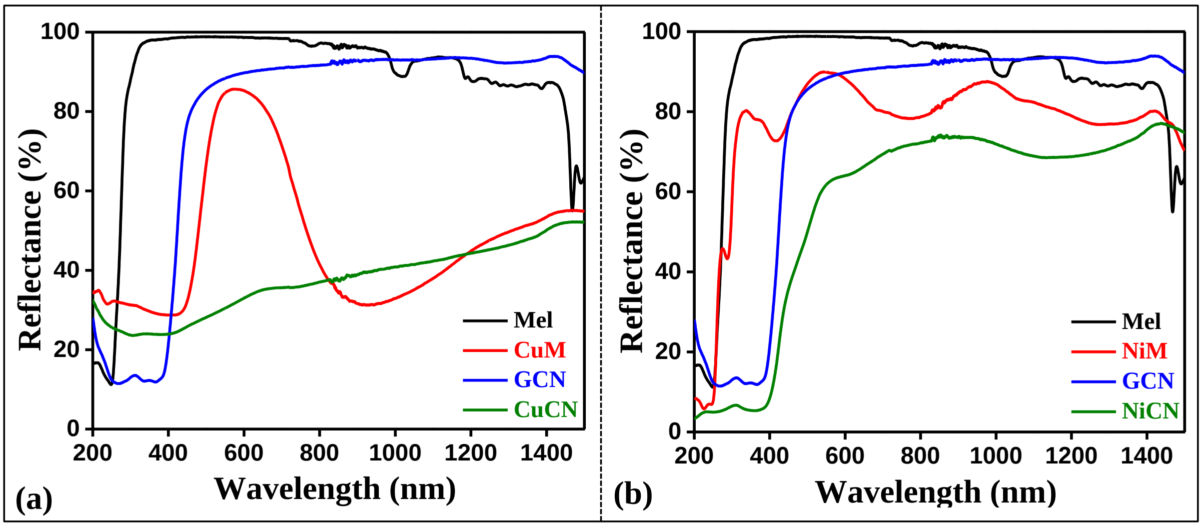

Fig. 6.27: UV-Vis DRS spectra of pristine melamine, pristine GCN, CuM and NiM intermediate compounds, and (a) CuCN and (b) NiCN

The electronic properties of pure GCN and CuCN have been studied by employing first principles calculations. Pure GCN monolayer is a planar two dimensional materials with optimized lattice parameter of 7.145 Å and space group P-6M2. The unit cell contains three types of non-equivalent nitrogen atoms (denoted as N1, N2 and N3 in **Fig. 6.28(a)**) and two types of non-equivalent carbon atoms (C1 and C2 as shown in **Fig. 6.28(a)**). The presence of different types of C and N atoms in the system is prominent from the Mulliken population analysis (**Fig. 6.30(a)**). The bonds lengths between N1-C2, N2-C1, N3-C1 and N3-C2 were calculated to be 1.39 Å, 1.48 Å, 1.33 Å and 1.33 Å respectively. The optimized lattice parameter and the calculated bond lengths agree very well with prior reports. The unit cell of GCN decorated with Cu is shown in **Fig. 6.28(b)**. The formation energy for such Cu decoration was calculated to be 1.37 eV using equation (5.16) given in Chapter 5, Section 3.3.4. As the GGA typically underestimate the electronic band gap we implemented the HSE06 functional for the electronic band-structure calculation which is represented in **Fig. 6.28(c,d)**.

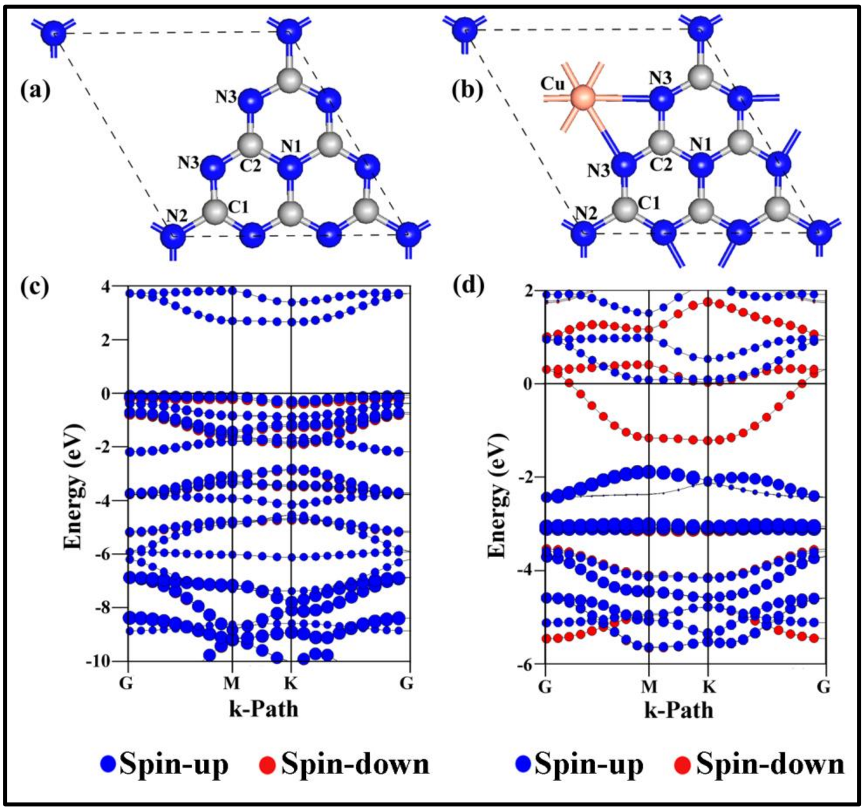

Fig. 6.28: Unit cell of (a) Pristine GCN and (b) Cu decorated GCN; the electronic band structure of (c) pristine GCN and (d) CuCN

Pure GCN was found to be a non-magnetic material with the bands of the up and down spin being completely merged over each other (**Fig.6.28**). The indirect band gap value was calculated to be 2.82 eV with the valence band maximum (VBM) located at the **Γ** (0, 0, 0) point and the conduction band minimum (CBM) situated at the **K** (-1/3, 2/3, 0) point in the reciprocal space. The orbital-wise contribution to the band-structure from each element was further computed for both the up and down spin together due to the non-magnetic nature of pure GCN. The highest occupied valence band in the band-structure of GCN is solely contributed by the p_y orbital of the N3 atoms with minor contribution from the p_x orbital of the same atom (**Fig. 6.29(b)**). The p orbitals of the N1 and N2 atoms only contribute very weakly near the VBM and have major contribution in the lower energy valence bands. The lowest unoccupied conduction band is formed by the major contribution of the p_z orbital of the C1 atoms with lower but substantial contribution from the C2-p_z orbitals as shown in **Fig. 6.29(a)**. Also, the N1-p_z orbitals have smaller contribution in forming the lowest unoccupied conduction band.

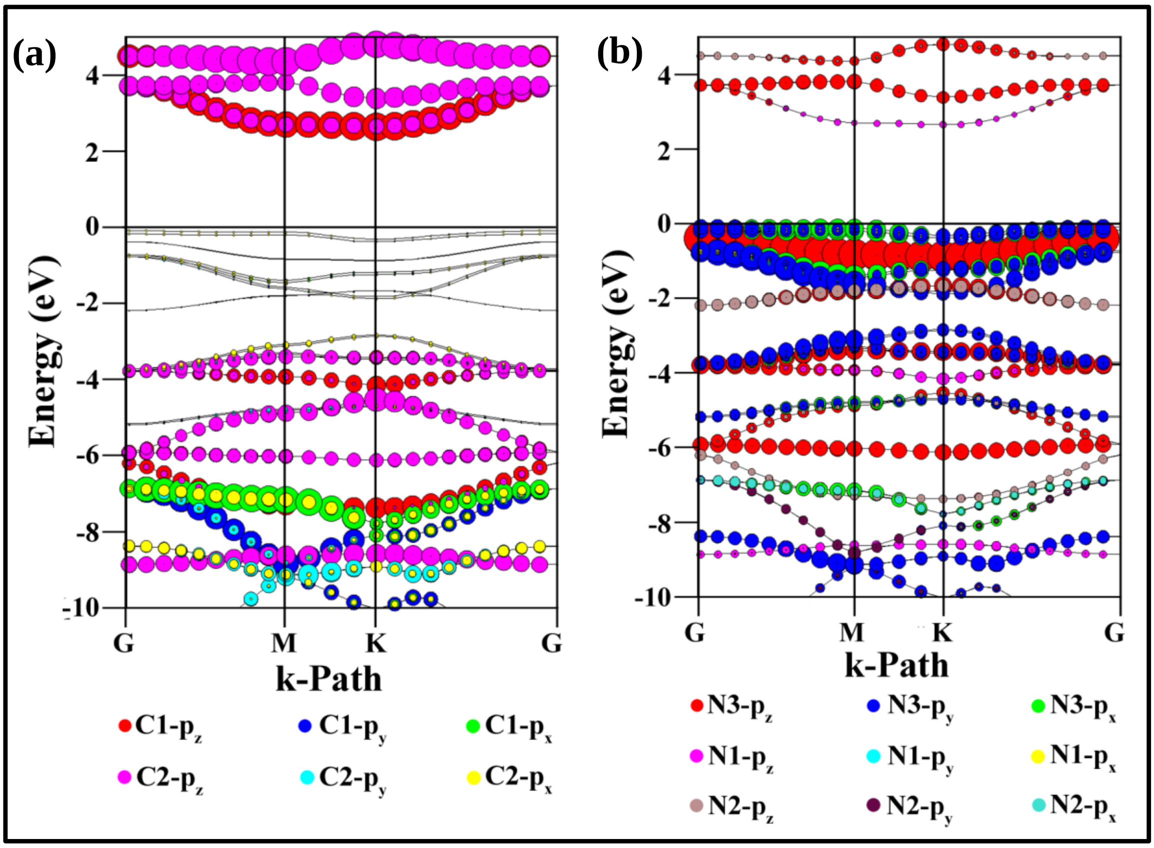

***Fig. 6.29**: Orbital projected band-structure of pure GCN (a) projected on the orbitals of C atoms, (b) projected on the orbitals of N atoms*

Within the valence bands, the p orbitals of C1 and C2 atoms have significant contribution only in the lower energy valence bands (from -3.0 eV and lower with respect to the Fermi level (E_F)) with zero contribution to the bands near VBM. **Fig. 6.31(a,b)** representing the highest occupied molecular orbital (HOMO) and lowest unoccupied molecular orbital (LUMO) of pure GCN reconfirms the observation stated from its electronic band-structure. From the **Fig. 6.31(a)**, it is prominent that the lone pairs associated with the N3 atoms residing in the plane of the GCN monolayer configure the HOMO which implicate that the lone pairs occupy the N-p_y orbitals in the ground state. The plot of the electron localization function (ELF) as shown in the **Fig. 6.33(a)** clearly depicts the covalent bonding between the

C and N atoms along with the lone pairs of N3 atoms oriented towards the hollow space within the plane of the GCN monolayer.

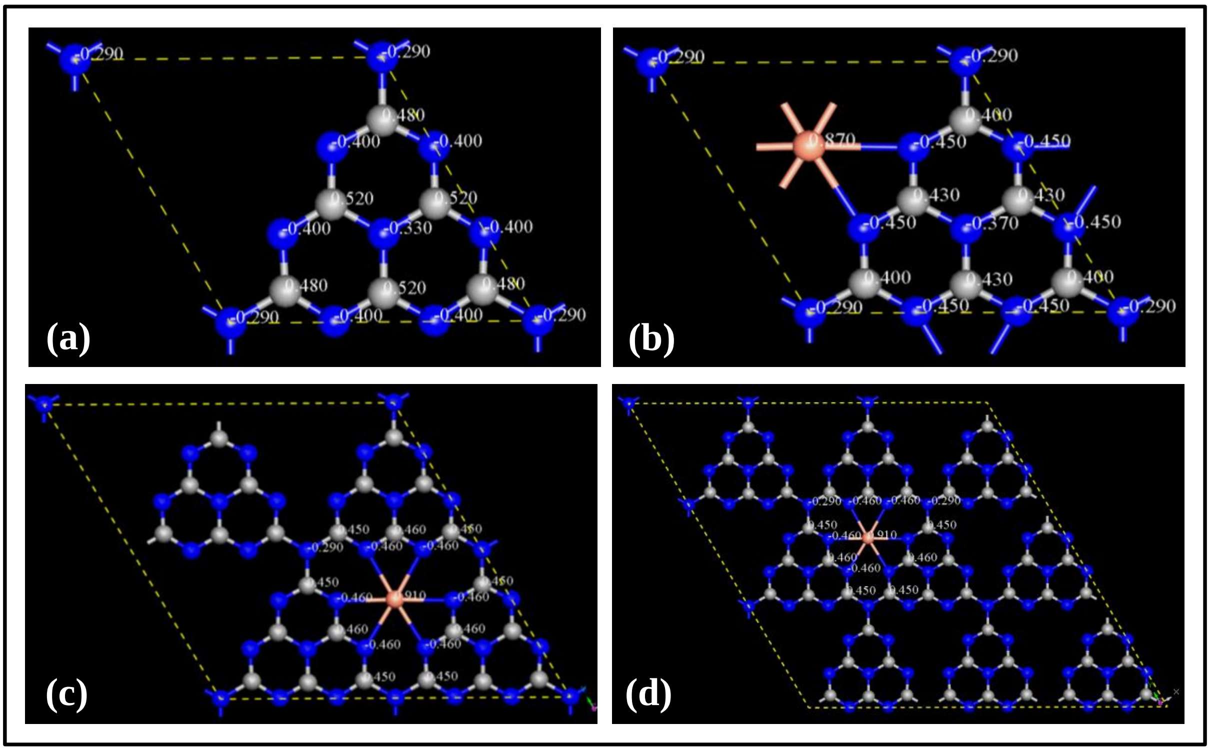

Fig. 6.30: Mulliken population analysis of (a) pristine GCN, (b) CuCN unit cell, (c) CuCN 2x2, and (d) CuCN 3x3

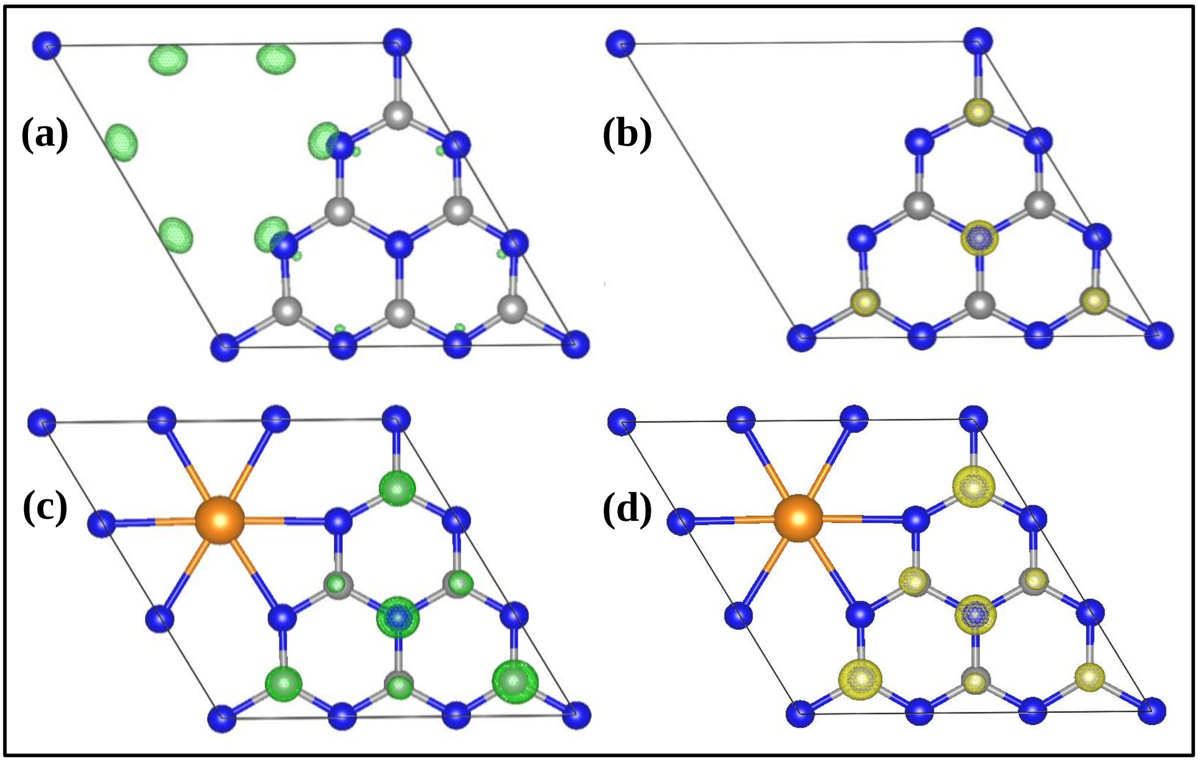

Fig. 6.31: (a) HOMO and (b) LUMO of pristine GCN; and (c) HOMO and (d) LUMO of Cu decorated GCN

To study the effect of Cu decoration in GCN towards the dye degradation process, (2×2×1) and (3×3×1) supercells of pure GCN were considered and one Cu atom was incorporated in each case, and the formation energies for Cu decoration was calculated to be 1.16 eV and 1.19 eV respectively. But at this point, to study the interaction between Cu and GCN and to investigate the changes in electronic properties upon Cu decoration, Cu was embedded in the GCN unit cell to reduce the computational cost. Cu was found to get adsorbed right in the middle of the hollow pore of the GCN monolayer maintaining the planarity of the system. The Cu atom interacts only with the N3 atoms with bond length of 2.38 Å between them. Mulliken population analysis shows accumulation of negative charge on the N3 atoms (by 0.05e compared to the pristine state) and the Cu atom resides as a positively charged center (0.87e) (**Fig. 6.30(b)**).

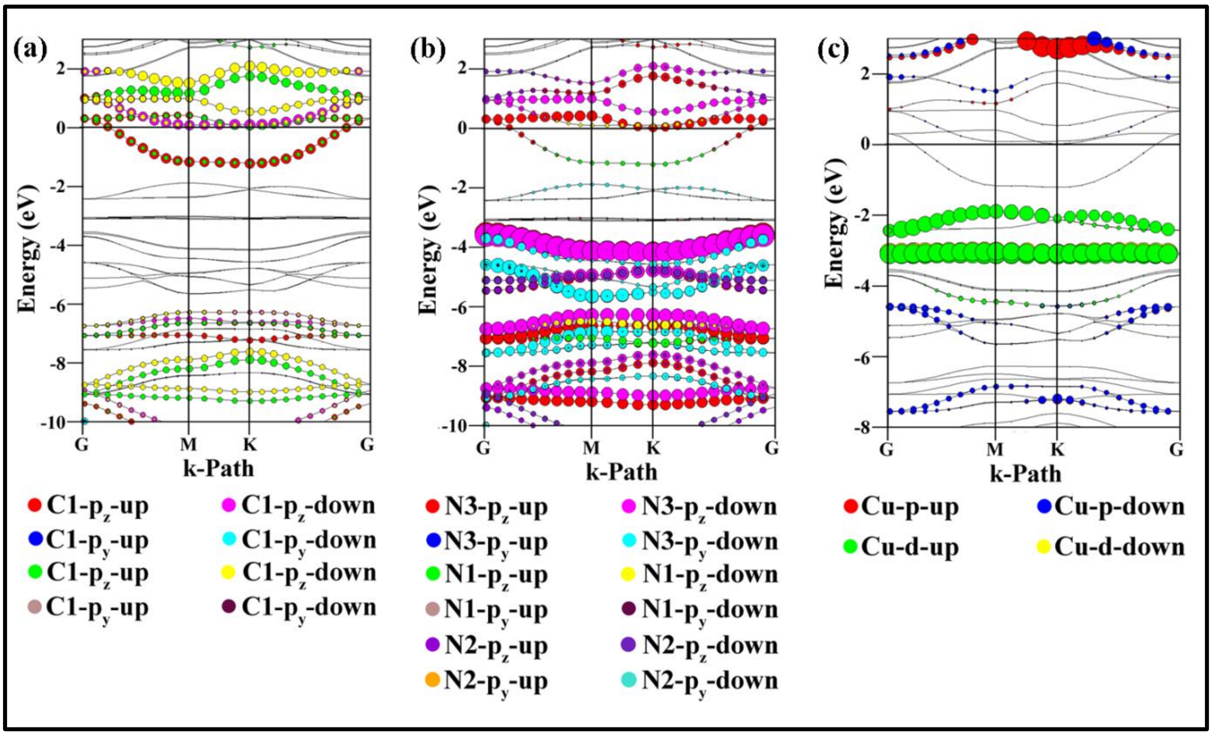

***Fig. 6.32**: Orbital projected band-structure of CuCN (a) projected on the orbitals of C atoms, (b) projected on the orbitals of N atoms, (c) projected on the orbitals of Cu atoms*

The semiconducting nature of pure GCN was modulated into a half-metallic one with band crossing the E_F for one kind of spin whereas bands corresponding to the opposite spin representing semiconducting nature with direct band gap of value 1.98 eV at the E_F (**Fig. 6.28(d)**). The VBM and CBM were both found to be located at the **M** (0, 1/2, 0) point in the reciprocal space. The spin splitting was observed only near the E_F at the valence band and at the conduction band with the up and down spin states of the p_z orbital of C1, C2, N1 and N3 forming degenerate energy levels as shown in **Fig. 6.32(a,b)**. The most prominent contribution in forming the degenerate bands was from the C1-p_z and C2-p_z orbitals. For simpler representations, the orbital decomposed band structures were plotted only for the p_y and p_z orbitals of the C and N atoms. The band formed by mostly the C1-p_z-up orbitals with minor contribution from the C2-p_z-up and N1-p_z-up orbitals intersects the E_F establishing the metallic nature CuCN for one type of spins. For the opposite spin, the C1-p_z-down and C2-p_z-down compose the lowest unoccupied conduction band and the Cu-d orbitals solely form the highest occupied valence band establishing the semiconducting nature and thus rendering CuCN as half-metallic (**Fig. 6.32(c)**). The top of the valence band in the semiconducting band-structure is solely contributed by the Cu-d bands with no spin splitting.

The HOMO and LUMO for CuCN are represented in **Fig. 6.31(c,d)** which perfectly corroborates with the observations from its electronic band-structure. The ELF plot of CuCN is shown in **Fig. 6.33(b)**. Although the ELF plot fails to represent the coordination bonds between N3 and Cu, the symmetric distribution of the lone pairs around the Cu atoms as compared to the slightly distorted distribution of the same lone pairs in case of pure GCN represents equivalent bonding between the six N3 atoms and the Cu atom which is situated right at the middle of the hollow pore of the GCN unit cell.

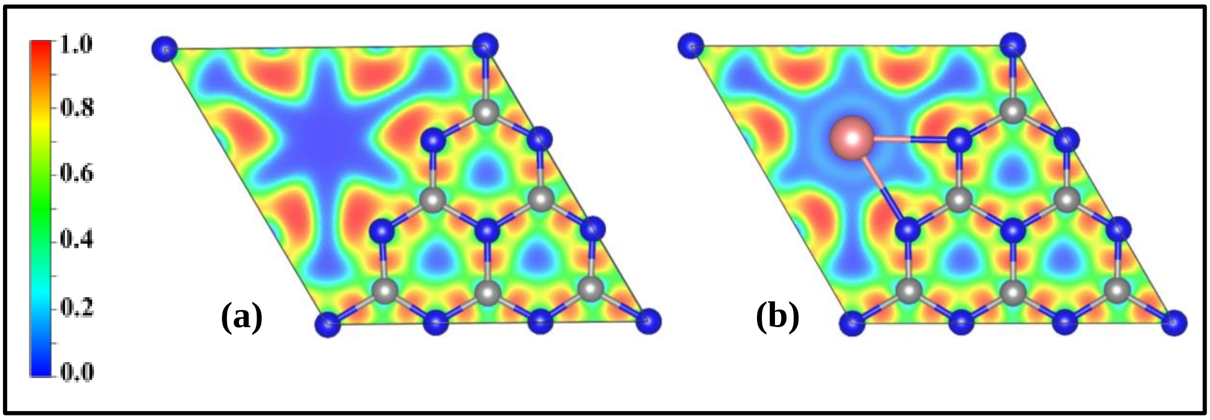

Fig. 6.33: *Electron Localization Function (ELF) of (a) pure GCN and (b) CuCN*

We further calculated the total density of states (TDOS) and projected density of states (PDOS) of the Cu decorated (2×2×1) and (3×3×1) GCN cell within the GGA to shed light on the electronic properties of those systems (**Fig. 6.34** and **Fig. 6.35**). The aid of GGA was taken into account due to the fairly large area of those systems. Both CuCN cell of dimension (2×2×1) and (3×3×1) were found to be metallic in nature with spin polarization at E_F much reduced compared to the Cu decorated GCN unit cell. In both the cases the highest occupied band below the E_F is formed prominently by the Cu-d orbitals (**Fig. 6.34(d)** and **Fig. 6.35(d)**) whereas the system is rendered metallic as the bands formed by C1-p_z and C2-p_z orbital intersects the E_F (**Fig. 6.34(b)** and **Fig. 6.35(b)**) similar to the Cu-decorated GCN unit cell case as discussed earlier.

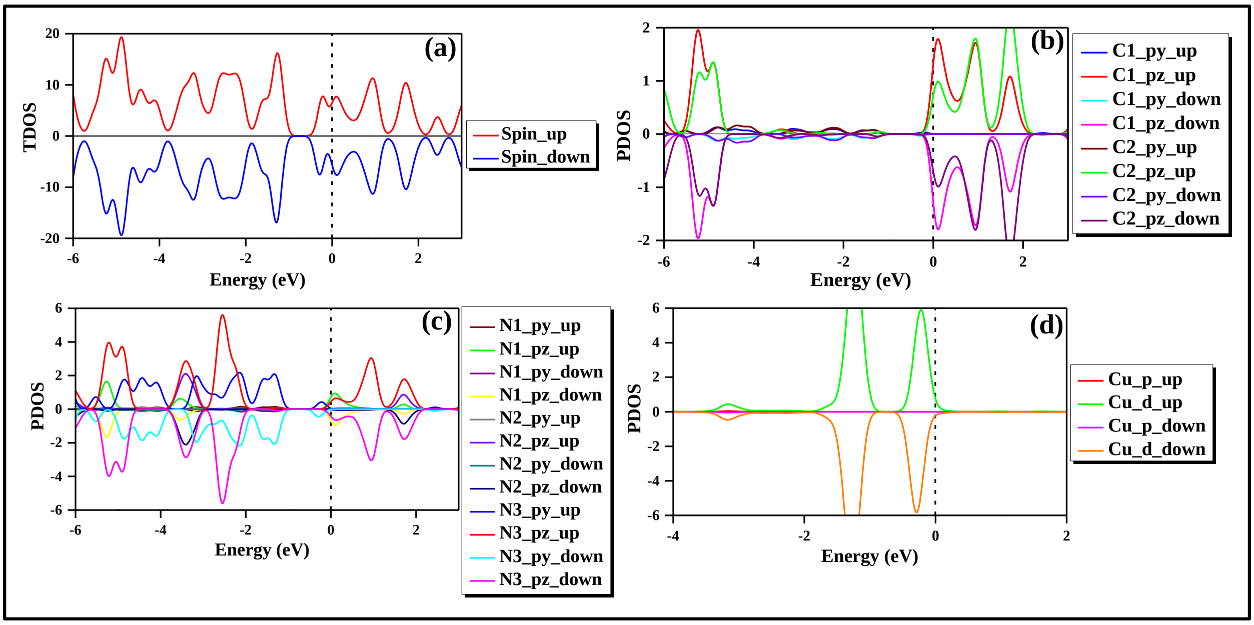

***Fig. 6.34**: The total density of states (TDOS) and projected density of states (PDOS) of the Cu decorated (2×2×1) GCN cell; (a) TDOS, (b) PDOS of C1 and C2, (c) PDOS of N1, N2 and N3, (d) PDOS of Cu*

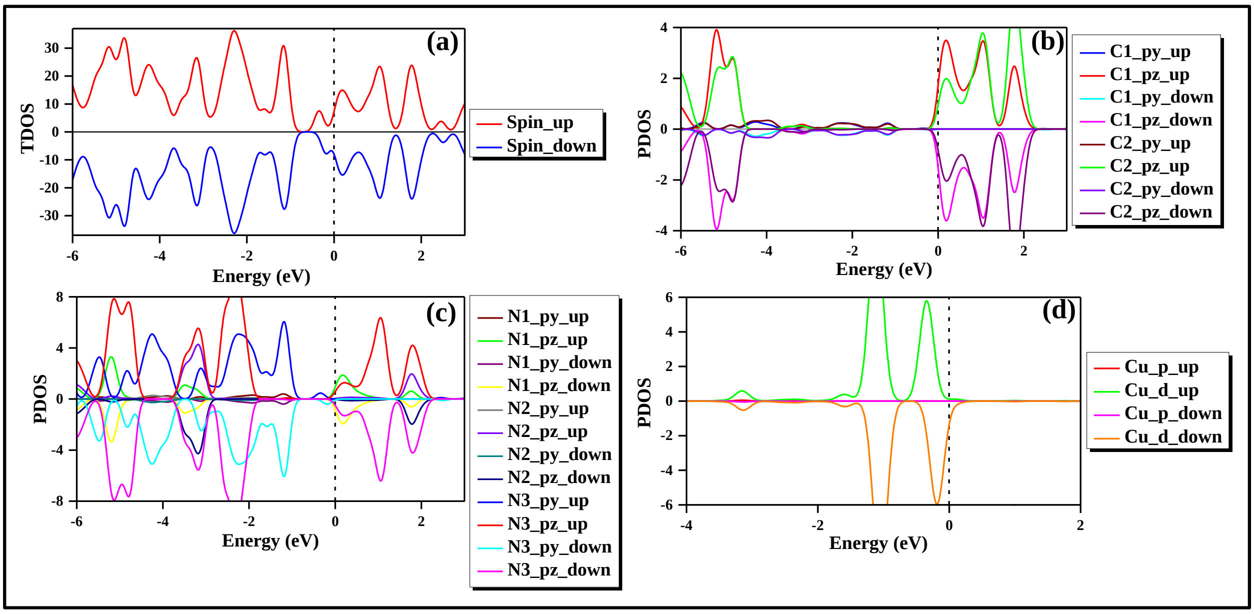

***Fig. 6.35:** The total density of states (TDOS) and projected density of states (PDOS) of the Cu decorated (3×3×1) GCN cell; (a) TDOS, (b) PDOS of C1 and C2, (c) PDOS of N1, N2 and N3, (d) PDOS of Cu*

At the E_F, the contribution from C1-p_z is relatively higher than the contribution of C2-p_z for both of the systems. Our study reveals that decorating GCN monolayer with Cu renders the systems metallic and as the concentration of Cu increases the amount of spin polarization at the Fermi level increases drastically, eventually opening band gap for one type of spin, hence making the system half-metallic. The Mulliken population analysis for those systems shows similar but slightly higher accumulation of charge over the N3 bonded with Cu (**Fig. 6.30(c,d)**). The amount of positive charge over Cu also increases as the concentration of Cu in the GCN system decreases (**Fig. 6.30(c,d)**).

In the above sections, triazine-based polymers including GCN have been characterized in details by various instruments and analytical techniques to reveal their different characteristics. The detailed analysis of MEG_{10} polymer, pristine and exfoliated GCN, and doped-GCN samples validated their proper phase formation, chemical structures, morphologies, and optical and electronic properties. All the necessary analyses proved the successful development of the samples. In the following section, these samples will be utilized for application purposes in the field of wastewater treatment. The results obtained from different experiments will be discussed in details, and some plausible mechanisms will be proposed to establish the samples as promising nanomaterials for environmental remediation.

CHAPTER 6:

RESULTS AND DISCUSSION

PART 2

Fluorescence Detection of Mercury (Hg^{2+}) Heavy Metal by MEG_{10} Polymer

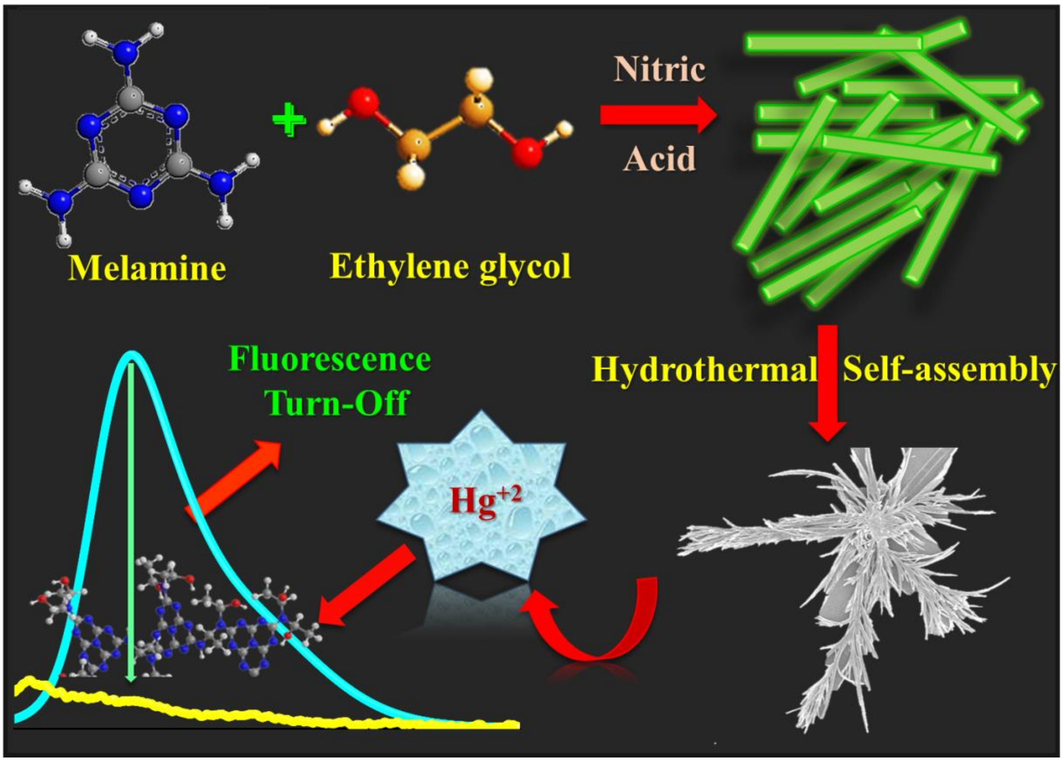

6.4. Fluorescence detection of Hg^{2+} by MEG_{10}

The high toxicity of mercury ions arise from its strong affinity towards the S-atoms of biological building blocks. So, even a trace quantity of this metal (0.002 mg/L as recommended by WHO) is dangerous for human health. Furthermore, owing to its small ionic radius and high solvation energy, Hg^{2+} ions remain encapsulated by water molecules for which its detection is a challenging task. Owing to the impressive affinity of Hg^{2+} with sulphur, triazine based polymers are generally modified with sulphur based thiol/thioether-groups to improve the sensing and removal property. Introduction of sulphur groups has the advantage of forming strong unsaturated coordination with mercury ions and subsequent functionalization leads to the many-fold enhancement of the detection and removal efficiency [294]. Till date, there are very few reports on Hg^{2+} ion sensing without the as mentioned modification of triazine-based polymers following functionalization with sulphur related groups. The polymer reported in the present work interestingly exhibits inherent affinity towards Hg^{2+} and the sensitivity observed in our case is comparable to the sulphur based conjugated polymers.

The importance of ultra-trace detection of Hg^{2+} ions with high level of selectivity and sensitivity has contemporary significance. Therefore, considering the salient chemical as well as the optical properties of covalent framework polymers, we focused upon the development of crystalline triazine-based organic polymers with fibrous morphology for the detection of potentially toxic Hg^{2+} in water. Crystalline polymers have highly defined lattice structure along with very high surface electron density which attributes to their significant photoluminescence property [267]. The inherent crystallinity of the polymer emerges from its highly crystalline precursor melamine. This rod like structure can easily self-assemble and exhibits more exposed surface along with protruded organic functionalities.

In this work, the as-synthesized thermally stable and crystalline nitrogen-rich melamine-based covalent polymer nanodendrite MEG_{10} has been used to demonstrate the nanomolar level detection of Hg^{2+} ions through fluorescence quenching of these photoluminiscent nanodendrites without the functionalization with any sulphur mediated groups. MEG_{10} polymer has been used as a fluorescent metal ion detector with high selectivity and sensitivity for Hg^{2+} ions even in presence of multi-species ions in the solution as shown in **Fig. 6.36(a-c)**. The Stern-Volmer plot, (I_0/I) versus [Q], is given in **Fig. 6.36(c)** and K_{sv} of each analyte are obtained from the respective slopes of the linear fit at low range of [Q], following equation (5.3) given in chapter 5, section 5.3.1.3.

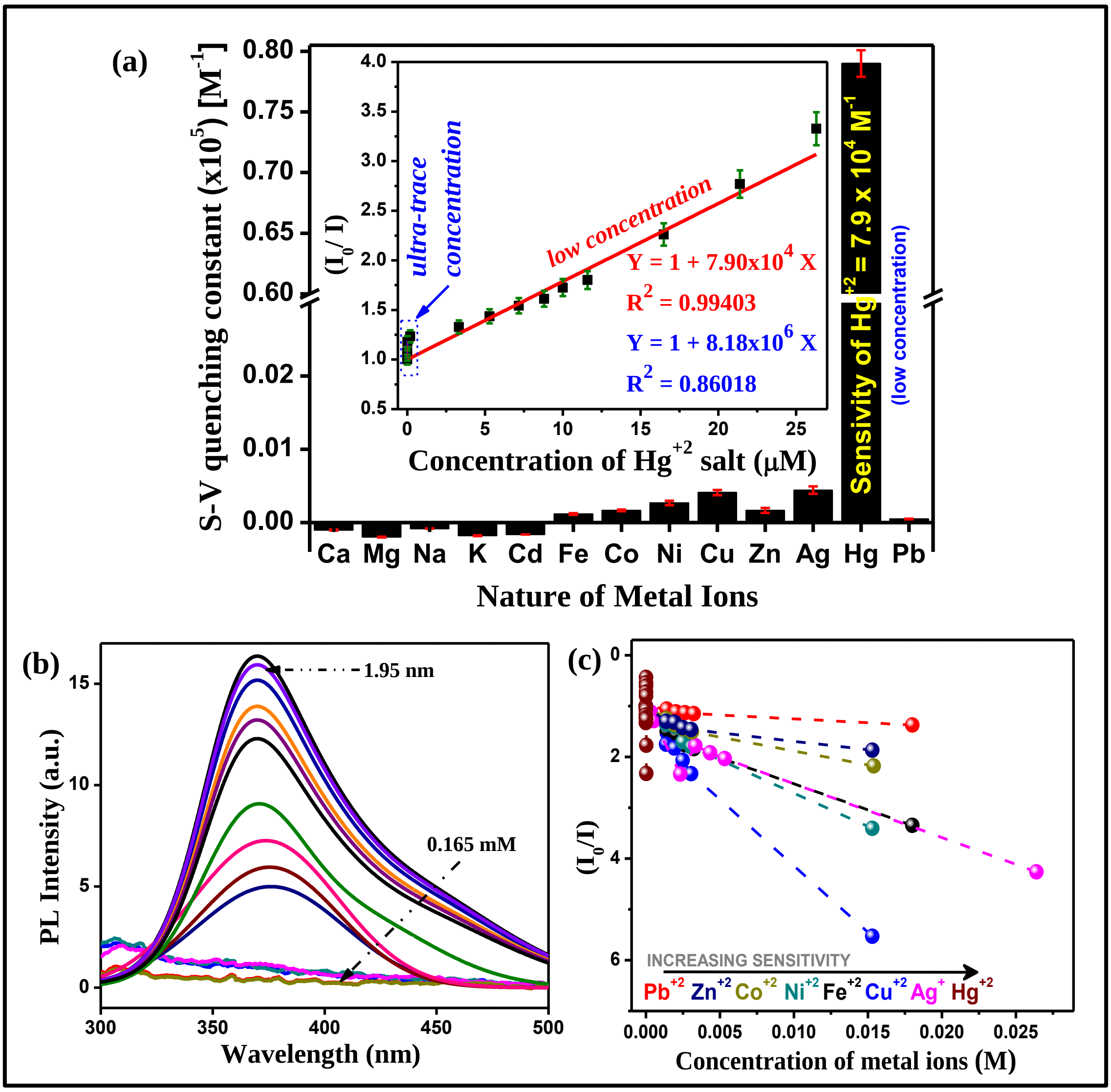

Fig. 6.36: *(a) Sensing selectivity of* MEG_{10} *towards different metal ions. (Inset of (a)) Stern-Volmer plot,* (I_0/I) *vs concentration of* Hg^{2+} *salt [Q], showing two linear responses for ultra-trace and low concentrations with* $K_{S\text{-}V}$ *of* (8.18×10^6) *and* (7.9×10^4) M^{-1} *respectively when* $[MEG_{10}]$ *= 0.5 mg/mL at 25 °C. (b) Room temperature PL quenching of aqueous* MEG_{10} *solution in presence of different concentration of* Hg^{2+} *salt at 25 °C. (c) Change in PL intensity* $[(I_0\text{-}I)/I]$ *versus concentration of different transition metal ions (*$[MEG_{10}]$ *= 0.5 mg/mL, 25 °C)*

It is clearly revealed from **Fig. 6.36(a) (inset)** that the Stern-Volmer plot does not follow the conventional linear nature throughout the whole concentration range which perhaps can be attributed to the fact that both static and dynamic quenching processes occur in the system [295,247]. The values of $K_{S\text{-}V}$ and L_D as obtained for both the two responses for Hg^{2+} at two different concentration ranges (0 - 1.95×10^{-7} M and 3.33×10^{-6} - 2.63×10^{-5} M, respectively)

[247] are given in the **Table 6.3** along with those from other references for comparison. With further increase in the concentration of mercury ions above 2.63x10^{-5} M, no more fluorescence quenching can be observed which indicates the possibility of exhaustion of Hg^{2+} binding sites on the surface of MEG_{10}. The values of L_D are obtained following equation (5.4) given in chapter 5, section 5.3.1.3.

In general, the fluorescence quenching mechanism in conjugated polymers is a complex phenomenon arising due to the transfer of energy throughout the conjugated structure which subsequently results in the mixture of static and dynamic quenching phenomena [296]. As observed from the Stern-Volmer plot, both complex formation and collisional quenching occurs in the MEG_{10}-Hg^{2+} system yielding the occurrence of static and dynamic quenching, respectively. Molecular contact between the fluorescent MEG_{10} and the Hg^{2+} quencher is required for both the quenching phenomena. It is highly possible that during collisional or dynamic quenching, the Hg^{2+} ions diffuse into the fluorescent MEG_{10} when MEG_{10} is in the excited state lifetime. When contact between the fluorescent polymer and the quencher molecules takes place, MEG_{10} returns to the ground state but no emission of photon occurs. On the other hand, Hg^{2+} ions can also form stable non-fluorescent complexes with the MEG_{10} polymer in the ground state itself thereby resulting in static quenching. Melamine contributes the π-conjugated system whereas the glycol group acts as oxygen donor during the formation of the MEG_{10} polymer. The additive effects of both the groups are the major attributions to the selective sensing of mercury ions. The Hg^{2+} ions significantly interact with the N-atoms of the π- conjugated heptazine units and also with the associated oxygen atoms in the MEG_{10} polymers forming a reversible non-fluorescent complex between MEG_{10} and Hg^{2+}, thereby resulting in the PL quenching of the polymer. Moreover, Hg^{2+} have a larger ionic radius as compared to other metal ions so the polarization and deformation effects happen more favourably when interaction occurs with the nitrogen atoms of the polymer [248]. The negative surface charge of MEG_{10} as evident from the Zeta potential analysis is also one of the primary reasons for its effective interaction with the positively charged Hg^{2+} ions. In presence of low concentration of MEG_{10} (= 0.5 mg/mL) the observed limit of detection (L_D) of Hg^{2+} ions is 0.03 and 3.6 ppb for the two responses of the Stern-Volmer (S-V) plot in ultra-trace and low concentration ranges with respective S-V constants of 8.18 x 10^6 and 7.9 x 10^4 M^{-1} (refer to inset of **Fig. 6.36(a)**). The sensitivity of this polymer is higher than some of the recently reported metal-free organic polymers [248,297,298] and is comparable to the work of Barman et al. [299]. The observed L_D values for MEG_{10} are lower than the safety limits of Hg^{2+} concentrations in drinking water as recommended by WHO (~2 ppb). It is to be noted that the counter-anions used for the complete range of metal salts are nitrates.

Table 6.3. Comparative studies of sensitivity of different organic polymers towards Hg^{2+} ions:

Sensing Material	[Sensing Material] (mg/mL)	K_{S-V} (M^{-1})	L_D (ppb)	Normalized K_{S-V} =K_{S-V}/[Sensing Material] ($M^{-1}\cdot mg^{-1}\cdot mL$)
MEG_{10}	0.5	8.18×10^6	0.03	16.36×10^6
		7.9×10^4	3.6	15.8×10^4
g-CNQDs [299]	0.5	2.7×10^7	0.02	5.4×10^7
PANI/C dots [248]	--	7.519×10^6	5.86	--
HCMP-1 [297]	0.8	1.1×10^4	27.2	1.375×10^4
COF-LZU8 [298]	0.003	86.31×10^6	25	2.88×10^{10}
CTFQD [300]	0.07	-	0.02	-
NOP-28 [301]	-	3.7×10^4	12	-

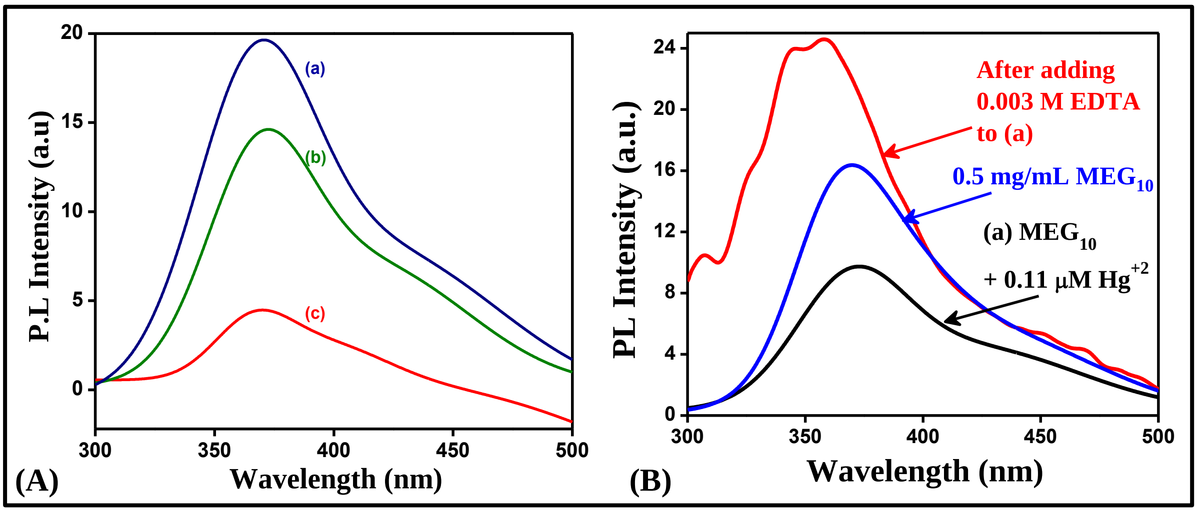

***Fig. 6.37**: (A) PL of pure MEG_{10} (a), MEG_{10} in presence of mixture of ions (Fe^{2+}, Co^{2+}, Ni^{2+}, Cu^{2+}, Zn^{2+} and Ag^{+}) (b), and MEG_{10} in presence of mixture of ions (Fe^{2+}, Co^{2+}, Ni^{2+}, Cu^{2+}, Zn^{2+} and Ag^{+}) after addition of Hg^{2+} (c). (B) Recovery of PL after treatment of the Hg^{2+}-binded MEG_{10} with 0.003M EDTA solution*

A comparative study of mercury ion sensing as obtained from existing reports are listed in **Table 6.3.** As observed from **Table 6.3**, Ding et al. [298] obtained a high value of $K_{S\text{-}V}$ in detection of Hg^{2+} by thioether-functionalized COF (COF-LZU8). The introduction of sulphur groups into the COF material significantly enhanced the sensing activity, thus a higher sensitivity compared to MEG_{10} was observed in this case. On the other hand, our MEG_{10} polymeric material showed quite improved sensing activity compared to the hypercrosslinked fluorescent conjugated polymer HCMP-1 as developed by Xiang et al. [297].

Fig. 6.37(A) shows the fluorescence quenching of MEG_{10} polymer in presence of a combination of different heavy metal ions. When a mixture of Fe^{2+}, Co^{2+}, Ni^{2+}, Cu^{2+}, Zn^{2+} and Ag^{+} is added into the solution, there is a significant quenching in the fluorescence intensity of MEG_{10} (refer to **(b)** of **Fig. 6.37(A)**). Interestingly, when Hg^{2+} ions are added in this mixture solution, the fluorescence emission intensity of MEG_{10} reduces drastically as evident from **(c)** of **Fig. 6.37(A)**. Furthermore, MEG_{10} showed good ON/OFF fluorescence switching in presence of EDTA and Hg^{2+} ions as the former extracts out the bonded Hg^{2+} ions from MEG_{10} sites (**Fig. 6.37(B)**). This observation led to the fact that the PL spectra have been rescued by addition of strong metal ion chelator EDTA, which suggests that, the interaction of MEG_{10} with Hg^{2+} is completely reversible. This also indicates that the unbound components, i.e., Hg^{2+} and MEG_{10} are probably in rapid equilibrium with the bound species [302].

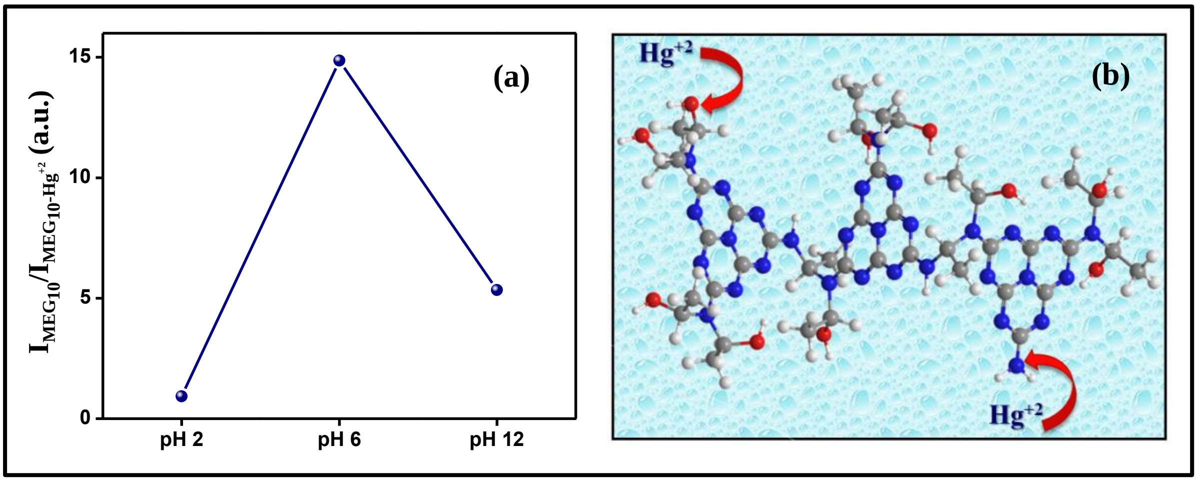

Fig. 6.38: (a) Intensity ratio plot of MEG_{10} and MEG_{10}-Hg^{2+} complexes at pH 2, 6 and 12. (b) Plausible interaction of Hg^{2+} ions with the peripheral electron donating oxygen and nitrogen ligands of MEG_{10}

The change in the PL intensity ratio for the MEG_{10} polymer and the MEG_{10}-Hg^{2+} complexes for acidic, neutral and basic pH is shown in **Fig. 6.38(a)**. It was observed that the fluorescence intensity for MEG_{10} was highest at pH12 which gradually decreased with decrease in the pH value. Interestingly, upon addition of 0.116 mM of Hg^{2+} solution and again varying the pH, it was observed from the intensity ratio plot that the best sensing property was obtained in a solution at pH6 followed by pH12 whereas the sensing property got drastically hindered in acidic medium. This can be attributed to the fact that the existing amine groups in the MEG_{10} polymer undergoes protonation under acidic conditions to generate positively charged sites consisting of $-NH_3^+$ groups which are beneficial for the adsorption of negatively charged anionic heavy metals rather than positively charged Hg^{2+} ions. The increase in the overall positive charge on the surface of the polymer at a lower pH value hinders the interaction with cations. Hence, MEG_{10} shows significant sensing ability in neutral to basic media whereas negligible sensing property in acidic medium.

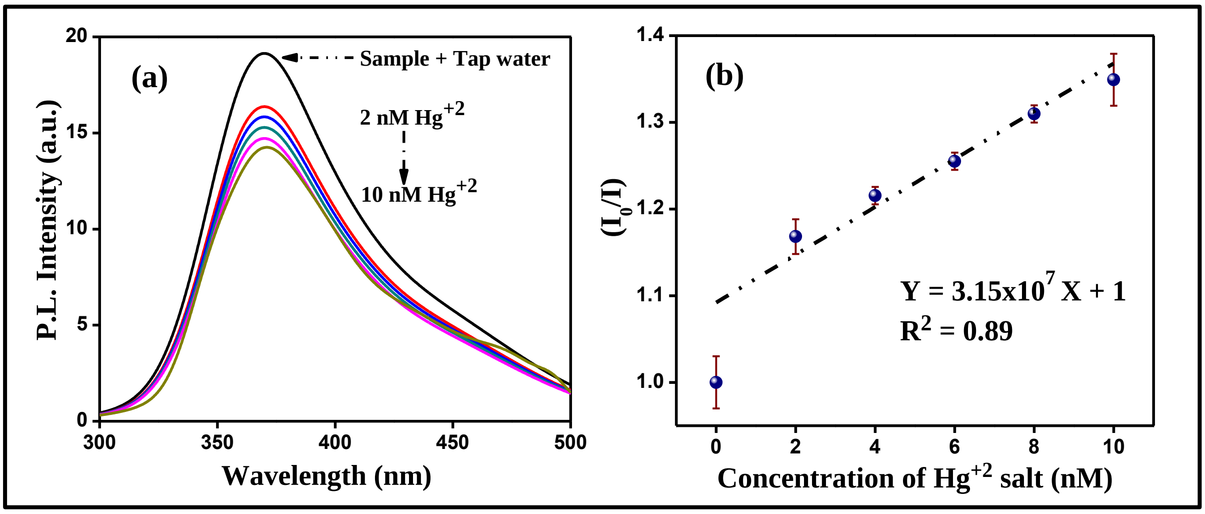

***Fig. 6.39**: (a) Room temperature PL quenching of aqueous MEG_{10} solution in tap water in presence of different concentration of salts. (b) Change in PL intensity $[I_0/I]$ versus different concentration of Hg^{2+} metal ions in tap water $[MEG_{10}]$ = 0.5 mg/mL*

The MEG_{10} polymer was further employed to detect trace mercury ions present in tap water samples to prove its practical applicability. The procedure is given in details in section 5.3.1.2. of chapter 5. **Fig. 6.39(a)** shows that the fluorescence intensity of MEG_{10} decreased with increased concentrations of Hg^{2+}. The corresponding calibration curve of (I_0/I) vs. Hg^{2+} concentration is given in **Fig. 6.39(b)** which shows a reasonably well linear correlation (R^2 = 0.89). Hence it can be inferred that MEG_{10} polymer can successfully distinguish between tap water and the water that has been injected with 2 nM Hg^{2+} concentrations in spite of the presence of various other minerals and organic elements in tap water.

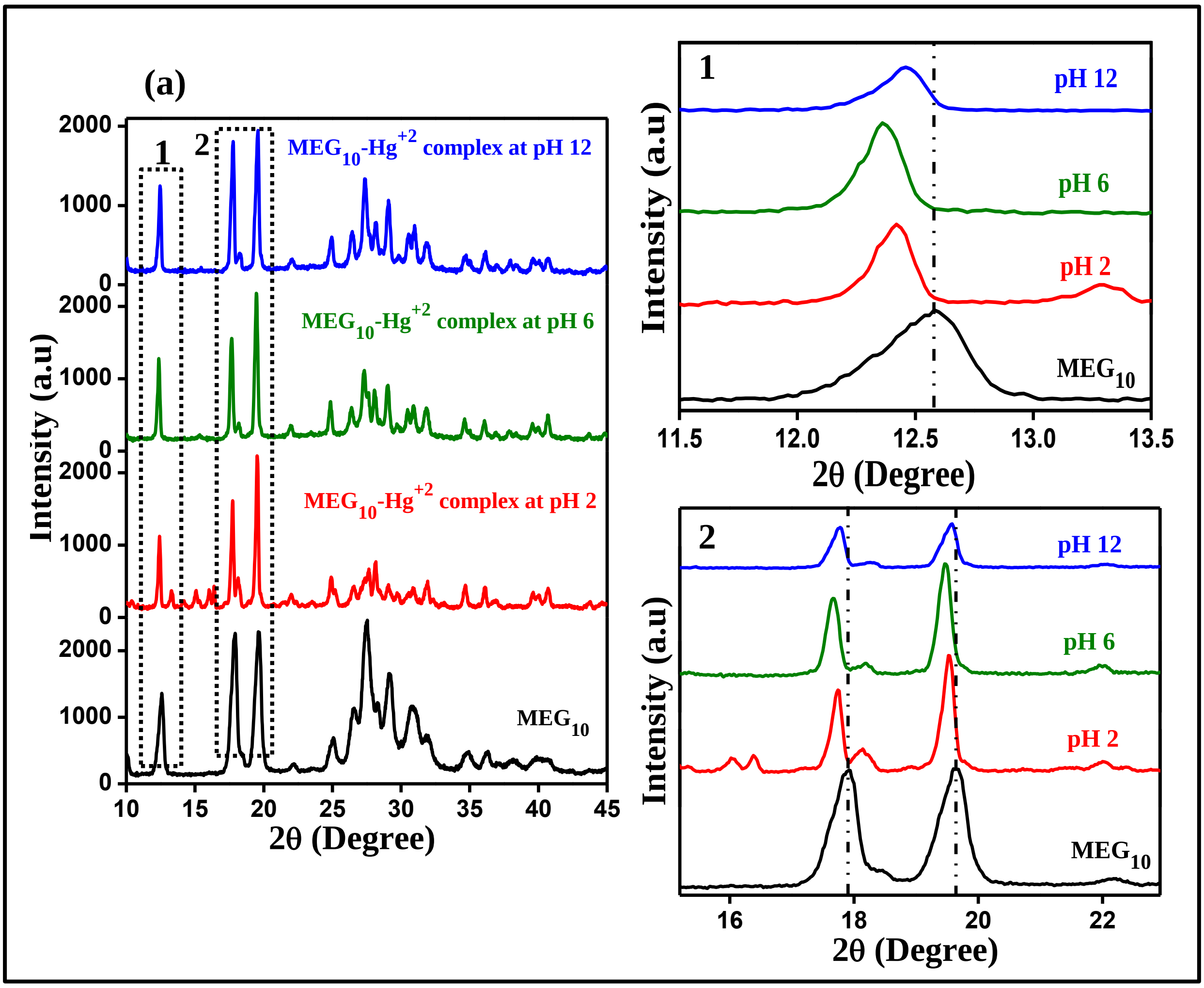

Fig. 6.40: *(a) XRD analysis of MEG$_{10}$ after Hg^{2+} adsorption at different pH values of 2, 6 and 12. Magnified XRD plot of the (1) (001) plane and (2) (-201) and (200) planes of MEG$_{10}$ after Hg^{2+} adsorption*

Fig. 6.40(a) shows the XRD pattern of MEG$_{10}$-Hg^{2+} complexes formed after Hg^{2+} adsorption on the polymer at different pH values of 2, 6 and 12 along with the XRD plot of pure MEG$_{10}$. It can be seen that at acidic pH(2) there are presence of peaks in-between 13.3° to 16° corresponding to HgO along with the characteristic peaks of MEG$_{10}$ with reduced intensity. However, at pH 6 and 12, there are no signs of mercury related peaks and only the peaks corresponding to MEG$_{10}$ can be observed with decreased intensity. The magnified images of the (001) plane and the (-201) and (200) planes after inclusion of Hg^{2+} ions are shown in **Fig. 6.40 (1)** and **(2)**, respectively. There is a significant shifting to lower 2Θ values after Hg^{2+} incorporation and the maximum shift can be observed at pH 6. This shifting results from the increased interlayer spacing caused by the incorporation of Hg^{2+} ions in the interstitial sites of the MEG$_{10}$ polymer. The introduction of Hg^{2+} ions also leads to the reduced intensity of the characteristic planes of MEG$_{10}$ due to the hindrance in crystal growth. At pH 2, mercury groups remain associated as separate entities with the MEG$_{10}$ polymer thereby showing negligible sensing phenomena. However with increase in the pH values, mercury gets incorporated into the different planes of MEG$_{10}$ forming coordination complexes with the polymer due to chemisorption. Hence, the sensing property is significantly enhanced.

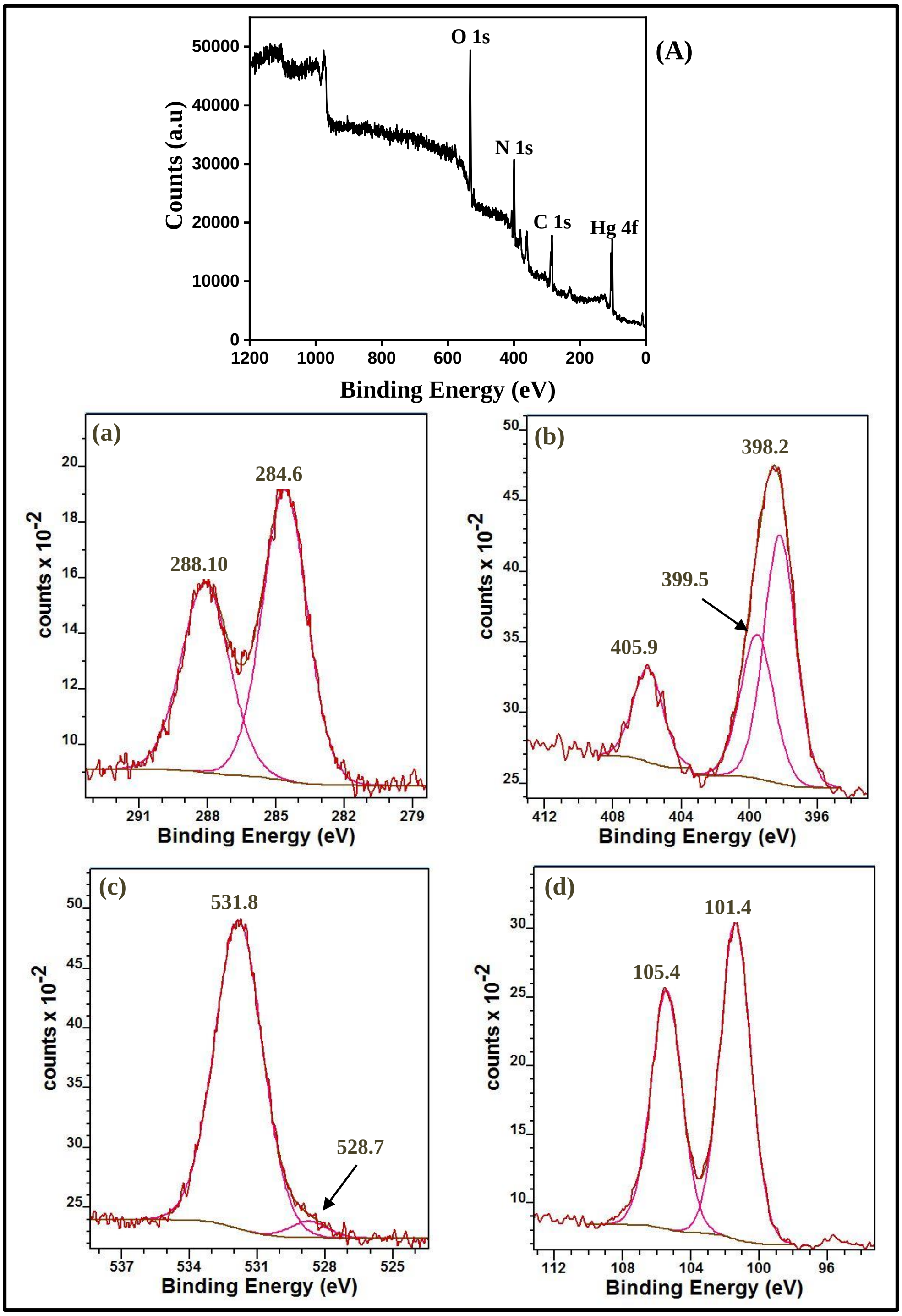

Fig. 6.41: *XPS spectra of MEG$_{10}$ after Hg^{2+} adsorption: (A) XPS survey scan; Elemental scan of (a) C1s, (b) N1s, (c) O1s spectra and (d) Hg4f spectra*

XPS analysis of set 5 (refer **Table 5.1**) was carried out to understand the nature of interaction between Hg^{2+} ions with the polymer. **Fig. 6.41** shows some prominent changes in the O1s and N1s XPS profiles of Hg^{2+}-MEG_{10} mixture owing to the interaction between Hg^{2+} ions with the O and N atoms of the polymer. This accounts for the quenching of PL of MEG_{10}. Deconvolution of the C1s spectra reveals that the intensity of peak at 288.1 eV has been suppressed with respect to the peak at 284.6 eV, which confirms that the C-O bonding is affected in presence of Hg^{2+} ions. The N1s spectra shows deconvoluted peaks at 399.5 and 398.2 eV along with the π-π^* satellite peak at 405.9 eV ($\Delta = 7.7$ eV). The O1s peak ascribed to the C-O group also shifts to 531.8 eV from 530.5 eV. These prominent changes in the XPS profile with respect to MEG_{10} (shown in **Fig. 6.8**) are related to the binding of the Hg^{2+} ions with the O and N atoms of MEG_{10}. Furthermore, the XPS profile of Hg4f, given in **Fig. 6.41(d)**, shows the two symmetric $4f_{7/2}$ and $4f_{5/2}$ peaks at 101.4 and 105.4 eV characteristic of Hg^{2+}. The XPS survey scan given in **Fig. 6.41(A)** shows the presence of mercury along with the characteristic peaks of C, O, and N.

The lone pairs of electrons in both the oxygen bonded and nitrogen bonded groups render electron donating feature in MEG_{10} polymer for effective interaction with Hg^{2+} ions. The heavy metal Hg^{2+} ion has the ability to form strong chelates with the -N≡C linkages and –O- bridges where stable coordination bonds are formed as the interaction between the metal ions and electron donating lone pairs based ligands of MEG_{10}. Most possibly this chelation process of Hg^{2+} ions with nitrogen and oxygen atoms of the polymer brought them into close proximity with each other. This resulted in the utilization of the lone pairs and subsequent reduction in the photogenerated charge carriers. The energy and electron transfer from the π-conjugation framework of MEG_{10} to the unoccupied orbitals of the metal complex along with possible aggregation of the polymer chains by the metal ions are the plausible causes behind the observed fluorescence quenching. A similar mechanism was suggested by Xiang et al. who reported the fluorescence detection of Hg^{2+} ions resulting from the high affinity of their polymer sample towards mercury [297]. They reported an L_D value of 27.2 ppb which is much inferior to that obtained for MEG_{10} in our study. Zhu et al. reported highly sensitive Hg^{2+} ions sensing by covalent triazine-based framework which was rapidly exfoliated and subsequently cut into N-doped carbon quantum dots [300].

The HSAB theory predicts the conventional pattern followed by different metals for different ligands based on their relative affinities where hard metals are found to interact more strongly with hard ligands and soft metals with soft ligands. This explains the preferential strong interaction of soft d-block metal cation Hg^{2+} with soft sulphur based groups rather than nitrogen based ligands [302]. However, it is also noted that organic ligands constituting of unsaturated nitrogen atoms can be considered as soft Lewis bases [303]. Owing to this property they can exhibit impressive tendency to generate stable coordination complexes with various transition metal ions, most specifically with those ions which can be contemplated as soft Lewis acids thereby resulting in the formation of covalent complexes. Moreover the carbon atoms form weak π bonds with the peripheral nitrogen atoms which results in the accumulation of more electron density on the N atoms. The enhanced electron density on the edge-terminated nitrogen atoms increases its donating capability and thereby its soft base nature [304]. It is extremely possible that similar phenomena also occur on the peripheral oxygen atoms. In this work, in absence of any sulphur based ligands, the crystal structure of MEG_{10} polymer helps in the possible binding of Hg^{2+} through covalent nitrogen-mercury bond and this is more stable than the bonds formed with other metal ions. Hence the N-Hg-N covalent bond forms a much stronger complex compared to those produced by other metals ions thereby resulting in the highly selective sensing accompanied with significant large quenching effect [305]. After Hg^{2+}, Ag^{+} is another soft acid which can readily interact with donor nitrogen ligands and can thereby compete with mercury ions in terms of selectivity. Interestingly, MEG_{10} shows negligible sensitivity towards Ag^{+} as compared to Hg^{2+} ions. Moreover the specific selectivity of MEG_{10} for Hg^{2+} ions can also be revealed from the high association coefficient value of Hg^{2+} even at low concentrations (K_{S-V} value being $7.9x10^{4}$ M^{-1}) as compared to Ag^{+} ions (K_{S-V} value = $0.041x10^{4}$ M^{-1}) for the same concentrations. This value suggests that Hg^{2+} ions have 192 times more selectivity over Ag^{+}. The possible interaction mechanism of mercury ions with the donor nitrogen and oxygen atoms of MEG_{10} polymer has been shown in **Fig. 6.38(b).**

The fluorescence time decay plots of MEG_{10} and Hg^{2+} attached MEG_{10} complexes are shown in **Fig. 6.42(a,b)**. The corresponding values as obtained from the time decay measurements are listed in **Table 6.4** where τ_1 and τ_2 are the decay lifetime of luminescence and B_1 and B_2 are the weighting parameters. It can be seen that the pure MEG_{10} sample shows single-exponential decay nature with only one τ_1 component of 1.809±0.009 ns. Interestingly after the addition of Hg^{2+} ions the time decay curve takes bi-exponential nature with the generation of a second τ_2 component of 9±6.46 ns. A marginal decrease in the τ_1 component of MEG_{10}-Hg^{2+} complex is observed compared to that of pure MEG_{10} with a value of 0.535±0.01 ns. The generation of two decay centres may arise due to two contributions, one from the free MEG_{10}

and the other from an intermediate state which resulted from the attachment of mercury ions on the polymer surface [306]. The interaction between MEG_{10} and Hg^{2+} creates a supplementary fluorescence quenching pathway possibly due to the transfer of excitation energy and/or charge from the ligand of MEG_{10} to the d-orbital of Hg^{2+}.

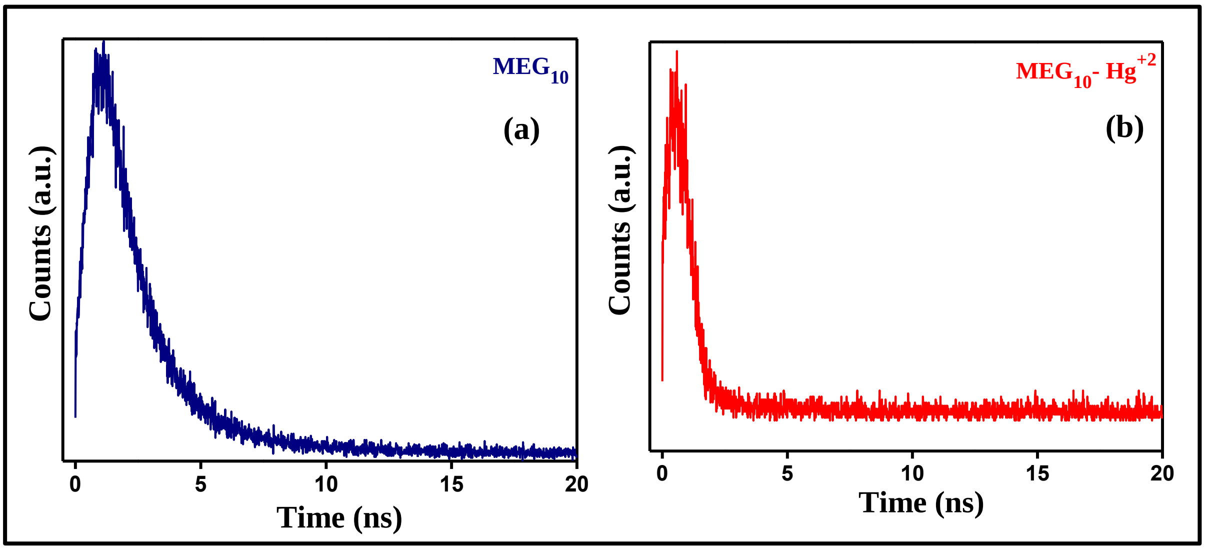

***Fig. 6.42**: Fluorescence time decay of (a) MEG_{10} and (b) MEG_{10}-Hg^{2+} complex at an excitation and emission wavelength of 257.8 nm and 369.4 nm, respectively*

Table 6.4. Values of different parameters as obtained from fluorescence time decay measurements:

Sample	τ_1	τ_2	B_1	B_2	A	χ^2
MEG_{10}	1.809±0.009 ns	-	379.551	-	7.873	1.227
MEG_{10}-Hg^{+2}	0.535±0.01 ns	9±6.46 ns	126.230	1.331	1.506	1.228

In summary, MEG_{10} has been demonstrated as a highly selective and sensitive Hg^{2+} ion sensors with sensitivity of Hg^{2+} ions about $8.18\text{x}10^6$ M^{-1} for ultra-trace mercury concentration at a pH value of 6. The limit of detection was also found to be extremely low ~0.03 ppb. The combined effect of the electron donating nitrogen and oxygen based ligands constituting the polymer resulted in the selective sensing of mercury ions. MEG_{10} polymer stands out in this regard owing to the fact that it can inherently detect mercury ions without any sulphur mediated functionalization as required for other existing triazine based polymers for mercury ion sensing. The polymer was also found to detect Hg^{2+} ions in real tap water samples which proved its practical feasibility. In future, this material may be commercially used to selectively sense Hg^{2+} ions owing to its cheap and non-toxic nature.

Photocatalytic degradation of toxic pollutants by exfoliated GCN

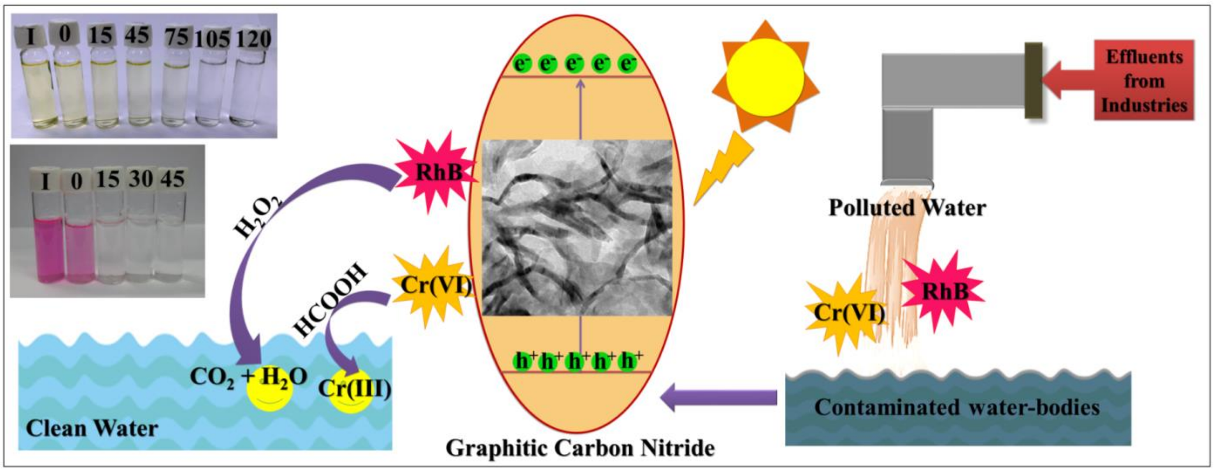

6.5. Photocatalytic degradation of toxic pollutants by exfoliated GCN

As discussed previously, RhB dye is a toxic chemical compound released by the textile industry that can cause disastrous effects on human health, as well as negatively impact water resources [307]. Another hazardous inorganic micro-pollutant that is released at an alarming rate from leather tanning, electroplating, and alloy manufacturing plants is hexavalent chromium (Cr(VI)) [136,137]. The reduction of Cr(VI) to its less-toxic form, Cr(III), is considered a novel approach to greatly alleviate the toxicity of hexavalent chromium in the environment. Thus, it is necessary to properly treat pollutant-laden wastewater before it is discharged into the natural environment.

Heterogeneous photocatalysis is an advanced AOP method frequently used for the remediation of industrial wastewater [308]. A suitable photocatalyst is employed to non-selectively degrade the pollutant effluents into non-toxic end products under light illumination [308]. The primary criterion for a promising photocatalyst is preventing the recombination of the photogenerated electrons and holes so that reactive species, such as •OH and superoxide radicals ($\bullet O_2^-$), can be easily produced to participate in redox reactions to achieve complete mineralisation of toxic pollutants. In this regard, certain electron and hole scavengers are employed to accelerate and ameliorate the degradation or reduction procedure of the toxic pollutants. H_2O_2 is an environmental-friendly electron-capturing agent. When added to a catalytic system, it can enhance the photocatalytic response significantly by generating •OH radicals in the presence of light [309]. Similarly, formic acid (FA/HCOOH) is a small molecular weight organic acid generally used in redox reactions as an electron and hydrogen donor [310]. Due to its non-toxic nature, FA is considered a green sacrificial agent. FA can consume the positively charged photogenerated holes in the valence band of the photocatalyst material to generate $\bullet CO_2^-$ radicals. These radicals can oxidise $HCrO_4^-$ to CO_2 and H_2O [311]. In addition, due to the capture of the holes by FA, a higher amount of negatively charged electrons can participate in the Cr(VI) reduction process. This enhances the overall catalytic efficiency [136].

In the present work, GCNX sample was used for the photocatalytic degradation of RhB dye in the presence of H_2O_2 and for reducing Cr(VI) to Cr(III) in the presence of FA. Both studies have been performed in the presence of a visible light source. Extensive experimentations have been conducted by varying the catalyst dosage, the initial pollutant (RhB and Cr(VI)) concentration, the concentrations of H_2O_2 and FA, and pH. Statistical analysis of the catalytic performance in the degradation of both pollutants has been validated by response surface methodology (RSM), which predicted the optimal catalytic conditions. The reduction efficiency of the GCN catalyst has been further explored using density functional theory (DFT)-based first-principles calculations.

6.5.1. Photocatalytic degradation of RhB dye:

The hazardous pollutant RhB has been degraded by the as-synthesised samples under visible light illumination in the presence of H_2O_2. The RhB dye solution shows the highest absorption intensity around 554 nm, as observed from the UV-vis spectra.

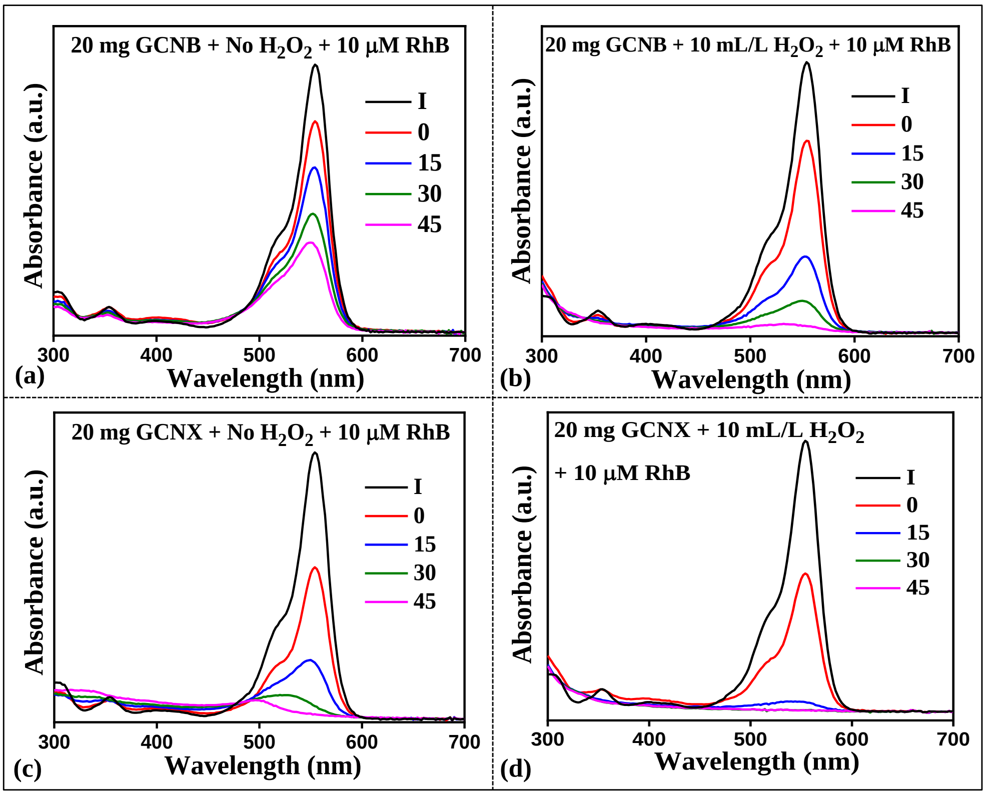

***Fig. 6.43**: Absorbance spectra of RhB in presence of (a) GCNB and no H_2O_2, (b) GCNB and H_2O_2, (c) GCNX and no H_2O_2, (d) GCNX and H_2O_2*

The absorbance spectra of RhB for different catalytic conditions are given in **Fig. 6.43**. In the absence of H_2O_2, upon visible-light irradiation up to 45 min, 20 mg of GCNB can only partially degrade 10 μM of RhB (**Fig. 6.43(a)**), whereas the same amount of GCNX can completely degrade the same concentration of RhB (**Fig. 6.43(c)**). However, the catalytic efficiency of both samples is significantly improved when H_2O_2 is introduced into the system. In **Fig. 6.43(b)**, 20 mg of GCNB can completely degrade 10 μM of RhB within 45 min in 10 mL/L H_2O_2. The same amount of GCNX more efficiently achieves 100% degradation of RhB within 30 min in the presence of 10 mL/L H_2O_2 (**Fig. 6.43(d)**).

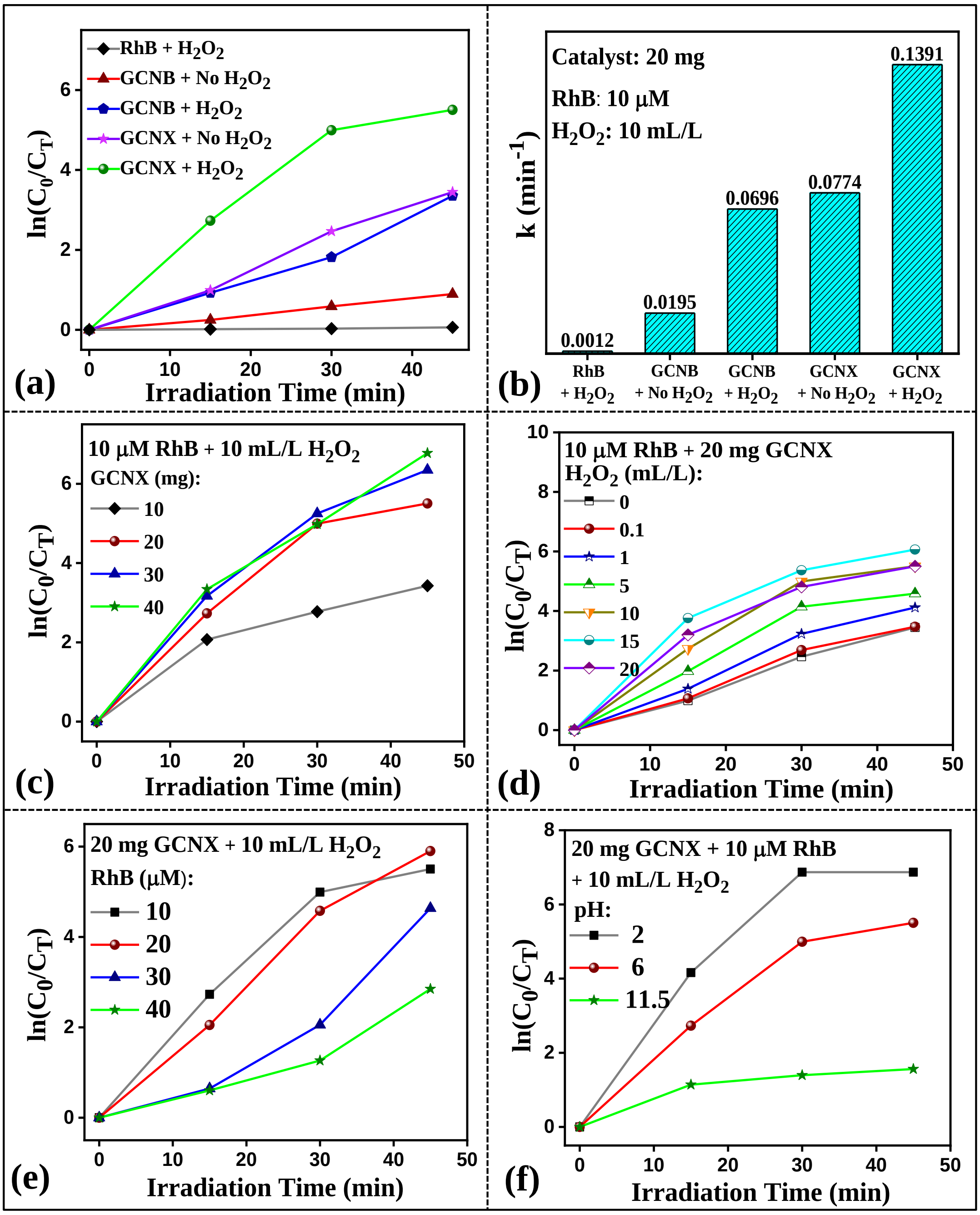

***Fig. 6.44**: (a) $\ln(C_0/C_T)$ plots for various catalytic conditions; (b) bar graphs showing the rate constant values; $\ln(C_0/C_T)$ plots for variation in (c) catalyst dosage, (d) H_2O_2 concentration, (e) RhB concentration, and (f) pH*

The $\ln(C_0/C_T)$ vs. time plots for all conditions are shown in **Fig. 6.44(a)**, and the calculated rate constant values are shown in **Fig. 6.44(b).** The rate constant values have been calculated following equation (5.8) given in chapter 5, section 5.3.2.3. The best catalytic system has a 'k' value of 0.1391 min^{-1}. Furthermore, without any catalyst, H_2O_2 alone cannot degrade

RhB under visible light illumination (**Fig. 6.45(a)**). The digital images of the RhB solutions at different time intervals in the presence of GCNX and the absence of H_2O_2 are shown in **Fig. 6.45(b),** and the digital images in the presence of both GCNX and H_2O_2 are shown in **Fig. 6.45(c)**.

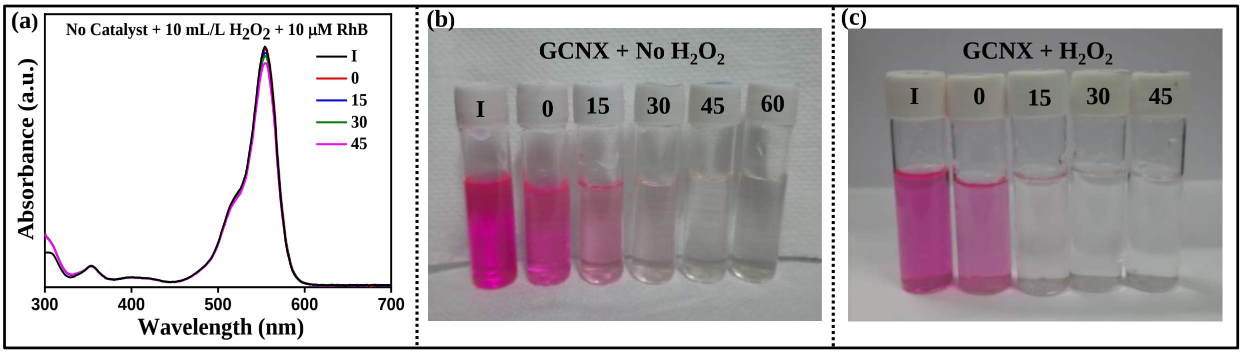

***Fig. 6.45**: (a) Absorbance spectra of 10 µM RhB in absence of GCNX (concentration of H_2O_2: 10 mL/L); digital images of RhB solution (b) in presence of GCNX and absence of H_2O_2, and (c) in presence of both GCNX and H_2O_2*

The effect of the amount of catalyst on the catalytic activity has been analysed by varying the amounts of GCNX and keeping the concentration of RhB and H_2O_2 fixed at 10 µM and 10 mL/L, respectively. The corresponding $\ln(C_0/C_T)$ plot is shown in **Fig. 6.44(c)**. With an increased amount of catalyst, the reaction rate increases significantly because more catalyst provides more active sites for the photocatalytic reactions. The highest rate constant, 0.1601 min^{-1}, is obtained for 40 mg of catalyst, as seen in **Fig. 6.46(a)**.

The effect of H_2O_2 concentration on the degradation of 10 µM of RhB dye has been further studied by using a constant amount of catalyst, 20 mg. From the $\ln(C_0/C_T)$ plot (**Fig. 6.44(d)**), the reaction rate initially increases with increasing H_2O_2 concentration; however, after a certain amount of H_2O_2 is added, the reaction rate decreases significantly. The rate constants for all H_2O_2 concentrations are given in **Fig. 6.46(b)**. The highest reaction rate (0.1556 min^{-1}) is obtained for 15 mL/L H_2O_2. The increase in H_2O_2 in the catalytic system generates more hydroxyl radicals in the solution, enhancing the photocatalytic degradation rate. H_2O_2 can generate •OH radicals by effectively scavenging photogenerated electrons from the conduction band (CB) of the photocatalyst material.

$$H_2O_2 + e^- \longrightarrow {}^{\bullet}OH + OH^- \quad \ldots\ldots\ldots\ (6.1)$$

When there is a low concentration of H_2O_2 in the system, the amount of active hydroxyl radicals generated on the photocatalyst surface also remains low. Thus, the degradation rate is much slower. However, when the concentration of H_2O_2 in the solution becomes too high (here, 20 mL/L), the H_2O_2 molecules start competing with the pollutant molecules for adsorption on the catalyst surface, blocking the active sites [312]. Moreover, H_2O_2 can scavenge the •OH radicals at higher concentrations to generate hydroperoxyl radicals (•OOH). These •OOH radicals further scavenge hydroxyl radicals, thereby decreasing the number of active radicals in the system [313]. Excess H_2O_2 possess the ability to scavenge the photogenerated holes (h^+) to form •OOH radicals. Notably, •OOH radicals are much less reactive than •OH; thus, they do not contribute to dye degradation.

$•OH + H_2O_2 \longrightarrow H_2O + •OOH$ ……… (6.2)

$•OH + •OOH \longrightarrow H_2O + O_2$ ……… (6.3)

$h^+ + H_2O_2 \longrightarrow H^+ + •OOH$ ……… (6.4)

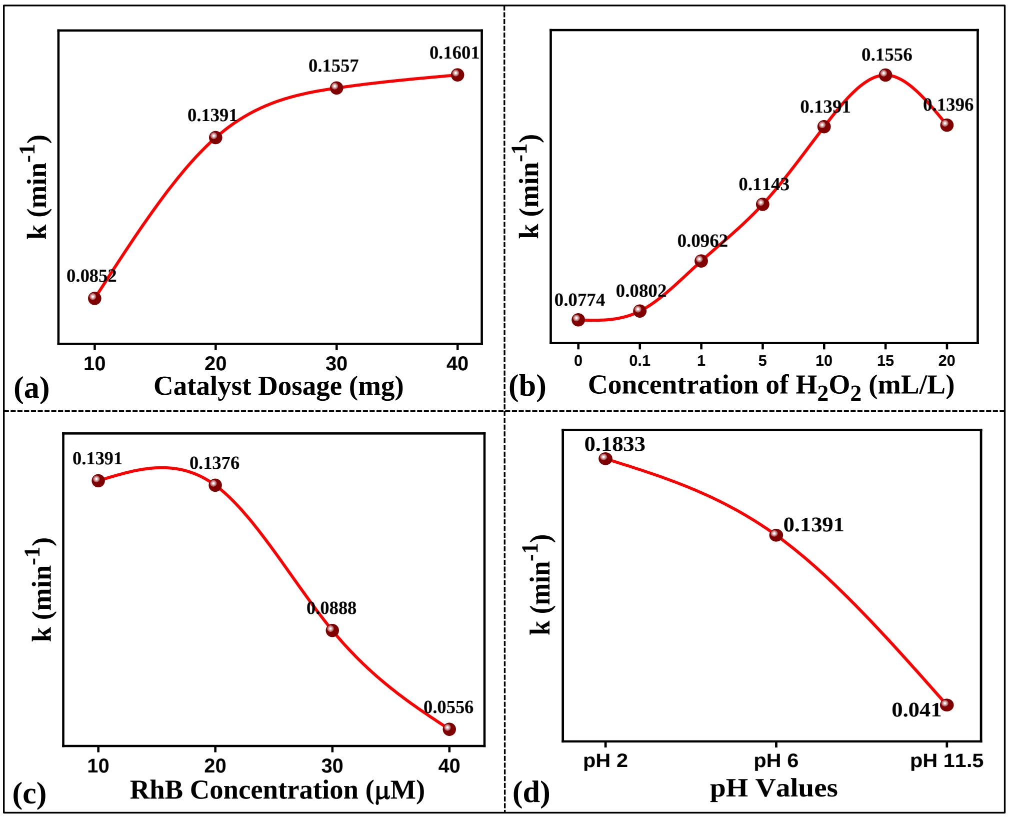

***Fig. 6.46**: Rate constant plots for variation in (a) catalyst dosage, (b) H_2O_2 concentration, (c) RhB concentration, and (d) pH*

The effect of the initial concentration of pollutant has also been studied by increasing the concentration of the RhB dye solution from 10 to 40 µM. During the experiments, the GCNX amount was kept fixed at 20 mg and the H_2O_2 concentration was maintained at 10 mL/L. The corresponding $\ln(C_0/C_T)$ plot is given in **Fig. 6.44(e)**. There is a slight decrease in the reaction rate on increasing the concentration from 10 to 20 µM. However, further increases in the concentration result in a drastic reduction in the degradation rate. The highest value of k

($0.1391\ \text{min}^{-1}$) is obtained from 10 µM RhB. Several monolayers of adsorbed RhB molecules can be formed on the GCN surface at a moderately high (>10 µM) dye concentration. Until a critical concentration limit is reached for the pollutant, the surface of the photocatalyst is not fully covered with dye, leading to a constant reaction rate [314]. On further increasing the concentration of the pollutant, the adsorbed dye molecules occupy most of the catalytic photoactive sites on the catalyst surface, which is the primary cause of a reduced reaction rate [315]. As the number of dye compounds adsorbed on the photocatalyst surface increases, the requirement for active radicals, such as •OH and $•O_2^-$, for degradation also increases proportionately. However, for a given intensity of the visible light, amount of photocatalyst, and period of irradiation, the generation of photo-induced active radicals in the catalytic system remains constant. Thus, for an increased dye concentration, the available active radicals are insufficient to degrade high amounts of pollutants, leading to a decreased degradation rate [315]. Also, at high pollutant concentrations, the light infiltration into the catalytic solution is reduced [316]. The catalytic rate constants obtained for different RhB concentrations are shown in **Fig. 6.46(c)**.

The catalytic activity of GCNX has been studied at three different pHs (acidic pH 2, neutral pH 6, and basic pH 11.5). The experimental conditions were maintained at 20 mg GCNX, 10 mL/L H_2O_2 and RhB concentration of 10 µM. The $\ln(C_0/C_T)$ plots and the associated rate constant plots are shown in **Fig. 6.44(f)** and **Fig. 6.46(d),** respectively. The catalyst dosage, H_2O_2 concentration, and RhB concentration are maintained at 20 mg, 10 mL/L, and 10 µM, respectively. The best degradation rate is obtained at an acidic pH with a rate constant of $0.1833\ \text{min}^{-1}$ because a lower pH is generally favourable for generating •OH radicals. The rate decreases drastically at the basic pH value because, in alkaline conditions, the surface of the photocatalyst becomes negatively charged due to the adsorption of OH^- ions. The •OH active species are rapidly scavenged on reacting with these OH^- ions to generate $•H_2O_2$ or •OOH radicals through radical–radical reactions [312]. Thus, the active hydroxyl radicals lose the opportunity to react with dye molecules, and a reduction in the catalytic efficiency occurs at higher pH.

Effluents released from textile factories contain inorganic salts along with residual dyes. These salts act as exhausting agents when dyeing cellulose fabrics [317]. The effect of these co-existing species on photocatalytic dye degradation by GCNX has been studied by measuring the catalytic activities in the presence of different types of inorganic anions. The corresponding C_T/C_0 plots and bar graph depicting the rate constants are given in **Fig.**

6.47(a,b). The catalyst amount, H_2O_2 and RhB concentrations were maintained at 20 mg, 10 mL/L, and 20 μM, respectively.

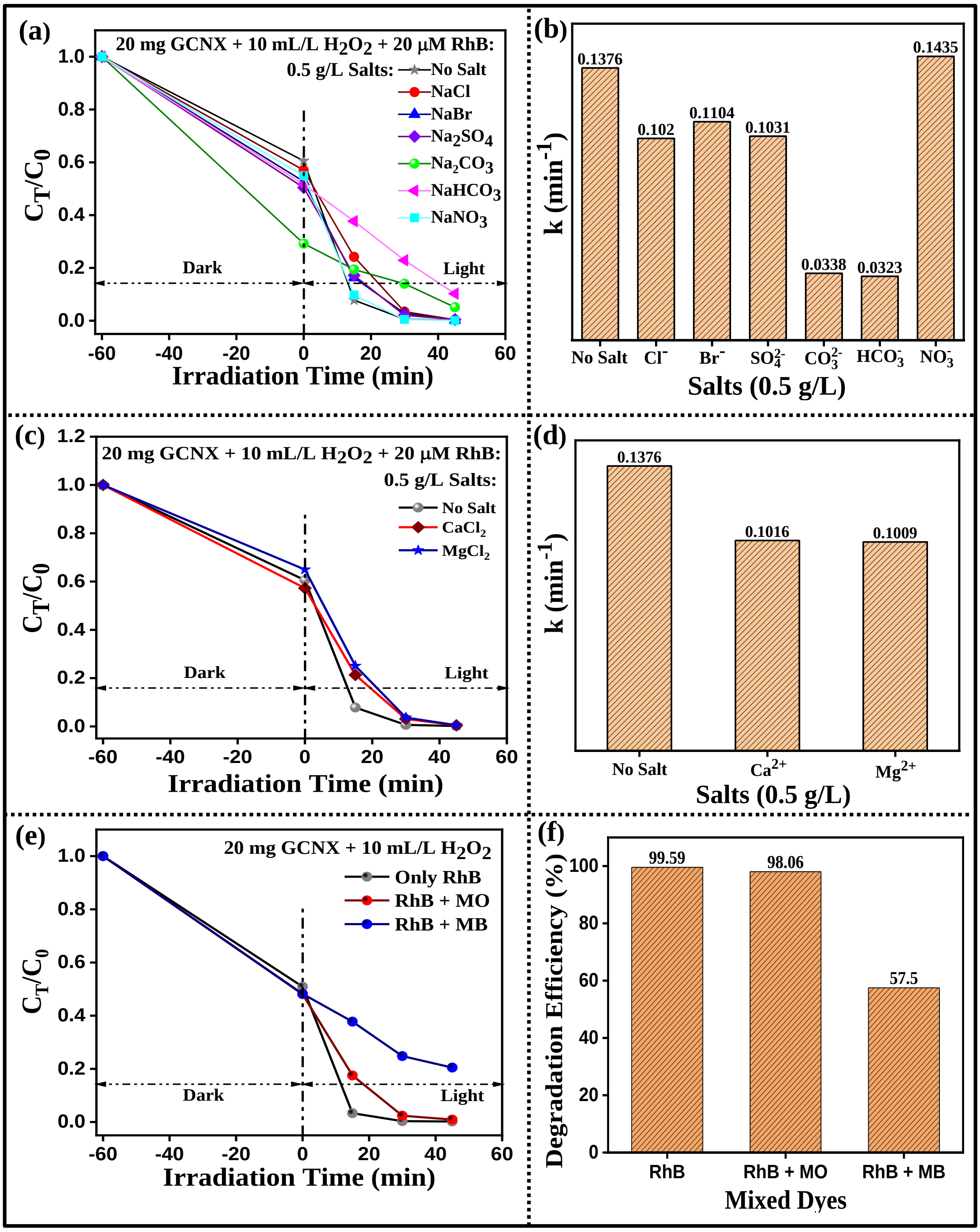

***Fig. 6.47**: C_T/C_0 plots obtained in presence of (a) anionic salts, (c) cationic salts, and (e) different types of textile dyes; bar graphs showing the rate constant values for (b) anionic salts, and (d) cationic salts; and (f) degradation efficiency values for different mixed dyes in 45 min irradiation time*

In the presence of anions such as Cl^-, Br^-, SO_4^{2-}, CO_3^{2-}, and HCO_3^-, the degradation rate significantly decreases, whereas for NO_3^-, the reaction rate improves. The competitive adsorption of these anions decreases the chances of the adsorption of RhB on the GCN surface, decreasing the degradation rate. Also, these negatively charged ions can react with the photogenerated holes, reducing the generation of active radicals required for dye degradation. Cl^- ions scavenge •OH radicals and, upon reacting with •OH, form $\cdot Cl^-$ and $\cdot Cl_2^-$ radicals. These radicals possess inferior oxidising abilities than •OH radicals, thus decreasing the catalytic activity [318]. Br^- ions are also scavengers of •OH radicals; thus, the rate constant decreases to 0.1104 min^{-1} in their presence. The reaction rates are mainly reduced in the presence of carbonate and bicarbonate ions. Like Cl^- and Br^-, HCO_3^- ions scavenge •OH active radicals and generate $\bullet CO_3^-$ radicals with poor oxidising capability in aqueous solution [319]. Moreover, adding HCO_3^- increases the pH of the solution, thereby suppressing the formation of •OH radicals. However, the presence of NO_3^- ions in the solution accelerates the degradation rate, with a rate constant of 0.1435 min^{-1}. NO_3^- ions directly or indirectly help generate of •OH radicals [320]:

$NO_3^- + h\nu \longrightarrow NO_2^- + O$ ………. (6.5)

$NO_3^- + H_2O + h\nu \longrightarrow NO_2^- + OH^- + \bullet OH$ ………. (6.6)

$O + H_2O \longrightarrow 2\bullet OH$ ………. (6.7)

The effect of inorganic cations has also been studied by introducing cationic salts into the catalytic system. The C_T/C_0 plots and bar diagram depicting the rate constants are given in **Fig. 6.47(c,d)**. The surface of GCN is negatively charged [312]; thus, the positively charged Ca^{2+} or Mg^{2+} ions can be adsorbed on the GCN surface, blocking these sites for RhB adsorption. The presence of these cations on the GCN surface prevents the approach of RhB (a cationic dye) to the catalyst surface, where some •OH radicals are generated, decreasing the dye degradation rate.

The wastewater emanated from textile and dyeing factories contains not a single type of dye but mixtures of different dye compounds. The presence of other dyes can interfere with the catalytic degradation of RhB. In this work, apart from RhB, two other commonly emitted dye compounds have been chosen to analyse the effects of their presence in the catalytic solution on the RhB reduction efficiency. These dyes are methyl orange (MO) and methylene blue (MB). The absorbance spectra of RhB + MO and RhB + MB solutions are shown in **Fig. 6.48(a,b)**, respectively. The characteristic peaks of MO and MB are visible in the respective spectra, along with the prominent peak of RhB. In the presence of 20 mg of GCNX and 10 mL/L H_2O_2, the RhB + MO mixture solution is completely degraded within 45 min, with a degradation efficiency of 98.06%. However, under the same catalytic condition, the RhB degradation efficiency is significantly reduced for the combination of RhB + MB solution. GCNX acts as a very good adsorbent for the MB dye: after dark-stirring for 1 hr. prior to switching-on the visible-light source, most of the MB dye molecules are adsorbed on the GCNX surface. This blocks almost all the catalytic reactive sites required for the adsorption of the RhB dye and also obstructs visible light absorption by the catalyst. Thus, a decreased degradation rate is observed; only 57.5% efficiency is achieved after 45 min of light irradiation. The corresponding (C_T/C_0) vs. time plots and bar graph depicting the efficiency values are shown in **Fig. 6.47(e,f)**.

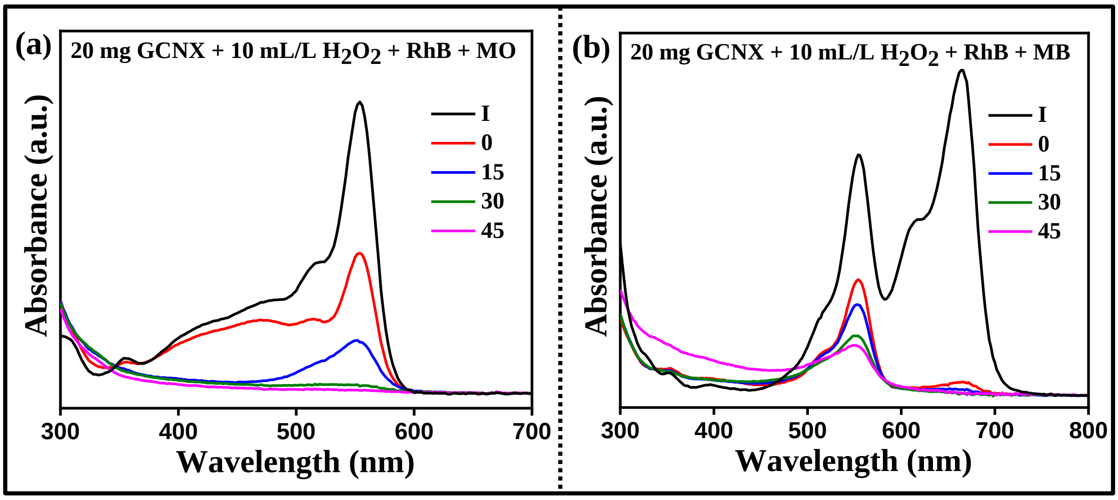

Fig. 6.48: *Absorbance spectra of (a) RhB + MO and (b) RhB + MB mixed dye solutions in presence of 20 mg of GCNX and 10 mL/L of* H_2O_2

Scavenging tests have been performed to determine the active radicals participating in the photocatalytic degradation of RhB dye. The degradation rate decreases in the presence of isopropyl alcohol (IPA) and ethylenediamine tetraacetic acid (EDTA), whereas the activity rate increases in the presence of $AgNO_3$, as observed from the C_T/C_0 and bar graph plots shown in **Fig. 6.49(a,b)**. IPA and EDTA scavenge •OH radicals and holes respectively. The decreased catalytic rate indicates that •OH and photogenerated h^+ are the main active species helping the dye degradation process. However, the increased reaction rate when $AgNO_3$ is added into the system is because $AgNO_3$ can consume the photogenerated electrons when it acts as an electron scavenger. This, in turn, helps to prevent electron–hole recombination, causing more h^+ to become available in the system to degrade the dye [321]. The formation of •OH radicals is further confirmed by fluorescence emission on the addition of terephthalic acid (TA) to the catalytic system. The corresponding PL emission spectra are shown in **Fig. 6.49(c)**. Upon irradiation with visible light in the presence of H_2O_2, •OH radicals are formed from the photocatalyst. TA directly reacts with these •OH radicals to generate a highly fluorescent compound, 2-hydroxyterephthalic acid. This compound exhibits its highest emission intensity at 425 nm upon excitation at a wavelength of 315 nm [322]. With increased irradiation time, the PL emission intensity increases proportionately. This suggests an increase in the concentration of the photogenerated hydroxyl radicals in the catalyst-dispersed solution.

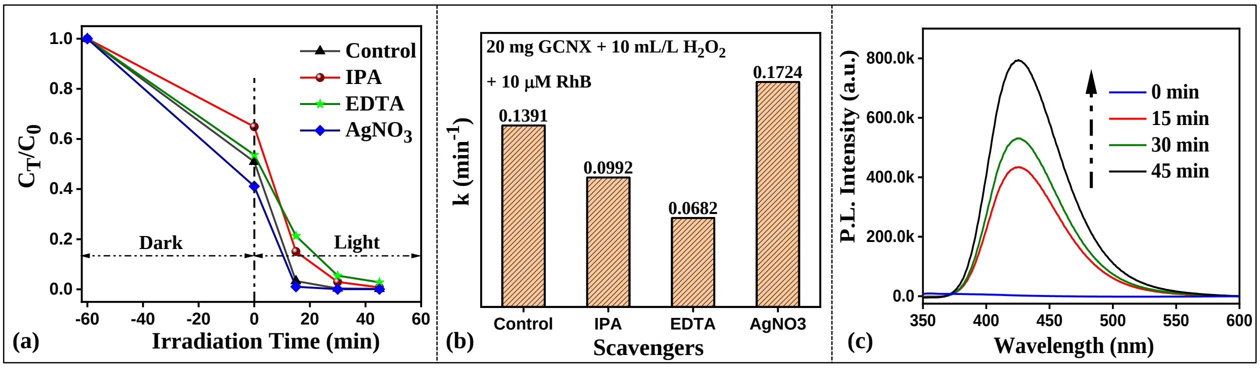

Fig. 6.49: *(a) C_T/C_0 plots in presence of different radical scavengers, (b) bar graphs showing the rate constant values, (c) P.L. emission spectra after addition of TA to detect •OH radicals*

Table 6.5 shows the values of slope and adj. R^2 obtained from the linearized and non-linearized fits of the pseudo-first-order reaction model for RhB dye degradation in the presence of different catalytic conditions. **Fig. 6.50(a-d)** shows the pseudo-first order non-linear exponential fitting and linearized fitting of RhB dye degradation by GCNB in absence and presence of H_2O_2. **Fig. 6.51(a-d)** shows similar plots for RhB dye degradation by GCNX in absence and presence of H_2O_2.

Table 6.5. Values of slope and adj. R^2 obtained from linearized and non-linearized fits of the pseudo-first-order reaction model for RhB dye degradation:

Catalytic Conditions	**Non-Linearly Fitted Data**		**Linearly Fitted Data**	
	Slope (k) (min^{-1})	**Adj. R^2**	**Slope (k) (min^{-1})**	**Adj. R^2**
10 mg GCNX + 10 mL/L H_2O_2 + 10 μM RhB	0.13113 ± 0.01436	0.9955	0.08523 ± 0.00942	0.95285
20 mg GCNX + 10 mL/L H_2O_2 + 10 μM RhB	0.18171 ± 0.00267	0.99997	0.13919 ± 0.01325	0.96471
30 mg GCNX + 10 mL/L H_2O_2 + 10 μM RhB	0.21082 ± 0.00352	0.99998	0.15576 ± 0.01244	0.97495
40 mg GCNX + 10 mL/L H_2O_2 + 10 μM RhB	0.22186 ± 0.00615	0.99996	0.1601 ± 0.01077	0.98213
20 mg GCNX + No H_2O_2 + 10 μM RhB	0.07092 ± 0.00392	0.99668	0.07741 ± 0.00233	0.99638
20 mg GCNX + 0.1	0.07571 ± 0.00412	0.99706	0.08028 ± 0.00351	0.9924

mL/L H_2O_2 + 10 µM RhB				
20 mg GCNX + 1 mL/L H_2O_2 + 10 µM RhB	0.09476 ± 0.00295	0.99933	0.0962 ± 0.0042	0.99243
20 mg GCNX + 5 mL/L H_2O_2 + 10 µM RhB	0.13209 ± 0.00222	0.9999	0.11438 ± 0.00971	0.97177
20 mg GCNX + 15 mL/L H_2O_2 + 10 µM RhB	0.25011 ± 0.0078	0.99997	0.15565 ± 0.01899	0.943
20 mg GCNX + 20 mL/L H_2O_2 + 10 µM RhB	0.21235 ± 0.00712	0.99992	0.13961 ± 0.01531	0.95359
20 mg GCNX + 10 mL/L H_2O_2 + 20 µM RhB	0.1375 ± 0.0018	0.99995	0.13769 ± 0.00553	0.99359
20 mg GCNX + 10 mL/L H_2O_2 + 30 µM RhB	0.05577 ± 0.00812	0.97145	0.0888 ± 0.01152	0.93604
20 mg GCNX + 10 mL/L H_2O_2 + 40 µM RhB	0.04481 ± 0.00401	0.98481	0.05562 ± 0.00597	0.95548
20 mg GCNB + No H_2O_2 + 10 µM RhB	0.01919 ± 0.0007	0.99427	0.01954 ± 0.0004	0.99747
20 mg GCNB + 10 mL/L H_2O_2 + 10 µM RhB	0.06247 ± 0.00198	0.99867	0.06962 ± 0.00379	0.98825
20 mg GCNX + 10 mL/L H_2O_2 + 10 µM RhB @pH 2	0.27736 ± 0.00325	1	0.18339 ± 0.02472	0.93108
20 mg GCNX + 10 mL/L H_2O_2 + 10 µM RhB @pH 11.5	0.0548 ± 0.01101	0.92076	0.04101 ± 0.00639	0.90956
20 mg GCNX + 10 mL/L H_2O_2 + 20 µM RhB + 0.5 g/L NaCl	0.06818 ± 0.00855	0.98317	0.1020 ± 0.00842	0.97331
20 mg GCNX + 10 mL/L H_2O_2 + 20 µM RhB + 0.5 g/L NaBr	0.08301 ± 0.00472	0.99727	0.1104 ± 0.00763	0.98114
20 mg GCNX + 10 mL/L H_2O_2 + 20 µM RhB + 0.5 g/L Na_2SO_4	0.07932 ± 0.00697	0.99313	0.1031 ± 0.00503	0.99055
20 mg GCNX + 10 mL/L H_2O_2 + 20 µM RhB + 0.5 g/L Na_2CO_3	0.02961 ± 0.00337	0.96338	0.03389 ± 0.00382	0.95114
20 mg GCNX + 10 mL/L H_2O_2 + 20 µM RhB + 0.5 g/L $NaHCO_3$	0.02847 ± 0.0032	0.96498	0.03234 ± 0.00291	0.96835
20 mg GCNX + 10 mL/L H_2O_2 + 20 µM RhB + 0.5 g/L $NaNO_3$	0.11805 ± 0.00449	0.99935	0.14357 ± 0.00575	0.99361
20 mg GCNX + 10	0.07431 ± 0.00709	0.99114	0.10162 ± 0.00628	0.98489

mL/L H_2O_2 + 20 μM RhB + 0.5 g/L $CaCl_2$				
20 mg GCNX + 10 mL/L H_2O_2 + 20 μM RhB + 0.5 g/L $MgCl_2$	0.07249 ± 0.0074	0.98954	0.10091 ± 0.00669	0.98264
20 mg GCNX + 10 mL/L H_2O_2 + 10 μM RhB + IPA	0.09816 ± 0.00112	0.99992	0.09926 ± 0.00126	0.99936
20 mg GCNX + 10 mL/L H_2O_2 + 10 μM RhB + EDTA	0.06615 ± 0.00353	0.99654	0.06829 ± 0.00296	0.99251
20 mg GCNX + 10 mL/L H_2O_2 + 10 μM RhB + $AgNO_3$	0.24492 ± 0.0026	1	0.17247 ± 0.02191	0.93845

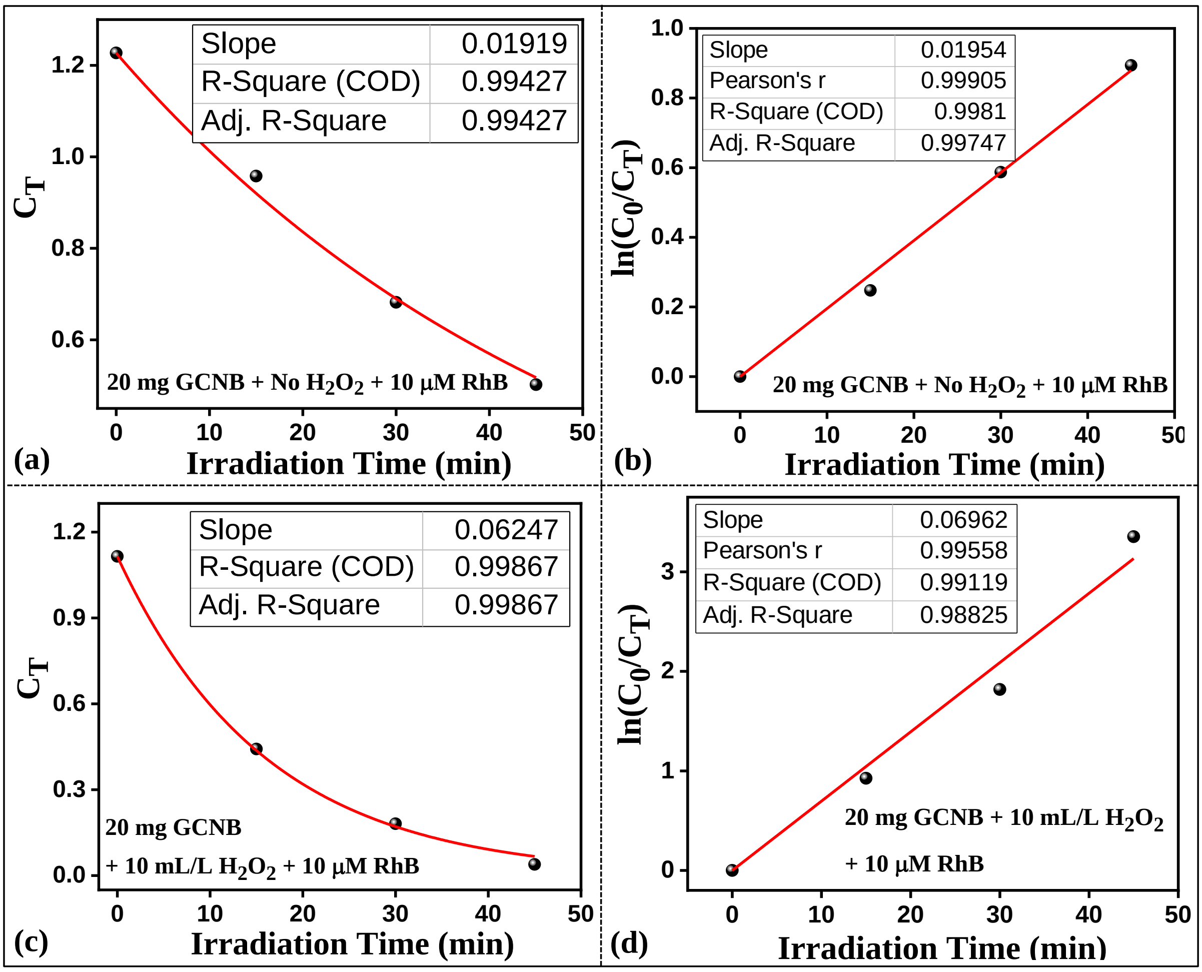

Fig. 6.50: *Pseudo-first order (a,c) non-linear exponential fitting, and (b,d) linearized fitting of RhB dye degradation by GCNB catalyst in presence and absence of* H_2O_2*.*

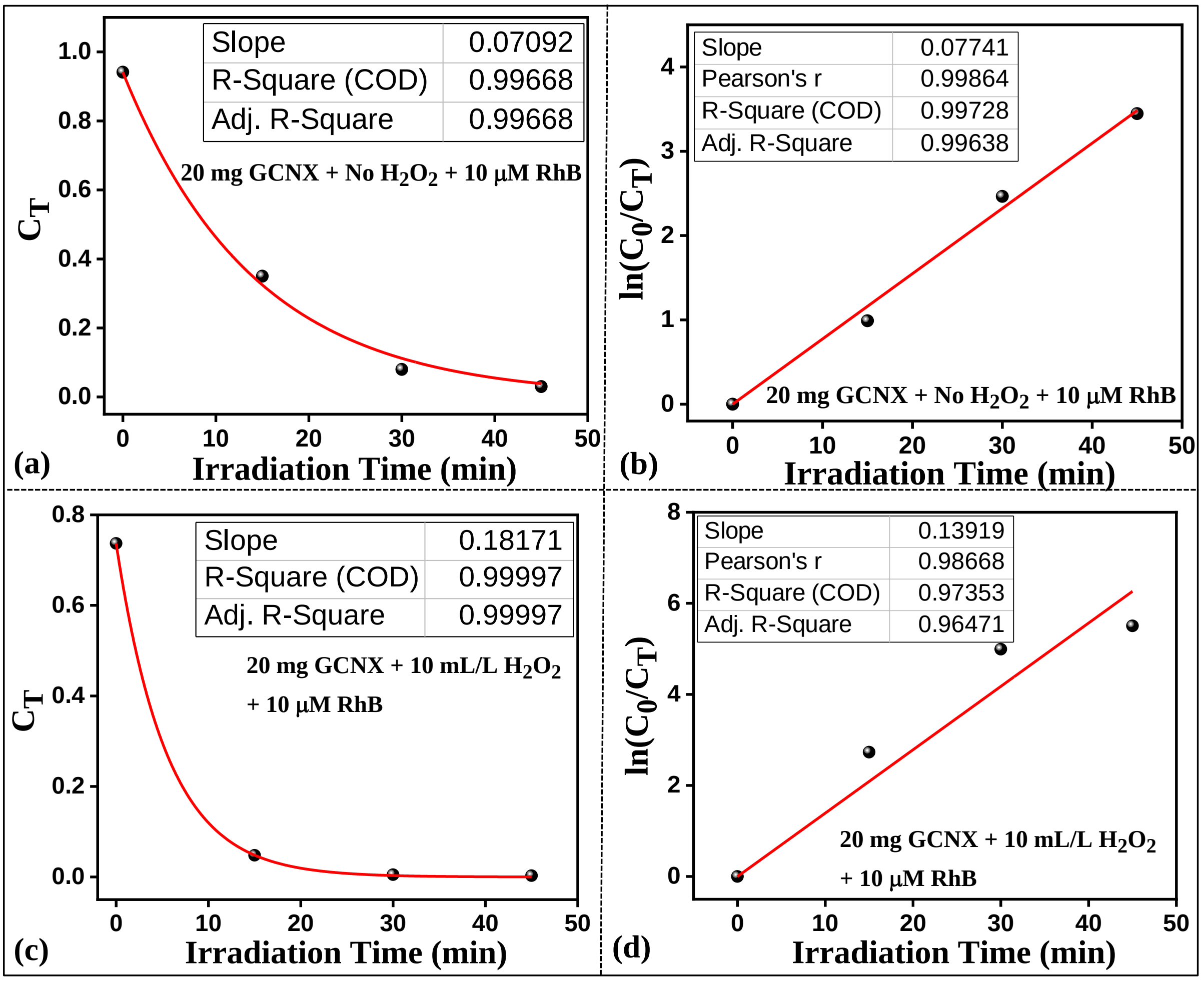

(a)

Slope	0.07092
R-Square (COD)	0.99668
Adj. R-Square	0.99668

(b)

Slope	0.07741
Pearson's r	0.99864
R-Square (COD)	0.99728
Adj. R-Square	0.99638

(c)

Slope	0.18171
R-Square (COD)	0.99997
Adj. R-Square	0.99997

(d)

Slope	0.13919
Pearson's r	0.98668
R-Square (COD)	0.97353
Adj. R-Square	0.96471

Fig. 6.51: *Pseudo-first order (a,c) non-linear exponential fitting, and (b,d) linearized fitting of RhB dye degradation by GCNX catalyst in presence and absence of* H_2O_2.

6.5.2. Photocatalytic reduction of hexavalent chromium (Cr(VI)):

The GCNX photocatalyst has been further utilised for effectively reducing Cr(VI) to Cr(III) in an aqueous solution in the presence of FA. The reduction efficiency has been calculated following equation (5.10), given in chapter 5, section 5.3.2.3. The aqueous solution of Cr(VI) shows a maximum absorption intensity at 350 nm, and the corresponding spectra of 0.8 mg/mL Cr(VI) in the presence of 20 mg of GCNX and 0.8 mL of FA under visible light illumination are shown in **Fig. 6.52(a)**. FA alone cannot reduce Cr(VI) to Cr(III) in the absence of any catalyst material (**Fig. 6.53(a)**). Moreover, when FA is not added to the system, pristine GCNX does not exhibit any sign of catalytic activity in reducing Cr(VI) (**Fig. 6.53(b)**). The presence of both factors leads to the complete reduction of Cr(VI) to Cr(III) within 120 min. The corresponding C_T/C_0 plot and bar graph plot for reduction efficiency are given in **Fig. 6.52(b,c),** respectively, showing that 68.4% efficiency is achieved within 75 min by GCNX. The digital image in **Fig. 6.53(c)** shows the decolouration of Cr(VI) with time.

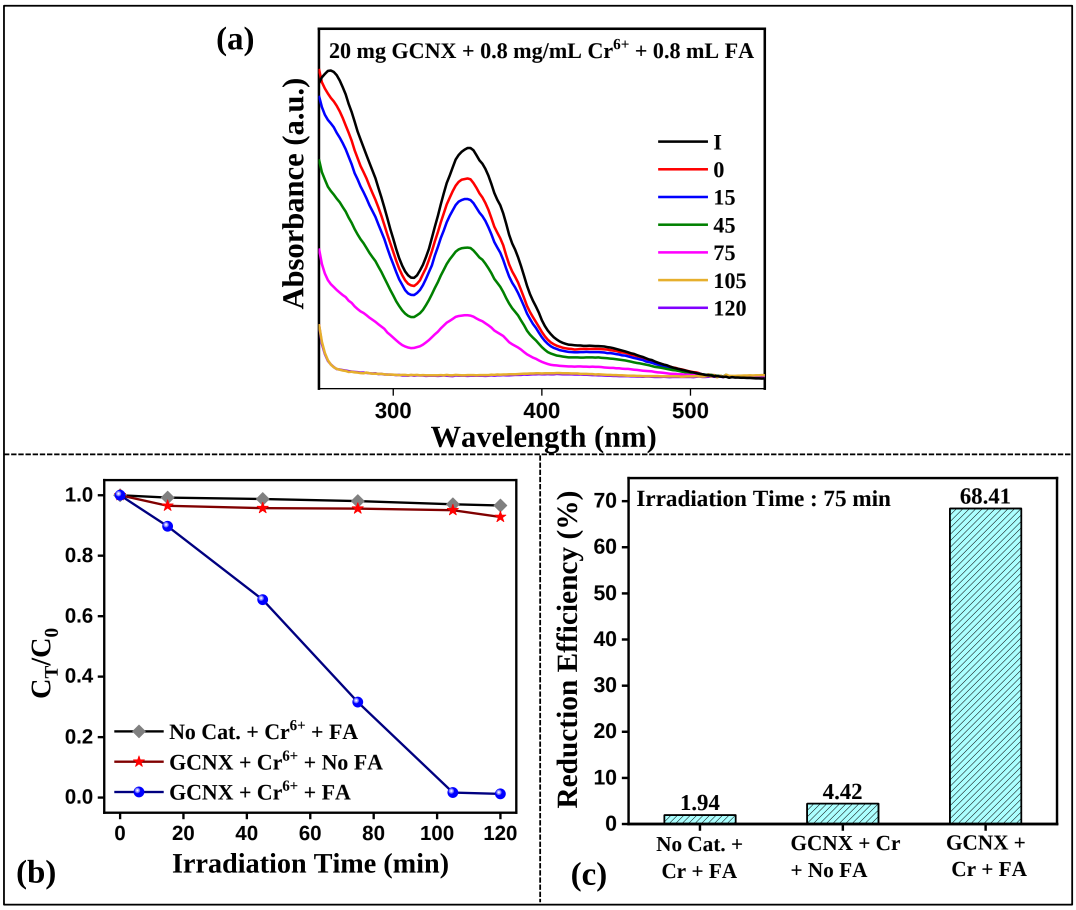

***Fig. 6.52**: (a) Absorbance spectra of Cr(VI) in presence of GCNX and FA, (b) C_T/C_0 plots for different catalytic conditions, (c) bar graphs showing the reduction efficiency for different catalytic conditions*

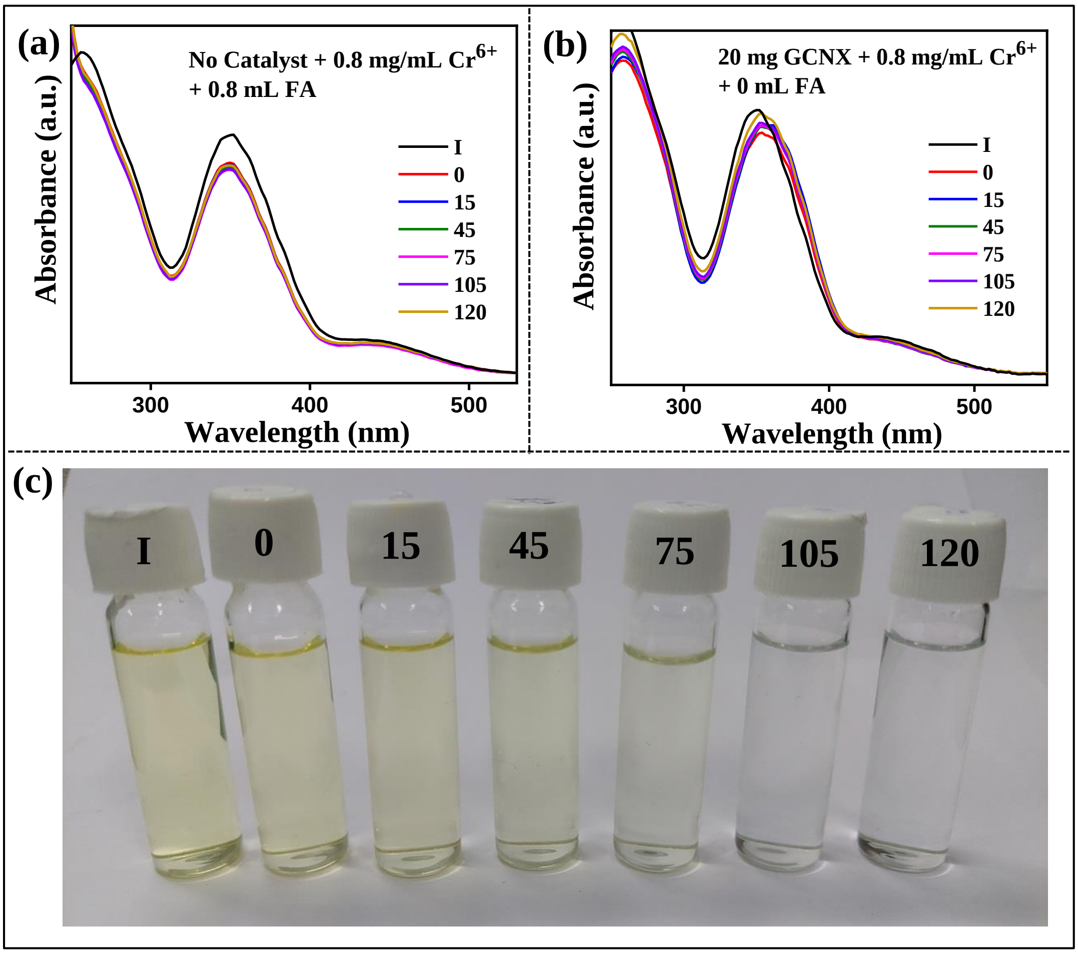

Fig. 6.53: *Absorbance spectra of 0.8 mg/mL Cr(VI) in presence of (a) 0.8 mL FA and in absence of catalyst, and (b) 20 mg GCNX and in absence of FA; (c) digital image showing the decolouration of Cr(VI) with time*

The effect of increasing the FA amount on the photocatalytic reduction of Cr(VI) has also been studied, and the corresponding C_T/C_0 plot and η% plots are shown in **Fig. 6.54(a,b)**. During the experiments, the GCNX amount was maintained at 20 mg, whereas Cr(VI) concentration was kept constant at 0.8 mg/mL. On increasing the FA amount, the catalytic reduction efficiency increases linearly; however, after a specific limit, the efficiency becomes saturated with no further improvement. FA, an electron donor, can capture the positively charged photogenerated h^+ from the valence band (VB) of the catalyst, preventing the recombination of charge carriers. Thus, a higher amount of negatively charged electrons is available to photo-degrade Cr(VI), and the efficiency of the process is enhanced. However, further increasing the amount of FA does not improve the efficiency. Excess FA can lead to the scavenging of larger amounts of holes, causing a lack of holes to conduct the reduction reactions. Cr(VI) exists in the solution in the forms of $Cr_2O_7^{2-}$, $HCrO_4^-$, and CrO_4^{2-}. Excess

FA can compete with these radicals to be adsorbed on the GCN. This also reduces the reduction efficiency of the catalyst [323].

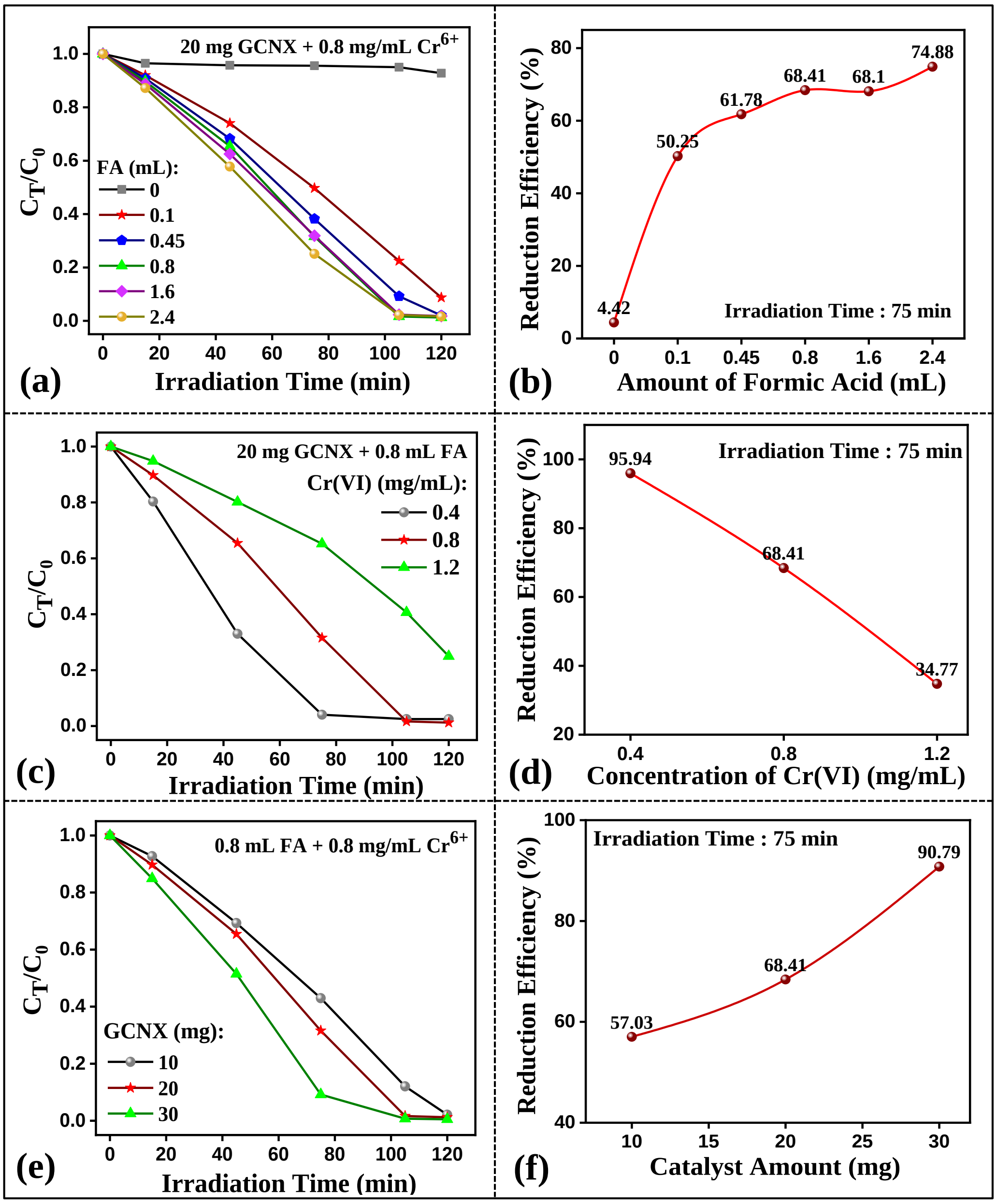

***Fig. 6.54**: C_T/C_0 plots for variation in (a) amount of FA, (c) concentration of Cr(VI), and (e) catalyst amount; reduction efficiency plots for variation in (b) amount of FA, (d) concentration of Cr(VI), and (f) catalyst amount*

The effect of the initial Cr(VI) concentration on the reduction efficiency has been studied further by varying the Cr(VI) concentration between 0.4, 0.8, and 1.2 mg/mL and keeping the catalyst and FA constant at 20 mg and 0.8 mL, respectively. The C_T/C_0 and η% plots are shown in **Fig. 6.54(c,d),** respectively. As observed from the plots, for 0.4 mg/mL Cr(VI) concentration, the complete reduction is achieved within 75 min of visible light irradiation with a reduction efficiency of 95.94%. On increasing the concentration, a significant decrease in efficiency (34.77%) is observed. The most plausible explanation is that a higher concentration of Cr(VI) blocks the active sites on the catalyst surface and hinders the GCN catalyst with screening or shielding effects [324]. This, in turn, reduces the activity of FA and slows the Cr(VI) degradation..

Subsequently, the effect of the catalyst dosage on the reduction of Cr(VI) has been studied by keeping the initial concentration of Cr(VI) and volume of FA fixed at 0.8 mg/mL and 0.8 mL, respectively, and varying the GCNX between 10, 20, and 30 mg. The C_T/C_0 and η% plots are shown in **Fig. 6.54(e,f),** respectively. The photocatalytic rate increases with increased catalyst dosage, and 90.79% efficiency is achieved within 75 min of light illumination for 30 mg of catalyst. With an increased amount of catalyst, the total number of photocatalytic active sites on the catalyst surface increases, increasing the number of electrons contributing to the photo-assisted reduction of Cr(VI).

The photocatalytic reduction efficiency depends significantly on the pH of the catalytic solution, and its effect has been studied by varying the pH between 2, 5, 6.5, 9, and 11.5. The absorbance spectra are shown in **Fig. 6.55(a-d)**. The best catalytic activity is observed at an acidic pH value (98.35% reduction efficiency achieved in 105 min). As the pH of the solution increases, the reduction rate of Cr(VI) by GCNX reduces drastically. No catalytic activity is observed at basic pH values, as seen in the C_T/C_0 and η% plots in **Fig. 6.55(e,f)**. The dominant species of chromium(VI) that can exist in aqueous solution are $HCrO_4^-$, $Cr_2O_7^{2-}$, and CrO_4^{2-} [325]. $HCrO_4^-$ is the most reactive form of Cr(VI), which is generated at an acidic pH, preferably < 3. Lower pH values also provide a thermodynamically feasible condition for reducing Cr(VI) to Cr(III). At neutral pH, the dominant Cr(VI) species is $Cr_2O_7^{2-}$, which is less reactive than $HCrO_4^-$. Thus catalytic efficiency starts to drop at neutral pH. The absorbance spectra of Cr(VI) for the basic pH values 9 and 11.5 (**Fig. 6.55(c,d)**) show that there are two peaks at 273 and 372 nm. These peaks occur due to the generation of the least reactive species of Cr(VI), i.e., CrO_4^{2-}. Alkaline media can also cause the precipitation of Cr(III) ions in the form of $Cr(OH)_3$ on the surface of the photocatalyst, thereby hindering its catalytic ability. Adding FA provides a suitable pH environment (pH = 2) to efficiently carry out the photo-reduction of Cr(VI) by generating the highly active species $HCrO_4^-$.

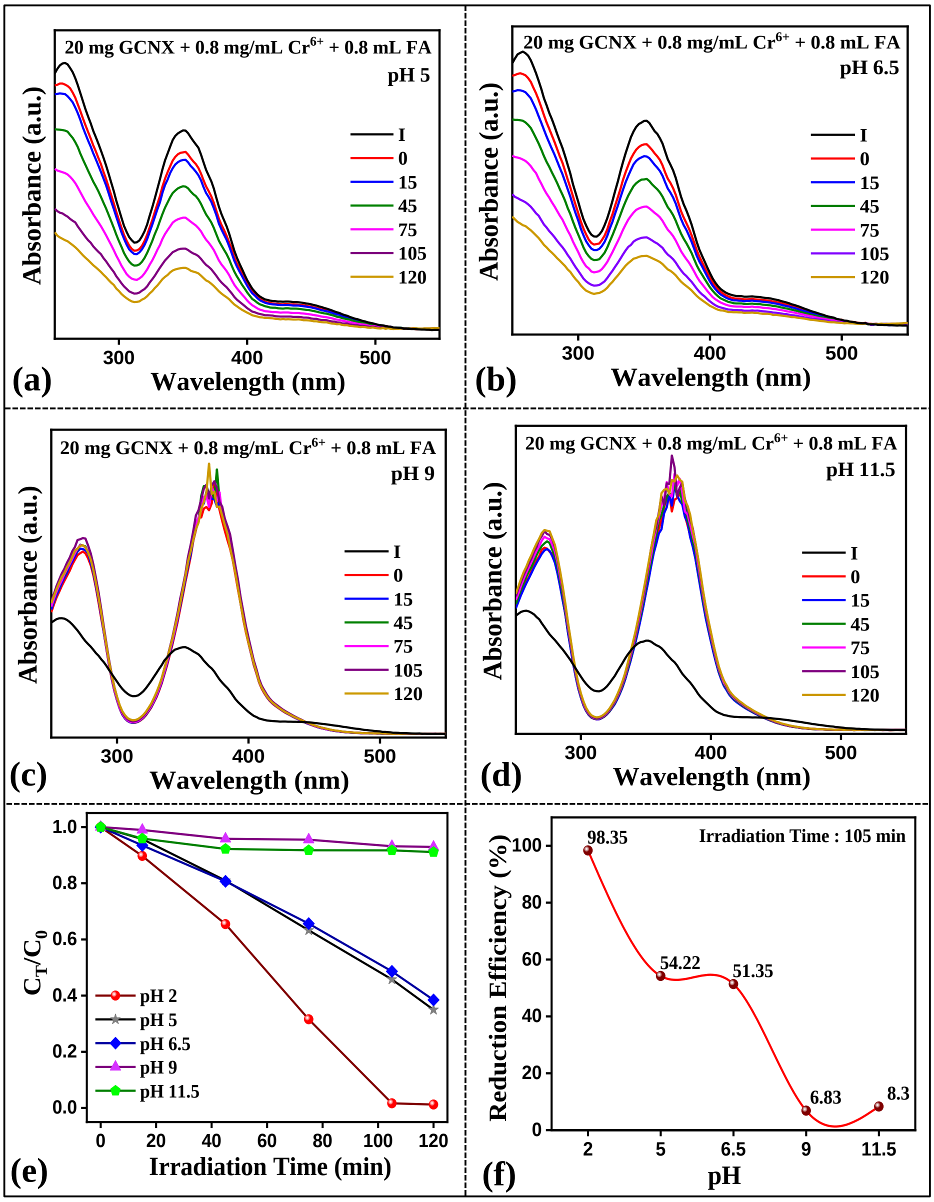

Fig. 6.55: *Absorbance spectra of 0.8 mg/mL Cr(VI) in presence of 20 mg of GCNX and 0.8 mL FA at pH values (a) 5, (b) 6.5, (c) 9, and (d) 11.5; (e) C_T/C_0 plots of Cr(VI) reduction by GCNX in different pH conditions and (f) reduction efficiency plots for different pH values*

Organic acids are considered hole scavengers and reducing agents in photocatalytic reactions and often exist in aquatic environments. The effect of adding different organic acids, such as citric acid (CA), oxalic acid (OA), and EDTA, has also been investigated. CA and OA contain small molecular weight carboxylate functional groups containing acids; the only difference is the number of α-hydroxyl groups. The C_T/C_0 and η% plots are shown in **Fig. 6.56(a,b)**. The best reduction efficiency is achieved in the presence of OA (98.53%), followed by CA (83.44%) and FA (77.53%) upon irradiation of the catalytic system up to 105 min. Like FA, CA, and OA can also scavenge the photogenerated holes, increasing the availability of electrons for the photocatalyst. This promotes the efficient reduction of Cr(VI) by capturing electrons [326]. However, the reduction of Cr(VI) is severely affected negatively in the presence of EDTA. This could be due to the intervention of the adsorbed EDTA molecules on Cr(VI) ions accessing the GCNX surface [326]. **Fig. 6.56(c,d)** show the C_T/C_0 and η% plots for Cr(VI) reduction in varying amounts of OA. With an increased concentration of OA in the catalytic solution, the reduction efficiency increases proportionately. Within 105 min, 98.53% efficiency is achieved in the presence of 0.1 g of OA. However, OA can reduce Cr(VI) to Cr(III) to some extent without any catalyst.

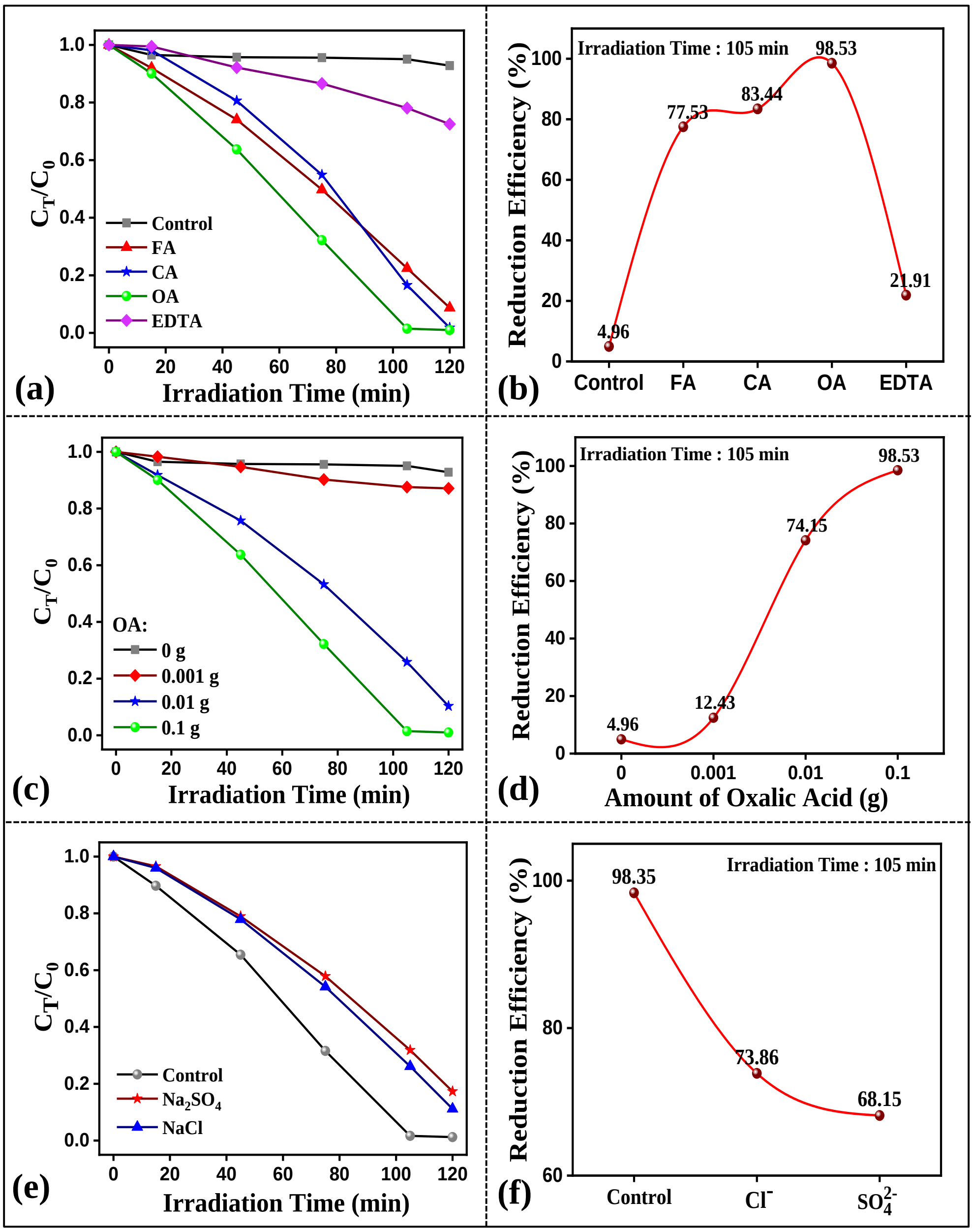

***Fig. 6.56**: C_T/C_0 plots of Cr(VI) reduction by GCNX in presence of (a) different organic acids, (c) different amount of OA, and (e) different inorganic anions; reduction efficiency plots in presence of (b) different organic acids, (d) different amount of OA, and (f) different inorganic anions*

The effect of some dissolved inorganic species like Cl^{-} and SO_4^{2-} in the photocatalytic solution on the Cr(VI) reduction by GCNX and FA have been analysed. The associated C_T/C_0 and reduction efficiency plots are shown in **Fig. 6.56(e,f)**. The presence of these ions significantly hampers the catalytic activity due to the competition between the anions and Cr(VI) ions for the active catalytic sites on the GCNX surface. Cl^{-} and SO_4^{2-} are more rapidly adsorbed than Cr(VI) on GCNX, forming a film on its surface that restricts the Cr(VI) adsorption [327]. Additionally, these anions act as radical scavengers, reducing the catalytic activity [328].

6.5.3. Reusability and practical application of GCNX photocatalyst:

The as-synthesised GCNX sample proved to be a durable photocatalyst material because it can be recycled for several catalytic cycles of degrading both RhB and Cr(VI). In this work, a sample has been reused up to four times for RhB degradation and up to three times for Cr(VI) reduction. From the bar diagram shown in **Fig. 6.57(a)** and the $\ln(C_0/C_T)$ plot shown in **Fig. 6.57(b)**, the removal efficiency values after each catalytic cycle for RhB degradation slightly decrease from the preceding cycle due to the loss of active catalytic sites with each repeated cycle. The loss of sample after each cycle is another plausible reason. Similarly, for Cr(VI) reduction, the catalytic efficiency decreases after three cycles, as observed from the bar graph plot and C_T/C_0 plot shown in **Fig. 6.57(c,d)**.

The XRD spectra of GCNX taken after RhB catalysis and Cr(VI) reduction are shown in **Fig. 6.57(e)**. Compared with the XRD spectra of GCNX taken before catalytic activity, the phase of the photocatalyst has been retained after its catalytic performance, and there are no new peaks related to the pollutants. Moreover, the XPS spectra of GCNX after Cr(VI) reduction are provided in **Fig. 6.57(f)**. Besides the characteristic elements C, N, and O, a very minute amount (0.01%) of Cr is also detected in the sample. Upon magnifying the Cr2p3 spectra (shown in the inset of **Fig. 6.57(f)**), a single peak at 576.8 eV can be observed, which is assigned to Cr(III) [329]. This suggests that Cr(VI) is successfully reduced to Cr(III) in the presence of GCNX. Moreover, it also indicates that significantly less Cr(III) is deposited on the GCNX surface after catalysis, which does not prevent the reuse of the catalyst material [330]. Hence, the as-synthesised GCNX proved a stable catalyst for wastewater remediation.

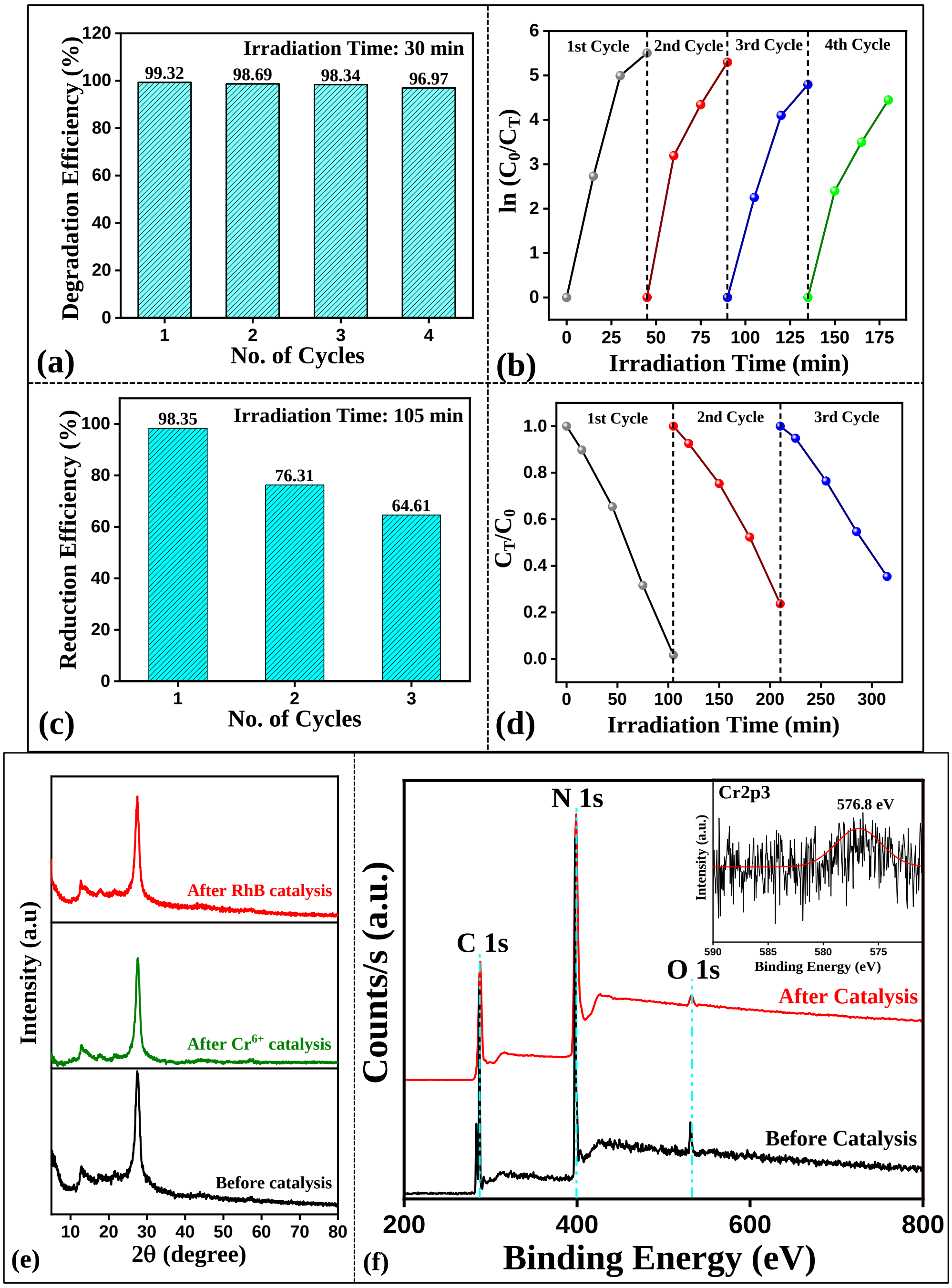

***Fig. 6.57**: Bar graphs showing the efficiency values of different catalytic cycles for (a) RhB degradation, and (c) Cr(VI) reduction; (b) ln(C_0/C_T) plots for different cycles of RhB degradation, and (d) C_T/C_0 plots for three repeated reduction cycles of Cr(VI,) (e) XRD plots of GCNX before catalysis and after RhB and Cr(VI) reduction; (f) XPS spectra of GCNX before and after Cr(VI) reduction, inset of (f): Cr2p3 spectra*

To evaluate the practicability of the GCNX catalyst in real-life wastewater treatment, GCNX has been utilised to degrade RhB and Cr(VI) in actual water samples collected from tap and river water [331-334]. Similar catalytic procedures for the photo-reduction of RhB and Cr(VI) have been performed in these water systems. The C_T/C_0 plots along with the bar graph of degradation efficiencies as obtained for RhB degradation in presence of real water samples are shown in **Fig. 6.58(a,b)**. Compared to de-ionised (DI) water, the catalytic efficiency is reduced slightly for the real-world water systems.

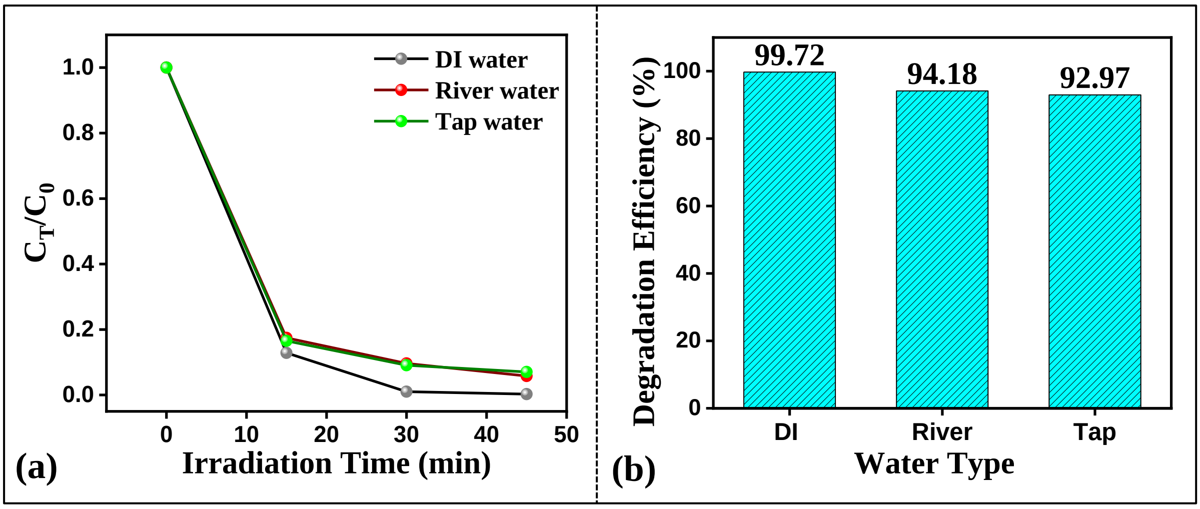

Fig. 6.58: (a) C_T/C_0 plots for RhB degradation in presence of different types of water environment, (b) bar graph showing the corresponding degradation efficiency in 45 min irradiation time

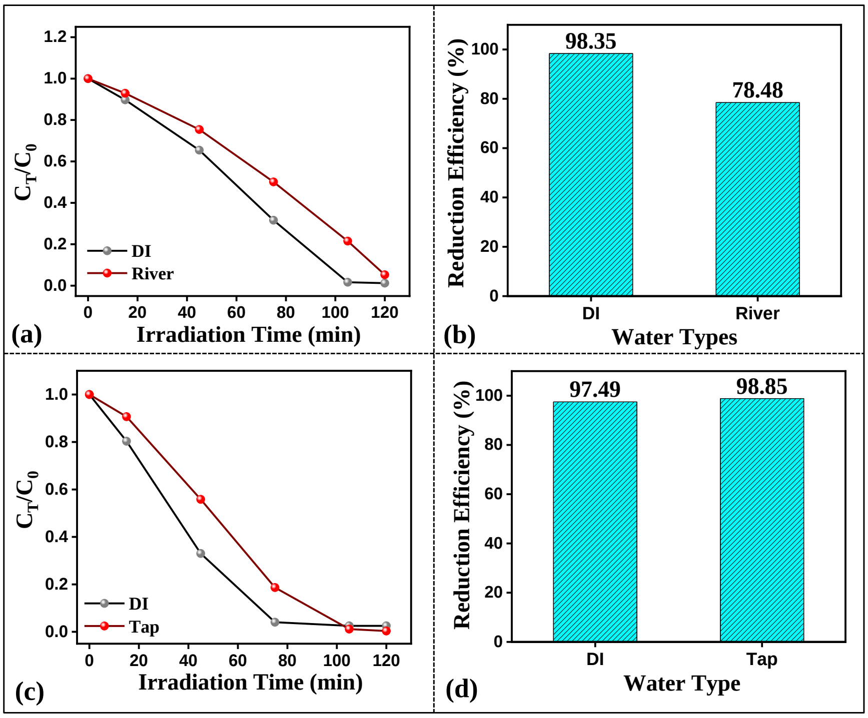

Fig. 6.59: C_T/C_0 plots for Cr(VI) reduction in presence of (a) river water, and (c) tap water; (b,d) bar graphs showing the respective reduction efficiencies in 105 min irradiation time

For reduction of Cr(VI), the C_T/C_0 plots and bar graphs depicting the removal efficiencies are shown in **Fig. 6.59(a,b)** and **Fig. 6.59(c,d)** for river and tap water, respectively. Similarly to RhB, the reduction efficiency is significantly hindered for the river water system. Natural water sources consist of various inorganic cations, anions, and natural and dissolved organic matter, which co-exist with hazardous pollutants [333]. The existence of these entities most likely results in the scavenging of photocatalytic active species along with blocking the reactive surface sites of the catalyst, limiting visible light absorption. However, the GCNX catalyst still exhibits impressive performance in the catalytic reduction of toxic pollutants in natural water samples with high removal efficiencies. The almost unchanged catalytic activity of GCNX in reducing toxic pollutants in such water samples further highlights its excellent prospects for applications in wastewater remediation.

6.5.4. Statistical evaluation of photocatalytic activity:

Unlike traditional optimisation methods, which do not take into account the effects of the combination of catalytic parameters, RSM is a combined mathematical and statistical technique that has been used extensively to determine the optimal catalytic condition by analysing the effects of parameters and the strong interactions between different parameters [249]. RSM is explicitly used when various factors intervene in the catalytic optimisation process. Box–Behnken Design (BBD) is one of the most used RSM designs, which is convenient for fitting quadratic surfaces and well-suited to evaluate the optimisation process [250]. The detailed modelling techniques and associated equations have been provided in section 5.3.2.4. of chapter 5.

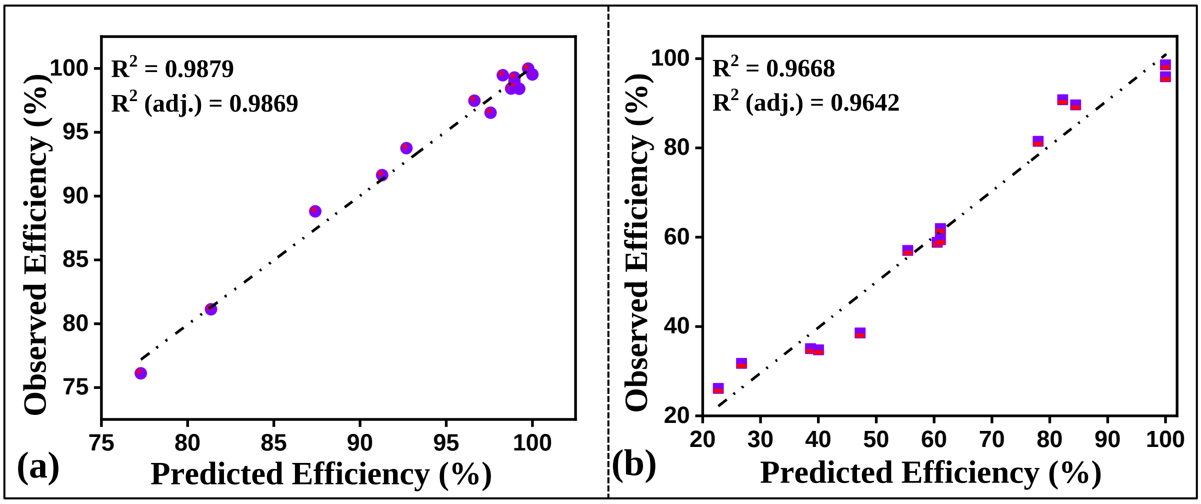

***Fig. 6.60**: Observed efficiency vs. predicted efficiency plots for (a) RhB and (b) Cr(VI) reduction*

Fig. 6.60(a,b) depict the observed efficiency vs. predicted efficiency plots for RhB and Cr(VI) reduction. Both plots are linear, and the observed efficiency matches the predicted efficiency values. For RhB degradation, the coefficient of determination (R^2) of the linear plot is 0.9879, and the adjusted coefficient of determination (adj. R^2) equals 0.9869. Similarly, for Cr(VI) reduction, the R^2 and the adj. R^2 values are 0.9668 and 0.9642, respectively. Since the above values are close to 1, the BBD model is robust for present experimental results [335].

The interaction between the amount of catalyst and the H_2O_2 concentration on the decolourisation of RhB dye when the RhB concentration is constant at 20 μM has been determined via the contour plot, as shown in **Fig. 6.61(a)**. The associated surface plot of efficiency is shown in **Fig. 6.61(b)**. Nearly 100% degradation efficiency is achieved by simultaneously increasing the amount of catalyst and the concentration of H_2O_2. However, a slight decrease in efficiency is observed when the H_2O_2 concentration exceeds 15 mL/L. The region of best efficiency is shown in dark green and lies between a catalyst dosage of 20–30 mg and an H_2O_2 concentration of 7.5–15 mL/L.

The effect of the interaction between the catalyst amount and the RhB concentration on the degradation efficiency when the H_2O_2 concentration is constant at 10 mL/L is seen in the contour and surface plots shown in **Fig. 6.61(c,d)**. The degradation efficiency increases with simultaneously increased catalyst amount and RhB concentration. However, after the concentration of RhB rises above 24 μM, the efficiency starts to decrease, and a further increase in catalyst amount does not improve the efficiency. With less catalyst and high RhB concentration, the efficiency is poor. The region of maximum efficiency lies between a catalyst dosage of 18–27.5 mg and a RhB concentration of 10–24 μM. The available active radicals generated in the catalytic system are insufficient to fully degrade high concentration of RhB pollutant, leading to a decreased degradation rate, which has also been observed experimentally.

Finally, the effect of the interaction between the concentrations of H_2O_2 and RhB on the degradation efficiency has been studied by keeping the amount of catalyst constant at 20 mg. **Fig. 6.61(e,f)** shows the corresponding contour and surface plots. High efficiency is achieved when the H_2O_2 concentration is high, and the RhB concentration is low. With increased RhB concentration, the degradation efficiency decreases rapidly. The region of maximum efficiency is between an H_2O_2 concentration of 7–15 mL/L and an RhB concentration of 10–22 μM. As determined from the Minitab software, the optimal catalytic condition to achieve 100% degradation efficiency is when the amount of catalyst is 23.13 mg, the H_2O_2 concentration is 15 mL/L, and the RhB concentration is 17.68 μM.

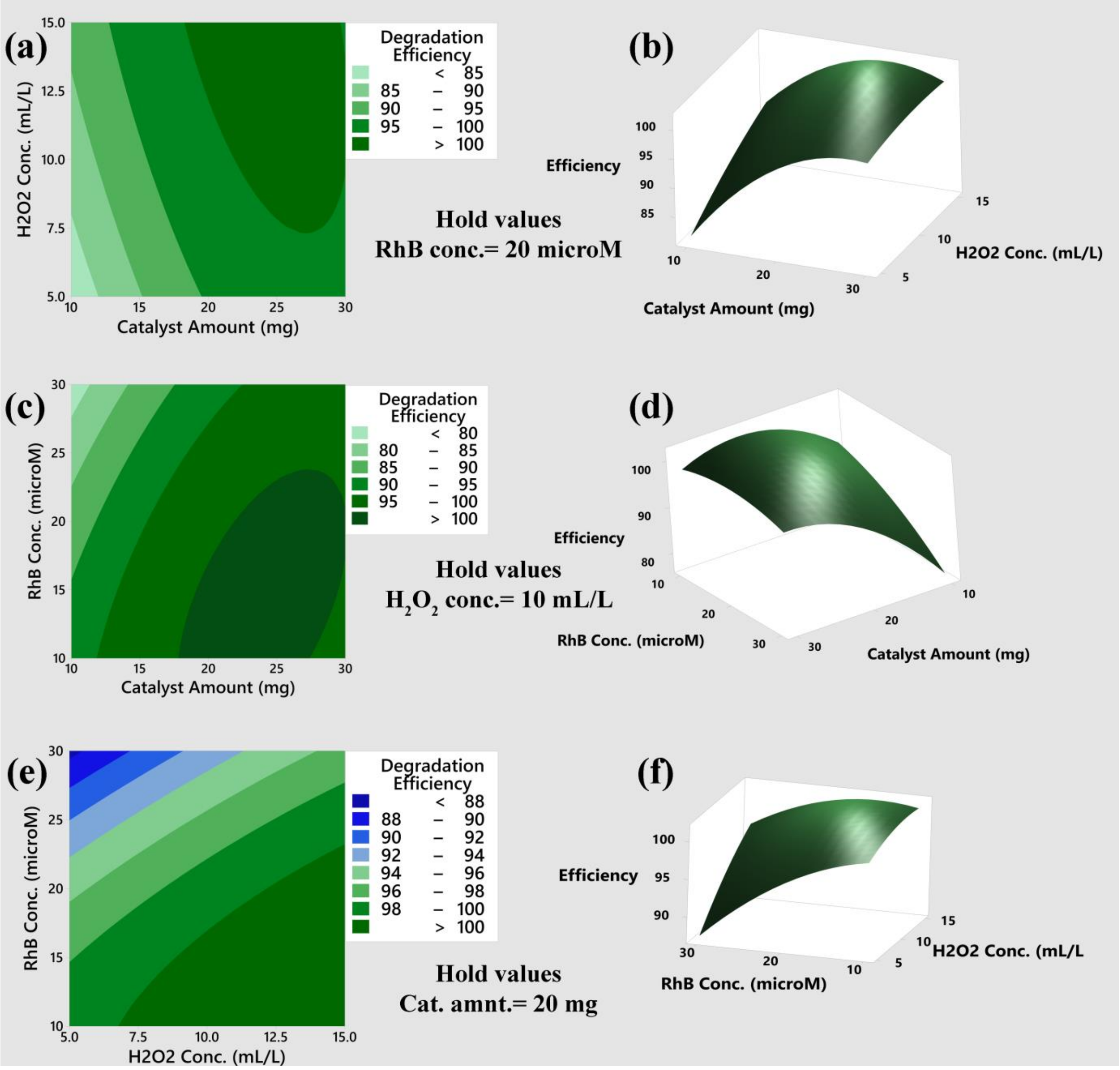

***Fig. 6.61**: Contour plots of efficiency (%) vs. (a) H_2O_2 concentration and catalyst amount, (c) RhB concentration and catalyst amount, and (e) RhB concentration and H_2O_2 concentration; surface plots of efficiency (%) vs. (b) H_2O_2 concentration and catalyst amount, (d) RhB concentration and catalyst amount, and (f) RhB concentration and H_2O_2 concentration*

For Cr(VI) reduction, the contour and surface plots are separately drawn for different catalytic parameters to understand the interactions between them. **Fig. 6.62(a,b)** show the contour and surface plots for catalyst amount vs. FA amount when the Cr(VI) concentration is fixed at 0.8 mg/mL. The degradation efficiency increases proportionately when the amounts of GCNX and FA are simultaneously increased. The maximum efficiency is achieved near the highest values, at 30 mg of catalyst and 0.8 mL of FA.

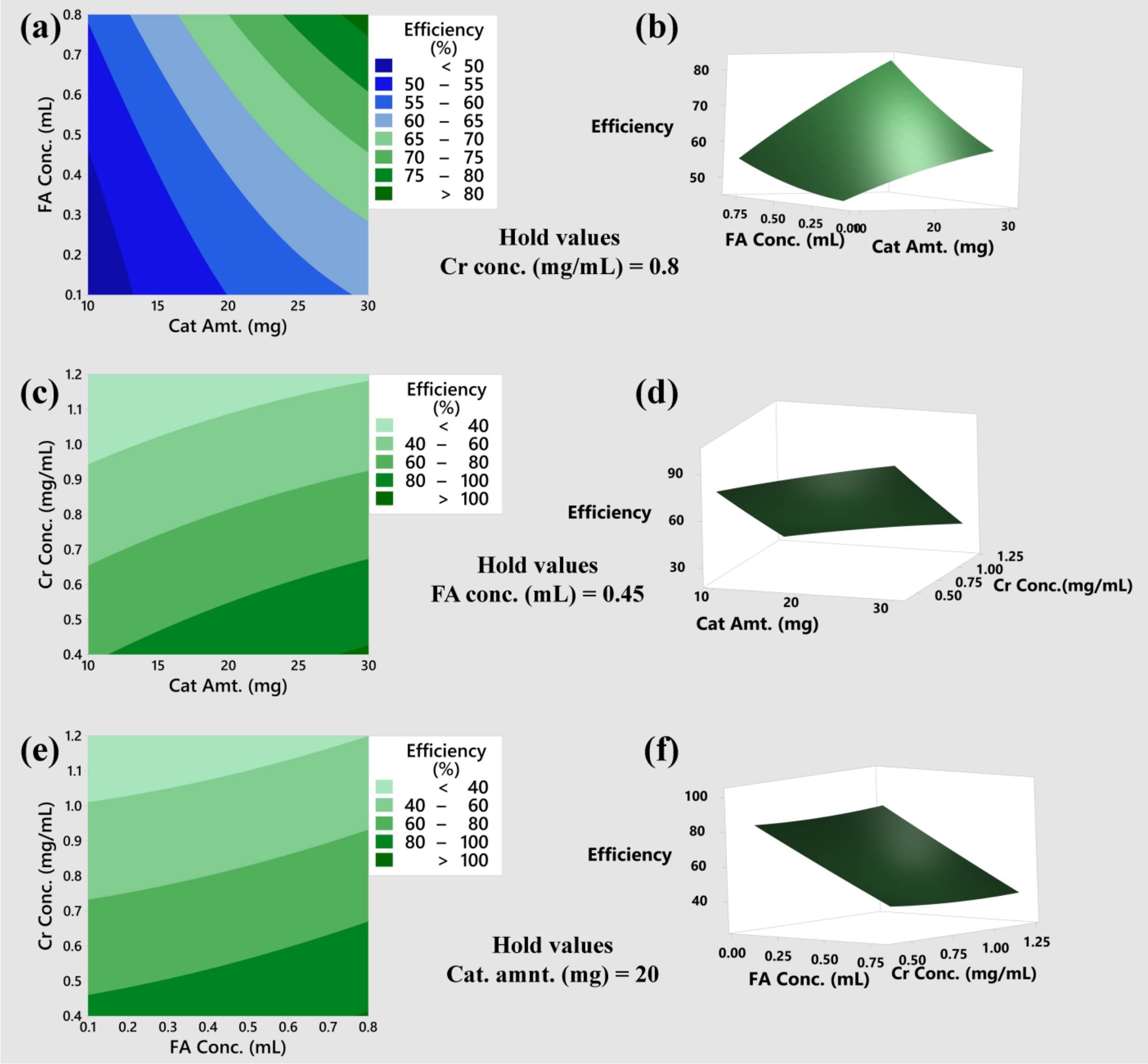

***Fig. 6.62**: Contour plot of efficiency (%) vs. (a) FA and catalyst amount, (c) Cr(VI) concentration and catalyst amount, and (e) Cr(VI) concentration and FA amount; surface plot of efficiency (%) vs. (b) FA and catalyst amount, (d) Cr(VI) concentration and catalyst amount, and (f) Cr(VI) concentration and FA amount*

Furthermore, the effect of the interaction between the amount of catalyst and Cr(VI) concentration on reduction efficiency has been studied by keeping the amount of FA fixed at 0.45 mL. The efficiency increases with increased catalyst amount and decreases with increased Cr(VI) concentration. The best catalytic activity is observed at nearly 30 mg of catalyst and a Cr(VI) concentration of 0.4 mg/mL. **Fig. 6.62(c,d)** shows the corresponding contour and surface plots.

Finally, the effect of the interaction between the FA and Cr(VI) concentrations on the efficiency has been studied by keeping the amount of catalyst fixed at 20 mg. From the contour and surface plots shown in **Fig. 6.62(e,f),** the catalytic activity increases with increased FA amount and decreases with decreased Cr(VI) concentration. The best catalytic efficiency occurs at 0.8 mL of FA and a Cr(VI) concentration of 0.4 mg/mL. As determined using the Minitab software, the optimal catalytic conditions are 30 mg of GCNX, 0.8 mL of FA, and 0.4 mg/mL of Cr(VI).

6.5.5. Plausible mechanism of GCN catalytic activity:

We further probed the activity of GCN in the reduction of RhB and Cr(VI) using first-principles calculations. The XPS data reveals the presence of C-N, C=O and C-OH bonds in the catalytic system. These bonds are most likely to be present due to the functionalisation and saturation of the dangling bonds at the edge of the GCN blocks by functional groups such as amine ($-NH_2$), carbonyl (-C=O) and hydroxyl (-OH). The theoretical calculations in this work are conducted for small quantum dots of GCN. The dangling bonds present at the edge of the quantum dots are saturated with these functional groups to reciprocate their presence in the synthesized GCN.

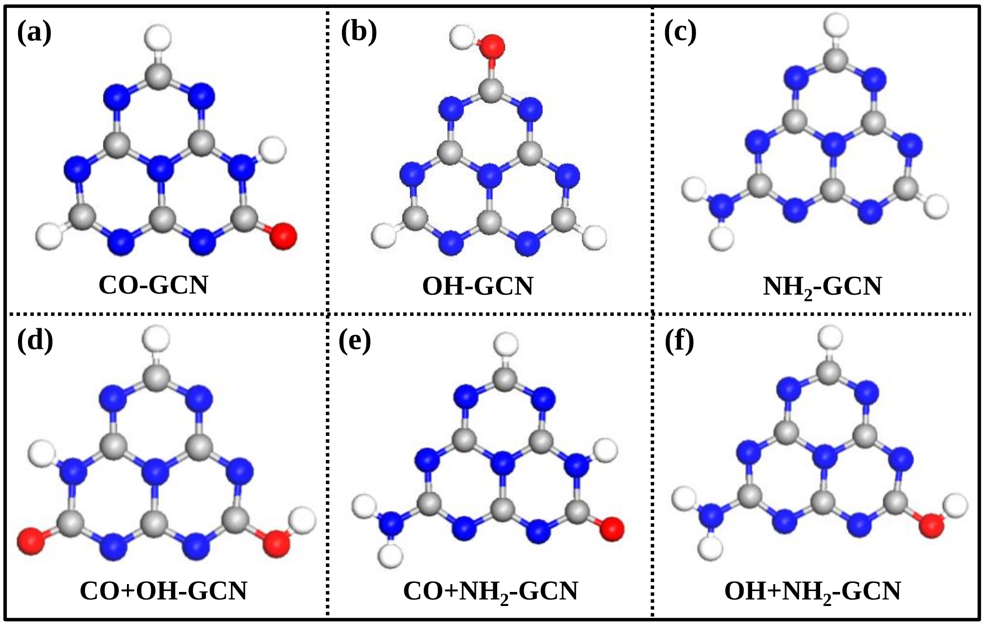

Fig. 6.63: *Optimised configurations of the edge-functionalised GCN quantum dots structures for six systems: (a) CO-GCN, (b) OH-GCN, (c)* NH_2*-GCN, (d) CO+OH-GCN, (e) CO+*NH_2*-GCN, and (f) OH+*NH_2*-GCN*

The optimised configurations of the edge-functionalised GCN quantum dot structures are shown in **Fig. 6.63(a-f)**. Six different systems are modelled: CO-GCN, OH-GCN, NH_2-GCN, CO+OH-GCN, CO+NH_2-GCN and OH+NH_2-GCN (**Fig. 6.63(a-f)**). All the edge-functionalised GCN configurations are found to be semiconducting with band gap values ranging from 2.24 to 2.57 eV. The total density of states (TDOS) of all the edge-functionalised GCNs is presented in **Fig. 6.64(a-f)**. All the systems are completely non-spin polarised in nature. When subject to illumination with proper wavelengths, the GCN systems produce photogenerated electrons (e^-) and holes (h^+) which reside momentarily in the CB and VB, respectively. For those photogenerated charge carriers to participate in the reduction of RhB or Cr(VI), the recombination of the e^-/h^+ pairs must be avoided by incorporating a suitable redox couple within the system that captures the photogenerated electrons and holes.

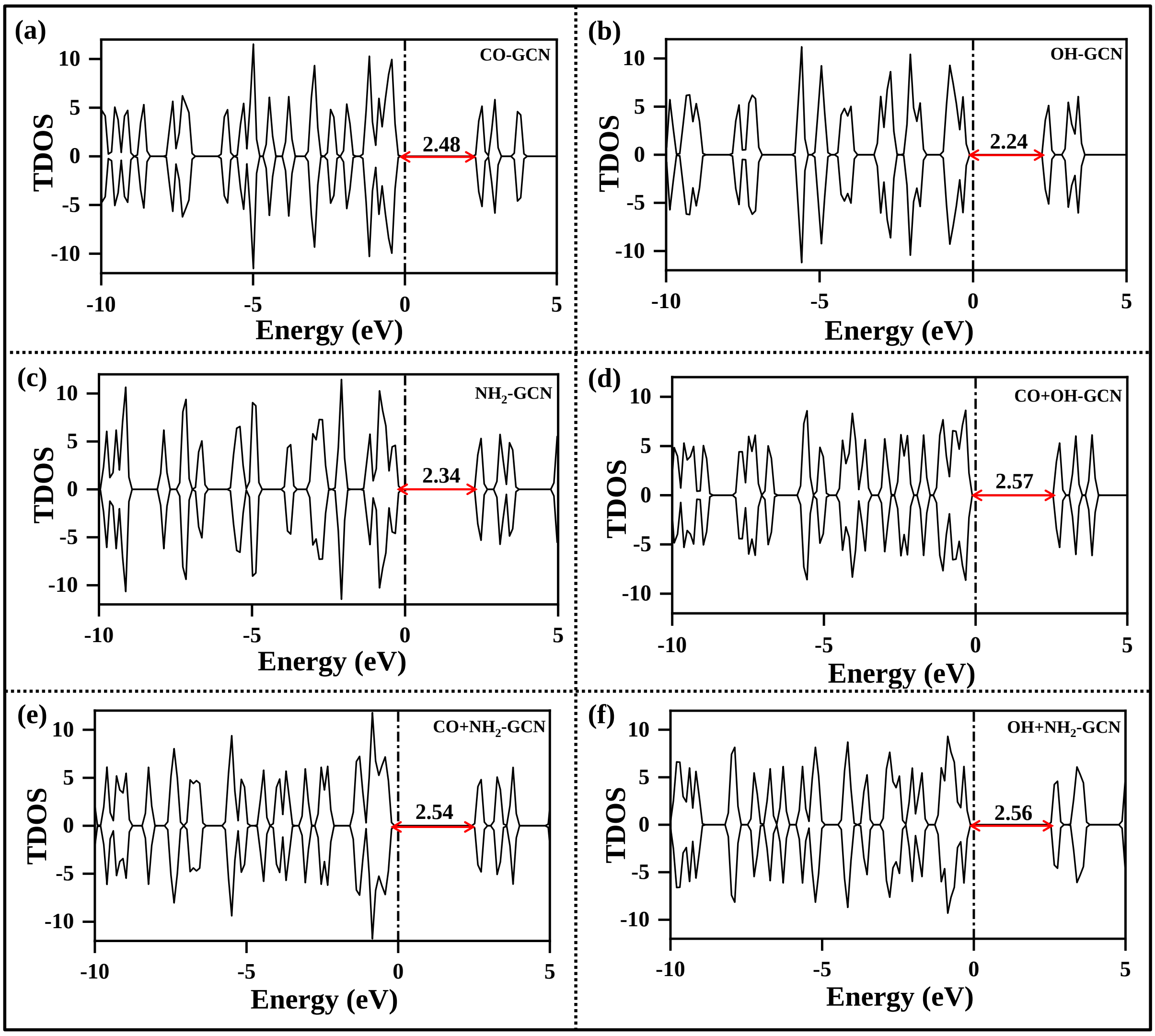

Fig. 6.64: *The total density of states (TDOS) of all the edge-functionalised GCN systems: (a) CO-GCN, (b) OH-GCN, (c) NH_2-GCN, (d) CO+OH-GCN, (e) CO+NH_2-GCN, and (f) OH+NH_2-GCN*

In the present study, H_2O_2, HCOOH and H_2O are expected to accept photogenerated electrons and holes to prevent their recombination through redox reactions, generating the products that are sought to reduce RhB and Cr(VI). Active •OH radicals reduce the RhB molecules in a photocatalytic reduction process. If the CB energy level of the semiconductor is more negative (in the normal hydrogen electrode (NHE) scale) than the reduction potential of •OH/H_2O_2 (+0.5 V vs. NHE), then the H_2O_2 molecules can capture the photogenerated electrons to produce •OH via the following reaction:

$$\boldsymbol{H_2O_2 + e_{CB}^- \rightarrow OH^- + \bullet OH} \qquad \text{……….} (6.8)$$

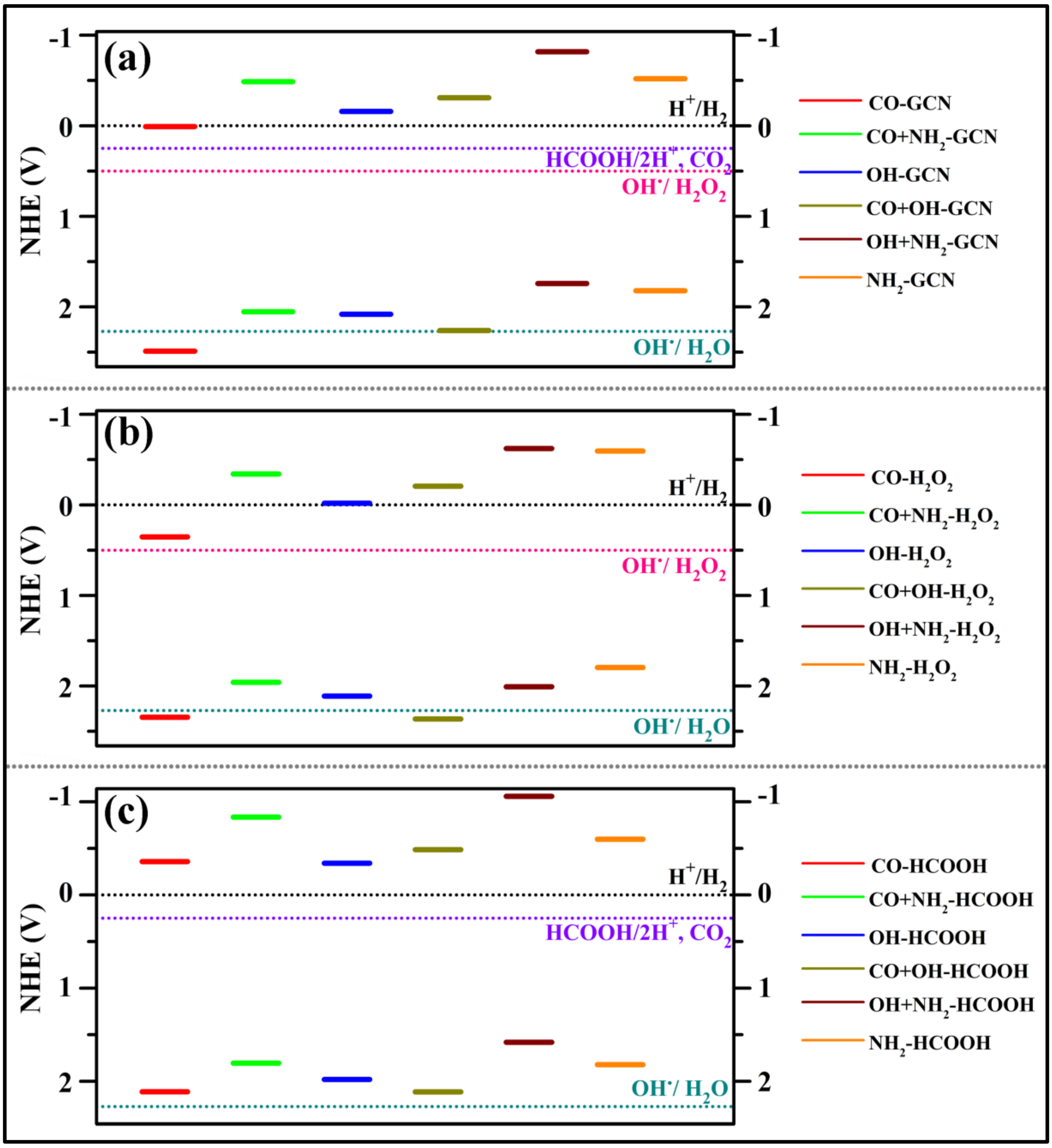

Fig. 6.65*: Band alignment diagrams of (a) edge-functionalised GCN systems, (b) adsorbed-H_2O_2 GCN systems, and (c) adsorbed-HCOOH GCN systems*

In contrast, H_2O can produce •OH radicals if the reduction potential of •OH/H_2O (+2.27 V vs. NHE) is less positive than the VB energy level of the semiconductor, following the reaction given below:

$$\boldsymbol{H_2O + h_{VB}^+ \rightarrow \bullet OH + H^+} \qquad \text{……….} (6.9)$$

As for the edge-functionalised GCN blocks considered in the present study, the conduction band minimum (CBM) is at a more negative value in the NHE scale with respect to the reduction potential of •OH/H_2O_2, as shown in **Fig. 6.65(a)**. The valence band maximum (VBM) is found to be located at higher values than the reduction potential of •OH/H_2O for all the edge-functionalised GCN systems except CO-GCN. Thus, for the GCN photocatalyst, H_2O_2 is expected to be the predominant source of •OH instead of the H_2O molecules by capturing the photogenerated electrons and preventing electron–hole recombination.

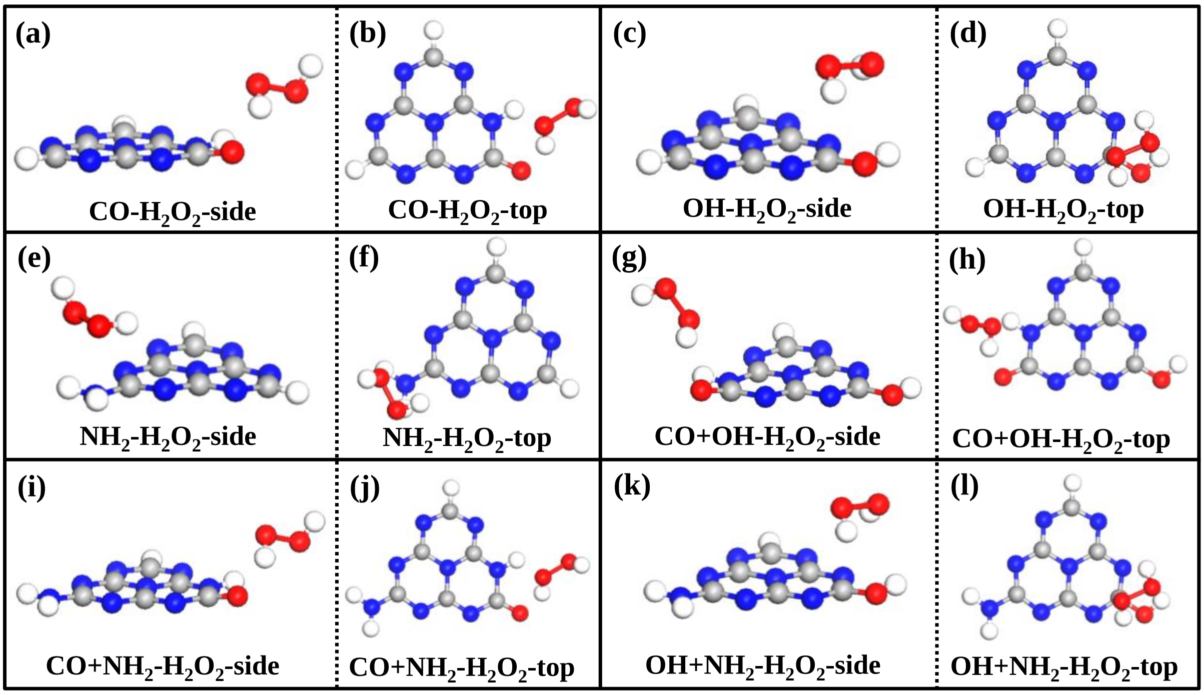

Fig. 6.66: *The optimised configurations of the H_2O_2 molecules adsorbed on the GCN blocks in both side and top views: (a) CO-H_2O_2-side, (b) CO-H_2O_2-top, (c) OH-H_2O_2-side, (d) OH-H_2O_2-top, (e) NH_2-H_2O_2-side, (f) NH_2-H_2O_2-top, (g) CO+OH-H_2O_2-side, (h) CO+OH-H_2O_2-top, (i) CO+NH_2-H_2O_2-side, (j) CO+NH_2-H_2O_2-top, (k) OH+NH_2-H_2O_2-side, and (l) OH+NH_2-H_2O_2-top*

For the H_2O_2 molecules to capture electrons from the edge-functionalised GCN systems, they must interact strongly with the GCN blocks. Hence, the adsorption of the H_2O_2 molecules on the edge-functionalised GCN configurations has been investigated. The optimised configurations of the H_2O_2 molecules adsorbed on the GCN blocks in the energetically most favourable adsorption conditions are shown in **Fig. 6.66(a-l)**. Although the interaction in all the cases is via the weak van der Waals forces, the adsorption process is exothermic on all the edge-functionalised GCN systems, indicating strong binding between the GCN blocks and the H_2O_2 molecules. Such strong interactions can facilitate the transfer of electrons from the GCN blocks to the H_2O_2 molecules. The adsorption energy values for H_2O_2 adsorption in the most favourable adsorption scenarios are given in **Table 6.6**. The H_2O_2 adsorption is strongest on the CO-GCN and CO+NH_2-GCN systems, with adsorption energy values of −0.34 eV and −0.36 eV, respectively. The H_2O_2 molecule is adsorbed via an interaction with the –C=O functional group only on systems that also contain other functional groups. For the OH+NH_2-GCN system, the H_2O_2 molecule is bonded to the photocatalyst via an interaction with the –OH functional group. The position of the VBMs and CBMs of the adsorbed-H_2O_2 GCN systems are represented in **Fig. 6.65(b)** within the NHE scale. The CBMs of the GCN systems after H_2O_2 adsorption shift to more positive values than the same for the bare GCN systems. This indicates the transfer of an electron to the H_2O_2 molecule from the GCN system after adsorption. An exception of this is observed only for the NH_2-GCN system.

Electrons are transferred from the CBMs of the bare GCN blocks to lower energy levels in the adsorbed-H_2O_2 configurations. The CBMs of the adsorbed-H_2O_2 edge-functionalised GCN systems remain more negative than the •OH/H_2O_2 reduction potential. This suggests that the CBMs of adsorbed-H_2O_2 edge-functionalised GCNs act as intermediate trapping levels for the electrons, and the H_2O_2 molecules are almost reduced into active ·OH radicals. Hence, H_2O_2 plays the most crucial role in producing active •OH radicals by capturing the photogenerated electrons from the semiconducting GCN blocks. The amount of shift of the CBM to a more positive value is the maximum for H_2O_2 adsorption on CO-GCN. Notably, the adsorption energy is the least negative for H_2O_2 adsorption on NH_2-GCN. This is the only system for which the CBM shifts to a more negative value after H_2O_2 adsorption, and indicates that electrons are rarely to be transferred from the GCN photocatalyst to the H_2O_2 molecules via the –NH_2 group.

Table 6.6. The adsorption energy values for H_2O_2 adsorption in the most favourable adsorption scenario:

System	**H_2O_2 adsorption energy (eV)**
CO-GCN	-0.34
OH-GCN	-0.14
NH_2-GCN	-0.10
CO+OH-GCN	-0.21
CO+NH_2-GCN	-0.36
OH+NH_2-GCN	-0.17

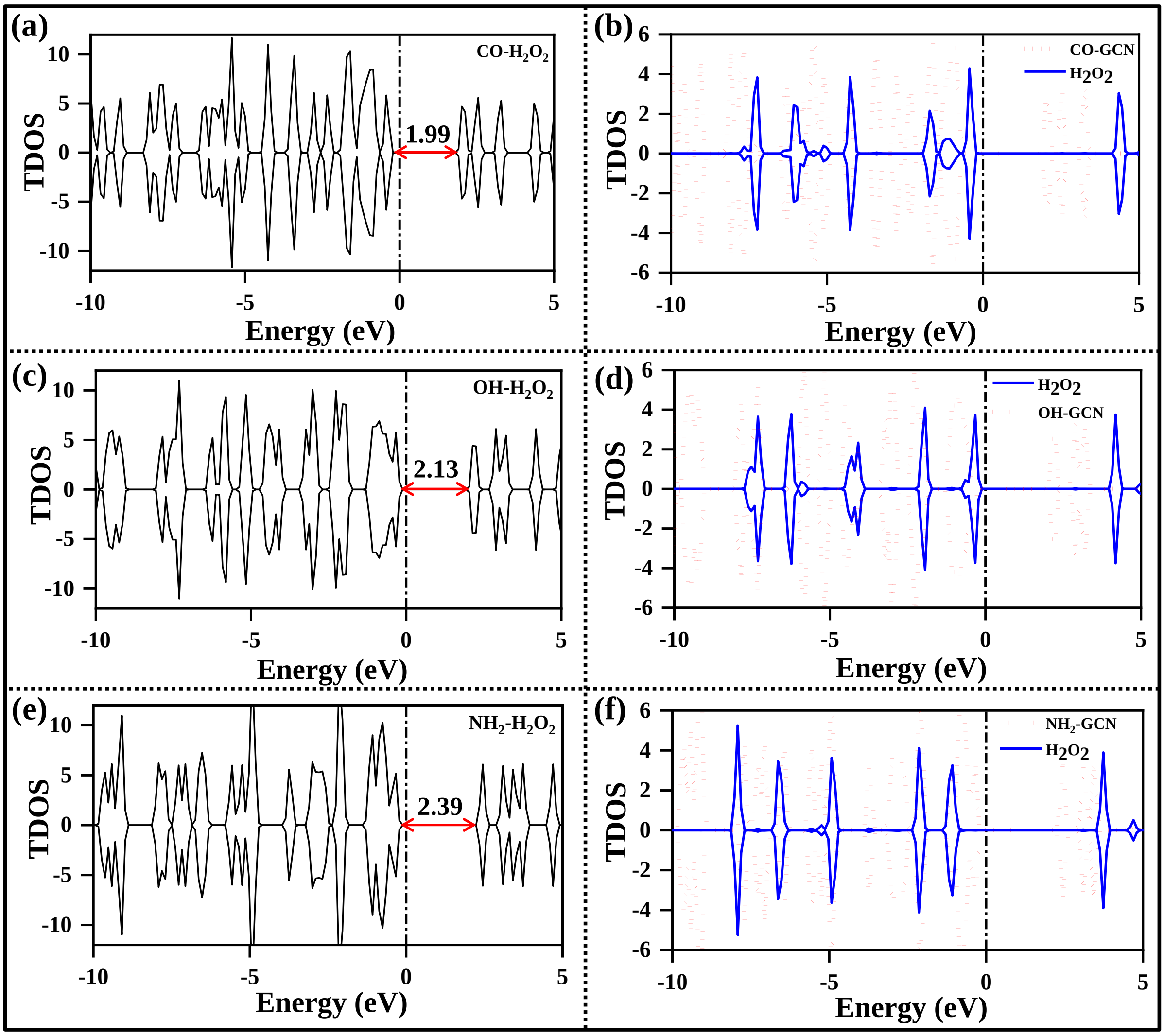

Fig. 6.67: *TDOS of the adsorbed-H_2O_2 configurations: (a) CO-H_2O_2, (c) OH-H_2O_2, (e) NH_2-H_2O_2; the contribution from the GCN quantum dots and adsorbed H_2O_2 molecules to the TDOS of all the adsorbed configurations: (b) CO-GCN, (d) OH-GCN, (f) NH_2-GCN*

The TDOS of the adsorbed-H_2O_2 configurations are represented in **Fig. 6.67(a,c,e,g,i,k)**. The band gap is smaller than the bare GCN configuration for all the systems except for H_2O_2 adsorbed on NH_2-GCN and OH+NH_2-GCN. The contributions to the TDOS from the GCN quantum dots and adsorbed H_2O_2 molecules of all the adsorbed configurations are shown in **Fig. 6.67(b,d,f,h,j,l)**. H_2O_2 contributes to the VBMs for all the adsorbed configurations except NH_2-GCN, for which the GCN system is the sole contributor to the VBs states just below the Fermi level (**Fig. 6.67(e,f)**).

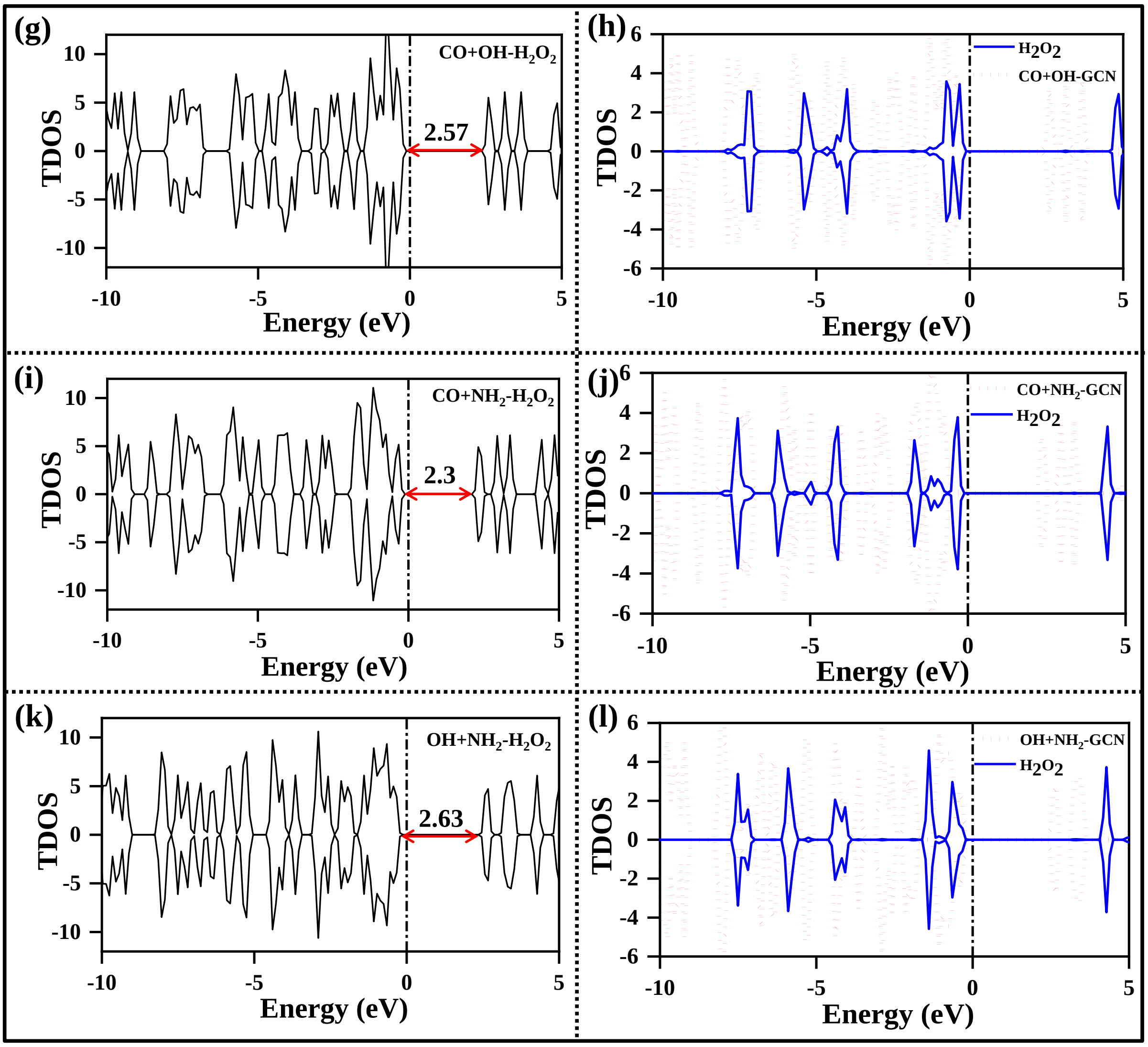

Fig. 6.67(continued): *TDOS of the adsorbed-H_2O_2 configurations: (g) CO+OH-H_2O_2, (i) CO+NH_2-H_2O_2, (k) OH+NH_2-H_2O_2; the contribution from the GCN quantum dots and adsorbed H_2O_2 molecules to the TDOS of all the adsorbed configurations: (h) CO+OH-GCN, (j) CO+NH_2-GCN, (l) OH+NH_2-GCN*

The reduction of Cr(VI) into Cr(III) occurs via the reaction of molecules containing Cr(VI) with nascent hydrogen. For all the edge-functionalised GCN systems except CO-GCN, the CBMs are situated at negative values within the NHE scale, whereas for the CO-GCN system, the CBM is situated at 0 V vs. NHE (**Fig. 6.65(a)**). If there are H^+ ions present in the solvent, they would very likely capture the photogenerated electrons and produce nascent hydrogen. If the VB level of the semiconductor is more positive than the reduction potential of HCOOH/2H^+, CO_2 (+0.25 V vs. NHE), FA (HCOOH) could act as the source of H^+ through its oxidation by capturing photogenerated holes via the following reaction:

$$\boldsymbol{3HCOOH_{(aq)} \rightarrow 2CO_2 + 6e^- + 6H^+} \ldots\ldots\ldots (6.10)$$

As shown in **Fig. 6.65(a)**, the VBMs of all the edge-functionalised GCNs are at more positive values than the reduction potential of $HCOOH/2H^+$, CO_2. Hence, HCOOH is very likely to capture the photogenerated holes from the semiconducting GCN systems to produce H^+ ions and prevent electron–hole recombination. The adsorption of HCOOH molecules on edge-functionalised GCN blocks is exothermic: a negative adsorption energy is calculated using equation (6.10). The adsorption energy values for HCOOH adsorption on different edge-functionalised GCN systems are represented in **Table 6.7**. The negative values of the adsorption energy reveal a strong interaction between the adsorbed-HCOOH molecules and the edge-functionalised GCN blocks. The interaction of the HCOOH molecules with the GCN blocks is found to be via van der Waals or hydrogen bonding. The optimised configurations of HCOOH molecules adsorbed on edge-functionalised GCNs are represented in **Fig. 6.68(a-l)**. As in the H_2O_2-adsorption scenario, the HCOOH interacts with the GCN blocks via the –C=O functional group even when other functional groups are present in the adsorbent system. The strongest adsorption of HCOOH is found on the CO-GCN and the CO+OH-GCN systems, with adsorption energy values of −0.19 eV in both cases.

Table 6.7. The adsorption energy values for HCOOH adsorption on different edge-functionalised GCN systems:

System	HCOOH adsorption energy (eV)
CO-GCN	-0.19
OH-GCN	-0.11
NH_2-GCN	-0.14
CO+OH-GCN	-0.19
CO+NH_2-GCN	-0.18
OH+NH_2-GCN	-0.09

The position of the VBMs and CBMs of the adsorbed-HCOOH configurations are shown in **Fig. 6.65(c)** with respect to the NHE scale. The VBMs of all the adsorbed-HCOOH configurations are calculated as less positive or more negative than the bare GCN blocks. Notably, the VBMs of the HCOOH-adsorbed GCN blocks are located at more positive values than the $HCOOH/2H^+$, CO_2 reduction potential. This indicates that the photogenerated holes are indeed captured by the adsorbed HCOOH molecules and are residing at an intermediate energy level prior to the oxidation of HCOOH into CO_2 and H^+. The upwards shift of the VBMs of the adsorbed-HCOOH systems within the NHE scale shows the dominant role the

HCOOH solvent molecules play in producing H^+ ions, which is pivotal in reducing Cr(VI) to Cr(III).

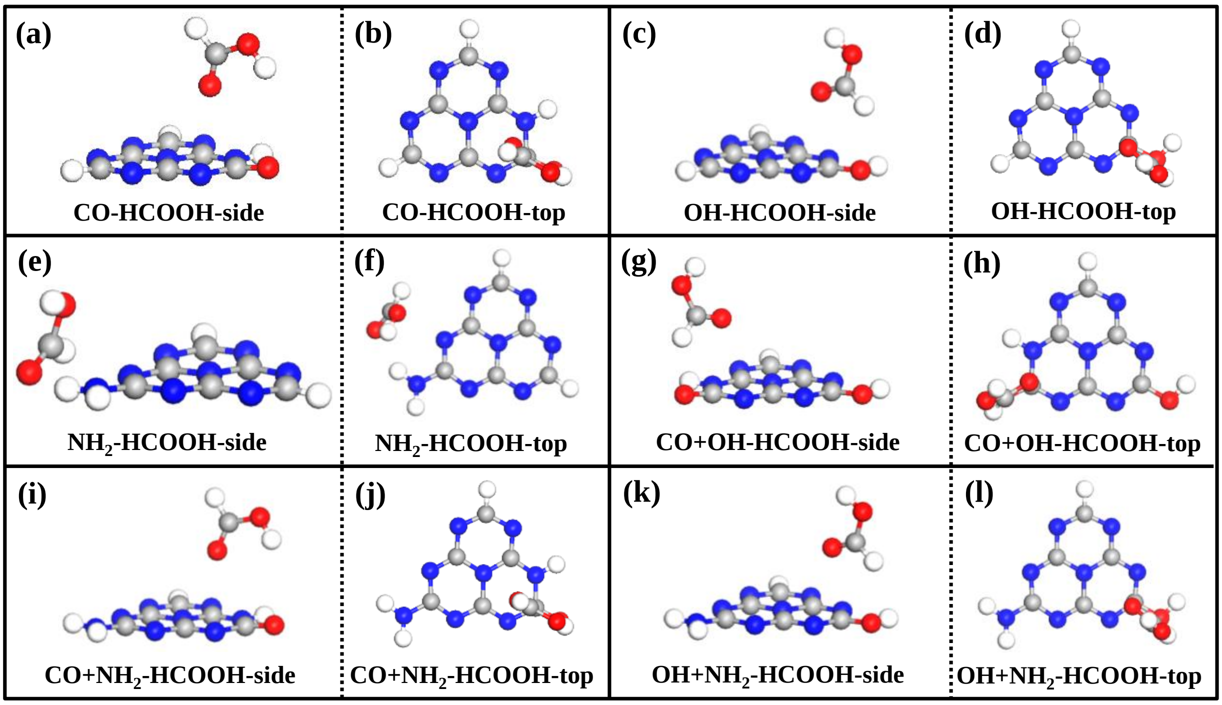
(a) CO-HCOOH-side
(b) CO-HCOOH-top
(c) OH-HCOOH-side
(d) OH-HCOOH-top
(e) NH_2-HCOOH-side
(f) NH_2-HCOOH-top
(g) CO+OH-HCOOH-side
(h) CO+OH-HCOOH-top
(i) CO+NH_2-HCOOH-side
(j) CO+NH_2-HCOOH-top
(k) OH+NH_2-HCOOH-side
(l) OH+NH_2-HCOOH-top

Fig. 6.68: *The optimised configurations of the adsorbed HCOOH molecules on the GCN blocks in both side and top views: (a) CO-HCOOH-side, (b) CO-HCOOH-top, (c) OH-HCOOH-side, (d) OH-HCOOH-top, (e)* NH_2*-HCOOH-side, (f)* NH_2*-HCOOH-top, (g) CO+OH-HCOOH-side, (h) CO+OH-HCOOH-top, (i) CO+*NH_2*-HCOOH-side, (j) CO+*NH_2*-HCOOH-top, (k) OH+*NH_2*-HCOOH-side, and (l) OH+*NH_2*-HCOOH-top*

The TDOS of the adsorbed-HCOOH GCN systems are represented in **Fig. 6.69(a,c,e,g,i,k)**. For all cases, the band gap increases compared to the band gap of the bare GCN systems. The individual contribution of the edge-functionalised GCN and adsorbed HCOOH molecule to the TDOS is shown in **Fig. 6.69(b,d,f,h,j,l)**. In contrast to H_2O_2 adsorption, the density of states (DOS) just below the Fermi level are contributed by only the GCN blocks for all the adsorbed-HCOOH edge-functionalised GCN configurations. The absence of an occupied DOS adjacent to the Fermi level for the adsorbed HCOOH molecules most likely corresponds to the capture of the photogenerated holes by the adsorbed HCOOH molecule.

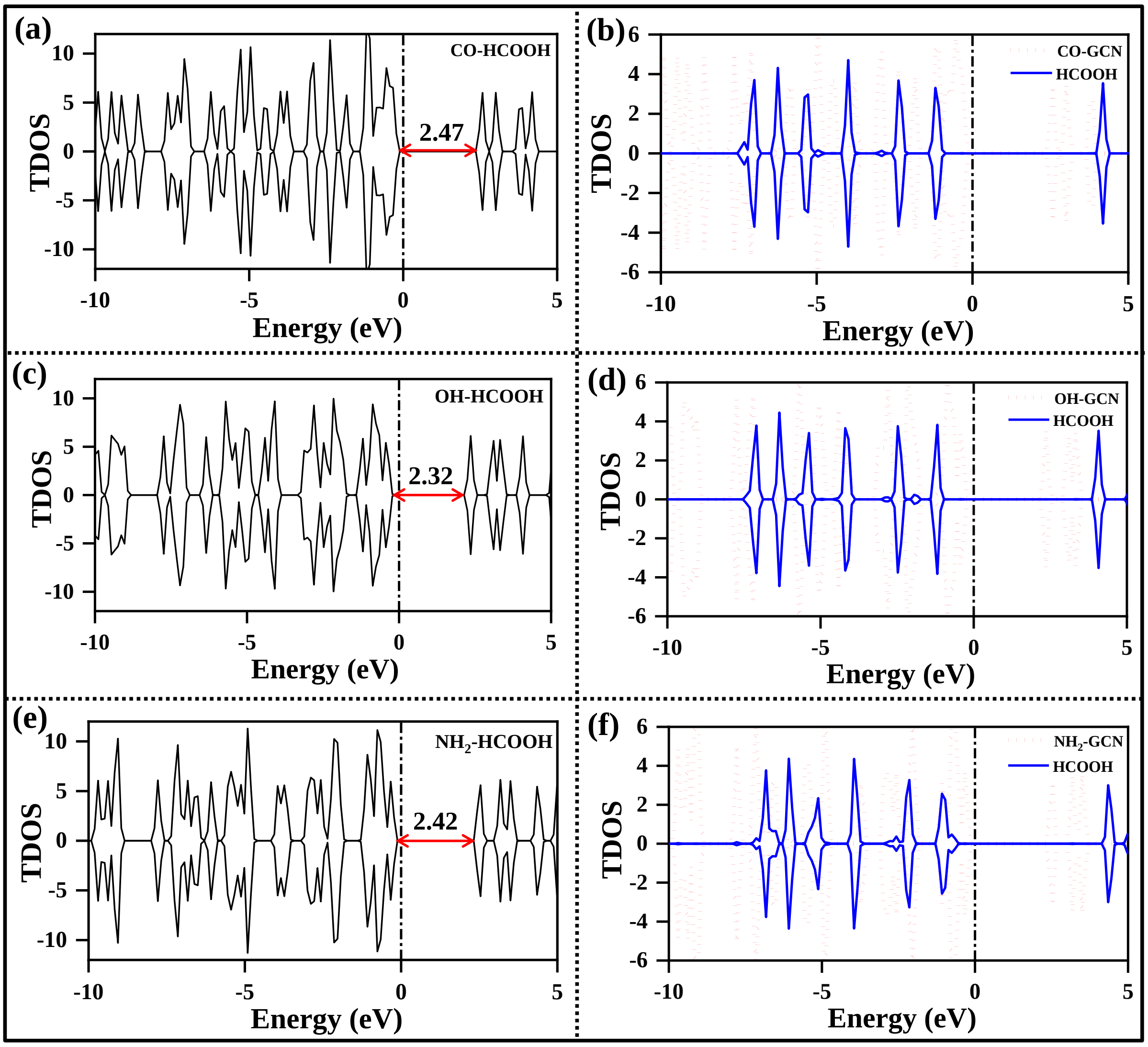

Fig. 6.69: *TDOS of the adsorbed-HCOOH configurations: (a) CO-HCOOH, (c) OH-HCOOH, (e) NH_2-HCOOH; the contribution from the GCN quantum dots and adsorbed HCOOH molecules to the TDOS of all the adsorbed configurations: (b) CO-GCN, (d) OH-GCN, (f) NH_2-GCN*

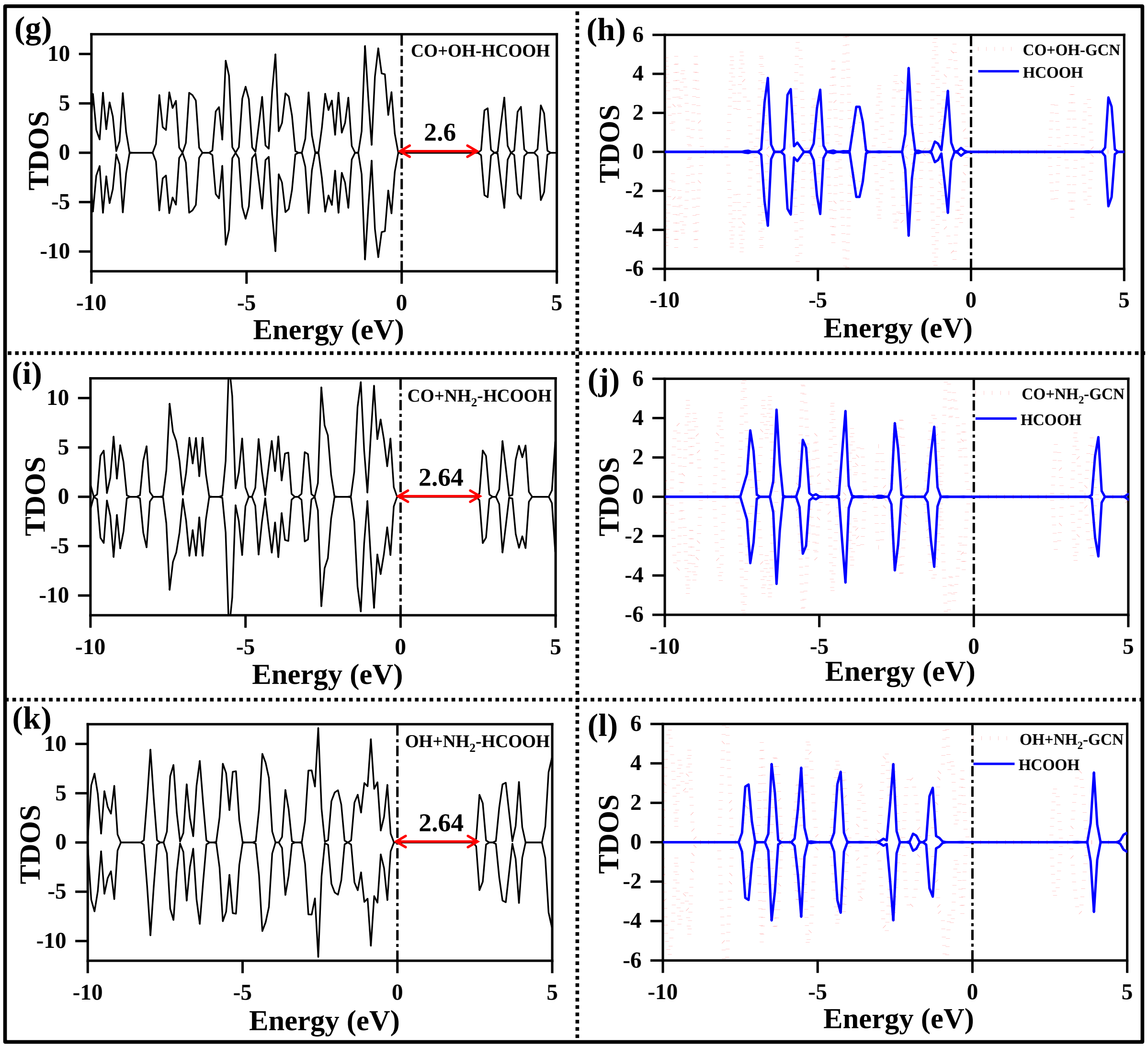

Fig. 6.69(continued): *TDOS of the adsorbed-HCOOH configurations (g) CO+OH-HCOOH, (i) CO+NH$_2$-HCOOH, (k) OH+NH$_2$-HCOOH; the contribution from the GCN quantum dots and adsorbed H_2O_2 molecules to the TDOS of all the adsorbed configurations: (h) CO+OH-GCN, (j) CO+NH$_2$-GCN, (l) OH+NH$_2$-GCN*

The active sites for RhB adsorption on the edge-functionalised GCN systems have been further evaluated. Three sites on RhB, the O atom of the C-O-C bond, one of the N atoms, and the COOH functional group have been considered to study their interaction with the GCN blocks. **Fig. 6.70** and **Fig. 6.71** show the interaction of a RhB molecule with the GCN blocks and their computed ground state energy for interaction via different active sites. The lowest energy configurations are found when RhB interacts via the COOH functional group with the GCN systems for CO-GCN, OH-GCN, CO+OH-GCN, CO+NH$_2$-GCN and OH+NH$_2$-GCN (**Fig. 6.70(c,f)**) and **Fig. 6.71(c,f,i)**). For NH$_2$-GCN, the most stable interaction occurs between the –NH$_2$ group of NH$_2$-GCN and the C-O-C of RhB (**Fig. 6.70(g,h)**). In most cases, the interactions are via hydrogen bonds.

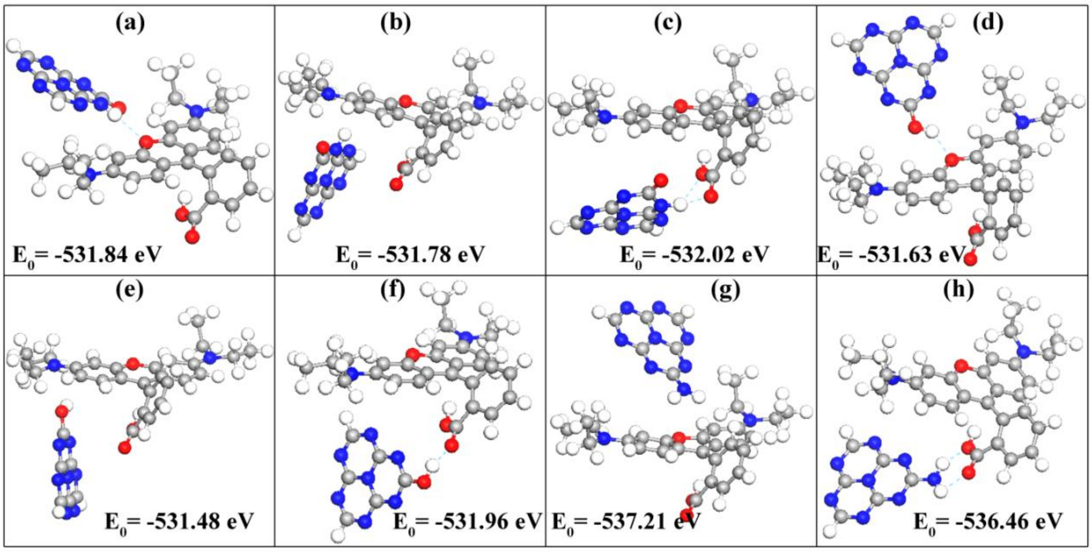

***Fig. 6.70**: Interaction of RhB with the edge-functionalised GCN and their optimised configurations for (a-c) CO-GCN, (d-f) OH-GCN, and (g,h) NH_2-GCN. The ground state energy (E_0) of the optimised configuration as obtained from DFT calculations are also given for each RhB adsorbed configuration*

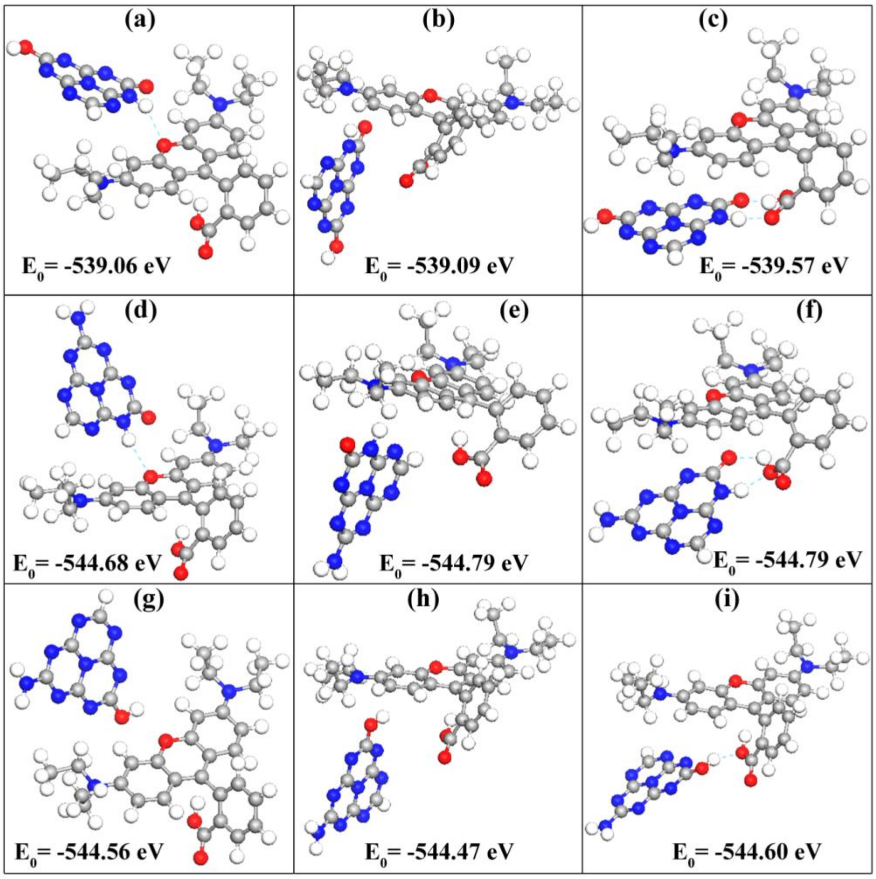

***Fig. 6.71**: Interaction of RhB with the edge-functionalised GCN and their optimised configurations for (a-c) CO+OH-GCN, (d-f) CO+NH_2-GCN, and (g-i) OH+NH_2-GCN. The ground state energy (E_0) of the optimised configuration as obtained from DFT calculations are also given for each RhB adsorbed configuration*

Experimental findings described that the modified GCN with improved properties helped efficiently reduce commonly existing toxic pollutants in wastewater. The visible light–induced photo-reduction of these pollutants was facilitated by the electron-capturing H_2O_2 and hole-capturing FA. In the presence of 20 mg of an optimal catalyst and an H_2O_2 concentration of 10 mL/L, 10 μM RhB solution was completely degraded to its non-toxic end products within 30 min. This amount of catalyst in the presence of 0.8 mL of FA could achieve about 100% efficiency in reducing 0.8 mg/mL Cr(VI) solution to Cr(III) within 2 hr. Optimisation of the catalytic activity and in-depth analysis of the interaction between the factors contributing to the enhanced catalytic performance was achieved by conducting various experiments by varying different influencing parameters and applying statistical modelling with RSM analysis. The rate constant and photo-reduction efficiency values increased proportionately with increased amounts of catalyst. Similarly, with increasing concentrations of electron-capturing and hole-capturing agents for the reduction of RhB and Cr(VI), respectively, the efficiency enhanced proportionately. However, after a specific limit, the catalytic activity was exhausted. The catalytic efficiency was hindered by increasing the initial concentration of pollutants. The Box–Behnken design was chosen to determine the optimal operating conditions for reducing both pollutants, which was evaluated using Minitab. Additionally, the plausible mechanism driving the catalytic activity of GCN was further analysed and validated by employing first-principles calculations. The band position of the VBM and CBM of different edge-functionalised GCN blocks in the NHE scale revealed their ability to reduce RhB and Cr(VI) through transferring photogenerated electrons and holes, respectively. The shift of the CBM to a more positive value upon H_2O_2 adsorption and the VBM to a more negative value upon HCOOH adsorption indicated the transfer of photogenerated electrons and holes, respectively, to the adsorbate molecules. This phenomenon proactively produced active radicals and ions to reduce RhB and Cr(VI). It may be concluded that the as-synthesised metal-free, non-toxic, exfoliated, pristine GCN with a high surface area could be successfully applied in wastewater treatment plants owing to its facile synthesis procedure. The stable and reusable GCNX catalyst could facilitate the rapid treatment of wastewater containing hazardous dyes and Cr(VI) in the presence of readily available and environmental-friendly electron-capturing and hole-capturing reagents, respectively. Thus, this work paves the way for applying this material and method in wastewater remediation.

Cu-doped and Ni-doped GCN for catalytic reduction of toxic pollutants

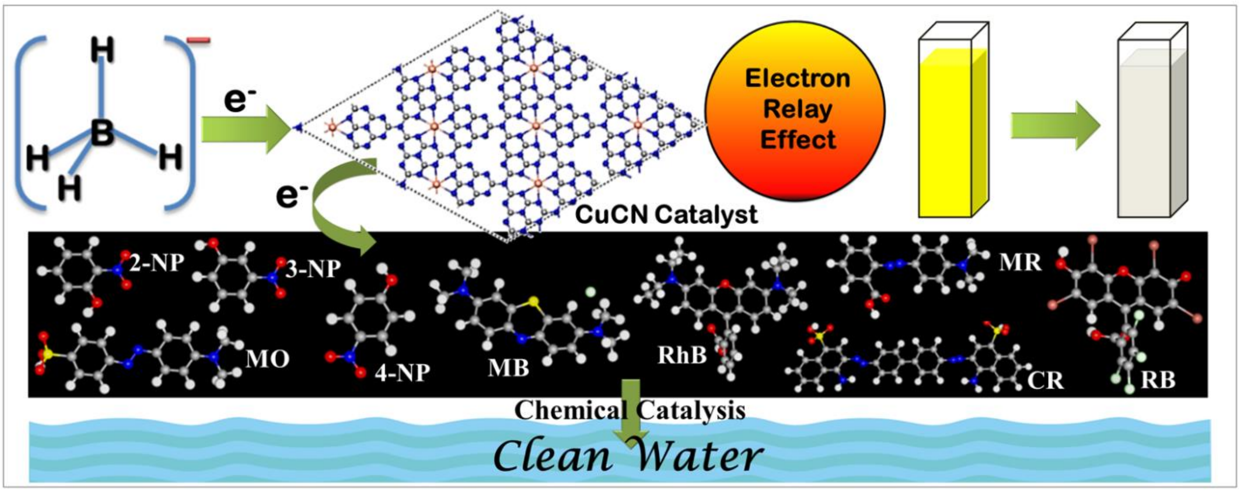

6.6. Cu-doped and Ni-doped GCN for catalytic reduction of toxic pollutants

Organic pollutants like methyl orange, methylene blue, rhodamine B, Congo red, methyl red, rose Bengal, and nitrophenol compounds are some conventional toxic chemicals released into rivers and ponds on a regular basis without following any regulations and guidelines. Most of these chemicals are considered as extremely hazardous and are on the “priority pollutant” lists of many environmental organizations [336]. The stability of these undesirable compounds in the environment makes them immensely difficult to be treated and removed in order to achieve a cleaner and sustainable ecosystem.

In recent times, heterogeneous chemical catalysis mediated by electron relay effect in presence of a reducing agent like $NaBH_4$ have gained much prominence owing to many advantages of this process as compared to traditional adsorption and photocatalysis methods. This is a relatively more efficient and economical method through which toxic pollutants are effectively degraded to non-toxic compounds within a very short time. Upon extensive literature survey, it has been concluded that most of the existing reports employing this technique for reduction of pollutants are based on noble metal loading in GCN which limits their practical feasibility because of the high cost, poor availability, and controlled synthesis techniques of noble metal nanoparticles. Comparatively, transition metals like Cu and Ni are earth abundant and much more economical for practical usage. In current scenario, very few researches have been conducted on the detailed experimental and theoretical insights into the degradation of different types of toxic pollutants by $NaBH_4$ assisted chemical reduction.

In the present work, the as-developed Cu doped and Ni decorated GCN have been extensively utilized for the catalytic degradation of a vast range of pollutants present in waste-water like 4-nitrophenol, 3-nitrophenol, 2-nitrophenol, methyl orange, methylene blue, methyl red, congo red, rose Bengal and rhodamine B dyes by $NaBH_4$ mediated electron relay process. This work also deals with the substantial variations in several parameters like catalyst dosage, $NaBH_4$ concentration, pH, and concentration of pollutants which have been performed to understand their effect on catalytic activity. Moreover, a detailed theoretical analysis have been performed by first principles DFT calculations to elucidate the chain of reactions taking place during the degradation of 4-nitrophenol, methyl orange, and methylene blue to their reduced non-toxic end products and also to determine the most plausible reaction routes along with theoretical efficiencies. Most existing reports have not dealt with the catalytic activity of such an extensive range of pollutants along with the precise mechanism of the dye degradation procedure; thus limiting their practical implementation in waste-water remediation. The current work thus provides a detailed experimental and theoretical approach towards the impressive catalytic activity of metal decorated GCN.

6.6.1. Catalytic reduction of nitrophenol compounds by CuCN and NiCN:

The detailed catalytic procedures and related mathematical calculations to evaluate the rate constant values have been discussed in chapter 5. The pseudo-first order rate constant values have been calculated following equation (5.15), given in chapter 5, section 5.3.3.3. It can be observed from **Fig. 6.72** that mild yellow-coloured 4-nitrophenol (4-NP) solution dissolved in water medium in pristine condition exhibits an absorption peak at 316 nm. This peak shifts considerably to a higher wavelength around 400 nm upon addition of $NaBH_4$ due to the formation of 4-nitrophenolate ions. The colour of the solution turns to bright yellow in presence of $NaBH_4$. The gradual disappearance of this peak at 400 nm along with simultaneous emergence of a new peak around 297 nm suggests the formation of 4-aminophenol (4-AP) by reduction of 4-NP in presence of $NaBH_4$. The solution turns colourless after completion of the reaction procedure.

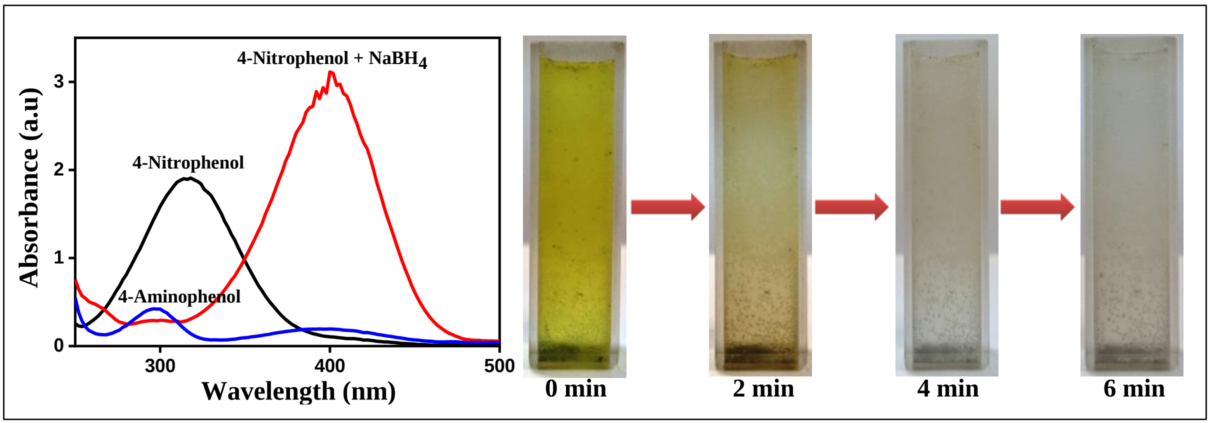

Fig. 6.72: *Absorption spectra of pure 4-NP solution without* $NaBH_4$ *addition, absorption after addition of* $NaBH_4$ *in 4-NP solution, and absorption spectra of 4-aminophenol; digital images showing the gradual transformation of 4-NP to 4-AP in presence of CuCN catalyst and* $NaBH_4$

6.6.1.1. Effect of various parameters on the catalytic activity:

From the absorption spectra of 1 mM 4-NP, shown in **Fig. 6.73(a)**, it can be observed that complete reduction of the pollutant was achieved within 5 min in presence of 4 mg CuCN catalyst and 0.1 M of $NaBH_4$. Variation in the $NaBH_4$ concentrations were performed by keeping the catalyst amount fixed to 4 mg and 4-NP concentration fixed to 1 mM. By increasing the concentration of $NaBH_4$ from 0.01 M to 1 M and keeping the catalyst dosage constant at 4 mg, the rate of reduction of 4-NP to 4-AP increases proportionately. The $\ln(C_0/C_T)$ vs. time plots for varying concentrations of $NaBH_4$ are shown in **Fig. 6.73(b)**. Increased concentration of $NaBH_4$ in the solution contributes more electrons in the catalytic system, thereby facilitating the electron relay effect. The pseudo-first order rate constant (k) values calculated by following equation (5.15) obtained for different concentrations of $NaBH_4$ for 4 mg CuCN catalyst are listed in **Table 6.8**.

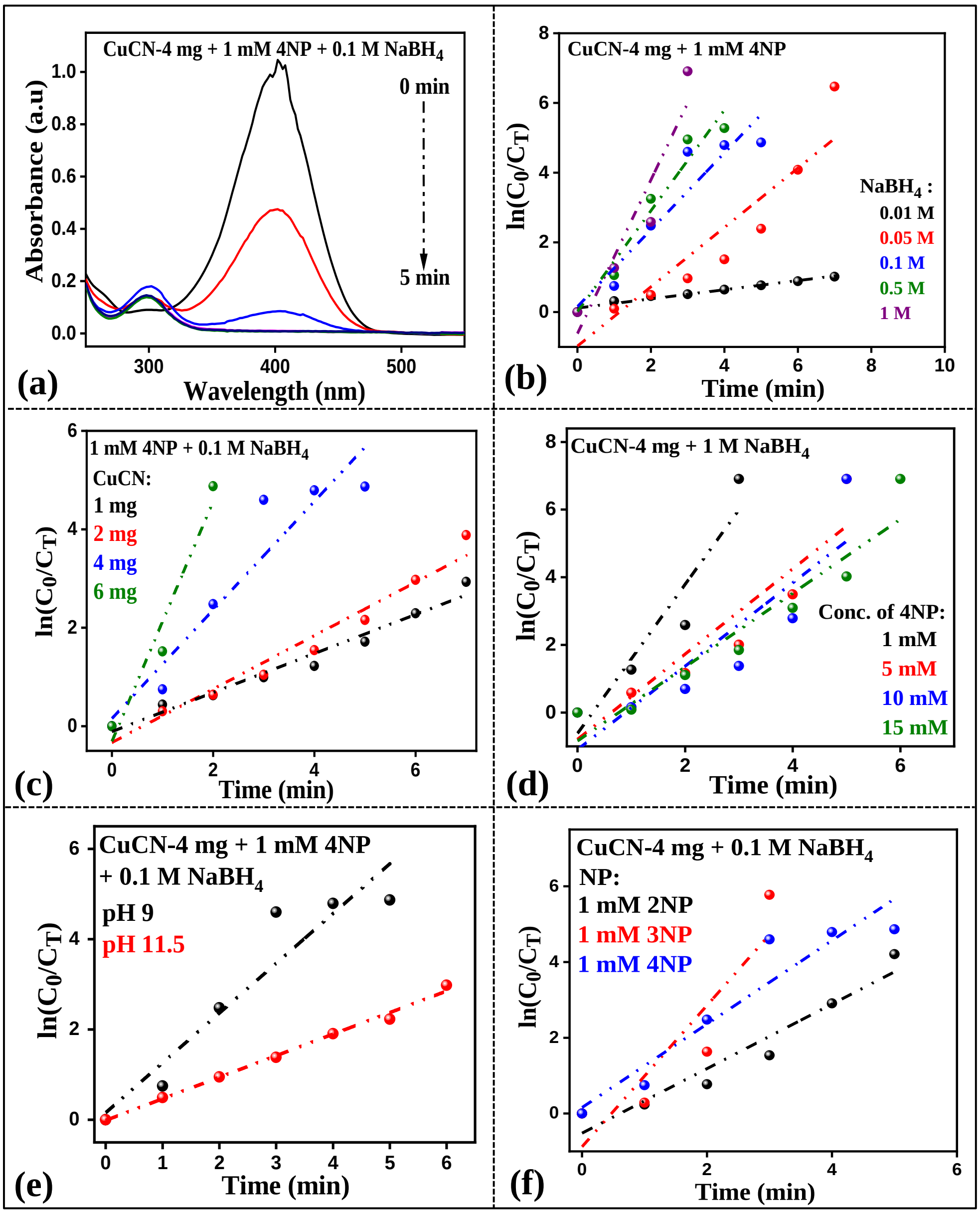

***Fig. 6.73**: (a) Absorption spectra of 4-NP in presence of 4 mg CuCN and 0.1 M $NaBH_4$; Pseudo-first order rate kinetics plot for degradation of 4-NP by CuCN in presence of (b) varying concentrations of $NaBH_4$, (c) varying dosages of CuCN, (d) varying concentrations of 4-NP, (e) at pH 9 and 11.5; and (f) pseudo-first order rate kinetics plot for degradation of different NP compounds by CuCN catalyst*

The effect of catalyst dosage on the catalytic reduction of 4-NP was further evaluated by varying the dosages of CuCN catalyst as 1, 2, 4, and 6 mg. The concentration of 4-NP and $NaBH_4$ was maintained constant at 1 mM and 0.1 M respectively. The corresponding kinetics plot is shown in **Fig. 6.73(c)** along with the rate constant values for each dosage. It is observed that the reduction rate increases with the increase in the amount of catalyst in the solution, which may be due to the increased availability of catalytic active sites, thereby enhancing the reduction efficiency significantly. Subsequently the variation in the concentrations of 4-NP were performed by keeping the CuCN amount constant at 4 mg, whereas, the concentration of $NaBH_4$ was maintained at 1 M. In these experimental runs, concentrations of the stock solution of 4-NP were increased as 5, 10, and 15 mM. The corresponding rate kinetics plot is shown in **Fig. 6.73(d)**. It is evident that 4 mg CuCN is capable of effectively attenuating high concentrations of 4-NP within reasonable time period. However, the ‘k’ values decrease considerably with increasing concentration of 4-NP. The values obtained from rate kinetics plots are listed in **Table 6.8**.

It is noted that the stock solution of 4-NP has a neutral pH of 7, whereas the stock solution of 0.1 M $NaBH_4$ exhibits a slightly basic pH value. Hence the reaction solution (4-NP + $NaBH_4$) inside the cuvette has a pH value of 9. The catalytic activity of 4 mg CuCN in reduction of 1 mM 4-NP was studied at a basic pH value (pH = 11.5) by adding appropriate amount of 0.1 M of NH_4OH in the reaction solution. The rate kinetics plot at basic pH is shown in **Fig. 6.73(e)** and the corresponding rate constant value is listed in **Table 6.8**. It can be observed from the rate kinetics plot that the rate of degradation gets significantly hindered at pH 11.5 suggesting possible inhibition of the reaction at a high pH value. This may be attributed to the fact that the rate of hydrolysis of borohydride ions decreases considerably with increase in pH [337]. It is also to be mentioned here that 4-NP solution interacts drastically with any type of acids; hence we could not perform the catalytic study at acidic pH. A very small concentration (0.1 M) of any acid reacted vigorously with 4-NP, immediately turning the 4-NP solution colourless. However there is a report on reduction of 4-NP at pH 5 by Lin et al. [337] but they did not decrease the pH beyond this value. They observed significant increase in the catalytic rate at low pH.

Similar experimental studies were performed with the NiCN sample. **Fig. 6.74(a)** shows the absorption spectra of 1 mM 4-NP in presence of 4 mg catalyst and 0.3 M of $NaBH_4$. Increasing the concentration of $NaBH_4$ led to faster degradation rate of 4-NP. The rate kinetics plot for varying concentrations of $NaBH_4$ (0.1, 0.3, and 0.5 M) are demonstrated in

Fig. 6.74(b). With increase in $NaBH_4$ concentration to 0.5 M, complete reduction occurred within 1 min. The corresponding rate constant values are listed in **Table 6.8**.

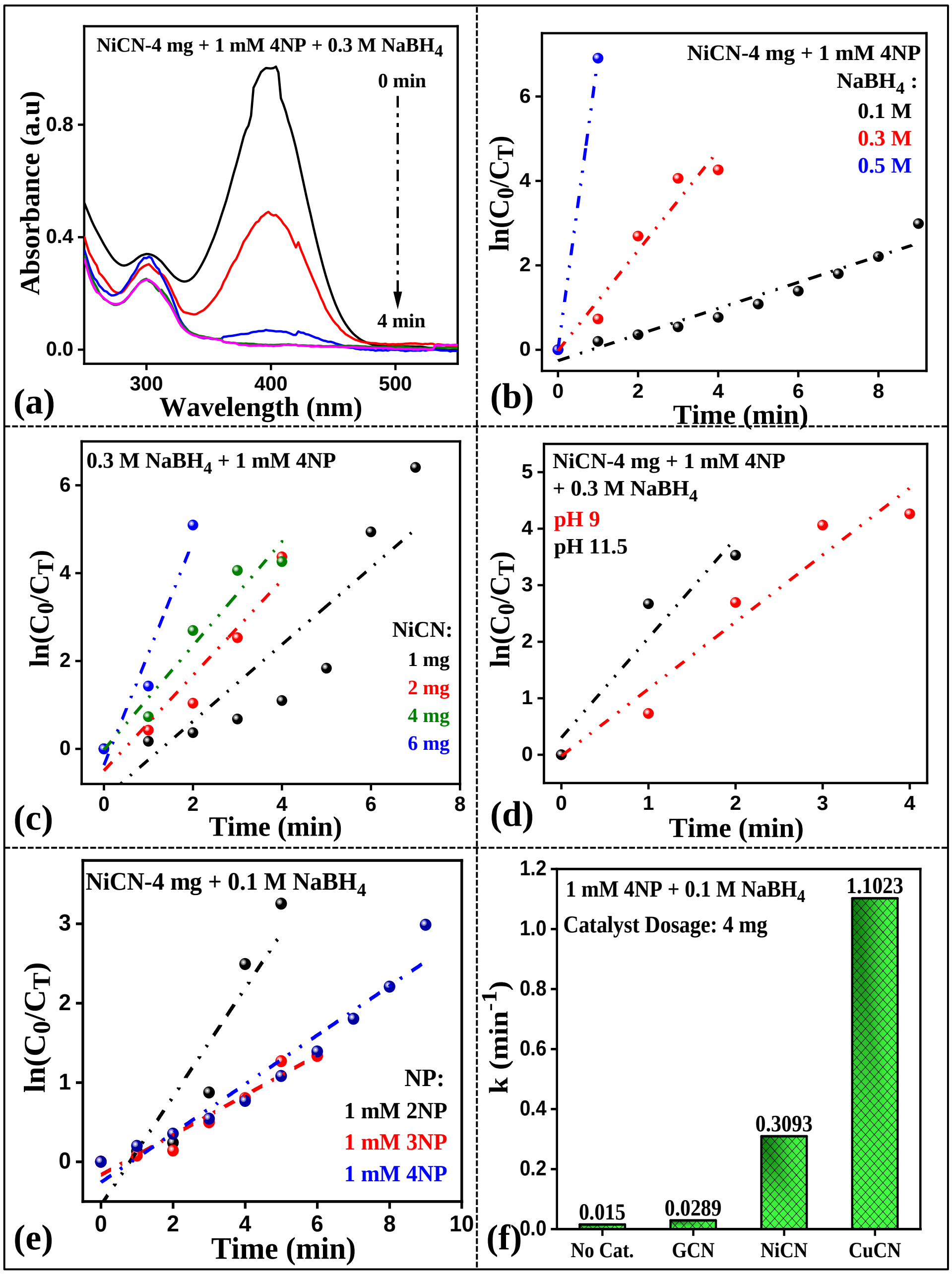

***Fig. 6.74**: (a) Absorption spectra of 4-NP in presence of 4 mg NiCN and 0.3 M $NaBH_4$; Pseudo-first order rate kinetics plot for degradation of 4-NP by NiCN in presence of (b) varying concentrations of $NaBH_4$; (c) varying dosages of NiCN; (d) at pH values of 9 and 11.5; (e) pseudo-first order rate kinetics plot for degradation of different NP compounds by NiCN catalyst; and (f) bar graph showing the pseudo-first order rate constant values for degradation of 4-NP by pristine GCN, NiCN, CuCN and in absence of any catalyst*

The effect of amount of catalyst on the catalytic activity of 4-NP reduction was studied in the present work. The rate kinetics plot in presence of varying dosage of NiCN (1, 2, 4, and 6 mg) and 0.3 M $NaBH_4$ for the reduction of 1 mM 4-NP is shown in **Fig. 6.74(c)**. Like CuCN, the best activity is observed at a NiCN catalyst dosage of 6 mg. The rate of reduction of 4-NP increases proportionately with the increase in NiCN catalyst dosage, since more amount of catalyst is present to attack the target pollutant and reduce it to its final non-toxic product. The catalytic activity of NiCN at a basic pH of 11.5 can be investigated from the rate kinetics plot shown in **Fig. 6.74(d)**. Interestingly, unlike CuCN, the rate of reduction of 4-NP increased significantly at a high pH value. The 'k' value is listed in **Table 6.8**.

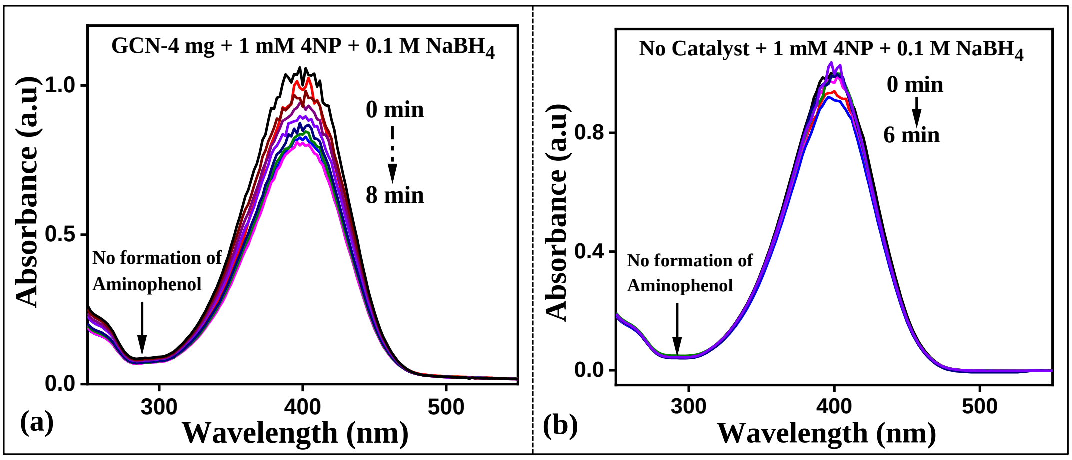

***Fig. 6.75**: Absorption spectra of 4-NP in presence of 0.1 M $NaBH_4$ and (a) 4 mg pure GCN, and (b) in absence of any catalyst*

Fig. 6.75(a) shows the absorption spectra of 1 mM 4-NP in presence of 4 mg of GCN and 0.1 M $NaBH_4$, whereas, **Fig. 6.75(b)** shows the absorption spectra of 1 mM 4-NP in the presence of only 0.1 M $NaBH_4$ and in absence of any catalyst. It can be clearly observed that 4-NP does not exhibit any sign of reduction in absence of any catalyst or in presence of pristine GCN. The rate constant values as obtained for all the catalysts and no catalysts are depicted in a bar diagram shown in **Fig. 6.74(f)**. It can be observed that in absence of any catalyst, and in the presence of GCN, the 'k' value seems negligible as compared to the values obtained in presence of NiCN and CuCN catalyst. For the same dosage of catalyst, and same concentrations of 4-NP and $NaBH_4$, CuCN have the highest rate constant value which indicates that it is the most effective catalyst in degrading 4-NP.

CuCN and NiCN catalysts were further utilized for the chemical reduction of 2-NP and 3-NP. **Fig. 6.76(a,b)** shows the absorption spectra of 1 mM of 2-NP and 3-NP respectively in presence of 4 mg CuCN and 0.1 M $NaBH_4$. The corresponding $\ln(C_0/C_T)$ plot is given in **Fig. 6.73(f)** from where it can be stated that CuCN shows highest catalytic activity in reducing 3-NP followed by 4-NP and 2-NP. Similar experiments were performed by NiCN (4 mg) in presence of 1 mM 2-NP and 3-NP and 0.1 M $NaBH_4$ (**Fig. 6.76(c,d)**). The rate kinetics plot as shown in **Fig. 6.74(e)** reveals that NiCN exhibits highest activity for 2-NP, followed by 4-NP and 3-NP. The calculated 'k' values are listed in **Table 6.8**.

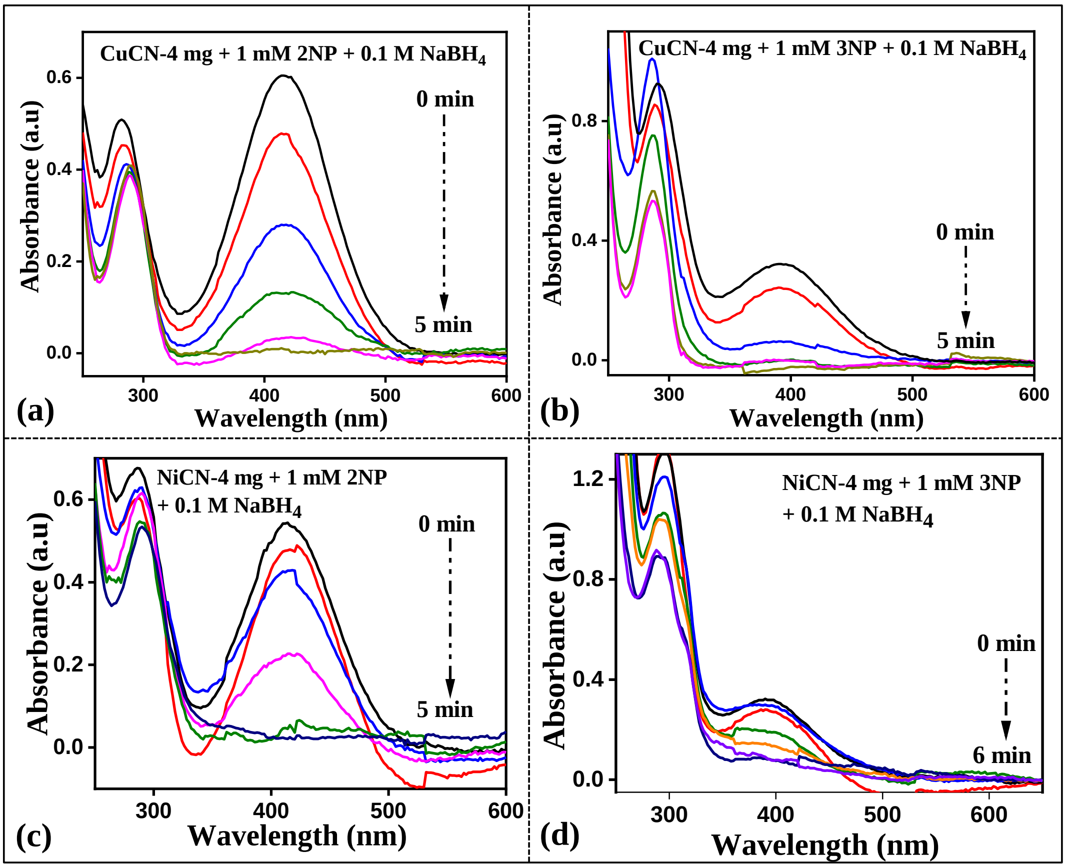

Fig. 6.76: Absorption spectra of (a) 2-NP and (b) 3-NP in presence of 4 mg CuCN and 0.1 M $NaBH_4$. Absorption spectra of (c) 2-NP and (d) 3-NP in presence of 4 mg NiCN and 0.1 M $NaBH_4$

6.6.1.2. Reusability test of the catalysts:

The stability of both the catalysts was examined by reusing them for more than one catalytic cycle. This was performed by extracting the used catalyst from the dye-$NaBH_4$ solution after completion of a particular catalytic cycle through filtration, then washing it repeatedly with DI water, and finally drying it at 50 °C to obtain the product.

The CuCN sample was reused up to four catalytic cycles and the corresponding C_T/C_0 plot is drawn in **Fig. 6.77(a)**. From the bar diagram in **Fig. 6.77(b)**, it can be observed that the rate constant values decrease considerably with each repeating cycle which indicates the gradual loss of efficiency of the catalyst. The NiCN sample was reused following similar procedures for three catalytic cycles. From the C_T/C_0 plot (**Fig. 6.77(c)**) and the bar graph (**Fig. 6.77(d)**), it is revealed that the rate constant values decrease with increase in catalytic cycles.

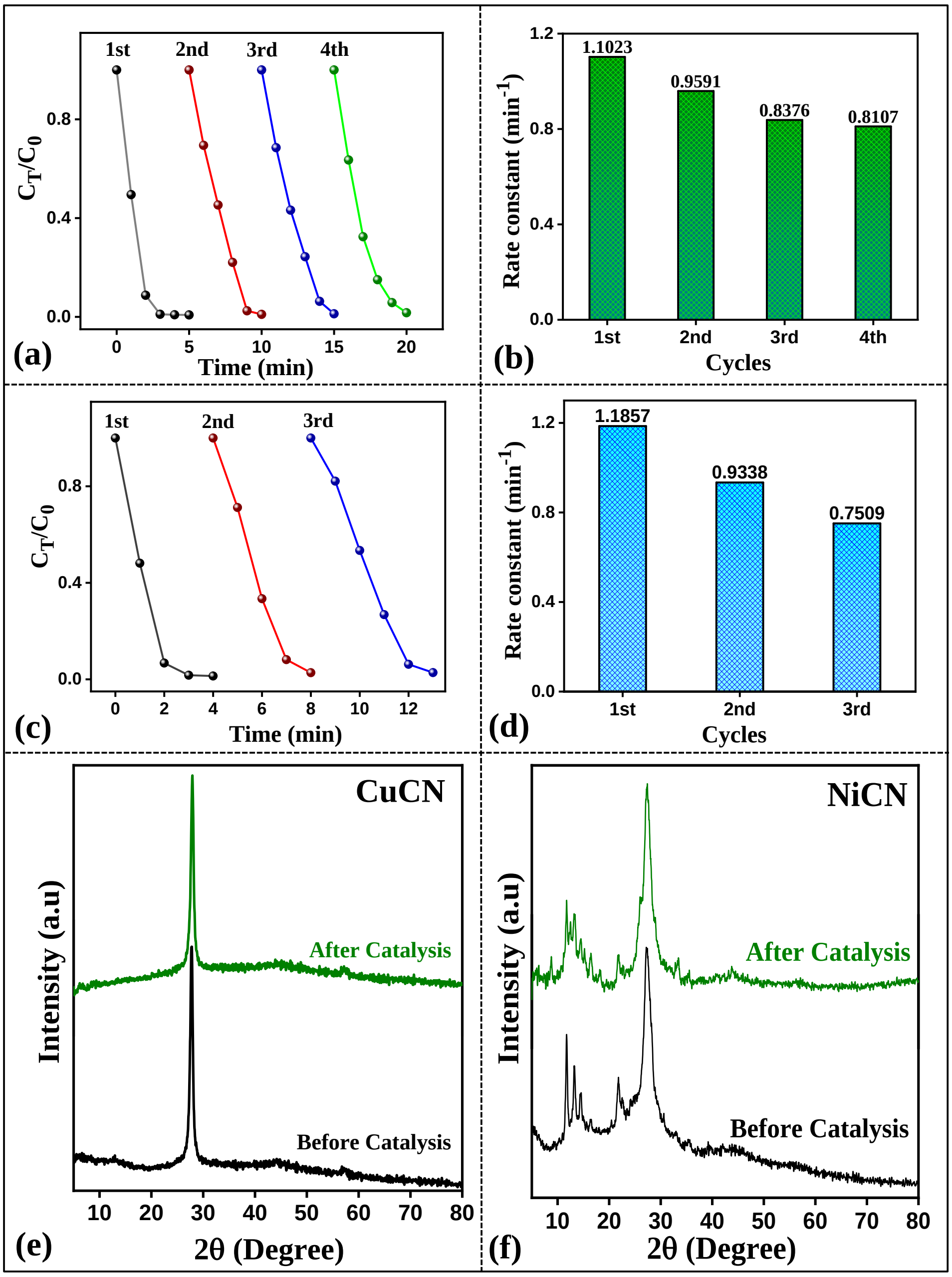

***Fig. 6.77**: (a) Catalytic activity of CuCN in degrading 4-NP up to four cycles, (b) rate constant values for the four catalytic cycles; (c) Catalytic activity of NiCN in degrading 4-NP up to three cycles, (d) rate constant values for the three catalytic cycles; (e) XRD plot of CuCN catalyst before and after catalytic activity; and (f) XRD plot of NiCN catalyst before and after catalytic activity*

The XRD spectra of CuCN and NiCN after catalysis reaction are shown in **Fig. 6.77(e)** and **Fig. 6.77(f)** respectively. On comparison with their respective XRD spectra before catalysis, it is revealed that both the samples retain their characteristic phases with no indication of any new peaks and no change in phases. This indicates that both the catalysts exhibit significant stability during the catalytic reactions. However, the NiCN sample showed some mixed nickel phases like nickel oxide and metallic nickel related peaks after the second cycle and the sample colour also changed from pale yellow to brown. Owing to this, NiCN was not further used for catalytic tests.

Table 6.8. Rate constant values and degradation time of nitrophenol compounds in presence of pure GCN, CuCN and NiCN catalysts:

Catalyst	Pollutants	Catalyst amount (mg)	Conc. of Pollutants (mM)	Conc. of $NaBH_4$ (M)	Degradation Time (min)	Rate Constant (min^{-1})
CuCN	4-NP	4	1	0.01	> 7	0.1312
CuCN	4-NP	4	1	0.05	7	0.8507
CuCN	4-NP	4	1	0.1	5	1.1023
CuCN	4-NP	4	1	0.5	4	1.4452
CuCN	4-NP	4	1	1	3	2.2042
CuCN	4-NP	2	1	0.1	7	0.5424
CuCN	4-NP	6	1	0.1	2	2.4378
CuCN	4-NP	1	1	0.1	> 7	0.3963
CuCN	4-NP	4	5	1	5	1.2601
CuCN	4-NP	4	10	1	5	1.2321
CuCN	4-NP	4	15	1	6	1.0920
CuCN	4-NP	4	1@pH 11.5	0.1	> 6	0.4773
CuCN	2-NP	4	1	0.1	5	0.8519
CuCN	3-NP	4	1	0.1	5	1.8669
NiCN	4-NP	4	1	0.1	> 9	0.3093
NiCN	4-NP	4	1	0.3	4	1.1857
NiCN	4-NP	4	1	0.5	1	6.9077
NiCN	4-NP	1	1	0.3	7	0.8751
NiCN	4-NP	2	1	0.3	4	1.0847
NiCN	4-NP	6	1	0.3	2	2.5472
NiCN	4-NP	4	1@pH 11.5	0.3	2	1.7650
NiCN	2-NP	4	1	0.1	5	0.6854
NiCN	3-NP	4	1	0.1	6	0.2515
GCN	4-NP	4	1	0.1	----	0.0289
No Cat.	4-NP	----	1	0.1	----	0.015

6.6.2. Catalytic reduction of methyl orange (MO) by CuCN and NiCN:

Methyl orange, an anionic azo dye, is a toxic effluent released into water environment primarily from textile industries and also from pharmaceutical, paper, cosmetics, food printing and leather industries [149]. The high solubility of MO in aqueous medium accompanied with its azo-group induced non-biodegradable carcinogenic nature can cause extreme hazardous effects on human health like vomiting tendency, diarrhoea and breathing problem [149]. The UV spectrum of pristine MO dye solution exhibits a prominent absorption peak at 464 nm and a smaller hump near 265 nm before the onset of catalytic activity. The peak at 464 nm originates from the delocalization of π electrons along the -

N=N- azo bond of MO [229] while the hump at 265 nm arises from the aromatic benzene ring of MO as reported by Shen et al. [338]. In presence of catalyst and $NaBH_4$, the intense band at 464 nm quickly disappears while the hump at 265 nm undergoes significant shifting to lower wavelength (256 nm) along with increase in the intensity of the particular band. This is accompanied with changing of the bright orange colour of the solution to completely colourless. These observations suggest the possible reduction of MO by destroying its -N=N- azo bond to produce non-toxic end products of N, N'-dimethyl-p-phenylenediamine and sodium salt of sulphanilic acid [339,229].

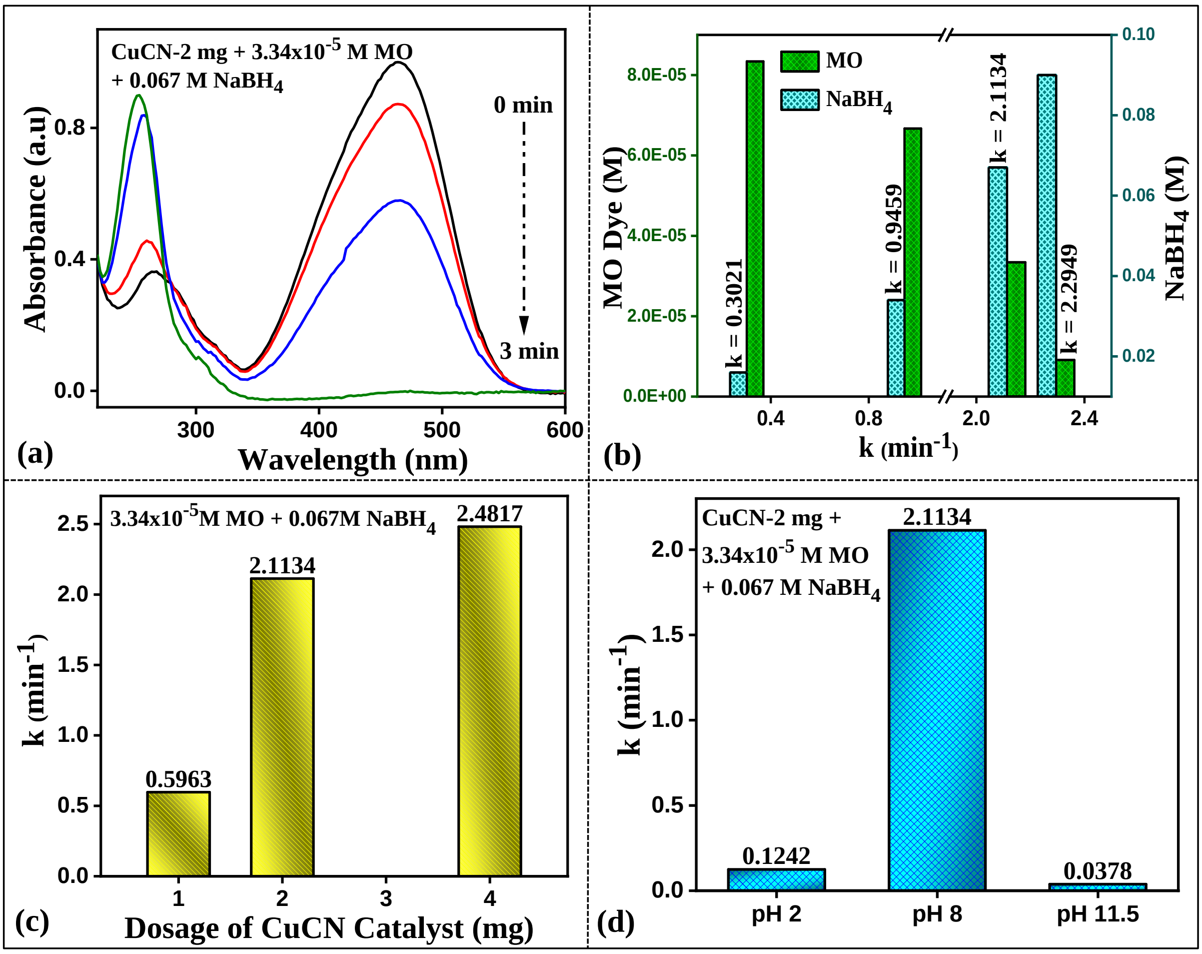

Fig. 6.78: *(a) Absorption spectra of MO dye in presence of CuCN and $NaBH_4$; bar graph plots showing rate constant values in presence of (b) varying concentrations of MO and $NaBH_4$, (c) different dosages of CuCN, (d) acidic, neutral and basic pH*

6.6.2.1. Effect of various parameters on the catalytic activity:

Fig. 6.78(a) shows the absorption spectra of 0.03 mM MO in presence of 0.067 M of $NaBH_4$ and 2 mg CuCN catalyst. The bar graph plot shown in **Fig. 6.78(b)** depicts the rate constant values calculated at different concentrations of MO and $NaBH_4$ keeping the CuCN dosage fixed at 2 mg are shown. For the lowest concentration of MO dye, i.e. 0.009 mM, 2 mg

CuCN could achieve 100% degradation within 3 min. With gradual increase in the dye concentration from 0.009 mM to 0.08 mM and simultaneous decrease in the $NaBH_4$ concentration from 0.09 M to 0.016 M, the reduction rate of MO decreases significantly. Next, the $NaBH_4$ and MO concentrations were fixed at 0.067 M and 0.03 mM respectively while the CuCN catalyst dosage was varied as 1, 2, and 4 mg. The corresponding bar graph plot is given in **Fig. 6.78(c)**. With increase in CuCN amount, the rate constant values show a significant increment.

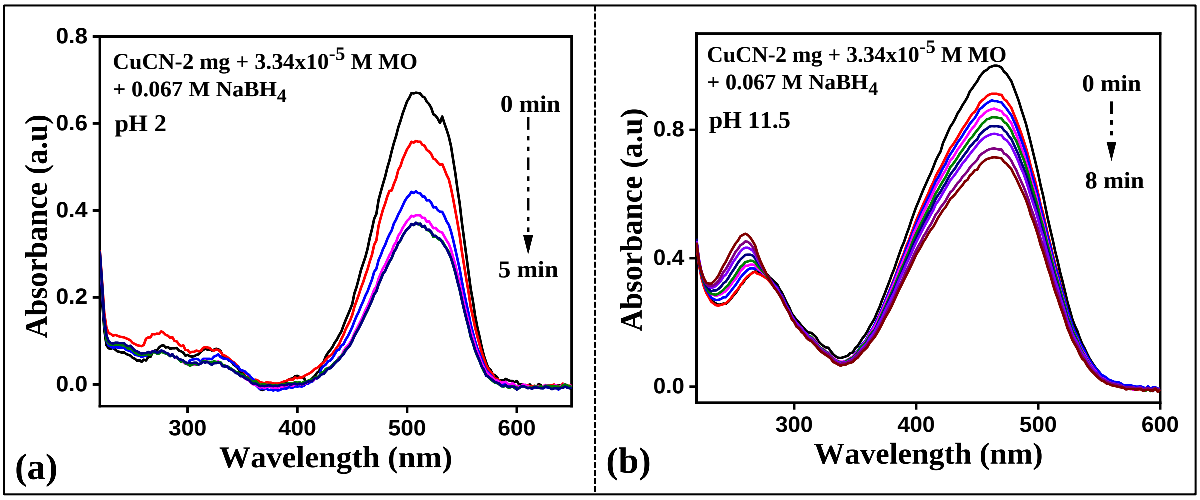

***Fig. 6.79**: Absorption spectra of 0.03 mM MO dye in presence of 0.067 M $NaBH_4$ and 2 mg CuCN at (a) acidic pH value of 2, and (b) basic pH value of 11.5*

For the pH variation studies, few drops of 0.1 M HCl and 0.1 M of NH_4OH were added into the reaction solution to make the pH 2 and 11.5 respectively. At acidic pH, the orange colour of the MO solution quickly turned red along with noticeable shift in the characteristic UV peak to a higher wavelength of 510 nm; whereas no visible change was observed at basic pH. It can be seen from the bar graph plot in **Fig. 6.78(d)** that in presence of 2 mg CuCN and 0.067 M $NaBH_4$, the reduction rate of 0.03 mM MO is significantly hindered, both at acidic and basic pH. The corresponding absorption spectra of MO at pH 2 and 11.5 are exhibited in **Fig. 6.79(a,b)**, respectively. The rate constant values for all these variations in the reaction parameters are listed in **Table 6.9**.

The NiCN catalyst was similarly employed for the reduction of MO dye. For 2 mg NiCN catalyst dosage, two variations in the concentration of $NaBH_4$ (0.067 M and 0.034 M) and MO (0.03 mM and 0.06 mM) were performed. The absorbance spectra of 0.03 mM MO in presence of 0.067 M $NaBH_4$ and 2 mg NiCN is shown in **Fig. 6.80(a)**. The bar graph plot in **Fig. 6.80(b)** helps to elucidate the rate constant values which are listed in **Table 6.9**.

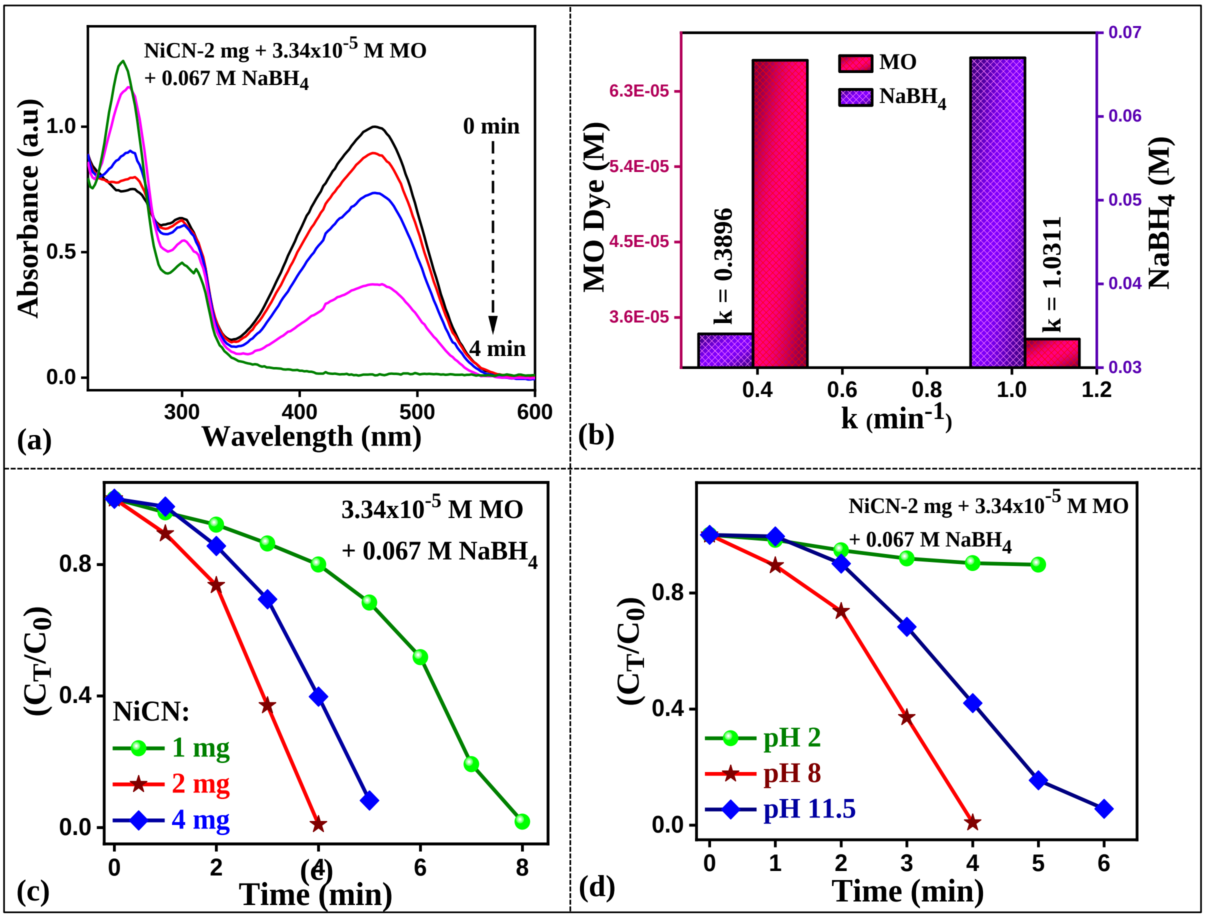

Fig. 6.80: (a) Absorption spectra of 0.03 mM MO and 0.067 M $NaBH_4$ in presence of 2 mg NiCN, (b) bar graph plot showing rate constant values for variation in MO dye and $NaBH_4$ concentration, (c) intensity ratio plot for variation in NiCN catalyst amount, and (d) intensity ratio plot for variation in pH values

Furthermore, the effect of catalyst dosage on the reaction kinetics was also studied by varying the amount of NiCN and fixing the concentrations of MO and $NaBH_4$ to 0.03 mM and 0.067 M, respectively. It can be speculated from the intensity ratio plot (C_T/C_0) shown in **Fig. 6.80(c)** that degradation rate increased considerably at a higher catalyst dosage of 4 mg compared to that observed for 1 mg NiCN. However the best reduction rate was observed at 2 mg NiCN dosage. The ‘k’ value decreases significantly at 4 mg dosage (0.4399 min^{-1}) possibly due to the agglomeration of the catalyst. Variation in pH was also performed for the NiCN catalyst following similar procedure like CuCN. From the C_T/C_0 plot (shown in **Fig. 6.80(d)**), it can be observed that the reduction rate is greatly hindered at both these pH values. The rate constant values listed in **Table 6.9** confirm these observations.

The absorption spectra given in **Fig. 6.81(a)** and **Fig. 6.81(b)** show the reduction of 0.03 mM MO dye in presence of 2 mg pristine GCN and in absence of any catalyst. The $NaBH_4$

concentration in all cases is 0.067 M. It can be observed that in both cases, negligible amount of reduction takes place suggesting the inefficiency of pure GCN as a catalyst material. **Fig. 6.81(c)** shows the bar graph depicting rate constant values of all the catalysts and no catalyst. The associated rate constant values are tabulated in **Table 6.9** and are also evident from the bar graph. Experimental results confirm that CuCN is the most efficient catalyst of all in its ability to degrade MO.

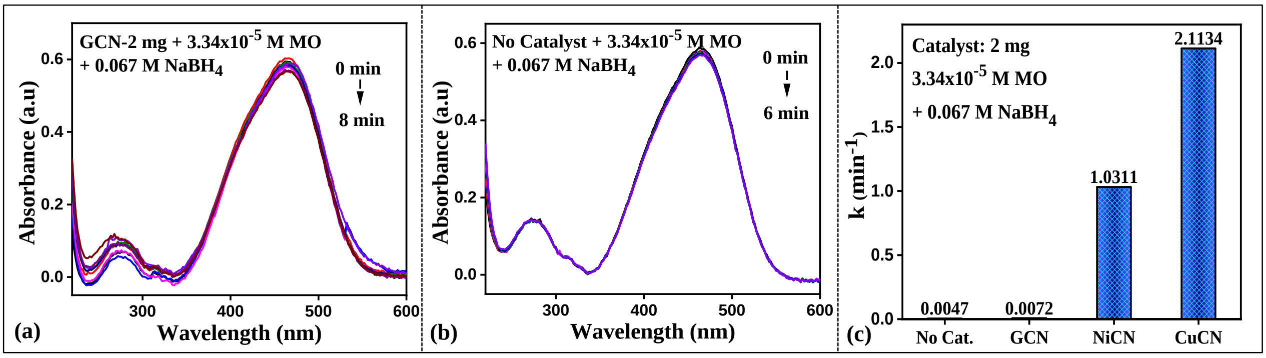

Fig. 6.81: Absorption spectra of 0.03 mM MO and 0.067 M NaBH$_4$ in presence of (a) 2 mg pure GCN, (b) in absence of any catalyst; (c) bar graph plot showing the rate constant values for different catalysts

6.6.3. Catalytic reduction of methyl red (MR) by CuCN and NiCN:

MR is an azo group containing anionic dye used in large-scale in textile and paper printing industries [340]. This potential carcinogenic and mutagenic toxic pollutant can cause many detrimental effects on human body like respiratory distress, irritation in eyes and skin, and can also affect the digestive tract if inhaled or swallowed accidentally [340]. The CuCN catalyst was utilized for the reduction of MR dye following the same procedure. MR at a neutral to basic pH exhibits an intense peak at 431 nm [341] which gives its stark reddish-yellow colour.

6.6.3.1. Effect of various parameters on the catalytic activity:

It can be observed from the absorption spectra given in **Fig. 6.82(a)** that 2 mg CuCN catalyst can degrade 0.03 mM MR dye within 4 min in presence of 0.067 M NaBH$_4$. The bar graph plot shown in **Fig. 6.82(b)** reveals that with increase in MR concentration and simultaneous decrease in NaBH$_4$ concentration, there is not much significant decrease in the rate of reduction. The variation in dye and NaBH$_4$ concentration is performed by keeping the CuCN dosage constant at 2 mg. The rate constant values obtained after linear fitting of the rate kinetics plots are listed in **Table 6.9**.

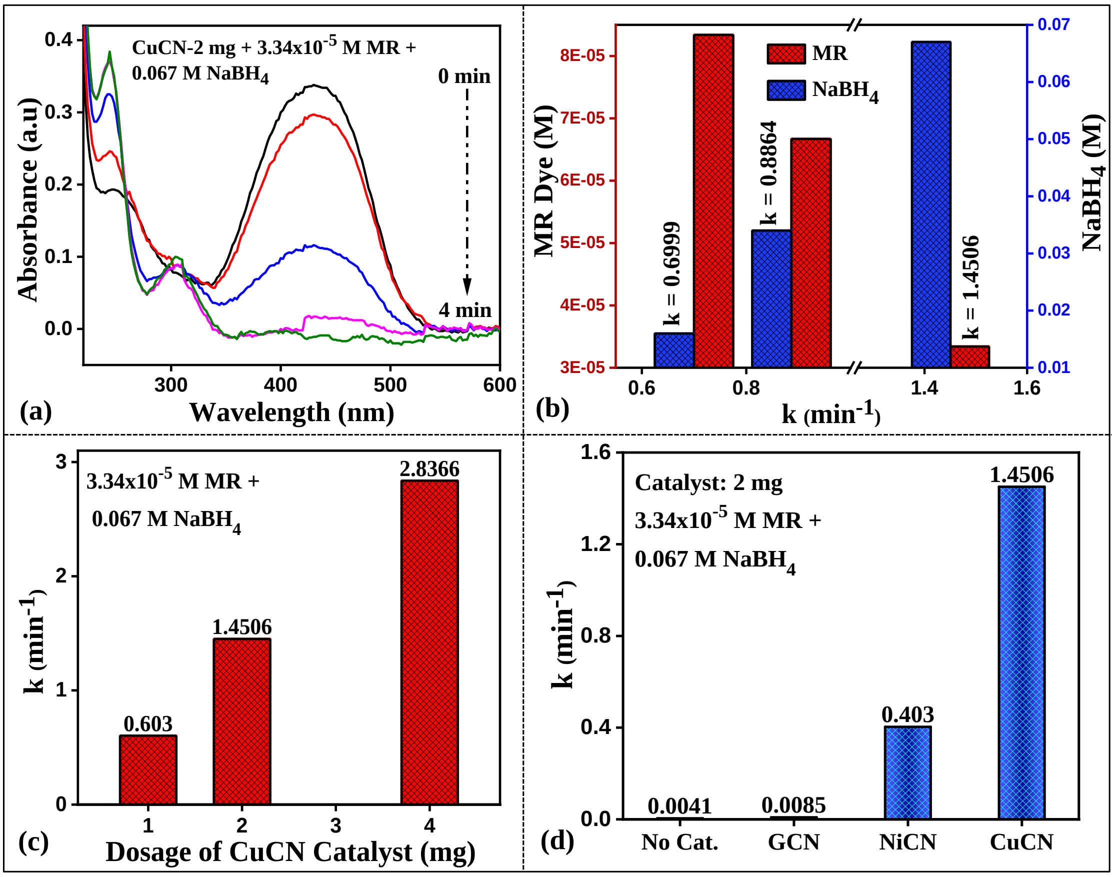

Fig. 6.82: *(a) Absorption spectra of MR dye in presence of CuCN and $NaBH_4$; bar graph plots in presence of (b) varying concentrations of MR and $NaBH_4$, and (c) different dosages of CuCN, (d) bar graph plot of rate constant values in presence of different catalysts and in absence of any catalyst*

The effect of amount of CuCN catalyst on the catalytic reduction of MR dye has further been evaluated experimentally. It has been observed that on lowering the catalyst dosage to 1 mg, reduction rate of 0.03 mM MR decreases; whereas increasing the CuCN amount to 4 mg, nearly 100% reduction of the same concentration of MR is achieved within few minutes. The bar graph plot given in **Fig. 6.82(c)** confirms the observation. The absorption spectra in **Fig. 6.83(b,c)** show the catalytic activity in reduction of MR in presence of 2 mg GCN and in absence of any catalyst. No sign of reduction is observed in these two cases. However, 2 mg NiCN can degrade 0.03 mM MR within 7 min in presence of 0.067 M $NaBH_4$ as observed from **Fig. 6.83(a)**. The bar graph showing the rate constant values are depicted in **Fig. 6.82(d)**. This observation again proves that CuCN is the most efficient catalyst in reduction of MR dye.

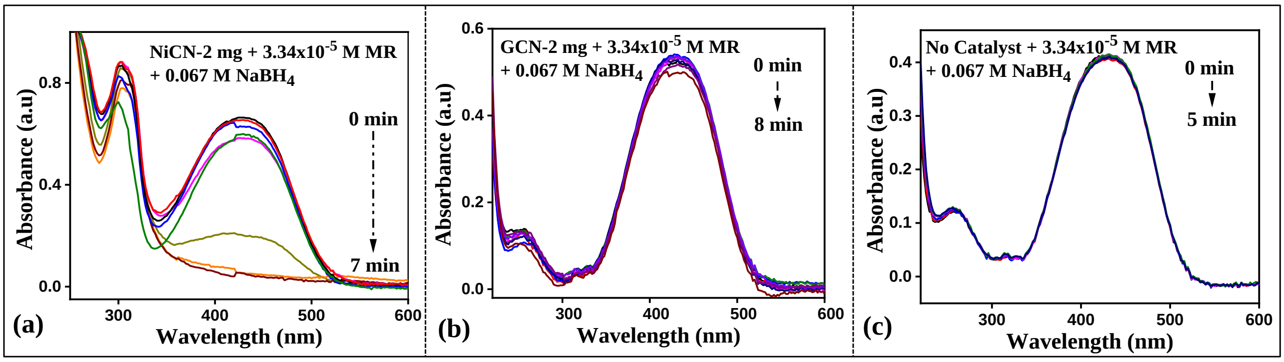

***Fig. 6.83**: Absorption spectra of 0.03 mM MR dye in presence of 0.067 M NaBH$_4$ and (a) 2 mg NiCN, (b) 2 mg pristine GCN, and (c) in absence of any catalyst*

6.6.4. Catalytic reduction of Congo red (CR) by CuCN and NiCN:

CR is a toxic carcinogenic anionic benzidine-based azo dye released from a number of industries including textile, plastic, tannery, paper, food and distilleries [342]. This pollutant is extremely hazardous to living organisms and can cause severe effects on human health like gastrointestinal disorders, diarrhoea, allergy, liver tumour etc. [146]. CR dye exhibits two prominent absorption peaks at 490 nm 340 nm in aqueous medium before the starting of catalysis reaction. The band at 490 nm arises due to π-π* transition whereas that at 340 nm occurs due to the n- π* transition along the -N=N- azo bond of CR [343]. In presence of catalyst and NaBH$_4$, the intensity of these two main peaks decreases gradually whereas a new peak emerges at 250 nm due to the formation of free amino (-NH$_2$) based intermediates as a result of the reduction of CR that occurs at the -N=N- azo site [146].

6.6.4.1. Effect of various parameters on the catalytic activity:

It has been observed from **Fig. 6.84(a)** that 2 mg CuCN can degrade 0.03 mM CR within 4 min in presence of 0.067 M NaBH$_4$. The concentration of CR and NaBH$_4$ were simultaneously varied to study their effect on the reduction activity. The rate constant values obtained from the ln(C_0/C_T) plots are depicted as bar graphs in **Fig. 6.84(b)** and the values are listed in **Table 6.9**.

The effect of catalyst dosage on the degradation activity of CR was performed by varying the CuCN catalyst amounts as 1, 2, and 4 mg, and simultaneously keeping the concentration of CR and NaBH$_4$ fixed at 0.03 mM and 0.067 M, respectively. The bar graph plot shown in **Fig. 6.84(c)** gives the calculated rate constant 'k' values. With increase in CuCN amount, the rate constant values increase proportionately. Hence it can be stated that the rate of reduction of CR increases with increase in $NaBH_4$ concentration, increase in catalyst amount, and decrease in CR concentration.

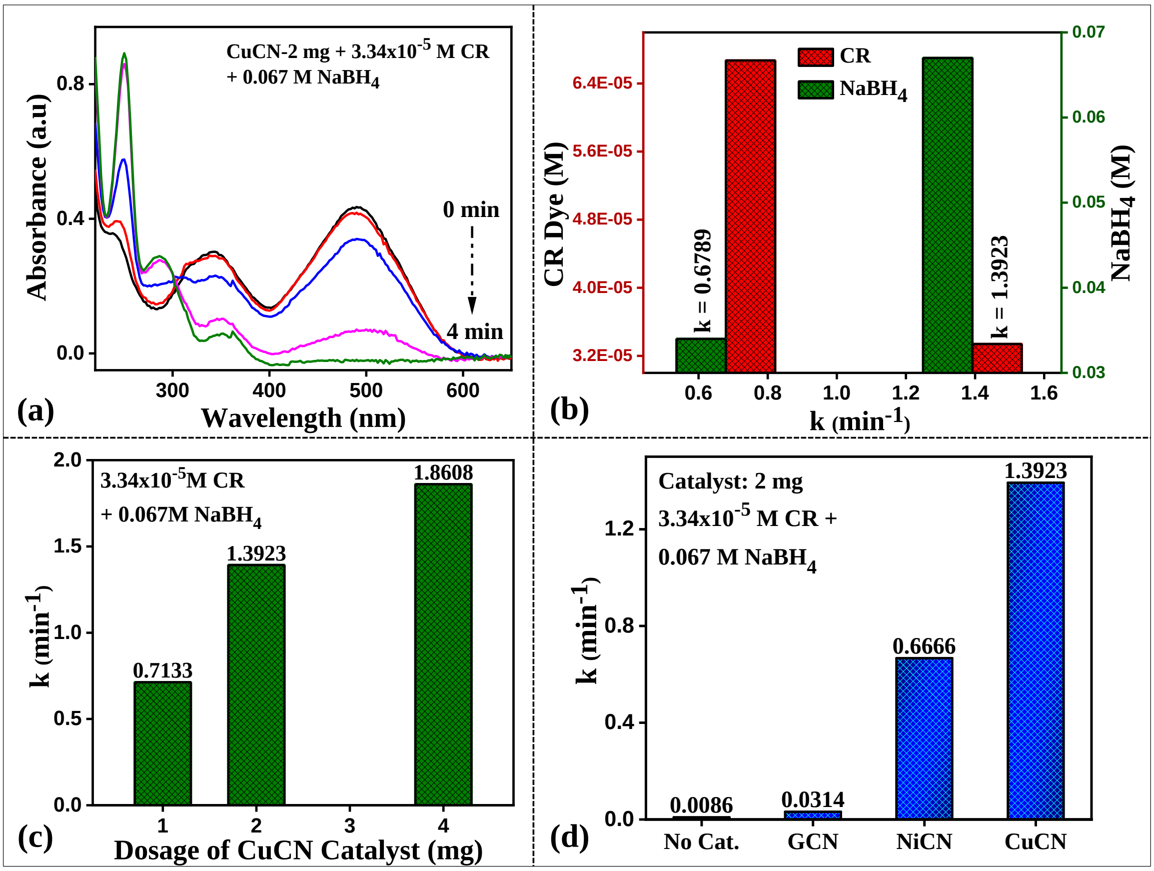

***Fig. 6.84**: (a) Absorption spectra of CR dye in presence of CuCN and $NaBH_4$; bar graph plots showing rate constant values in presence of (b) varying concentrations of CR and $NaBH_4$, and (c) different dosages of CuCN, (d) bar graph plot of rate constant values in presence of different catalysts and in absence of any catalyst*

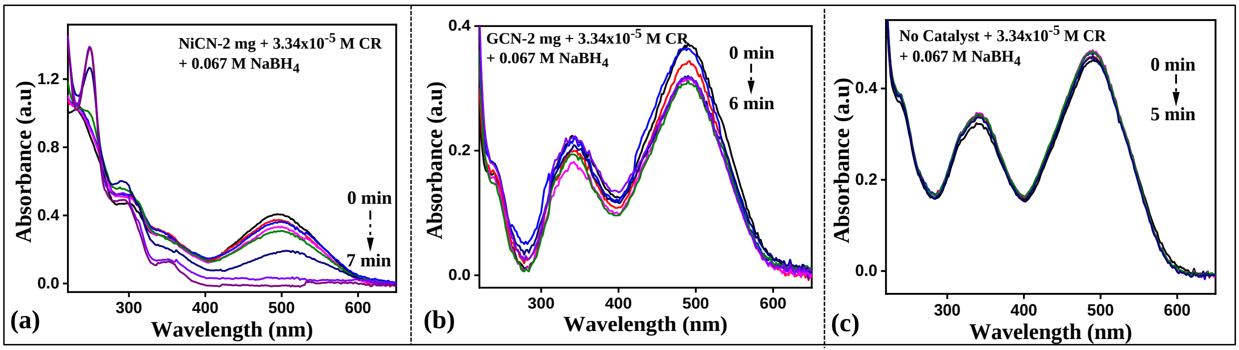

***Fig. 6.85**: Absorption spectra of 0.03 mM CR and 0.067 M $NaBH_4$ in presence of (a) 2 mg NiCN, (b) 2 mg pure GCN, and (c) in absence of any catalyst*

The absorption spectra of 0.03 mM CR in presence of 2 mg NiCN and 2 mg GCN in presence of 0.067 M $NaBH_4$ and that of the same concentration of CR and $NaBH_4$ without any catalyst are shown in **Fig. 6.85(d),(e),** and **(f),** respectively. The respective rate constant values can be obtained from the bar graph given in **Fig. 6.84(d)** for all samples. From this observation, it can be inferred that CuCN is again the most effective catalyst in reduction of CR.

6.6.5. Catalytic reduction of methylene blue (MB) by CuCN and NiCN:

MB is a thiazin group containing cationic dye emitted into the water environment primarily from paper printing and silk and cotton dying industries [344]. The complex structure of MB along with its impressive solubility in water medium and high stability against all conditions renders its non-biodegradable toxic nature [344]. MB can cause many adverse effects on human health like jaundice, cyanosis, diarrhoea, tissue necrosis and heart diseases [148]. The UV spectrum of unprotonated MB shows two main peaks situated at 611 nm and 663 nm which give its characteristic bright blue colour [345]. In presence of catalyst, MB gets reduced to its colourless non-toxic form which is called leucomethylene blue (LMB) [345]. The effect of variation in the MB dye concentration along with variation in $NaBH_4$ concentration was performed.

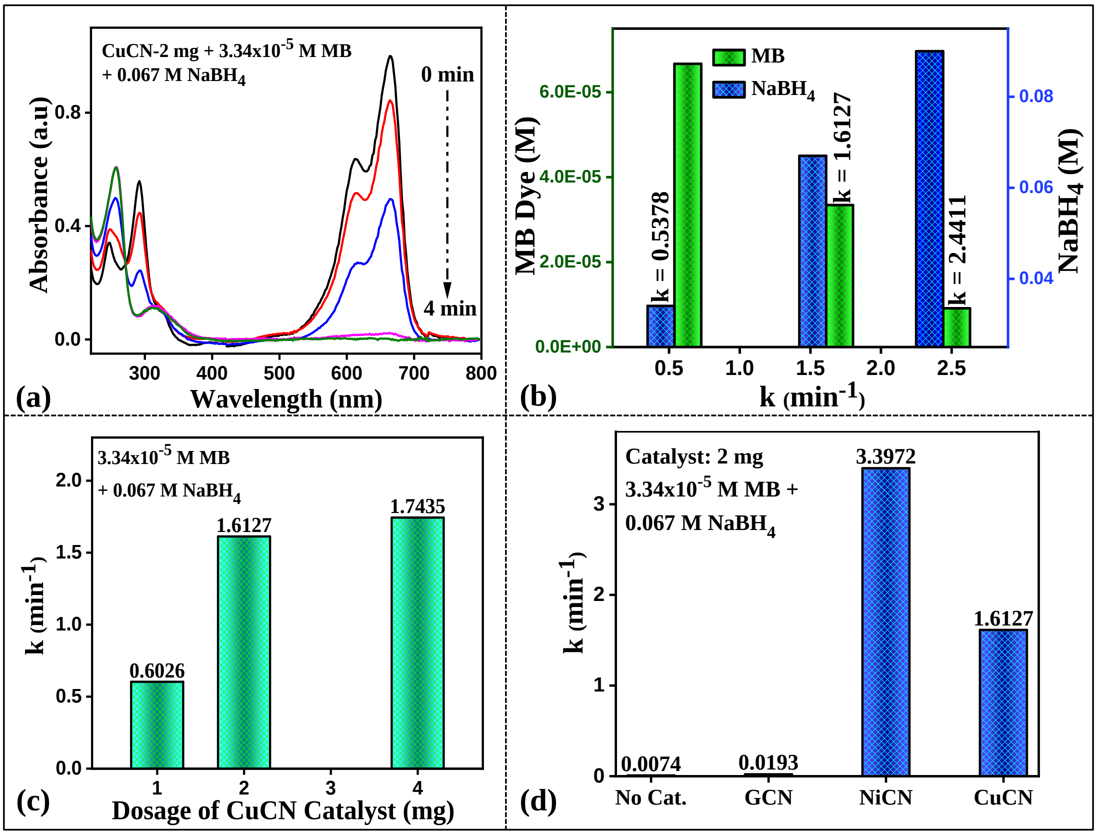

***Fig. 6.86**: (a) Absorption spectra of MB dye in presence of CuCN and $NaBH_4$; bar graph plots showing rate constant values in presence of (b) varying concentrations of MB and $NaBH_4$, and (c) different dosages of CuCN, (d) bar graph plot of rate constant values in presence of different catalysts and in absence of any catalyst*

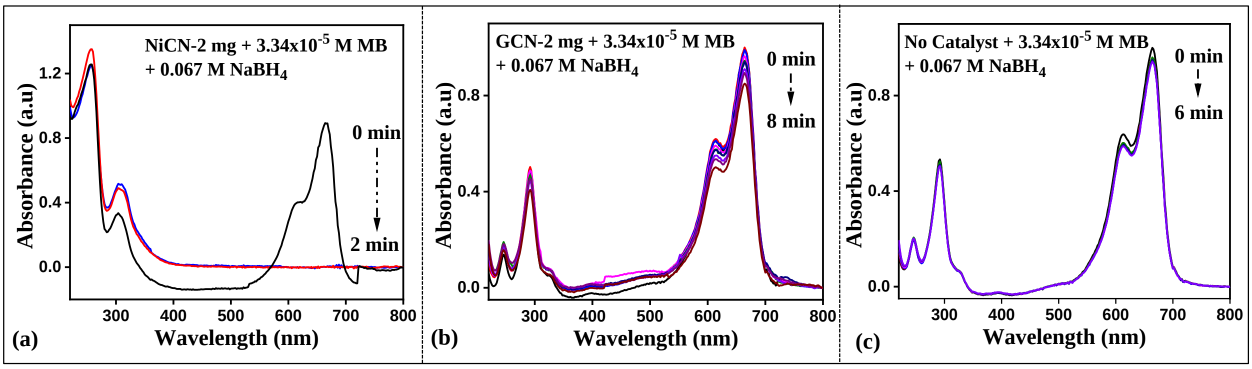

***Fig. 6.87**: Absorption spectra of 0.03 mM MB dye in presence of 0.067 M $NaBH_4$ and (a) 2 mg NiCN, (b) 2 mg pristine GCN, and (c) in absence of any catalyst*

6.6.5.1. Effect of various parameters on the catalytic activity:

The absorption spectrum in **Fig. 6.86(a)** shows that 2 mg CuCN takes 4 min to completely degrade 0.03 mM of MB dye. The effect of variation in MB dye and $NaBH_4$ concentrations are evident from the bar graph plot given in **Fig. 6.86(b)**, which confirms that reduction rate decreases proportionately with increase in the concentration of MB and simultaneous decrease in the $NaBH_4$ concentration. The rate constant values as obtained are shown in the bar graph plot as well as listed in **Table 6.9**.

The effect of catalyst dosage on the reduction of MB dye was also examined in presence of 1, 2, and 4 mg catalyst amounts. On increasing the catalyst amount from 1 mg to 4 mg, decolouration of MB dye proceed at a much faster rate. The bar graph plots showing the rate constant values for all catalyst dosages are given in **Fig. 6.86(c)**.

MB dye remains non-degradable in presence of only 0.067 M $NaBH_4$ and no catalyst as evident from the absorption spectrum in **Fig. 6.87(c)**. In presence of bare GCN, negligible amount of reduction occur up-to 8 min of catalytic activity (**Fig. 6.87(b)**). Interestingly, 2 mg NiCN exhibits superior catalytic activity in reducing 0.03 mM MB within 2 min (**Fig. 6.87(a)**). The rate constant values as obtained for all the catalysts are plotted in the bar graph in **Fig. 6.86(d).** In this case, NiCN sample proved to be the most efficient catalyst among others.

6.6.6. Catalytic reduction of rhodamine B (RhB) by CuCN and NiCN:

RhB, a cationic dye consisting of xanthene group, is one of the most hazardous effluents emitted from textile, paint, cosmetics, paper and leather industries [307]. This synthetic dye when released in the environment can cause carcinogenic effects, neurotoxicity and oxidative stress in humans along with toxicity of the reproductive system [146,147]. If accidentally inhaled or ingested, RhB can also cause irritation in eyes, throat, nose, and skin and also pain in the chest [146]. The intense pink colour of the RhB dye aqueous solution occurs due to the prominent absorption band at 554 nm in the UV spectrum. RhB possess a conjugated xanthene structure before the onset of catalytic activity [346]. In presence of catalyst and NaBH$_4$, this conjugated xanthene structure gets destroyed leading to the formation of the leuco form of RhB and eventual decolourisation of the dye [[346]. This is evident from the decrease in the intensity of the characteristic peak at 554 nm along with the simultaneous generation of a new peak at 237 nm which confirms the de-ethylation phenomenon of RhB. The catalysts and NaBH$_4$ are capable of forming aromatic amines (-NH$_2$) groups N-de-ethylated molecules at the -N(C$_2$H$_5$)$_2$ site where the de-ethylation of RhB takes place [347]. The origin of the peak at 237 nm is due to these de-ethylated compounds formed as a result of reduction of RhB [146].

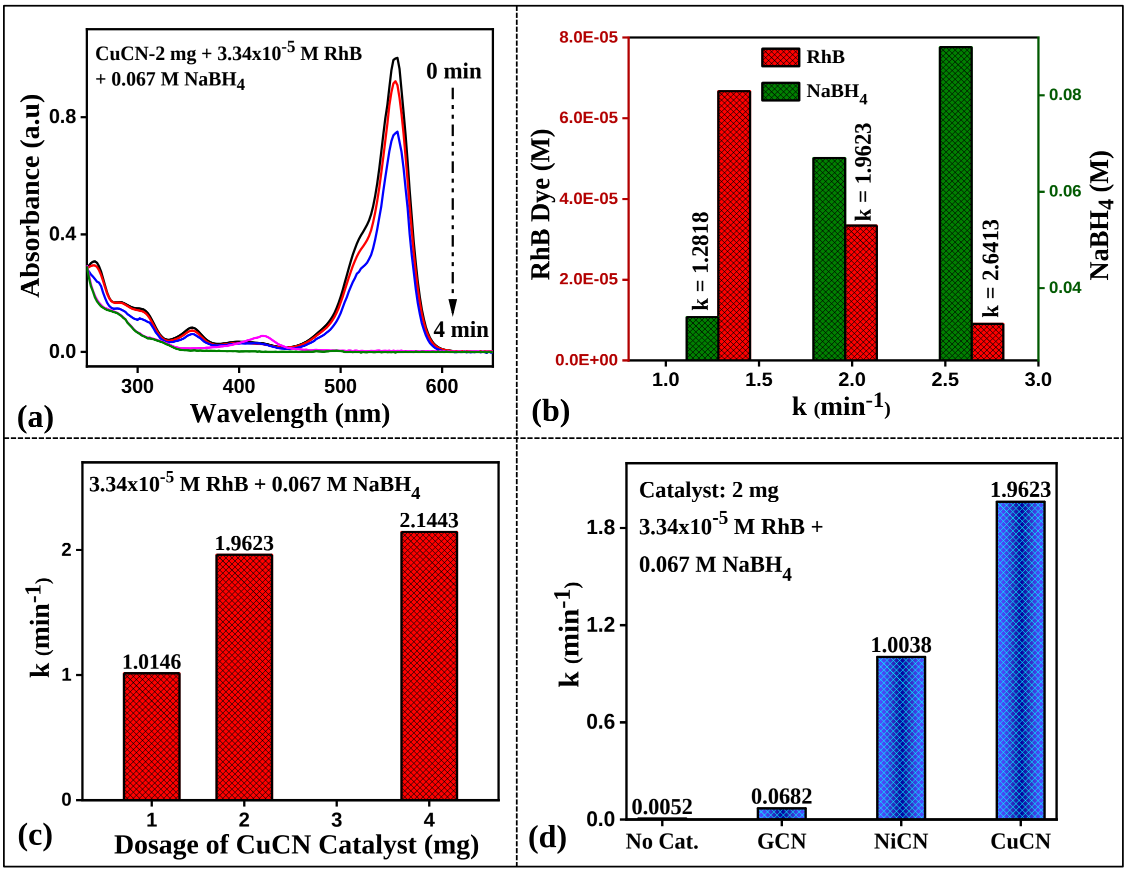

Fig. 6.88*: (a) Absorption spectra of RhB dye in presence of CuCN and NaBH$_4$; bar graph plots showing rate constant values in presence of (b) varying concentrations of RhB and NaBH$_4$, and (c) different dosages of CuCN, (d) bar graph plot of rate constant values in presence of different catalysts and in absence of any catalyst*

6.6.6.1. Effect of various parameters on the catalytic activity:

At first, the concentrations of RhB were varied as 0.009, 0.03, and 0.06 mM; while the $NaBH_4$ concentrations were simultaneously changed from 0.09 M, 0.067 M to 0.034 M respectively. The absorption spectrum of 0.03 mM RhB is shown in **Fig. 6.88(a).** The CuCN catalyst amount was kept constant at 2 mg. In all the cases, a certain amount of induction period is noticed, which increases with increase in dye concentration. After the induction time, the RhB dye quickly degrades to colourless non-toxic compound. The bar graph plot showing the rate constant values in presence of different concentrations of $NaBH_4$ and RhB dye is plotted in **Fig. 6.88(b)**.

The effect of catalyst dosage on the catalytic reduction rate was also studied. The bar graph plot shown in **Fig. 6.88(c)** reveals the catalytic activity of 1, 2, and 4 mg CuCN in complete degradation of 0.03 mM RhB in presence of 0.067 M $NaBH_4$. The rate constant values as obtained for all the variations are listed in the bar graph as well as in **Table 6.9**.

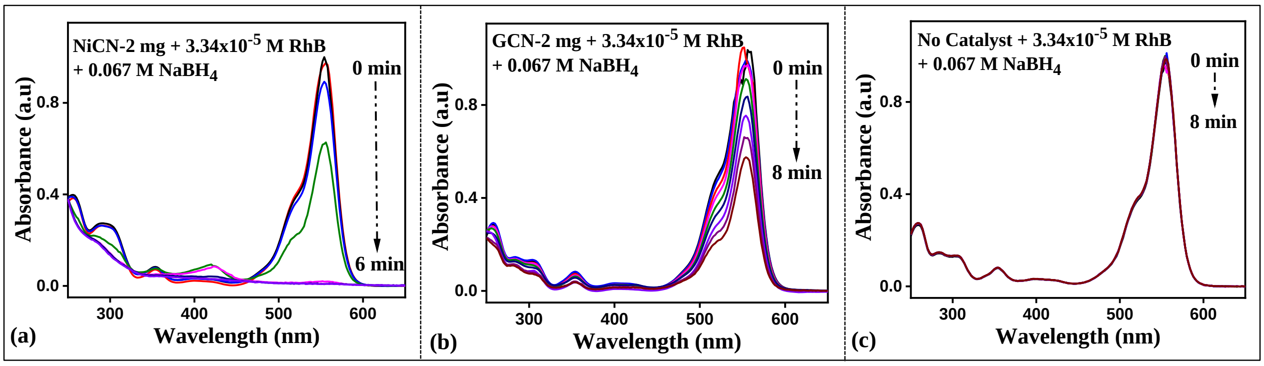

***Fig. 6.89**: Absorption spectra of 0.03 mM RhB dye in presence of 0.067 M $NaBH_4$ and (a) 2 mg NiCN, (b) 2 mg pristine GCN, and (c) in absence of any catalyst*

It can be seen from the absorption spectra in **Fig. 6.89(c)** that RhB does not undergo any reduction in presence of $NaBH_4$ solely and in absence of any catalyst. However, RhB exhibits considerable degradation in presence of 2 mg pristine GCN as observed from the absorption spectra in **Fig. 6.89(b)**. Though the rate of reduction is significantly inferior as compared to that in presence of CuCN and NiCN; however the degradation rate cannot be ignored. The absorption spectra of 0.03 mM RhB in presence of 2 mg NiCN is shown in **Fig. 6.89(a)**. The rate constant values as calculated for no catalyst, GCN, NiCN and CuCN are observed from the bar graph in **Fig. 6.88(d)**. The CuCN catalyst again proves to be highly efficient in degrading RhB dye among all other samples.

6.6.7. Catalytic reduction of rose Bengal (RB) by CuCN and NiCN:

RB is a bright pink coloured anionic xanthene dye which is extensively released from insecticides manufacturing industries, dyes and printing industries and textile industries [348]. It can cause serious deleterious effects on the stomach, liver and corneal epithelium of human beings [349]. In case of accidental inhalation, ingestion or contact with skin, it can result in irritation, itching sensation and inflammation. In aqueous medium RB exhibits a broad absorption band at 549 nm.

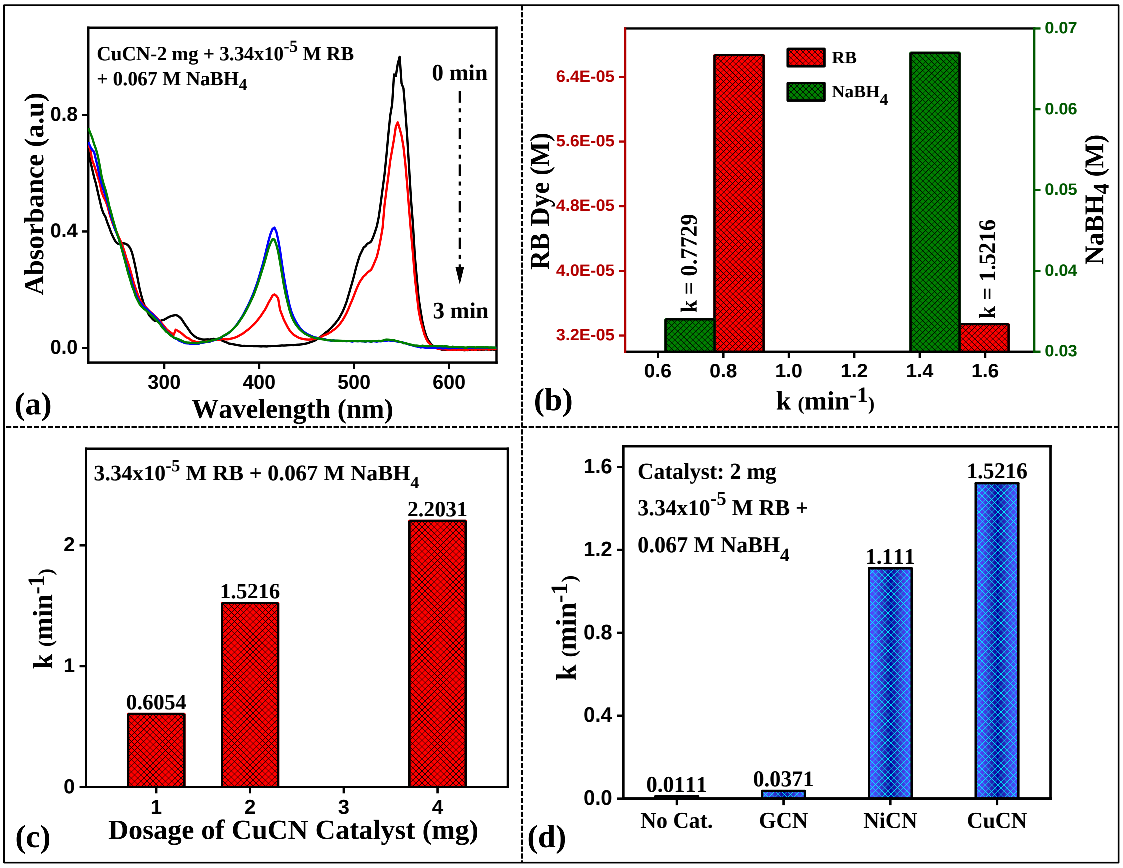

Fig. 6.90: (a) Absorption spectra of RB dye in presence of CuCN and NaBH$_4$; bar graph plots showing the rate constant values in presence of (b) varying concentrations of RB and NaBH$_4$, and (c) different dosages of CuCN, (d) bar graph plot of rate constant values in presence of different catalysts and in absence of any catalyst

6.6.7.1. Effect of various parameters on the catalytic activity:

The absorption spectra of 0.03 mM RB dye in presence of 2 mg CuCN catalyst and 0.067 M NaBH$_4$ is shown in **Fig. 6.90(a)**. The intensity of the characteristic peak at 549 nm decreases with time along with the simultaneous generation of a new peak at 416 nm. The intensity of this peak increases as the catalytic reduction reaction proceeds towards the end. This result is in consistent and well corroborated with the observations by Kumar et al. [350]. The bar graph plots showing the rate constant values for varying concentrations of RB and $NaBH_4$ keeping the catalyst amount unchanged is shown in **Fig. 6.90(b)**.

The effect of varying dosage of CuCN catalyst on the RB reduction activity has been performed experimentally. The bar graph plot depicting the rate constant values for all dosages of CuCN (1, 2, and 4 mg) are shown in **Fig. 6.90(c)**. With increase in amount of catalyst, the rate constant values increase considerably. All these ‘k’ values are also given in **Table 6.9**.

Fig. 6.91(a-c) shows the absorption spectra of 0.03 mM RB in presence of 2 mg NiCN, 2 mg GCN, and in absence of any catalyst. When only 0.067 M $NaBH_4$ is present in the reaction system without any catalyst, no sign of reduction of RB is observed. Similar result is also observed in presence of 2 mg pure GCN. However, catalytic activity is significantly improved in presence of 2 mg NiCN. The rate constant values are depicted in the bar graph of **Fig. 6.90(d)**. This observation again infers that CuCN is the most effective catalyst in reduction of RB dye.

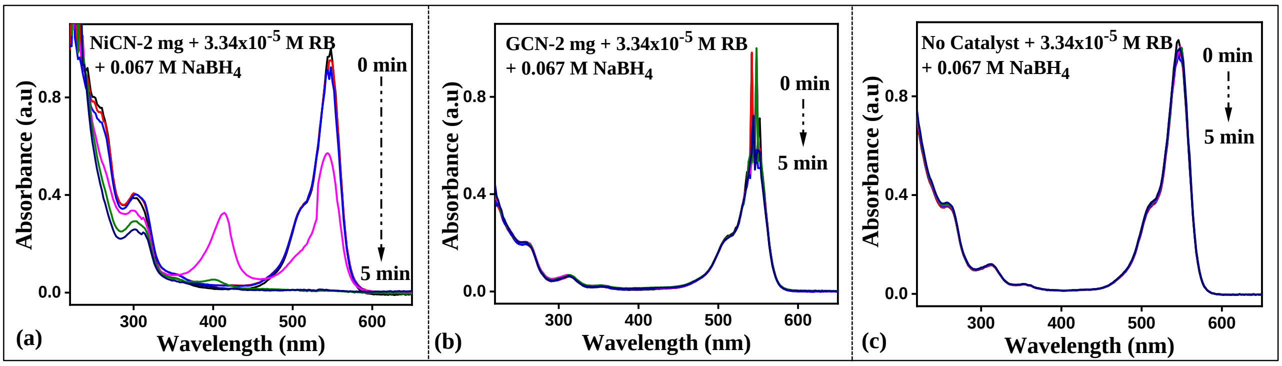

Fig. 6.91*: Absorption spectra of 0.03 mM RB and 0.067 M $NaBH_4$ in presence of (a) 2 mg NiCN, (b) 2 mg pure GCN, and (c) in absence of any catalyst*

6.6.8. Catalytic reduction of mixed dye by CuCN and NiCN:

We performed the catalytic reduction of a mixture of toxic dyes to establish the as-synthesized material as a potential catalyst for its practical utilization in waste-water remediation. Initially, a bright reddish-orange coloured mixture solution consisting of equal molar concentrations of methyl orange, methyl red, and Congo red dyes was prepared and termed as Mixed Dye 1 (Mxd. Dye 1). The UV-Vis absorption bands of MO, MR and CR are at 464 nm, 430 nm, and 490 nm. Due to the very high intensity of the MO dye, the absorption peak of MO supresses the absorption peaks of MR and CR.

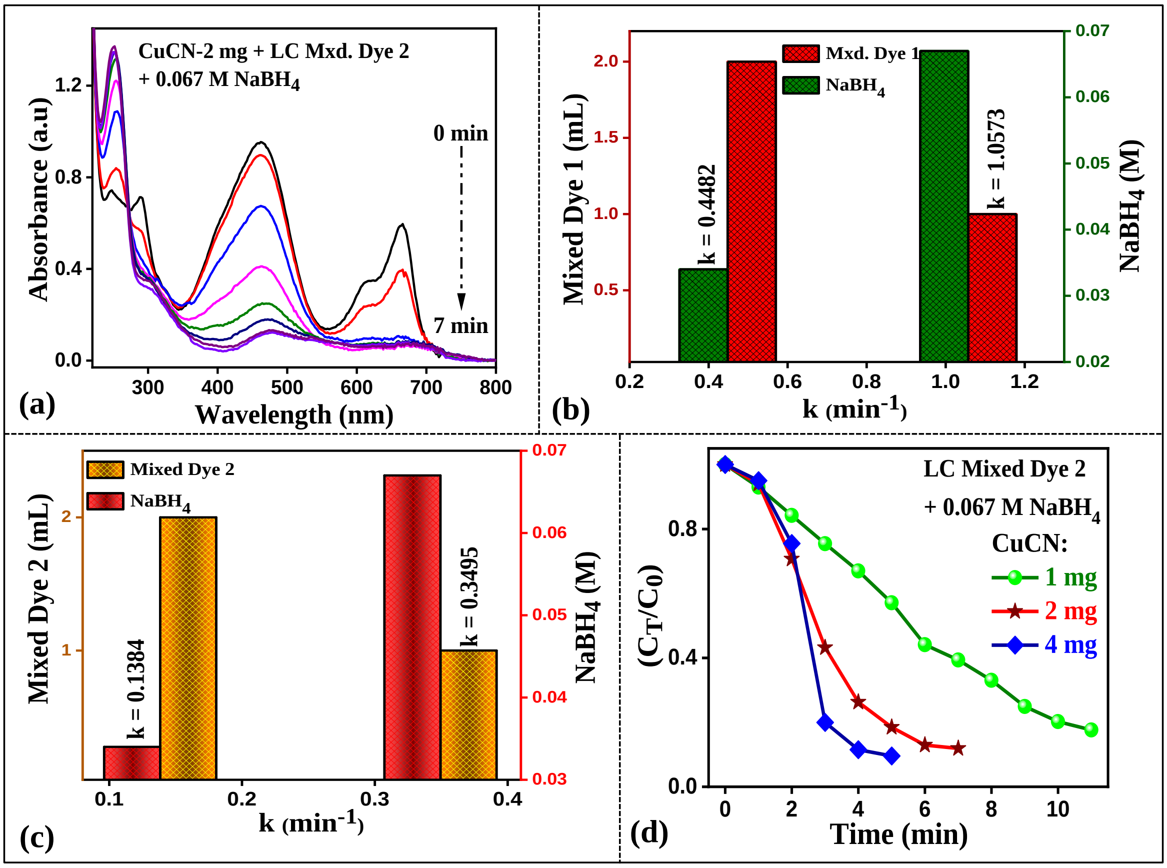

***Fig. 6.92**: (a) Absorption spectra of low concentration (LC) Mxd. dye 2 solution in presence of CuCN and $NaBH_4$; bar graph plots in presence of (b) varying concentrations (low and high: LC and HC) of Mxd. Dye 1 solution and $NaBH_4$, (c) varying concentrations (LC and HC) of Mxd. Dye 2 solution and $NaBH_4$, and (d) intensity ratio plot for different dosages of CuCN for degradation of LC Mxd. Dye 2 solution*

The absorption spectrum of low concentration (LC) Mxd. Dye 1 is shown in **Fig. 6.93(a)** which reveals a dominant peak at 458 nm and this corresponds to the average of the absorption peaks of the three dyes. In presence of 2 mg CuCN and 0.067 M $NaBH_4$, this LC mixed-dye 1 solution gets completely degraded within 6 min. However, on increasing the concentration of this mixture solution (HC), and reducing the $NaBH_4$ concentration, relatively longer time was required for complete degradation (**Fig. 6.93(b)**). The bar graph plot is shown in **Fig. 6.92(b)** and the rate constant values obtained are given in **Table 6.9** and also in the bar graph.

Next, some amount of 0.1 mM MB dye solution was added into Mxd. Dye 1 solution to form a blackish-green coloured mixed solution which was termed as Mxd. Dye 2. The absorption spectra of this Mxd. Dye 2 solution show two distinct bands at 458 nm and 665 nm corresponding to Mxd. Dye 1 solution and MB dye respectively. It can be seen from **Fig. 6.92(a)** that 2 mg CuCN can effectively degrade low concentration (LC) of this dye solution (total amount of solution inside quartz cuvette = 3 mL) within 7 min in presence of 0.067 M $NaBH_4$. 2 mg CuCN takes slightly longer time (14 min) to degrade high concentration (HC) of Mxd. Dye 2 solution in presence of 0.034 M $NaBH_4$ (**Fig. 6.93(c)**). It can be seen from the absorption spectra that the intensity of the MB related peaks decreases much faster than that of the mixed dye solution 1. The corresponding bar graph plot showing the rate constant values for different concentrations of the mixed dye 2 solutions and $NaBH_4$ are shown in **Fig. 6.92(c)**.

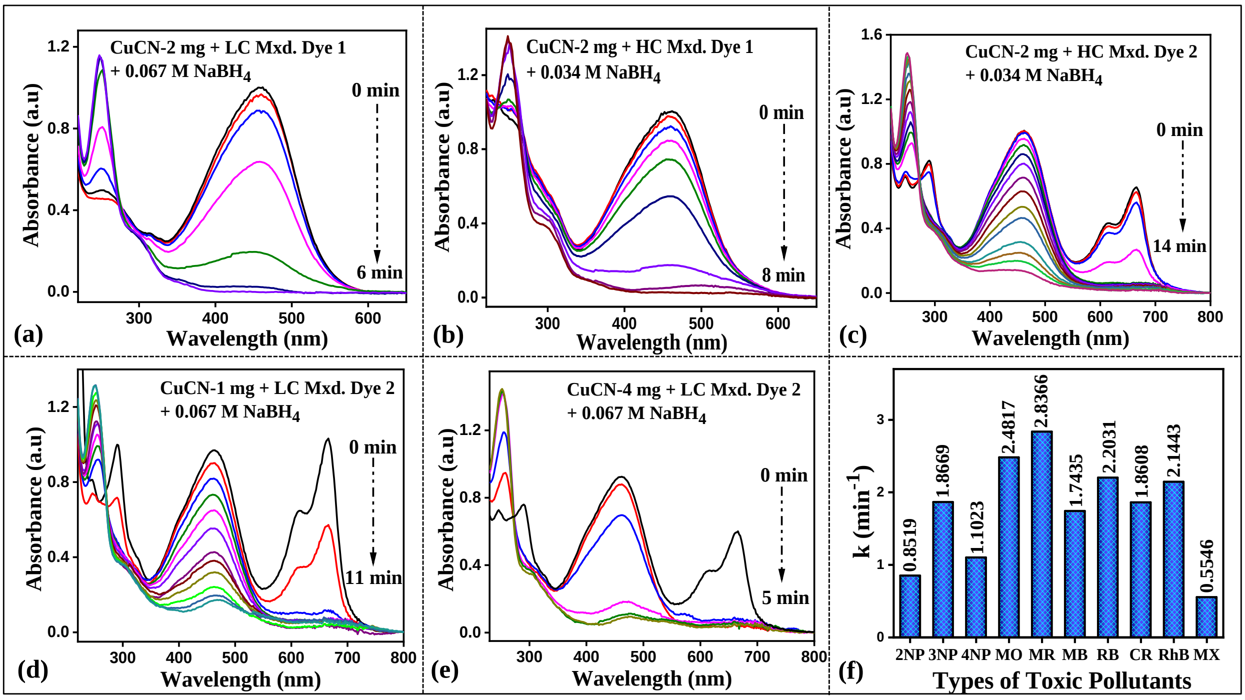

Fig. 6.93: Absorption spectra of (a) low concentration (LC) Mixed dye 1 and 0.067 M $NaBH_4$, and (b) high concentration (HC) Mixed dye 1 and 0.034 M $NaBH_4$ in presence of 2 mg CuCN; (c) absorption spectra of HC Mixed dye 2 in presence of 0.034 M $NaBH_4$ and 2mg CuCN; absorption spectra of LC Mixed dye 2 in presence of 0.067 M $NaBH_4$ and (d) 1 mg CuCN, and (e) 4 mg CuCN. (f) Bar graph plot depicting the rate constant values in degradation of all toxic pollutants by CuCN catalyst [catalyst (CuCN) dose: 4 mg, conc. of NP compounds: 1 mM, conc. of dyes: 0.1 mM, and conc. of $NaBH_4$ stock solution: 0.1 M]

Fig. 6.93(d) and **Fig. 6.93(e)** show the absorption spectra of LC Mxd. Dye 2 solution in 0.067 M $NaBH_4$ and in presence of 1 mg CuCN and 4 mg CuCN respectively. The intensity ratio plots for all catalyst dosages are shown in **Fig. 6.92(d)** and the corresponding rate constant values as acquired are listed in **Table 6.9**. Hence it can be concluded that the rate of reduction of mixed-dye increases with increase in the catalyst dosage and $NaBH_4$ concentration whereas decreases with increase in dye concentration and simultaneous decrease in $NaBH_4$

concentration. A bar graph shown in **Fig. 6.93(f)** depicts the rate constant values for degradation of all toxic pollutants by CuCN catalyst.

Table 6.9. Rate constant values and degradation time of all dye pollutants in presence of pure GCN, CuCN and NiCN catalysts [Concentration of dye stock solutions: 0.1 mM].

Catalyst	**Pollutants**	**Catalyst amount (mg)**	**Conc. of Dyes in cuvette (mM)**	**Conc. of $NaBH_4$ in cuvette (M)**	**Degradation Time (min)**	**Rate Constant (min^{-1})**
CuCN	MO	2	0.03	0.067	3	2.1134
CuCN	MO	2	0.009	0.09	3	2.2949
CuCN	MO	2	0.06	0.034	6	0.9459
CuCN	MO	2	0.08	0.016	10	0.3021
CuCN	MO	1	0.03	0.067	8	0.5963
CuCN	MO	4	0.03	0.067	3	2.4817
CuCN	MO	2	0.03@pH 2	0.067	> 5	0.1242
CuCN	MO	2	0.03@pH 11.5	0.067	> 8	0.0378
NiCN	MO	2	0.03	0.067	4	1.0311
NiCN	MO	2	0.06	0.034	8	0.3896
NiCN	MO	1	0.03	0.067	8	0.3743
NiCN	MO	4	0.03	0.067	5	0.4399
NiCN	MO	2	0.03@pH 2	0.067	> 5	0.0235
NiCN	MO	2	0.03@pH 11.5	0.067	6	0.4677
GCN	MO	2	0.03	0.067	----	0.0072
No Cat.	MO	----	0.03	0.067	----	0.0047
CuCN	MR	2	0.03	0.067	4	1.4506
CuCN	MR	2	0.06	0.034	5	0.8864
CuCN	MR	2	0.08	0.016	5	0.6999
CuCN	MR	1	0.03	0.067	6	0.603
CuCN	MR	4	0.03	0.067	2	2.8366
NiCN	MR	2	0.03	0.067	7	0.403
GCN	MR	2	0.03	0.067	----	0.0085
No Cat.	MR	----	0.03	0.067	----	0.0041
CuCN	CR	2	0.03	0.067	4	1.3923
CuCN	CR	2	0.06	0.034	8	0.6789
CuCN	CR	1	0.03	0.067	7	0.7133
CuCN	CR	4	0.03	0.067	3	1.8608
NiCN	CR	2	0.03	0.067	7	0.6666
GCN	CR	2	0.03	0.067	----	0.0314
No Cat.	CR	----	0.03	0.067	----	0.0086
CuCN	RB	2	0.03	0.067	3	1.5216
CuCN	RB	2	0.06	0.034	5	0.7729
CuCN	RB	1	0.03	0.067	5	0.6054
CuCN	RB	4	0.03	0.067	2	2.2031
NiCN	RB	2	0.03	0.067	5	1.111
GCN	RB	2	0.03	0.067	----	0.0371
No Cat.	RB	----	0.03	0.067	----	0.0111
CuCN	RhB	2	0.009	0.09	3	2.6413
CuCN	RhB	2	0.03	0.067	4	1.9623
CuCN	RhB	2	0.06	0.034	4	1.2818
CuCN	RhB	1	0.03	0.067	5	1.0146
CuCN	RhB	4	0.03	0.067	3	2.1443
NiCN	RhB	2	0.03	0.067	6	1.0038
GCN	RhB	2	0.03	0.067	----	0.0682
No Cat.	RhB	----	0.03	0.067	----	0.0052
CuCN	MB	2	0.009	0.09	3	2.4411
CuCN	MB	2	0.03	0.067	4	1.6127
CuCN	MB	2	0.06	0.034	9	0.5378

CuCN	MB	1	0.03	0.067	7	0.6026
CuCN	MB	4	0.03	0.067	4	1.7435
NiCN	MB	2	0.03	0.067	2	3.3972
GCN	MB	2	0.03	0.067	----	0.0193
No Cat.	MB	----	0.03	0.067	----	0.0074
CuCN	Mxd. Dye 1	2	LC	0.067	6	1.0573
CuCN	Mxd. Dye 1	2	HC	0.034	8	0.4482
CuCN	Mxd. Dye 2	2	LC	0.067	7	0.3495
CuCN	Mxd. Dye 2	2	HC	0.034	14	0.1384
CuCN	Mxd. Dye 2	1	LC	0.067	11	0.1655
CuCN	Mxd. Dye 2	4	LC	0.067	5	0.5546

6.6.9. Discussion on results with plausible reaction mechanism:

The toxic pollutants considered for reduction in the present work can be broadly divided into two categories: anionic and cationic compounds. Rhodamine B and Methylene Blue are cationic dyes whereas Methyl Orange, Methyl Red, Congo Red and Rose Bengal fall under the category of anionic dyes. The Nitrophenol pollutants in presence of $NaBH_4$ form anionic compounds. The primary criterion for $NaBH_4$ induced chemical catalysis reactions is simultaneous adsorption of both the pollutants and $NaBH_4$ on the as-prepared catalyst surface. The next criterion is the relay of electrons from the $NaBH_4$ to the toxic pollutants via the catalyst material [351]. From the above experimental observations it can be clearly stated that the pollutants do not undergo any reduction in absence of catalyst material. The sole presence of $NaBH_4$ is not sufficient to carry out any reduction reaction. This is because of the existence of a very high reaction kinetic barrier between the pollutant compounds and $NaBH_4$ which prevents the transfer of electrons between them and also due to the mutually repelling nature of the negatively charged BH_4^- and 4 nitrophenolate ions [352]. This leads to the important requirement of an efficient catalyst which can effectively participate in the electron-relay process by significantly reducing this huge redox potential difference between $NaBH_4$ and the pollutants. In aqueous medium, $NaBH_4$ undergoes ionization to generate BH_4^- radicals which are highly nucleophilic in nature. They donate electrons to the catalyst material which in turn relays them to the adsorbed pollutants on the catalyst surface. In order to depict the role of $NaBH_4$ as electron donor, electron scavenging test by purging oxygen in the catalytic system was carried out (see **Fig. 6.94(a,b)**).

The CuCN catalyst dispersed solution of 4-NP was purged with oxygen for 5 min before adding the $NaBH_4$ solution to initiate the catalytic reaction. Upon addition of $NaBH_4$, the borohydride ions react with dissolved oxygen in water at a much faster rate than with nitrophenol pollutant [353]. The absorbance graph of 4-NP after oxygen purging in presence of the CuCN catalyst along with the corresponding C_T/C_0 plot is shown in the following figure (**Fig. 6.94(a,b)**). It can be seen from the graphs that upon oxygen purging, an induction period of several minutes was observed along with a decrease in the reaction rate. The catalytic reduction of 4-NP to 4-AP proceeded at a much slower rate in the oxygen-purged system. This observation is similar to the report by Ballauff et al. [354], who suggested the possible phenomenon of dissolved oxygen in water reacting with $NaBH_4$ much readily while 4-NP molecules do not react. Only after maximum oxygen has been consumed will 4-NP get reduced to 4-AP. The presence of oxygen in the system consumes the electrons from the borohydride ions, as a result of which the electron relay effect between $NaBH_4$ and the pollutants via the catalyst will get hampered leading to a decrease in the reduction rate.

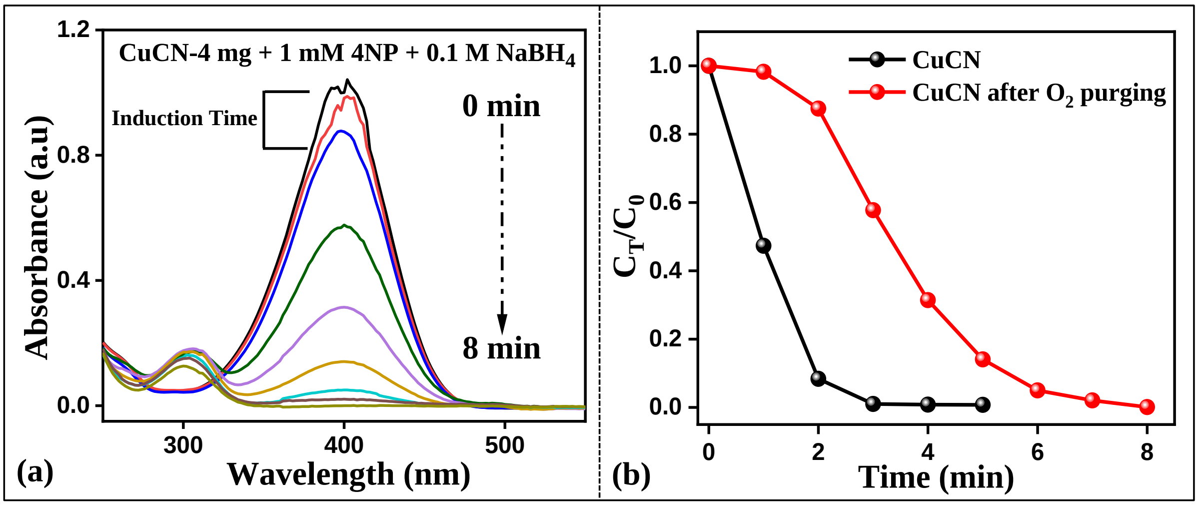

***Fig. 6.94**: (a) Absorbance plot of 4-NP reduction by CuCN catalyst after oxygen purging for 5 min; (b) Corresponding C_T/C_0 plot*

Furthermore, thorough theoretical investigation of the dye degradation mechanisms on the pure GCN and CuCN by means of density functional theory (DFT) based calculations was carried out. From the catalytic performance analysis, it can be observed that CuCN exhibits the best catalytic efficiency in terms of degradation time and rate constant values for the degradation of most of the pollutants. Hence we have selected only CuCN catalyst system to study the plausible mechanism by DFT calculations.

6.6.9.1. Degradation mechanism of 4-Nitrophenol:

The conversion of 4-NP to 4-Aminophenol (4-AP) occurs through an electron relay and subsequent hydrogenation process mediated by the $NaBH_4$ molecule. $NaBH_4$ unambiguously plays the role of electron donor to the catalyst (GCN/CuCN) surface as it dissociates into Na^+ and BH_4^- upon interaction with the catalyst surface and the hence produced H^- play the essential role of the reducing element [355,356]. In contrary, lots of ambiguity is still present about the source of hydrogen atoms present in the converted 4-AP molecule [109]. Arguably, both the H^- from $NaBH_4$ and the H^+ from water solution can be the source for hydrogenation of 4-NP. Both the O and N atom of the Nitro group ($-NO_2$) of 4-NP are highly electron rich negatively charged center. Hence, it is highly unlikely for the H^- ion to take part in the hydrogenation process overcoming the electrostatic repulsive barrier. Yet both the H^+ and H^- have been proposed as the source of hydrogen in the converted 4-AP in literature [355-357].

In this regard, both the reaction pathways involving H^+ from water/ H^- from $NaBH_4$ as the hydrogen source was investigated theoretically including all possible intermediate reaction routes to isolate the most feasible reaction mechanism for the conversion of 4-NP to 4-AP. Strong adsorption of the reactant (4-NP) on the catalyst surface is another necessary condition to secure transfer of the electrons from the catalyst surface to the 4-NP molecule. To begin with, the adsorption of 4-NP molecule in two different orientations (namely, N-down: 4-NP interacts with the catalyst surface via the N atom of $–NO_2$; and N-up: 4-NP interacts with the catalyst surface via the O atom of –OH) on various sites over the GCN surface was carried out. Similar to the experimental observations, the 4-NP molecules only interact with the GCN surface via weak van der Waals interaction without forming any chemical bonds (distance from the GCN surface > 2.5 Å) for both the orientation violating the strong adsorption criteria of the 4-NP molecule with the catalyst surface to complete the electron relay process rendering pure GCN as a poor catalyst to reduce 4-NP into 4-AP. In this regard, rest of the reaction steps for the conversion was ignored for GCN. Decorating the GCN surface with Cu on the other hand significantly improves the scenario as strong exothermic chemisorption was observed for both the N-up and N-down orientations (adsorption energy values -2.57 eV and -1.88 eV respectively).

The adsorption in the N-up orientation is slightly stronger as evident from the adsorption energy values. Subsequently, rest of the reaction pathway was carried out with both H^+ and H^- acting as the hydrogen source for both the adsorbed orientations. Following the reaction pathway involving H^- as the hydrogen source, energy barrier was observed for N-up orientation during the conversion between the reaction intermediates from reaction coordinate (2) to (3) and from (4) to (5) i.e. the first and second hydrogenation process. In contrary, the reaction proceeds smoothly for 4-NP adsorbed in N-down configuration with a very small energy barrier (between the reaction intermediate from reaction coordinate (4) to (5)) expected to be overcome easily with external perturbation during the second hydrogenation process.

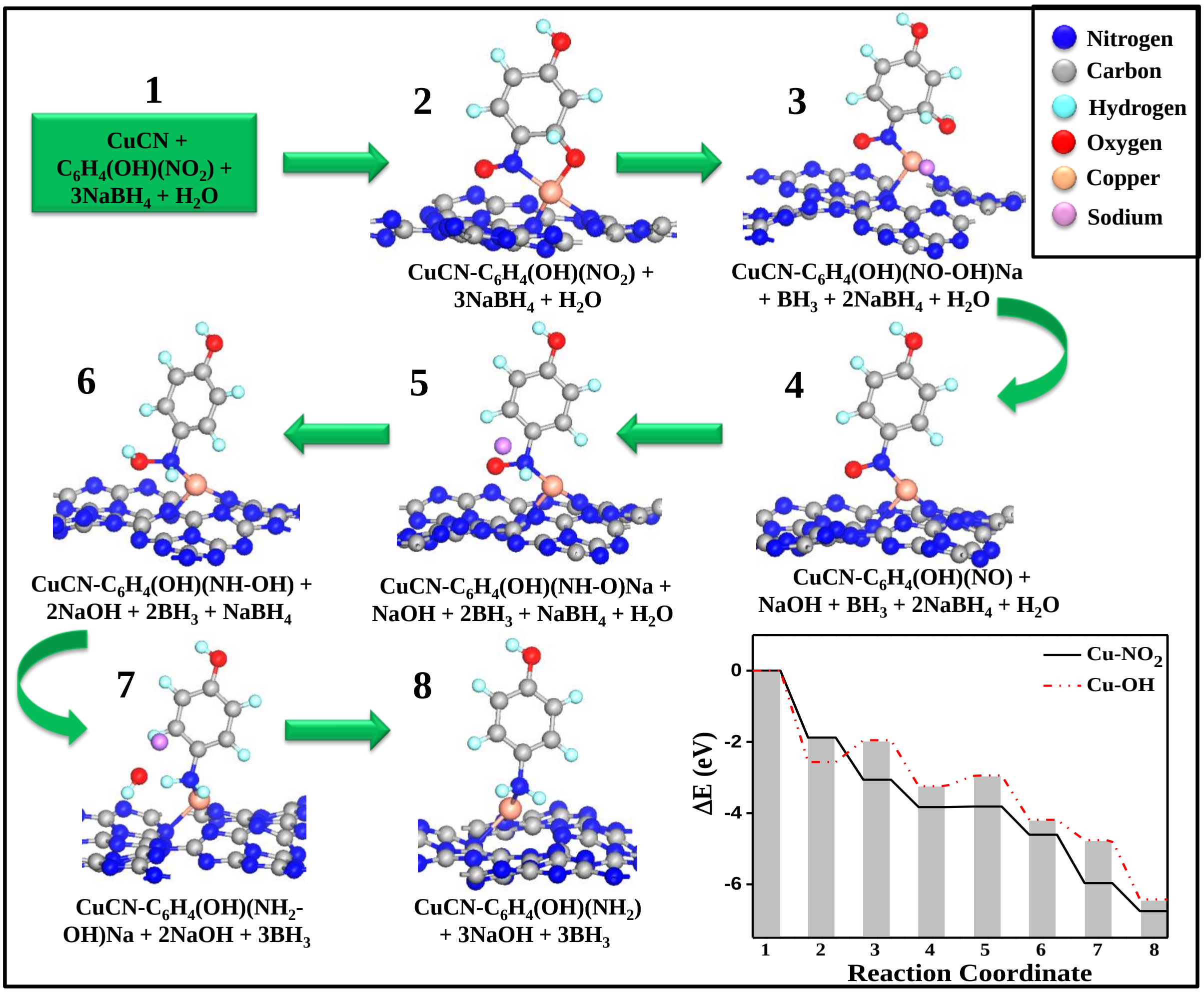

Fig. 6.95: *The reaction intermediates for reaction pathway involving H^- for the energetically favorable N-down (Cu-NO_2) adsorbed configuration of 4-NP on CuCN. The energy profile for both N-up (Cu-OH) and N-down configuration of the whole reaction process is shown at the bottom right corner of the figure.*

Notably, the conversion from reaction coordinate (4) to (5) involves the first hydrogenation of the N atom. While in pristine state the N atom holds a small positive charge over it, after adsorption on the CuCN surface the charge over N becomes negative as shown from the Mulliken population analysis in **Fig. 6.96(a,b)**. The small barrier corresponds to energy required to overcome the electrostatic repulsion for the H^- ion. The energy profiles of the whole reaction pathway involving H^- as the hydrogen source for both the orientations are shown in **Fig. 6.95** along with the atomistic configurations of each reaction intermediate for the preferable reaction pathway i.e. for N-down adsorbed configuration.

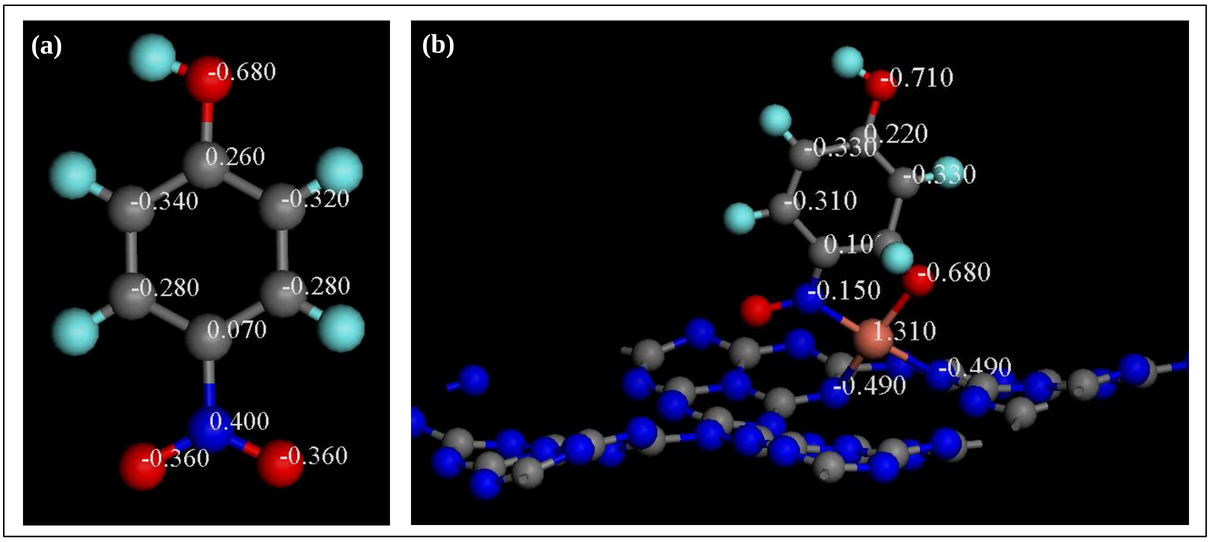

***Fig. 6.96**: Mulliken population analysis of (a) isolated 4-NP pollutant molecule, and (b) 4-NP adsorbed on CuCN*

The whole reaction pathway involving H^- as studied from the first principles calculation is as follows:

(1) CuCN + $C_6H_4(OH)(NO_2)$ + $3NaBH_4$ + H_2O → (2) CuCN-$C_6H_4(OH)(NO_2)$ + $3NaBH_4$ + H_2O → (3) CuCN-$C_6H_4(OH)(NO\text{-}OH)Na$ + BH_3 + $2NaBH_4$ + H_2O → (4) CuCN-$C_6H_4(OH)(NO)$ + NaOH + BH_3 + $2NaBH_4$ + H_2O → (5) CuCN-$C_6H_4(OH)(NH\text{-}O)Na$ + NaOH + $2BH_3$ + $NaBH_4$ + H_2O → (6) CuCN-$C_6H_4(OH)(NH\text{-}OH)$ + 2NaOH + $2BH_3$ + $NaBH_4$ → (7) CuCN-$C_6H_4(OH)(NH_2\text{-}OH)Na$ + 2NaOH + $3BH_3$ → (8) CuCN-$C_6H_4(OH)(NH_2)$ + 3NaOH + $3BH_3$.

In case of the reaction pathway involving H^+ as the hydrogen source, a sizable amount of reaction barrier was still observed for 4-NP adsorbed in N-up orientation whereas a monotonically exothermic energy profile was observed for N-down orientation representing a spontaneous reaction mechanism. The reaction pathway involving H^+ was found as follows:

(1) CuCN + $C_6H_4(OH)(NO_2)$ + $6H^+$ + $6e^-$ → (2) CuCN-$C_6H_4(OH)(NO_2)$ + $6H^+$ + $6e^-$ → (3) CuCN-$C_6H_4(OH)(NO\text{-}OH)$ + $5H^+$ + $5e^-$ → (4) CuCN-$C_6H_4(OH)(NO)$ + H_2O + $4H^+$ + $4e^-$ → (5) CuCN-$C_6H_4(OH)(N\text{-}OH)$ + H_2O + $3H^+$ + $3e^-$ → (6) CuCN-$C_6H_4(OH)(NH\text{-}OH)$ + H_2O + $2H^+$ + $2e^-$ → (7) CuCN-$C_6H_4(OH)(NH)$ + $2H_2O$ + H^+ + e^- → (8) CuCN-$C_6H_4(OH)(NH_2)$ + $2H_2O$.

The energy profiles for both the orientations as well as the structures of each reaction intermediate of the preferable pathway are represented in **Fig. 6.97**. Prominently, the reaction mechanism involving H^+ as the hydrogen source with 4-NP adsorbed in the N-down configuration dictates the most facile conversion route from 4-NP to 4-AP. The more efficient reaction pathways of the N-down adsorbed configuration irrespective of the hydrogen source owe to the shorter transmission channel for the electron to move from the catalyst surface to active sites in the adsorbed reactant molecule. Notably, the reaction barrier appears only during the hydrogenation processes for both the adsorbed orientations when H^- works as the hydrogen source owing to the electrostatic repulsion. The absence of any reaction barrier involving H^+ in N-down configuration denotes that water is the most probable source of hydrogen in the product 4-AP molecule.

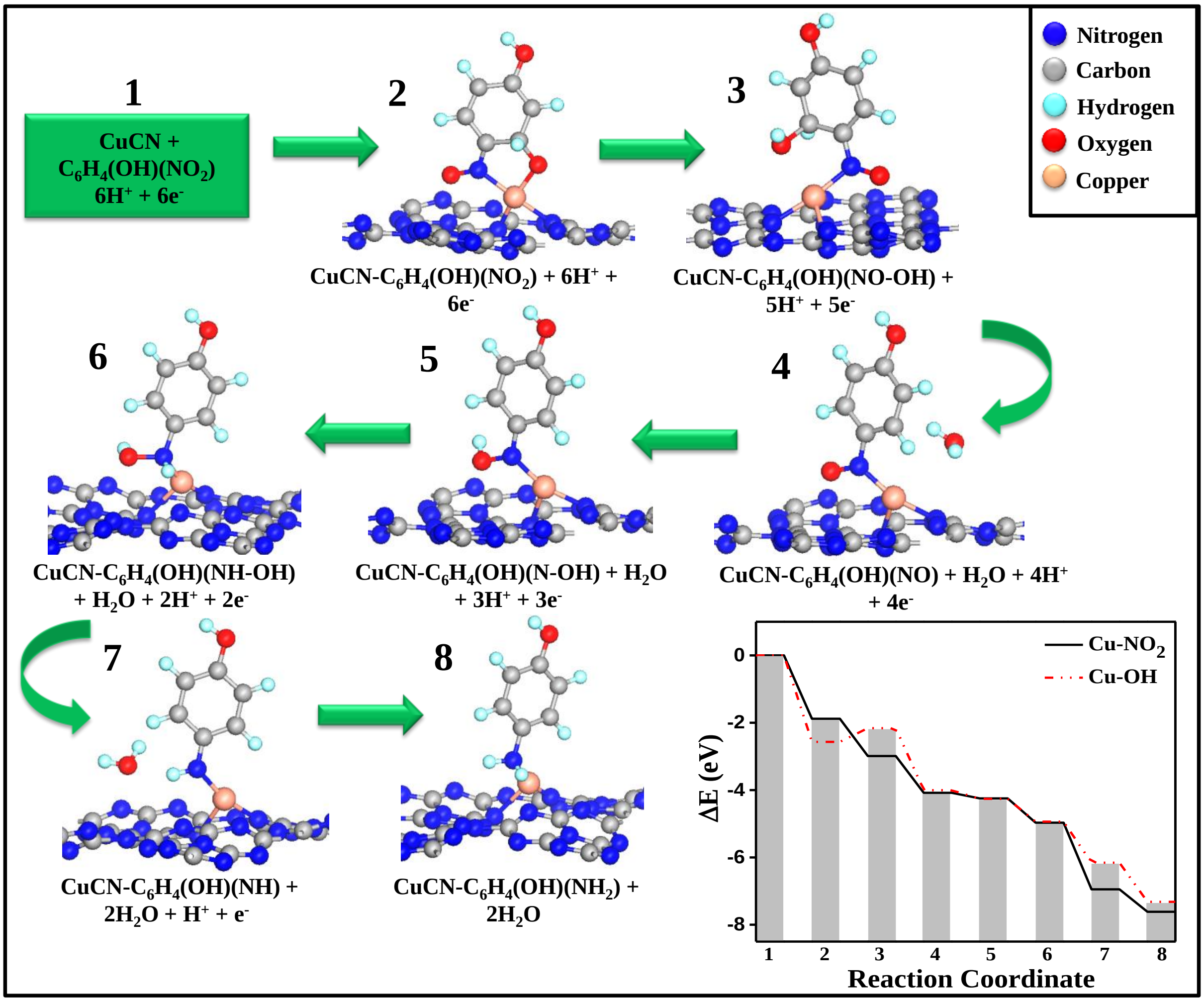

***Fig. 6.97**: The reaction intermediates for reaction pathway involving H^+ for the energetically favorable N-down ($Cu\text{-}NO_2$) adsorbed configuration of 4-NP on CuCN. The energy profile for both N-up (Cu-OH) and N-down configuration of the whole reaction process is shown at the bottom right corner of the figure.*

6.6.9.2. Degradation mechanism of MO dye:

In the subsequent discussion, the degradation mechanism of another harmful dye methyl orange (MO) was studied using DFT calculations. The interaction of MO with pure GCN was found to be even weaker compared to 4-NP as the lowest distance of the MO molecule was found to be as high as 2.91 Å in its most favorable physically adsorbed configuration on GCN. Undoubtedly, GCN would not be able to reduce and degrade MO into non-harmful products as the weak interaction between the host and the MO would most likely break the necessary electron relay process. In this regard, GCN was decorated again with Cu and the catalytic activity of CuCN was further explored for the MO dye degradation process.

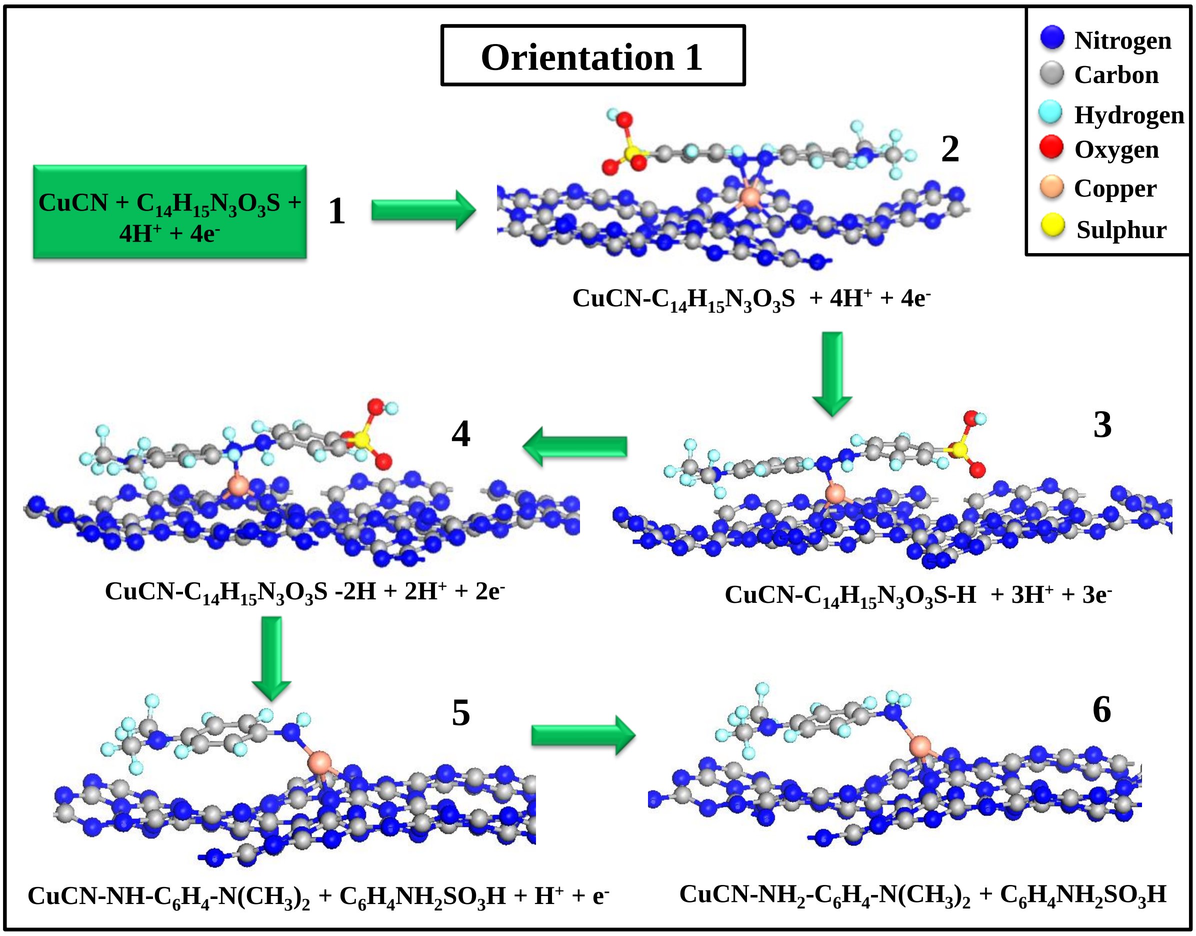

***Fig. 6.98**: The reaction intermediates for reaction pathway involving H^+ for the energetically less favorable adsorbed configuration Orientation 1 of MO on CuCN*

The adsorption of MO on CuCN was studied for different orientations of the MO molecule with interaction of end S and N atom and the middle N atoms with Cu including both ends on and side on orientations for each being taken into account. Just like the case of 4-NP, Cu acts as an active site for MO adsorption and converts the weak physical bond into strong chemical one through exothermic adsorption process. In terms of adsorption energy, the most favorable adsorption configurations were found when the middle N atoms interact with the Cu atom in both side on (orientation 1 in **Fig. 6.98**) and end on (orientation 2 in **Fig. 6.99(a)**) configurations.

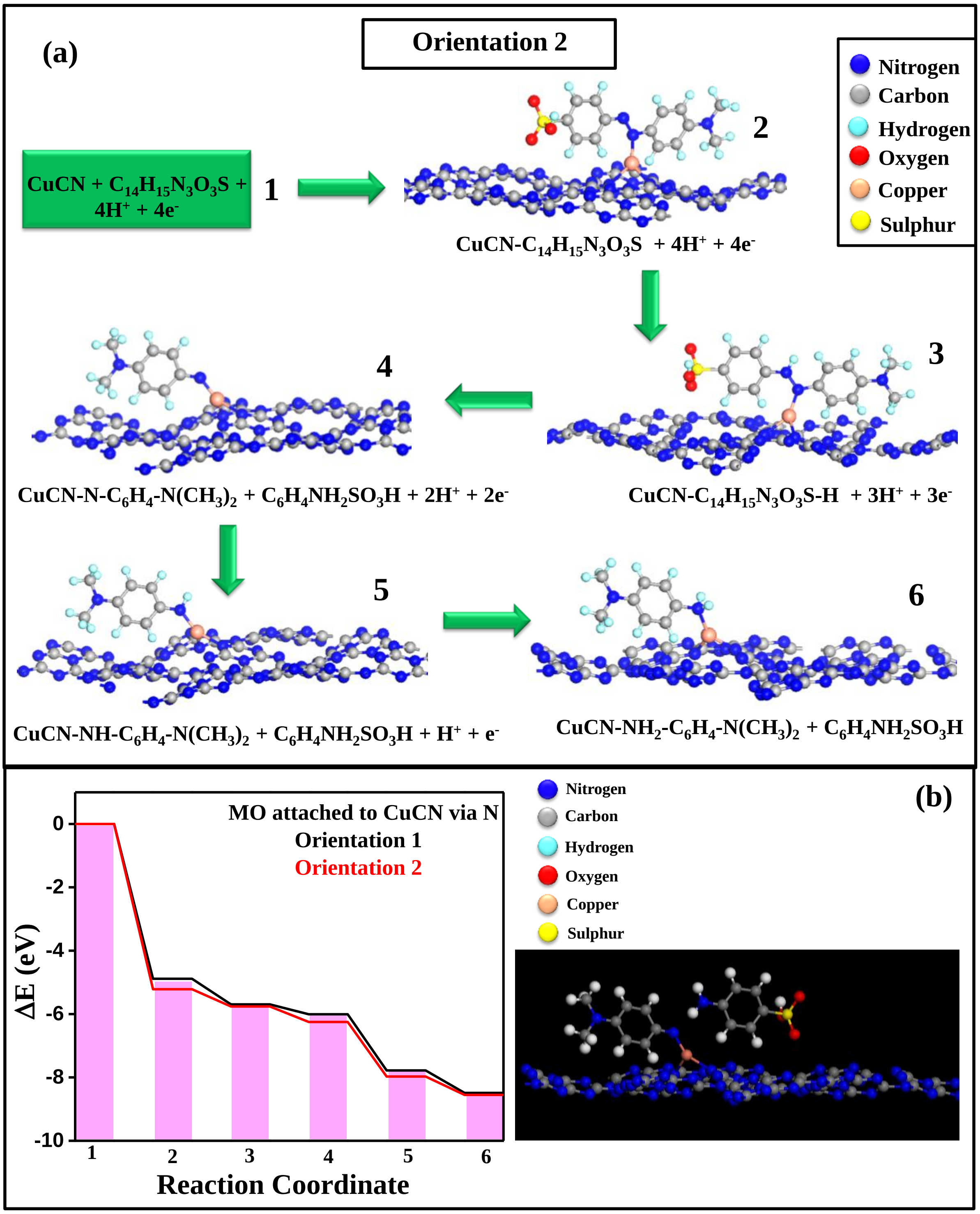

***Fig. 6.99**: (a) The reaction intermediates for reaction pathway involving H^+ for the energetically favorable adsorbed configuration Orientation 2 of MO on CuCN; (b) The energy profile for both adsorbed orientations 1 and 2 of the whole reaction process; and the optimized structure formed after first hydrogenation, i.e., the formation and desorption of sodium salt of sulphanilic acid*

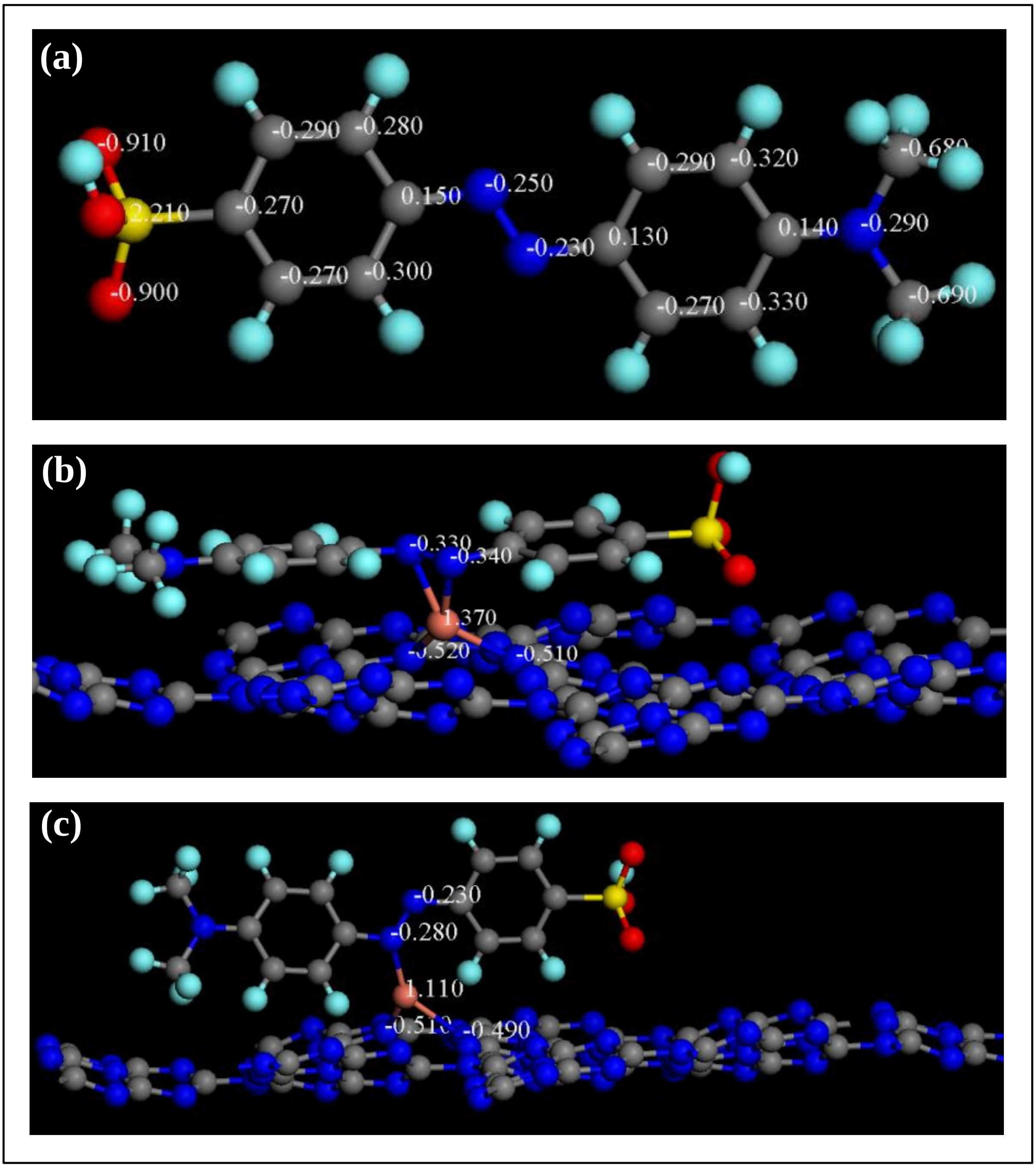

***Fig. 6.100**: Mulliken population analysis of (a) isolated MO molecule; and of MO adsorbed on CuCN via (b) Orientation 1, and (c) Orientation 2*

In the orientation 2, Cu forms chemical bond with only one N atom whereas both the N atoms become bonded with Cu upon adsorption in orientation 1. Notably, the Mulliken charge on both the N atoms are almost identical in its pristine state (-0.25e and -0.23e as shown in **Fig. 6.100(a)**) and it remains so with slight increment in the negative charge values (-0.34e and -0.33e) as shown in **Fig. 6.100(b)** after adsorption on CuCN in orientation 1. In case of adsorption in orientation 2, the difference between the charges on the middle N atoms becomes more prominent (-0.28e and -0.23e as represented in **Fig. 6.100(c)**). Although the adsorption energy values for the two orientations differs by little, MO adsorbed in orientation 2 is slightly more stable (by -0.33 eV) in terms of adsorption energy. For the subsequent steps of the degradation process, the H^+ from the water was considered as the source hydrogen element as similar to 4-NP.

MO is an anionic dye which is expected to be reduced into non-harmful products through hydrogenation of the electron rich and negatively charged N atoms bonded with Cu. Also, $NaBH_4$ works as the well-established donor of electron to complete the degradation process just like the reduction of 4-NP. The energy profiles of the degradation process of MO on CuCN which were evaluated taking the enthalpy of the system at first reaction coordinate as reference shows a spontaneous degradation process of MO for both the adsorbed orientations, albeit the route of the degradation process was found to be different for the two orientations (**Fig. 6.99(b)**). One of the expected product sodium salt of sulphanilic acid formed at the 3rd hydrogenation step (conversion from reaction coordinate 4 to 5) for orientation 1 whereas the same product formed right after 2nd coupled H^+ and e^- transfer for MO adsorbed orientation 2 (**Fig. 6.98** and **Fig. 6.99(a)**).

The detailed reaction pathway for MO degradation as found from the theoretical calculation is as follows:

For orientation 1: (1) $CuCN + C_{14}H_{15}N_3O_3S + 4H^+ + 4e^- \rightarrow$ (2) $CuCN\text{-}C_{14}H_{15}N_3O_3S + 4H^+ + 4e^- \rightarrow$ (3) $CuCN\text{-}C_{14}H_{15}N_2(NH)O_3S + 3H^+ + 3e^- \rightarrow$ (4) $CuCN\text{-}C_{14}H_{15}N(NH)(NH)O_3S + 2H^+ + 2e^- \rightarrow$ (5) $CuCN\text{-}C_8H_{10}N(NH) + C_6H_7NSO_3 + H^+ + e^- \rightarrow$ (6) $CuCN\text{-}C_8H_{10}N(NH_2) + C_6H_7NSO_3$

And for orientation 2: (1) $CuCN + C_{14}H_{15}N_3O_3S + 4H^+ + 4e^- \rightarrow$ (2) $CuCN\text{-}C_{14}H_{15}N_3O_3S + 4H^+ + 4e^- \rightarrow$ (3) $CuCN\text{-}C_{14}H_{15}N_2(NH)O_3S + 3H^+ + 3e^- \rightarrow$ (4) $CuCN\text{-}C_8H_{10}N_2 + C_6H_7NSO_3 + 2H^+ + 2e^- \rightarrow$ (5) $CuCN\text{-}C_8H_{10}N(NH) + C_6H_7NSO_3 + H^+ + e^- \rightarrow$ (6) $CuCN\text{-}C_8H_{10}N(NH_2) + C_6H_7NSO_3$.

Notably, the N present in the sodium salt of sulphanilic acid was not bonded to Cu after initial adsorption for orientation 2 and which paved the path for the quick transformation and desorption of the product in contrast to orientation 1 where both the N atoms were bonded to the Cu atom with identical charge distribution (**Fig. 6.100(b,c)**). The different types of charge distribution over the middle N atoms in different adsorbed orientations also most certainly play a crucial role in determining the intermediate reaction routes. Although, spontaneous degradation process was found for both the orientations, energy of the reaction intermediates through the pathway from orientation 2 are lower in energy compared to orientation 1 throughout the whole reaction process. Prominently, the pathway described from adsorbed orientation 2 would dominate the degradation process of MO on CuCN.

6.6.9.3. Degradation mechanism of MB dye:

Finally, the activity of both pure GCN and CuCN is theoretically explored in this subsection towards the degradation of another harmful dye methylene blue (MB). Similar to its adsorption capability towards 4-NP and MO, GCN was found to be inert towards the chemical adsorption of MB, hence corroborating its poor performance towards any dye degradation processes. Thus the aid of decorating the GCN layer with Cu was contemplated again to improve its performance towards the dye degradation process. Notably, as per prior reports, MB is a cationic dye with the two end N atoms possessing partially positive charge on them unlike previously discussed 4-NP and MO. The presence of higher amount of negative charge on the middle N atom compared to the end N atoms can also be seen clearly from the representation of Mulliken charge analysis (**Fig. 6.103(a)**).

In this regard, the adsorption of MB over CuCN was investigated with both types of N as well as the S atom interacting with Cu in different orientations. MB gets adsorbed onto CuCN weakly via the cationic N site whereas strong exothermic adsorption was found via both the anionic N and S sites with the interaction via anionic N in side on mode being slightly stronger with relatively lower adsorption energy (**Table 6.10**). The Mulliken population analysis reveals the highest accumulation of negative charge over the N atom that is interacting with Cu upon bonding which indicates stronger attractive electrostatic interaction between the N and Cu atoms resulting in the lowest adsorption energy for MB on CuCN as evident from **Table 6.10** and **Fig. 6.103(b-d)** compared to other dyes considered above. Although MB is cationic in nature, its degradation and conversion into Leuco MB (LMB) is expected through the hydrogenation of the negatively charged N atom. Hence, from the prior observations for other dyes, the H^+ from water is anticipated to be the source of hydrogen for the hydrogenation process. But the cationic nature of MB laid a path for detailed analysis. Hence, both the H^+ from water as well as H^- from $NaBH_4$ were considered parallely as the source of hydrogen and two different pathways are proposed in the present investigation. The reaction pathway involving H^+ is as given below (schematic representation in **Fig. 6.101**):

(1) CuCN + $C_{16}H_{18}N_3S$ + H^+ + e^- → (2) CuCN-$C_{16}H_{18}N_3S$ + H^+ + e^- → (3) CuCN-$C_{16}H_{18}N_2(NH)S$.

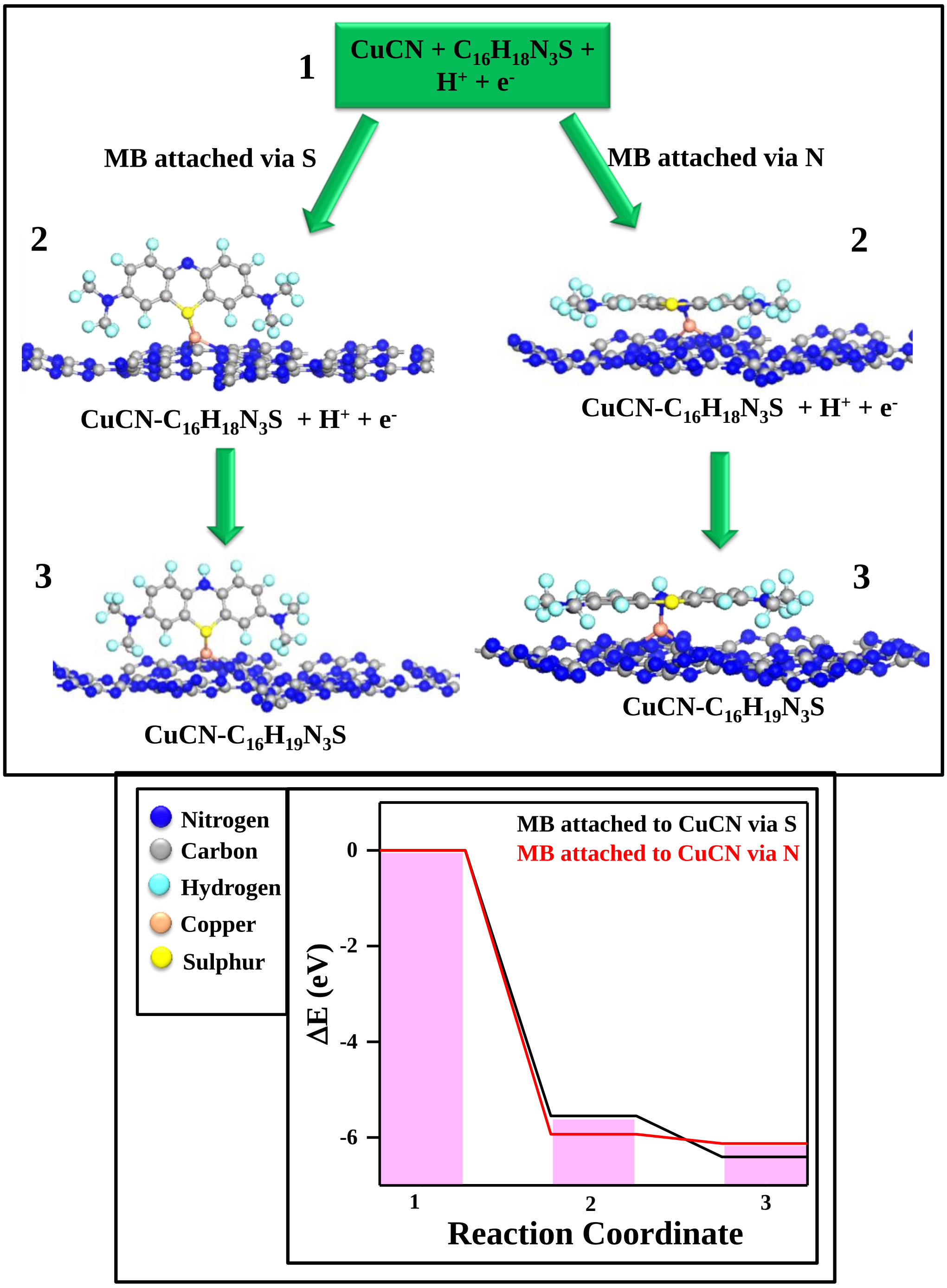

***Fig. 6.101**: The reaction intermediates for reaction pathway involving H^+ for both the adsorbed configuration of MB on CuCN via S and N sites; and the energy profile for both the adsorbed orientations of the whole reaction process are shown in the bottom right corner of the figure*

And the reaction pathway involving H^- as found from the DFT calculation is as follows (schematic representation in **Fig. 6.102**):

(1) $CuCN + C_{16}H_{18}N_3SCl + NaBH_4 \rightarrow$ (2) $CuCN\text{-}C_{16}H_{18}N_3SCl + Na^+ + BH_3 + H^- \rightarrow$ (3) $CuCN\text{-}C_{16}H_{18}N_2(NH)S + NaCl + BH_3$.

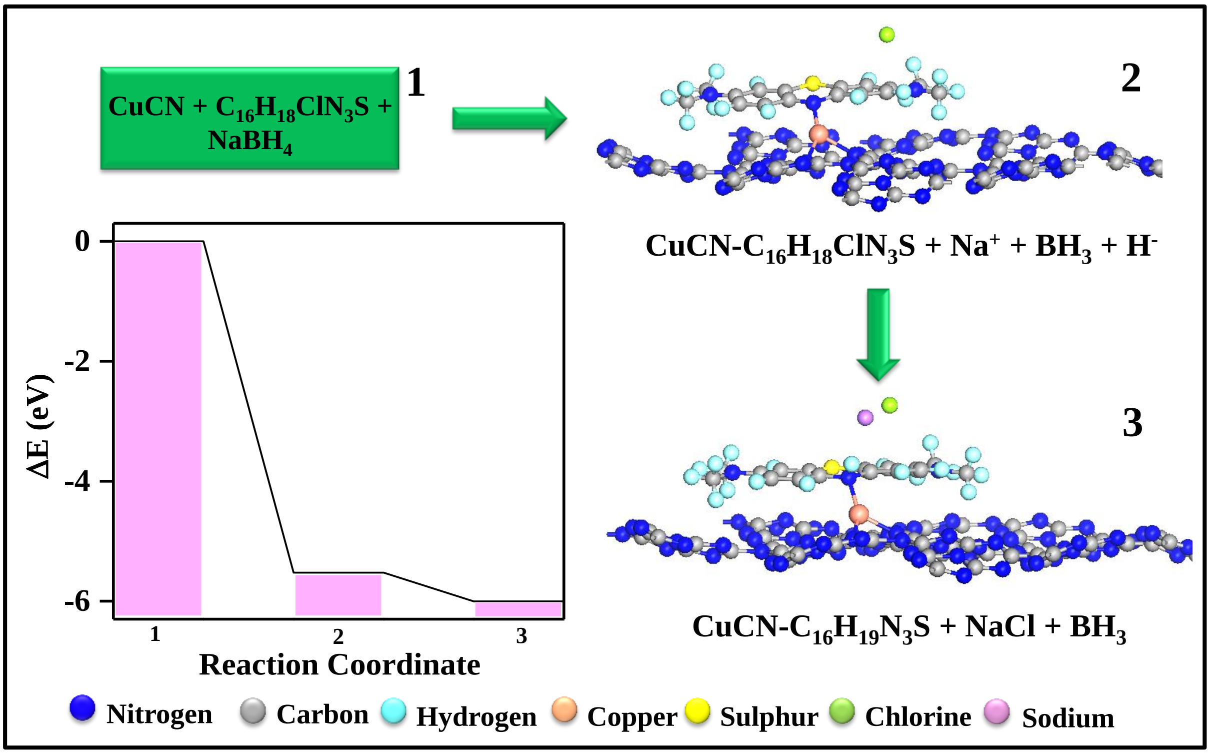

Fig. 6.102: *The reaction intermediates for reaction pathway involving* H^- *for the most favorable adsorbed orientation of MB (with Cl) on CuCN*

Spontaneous reaction pathways were found involving both H^+/ H^- as the hydrogen source with similar energy profiles. Although, in the pathway involving H^+ was spontaneous only for MB interacting with CuCN via the S site whereas the spontaneous pathway involving H^- was found for MB adsorbed via N in side on configuration. Notably, to reduce the complexity and computational cost, Cl^- was omitted during structural optimization of all the reaction intermediates for the pathway entailing H^+ as it does not take part in the reaction directly. Among all the dyes, the adsorption of MB via N in side on mode is found to be the strongest in terms of adsorption energy (**Table 6.10**) due to the greatest negative charge density on the interacting N atom in its pristine condition which produces strongest electrostatic attraction between the N atom and the metal Cu atom. The results from the free energy profiles of MB degradation process on CuCN suggest that MB would be reduced on CuCN through both the pathways competitively.

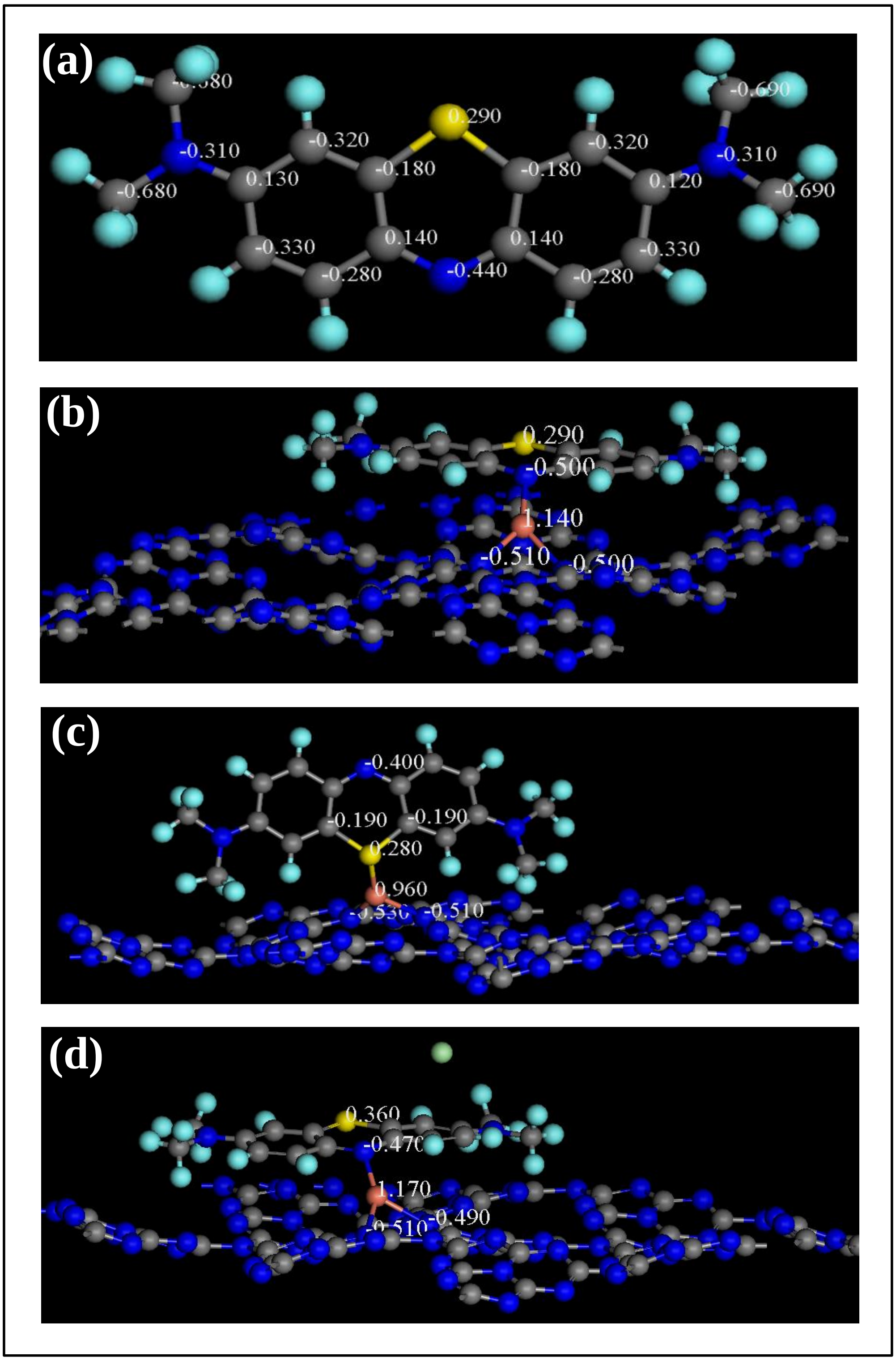

***Fig. 6.103**: Mulliken population analysis of (a) isolated MB molecule; MB adsorbed on CuCN via (b) N atom, and (c) S atom; and (d) Mulliken population analysis of MB with Cl adsorbed on CuCN*

Table 6.10. Chemisorption energies of 4-NP, MO and MB on CuCN in different orientations:

Pollutants	Orientation of the adsorbed configuration	Adsorption energy (eV)
4-NP	O atom bonded with Cu (N-up)	-2.57
	N atom bonded with Cu (N-down)	-1.88
MO	Middle N atoms bonded with Cu in side on mode (orientation 1)	-4.89
	Middle N atoms bonded with Cu in end on mode (orientation 2)	-5.22
	Edge N atom bonded with Cu	-4.60
	Edge S atom bonded with Cu	-4.82
MB (with Cl$^-$)	Anionic (middle) N atom bonded with Cu in end on mode	-5.17
	Anionic (middle) N atom bonded with Cu in side on mode	-5.58
	S atom bonded with Cu	-5.26
MB (without Cl$^-$)	Anionic (middle) N atom bonded with Cu in end on mode	-5.73
	Anionic (middle) N atom bonded with Cu in side on mode	-5.93
	S atom bonded with Cu	-5.55
	Cationic (end) N atom bonded with Cu	-4.38

A comparison chart is given in **Table 6.11** which compares the activity of CuCN and NiCN catalyst materials in terms of normalized rate constant values and degradation time with prior reports on doped and composite based GCN materials.

Table 6.11. Comparison of degradation activity of CuCN and NiCN catalysts with prior reports in terms of normalized rate constant values and degradation time.

Catalyst	Pollutant Conc.	NaBH$_4$ Conc.	Catalyst Dosage (mg)	Time (min)	Apparent Rate Constant (min^{-1})	Normalized Rate Constant (min^{-1} g^{-1})
Ag/GCN [219]	4-NP, 1.03x10^{-4} M (150 mL)	0.3 M (3 mL)	15	14	0.186	12.4
Pd/Au@GCN-N [225]	14.37 mM (1 mL)	1.43 M (1 mL)	0.25	5	0.7907	3162.8
Pd@GCN [358]	4-NP, 0.01 M (100 μL)	0.5 M (25 μL)	0.025	10	0.4374	17496
Ag-NH$_2$/GCN [359]	4-NP, 1x10^{-4} M (3 mL)	0.3 M (0.1 mL)	3	0.5	9.558	3186
Cu/GCN [226]	4-NP, 0.01 M (40 μL)	0.5 M (80 μL)	0.05	6	1.116	22320
Au/CeO$_2$/GCN	4-NP, 0.12 mM	0.04 M (250	1	0.67	6.3768	6376.8

[360]	(2 mL)	µL)				
Pd/GCN [221]	4-NP, 0.145 mM (2.5 mL)	1 M (50 µL)	0.0000125	6	0.76	6.08x10^{7}
Au@S-GCN [234]	4-NP, 1 mM (10 mL)	1 mM (1 mL)	0.5	5	0.751	1502
Copper Oxide-GCN [228]	4-NP, 5x10^{-5} M (3 mL)	1.6 mM (3 mL)	1	4	1.19	1190
GCN/Bi$_2$O$_2$CO$_3$/CoFe$_2$O$_4$ [230]	4-NP, 10 mM (2 mL)	0.05 M (20 mL)	----	5	0.783	----
Ag-Cu$_x$O-GCN [232]	4-NP, 100 ppm (1.5 mL)	0.01 M (1.5 mL)	0.05	4	0.334	6680
Au-GCN [361]	4-NP, 10 mg/L (50 mL)	0.1 g/mL (75 µL)	1	10	0.356172	356.172
Pd/Fe$_3$O$_4$/GCN [362]	4-NP, 0.01 M (0.1 mL)	0.5 M (25 µL)	0.1	3.5	1.662	16620
Au/polydopamine-decorated GCN [233]	2-NP, 0.2 mM (15 mL)	10, 20, 40, 60, 80 mM (15 mL)	5	1	2.904	580.8
	4-NP, 0.2 mM (15 mL)			1	3.084	616.8
	MO, 0.2 mM (15 mL)			0.67	5.298	1059.6
	CR, 0.2 mM (15 mL)			3	1.17	234
Au-GCN [222]	4-NP, 0.1 mM (2 mL)	0.1 M (1 mL)	0.0255	3.33	0.9726	38141
Pd/nitrogen-rich GCN [223]	4-NP [0.2 mM (0.2 mL)]	0.4 M (0.5 mL)	0.02	1	0.2526	1263
	MR [0.02 mM (0.2 mL)]			2	0.1266	421.8
	MB [0.02 mM (0.2 mL)]			1.33	0.1224	408
	RhB [0.02 mM (0.2 mL)]			1	0.2268	756
Ni doped GCN [47]	MO, 0.1 mM	0.1 M	1	4	1.4219	1421.9
Cu$_2$O/GCN [229]	MO, 0.1 mM (3 mL)	2x10^{-3} mM (0.3 mL)	1	4.7	1.3	1300
Cu^0/sodium alginate-GCN [363]	4-NP [0.07 mM (30 mL)]	0.1 M (5 mL)	16	6	0.384	24
	MO [0.07 mM (30 mL)]	0.1 M (5 mL)	16	17	0.135	8.4375
	CR [0.07 mM (30 mL)]	0.1 M (5 mL)	16	15	0.077	4.8125
CuCN [This Work]	2-NP [1 mM (0.3 mL)]	0.1 M (3 mL)	4	5	0.8519	212.97
	3-NP [1 mM (0.3 mL)]	0.1 M (3 mL)	4	5	1.8669	466.72
	4-NP [1 mM (0.3 mL)]	0.1 M (3 mL)	4	5	1.1023	273.95
	MO [0.1 mM (1 mL)]	0.1 M (2 mL)	2	3	2.1134	1056.7
	MR [0.1 mM (1 mL)]	0.1 M (2 mL)	2	4	1.4506	725.3
	CR [0.1 mM (1 mL)]	0.1 M (2 mL)	2	4	1.3923	696.15
	MB [0.1 mM (1 mL)]	0.1 M (2 mL)	2	4	1.6127	806.35

	RhB [0.1 mM (1 mL)]	0.1 M (2 mL)	2	4	1.9623	981.15
	RB [0.1 mM (1 mL)]	0.1 M (2 mL)	2	3	1.5216	760.8
NiCN [This Work]	2-NP [1 mM (0.3 mL)]	0. 1 M (3 mL)	4	5	0.6854	171.35
	3-NP [1 mM (0.3 mL)]	0.1 M (3 mL)	4	6	0.2515	62.87
	4-NP [1 mM (0.3 mL)]	0.3 M (3 mL)	4	4	0.3093	77.32
	MO [0.1 mM (1 mL)]	0.1 M (2 mL)	2	4	1.0311	515.55
	MR [0.1 mM (1 mL)]	0.1 M (2 mL)	2	7	0.403	201.5
	CR [0.1 mM (1 mL)]	0.1 M (2 mL)	2	7	0.6666	333.3
	MB [0.1 mM (1 mL)]	0.1 M (2 mL)	2	2	3.3972	1698.6
	RhB [0.1 mM (1 mL)]	0.1 M (2 mL)	2	6	1.0038	501.9
	RB [0.1 mM (1 mL)]	0.1 M (2 mL)	2	5	1.111	555.5

In conclusion, the metal decorated GCN samples exhibited superior $NaBH_4$-induced chemical catalytic activity in degradation of several toxic pollutants like 2-NP, 3-NP, 4-NP, MO, MR, CR, MB, RhB and RB within a very short time. Additionally, variation in catalyst dosage, $NaBH_4$ concentration, initial dye concentration, and pH were also performed to determine the optimum catalytic environment. Finally the CuCN sample was chosen as the best catalyst material based on its degradation performance to study a detailed plausible mechanism of the reduction reactions of 4-NP, MO and MB compounds by employing DFT calculations. The first principles studies supported the inactive nature of pure GCN towards dye degradation processes whereas Cu-decorated GCN initiated strong chemical bonding with the dyes through exothermic adsorption processes. For the conversion of 4-NP into 4-AP by CuCN, the source of hydrogen in the product molecule was revealed to be the water molecules present in the catalytic system. Similar source of hydrogen was revealed for the degradation of MO and two parallel reaction pathways were predicted from the monotonically exothermic energy profiles depending on the first hydrogenation site. For the reduction of the cationic dye MB, both water and $NaBH_4$ could competitively contribute in the hydrogenation process as revealed from the energy profiles. The present work thus provided detailed experimentation supported by vigorous theoretical analysis to establish CuCN as a potential water purifier that can be implemented in practical scenario owing to its capability in degrading a wide range of hazardous pollutants and their mixtures.

CHAPTER 7:

FINAL CONCLUSION & FUTURE SCOPES

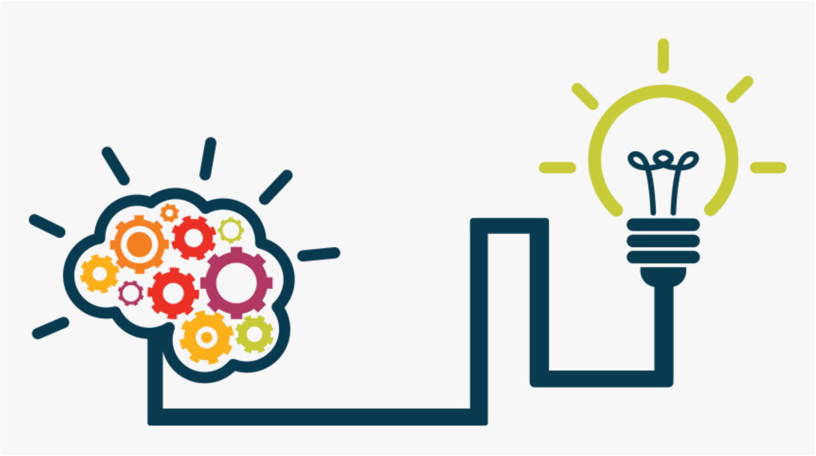

Final Conclusion and Future Scopes

The concluding chapter encapsulates the notable contributory findings and advancements made in the dissertation in the domains of wastewater treatment and environmental remediation using triazine-based nanomaterials. Additionally, this chapter highlights the potential avenues for future research in this particular field. The first segment of this chapter provides a summarized overview of the significant outcomes derived from the research works documented in this thesis. The subsequent segment delves into the potential areas of research works for further exploration and expansion in the aforementioned field.

7.1. Summary of the results:

An extensive survey and examination of existing literatures across various domains, encompassing synthesis and characterization of carbon- and nitrogen-based nanomaterials, and their application in wastewater remediation has been undertaken in the present dissertation. The primary aim was to rigorously identify the research challenges associated with the development of triazine-based nanomaterials and their subsequent utilization in purification of wastewater following simple methodologies. Within the scope of this research, synthesis of carbon- and nitrogen-based polymeric nanomaterials and their application potentials in the realm of wastewater treatment have been explored.

A novel triazine-based polymeric nanomaterial (MEG_{10}), having unique features, was synthesized following a facile solvothermal route. A very special class of triazine-based nanomaterial known as graphitic carbon nitride (GCN) was synthesized by adopting thermal treatment procedure. Enhancement of surface properties of GCN was achieved by thermal treatment followed by exfoliation technique. Furthermore, the inherent characteristics of the two-dimensional GCN matrix experienced a substantial enhancement through the incorporation of transition metals such as Cu and Ni. Metal incorporation into GCN was performed by chemical synthesis technique followed by thermal treatment procedure. All the as-synthesized nanomaterials were extensively characterized and investigated in details using characterization tools and various material testing analytical procedures to confirm the successful formation of their phases, structures, morphologies, and compositions.

In order to address the environmental concerns associated with the discharge of wastewater from various industrial sources, MEG_{10} triazine-based polymeric nanomaterial was implemented for the detection of Hg^{2+} heavy metal from aqueous environment. MEG_{10} demonstrated exceptional performance as a highly selective and sensitive sensor for Hg^{2+} ions, exhibiting a sensitivity of approximately $8.18x10^6$ M^{-1} for detecting ultra-trace Hg^{2+} concentrations. Notably, it also boasts an impressively low limit of detection, around ~0.03 ppb. This remarkable selectivity for Hg^{2+} ions can be attributed to the synergistic effects of electron-donating ligands or functional groups present in the polymer (mainly, nitrogen and oxygen-based ligands). MEG_{10} stands out in this context as it doesn't require sulfur-mediated functionalization, a necessity for other triazine-based polymers used in Hg^{2+} ion sensing. Moreover, the polymer has demonstrated its practical applicability by successfully detecting Hg^{2+} ions in real tap water samples. Considering its cost-effectiveness and non-toxic nature, MEG_{10} holds promise for potential commercial usage in the selective sensing of Hg^{2+} ions in the future.

Triazine-based GCN nanomaterial was employed as a photocatalyst material for the degradation of textile pollutants and reduction of Cr(VI) heavy metal after the modification of its surface area. This modified GCN exhibited enhanced properties, proving highly effective in the reduction of commonly encountered toxic pollutants found in wastewater. The photo-reduction of these contaminants induced by visible-light was made possible through the electron-capturing action of H_2O_2 and the hole-capturing capabilities of FA. Remarkably, with just only 20 mg of the optimal catalyst dosage and an H_2O_2 concentration of 10 mL/L, a 10 μM RhB solution was completely transformed into non-toxic products in a mere 30 minutes. Furthermore, employing this GCN catalyst in conjunction with 0.8 mL of FA achieved nearly 100% efficiency in reducing a 0.8 mg/mL Cr(VI) solution to Cr(III) in just 2 hours. The photocatalytic activity of GCN was optimized and a thorough analysis of the interactions among various influencing factors contributing to the improved catalytic performance was conducted through a series of experiments. These experiments involved varying influential parameters and employing statistical modelling, including RSM analysis. The Box–Behnken design was selected in order to identify the most favourable and optimal operational parameters for the simultaneous reduction of both pollutants, and these conditions were assessed using the Minitab software. Furthermore, the potential mechanism underlying GCN's catalytic activity was subjected to rigorous theoretical analysis implementing first-principles calculations. Analysing the band positions of the VBM and CBM for various edge-functionalized GCN blocks on the NHE scale revealed their capability to facilitate the reduction of RhB and Cr(VI) by efficiently transferring photogenerated e^-s and h^+s, respectively. In conclusion, exfoliated GCN, characterized by its substantial surface area, presented a promising solution for wastewater treatment facilities, by application of straightforward synthesis process. The stable, durable, and recyclable GCNX catalyst can expedite the efficient treatment of wastewater containing harmful contaminants like organic dyes and Cr(VI), employing readily accessible and environmentally friendly electron-capturing and hole-capturing agents, respectively. Consequently, this research can open up new avenues for the utilization of this nanomaterial in the realm of wastewater remediation.

The inclusion of transition metal ions, such as Cu^{2+} and Ni^{2+}, into the two-dimensional GCN network improved the properties of GCN considerably. The Cu-decorated and Ni-decorated GCN samples displayed superior chemical catalytic activity induced by $NaBH_4$, effectively degrading a range of toxic pollutants including 2-NP, 3-NP, 4-NP, MO, MR, CR, MB, RhB, and RB in a remarkably short timeframe. Moreover, vigorous experiments were conducted to assess the influence of catalyst dosage, $NaBH_4$ concentration, initial concentration of contaminants, and pH, aiming to identify the optimal catalytic conditions. It was observed experimentally that with increased catalyst amount and $NaBH_4$ concentration, the rate of catalytic activity increased manifolds. Ultimately, CuCN catalyst was selected as the most efficient catalyst based on its performance in degrading 4-NP, MO, and MB compounds, and the reduction mechanisms were further elucidated through detailed DFT calculations. This research work offers a comprehensive combination of experimental data and robust theoretical analysis, establishing CuCN as a promising water purification solution suitable for practical implementation. Its capacity to effectively degrade a diverse array of harmful contaminants, including complex mixtures of pollutants, underscores its potential as a valuable tool for water treatment.

7.2. Future prospects:

The research outlined in this dissertation holds significant relevance in the current context, as evidenced by recent literature, and offers possibilities for further exploration in the directions that follow.

In the present dissertation, only the scientific aspects of triazine-based nanomaterials have been ventured upon. Nevertheless, notable gaps persist in the progress of these nanomaterials within the realm of engineering applications. These nanomaterials have not reached a level of maturity suitable for widespread industrial utilization, mainly due to practical challenges such as production costs and yields. Exhaustive research works will be necessary to address these challenges in the future. Though GCN have found extensive use as adsorbents for eliminating organic pollutants like textile dyes, their development as effective adsorbents for the capture and removal of hazardous heavy metals and non-metals remains a less explored avenue. Detailed kinetic studies and adsorption isotherm studies for pristine and functionalized GCN nanomaterials for the removal of toxic heavy metals and non-metals are to be conducted in future research works. Moreover, regeneration studies and leaching effect analysis are to be carried out for practical applications. Extensive mathematical modelling and validation of theoretical model pertaining to these works are also to be tested.

The application of machine learning models in environmental contexts is becoming increasingly vital in our modern world. Utilizing data analysis and predictive analytics, these models are instrumental in tackling urgent environmental issues. Machine learning models help to analyse a large set of complex data generated by experimental procedures, thereby providing valuable insights into the various interacting parameters, and to identify accurately the optimal operating conditions. Different types of machine learning models will be implemented in some of my future research works concerning wastewater remediation to identify the best treatment condition.

References

1. P. Jangid, P. and M.P. Inbaraj, *Mater. Today: Proc.*, 2021, **43**, 2877-2881.
2. https://www.nano.gov
3. T.A. Saleh, *Environ. Technol. Innov.*, 2020, **20**, 101067.
4. K. Sakaushi and M. Antonietti, *Acc. Chem. Res.*, 2015, **48**, 1591-1600.
5. Y. Wang, X. Wang and M. Antonietti, *Angew. Chem. Int. Ed.*, 2012, **51**, 68-89.
6. Q. Yang, W. Wang, Y. Zhao, J. Zhu, Y. Zhu and L. Wang, *RSC Adv.*, 2015, **5**, 54978-54984.
7. Q. Lu, K. Eid, W. Li, A.M. Abdullah, G. Xu and R.S. Varma, *Green Chem.*, 2021, **23**, 5394-5428.
8. J. Ehrmaier, T.N. Karsili, A.L. Sobolewski and W. Domcke, *J. Phys. Chem. A*, 2017, **121**, 4754-4764.
9. S.C. Yan, Z.S. Li and Z.G. Zou, *Langmuir*, 2009, **25**, 10397-10401.
10. Y. Wang, J. Yao, H. Li, D. Su and M. Antonietti, *J. Am. Chem. Soc.*, 2011, **133**, 2362-2365.
11. J. Zhu, Y. Wei, W. Chen, Z. Zhao, A. Thomas, *Chem. Comm.*, 2010, **46**, 6965-6967.
12. M.H. Chan, R.S. Liu and M. Hsiao, *Nanoscale*, 2019, **11**, 14993-15003.
13. X. Li, Y. Wang, W. Tian and J. Cao, *ACS Omega*, 2019, **4**, 9645-9653.
14. L. He, M. Fei, J. Chen, Y. Tian, Y. Jiang, Y. Huang, K. Xu, J. Hu, Z. Zhao, Q. Zhang and H. Ni, *Mater. Today*, 2019, **22**, 76-84.
15. Y. Luo, Y. Yan, S. Zheng, H. Xue and H. Pang, *J. Mater. Chem. A*, 2019, **7**, 901-924.
16. A.A. Yadav, S.W. Kang and Y.M. Hunge, *J. Mater. Sci. Mater. Electron.*, 2021, **32**, 15577-15585.
17. M. Fronczak, M. Krajewska, K. Demby and M. Bystrzejewski, *J. Phys. Chem. C*, 2017, **121**, 15756-15766.
18. Q. Zhuang, L. Sun and Y. Ni, *Talanta*, 2017, **164**, 458-462.
19. N. Xu, R.L. Wang, D.P. Li, X. Meng, J.L. Mu, Z.Y. Zhou and Z.M. Su, *Dalton Trans.*, 2018, **47**, 4191-4197.
20. Y. Zhuang, Q. Zhu, G. Li, Z. Wang, P. Zhan, C. Ren, Z. Si, S. Li, D. Cai and P. Qin, *Mater. Res. Bull.*, 2022, **146**, 111619.
21. Z. Faraki and M.A. Bodaghifard, *Polycycl. Aromat. Compd.*, 2022, **43**, 1-18, 5940-5957.
22. T.K.A. Nguyen, T.T. Pham, H. Nguyen-Phu and E.W. Shin, *Appl. Surf. Sci.*, 2021, **537**, 148027.
23. T. Huang, Y. Fu, Q. Peng, C. Yu, J. Zhu, A. Yu and X. Wang, *Appl. Surf. Sci.*, 2019, **480**, 888-895.
24. H. Shan, S. Li, Z. Yang, X. Zhang, Y. Zhuang, Q. Zhu, D. Cai, P. Qin and J. Baeyens, *Chem. Eng. J.*, 2021, **426**, 130757.
25. N. Tahir, C. Krishnaraj, K. Leus and P. Van Der Voort, *Polymers*, 2019, **11**, 1326.
26. M. Liu, L. Guo, S. Jin and B. Tan, *J. Mater. Chem. A*, 2019, **7**, 5153-5172.
27. P. Kuhn, M. Antonietti and A. Thomas, *Angew. Chem., Int. Ed.*, 2008, **47**, 3450-3453.

28. L. Hao, J. Ning, B. Luo, B. Wang, Y. Zhang, Z. Tang, J. Yang, A. Thomas and L. Zhi, *J. Am. Chem. Soc.*, 2015, **137**, 219-225.
29. S.N. Talapaneni, T.H. Hwang, S.H. Je, O. Buyukcakir, J.W. Choi and A. Coskun, *Angew. Chem., Int. Ed.*, 2016, **55**, 3106-3111.
30. P. Puthiaraj, Y.R. Lee, S. Zhang and W.S. Ahn, *J. Mater. Chem. A*, 2016, **4**, 16288-16311.
31. G. Zhu, S. Shi, M. Liu, L. Zhao, M. Wang, X. Zheng, J. Gao and J. Xu, *ACS Appl. Mater. Interfaces*, 2018, **10**, 12612-12617.
32. L. Guo, Y. Niu, H. Xu, Q. Li, S. Razzaque, Q. Huang, S. Jin and B. Tan, *J. Mater. Chem. A*, 2018, **6**, 19775-19781.
33. J. Bi, W. Fang, L. Li, J. Wang, S. Liang, Y. He, M. Liu and L. Wu, *Macromol. Rapid Commun.*, 2015, **36**, 1799-1805.
34. Z.A. Ghazi, A.M. Khattak, R. Iqbal, R. Ahmad, A.A. Khan, M. Usman, F. Nawaz, W. Ali, Z. Felegari, S.U. Jan and A. Iqbal, *New J. Chem.*, 2018, **42**, 10234-10242.
35. T. Wang, K. Kailasam, P. Xiao, G. Chen, L. Chen, L. Wang, J. Li and J. Zhu, *Microporous Mesoporous Mater.*, 2014, **187**, 63-70.
36. J. Liebig, *Ann. Phar.*, 1834, **10**, 1-47.
37. J. Liu, H. Wang and M. Antonietti, *Chem. Soc. Rev.*, 2016, **45**, 2308-2326.
38. E.C. Franklin, *J. Am. Chem. Soc.*, 1922, **44**, 486-509.
39. M.L. Cohen, *Phys. Rev. B*, 1985, **32**, 7988.
40. A. Thomas, A. Fischer, F. Goettmann, M. Antonietti, J.O. Müller, R. Schlögl and J.M. Carlsson, *J. Mater. Chem.*, 2008, **18**, 4893-4908.
41. J. Zhu, P. Xiao, H. Li and S.A. Carabineiro, *ACS Appl. Mater. Interfaces*, 2014, **6**, 16449-16465.
42. F. Su, M. Antonietti and X. Wang, *Catal. Sci. Technol.*, 2012, **2**, 1005-1009.
43. X. Wang, K. Maeda, A. Thomas, K. Takanabe, G. Xin, J.M. Carlsson, K. Domen and M. Antonietti, *Nat. Mater*, 2009, **8**, 76-80.
44. X. Zhang, X. Xie, H. Wang, J. Zhang, B. Pan and Y. Xie, *J. Am. Chem. Soc.*, 2013, **135**, 18-21.
45. N. Rono, J.K. Kibet, B.S. Martincigh and V.O. Nyamori, *Crit. Rev. Solid State Mater. Sci.*, 2021, **46**, 189-217.
46. Y. Zhang, Q. Pan, G. Chai, M. Liang, G. Dong, Q. Zhang and J. Qiu, *Sci. Rep.*, 2013, **3**, 1-8.
47. D. Das, D. Banerjee, M. Mondal, A. Shett, B. Das, N.S. Das, U.K. Ghorai and K.K. Chattopadhyay, *Mater. Res. Bull.*, 2018, **101**, 291-304.
48. S. Wang, J. Zhang, B. Li, H. Sun and S. Wang, *Energ. Fuel.*, 2021, **35**, 6504-6526.
49. B. Kumru, D. Cruz, T. Heil, B.V. Schmidt and M. Antonietti, *J. Am. Chem. Soc.*, 2018, **140**, 17532-17537.
50. W. Xiong, S. Chen, M. Huang, Z. Wang, Z. Lu and R.Q. Zhang, *ChemSusChem*, 2018, **11**, 2497-2501.
51. N. Prakash, G. Kumar, M. Singh, A. Barvat, P. Pal, S.P. Singh, H.K. Singh and S.P. Khanna, *Adv. Opt. Mater.*, 2018, **6**, 1800191.
52. K. Li, F.Y. Su and W.D. Zhang, *Appl. Surf. Sci.*, 2016, **375**, 110-117.

53. S. Kang, L. Zhang, M. He, Y. Zheng, L. Cui, D. Sun and B. Hu, *Carbon*, 2018, **137**, 19-30.
54. O. Stroyuk, O. Raievska and D.R. Zahn, *RSC Adv.*, 2020, **10**, 34059-34087.
55. H. Liu, X. Wang, H. Wang and R. Nie, *J. Mater. Chem. B*, 2019, **7,** 5432-5448.
56. Z. Mo, H. Xu, Z. Chen, X. She, Y. Song, J. Wu, P. Yan, L. Xu, Y. Lei, S. Yuan and H. Li, *Appl. Catal. B: Environ.*, 2018, **225**, 154-161.
57. Y.L.T. Ngo, W.M. Choi, J.S. Chung and S.H. Hur, *Sens. Actuators B: Chem.*, 2019, **282**, 36-44.
58. X. Wang, S. Jiang, X. Huo, R. Xia, E. Muhire and M. Gao, *Nanotechnology*, 2018, **29**, 205702.
59. T.O. Ajiboye, A.T. Kuvarega and D.C. Onwudiwe, *Nano-Struct. Nano-Objects*, 2020, **24**, 100577.
60. M. Elshafie, S.A. Younis, P. Serp and E.A.M. Gad, *Egypt. J. Pet.*, 2020, **29**, 21-29.
61. A.P. Cote, A.I. Benin, N.W. Ockwig, M. O'Keeffe, A.J. Matzger and O.M. Yaghi, S*cience*, 2005, **310**, 1166-1170.
62. W. Zhang, C. Li, Y.P. Yuan, L.G. Qiu, A.J. Xie, Y.H. Shen and J.F. Zhu, *J. Mater. Chem.*, 2010, **20**, 6413-6415.
63. M.G. Schwab, B. Fassbender, H.W. Spiess, A. Thomas, X. Feng and K. Mullen, *J. Am. Chem. Soc.*, 2009, **131**, 7216-7217.
64. A. Modak, M. Pramanik, S. Inagaki and A. Bhaumik, *J. Mater. Chem. A*, 2014, **2**, 11642-11650.
65. H. Zhao, Z. Jin, H. Su, X. Jing, F. Sun and G. Zhu, *Chem. Commun.*, 2011, **47**, 6389-6391.
66. P. Puthiaraj and K. Pitchumani, *Green Chem.*, 2014, **16**, 4223-4233.
67. M.R. Liebl and J. Senker, *Chem. Mater.*, 2013, **25**, 970-980.
68. S.P. Lee, N. Mellon, A.M. Shariff and J.M. Leveque, In *IOP Conf. Ser.: Mater. Sci. Eng.*, 2017, **226**, 012173.
69. R. Peng, G. Chen, F. Zhou, R. Man and J. Huang, *Chem. Eng. J.*, 2019, **371**, 260-266.
70. L. Maya, D.R. Cole and E.W. Hagaman, *J. Am. Ceram. Soc.*, 1991, **74,** 1686-1688.
71. C. Bie, B. Cheng, J. Fan, W. Ho and J. Yu, *EnergyChem*, 2021, **3**, 100051.
72. J. Kouvetakis, M. Todd, B. Wilkens, A. Bandari and N. Cave, *Chem. Mater.*, 1994, **6**, 811-814.
73. I. Alves, G. Demazeau, B. Tanguy and F. Weill, *Solid State Commun.*, 1999, **109**, 697-701.
74. H. Montigaud, B. Tanguy, G. Demazeau, I. Alves and S. Courjault, *J. Mater. Sci.*, 2000, **35**, 2547-2552.
75. Y. Gu, L. Chen, L. Shi, J. Ma, Z. Yang and Y. Qian, *Carbon*, 2003, **41**, 2674-2676.
76. B.V. Lotsch and W. Schnick, *Chem. Mater.*, 2006, **18**, 1891-1900.
77. M.J. Bojdys, J.O. Müller, M. Antonietti and A. Thomas, *Chem. Eur. J.*, 2008, **14**, 8177-8182.
78. J. Zhang, X. Chen, K. Takanabe, K. Maeda, K. Domen, J.D. Epping, X. Fu, M. Antonietti and X. Wang, *Angew. Chem., Int. Ed.*, 2010, **49**, 441-444.
79. J. Liu, T. Zhang, Z. Wang, G. Dawson and W. Chen, *J. Mater. Chem.*, 2011, **21**, 14398-14401.

80. B. Bann and S.A. Miller, *Chem. Rev.*, 1958, **58**, 131-172.
81. P.M. Schaber, J. Colson, S. Higgins, D. Thielen, B. Anspach and J. Brauer, *Thermochim. Acta*, 2004, **424**, 131-142.
82. Y. Zheng, Z. Zhang and C. Li, *J. Photochem. Photobiol. A: Chem.*, 2017, **332**, 32-44.
83. S. Zhou, Y. Liu, J. Li, Y. Wang, G. Jiang, Z. Zhao, D. Wang, A. Duan, J. Liu and Y. Wei, *Appl. Catal. B: Environ.*, 2014, **158**, 20-29.
84. Q. Huang, J. Yu, S. Cao, C. Cui and B. Cheng, *Appl. Surf. Sci.*, 2015, **358**, 350-355.
85. S. Yao, S. Xue, S. Peng, M. Jing, X. Qian, X. Shen, T. Li and Y. Wang, *J. Mater. Sci. Mater. Electron.*, 2018, **29**, 17921-17930.
86. H.B. Fang, Y. Luo, Y.Z. Zheng, W. Ma and X. Tao, *Ind. Eng. Chem. Res.*, 2016, **55**, 4506-4514.
87. H.S. Zhai, L. Cao and X.H. Xia, *Chin Chem Lett .*, 2013, **24**, 103-106.
88. Y. Zhang, S. Zong, C. Cheng, J. Shi, X. Guan, Y. Lu and L. Guo, *Int. J. Hydrog. Energy*, 2018, **43**, 13953-13961.
89. P. Praus, L. Svoboda, M. Ritz, I. Troppová, M. Šihor and K. Kočí, *Mater. Chem. Phys.*, 2017, **193**, 438-446.
90. N.D. Shcherban, P. Mäki-Arvela, A. Aho, S.A. Sergiienko, P.S. Yaremov, K. Eränen and D.Y. Murzin, *Catal. Sci. Technol.*, 2018, **8**, 2928-2937.
91. M. Zhang, J. Xu, R. Zong and Y. Zhu, *Appl. Catal. B: Environ.*, 2014, **147**, 229-235.
92. R.M. Mohamed, *Ceram. Int.*, 2015, **41**, 1197-1204.
93. Z. Ye, W. Yue, M. Tayyab, J. Zhang and J. Zhang, *Dalton Trans.*, 2022, **51**, 18542-18548.
94. B.V. Lotsch and W. Schnick, *Chem. Eur. J.*, 2007, **13**, 4956-4968.
95. E. Kroke, M. Schwarz, E. Horath-Bordon, P. Kroll, B. Noll and A.D. Norman, *New J. Chem.*, 2002, **26**, 508-512.
96. B.V. Lotsch, M. Döblinger, J. Sehnert, L. Seyfarth, J. Senker, O. Oeckler and W. Schnick, *Chem. Eur. J.*, 2007, **13**, 4969-4980.
97. P. Niu, L. Zhang, G. Liu and H.M. Cheng, *Adv. Funct. Mater.*, 2012, **22**, 4763-4770.
98. W.S. Hummers Jr and R.E. Offeman, *J. Am. Chem. Soc.*, 1958, **80,** 1339-1339.
99. S. Yang, Y. Gong, J. Zhang, L. Zhan, L. Ma, Z. Fang, R. Vajtai, X. Wang and P.M. Ajayan, *Adv. Mater.*, 2013, **25**, 2452-2456.
100. H. Sun, X. Zhou, H. Zhang and W. Tu, *Int. J. Hydrog. Energy*, 2017, **42**, 7930-7937.
101. M.I. Chebanenko, N.V. Zakharova, A.A. Lobinsky and V.I. Popkov, *Semiconductors*, 2019, **53**, 2072-2077.
102. L. Jiang, X. Yuan, Y. Pan, J. Liang, G. Zeng, Z. Wu and H. Wang, *Appl. Catal. B: Environ.*, 2017, **217**, 388-406.
103. Y. Wang, Y. Wang, Y. Chen, C. Yin, Y. Zuo and L.F. Cui, *Mater. Lett.*, 2015, **139**, 70-72.
104. I.N. Reddy, L.V. Reddy, N. Jayashree, C.V. Reddy, M. Cho, D. Kim and J. Shim, *Chemosphere*, 2021, **264**, 128593.
105. H. Li, Y. Xia, T. Hu, Q. Deng, N. Du and W. Hou, *J. Mater. Chem. A*, 2018, **6**, 6238-6243.
106. S. Tonda, S. Kumar, S. Kandula and V. Shanker, *J. Mater. Chem. A*, 2014, **2**, 6772-6780.

107. P.W. Chen, K. Li, Y.X. Yu and W.D. Zhang, *Appl. Surf. Sci.*, 2017, **392**, 608-615.
108. T.H. Pham, S.H. Jung and T. Kim, *Sol. Energy*, 2021, **224**, 18-26.
109. X. Li and X. Gan, *J. Environ. Chem. Eng.*, 2022, **10**, 108290.
110. Z. Zhu, Y. Miao, G. Wang, W. Chen and W. Lu, *Environ. Technol.*, 2022, **43**, 2569-2580.
111. D.A. Gonçalves, R.P. Alvim, H.A. Bicalho, A.M. Peres, I. Binatti, P.F. Batista, L.S. Teixeira, R.R. Resende and E. Lorençon, *New J. Chem.*, 2018, **42**, 5720-5727.
112. T. Xiong, W. Cen, Y. Zhang and F. Dong, *Acs Catal.*, 2016, **6**, 2462-2472.
113. Z. Ge, A. Yu and R. Lu, *Materials Letters*, 2019, **250**, 9-11.
114. A. Kumar, S. Kashyap, M. Sharma and V. Krishnan, *Chemosphere*, 2022, **287**, 131988.
115. Q. Deng and Q. Li, *J. Mater. Sci.*, 2018, **53**, 506-515.
116. M. Fronczak, K. Demby, P. Strachowski, M. Strawski and M. Bystrzejewski, *Langmuir*, 2018, **34**, 7272-7283.
117. M. Zhou, G. Dong, F. Yu and Y. Huang, *Appl. Catal. B: Environ.*, 2019, **256**, 117825.
118. T.S. Bui, P. Bansal, B.K. Lee, T. Mahvelati-Shamsabadi and T. Soltani, *Appl. Surf. Sci.*, 2020, **506**, 144184.
119. X. Jin, J. Chen, X. Zeng, L. Xu, Y. Wu and F. Fu, *Biosens. Bioelectron.*, 2019, **128**, 45-51.
120. D.R. Paul, R. Sharma, P. Panchal, S.P. Nehra, A.P. Gupta and A. Sharma, *Int. J. Hydrog. Energy*, 2020, **45**, 23937-23946.
121. C. Li, Y. Wang, C. Li, S. Xu, X. Hou and P. Wu, *ACS Appl. Mater. Interfaces*, 2019, **11**, 20770-20777.
122. N. Cheng, J. Tian, Q. Liu, C. Ge, A.H. Qusti, A.M. Asiri, A.O. Al-Youbi and X. Sun, *ACS Appl. Mater. Interfaces*, 2013, **5**, 6815-6819.
123. https://www.un.org
124. https://www.hsph.harvard.edu/ehep/
125. A. Hasanbeigi and L. Price, *J. Clean. Prod.*, 2015, **95**, 30-44.
126. D. Das, A.K. Sharma, K.K. Chattopadhyay and D. Banerjee, *Curr. Anal. Chem.*, 2022, **18**, 309-340.
127. M.A. Hassaan, A. El Nemr and A. Hassaan, *Am. J. Environ. Sci. Eng.*, 2017, **1**, 64-67.
128. M.M. Rashid, M. Chowdhury and M.R. Talukder, *J. Environ. Chem. Eng.*, 2020, **8**, 104504.
129. E. Santoso, R. Ediati, Y. Kusumawati, H. Bahruji, D.O. Sulistiono and D. Prasetyoko, *Mater. Today Chem.*, 2020, **16**, 100233.
130. A. Elliott, W.E. Hanby and B.R. Malcolm, *Br. J. Appl. Phys.*, 1954, **5**, 377.
131. D. Das, B.K. Das, R. Sarkar, S. Mukherjee and K.K. Chattopadhyay, *Appl. Surf. Sci.*, 2022, **580**, 152137.
132. K.B. Narayanan and N. Sakthivel, *Bioresour. Technol.*, 2011, **102**, 10737-10740.
133. S.E. Bailey, T.J. Olin, R.M. Bricka and D.D. Adrian, *Water Res.*, 1999, **33**, 2469-2479.
134. N.K. Srivastava and C.B. Majumder, *J. Hazard. Mater.*, 2008, **151**, 1-8.
135. M. Shahbaz, M.Z. Hashmi, R.N. Malik and A. Yasmin, *Chemosphere*, 2013, **93**, 274-282.

136. C. Bao, M. Chen, X. Jin, D. Hu and Q. Huang, *J. Mol. Liq.*, 2019, **279**, 133-145.
137. W. Song, P. Ge, Q. Ke, Y. Sun, F. Chen, H. Wang, Y. Shi, X.L. Wu, H. Lin, J. Chen and C. Shen, *Chemosphere*, 2019, **221**, 166-174.
138. M. Owlad, M.K. Aroua, W.A.W. Daud and S. Baroutian, *Water Air Soil Pollut.*, 2009, **200**, 59-77.
139. S.S. Hassan, N.S. Awwad and A.H. Aboterika, *J. Hazard. Mater.*, 2008, **154**, 992-997.
140. S. Giraldo, I. Robles, A. Ramirez, E. Flórez and N. Acelas, *SN Appl. Sci.*, 2020, **2**, 1-17.
141. S.M. Wilhelm and N. Bloom, *Fuel Process. Technol.*, 2000, **63**, 1-27.
142. S. Joseph and B. Mathew, *J. Mol. Liq.*, 2015, **204**, 184-191.
143. I.A. Alaton and I.A. Balcioglu, *J. Photochem. Photobiol. A, Chem.*, 2001, **141**, 247-254.
144. M. Faisal, M.A. Tariq and M. Muneer, *Dyes Pigm.*, 2007, **72**, 233-239.
145. K.T. Chung and C.E. Cerniglia, *Mutat. Res./Rev. Genet. Toxicol.*, 1992, **277**, 201-220.
146. M. Ismail, M.I. Khan, S.B. Khan, M.A. Khan, K. Akhtar and A.M. Asiri, *J. Mol. Liq.*, 2018, **260**, 78-91.
147. M.R.R. Kooh, L.B. Lim, L.H. Lim and M.K. Dahri, *Environ. Monit. Assess.*, 2016, **188**, 1-15.
148. Y. Li, Q. Du, T. Liu, X. Peng, J. Wang, J. Sun, Y. Wang, S. Wu, Z. Wang, Y. Xia and L. Xia., *Chem. Eng. Res. Des.*, 2013, **91**, 361-368.
149. V.S. Munagapati, V. Yarramuthi and D.S. Kim, *J. Mol. Liq.*, 2017, **240**, 329-339.
150. C. Nistor, A. Oubiña, M.P. Marco, D. Barceló and J. Emnéus, *Anal. Chim. Acta*, 2001, **426**, 185-195.
151. M. Bilal, A.R. Bagheri, P. Bhatt and S. Chen, *J. Environ. Manage.*, 2021, **291**, 112685.
152. M. Capodici, A. Avona, V.A. Laudicina and G. Viviani, *Sci. Total Environ.*, 2018, **630**, 462-468.
153. D. Das, A. Mitra, R. Chatterjee, S. Sain and K.K. Chattopadhyay, *New J. Chem.*, 2019, **43**, 4364-4376.
154. F. Zahir, S.J. Rizwi, S.K. Haq and R.H. Khan, *Environ. Toxicol. Pharmacol.*, 2005, **20**, 351-360.
155. D. Das, B.K. Das, R. Sarkar, S. Mukherjee and K.K. Chattopadhyay, *Environ. Res.*, 2023, 115263.
156. K. Shekhawat, S. Chatterjee and B. Joshi, *Int. J. Adv. Res.*, 2015, **3**, 167-172.
157. L. Giraldo, A. Erto and J.C. Moreno-Piraján, *Adsorption*, 2013, **19**, 465-474.
158. B. Saha, S. Das, J. Saikia and G. Das, *J. Phys. Chem. C*, 2011, **115**, 8024-8033.
159. S.S. Fiyadh, M.A. AlSaadi, W.Z. Jaafar, M.K. AlOmar, S.S. Fayaed, N.S. Mohd, L.S. Hin and A. El-Shafie, *J. Clean. Prod.*, 2019, **230**, 783-793.
160. J. Wang and B. Chen, *Chem. Eng. J.*, 2015, **281**, 379-388.
161. A. Wu, J. Jia and S. Luan, *Colloids Surf. A: Physicochem. Eng. Asp.*, 2011, **384**, 180-185.
162. M. Salehi, D. Sharafoddinzadeh, F. Mokhtari, M.S. Esfandarani and S. Karami, *Clean Technol. Recycl.*, 2021, **1**, 1-33.

163. S. Wang, C.W. Ng, W. Wang, Q. Li and Z. Hao, *Chem. Eng. J.*, 2012, **197**, 34-40.
164. A. Molla, Y. Li, B. Mandal, S.G. Kang, S.H. Hur and J.S. Chung, *Appl. Surf. Sci.*, 2019, **464**, 170-177.
165. Q.I. Rahman, M. Ahmad, S.K. Misra and M. Lohani, *Mater. Lett.*, 2013, **91**, 170-174.
166. P. Peerakiatkhajohn, T. Butburee, J.H. Sul, S. Thaweesak and J.H. Yun, *Nanomaterials*, 2021, **11**, 1059.
167. G. Elango and S.M. Roopan, *J. Photochem. Photobiol. B, Biol.*, 2016, **155**, 34-38.
168. S. Taghavi Fardood, F. Moradnia and A. Ramazani, *Micro Nano Lett.*, 2019, **14**, 986-991.
169. J.R. Chiou, B.H. Lai, K.C. Hsu and D.H. Chen, *J. Hazard. Mater.*, 2013, **248**, 394-400.
170. K. Zhao, J. Wang, W. Kong and P. Zhu, *J. Environ. Chem. Eng.*, 2020, **8,** 103517.
171. F. Subhan, S. Aslam, Z. Yan and M. Yaseen, *J. Colloid Interface Sci.*, 2020, **578**, 37-46.
172. G. Shimoga, R.R. Palem, S.H. Lee and S.Y. Kim, *Metals*, 2020, **10**, 1661.
173. M.A. Malik, A.A. Alshehri and R. Patel, *J. Mater. Res. Technol.*, 2021, **12**, 455-470.
174. Y. Wang, P. Gao, Y. Wei, Y. Jin, S. Sun, Z. Wang and Y. Jiang, *J. Environ. Manage.*, 2021, **278**, 111473.
175. M. Li, B. Wang, X. An, Z. Li, H. Zhu, B. Mao, D.G. Calatayud and T.D. James, *Dyes Pigm.*, 2019, **170**, 107476.
176. D.Y. Wang, W.J. Wang, R. Wang, S.C. Xi and B. Dong, *Eur. Polym. J.*, 2021, **147**, 110297.
177. H. Hong, N. Wu, M. Han, Z. Guo, H. Zhan, S. Du and B. Chen, *Mater. Chem. Front.*, 2021, **5**, 6568-6574.
178. X. Guo, G. Yue, J. Huang, C. Liu, Q. Zeng and L. Wang, *ACS Appl. Mater. Interfaces*, 2018, **10**, 26118-26127.
179. W. Tang, Y. Tian, B. Li, Q. Liu, D. Wang, X. Jing, J. Zhang and S. Xu, *Spectrochim. Acta A, Mol. Biomol. Spectrosc.*, 2019, ***210***, 341-347.
180. N. Cheng, P. Jiang, Q. Liu, J. Tian, A.M. Asiri and X. Sun, *Analyst*, 2014, **139**, 5065-5068.
181. J. Tian, Q. Liu, A.M. Asiri, A.O. Al-Youbi and X. Sun, *Anal. Chem.*, 2013, **85**, 5595-5599.
182. W. Bian, H. Zhang, Q. Yu, M. Shi, S. Shuang, Z. Cai and M.M. Choi, *Spectrochim. Acta A, Mol. Biomol. Spectrosc.*, 2016, **169**, 122-127.
183. H. Huang, R. Chen, J. Ma, L. Yan, Y. Zhao, Y. Wang, W. Zhang, J. Fan and X. Chen, *Chem. Commun.*, 2014, **50**, 15415-15418.
184. H. Zhang, Y. Huang, Y. Zheng, J. Zhou, Q. Wu, Z. Zhang, F. Gan and W. Chen, *Spectrochim. Acta A, Mol. Biomol. Spectrosc.*, 2019, **217**, 141-146.
185. M. Afshari and M. Dinari, *J. Hazard. Mater.*, 2020, **385**, 121514.
186. C. Liu, M. Xia, M. Zhang, K. Yuan, F. Hu, G. Yu and X. Jian, *Polymer*, 2020, **194**, 122401.
187. J. Mohanraj, D. Durgalakshmi and R. Saravanan, *Environ. Pollut.*, 2021, **269**, 116172.
188. M. Yousefi, S. Villar-Rodil, J.I. Paredes and A.Z. Moshfegh, *J. Alloys Compd.*, 2019, **809**, 151783.

189. G. Xiao, Y. Wang, S. Xu, P. Li, C. Yang, Y. Jin, Q. Sun and H. Su, *Chin. J. Chem. Eng.*, 2019, **27**, 305-313.
190. D. Peng, W. Jiang, F.F. Li, L. Zhang, R.P. Liang and J.D. Qiu, *ACS Sustain. Chem. Eng.*, 2018, **6**, 11685-11694.
191. Y. Georgiou, E. Mouzourakis, A.B. Bourlinos, R. Zboril, M.A. Karakassides, A.P. Douvalis, T. Bakas and Y. Deligiannakis, *J. Hazard. Mater.*, 2016, **312**, 243-253.
192. M.M. Bello and A.A.A. Raman, *Environ. Chem. Lett.*, 2019, **17**, 1125-1142.
193. H. Sadegh and G.A. Ali, In *Research anthology on synthesis, characterization, and applications of nanomaterials*, 2021, 1230-1240, IGI Global.
194. Y. Du, H. Ai, Y. Liu and H. Liu, *Sustain. Energy Fuels.*, 2023, **7**, 1747-1754.
195. W.Y. Geng, X.X. Lu, H. Zhang, Y.H. Luo, Z.X. Wang, S.F. Guo, Z.Y. Zhou and D.E. Zhang, *Sep. Purif. Technol.*, 2022, **290**, 120829.
196. S. Sun and S. Liang, *Nanoscale*, 2017, **9**, 10544-10578.
197. D.P. Kumar, L.M. Nollen, A.P. Rangappa and T.K. Kim, *Environ. Res.*, 2022, **204**, 112362.
198. Y. Cui, Y. Tang and X. Wang, *Mater. Lett.*, 2015, **161**, 197-200.
199. C. Wang, H. Fan, X. Ren, J. Fang, J. Ma and N. Zhao, *Mater. Charact.*, 2018, **139**, 89-99.
200. R.C. Pawar, S. Kang, J.H. Park, J.H. Kim, S. Ahn and C.S. Lee, *Sci. Rep.*, 2016, **6**, 31147.
201. F. Wei, Y. Liu, H. Zhao, X. Ren, J. Liu, T. Hasan, L. Chen, Y. Li and B.L. Su, *Nanoscale*, 2018, **10**, 4515-4522.
202. H. Qi, Y. Liu, C. Li, X. Zou, Y. Huang and Y. Wang, *Mater. Lett.*, 2020, **264**, 127329.
203. Y. Wang, H. Cai, F. Qian, Y. Li, J. Yu, X. Yang, M. Bao and X. Li, *J. Colloid Interface Sci.*, 2019, **533**, 47-58.
204. P. Praus, A. Smýkalová, K. Foniok, P. Velíšek, D. Cvejn, J. Žádný and J. Storch, *Nanomaterials*, 2020, **10**, 193.
205. J.N. Zhu, X.Q. Zhu, F.F. Cheng, P. Li, F. Wang, Y.W. Xiao and W.W. Xiong, *Appl. Catal. B: Environ.*, 2019, **256**, 117830.
206. D. Das, D. Banerjee, B. Das, N.S. Das and K.K. Chattopadhyay, *Mater. Res. Bull.*, 2017, **89**, 170-179.
207. D.R. Paul, R. Sharma, P. Panchal, R. Malik, A. Sharma, V.K. Tomer and S.P. Nehra, *J. Nanosci. Nanotechnol.*, 2019, **19**, 5241-5248.
208. I.M. Sundaram and S. Kalimuthu, *Mater. Chem. Phys.*, 2018, **204**, 243-250.
209. T. Paul, D. Das, B.K. Das, S. Sarkar, S. Maiti and K.K. Chattopadhyay, *J. Hazard. Mater.*, 2019, **380**, 120855.
210. J.H. Wu, F.Q. Shao, S.Y. Han, S. Bai, J.J. Feng, Z. Li and A.J. Wang, *J. Colloid Interface Sci.*, 2019, **535**, 41-49.
211. D. Rattan Paul and S.P. Nehra, *Environ. Sci. Pollut. Res.*, 2021, **28**, 3888-3896.
212. D.R. Paul, R. Sharma, S.P. Nehra and A. Sharma, *RSC Adv.*, 2019, **9**, 15381-15391.
213. D.A. Erdogan, M. Sevim, E. Kısa, D.B. Emiroglu, M. Karatok, E.I. Vovk, M. Bjerring, Ü. Akbey, Ö. Metin and E. Ozensoy, *Top. Catal.*, 2016, **59**, 1305-1318.

214. X. Li, H. Zhang, J. Huang, J. Luo, Z. Feng and X. Wang, *Ceram. Int.*, 2017, **43**, 15785-15792.
215. S. Le, T. Jiang, Q. Zhao, X. Liu, Y. Li, B. Fang and M. Gong, *RSC Adv.*, 2016, **6**, 38811-38819.
216. S. Iqbal, A. Bahadur, S. Ali, Z. Ahmad, M. Javed, R.M. Irfan, N. Ahmad, M.A. Qamar, G. Liu, M.B. Akbar and M. Nawaz, *J. Alloys Compd.*, 2021, **858**, 158338.
217. F. Rezaei and M. Dinari, *Colloids Surf. A: Physicochem. Eng. Asp.*, 2021, **618**, 126441.
218. Subodh, K. Prakash and D.T. Masram, *ACS Appl. Polym. Mater.*, 2020, **3**, 310-318.
219. X. Wang, F. Tan, W. Wang, X. Qiao, X. Qiu and J. Chen, *Chemosphere*, 2017, **172**, 147-154.
220. T.B. Nguyen, C.P. Huang and R.A. Doong, *Appl. Catal. B: Environ.*, 2019, **240**, 337-347.
221. K. Gu, X. Pan, W. Wang, J. Ma, Y. Sun, H. Yang, H. Shen, Z. Huang and H. Liu, *Small*, 2018, **14**, 1801812.
222. X. Zhou, Y. Li, Y. Xing, X. Liu, X. Yu and Y. Yu, *J. Phys. Chem. Solids*, 2020, **142**, 109438.
223. Y. Kumar, S. Rani, J. Shabir and L.S. Kumar, *ACS Omega*, 2020, **5**, 13250-13258.
224. K. Saravanakumar, V.S. Priya, V. Balakumar, S.L. Prabavathi and V. Muthuraj, *Environ. Res.*, 2022, **212**, 113185.
225. W. Fang, Y. Deng, L. Tang, G. Zeng, Y. Zhou, X. Xie, J. Wang, Y. Wang and J. Wang, *J. Colloid Interface Sci.*, 2017, **490**, 834-843.
226. S. Huang, Y. Zhao and R. Tang, *RSC Adv.*, 2016, **6**, 90887-90896.
227. V. Nisha, S. Moolayadukkam, A. Paravannoor, D. Panoth, Y.H. Chang, S. Palantavida, S.J. Hinder, S.C. Pillai and B.K. Vijayan, *Inorg. Chem. Commun.*, 2022, **142**, 109598.
228. T. Aditya, J. Jana, A. Pal and T. Pal, *ACS Omega*, 2018, **3,** 9318-9332.
229. A. Mitra, P. Howli, D. Sen, B. Das and K.K. Chattopadhyay, *Nanoscale*, 2016, **8**, 19099-19109.
230. A. Kumar, A. Kumar, G. Sharma, H. Ala'a, M. Naushad, A.A. Ghfar, C. Guo and F.J. Stadler, *Chem. Eng. J.*, 2018, **339**, 393-410.
231. D. Ayodhya and G. Veerabhadram, *Mater. Res. Innov.*, 2020, **24**, 210-228.
232. A. Verma, S. Kumar, W.K. Chang and Y.P. Fu, *Dalton Trans.*, 2020, **49**, 625-637.
233. L. Qin, D. Huang, P. Xu, G. Zeng, C. Lai, Y. Fu, H. Yi, B. Li, C. Zhang, M. Cheng and C. Zhou, *J. Colloid Interface Sci.*, 2019, **534**, 357-369.
234. V. Balakumar, H. Kim, J.W. Ryu, R. Manivannan and Y.A. Son, *J. Mater. Sci Technol.*, 2020, **40**, 176-184.
235. E.O. Oseghe, S.O. Akpotu, E.T. Mombeshora, A.O. Oladipo, L.M. Ombaka, B.B. Maria, A.O. Idris, G. Mamba, L. Ndlwana, O.S. Ayanda and A.E. Ofomaja, *J. Mol. Liq.*, 2021, **344**, 117820.
236. K. H. J. Buschow, R. W. Cahn, M. C. Flemings, B. Ilschner, E. J. Kramer and S. Mahajan, Eds., “Encyclopedia of Materials—Science and Technology,” Vol. 1-11, Elsevier, New York, 2001.

237. A. Kaech, "An Introduction to Electron Microscopy Instrumentation. Imaging and Preparation. Zurich: Center for Microscopy and Image Analysis, University of Zurich", 2013.
238. H. Chandel, B. Wang and M.L. Verma, "Contributions of Nanomaterial-Based Fluorescent Biosensors for Monitoring Environmental Pollutants", 2022.
239. H.M. Rietveld, *Acta Crystallogr.*, 1967, **22**, 151-152.
240. H.M. Rietveld, *J. Appl. Crystallogr.*, 1969, **2**, 65-71.
241. R.A. Young and D.B. Wiles, *J. Appl. Crystallogr.*, 1982, **15**, 430-438.
242. L. Lutterotti, MAUD (Materials Analysis Using Diffraction), 2016 (http://maud.radiographema.eu/).
243. R. A. Young (ed.), *The Rietveld Method*, 1996, International Union of Crystallography, Oxford University Press, New York.
244. G. Caglioti, A.T. Paoletti and F.P. Ricci, *Nucl. Instrum.*, 1958, **3**, 223-228.
245. H.R. Wenk, L. Lutterotti and S.C. Vogel, *Powder Diffr.*, 2010, **25**, 283-296.
246. W.A. Dollase, *J. Appl. Crystallogr.*, 1986, **19**, 267-272.
247. W. Lu, X. Qin, S. Liu, G. Chang, Y. Zhang, Y. Luo, A.M. Asiri, A.O. Al-Youbi and X. Sun, *Anal. Chem.*, 2012, **84**, 5351-5357.
248. X. Wang, J. Zhang, W. Zou and R. Wang, *RSC Adv.*, 2015, **5**, 41914-41919.
249. F. Madjene, M. Assassi, I. Chokri, T. Enteghar and H. Lebik, *Water Environ. Res.* 2021, **93**, 112-122.
250. G. Dogdu Okcu, T. Tunacan and E. Dikmen, *J. Environ. Sci. Health, Part A*, 2019, **54**, 136-145.
251. G. Kresse and J. Hafner, *Phys. Rev. B*, 1993, **47**, 558.
252. G. Kresse and J. Hafner, *Phys. Rev. B*, 1994, **49**, 14251.
253. P.E. Blöchl, *Phys. Rev. B*, 1994, **50**, 17953.
254. J.P. Perdew, K. Burke and M. Ernzerhof, *Phys. Rev. Lett.*, 1996, **77**, 3865.
255. S. Grimme, S. Ehrlich and L. Goerigk, *J. Comput. Chem.*, 2011, **32**, 1456-1465.
256. D. Ayodhya and G. Veerabhadram, *FlatChem*, 2019, **14**, 100088.
257. G. Kresse and J. Furthmüller, *Comput. Mater. Sci.*, 1996, **6**, 15-50.
258. G. Kresse and J. Furthmüller, *Phys. Rev. B*, 1996, **54**, 11169.
259. A.V. Krukau, O.A. Vydrov, A.F. Izmaylov and G.E. Scuseria, *J. Chem. Phys.*, 2006, **125**, 224106.
260. S. Grimme, *J. Comput. Chem.*, 2006, **27**, 1787-1799.
261. M.D. Segall, P.J. Lindan, M.A. Probert, C.J. Pickard, P.J. Hasnip, S.J. Clark and M.C. Payne, *J. Phys. Condens. Matter*, 2002, **14**, 2717.
262. A. Cousson and F. Fillaux, *Acta Crystallogr. Sect. E: Struct. Rep. Online*, 2005, **61**, o222-o224.
263. S. Sain, A. Kar, A. Patra and S.K. Pradhan, *CrystEngComm*, 2014, **16**, 1079-1090.
264. S. Kundu, S. Sain, M. Yoshio, T. Kar, N. Gunawardhana and S.K. Pradhan, *Appl. Surf. Sci.*, 2015, **329**, 206-211.
265. H. Zhou, S. Xu, H. Su, M. Wang, W. Qiao, L. Ling and D. Long, *Chem. Commun.*, 2013, **49**, 3763-3765.
266. P. Kaur, J.T. Hupp and S.T. Nguyen, *ACS Catal.*, 2011, **1**, 819–835.

267. L.K. Shrestha, Y. Yamauchi, J.P. Hill, K.I. Miyazawa and K. Ariga, *J. Am. Chem. Soc.*, 2013, **135**, 586-589.
268. B. Jürgens, E. Irran, J. Senker, P. Kroll, H. Müller and W. Schnick, *J. Am. Chem. Soc.*, 2003, **125**, 10288-10300.
269. K. Krishnan and R.S. Krishnan, In *Proc. Indian Acad. Sci. – Sect. A*, 1966, August (Vol. 64, No. 2, 111-122), New Delhi: Springer India.
270. J. Jiang, L. Ou-yang, L. Zhu, A. Zheng, J. Zou, X. Yi and H. Tang, *Carbon*, 2014, **80**, 213-221.
271. G. Kesavan and S.M. Chen, *Diam. Relat. Mater.*, 2020, **108**, 107975.
272. X. Yuan, C. Zhou, Y. Jin, Q. Jing, Y. Yang, X. Shen, Q. Tang, Y. Mu and A.K. Du, *J. Colloid Interface Sci.*, 2016, **468**, 211-219.
273. J. Liu, T. Zhang, Z. Wang, G. Dawson and W. Chen, *J. Mater. Chem.*, 2011, **21**, 14398-14401.
274. L. Tan, J. Xu, X. Zhang, Z. Hang, Y. Jia and S. Wang, *Appl. Surf. Sci.*, 2015, **356**, 447-453.
275. B. Zhu, P. Xia, Y. Li, W. Ho and J. Yu, *Appl. Surf. Sci.*, 2017, **391**, 175-183.
276. J. Gao, Y. Wang, S. Zhou, W. Lin and Y. Kong, *ChemCatChem*, 2017, **9**(9), 1708-1715.
277. H. Liu, D. Chen, Z. Wang, H. Jing and R. Zhang, *Appl. Catal. B: Environ.*, 2017, **203**, 300-313.
278. D. Das, D. Banerjee, D. Pahari, U.K. Ghorai, S. Sarkar, N.S. Das and K.K. Chattopadhyay, *J. Lumin.*, 2017, **185**, 155-165.
279. H. Chand, P. Choudhary, A. Kumar, A. Kumar and V. Krishnan, *J. CO2 Util.*, 2021, **51**, 101646.
280. Z. Ding, X. Chen, M. Antonietti and X. Wang, *ChemSusChem*, 2011, **4**, 274-281.
281. J. Fang, H. Fan, Z. Zhu, L.B. Kong and L. Ma, *J. Catal.*, 2016, **339**, 93-101.
282. B. Yue, Q. Li, H. Iwai, T. Kako and J. Ye, *Sci. Technol. Adv. Mater.*, 2011, **12**.
283. L. Li, M. Liang, J. Huang, S. Zhang, Y. Liu and F. Li, *Environ. Sci. Pollut. Res.*, 2020, **27**, 29391-29407.
284. S. Cao, J. Low, J. Yu and M. Jaroniec, *Adv. Mater.*, 2015, **27**, 2150-2176.
285. A. Kumar, K.R. Shankar, A. Kumar, G. Harith and V. Krishnan, *J. Environ. Chem. Eng.*, 2021, **9**, 105147.
286. Y. Li, W. Ho, K. Lv, B. Zhu and S.C. Lee, *Appl. Surf. Sci.*, 2018, **430**, 380-389.
287. G. Darabdhara, J. Bordoloi, P. Manna and M.R. Das, *Sens. Actuators B: Chem.*, 2019, **285**, 277-290.
288. https://xpssimplified.com/elements/nickel.php
289. A.N. Mansour and C.A. Melendres, *Surf. Sci. Spectra*, 1994, **3**, 255-262.
290. P. Chaudhary and P.P. Ingole, *Electrochim. Acta*, 2020, **357**, 136798.
291. X. Zou, R. Silva, A. Goswami and T. Asefa, *Appl. Surf. Sci.*, 2015, **357**, 221-228.
292. H. Dou, L. Chen, S. Zheng, Y. Zhang and G.Q. Xu, *Mater. Chem. Phys.*, 2018, **214**, 482-488.
293. S. Hu, X. Qu, P. Li, F. Wang, Q. Li, L. Song, Y. Zhao and X. Kang, *Chem. Eng. J.*, 2018, **334**, 410-418.
294. N. Huang, L. Zhai, H. Xu and D. Jiang, *J. Am. Chem. Soc.*, 2017, **139**, 2428-2434.

295. S. Liu, J. Tian, L. Wang, Y. Zhang, X. Qin, Y. Luo, A.M. Asiri, A.O. Al-Youbi and X. Sun, *Adv. Mater.*, 2012, **24**, 2037-2041.
296. J.M. García, F.C. García, F. Serna and J.L. de la Peña, *Polym. Rev.*, 2011, **51**, 341-390.
297. L. Xiang, Y. Zhu, S. Gu, D. Chen, X. Fu, Y. Zhang, G. Yu, C. Pan and Y. Hu, *Macromol. Rapid Commun.*, 2015, **36**, 1566-1571.
298. S.Y. Ding, M. Dong, Y.W. Wang, Y.T. Chen, H.Z. Wang, C.Y. Su and W. Wang, *J. Am. Chem. Soc.*, 2016, **138**, 3031-3037.
299. S. Barman and M. Sadhukhan, *J. Mater. Chem.*, 2012, **22**, 21832-21837.
300. Y. Zhu, M. Qiao, W. Peng, Y. Li, G. Zhang, F. Zhang, Y. Li and X. Fan, *J. Mater. Chem. A*, 2017, **5**, 9272-9278.
301. Y. Fu, W. Yu, W. Zhang, Q. Huang, J. Yan, C. Pan and G. Yu, *Polym. Chem.*, 2018, **9**, 4125-4131.
302. J.M. Thomas, R. Ting and D.M. Perrin, *Org. Biomol. Chem.*, 2004, **2**, 307-312.
303. H. Tavallali, H. Shafiekhani, M.K. Rofouei and M. Payehghadr, *J. Braz. Chem. Soc.*, 2014, **25**, 861-866.
304. N.D. Rudd, H. Wang, E.M. Fuentes-Fernandez, S.J. Teat, F. Chen, G. Hall, Y.J. Chabal and J. Li, *ACS Appl. Mater. Interfaces*, 2016, **8**, 30294-30303.
305. P. Bairi, P. Chakraborty, B. Roy and A.K. Nandi, *Sens. Actuators B: Chem.*, 2014, **193**, 349-355.
306. H.S. Jung, P.S. Kwon, J.W. Lee, J.I. Kim, C.S. Hong, J.W. Kim, S. Yan, J.Y. Lee, J.H. Lee, T. Joo and J.S. Kim, *J. Am. Chem. Soc.*, 2009, **131**, 2008-2012.
307. M.K. Dahri, M.R.R. Kooh and L.B. Lim, *Adv. Phys. Chem.*, 2016, **2016**.
308. K. Badvi and V. Javanbakht, *J. Clean. Prod.*, 2021, **280**, 124518.
309. Y. Li, X. Wang, X. Wang, Y. Xia, A. Zhang, J. Shi, L. Gao, H. Wei and W. Chen, *Colloids Surf. A: Physicochem. Eng. Asp.*, 2021, ***618***, 126445.
310. N. Wang, L. Zhu, K. Deng, Y. She, Y. Yu and H. Tang, *Appl. Catal. B: Environ.*, 2010, **95**, 400-407.
311. V. Hasija, P. Raizada, P. Singh, N. Verma, A.A.P. Khan, A. Singh, R. Selvasembian, S.Y. Kim, C.M. Hussain, V.H. Nguyen and Q. Van Le, *Process Saf. Environ. Prot.*, 2021, **152**, 663-678.
312. H. Lin, Y. Liu, J. Deng, S. Xie, X. Zhao, J. Yang, K. Zhang, Z. Han and H. Dai, *J. Photochem. Photobiol. A: Chem.*, 2017, **336**, 105-114.
313. M. Su, C. He, V.K. Sharma, M. Abou Asi, D. Xia, X.Z. Li, H. Deng and Y. Xiong, *J. Hazard. Mater.*, 2012, **211**, 95-103.
314. K.M. Reza, A.S.W. Kurny and F. Gulshan, *Appl. Water Sci.*, 2017, **7**, 1569-1578.
315. S. Ahmed, M.G. Rasul, W.N. Martens, R. Brown and M.A. Hashib, *Water Air Soil Pollut.*, 2011, **215**, 3-29.
316. H. Ullah, E. Viglašová and M. Galamboš, *Processes*, 2021, **9**, 263.
317. C. Zhang, Y. Dong, B. Li and F. Li, *J. Clean. Prod.*, 2018, **177**, 245-253.
318. K.Y.A. Lin and J.T. Lin, *Chemosphere*, 2017, **182**, 54-64.
319. X. Wu, X. Gu, S. Lu, M. Xu, X. Zang, Z. Miao, Z. Qiu and Q. Sui, *Chem. Eng. J.*, 2014, **255**, 585-592.

320. H. Zhu, R. Jiang, L. Xiao, Y. Chang, Y. Guan, X. Li and G. Zeng, *J. Hazard. Mater.*, 2009, **169**, 933-940.
321. P. Niu, G. Wu, P. Chen, H. Zheng, Q. Cao and H. Jiang, *Front. Chem.*, 2020, **8**, 172.
322. A. Pavanello, A. Blasco, P.F. Johnston, M.A. Miranda and M.L. Marin, *Catalysts*, 2020, **10**, 774.
323. Q. Xu, R. Li, C. Wang and D. Yuan, *J. Alloys Compd.*, 2017, **723**, 441-447.
324. Y. Liu, H. Yang and T. Chen, *RSC Adv.*, 2022, **12**, 4550-4561.
325. O.M. Bankole, T.D. Olorunsola and A.S. Ogunlaja, *J. Photochem. Photobiol. A: Chem.*, 2021, **405**, 112934.
326. M.R. Samarghandi, J.K. Yang, O. Giahi and M. Shirzad-Siboni, *Environ. Technol.*, 2015, **36**, 1132-1140.
327. S. Pu, Y. Hou, H. Chen, D. Deng, Z. Yang, S. Xue, R. Zhu, Z. Diao and W. Chu, *Catalysts*, 2018, **8**, 251.
328. Y. Qi, Y. Fan, T. Liu and X. Zheng, *Chemosphere*, 2020, **261**, 127824.
329. H. Li, F. Deng, Y. Zheng, L. Hua, C. Qu and X. Luo, *Environ. Sci. Nano*, 2019, **6**, 3670-3683.
330. C. Zhu, Y. Li, Y. Zhang, J. Liu, X.Q. Hao and M.P. Song, *Colloids Surf. A: Physicochem. Eng. Asp.*, 2022, **642**, 128657.
331. Y.P. Moreno, W.L. da Silva, F.C. Stedile, C. Radtke and J.H. dos Santos, *Appl. Surf. Sci. Adv.*, 2021, **3**, 100055.
332. C. Gong, F. Chen, Q. Yang, K. Luo, F. Yao, S. Wang, X. Wang, J. Wu, X. Li, D. Wang and G. Zeng, *Chem. Eng. J.*, 2017, **321**, 222-232.
333. S. Luo, S. Li, S. Zhang, Z. Cheng, T.T. Nguyen and M. Guo, *Sci. Total Environ.*, 2022, **806**, 150662.
334. N. Sharma, A.K. Dey, R.Y. Sathe, A. Kumar, V. Krishnan, T.D. Kumar and C.M. Nagaraja, *Catal. Sci. Technol.*, 2020, **10**, 7724-7733.
335. H. Chaker, N. Ameur, K. Saidi-Bendahou, M. Djennas and S. Fourmentin, *J. Environ. Chem. Eng.*, 2021, **9**, 104584.
336. K.B. Narayanan and N. Sakthivel, *Bioresour. Technol.*, 2011, **102**, 10737-10740.
337. F.H. Lin and R.A. Doong, *Appl. Catal. A: Gen.*, 2014, **486**, 32-41.
338. T. Shen, C. Jiang, C. Wang, J. Sun, X. Wang and X. Li, *RSC Adv.*, 2015, **5**, 58704-58712.
339. L.Q. Zheng, X.D. Yu, J.J. Xu and H.Y. Chen, *Chem. Commun.*, 2015, *51*, 1050-1053.
340. C. Sahoo, A.K. Gupta and A. Pal, *Desalination*, 2005, **181**, 91-100.
341. J.H. Zhang, Q. Liu, Y.M. Chen, Z.Q. Liu and C.W. Xu, *Acta Phys.-Chim. Sin.*, 2012, **28**, 1030-1036.
342. R. Ahmad and R. Kumar, *Appl. Surf. Sci.*, 2010, **257**, 1628-1633.
343. B.R. Ganapuram, M. Alle, R. Dadigala, A. Dasari, V. Maragoni and V. Guttena, *Int. Nano Lett.*, 2015, **5**, 215-222.
344. C. Hou, B. Hu and J. Zhu, *Catalysts*, 2018, **8**, 575.
345. R. Begum, J. Najeeb, A. Sattar, K. Naseem, A. Irfan, A.G. Al-Sehemi and Z.H. Farooqi, *Rev. Chem. Eng.*, 2020, **36**, 749-770.
346. S. Ma, X. Chen, B. Zhao, L. Li and W. Fu, *Chem. Eng. Technol.*, 2018, **41**, 149-156.

347. Z. He, C. Sun, S. Yang, Y. Ding, H. He and Z. Wang, *J. Hazard. Mater.*, 2009, **162**, 1477-1486.
348. S. Ameen, H.K. Seo, M.S. Akhtar and H.S. Shin, *Chem. Eng. J.*, 2012, **210**, 220-228.
349. H.M. Tabery, *Acta Ophthalmol. Scand*, 1998, **76**, 142-145.
350. S. Kumar and R.K. Sharma, *Catal. Lett.*, 2019, **149**, 2268-2278.
351. M.M. Khan, J. Lee and M.H. Cho, *J. Ind. Eng. Chem.*, 2014, **20**, 1584-1590.
352. Z. Zhang, C. Shao, Y. Sun, J. Mu, M., Zhang, P. Zhang, Z. Guo, P. Liang, C. Wang and Y. Liu, *J. Mater. Chem.*, 2012, **22,** 1387-1395.
353. S. Saha, A. Pal, S. Kundu, S. Basu and T. Pal, *Langmuir*, 2010, **26**, 2885-2893.
354. Y. Mei, Y. Lu, F. Polzer, M. Ballauff and M. Drechsler, *Chem. Mater.*, 2007, **19**, 1062-1069.
355. S. Bae, S. Gim, H. Kim and K. Hanna, *Appl. Catal. B: Environ.*, 2016, **182**, 541-549.
356. X. Kong, H. Zhu, C. Chen, G. Huang and Q. Chen, *Chem. Phys. Lett.*, 2017, **684**, 148-152.
357. Z. Wang, R. Su, D. Wang, J. Shi, J.X. Wang, Y. Pu and J.F. Chen, *Ind. Eng. Chem. Res.*, 2017, **56**, 13610-13617.
358. Y. Zhao, R. Tang, and R. Huang, *Catal. Lett.*, 2015, **145,** 1961-1971.
359. P. Veerakumar, N. Dhenadhayalan, K.C. Lin, and S.B. Liu, *Chem. Select*, 2017, **2**, 1398-1408.
360. M. Kohantorabi, and M.R. Gholami, *Appl. Phys. A*, 2018, **124**, 1-17.
361. Y. Fu, T. Huang, B. Jia, J. Zhu, and X. Wang, *Appl. Catal. B: Environ.*, 2017, **202**, 430-437.
362. Y. Yang, and R. Tang, *Chem. Lett.*, 2018, **47**, 544-547.
363. S.B. Khan, S. Ahmad, T. Kamal, A.M. Asiri, and E.M. Bakhsh, *Int. J. Biol. Macromol.*, 2020, **164**, 1087-1098.

NJC

PAPER

Cite this: DOI: 10.1039/c8nj06119j

A morphology-tailored triazine-based crystalline organic polymer for efficient mercury sensing†

Dimitra Das,‡[a] Anuradha Mitra,‡§[b] Rituparna Chatterjee,[a] Sumanta Sain[c] and Kalyan Kumar Chattopadhyay *[ab]

Received 3rd December 2018,
Accepted 28th January 2019

DOI: 10.1039/c8nj06119j

rsc.li/njc

Hydrothermal synthesis of a novel crystalline, highly cross-linked and thermally-stable triazine-based organic polymer with nanodendritic morphology has been reported. A Rietveld whole profile fitting method has been deployed to elucidate the crystal structure of the polymer. The polymer has been found to be composed of monoclinic melamine having space group $P2_1/a$. FTIR and Raman spectroscopic analysis provided a detail insight into the chemical structure of the as-synthesized polymer. XPS and NMR analyses were carried out for further understanding the different types of linkages required to create the backbone of the polymer. The unique rod-like morphology of the triazine-based polymer has been revealed by FESEM and TEM studies. Furthermore, a plausible mechanism for nanodendrite formation has been proposed. Interestingly, this polymer has been found to selectively detect Hg^{2+} ions at an extremely low concentration through fluorescence quenching with a detection limit as low as 0.03 ppb. The sensing phenomenon has also been explained in detail to understand the applicability of the material. Until now most of the existing studies have reported that triazine-based polymers for mercury ion sensing required the introduction of sulphur-based groups and subsequent fuctionalization owing to the high affinity of Hg^{2+} towards sulphur. However, the inherent impressive sensitivity of our polymer sample towards Hg^{2+} is the very first report in the field of highly crystalline triazine-based polymers without the necessity of any modification by sulphur mediation for mercury ion detection.

Introduction

Porous organic polymers (POPs), constructed from light elements such as C, H, N, O, S, and B atoms, are an emergent class of non-toxic, metal-free, environmentally benign advanced materials. These materials are being used in gas separation and storage, catalysis, and environmental remediation.[1,2] Among the various groups of POPs, this article mainly focuses on covalent triazine-based polymers (CTPs) with a functional triazine group. These are a very significant class of porous organic materials due to their remarkable stability arising from strong covalent bonds. Besides, the symmetry and structural attributes of the triazine core make them an appealing candidate for investigating a wide range of material characteristics such as nonlinear optical, liquid crystalline and luminescent properties. Triazine-based derivatives are specifically used in supramolecular chemistry, since they can conventionally form hydrogen bonds, favour π–π contacts, and they were recently revealed to be involved in interesting anion–π interactions.[3] In addition to their tunable functionalities, their crystalline structure, morphology, pore-structure and surface area can be tuned to produce optimized triazine-based POPs (TPOPs), thus making them suitable for targeted applications. For instance, crystalline TPOPs, possessing stable ultra-micropores, have been found to be suitable for CO_2 adsorption,[4–6] whereas amorphous mesoporous TPOP adsorbents have been employed by some researchers for the removal of heavy metal ions and organic molecules.[7,8] The versatility of crystalline TPOPs is noteworthy owing to the rigid and stable structural framework constructed by the organic backbone, thereby rendering significant technological advantages over their amorphous counterparts.[9] This may be due to the fact that amorphous covalent frameworks have hydrogen bonds which perhaps hinder electron conduction across the plane possibly leading to poor conductivity.[10] Moreover, crystalline POPs have the ability to decrease structural defects by adjusting themselves thereby forming the most thermodynamically

---

[a] *School of Materials Science and Nanotechnology, Jadavpur University, Kolkata 700032, India*

[b] *Department of Physics, Jadavpur University, Kolkata 700032, India. E-mail: kkc.juphy@gmail.com*

[c] *Department of Materials Science, Indian Association for the Cultivation of Science, Jadavpur, Kolkata 700 032, India*

† Electronic supplementary information (ESI) available: Characterizations of MEG_{10}. See DOI: 10.1039/c8nj06119j

‡ Equal contribution.

§ Present address: Aditya Birla Science and Technology Co. Pvt. Ltd, Panvel, Raigad 410208, India.

Environmental Research 221 (2023) 115263

Contents lists available at ScienceDirect

Environmental Research

journal homepage: www.elsevier.com/locate/envres

Highly exfoliated graphitic carbon nitride for efficient removal of wastewater pollutants: Insights from DFT and statistical modelling

Dimitra Das [a], Bikram Kumar Das [b,1], Ratna Sarkar [b], Somnath Mukherjee [c], Kalyan Kumar Chattopadhyay [a,b,*]

[a] *School of Materials Science and Nanotechnology, Jadavpur University, 188, Raja S.C. Mallick Road, Kolkata, 700032, India*
[b] *Department of Physics, Jadavpur University, 188, Raja S.C. Mallick Road, Kolkata, 700032, India*
[c] *Department of Civil Engineering, Jadavpur University, 188, Raja S.C. Mallick Road, Kolkata, 700032, India*

ARTICLE INFO

Keywords:
Graphitic carbon nitride
Exfoliation
Water remediation
Photocatalysis
Statistical evaluation
First-principles

ABSTRACT

The present work entails the synthesis of thermally modified graphitic carbon nitride (GCN) using a two-step thermal treatment procedure and its subsequent use in the photocatalytic reduction of toxic pollutants such as rhodamine B dye (RhB) and chromium (VI) (Cr(VI)) from aquatic environments. The as-synthesised exfoliated GCN (GCNX) is characterised by X-ray diffraction (XRD) analysis, Fourier transform infrared (FTIR) spectroscopy, X-ray photoelectron spectroscopy (XPS), energy-dispersive X-ray spectroscopy (EDS), Brunauer–Emmett–Teller analysis (BET), diffuse reflectance spectroscopy (DRS), photoluminescence spectroscopy (PL), field emission scanning electron microscopy (FESEM), and transmission electron microscopy (TEM). These characterisations helped to elucidate the phase formation, chemical structure, composition, surface area, optical properties, and morphology of the sample. With assistance from a visible light source, GCNX can degrade RhB dye within 30 min in the presence of hydrogen peroxide (H_2O_2) and reduce Cr(VI) to Cr(III) in under 2 h in the presence of formic acid (FA/HCOOH). Variations in different catalytic parameters, including catalyst amount, pH of the solution, initial RhB or Cr(VI) concentration, and variation in H_2O_2 or FA concentration, are performed to inspect their effects on the photodegradation activity of GCNX. Moreover, the GCNX catalyst exhibits impressive stability and reusability. A thorough statistical evaluation follows the response surface methodology to understand the complex interaction between the factors contributing to the catalytic activity. The band alignment of differently functionalised GCN blocks in their pristine form and their H_2O_2/FA-adsorbed states is investigated using first-principles calculations to provide a further understanding of the RhB and Cr(VI) reduction mechanisms. The modified GCN can thus be effectively employed as a low-cost material for removing contamination from aquatic environments.

1. Introduction

Due to their excellent optical properties, semiconducting materials are extensively utilised in degrading conventional wastewater pollutants by photocatalysis technology. Many investigations have been conducted on the photocatalytic applications of different types of semiconducting materials, including metal oxides (e.g. TiO_2 and ZnO), metal sulphides (e.g. CdS and MoS_2), metal phosphides, and non-metallic semiconductors [Guo et al., 2022]. Among these materials, graphitic carbon nitride (GCN) has emerged as a superior photocatalyst with exciting properties. This metal-free nitrogen-rich layered material with an appropriate wide band gap for visible light has been widely employed for the photocatalytic degradation of hazardous pollutants from aquatic environments [Nguyen et al., 2021; Yadav et al., 2021]. Moreover, GCN is a highly thermally stable material that exhibits chemical stability under ambient conditions due to its electron-rich π-conjugated two-dimensional network [Dong et al., 2014; Rana and Minceva, 2021]. The material can be synthesised on a large scale by following simple synthesis strategies employing convenient, low-cost raw precursors, such as urea and melamine. However, GCN has yet to be applied widely because of its drawbacks, which include poor specific surface area, fewer active sites, and a high rate of recombination of electron–hole pairs

---

* Corresponding author. School of Materials Science and Nanotechnology, Jadavpur University, 188, Raja S.C. Mallick Road, Kolkata, 700032, India.
E-mail addresses: kalyan_chattopadhyay@yahoo.com, kkc.juphy@gmail.com (K.K. Chattopadhyay).

[1] Present Address: BCAM – Basque Center for Applied Mathematics, Alameda de Mazarredo 14, E-48009, Bilbao, Spain.

https://doi.org/10.1016/j.envres.2023.115263
Received 26 September 2022; Received in revised form 6 January 2023; Accepted 9 January 2023
Available online 12 January 2023

Applied Surface Science 580 (2022) 152137

Contents lists available at ScienceDirect

Applied Surface Science

journal homepage: www.elsevier.com/locate/apsusc

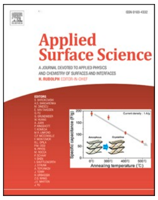

Full Length Article

Copper and nickel decorated g-C_3N_4 as superior catalysts for reduction of toxic pollutants: A combined experimental and theoretical approach

Dimitra Das [a], Bikram Kumar Das [b], Ratna Sarkar [b], Somnath Mukherjee [c], Kalyan Kumar Chattopadhyay [a,b,*]

[a] School of Materials Science and Nanotechnology, Jadavpur University, 188, Raja S.C. Mallick Road, Kolkata 700032, India
[b] Department of Physics, Jadavpur University, 188, Raja S.C. Mallick Road, Kolkata 700032, India
[c] Department of Civil Engineering, Jadavpur University, 188, Raja S.C. Mallick Road, Kolkata 700032, India

ARTICLE INFO

Keywords:
Graphitic carbon nitride
$NaBH_4$ induced catalysis
Electron relay
Pollutants degradation
Waste-water remediation
First principles

ABSTRACT

Catalytic reduction of pollutants employing the concept of electron-relay effect between sodium borohydride ($NaBH_4$) and pollutant compounds, both adsorbed on catalyst surface, is one of the most effective and facile techniques among other conventional procedures. In this work, potential catalysts were developed by incorporating Cu and Ni into two-dimensional conjugated network of g-C_3N_4 to modify its surface properties for subsequent application in rapid degradation of hazardous waste-water pollutants. Exhaustive experiments including variation of various parameters such as catalyst-dosage, $NaBH_4$ concentration, pollutants concentration, and pH were performed to analyse the role of metal ad-atoms, determine the best catalyst, and propose the optimum catalytic degradation conditions for each harmful pollutant and their mixtures separately for practical implementations. The as-proposed superiority of the catalyst was validated through first-principles calculations. The experimental results established the materials to be highly efficient catalysts in terms of degradation time and various catalytic parameters in reduction of a vast range of pollutants. In-depth theoretical analysis was performed to understand the role played by Cu-atom incorporation towards dye degradation mechanisms. The most feasible reaction routes for selected pollutants were identified and represented at the atomic reaction level portraying the role of $NaBH_4$ and aqueous electrolyte in the electron-relay process.

1. Introduction

The enormous influx of toxic pollutants into the natural environment from innumerable industrial sources poses as a drastic threat to the ecosystem in recent times. Chemical industries manufacturing textile, pharmaceutical and explosive products are the sources of immensely harmful and non-degradable effluents which cause inimical effects on human health by polluting the nature's water bodies. Conventional textile dyes like Methyl orange, Methylene blue, Rhodamine B, Congo red, Methyl red and Rose Bengal are released into rivers and ponds on a regular basis without following any regulations and guidelines. These chemical compounds are extremely difficult to degrade and they are capable of forming impenetrable layers on water surface thereby preventing the sunlight to reach the bottom of the aquatic ecosystem where bio-organisms thrive [1]. Nitrophenol compounds are generally released from pesticide, leather and explosive industries and are typically used in the making of drugs, fungicides, insecticides and also as dyes to darken leather [2]. 4-Nitrophenol is considered to be extremely hazardous and is on the "priority pollutant" lists of many environmental organizations [2]. Nitrophenol compounds are mostly carcinogenic and mutagenic in nature [3] and can cause severe hazardous effects on human body like irritation in throat, nose, lungs and skin, stomach-upset, fatigue, affect the central nervous system and can even cause death in extreme cases. The stability of these undesirable compounds in the environment makes them immensely difficult to be treated and removed in order to achieve a cleaner and sustainable ecosystem.

Conventional methods used for degradation and/or removal of these compounds from waste-water are adsorption [4], advanced oxidation processes [5] including Fenton and photo-Fenton based reactions, photocatalytic degradation [6,7], biological treatment [8], chemical precipitation [9] and others. In recent times, heterogeneous chemical catalysis mediated by electron relay effect in presence of a reducing agent like $NaBH_4$ have gained much prominence owing to many advantages of this process as compared to traditional adsorption and

---

* Corresponding author at: School of Materials Science and Nanotechnology, Jadavpur University, 188, Raja S.C. Mallick Road, Kolkata 700032, India.
E-mail address: kkc.juphy@gmail.com (K. Kumar Chattopadhyay).

https://doi.org/10.1016/j.apsusc.2021.152137
Received 27 August 2021; Received in revised form 19 November 2021; Accepted 3 December 2021
Available online 8 December 2021

J. Indian Chem. Soc.,
Vol. 96, April 2019, pp. 455-460

Magnesium incorporated graphitic carbon nitride for effective removal of fluoride ions

Dimitra Das[a], Kalyan Kumar Chattopadhyay[b] and Somnath Mukherjee[c]*

[a]School of Materials Science and Nanotechnology, [b]Department of Physics, [c]Department of Civil Engineering,

Jadavpur University, Kolkata-700 032, India

E-mail: mukherjeesomnath19@gmail.com

Manuscript received online 01 February 2019, accepted 25 March 2019

In the present investigation, magnesium (Mg) doped graphitic carbon nitride (GCN) synthesized in nanotechnology laboratory has been used as a nano-adsorbent material for effective removal of fluoride (F^-) ions from water. The material has been characterized by different techniques like XRD, FTIR, and FESEM to get a detailed insight into their properties. The batch adsorption experiments have been performed by varying different influencing parameters viz. adsorbent amount, initial fluoride concentration and pH. The experimental data revealed that the adsorption capacity of fluoride by Mg doped GCN depends on the above parameters. The thermodynamic parameters, kinetic reaction orders and isotherm plots are also fitted in accordance with the conventional models based on experimental findings.

Keywords: Magnesium doping, graphitic carbon nitride, fluoride, isotherm modelling, adsorption kinetics.

Introduction

Fluoride in trace amount (0.6 mg/L, as per WHO) is one of the essential non-metals that have been considered favourable for bone and enamel developments for living mammals. However, fluoride ingestion in excessive amount can lead to severe detrimental effects like fluorosis[1]. In India, a large number of people of different states severely suffer from fluorosis whereas more than 62 million people remain exposed to it due to presence of excess fluoride level in ground water used for drinking[2,3]. Fluoride laden waste water also emanate from industries like glass manufacturing, rock phosphate production units etc. Several processes on fluoride removals are reported in the literatures but the most effective and common tool for fluoride attenuation process is adsorption as advocated by earlier researchers. Nalgonda technique[4] is one of the extensive adsorption methods used at large in India owing to its facile operative method. Activated charcoal, alumina, fish bone, charcoal, bio-chars, clay minerals etc. are used as adsorbent material for fluoride decontamination[5].

Recently nanomaterials are being applied for water and waste-water treatment as a smart and sustainable candidate for the above purpose. Graphitic carbon nitride is one such nanomaterial which possesses significant surface area and is easily synthesized from viable cheap precursor like urea in a large scale. The large surface helps in better adsorption of metal/non-metal ions depending upon the surface charge. However, pure GCN has a negative surface charge owing to the edge terminated nitrogen lone pairs that limits adsorption of fluoride ions. To overcome this restriction, GCN has been doped with magnesium which leads to the generation of a positive surface charge on the GCN layers thereby improving the surface adsorption properties. Mg is easily available, economic and environment friendly as compared to other available transition metals. The utilization of Mg doped GCN as a nano-adsorbent for fluoride removal from water environment is perhaps a new application of adsorption process.

Experimental

Urea (CH_4N_2O) and Magnesium chloride hexahydrate ($MgCl_2.6H_2O$) with 99.99% purity were used for synthesis purposes. In the synthesis procedure, requisite amount of $MgCl_2.6H_2O$ was intimately mixed with 10 g of urea in a mortar-pestle followed by drying the mixed product in an oven at 100ºC for 24 h. The dried product was then put in a well-covered crucible made of alumina accompanied with a lid in order to check any probable gas loss. The mixture was thermally treated in a muffle furnace at 550ºC for 4 h at 5ºC/min ramp. After allowing an ambient cooling in room tempera-

Materials Today: Proceedings 44 (2021) 444–452

Contents lists available at ScienceDirect

Materials Today: Proceedings

journal homepage: www.elsevier.com/locate/matpr

Sodium borohydride assisted reduction of toxic pollutants by silver coordinated melamine based polymeric material

Dimitra Das [a,*], Ratna Sarkar [b], Somnath Mukherjee [c], Kalyan Kumar Chattopadhyay [a,b]

[a] School of Materials Science and Nanotechnology, Jadavpur University, Kolkata 700032, India
[b] Department of Physics, Jadavpur University, Kolkata 700032, India
[c] Environmental Engineering Section, Department of Civil Engineering, Jadavpur University, Kolkata 700032, India

ARTICLE INFO

Article history:
Received 7 September 2020
Received in revised form 15 September 2020
Accepted 28 September 2020
Available online 4 November 2020

Keywords:
Coordination polymer
4-Nitrophenol
Methyl orange
Sodium borohydride
Waste-water remediation

ABSTRACT

The present work involves the development of a Silver-Melamine (Ag-M) based coordination polymer and its utilization in degrading different toxic pollutants from waste-water by sodium borohydride ($NaBH_4$) induced chemical reduction technique. Detailed characterizations include XRD, FTIR, FESEM, TEM and DRS which reveal the phase formation, nature of chemical bonds and rod-like morphology of the sample. Ag-M exhibits superior activity in $NaBH_4$-assisted degradation of 4-Nitrophenol and Methyl orange to non-toxic end products within 6 min. Several variations of the parameters influencing the reduction activity have been performed and a plausible mechanism has been proposed to understand the chain of reactions taking place.

Selection and peer-review under responsibility of the scientific committee of the International Conference on Materials, Processing & Characterization.

1. Introduction

Substantial flourish in the textile and chemical industries involving the manufacturing of synthetic dyes, pharmaceuticals, plasticizers, various industrial solvents, and explosives has essentially led to the alarming release of hazardous and toxic effluents in the natural environment causing monstrous effects on this planet and its inhabitants [1]. With extensive growth in the industrial sectors resulting from the exponetial increase in population, the world has experienced a rapid surge in the pollution and exhaustion of its natural resources, most importanty tthe aquatic ecosystem. Toxic, non-degradable,synthetic coloured dyes are continuously discharged into water-bodies in an appalling rate without undergoing any proper treatment or maintaing any regulatory measures. These dyes are chemical compounds having complex structures which are capable of causing severe negative impacts on human health by affecting the central nervous system, digestive system, renal system and reproductive system along with gastro-intestinal disorder, stomach problems, irritation in skin, nose, throat etc. [2,3]. Among all such pollutants, 4-Nitrophenol (4-NP) and Methyl Orange (MO) deserve extensive treatment owing to their additional carcinogenic and mutagenic property [4]. 4-NP is an extremely perilous pollutant having being considered as one of the “priority pollutants” by many organizations and is discharged in huge amounts from leather tanning, fungicide and pesticide manufacturing and explosive industries [5]. Apart from causing fatigue, stomach upset and skin irritation, it can significantly affect the CNS leading to death. MO, an orange coloured organic anioin dye compound consisting of a complex azo group and exhibitng high solubility in aqueous solution, is a very hazardous effluent from several industrial sources like textile, cosmetics, dye manufacturing, paper and leather industries [6]. The health hazards caused by this dye includes severe diarrhoea accompanied with nausea and vomiting tendency [6]. Moreover, discharge of synthetic dyes into water-bodies can also lead to adverse effects on aquatic organisms.

Degradation of dye by photocatalysis and removal of dye by adsorption are two of the most employed conventional methods for waste-water remediation. However, both of these water-treatment processes encounter certain limitations in their practical utilisation for wide-range industrial applications. The performance efficiency and simple operative nature of the adsorption process is

---

* Corresponding author.
E-mail address: dimitradas248@gmail.com (D. Das).

https://doi.org/10.1016/j.matpr.2020.09.755
2214-7853/© 2021 Elsevier Ltd. All rights reserved.
Selection and peer-review under responsibility of the scientific committee of the International Conference on Materials, Processing & Characterization.

Sodium Borohydride Assisted Catalytic Reduction of Toxic Pollutants by Carbon and Nitrogen Based Poly-meric Compounds: A Review

Dimitra Das, Kalyan Kumar Chattopadhyay, and Somnath Mukherjee

Abstract Water pollution is one of the greatest concerns in today's world which needs immediate attention and strict regulatory surveillance to prevent its paramount adverse effects on the environment. Chemical pollutants discharged from countless industries like textiles and pharmaceuticals contribute extensively to contaminating freshwater resources of this planet whereby causing deleterious effects on all living organisms including human beings. Coloured dyes like Rhodamine B, Methyl Orange, Methylene Blue etc. and phenolic compounds like 4-Nitrophenol are a few of such pollutants whose degradation and complete removal from water-bodies are of utmost importance to avert pernicious environmental consequences. One of the most efficient techniques includes chemical catalytic reduction of these harmful pollutant compounds in the presence of sodium borohydride and appropriate catalyst materials, and this is a rapid degradation procedure moderated by the electron-relay effect. Polymeric compounds comprised of carbon and nitrogen elements are a distinctive class of materials that procured massive prominence in recent times owing to their prospective applications in numerous practical fields, including wastewater purification. Substantial porosity and surface area, non-toxic nature, low-cost and high-yield of production along with notable stability and durability are some of the remarkable features possessed by these materials which in turn make them a promising and efficient contestant for catalytic activities. The present article will try to abridge the findings of several reported literature that have dealt with the sodium borohydride induced catalytic reduction of toxic pollutants emitted from industrial plants by pure and doped carbon and nitrogen based materials.

Keywords Water purification · Chemical catalysis · Sodium borohydride · Toxic pollutants · Carbon and nitrogen based materials · Electron-relay effect

---

D. Das (✉) · K. K. Chattopadhyay
School of Materials Science and Nanotechnology, Jadavpur University, Kolkata, India
e-mail: dimitradas248@gmail.com

S. Mukherjee
Department of Civil Engineering, Jadavpur University, Kolkata, India

Y. Yukselen-Aksoy et al. (eds.), *Sustainable Earth and Beyond*, Lecture Notes in Civil Engineering 370, https://doi.org/10.1007/978-981-99-4041-7_34

PhD Thesis

ORIGINALITY REPORT

8%

SIMILARITY INDEX

PRIMARY SOURCES

1	pubs.rsc.org Internet	6171 words — 7%
2	www.rsc.org Internet	701 words — 1%

EXCLUDE QUOTES	ON	EXCLUDE SOURCES	< 1%
EXCLUDE BIBLIOGRAPHY	ON	EXCLUDE MATCHES	< 10 WORDS